From Radicals to Triradicals: Soft X-ray Investigations of Thin Films and self-assembled Monolayers

Dissertation

der Mathematisch-Naturwissenschaftlichen Fakultät

der Eberhard Karls Universität Tübingen

zur Erlangung des Grades eines Doktors der Naturwissenschaften

vorgelegt von

Tobias Maximilian Junghöfer

aus Siegburg

Tübingen

2021

Gedruckt mit Genehmigung der Mathematisch-Naturwissenschaftlichen Fakultät der Eberhard Karls Universität Tübingen.

Tag der mündlichen Qualifikation:	01.09.2021
Dekan:	Prof. Dr. Thilo Stehle
1. Berichterstatterin:	apl. Prof. Dr. Maria Benedetta Casu
2. Berichterstatter:	Prof. Dr. Reinhold Fink

Dedicated to my parents Dipl.-Psych. Theodora Wirth-Junghöfer (†) and Dipl.-Psych. Martin Junghöfer.

"For a while the three companions remained silent, gazing after him. Then Aragorn spoke. 'They will look for him from the White Tower,' he said, 'but he will not return from mountain or from sea.' Then slowly he began to sing:

Through Rohan over fen and field where the long grass grows
The West Wind comes walking, and about the walls it goes.
'What news from the West, O wandering wind, do you bring to me tonight?
Have you seen Boromir the Tall by moon or by starlight?
'I saw him ride over seven streams, over waters wide and grey,
I saw him walk in empty lands until he passed away
Into the shadows of the North, I saw him then no more.
The North Wind may have heard the horn of the son of Denethor,
'O Boromir! From the high walls westward I looked afar,
But you came not from the empty lands where no men are.'

Then Legolas sang:

From the mouths of the Sea the South Wind flies, from the sandhills and the stones,
The wailing of the gulls it bears, and at the gate it moans.
'What news from the South, O sighing wind, do you bring to me at eve?
Where now is Boromir the Fair? He tarries and I grieve.
'Ask not of me where he doth dwell – so many bones there lie,
On the white shores and the dark shores under the stormy sky,
So many have passed down Anduin to find the flowing Sea.
Ask of the North Wind news of them the North Wind sends to me!'
'O Boromir! Beyond the gate the seaward road runs south,
But you came not with the wailing gulls from the grey sea's mouth'.

Then Aragorn sang again:

From the Gate of the Kings the North Wind rides, and past the roaring falls,
And clear and cold about the tower its loud horn calls.
'What news from the North, O mighty wind, do you bring to me today?
What news of Boromir the bold? For he is long away.'
'Beneath Amon Hen I heard his cry. There many foes he fought,
His cloven shield, his broken sword, they to the water brought.
His head so proud, his face so fair, his limbs they laid to rest,
And Rauros, golden Rauros-falls, bore him upon its breast.
'O Boromir! The Tower of Guard shall ever northward gaze,
To Rauros, golden Rauros-falls, until the end of days."

So they ended. Then they turned their boat and drove it with all the speed they could against the stream back to Parth Galen.
"You left the East Wind to me," said Gimli, "but I will say naught of it."
"That is as it should be," said Aragorn. "In Minas Tirith they endure the East Wind, but they do not ask it for tidings. But now Boromir has taken his road, and we must make haste to choose our own."

– J.R.R. Tolkien, The Lord of the Rings, The Two Towers, "The Departure of Boromir"[1]

Abstract

English Version

Organic thin films for electronic applications have become a well-established scientific field over the previous decades and have found their way into our daily lives as well. Organic radical thin films represent a subset of this field and are of great interest for potential applications in organic electronics based on the quantum effects that derive from their unpaired electrons. This includes their use as quantum bits in quantum computers, spin-filtering and spintronic devices, or novel data storage devices.
In this work several different organic radical thin films are investigated by the X-ray-based techniques of X-ray photoelectron spectroscopy (XPS) and near-edge X-ray fine structure (NEXAFS) spectroscopy, as well as atomic force microscopy (AFM). Herein are presented the publications of the first successful depositions of organic radical thin films of intact purely organic di- and triradicals deposited via organic molecular beam deposition (OMBD). These polyradicals exhibit combined spins of $S = \frac{1}{2}$, 1, and $\frac{3}{2}$. While these depositions represent a challenge due to the polyradicals' increased reactivity they are possible. The results presented here show that the controlled sublimation of these molecules is governed by bulk thermodynamics and the onset of decomposition in the thermogravimetric analysis (TGA) and that film stability is dependent on the delocalisation of the unpaired electrons in the molecule and the onset of decomposition in TGA as well.
The results on the viability and film stability of self-assembled monolayers of a modified perchlorotriphenylmethyl (PTM) radical covalently bound to a gold substrate are also presented. These monolayers are also investigated using XPS, NEXAFS, and AFM. The results show that the preparation leaves the radical character intact on the surface even with further on-surface modification of the molecules and that the resulting thing films exhibit good stability towards exposure to air.
These findings represent a substantial advancement in the field of organic radical thin films for use in quantum-based technologies.

Deutsche Version

Organische Dünnschichten für die Anwendung in organischer Elektronik haben sich über die letzten Dekaden zu einem etablierten Feld in den Natur- und Ingenieurswissenschaften entwickelt und haben sogar Einzug in unser tägliches Leben erhalten. Die Untergruppe der dünnen Schichten aus organischen Radikalen ist dabei von großem Interesse für potentielle Anwendungen in organischer Elektronik, welche auf den Quanteneffekten aufbaut, die sich aus den ungepaarten Elektronen ableiten. Diese beinhalten deren Verwendung als Quantenbit in Quantencomputern, in Spinfiltern oder spintronischen Geräten sowie neuartigen Datenspeichern.

Diese Arbeit zeigt die Untersuchungen von mehreren verschiedenen dünnen Schichten aus organischen Radikalen mittels Röntgenphotoelektronenspektroskopie (engl. „X-ray photoelectron spectroscopy“, XPS), Röntgen-Nahkanten-Absorptions-Spektroskopie (engl. „near-edge X-ray fine structure“, NEXAFS) sowie Rasterkraftmikroskopie (engl. atomic force microscopy, AFM). Es werden die Veröffentlichungen vorgestellt, die zum ersten Mal die erfolgreichen Abscheidungen von rein organischen Di- und Triradikalen mittels organischer Molekülstrahlabscheidung (engl. „organic molecular beam deposition“, OMBD) zeigen. Die untersuchten Polyradikale haben Gesamtspins von $S = \frac{1}{2}$, 1, und $\frac{3}{2}$. Die Abscheidung dieser Filme stellt wegen der erhöhten Reaktivität der Polyradikale eine Herausforderung dar. Dennoch ist sie möglich. Die hier vorgestellten Ergebnisse zeigen, dass die Sublimation der untersuchten Moleküle von der Thermodynamik des Festkörpers sowie dem Beginn der Zersetzung in der thermogravimetrischen Analyse (TGA) geherrscht wird. Die Stabilität der Schichten ist abhängig von der Delokalisierung der ungepaarten Elektronen und ebenfalls dem Beginn der Zersetzung in der TGA.

Ebenfalls zeigt diese Arbeit die Ergebnisse zu den kovalent auf eine Goldoberfläche gebundenen selbstorganisierten Monolagen eines modifizierten Perchlortriphenylmethylradikals (PTM) und deren Stabilität. Diese Monolagen wurden ebenfalls mittels der oben genannten Methoden XPS, NEXAFS und AFM untersucht. Die Ergebnisse zeigen, dass der Radikalcharakter der Moleküle, auch nach anschließender Modifikation auf der Oberfläche, erhalten bleibt und die Schichten eine gute Stabilität ob der Exposition gegenüber Luft aufweisen.

All diese Resultate stellen einen substantiellen Fortschritt auf dem Gebiet der dünnen Schichten organischer Radikale für Quanten-basierte Anwendungen dar.

Declaration

Ich erkläre hiermit, dass ich die zur Promotion eingereichte Arbeit mit dem Titel: „From Radicals to Triradicals: Soft X-ray Investigations of Thin Films and self-assembled Monolayers.“ selbständig verfasst, nur die angegebenen Quellen und Hilfsmittel benutzt und wörtlich oder inhaltlich übernommene Stellen (alternativ: Zitate) als solche gekennzeichnet habe.
Ich erkläre, dass die Richtlinien zur Sicherung guter wissenschaftlicher Praxis der Universität Tübingen (Beschluss des Senats vom 25.5.2000) beachtet wurden.
Ich versichere an Eides statt, dass diese Angaben wahr sind und dass ich nichts verschwiegen habe. Mir ist bekannt, dass die falsche Abgabe einer Versicherung an Eides statt mit Freiheitsstrafe bis zu drei Jahren oder mit Geldstrafe bestraft wird.

_____ _____

Ort, Datum Unterschrift

Acknowledgements

First and foremost I want to thank Prof Dr Maria Benedetta Casu for the opportunity to work for and learn from her. She provided excellent supervision and an enjoyable working environment from the first day.

I want to thank Prof Dr Thomas Chassé for providing access to his laboratory and further facilities and him and his group for welcoming me into their midst. I want to especially thank Dipl.-Chem. Hilmar Adler for his support with everything technical, Dr Peter Grüninger for his introduction to the instruments in the lab, and MEng Ivana Mršić, Dr Andreas Früh, and MSc Dustin Quinones for their help with the atomic force microscope.

Further thanks go to Dr Erika Giangrisostomi and Dr Ruslan Ovsyannikov for their support during our beamtimes at the LowDosePES beamline at the BESSYII synchrotron facility.

I also want to acknowledge Fero Digel, Gerd Vollmer, and Eberhard Braun as well as Karin Rein and Thomas Nieß for their excellent technical support.

Thanks also go the Deutsche Forschungsgemeinschaft (DFG) for funding my work through the project CA 852/11–1 “Interplay of structural and electronic properties and their impact on thin films of metal-free organic radicals.”.

Lastly I want to thank my parents Dipl.-Psych. Theodora Wirth-Junghöfer (†) and Dipl.-Psych Martin Junghöfer without whose support my studies would not have been possible or successful.

Contents

1. Introduction

Organic materials for application in electronics have been of interest in the chemical and physical fields for a long time.[2,3] They come with a variety of advantages when compared to the traditional inorganic semiconductors like flexibility in both molecular design (and consequently electronic properties) and macroscopic pliability.[4,5] They also reduce the need for toxic or hard to obtain and scarce resources like rare-earth metals.[6] These properties have lead to their widespread use in modern electronic devices from photovoltaics to smart phones with flexible displays.[7,8]

A subset of these are organic molecules that incorporate an additional degree of freedom in the form of a spin, and resulting magnetic moment, that it is possible to manipulate. It, for example, makes it possible to expand the use of organic thin films into the realms of quantum computing, with the unpaired electron serving as a quantum bit (or qubit), or spintronics.[9–12] Quantum computing uses the quantum states of a given bit to perform computations that are not possible or unsuitable for classical computing but requires those bits to be coherent for the time of the computation.[13,14] This makes it necessary to determine whether the films of a given molecule display long enough coherence time to be suitable for application. This has been shown to be the case by Ciccullo et al. for the Pyrene-Blatter radical, an important precursor to most radicals examined in this work.[15]
Molecules that contain such a spin usually come in two varieties: organic molecules containing one or more metal atoms and purely organic radicals. While the study of thin films of metal-containing organic molecules is a well-established field in which a lot of research has taken place, the field of purely organic radical thin films has only relatively recently gained traction.[16,17]

Based on the previous works on thin films of purely organic monoradicals[18–24] a large portion of this work aims to investigate the possibilities of purely organic di- and triradical thin films for the use in quantum-based organic electronics. The thermal deposition of

thin films of these polyradicals was deemed impossible due to the decreased thermal stability correlated with the increasing number of unpaired electrons.[25] Part of the publications presented in this work address the parameters in molecular design as well as experimental set-up that make the first successful depositions of purely organic polyradicals presented therein possible. These investigations are mainly carried out using X-ray spectroscopy methods that have proven to be a powerful tool for the investigation of previous monoradical thin films. They also aim to serve as a reference for the successful deposition of new polyradical thin films via organic molecular beam deposition (OMBD). The second part of the work examines the self-assembled monolayers of a hybrid organic/metallocene radical that was designed to incorporate the functionality of both the unpaired electron of the radical as well as allow access to the redox-chemistry of the metallocene. To this end this system uses a substrate and deposition technique more comparable to the industrial fabrication of electronic devices.

Thin film preparation can be achieved via several different means, each with their own advantages and disadvantages. The films examined in this work were all prepared in one of two ways: OMBD or a self-limiting wet chemical process resulting in self-assembled monolayers.
OMBD is a technique used for thin film formation in ultra-high vacuum (UHV) and is used for all polyradical thin films in this work. Like similar methods used for inorganic materials (e.g. molecular-beam epitaxy or MBE) it is used for the deposition of thin films with a high level of purity and allows for the fine adjustment of deposition parameters for optimal results. Against the background of quantum-based organic electronics, this highly controllable method is required in order to achieve the necessary controlled environment that these applications require.
Wet chemical processes are another option for film deposition. These allow for thin films to be deposited under less technically demanding conditions, making them a good option for laboratory use for the preparation and investigation of real-world surfaces. The lack of a need for UHV conditions also makes them attractive for industrial scale applications. The method used in this work relies on the immersion of a gold substrate in a solution of the radical that is relatively easy to perform without specialised equipment.

Chapter 1 gives in introduction to the field of organic electronics and the classes of materials examined here as well as an overview of the motivation behind this work.
Chapter 2 presents the theoretical background of both the materials and methods used in the investigations.
Chapter 3 establishes the details of the experimental set-ups and the data analysis.
Chapter 4 presents a summary of all the scientific findings regarding deposition parameters and thin film stability of the polyradicals as well as the investigation into the self-assembled monolayers.
Chapter 5 summarises the findings presented before and draws the comparison with the motivation.
Chapter 6 is the register of all the abbreviations, symbols, and units used here.
Chapter 7 list the publications written during the course of this work and establishes the contributions of all authors involved in them.
The appendices include the full texts, including supporting information, of all the publications this work is based on in ascending chronological order by date of publication, followed by the preprints of yet unpublished material.

2. Theoretical Background

This chapter will present the state of the art concerning the materials and substrates used in this thesis as well as the theoretical foundations of all methods used therein. It is sub-divided into a section concerning itself with the major radical moieties that make up the molecules used in this work and one detailing the theoretical background.

2.1. Materials

2.1.1. The Blatter Radical and its Derivates

This work focusses in large parts on derivatives of the 1,3-diphenyl-1,4-dihydro-1,2,4-benzotriazin-4-yl radical (figure 2.1) first published by Herbert M. Blatter in 1968[26] and consequently named the "Blatter radical". Stability is provided by a high degree of delocalisation throughout the aromatic system.[27]

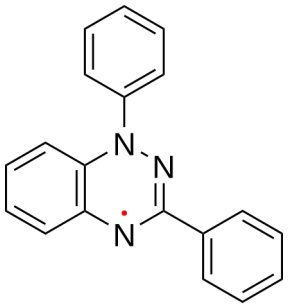

Figure 2.1.: Chemical structure of the stable Blatter radical.

2.1.1.1. The Pyrene-Blatter Radical

The Pyrene-Blatter radical (figure 2.2) is the combination of the Blatter radical and pyrene and represents the result of a design process intended to optimise the film-forming properties of the molecule by lowering its vapour pressure and increasing thermal stability of the films. It has a spin of $S = \frac{1}{2}$ with the spin-density mostly located in the triazinyl

moiety.[21] It is presented here as a point of reference and the foundation of this entire work.

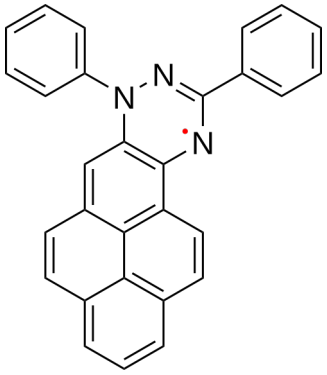

Figure 2.2.: Chemical structure of the stable Pyrene-Blatter radical.

2.1.1.2. The Nitronyl Nitroxide-Blatter Diradical

This molecule consists of a nitronyl nitroxide moiety bound to a Blatter radical, forming a diradical with a spin of $S = 1$. The spin-density of the unpaired electron is delocalised over the nitronyl nitroxide as well as most of the Blatter moieties with the exclusion of the phenyl group in the 3-position on the 1,2,4-benzotriazinyl group. It is referred to as "NN-Blatter" throughout this work. The relevant properties are listed in table 2.1 and the chemical structure can be seen in figure 2.3.

Table 2.1.: Properties of the NN-Blatter diradical.

Formula	$C_{26}H_{25}N_5O_2^{\bullet}$
Formula weight ($g\,mol^{-1}$)	560.67
Density ($g\,cm^{-3}$)	1.332
Spin	1
Magnetic interaction	strong AFM
Intramolecular ordering	1D chains

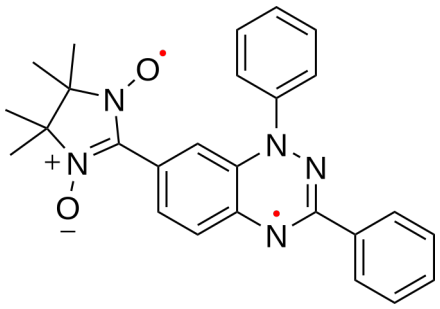

Figure 2.3.: Chemical structure of the stable NN-Blatter diradical.

2.1.1.3. The Fused Blatter-Blatter Diradical

This diradical is composed of two linked Blatter radicals in one of which the phenyl group in position 3 of the triazinyl moiety has been replaced by the benzene ring of the 1,2,4-benzotriazinyl moiety of the other Blatter radical. The resulting diradical has a spin of $S = 1$ with the spin-density of the unpaired electrons delocalised over most of the molecule excluding the terminal phenyl group and the *tert*-butyl group. It is referred to as "diBlatter" in this work. Its relevant properties are listed in table 2.2 and the chemical structure is shown in figure 2.4.

Table 2.2.: Properties of the diBlatter diradical.

Formula	$C_{36}H_{30}N_6{}^{2\bullet}$
Formula weight ($g\,mol^{-1}$)	546.66
Density ($g\,cm^{-3}$)	1.356
Spin	1
Magnetic interaction	AFM
Intramolecular ordering	1D chains

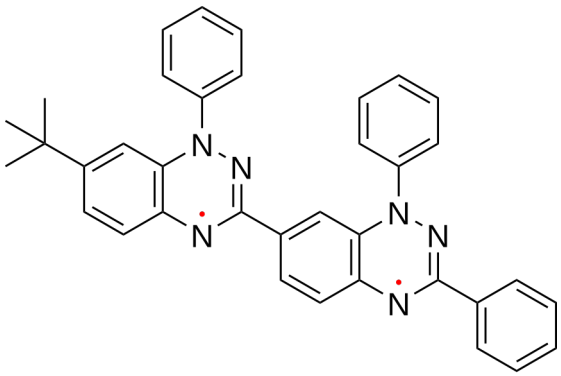

$C_{36}H_{30}N_6{}^{2\bullet}$

Figure 2.4.: Chemical structure of the stable diBlatter diradical.

2.1.1.4. The Di-Nitronyl Nitroxide-Blatter Triradical

This triradical is obtained by the addition of a further nitronyl nitroxide moiety to the NN-Blatter described above in the 3 position of the nitrogen-bound phenyl group. This results in a spin of $S = \frac{3}{2}$ and the molecule is referred to as "diNN-Blatter" throughout this work. Its relevant properties are listed in table 2.3 and the chemical structure is shown in figure 2.5.

Table 2.3.: Properties of the diNN-Blatter triradical.

Formula	$C_{33}H_{36}N_7O_4{}^{3\bullet}$
Formula weight ($g\,mol^{-1}$)	594.69
Density ($g\,cm^{-3}$)	1.303
Spin	$\frac{3}{2}$
Magnetic interaction	strong AFM
Intramolecular ordering	dimers

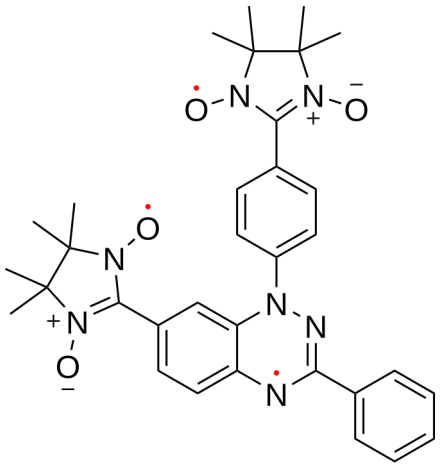

$C_{33}H_{36}N_7O_4^{3\bullet}$

Figure 2.5.: Chemical structure of the stable diNN-Blatter diradical.

2.1.2. The Benzodithiophene/Nitronyl Nitroxide-based Diradical

This diradical based on the heterocyclic Benzodithiophene molecule is obtained by the addition of two nitronyl nitroxide moieties at opposing sides of the molecule. This results in a diradical with two non-interacting radical moieties, each with a spin of $S = \frac{1}{2}$.[28] The spin-density of the unpaired electrons is delocalised over their respective nitronyl nitroxide groups with no interaction between the two groups over length of the molecule. It is referred to as "BDT-NN" throughout this work and its chemical structure is shown in figure 2.6 while the relevant properties are listed in table 2.4.

Table 2.4.: Properties of the BDT-NN diradical.

Formula	$C_{26}H_{34}N_4O_6S_2^{2\bullet}$
Formula weight ($g\,mol^{-1}$)	560.67
Density ($g\,cm^{-3}$)	1.332
Spin	$2 \times \frac{1}{2}$
Magnetic interaction	weak AFM
Intramolecular ordering	dimer

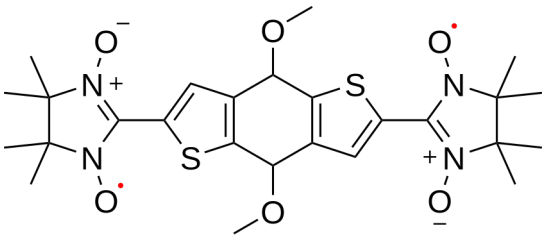

Figure 2.6.: Chemical structure of the stable BDT-NN diradical.

2.1.3. The Perchlorotriphenylmethyl Radical Derivate

The modified perchlorotriphenylmethyl (PTM) radical used is this work (figure 2.7) consists of a triphenylmethyl moiety in which all but two of the aromatic hydrogen atoms have been substituted by chlorine and the remaining two by an alkyne-terminated linker. The alkyne group serves the dual purposes of anchoring the radical to the gold substrate via a C−Au-bond and enabling the addition of a substituted ferrocene via a [3+2] cycloaddition called "click reaction" with a corresponding azide on the ferrocene.[29–31]

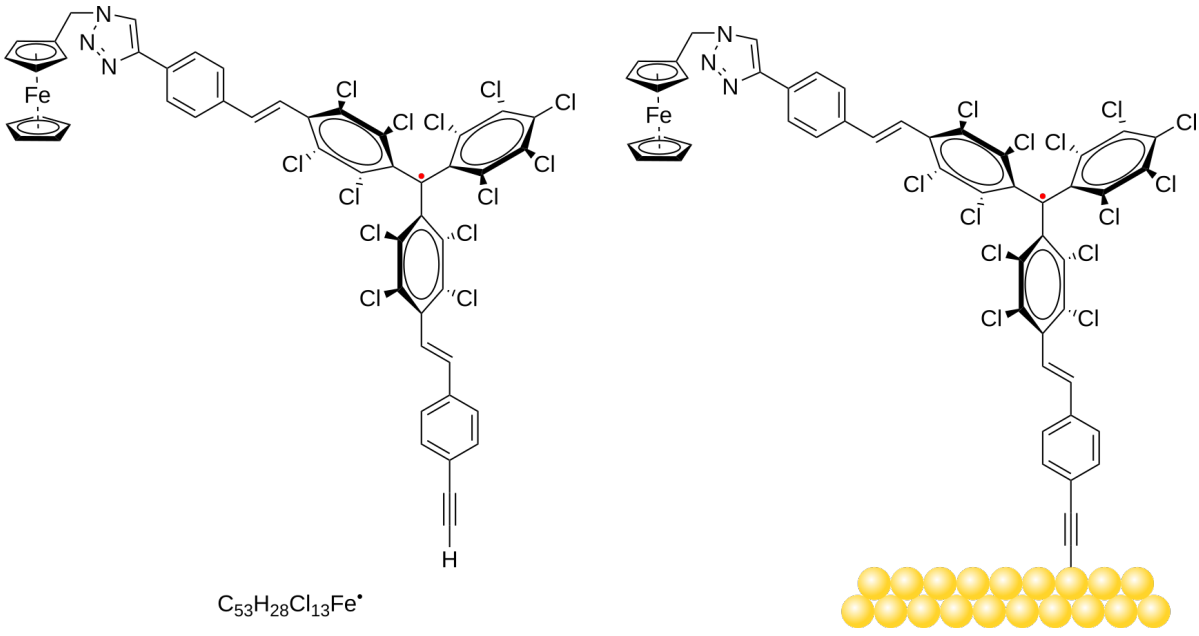

Figure 2.7.: Chemical structure of the stable PTM radical in solution (left) and bound to a gold surface (right).

2.1.4. Substrates

For all deposition experiments as well as drop-cast layers, single-side polished n-type silicon(111) wafers cut into 1 cm by 1 cm pieces were used. The wafers were cleaned of photoresist by two consecutive one hour runs of sonication in ethanol and acetone with subsequent rinsing with the respective solvent. By exposing the substrates to ambient air they develop a layer of amorphous SiO_2 which is inert.
Powder samples were prepared on Indium foil passivated by exposure to ambient air. The advantage of this substrate material lies in the fact that it is possible to firmly embed the radical crystals in the material counteracting the charging of the crystals upon irradiation during XPS measurements. This charging is a general problem in organic crystals due to their usually low conductivity and leads to shifts in binding energies between a few and several hundred eV making analysis of the spectra hard to impossible.[25]
For the experiments with PTM radical, template-stripped gold on glass was used as the substrate.[32] In order to fabricate these substrates, gold is deposited onto a super flat silicon wafer in UHV conditions after which an adhesive is applied to the resultant rough gold surface. By applying a a piece of glass to the adhesive and carefully stripping the gold from the silicon surface, a very flat and clean gold surface is generated from the former gold-silicon interface.[32]

2.2. Methods

2.2.1. Organic Molecular Beam Deposition

OMBD is a technique for depositing organic molecules onto a substrate in a highly controlled manner.[33] Low pressures in the ultra-high vacuum regime are needed for this method in order to guarantee a flux of non-interacting molecules, precluding reaction of the molecules in the gas phase. The use of such a method is necessitated by the dependence of film properties on evaporation conditions.[34,35] It is a derived from molecular beam deposition used for inorganic compounds which was first described in 1969.[36] As such it relies on an evaporation apparatus with a precisely controllable temperature which comes in the form of the Knudsen cell. As can be seen in figure 2.8 it consists of a ceramic and metal heat shield containing a quartz glass crucible into which the molecules are loaded. The crucible is heated via a heating filament integrated into the heat shield. A thermocouple is also integrated into the heat shield and a microprocessor-based digital electronic controller is used to precisely control the temperature and heating rate. When

the desired evaporation temperature is reached and stable, the shutter is opened, allowing the evaporated molecule to reach the substrate.

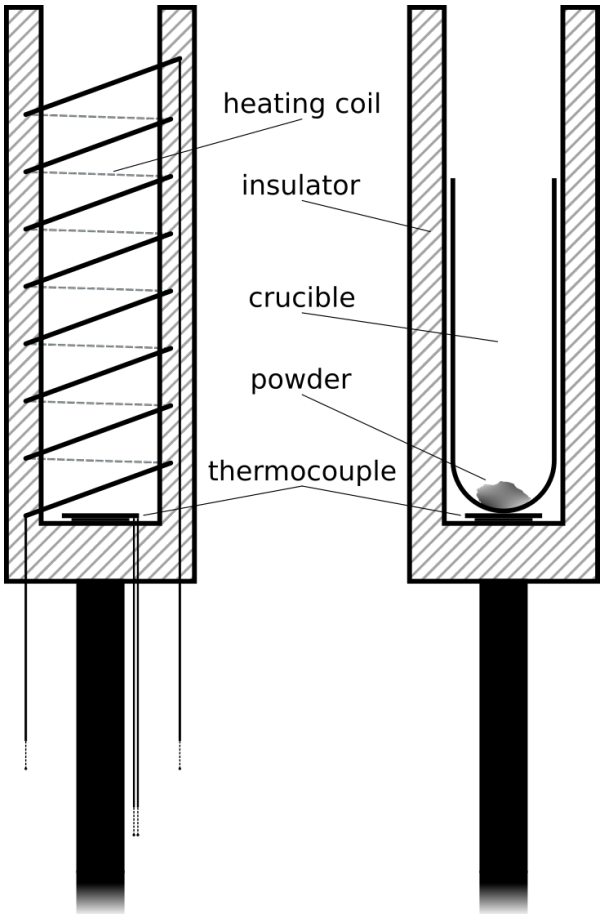

Figure 2.8.: Schematic image of a Knudsen cell.

2.2.1.1. Growth Modes

One important aspect is that the evaporation conditions have an influence on film morphology.[33] Besides that, a variety of kinetic and thermodynamic factors influence it as well.[37,38] The combination of these factors leads to three generally discussed growth modes that are observed in thin films.[33,37,38]

Frank-van-der-Merwe, or layer-by-layer, growth (figure 2.9, left side) is characterised by closed layers that grow one after the other. This growth mode is typical for systems in which the interaction between adsorbate and substrate is very strong (e.g. chemisorption) and the interaction between the adsorbate molecules is weak.

Volmer-Weber, or island, growth (figure 2.9 middle) occurs when the interaction between adsorbate molecules is stronger than the interaction between adsorbate and substrate

and is characterised by unconnected islands of the adsorbate. Additional material mostly gets incorporated into the existing islands rather than closing the gaps between them. Stranski-Krastanov growth (figure 2.9, right side) represents the intermediate case in which the adsorbate-substrate and adsorbate-adsorbate interactions are roughly equally strong. This first leads to the growth of a closed layer and transitions to island growth after that.

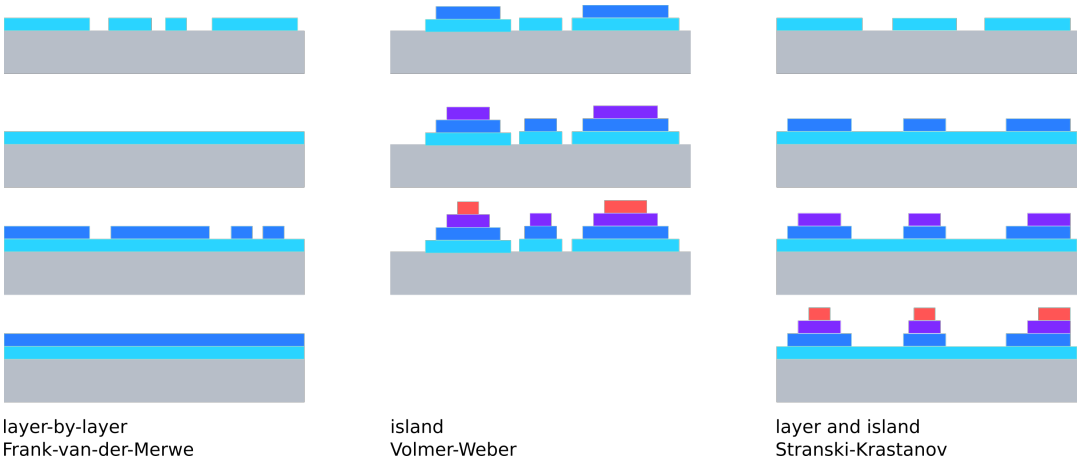

Figure 2.9.: Schematic image of different growth modes described for thin films.

2.2.2. X-Ray Photoelectron Spectroscopy

X-ray photoelectron spectroscopy (XPS) is a powerful method for the analysis of chemical and physical properties of materials. As such, it is the premier method used in this work. The basis of this method lies in the photoelectric effect first described by Heinrich Hertz in 1887 and Wilhelm Hallwachs in 1888.[39,40] The phenomenon was then mathematically described for the first time in 1905 by Albert Einstein who later received the Nobel Prize in physics for this work in particular.[41,42] This effect describes the interaction of electromagnetic radiation with the electron shells of the atoms in a given material. In the idealised one-electron picture, if a photon interacts with a bound electron, the electron is excited to a higher energetic state leaving behind an unoccupied state in the electron shell. If the energy of the photon is at or above the ionisation energy, the electron will be completely removed from the atom. The kinetic energy of the electron can then be measured and the binding energy calculated according to formula 2.1.

$$E_B = h\nu - E_{kin} \tag{2.1}$$

With E_B being the binding energy of the electron referenced to the vacuum state, h the Planck constant, ν the frequency of the incident light, and E_{kin} the measured kinetic energy of the electron.
Because the binding energies of electrons are specific for each element, this phenomenon lead to the development of photoelectron spectroscopy in the 1950s by Kai Siegbahn who published the first high-resolution spectrum of NaCl in 1956.[43] His further groundbreaking work on what was then termed "Electron Spectroscopy for Chemical Analysis" (ESCA) resulted in him winning the Nobel Prize for physics in 1981, exactly 60 years after Einstein.[44–47]
A further very important physical phenomenon for photoelectron spectroscopy is the so-called inelastic mean free path of the emitted photoelectron in the material. It is a measure for the distance a photoelectron can travel in the material before being re-absorbed into the electron shell of an atom. It approximately follows the so-called universal curve (equation 2.2) that was defined by Seah and Dench in 1979[48] and expanded upon by others.[49,50]

$$\lambda_n = \frac{A_n}{E_{kin}^2} + B_n\sqrt{E_{kin}} \tag{2.2}$$

where λ_n is the inelastic mean free path given in nm, A_n and B_n are empirical factors, and E_{kin} is the kinetic energy of the electron.
From the relations between $h\nu$ and E_{kin} and E_{kin} and λ we get one of the fundamental features of photoelectron spectroscopy; The dependency of the sampling depth from the energy of the incident X-rays. The information depth is usually given as 3λ as the depth at which, according to the Lambert-Beer law, 95 % of emitted photoelectrons are sampled. This relationship allows for the selective sampling of different regions in a film by varying the incident beam's energy, e.g. with a tunable synchrotron radiation source or by varying the incident angle.
There are several methods of generating the requisite X-rays, two of which were used in this work. The X-ray sources used in the home lab photoemission station mentioned in subsection 3.1 are regular X-ray tubes. In these, a water-cooled aluminium anode is bombarded by electrons generated via a heated tungsten filament cathode. The resulting X-rays, generated by a reverse of the photoelectric effect, are then focused onto the sample. As with the photoelectric effect, the energy of the resulting X-ray beam is element-specific. The more complicated synchrotron radiation source will be described in subsection 2.2.3.

The fact that a regular X-ray tube emits X-rays in a single, relatively narrow energy window gives rise for the need of an analyser that allows for a energy-dependant spectrum to be recorded. For this purpose, the hemispherical analyser shown in figure 2.10 is used. This type of analyser consists of two concentric electrodes between which a high-voltage potential is applied. Scanning through a range of voltages allows for the electrons emitted by the sample to be selectively focused on the detector. Several types of detectors exist

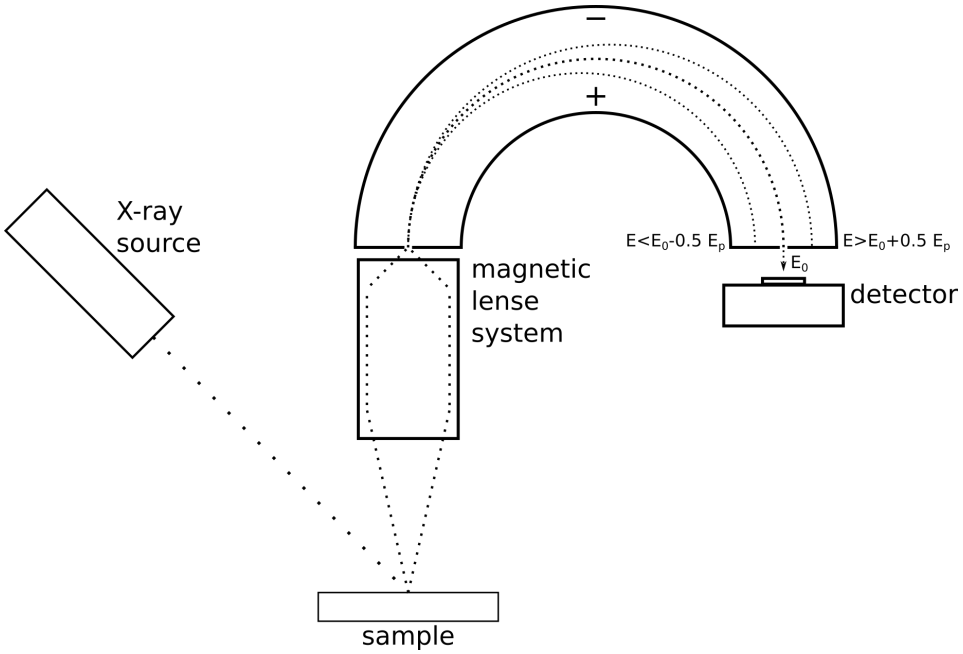

Figure 2.10.: Schematic image of a hemispherical electron analyser.

that are used in these devices, including charge-coupled devices (CCD) and electron multipliers/microchannel plate detectors.

2.2.3. Synchrotron Radiation Sources and Reliant Methods

Apart from the X-ray tubes mentioned above, another important source for electromagnetic radiation exists that offers properties not available in a lab set-up today. An electron synchrotron is in general a large facility that consists of five main components (figure 2.11). Electrons are first generated with an electron gun and accelerated in a small linear accelerator before being injected into a larger circular accelerator (booster ring) where they are accelerated to relativistic speeds. From there, they get injected into the so called storage ring where the actual generation of usable electromagnetic radiation takes place. This is achieved via a variety of devices all exploiting the fact that a relativistic

charge, travelling along a curved trajectory emits a narrow beam of light tangentially to the direction of its motion. The resulting energy loss in the electron is compensated for by radio-frequency generators installed along the storage ring. Along this narrow angle of light emittance, so-called beam lines are constructed which are equipped with highly sophisticated optics, suited for the desired wavelengths, as well as experimental stations for a large variety of purposes.[51] The combination of the intense light and the optics allows for the selection and scanning of a wide range of electromagnetic radiation, which is a prerequisite for many scientific methods including near-edge X-ray absorption fine structure (NEXAFS) spectroscopy and X-ray magnetic circular dichroism (XMCD).
The two types of photon sources used at the beam lines for experiments in this work are bending magnets (PM4 beam line at BESSYII) and undulators (P04 beam line at PETRAIII). Bending magnets are the simplest and oldest type of the photon sources. They are dipole magnets that keep the electron on their roughly circular orbit inside of the storage ring and produce light with a brilliance in the range of 10^{10} to 10^{14}.[51] Undulators, and their precursors the wigglers, are installed in a straight stretch on the storage ring and generate radiation via a periodically alternating series of dipole magnets that slightly redirect the electrons from their path. This produces a burst of light every half period that combines with the other bursts via constructive interference resulting in a narrow beam of light with a brilliance in the range of 10^{15} to 10^{21}.[51] Brilliance (or flux) is a measure for the usable light defined as follows:[51]

$$\text{brilliance} = \frac{\text{photons}}{\text{s} \cdot \text{mrad}^2 \cdot \text{mm}^2 \cdot 0.1\ \%\ \text{BW}} \tag{2.3}$$

where BW is the bandwidth of the photon beam.

2.2.3.1. Near-Edge X-Ray Absorption Fine Structure Spectroscopy

Fine structures in the X-ray absorption spectra were first reported on in the 1920s and 1930s. In 1920, Kossel published his findings on fine structures near the absorption edge[52,53] and laid the groundwork for what is today known as NEXAFS or X-ray absorption near edge structure (XANES) spectroscopy. The findings of Kronig on the fine structure further away from the absorption edge[54,55] take a similar place for extended X-ray absorption fine structure (EXAFS) spectroscopy.
In X-ray absorption spectroscopy, core-electrons are not excited to the vacuum level by the incident X-ray beam. Instead the sample is irradiated with an X-ray beam of varying

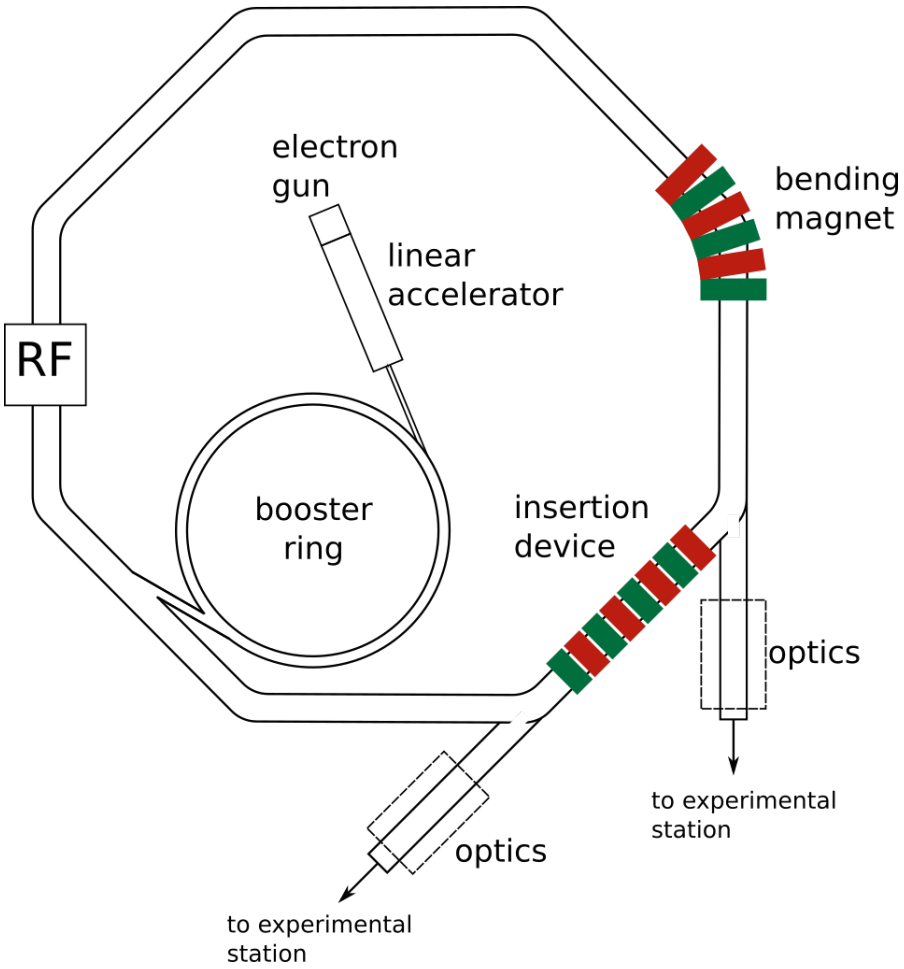

Figure 2.11.: Schematic image of a synchrotron radiation source.

photon energy around a defined absorption edge proving the precise energy for core electron to be excited into specific unoccupied states. As such NEXAFS spectroscopy probes the unoccupied electronic states close to the Fermi-level of a sample in the region up to about 100 eV above the absorption edge. That, in the case of organic molecules, means the transitions into the π^*- and σ^*-orbitals.

2.2.4. Microscopy

2.2.4.1. Atomic Force Microscopy

Atomic force microscopy (AFM) is a form of scanning probe microscopy first presented in the form of the scanning tunnelling microscope by Binning and Rohrer in 1985 for which they received the Nobel Price one year later.[56,57] The principles of the AFM including the experimental set-up and first measurements were first published by Binning et. al. in 1986.[58] In the case of the measurement modes used here it works by scanning an atomically sharp tip attached to a cantilever vibrating at a its resonance frequency over the sample while measuring changes in the amplitude via a laser focused on the reflective backside of the cantilever. Changes in the amplitude are the result of the interaction (both attraction and repulsion) of the tip with the substrate and can be attributed to a variety of phenomena like Van der Waals and electrostatic forces. A computer then translates these changes in amplitude into a topographic map of the surface with up to atomic resolution. These images can them be further analysed for factors like surface roughness, particle size, or layer thickness.[59]

2.2.4.2. Scanning Electron Microscopy

Scanning electron microscopy (SEM) is a method of microscopy which uses electrons in order to overcome the diffraction limit of visible light postulated by Abbe in 1873.[60] The diffraction limit is given as:

$$d = \frac{\lambda}{2n \sin \theta} \tag{2.4}$$

With d being the minimum resolvable distance, n being the refractive index of the medium, and θ being half the opening angle of the incident beam.
By using electrons with a de Broglie wavelength far below that of visible light, it is possible to resolve far smaller structures than would be possible with a conventional microscope. A disadvantage of this method is that non-conductive samples need to be specially prepared (e.g. by coating with gold) in order to avoid undue charging of the sample.
In general, a scanning electron microscope functions by focusing an electron beam onto a sample through a series of magnetic lenses in UHV conditions. There the electron beam interacts with the sample in various ways including elastic and inelastic scattering, the creation of secondary electrons, and the emission of electromagnetic radiation. Using different kinds of detectors, these, as well as the resultant sample current, can be used

for structural and chemical analysis of the surface of the sample.[61]

3. Experimental

3.1. Methods

3.1.1. Home Lab

3.1.1.1. X-Ray Photoemission Station

Due to the need for a maximally clean environment in general, most of the experiments presented here are conducted in an ultra-high vacuum apparatus. The used experimental station consists of four separate chambers dedicated to different steps in the preparation and analysis of the samples. To generate the pressures needed (up to 10^{-10} mbar) the experimental station is equipped with several turbomolecular pumps each backed by a separate membrane pump (10^{-4} mbar) which also serve as roughing pumps. Additionally, two kinds of getter pumps are used to further pump the system and maintain the desired pressure.

The preparation chamber is equipped with a power supply that allows for the heating of sample-holders in UHV conditions for annealing and cleaning by thermal desorption of contaminants. All of the SiO_2/Si(111) substrates prepared and measured in this experimental station were annealed for up to 16 h at a temperature of around 500 K. Cleanliness of the substrates is verified via XPS. Substrates still showing a significant amount of contamination are discarded. The base pressure in the preparation chamber is 3×10^{-9} mbar.

The separate organics chamber features a removable Knudsen-cell used for depositing the molecules on the cleaned substrates under controlled conditions. In order to avoid undue degradation of the molecules, no bake-out of the organics chamber was performed after loading the Knudsen-cell into the chamber. This leads to the higher and more variable base pressure given in table 3.1. The higher pressures of 3×10^{-6} to 3×10^{-5} mbar given there are typical for the first evaporation cycle of a given batch without a bake-out and improve to significantly lower pressures on the subsequent cycles. The temperature ranges used for evaporating the different molecules as well as the pressure ranges during

evaporation are shown in table 3.1. The evaporation temperature in the Knudsen cell is controlled via a K-type thermo-couple. The substrates are kept at room temperature during the deposition. The substrates with the deposited films are then transferred into the analysis chamber for XPS measurements. Powder samples are prepared by embedding the radical into passivated indium foil using a spatula. Drop coated samples are prepared from a solution of the triradical in toluene dropped onto the cleaned substrate with a micropipette.

Table 3.1.: Temperature and pressure ranges for the different radicals during deposition.

Molecule	**Temperature** (K)	**Pressure** (mbar)
Blatter	418	10^{-7} – 10^{-5}
NN-Blatter	363	10^{-6} – 10^{-5}
diNN-Blatter	375 – 383	10^{-8} – 10^{-5}
diBlatter	413 – 418	10^{-8} – 10^{-5}
BDT-NN	373 – 383	10^{-8} – 10^{-7}

The analysis chamber contains several radiation sources providing monochromatised (SPECS Focus 500/XR-50M) Al-$K\alpha$ (1486.6 eV) as well as non-monochromatised (VSW) Al-$K\alpha$ and Mg-$K\alpha$ (1254.6 eV) radiation. XPS measurements of freshly prepared films and ex-situ prepared SAMs were solely conducted with monochromatised Al-$K\alpha$ radiation while non-monochromatised Al-$K\alpha$ radiation was also used for some of the ex-situ prepared powder samples. The chamber is further equipped with a hemispherical analyser (SPECS Phoibos 150) which is used to measure the kinetic energy of the electrons resulting from the photoemission in the sample. Pass energies of 50 eV and 20 eV are used for overview spectra and specific core-level spectra respectively. All spectra are calibrated to the signal of their respective substrates as shown in table 3.2. The analyser uses a delay line detector, a variant of the microchannel plate detector. In order to avoid

Table 3.2.: Binding energies of substrate signals used for calibration.

Element	**Transition**	**Binding Energy**
Si	$2p$	99.80 eV
In	$3d_{5/2}$	443.90 eV
Au	$4f_{7/2}$	84.00 eV

damaging the radical films by prolonged beam exposure, only freshly prepared films were measured and the time of exposure was minimised. For experiments probing film

stability towards air exposure, beam exposure was further reduced in order to clearly attribute changes in the spectra to air exposure and not beam damage. This leads to a worse signal-to-noise ration in the respective spectra.

3.1.1.2. Atomic Force Microscopy

AFM measurements are conducted in ambient conditions using a Digital Instruments Nanoscope III Multimode AFM. For this, in-situ prepared samples are removed from their sample holders and fixed to an AFM sample holder using double-sided carbon tape. To reduce damage to the films, samples are stored in darkness from the time when they are taken out of UHV up until the AFM measurements take place. AFM is measured in tapping-mode using NCH n^+-silicon tips and ScanAsyst® mode using a silicon tip on a nitride lever backed with a reflective aluminium coating. Evaluation of the images is done with the free software Gwyddion.[62]

3.1.2. LowDosePES End-Station at BESSYII

NEXAFS and photon energy dependant XPS measurements were performed at the LowDosePES end-station, installed at the PM4 dipole beamline, at the third-generation synchrotron facility BESSYII (Helmholtz Zentrum Berlin).[63] The end-station is comprised of several chambers with the load-lock doubling as the chamber used for deposition. The different chambers are connected via a transfer chamber containing a carousel-mounted manipulator arm. Substrates for in-situ prepared samples are annealed in a dedicated chamber at a temperature of around 510 K. The temperature is controlled via an N-type thermocouple attached to the heating element. Substrates are heated for around 18 h and cleanliness is verified by XPS. Ex-situ prepared SAMs are directly transferred into the analysis chamber. The analysis chamber, which is used for both NEXAFS and XPS measurements, is equipped with an ArTOF spectrometer for measuring photoelectron spectra as well as capabilities to measure absorption spectra. A motorised manipulator provides the capability to measure at different angles relative to the incident beam. NEXAFS measurement angles are shown in table 3.3.
XPS spectra are calibrated to the same binding energies of the substrates as shown above with a further correction for the inherent energy drift of the system if necessary. NEXAFS spectra are normalised with the clean substrate spectra and the multibunch current to remove the substrate signal as well as the absorption of contaminants in the beamline and signal spikes generated by the injection of electrons into the storage ring.

To minimise beam-damage every measurement is taken on a new spot of the film.

Table 3.3.: Angles used for NEXAFS measurements for the different radical films.

Molecule	**Normal Incidence**	**Grazing Incidence**
Blatter	90 °	30 °
NN-Blatter		
SAMs		
diBlatter		25 °

3.1.3. Data Analysis

3.1.3.1. Fit Procedure

The best fit procedure used throughout this work is adapted from the method of Schöll et. al. used for closed-shell molecules.[64–67] In general, the individual calibrated core-level spectra are subjected to a linear background correction and subsequently normalised to the peak maximum. Based on previous publications and preliminary interpretation of the data, Voigt profiles (a convolution of Gauss and Lorentz curves) are used for each major contributing chemical environment in the molecule and a minimal number of satellite peaks is added. The fit parameters are refined under tight physical restraints until a reasonable agreement with the measured data is achieved. The width of the Lorentzian contribution is directly correlated with the lifetime of the core-hole after photoemission as is assumed as constant.[68,69] Values are given in table 3.4. The width of the Gaussian contribution is correlated with several experimental and device-dependant factors and needs to be adjusted accordingly. The fit procedure is further detailed in the supporting information in appendix B.

Table 3.4.: Values of the Lorentz-widths used for the fits for every relevant element.[64,70]

Element	**Transition**	**wL** (eV)
C	$1s$	0.08
N	$1s$	0.10
Cl	$2p$	0.10

3.1.3.2. Nominal Film Thickness

Nominal film thickness, meaning the film thickness under the assumption of a uniform and closed film, is calculated via the method published by Hill in 1976[71] using the

following simplified formula:

$$d = -\lambda_n \cos\theta \ln\left(\frac{I_1}{I_0}\right) \tag{3.1}$$

where d is the nominal film thickness, λ_n is the inelastic mean free path and θ the emission angle of the photoelectron, and I_1 and I_0 are the measured intensities of the substrate signal with and without the deposited film respectively. The integrated intensity of the Si $2p$ signals from the survey spectra (figure 3.1) are used to calculate the nominal thickness. A background correction is applied to the spectra so that the backgrounds are identical and the signals comparable. The Si $2p$ photoelectron when using Al-$K\alpha$ radiation have, according to equation 2.1, a binding energy of 1386.8 eV resulting in an inelastic mean free path of 3.17 nm. This value was obtained by linear regression of the data given in reference [49]. The value of $\cos\theta$ is 1 in normal emission, which was used in every measurement in the home lab.

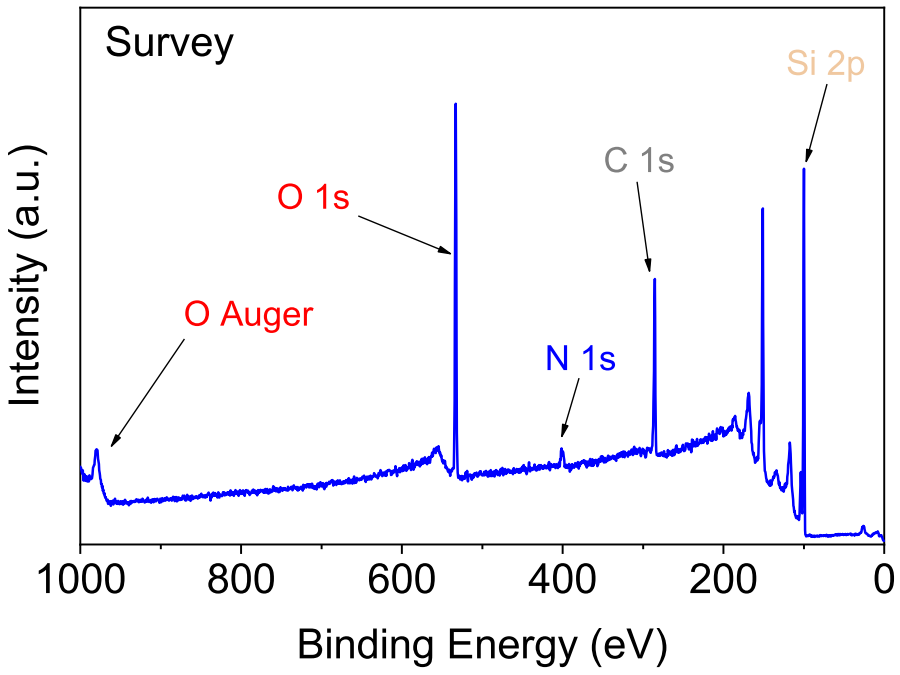

Figure 3.1.: Example of a survey spectrum of a diBlatter thin film typically used for the procedures above. Main features labelled with their respective sources.

3.1.3.3. Stoichiometry

Film stoichiometry was determined by calculating the ratio of the integrated intensities of the respective core levels after background correction from the survey spectra (figure 3.1). For this the integrated intensities need to be corrected by their respective relative sensitivity factors σ by simple division. These are given for all relevant elements in table 3.5.

Table 3.5.: Relative sensitivity factors used for calculation of film stoichiometry.[72,73]

Element	**Transition**	σ
C	$1s$	0.25
N	$1s$	0.42
Si	$2p$	0.27
Cl	$2p$	0.73
Fe	$2p$	3.00
Au	$4f_{7/2}$	2.80

4. Results and Discussion

4.1. Diradicals

4.1.1. Introduction

This chapter presents the first ever successful depositions of three different organic diradicals, NN-Blatter, diBlatter, and BDT-NN, and the investigation of their thin film stability. Being able to successfully deposit an intact diradical onto a surface is not only of academic interest, but also a crucial step towards the fabrication of functioning devices. The stability of the resultant films is of course similarly important for that goal. This chapter also discusses the chemical and physical factors that govern the process of a successful deposition as well as the morphology of the films.

Organic electronics have been of strong interest not only in academia but also for practical applications in recent decades.[74–80] Their popularity can be attributed to a series of properties that differentiate them from the widely used inorganic semiconductors and conductors. Unlike the classic inorganic semiconductors Silicon and Germanium, which are both brittle metalloids,[81] organic thin films often exhibit extended flexibility that makes it possible for them to be used in formerly unconventional shapes suited for a variety of settings.[82,83] Furthermore it is relatively easy to synthesise new organic molecules or modify existing ones in order to fine-tune their electronic properties like the band-gap or conductivity.[84] In order to achieve similar flexibility, inorganic semiconductors need to be doped with often rare (and thus expensive) and toxic elements. Great progress has been made, e.g., in the field of organic light-emitting devices where organic light-emitting diodes (OLEDs) are now commonplace as screens in mobile phones and television sets.[8] What differentiates the organic molecules presented in this work from other magnetic molecules studied for their potential use in electronics is their lack of metal atoms incorporated into the structure. As diradicals, they possess two unpaired electrons that give rise to a non-zero spin $\vec{s}$ and thus a magnetic moment $\vec{m}$ according to

$$\vec{m} = \gamma \vec{s} \tag{4.1}$$

where γ is the gyromagnetic ratio.
It is these unpaired electrons that make the diradicals potential candidates for application in electronics based on quantum phenomena like quantum computing, spintronics, and spin filtering.[15,85–87] The presence of more than one spin in the molecule compensates the disadvantage that organic molecules have of a relatively large volume compared to the often used single- or few-atom systems.[10,12,85,88]
The diradicals presented here represent two different cases of interaction between the two unpaired electrons. In the NN-Blatter and diBlatter molecules the two unpaired electrons are able to interact with each other leading to a combined spin S of 1 in both cases. BDT-NN represents the other case in which the two unpaired electrons do not couple, leading to two nominally separate units with a spin S of $\frac{1}{2}$ each.
Due to the highly reactive nature of organic diradicals it has been deemed practically impossible to successfully deposit them via controlled evaporation in UHV.[25]

4.1.2. Deposition and Evaporation Parameters

As shown in the respective publications in appendices A and D and figure 4.1, the focus of the presented data analysis are the N 1s and C 1s core level spectra. This is due to the spin densities of the radicals being mostly located in the nitrogen-containing moieties in all of the investigated molecules. O 1s spectra are not considered for the analysis because the signal is dominated by the intensity emitted by the oxygen atoms in the SiO_2 in the substrate which makes the evaluation very unreliable.

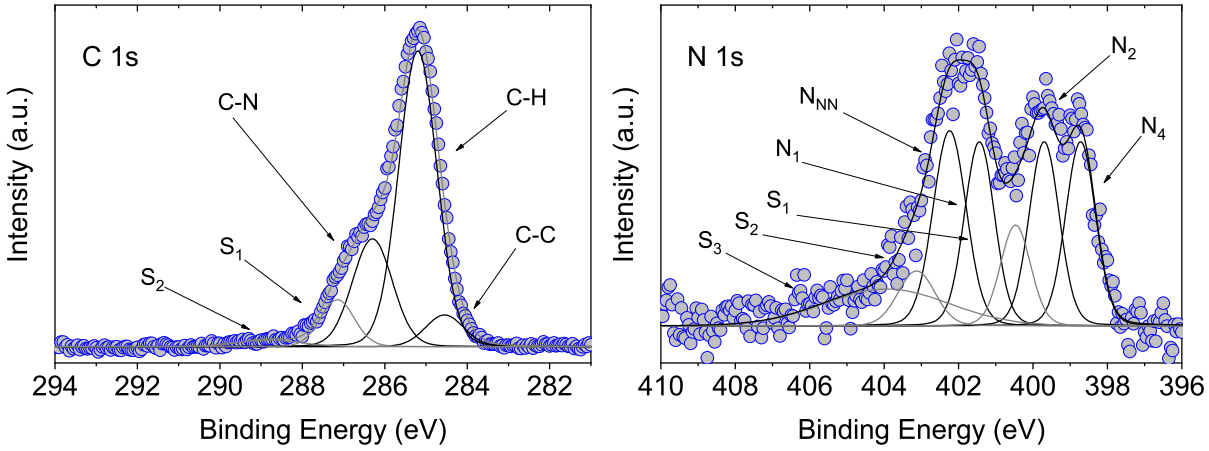

Figure 4.1.: Example of two normalised XPS spectra of a NN-Blatter diradical film with the results of their respective fit procedures.

There are two major steps to the successful deposition of any organic film via OMBD.

First the evaporation of the molecules in the Knudsen-cell and second the deposition on the substrate itself. Both of these have sets of parameters that govern their processes and that need to be understood in order for a successful deposition to be achievable. Gaining a good understanding of model systems like the ones studied here can also be used to predict the deposition behaviour of new molecules.
The first parameter looked at here is the evaporation temperature. Figure 4.2 illustrates that the evaporation temperature ranges leading to the successful deposition of the diradicals lie well below those of monoradicals previously investigated. By exceeding the upper temperature boundaries, one risks partial or complete degradation of the diradicals during the deposition. The lower limit of a feasible evaporation temperature is given by the crystal formation energy which needs to be overcome in order for the molecules to be able to change into the gas phase. The combination of these upper and lower temperature boundaries leads to a very narrow temperature range in which successful deposition of the intact molecules is possible.

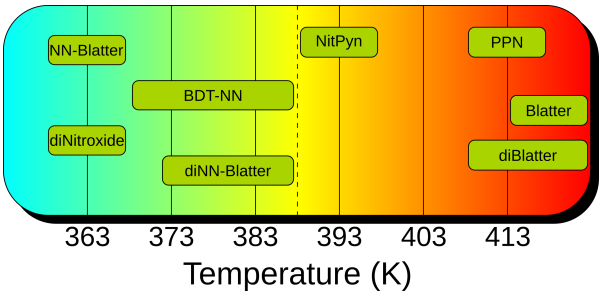

Figure 4.2.: Schematic representation of the temperature ranges used for the deposition of different organic radicals. Expanded from appendix D

The second major aspect is the monitoring of the formation of the films on the substrate. The initial qualitative assessment is carried out in situ by comparison of the line shape of the measured N 1s spectra with the expected line shape. In the case of the NN-Blatter, the expected line shape was obtained by the simple sum of previously measured spectra of the Pyrene-Blatter and nitronyl nitroxide radicals. The next, and most important, step of the process is the careful fit analysis of the N 1s and C 1s spectra carried out via the method detailed in chapter 3.1.3. In the cases of all three diradicals presented in this work, this best fit analysis confirms, by strong agreement with the theoretical stoichiometry of molecules, that all of them are in fact intact in the film. The full details on the fits for the NN-Blatter and BDT-NN diradicals are give in appendix C and its supporting information. The first hints of the growth mode of the films can be gained by plotting the attenuation of the substrate (Si 2p) signal versus the nominal film thickness as shown

in figure 4.3. By the slow attenuation of the signal, it is possible to ascertain that all three diradicals likely follow the Volmer-Weber growth mode described in chapter 2.2.1.1. This has been corroborated by AFM measurements for all three diradicals by showing islands on the surface. These can be either the result of the assumed Volmer-Weber or the Stranski-Krastanov growth modes but further investigation is needed in order to conclusively determine the prevailing mode. This is already a strong hint at the bulk formation thermodynamics of the diradicals being the major contributor to the film morphology as opposed to the interaction between the adsorbate and the substrate. In order to gain further insight into this topic, annealing experiments have been conducted in which the NN-Blatter film was heated, step-wise, and again measured by XPS. The relatively low temperatures at which the film completely desorbs (below 483 K) from the substrate are a further strong indication of the low degree of interaction between the two (appendix C).

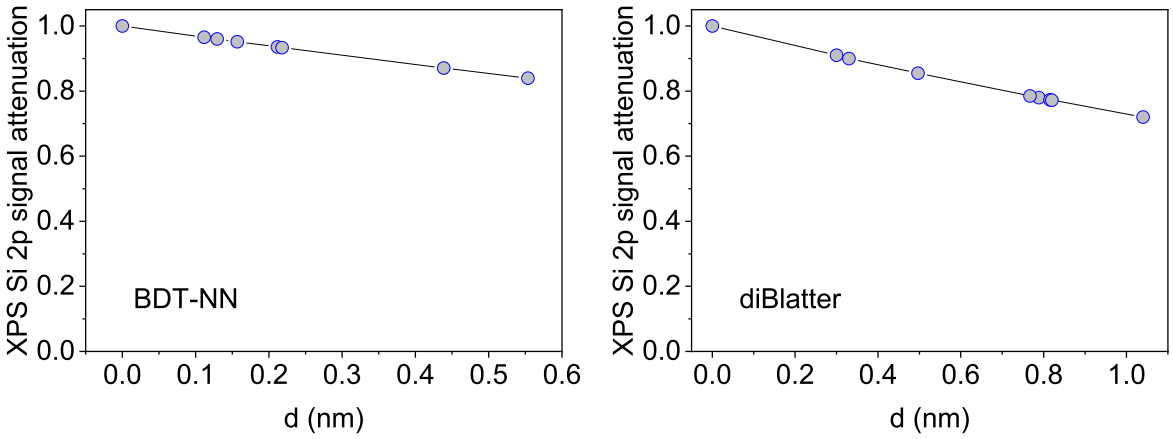

Figure 4.3.: Attenuation of the substrate signal plotted versus the nominal film thickness for two examples of BDT-NN and diBlatter thin films.

4.2. Triradical

4.2.1. Introduction

Analogous to chapter 4.1, the first successful deposition of a purely organic triradical is presented here based on the publication in appendix E. The diNN-Blatter triradical used here is described in section 2.1.1.4. The motivation for the use of this novel material is, in general, consistent with the previously discussed diradicals with the potential advantage

of one more unpaired electron in the molecule, increasing the density of usable spins in the film further. The analytical focus on the N 1*s* and C 1*s* core level spectra also remains the same.

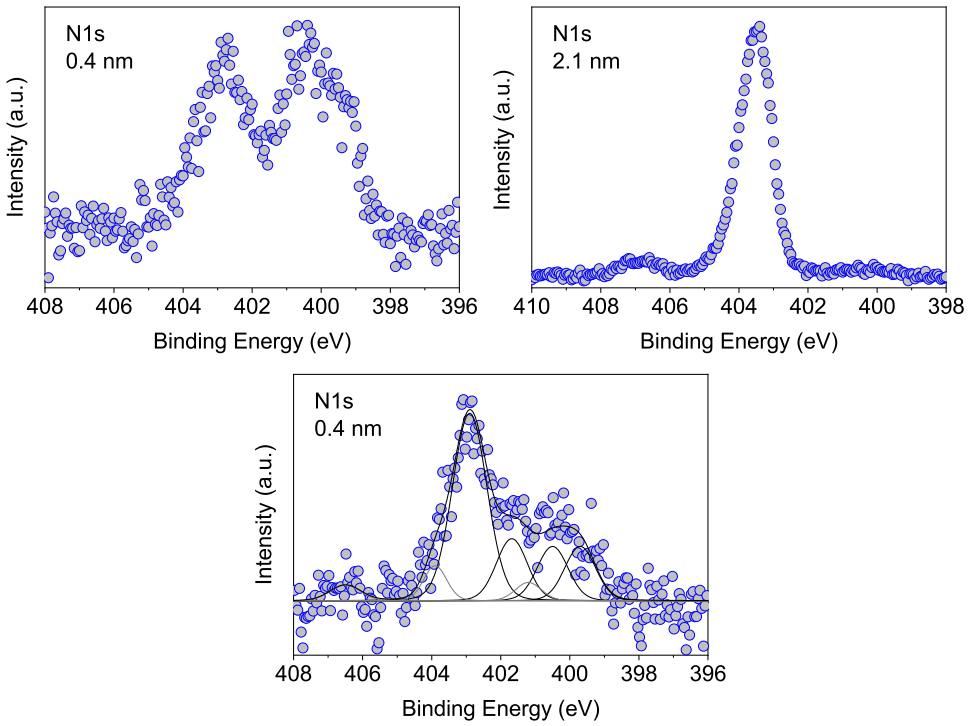

Figure 4.4.: Examples of the inconsistency in N 1*s* core level spectra of three diNN-Blatter thin films. Film with significant imino nitroxide fraction (top left) and aberrant line shape (top right). Thin film with fit showing expected stoichiometry of the intact triradical (bottom).

4.2.2. Deposition and Drop-Casting

The deposition of the diNN-Blatter triradical represents a significant challenge even compared to the previously discussed diradicals. Nonetheless it has proven possible to successfully deposit films of the intact triradical under UHV conditions. The examination of the overall film stoichiometry, careful fit analysis of the individual N 1*s* and C 1*s* core level spectra, as well as the comparison with powder spectra of these core levels clearly confirms this (Appendix E). Furthermore the triradical films are shown to also grow in the Volmer-Weber growth mode as supported by XPS, AFM, and SEM measurements. However the triradical films show a greater variance when compared to the mono- or diradicals (figure 4.4). We also observed some unsuccessful depositions that show

stoichiometries divergent from those expected (figures 4.4 and 4.5) for intact molecules and also differences in film morphology in AFM and SEM measurements. This suggests the presence of different intermolecular interactions in these films.
A new avenue of investigation was also pursued with the diNN-Blatter triradical in the preparation of drop-coated samples prepared by dropping a solution of the triradicals in toluene on the substrate via a pipette. These films are about two orders of magnitude thicker than the ones prepared by OMBD and show a stoichiometry in good agreement with the theoretical values.
This behaviour suggests that the factors making the successful deposition of the diradicals difficult have an even greater impact on the triradical, making it even more unstable and prone to react.

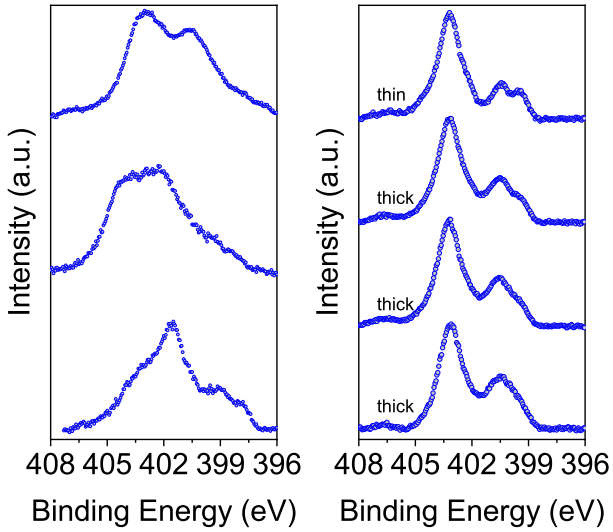

Figure 4.5.: Examples of N 1s core level spectra of three diNN-Blatter powder samples (left) and drop-coated samples (right).

4.3. Self-Assembled Monolayers of a Modified Perchlorotriphenylmethyl Radical

4.3.1. Introduction

The topic of this chapter is the self-assembled monolayers of a derivative of the PTM radical. The first concern is to verify that the radical character of the molecules is intact after deposition via several closely related wet chemical procedures. Furthermore the

orientation of the radicals relative to the surface as well as the stability of the monolayers are investigated (appendices B and C).
The motivation behind these studies is similar as the one described for the diradicals above, though the approach is a different one. The two main differences being the nature of the radical and the preparation method. While the diradicals derive their stability from the delocalisation of the unpaired electrons, the PTM radical derives its from the steric screening of the radical centre. Furthermore the wet chemical processes used for surface modification are undertaken partially in ambient conditions and partially in argon atmosphere negating the need for vacuum techniques and thus making the method potentially more suited for assembly line production.

4.3.2. Functionalisation of Gold Surfaces

The investigation into the viability of self-assembled monolayers of this specific derivative of the PTM radical focusses on two different synthetic scenarios. The first being the modification of a precursor radical already bound to the gold surface with azidomethylferrocene via a so-called click reaction (figure 4.6 and appendix B) and the second focussing on the differences between radical formation of the already ferrocene-substituted molecule before and after attachment to the gold surface (figure 4.8 and appendix C).

Charge transport measurements conducted by the group of N. Crivillers of the Institut de Ciència de Materials de Barcelona for the first case show a current density that is below the expected value for an experiment with a quantitative yield of the click reaction and above that of the unmodified molecule. With the value being around the midpoint between the two, this indicates a yield of ca 50 %. By measuring XPS survey spectra and calculating the stoichiometry as shown in section 3.1.3 this assertion can be supported. This is shown in the fact that the intensities of the Fe $2p$ and N $1s$ peaks in the survey spectra are consistently too low for a monolayer in which all of the radicals incorporated the azidomethylferrocene moiety. NEXAFS measurements conducted with these self-assembled monolayers give further insight into their properties (figure 4.7 and appendix B). First it is possible to confirm the integrity of the radical centre of the molecule by the presence of a pre-edge feature in the C-K edge spectrum characteristic for the electronic transition from the C $1s$ orbital into the singly-unoccupied molecular orbital (SUMO).[89,90] Second it is possible to calculate the molecular orientation relative to the surface from the dichroism between spectra measured at normal and grazing

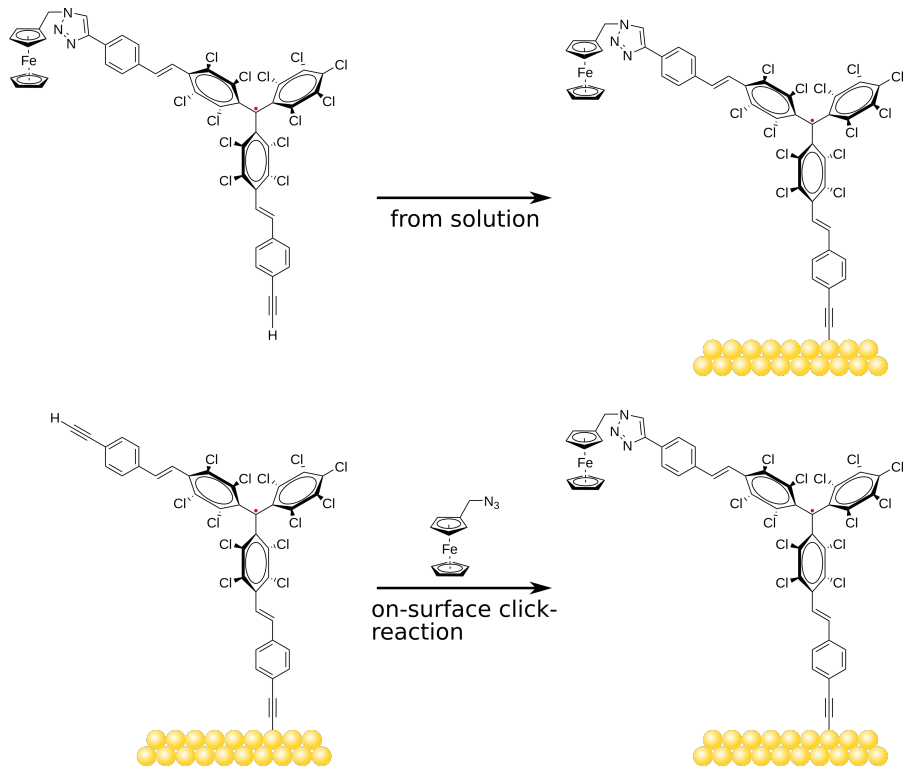

Figure 4.6.: The two approaches chosen for the preparation of the self-assembled monolayers in appendix B.

incidence using equation 4.2.[91]

$$\frac{1}{\tan^2 \alpha} = \frac{1}{2}\left(1 - \frac{1-q}{\sin^2 \theta_{p-pol} - q \sin^2 \theta_{s-pol}}\right) \tag{4.2}$$

where α is the angle between substrate and molecule, θ is the angle between the incident radiation and the surface and q is the ratio between the intensities for the different polarisations given as:

$$q = \frac{I(\theta_{p-pol})}{I(\theta_{s-pol})} \tag{4.3}$$

Due to the twisted nature of the PTM radical, the focus of this analysis is on the spectral features linked to the electronic transitions characteristic for the ferrocene moiety. Calculating the angle of the ferrocene moiety according to equation 4.2 results in an average angle of 21°–22° relative to the surface. These factors, i.e., low yield of the on-surface modification, the molecular orientation of the ferrocene moiety and the PTM radical twisting, could lead to a poor contact with the top electrode and lead to the

lack of current rectification observed in other self-assembled monolayers that include a redox-active ferrocene moiety.[92,93]

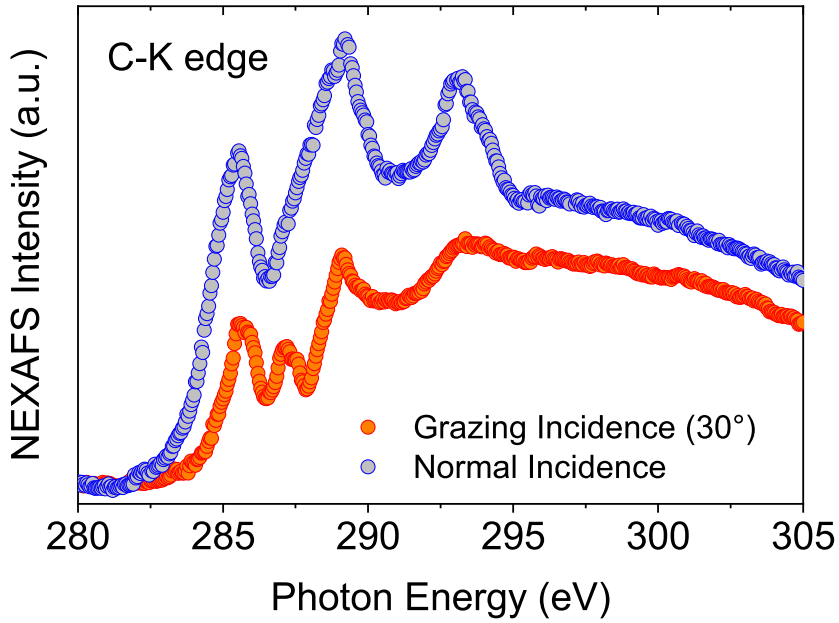

Figure 4.7.: Example of two NEXAFS spectra measured at the C-K edge showing the dichroism described and used to calculate the orientation of the $FeCp_2$ moiety in appendix B.

The second synthetic scenario, which includes the comparison of both radical monolayers with their diamagnetic counterpart (figure 4.8), reveals further information about the properties of the system. By careful analysis of the C 1*s* spectra of the para- and diamagnetic molecules it is possible to verify the intactness of the radical character in the samples after deposition. This manifests itself in a slight shift in the binding energy of the C−H component of the fit towards lower values as well as a narrowing of the component's peak of 0.4 eV from the diamagnetic to the paramagnetic molecule. This can be explained by more efficient screening of the core hole in the radicals and is congruent with the assertion of higher charge delocalisation due to the donor-acceptor character of the molecule in the presence of the unpaired electron and the ferrocene moiety described in appendix B.

Using synchrotron radiation with variable photon energy also makes it possible to gain further insight into the properties of the material by probing the monolayers at different depth (appendix C). Besides confirming the previously used assignment of satellite intensities to their respective main lines it is also possible to gain information about the structure of the films. We found that the C−Cl contributions to the overall signal grow

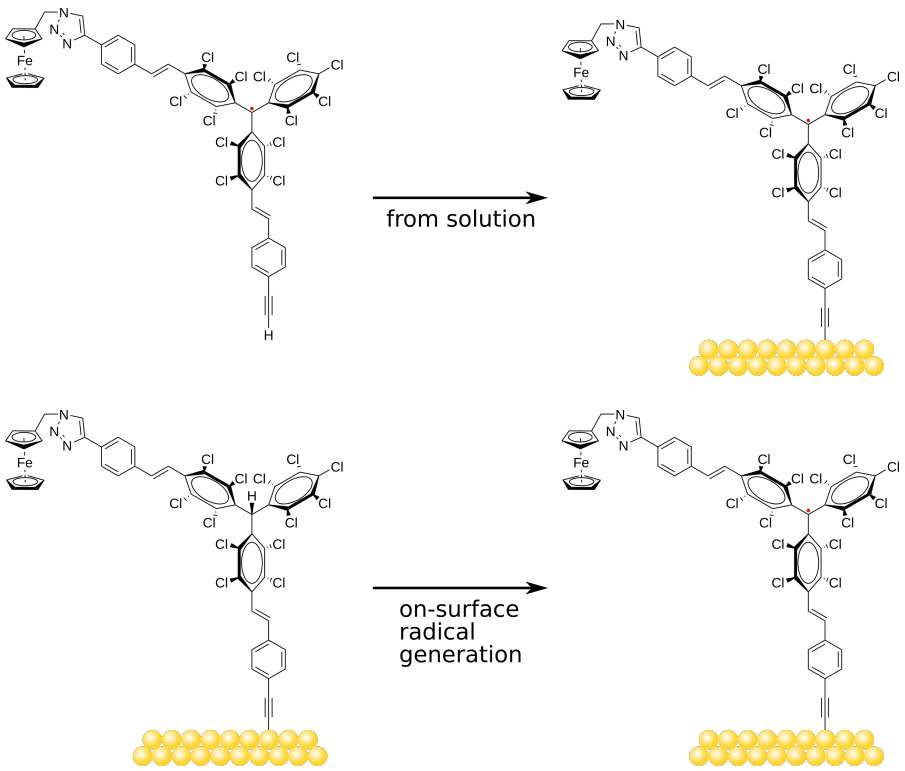

Figure 4.8.: The two approaches chosen for the preparation of the self-assembled monolayers in appendix C.

with increasing probing depth while the C−N contributions are higher in more surface-sensitive measurements indicating that there is a significantly different distance between the PTM moiety or the triazole moiety and the substrate surface (figure 4.8). From that it is possible to infer that the molecules are standing approximately perpendicular to the surface.
Furthermore the high degree of agreement between the respective fits confirms the robustness of the chosen parameters as well as the feasibility of the on-surface generation of the radical.

4.4. Stability

The stability of the films towards different environments is a critical factor in the context of the application of these types of di- and triradicals in real-world devices as well as for investigations carried out, by necessity, in ambient conditions. The general conditions and factors that need to be considered here differ greatly between the realms of pure synthesis, in which stability in solution and the bulk phase are usually the important concepts,

and surface science. Concepts like substrate and film morphology, adsorbate/substrate interaction, or molecular orientation become relevant in thin films and can lead to drastic changes in chemical and physical behaviour in the radicals. All radicals examined in this work are considered to be chemically "stable". While their syntheses are conducted under inert gas atmospheres, the final products can all be handled in air without degradation or even combustion. The same is not necessarily true for their thin films. Towards that end, experiments were conducted that test the various films' stability towards X-ray beam exposure and exposure to air. Furthermore, this data was correlated with ab initio DFT calculations done by Dr A. Calzolari of the CNR-NANO Istituto Nanoscienze in Modena in order to gain insight into the reasons for the observed behaviour.

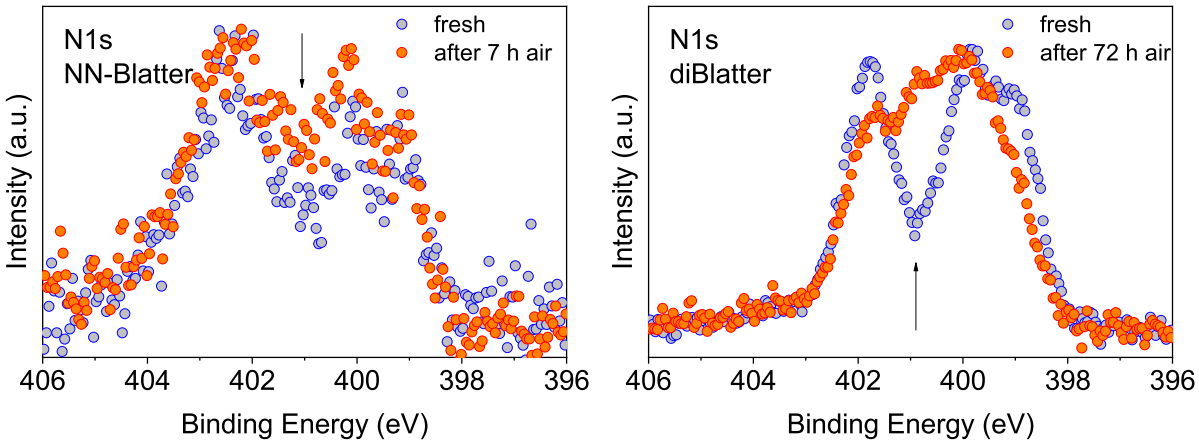

Figure 4.9.: Examples of N 1*s* core level spectra of NN-Blatter and diBlatter thin films after different exposure times showing the characteristic change of intensity in the region indicated by the arrows.

The main indicator for the degradation in these diradicals is a change in intensity in the N 1*s* spectrum with a shift in binding energies from above 400 eV in the case of the nitronyl nitroxide moiety and around 398 eV in the case of the Blatter moiety to around 400 eV (figure 4.9).[18,21] This change in intensity is caused mainly by two different processes whose corresponding binding energies coincide in the mentioned region. For the nitronyl nitroxide moieties, the main contribution is the loss of one of the oxygen atom resulting in an imino nitroxide radical (figure 4.11).[94,95] In the case of the Blatter moiety this intensity can be explained by a hydrogenation.[21,96] The corresponding new fit peak is labelled N* in the respective fits (Figure 4.10).

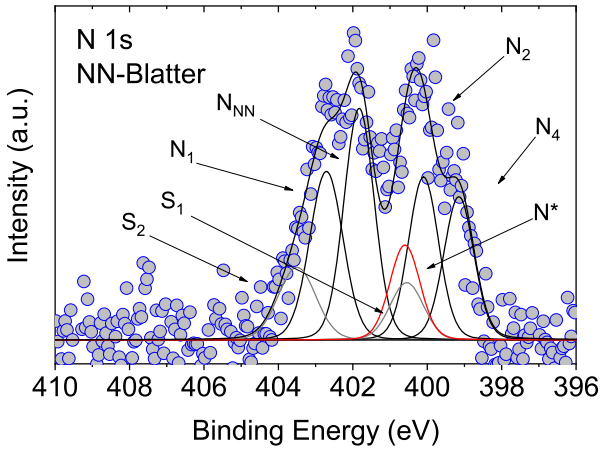

Figure 4.10.: Example of an N 1*s* core level spectrum of NN-Blatter after degradation with the result of the bets fit procedure showing the new contribution N* (highlighted in red).

The three diradical films show differing behaviour towards X-ray exposure. While the NN-Blatter and diBlatter films show little to no change in the N 1*s* line shape after prolonged exposure, the signal associated with the intact nitronyl nitroxide moiety completely vanishes even in measurements of under three hours for BDT-NN (appendices D and F).

Exposing the films to air reveals two major interesting factors. First, films of all three of the diradicals show greatly reduced stability when compared to the films made up of the monoradicals that form the basis of their molecular structure. Pyrene-Blatter films have shown air stability of several months before showing the first signs of degradation.[21] In contrast, films of the NN-Blatter and diBlatter diradicals show minor degradation already after a couple of hours and major degradation after a small number of days of air exposure. The of X-ray induced degradation and low signal strength of the principal core level spectra even results in the the study of degradation by air exposure not being feasible for the case of BDT-NN films. Correlating the results of the stability experiments with the radicals' physical properties (appendices D and F) it becomes evident, that there is a correlation between the degree of delocalisation of the unpaired electrons and the stability of the diradical films while the distance between the radical sites and the degree and type of magnetic interaction do not play a role. In both cases of the films more resistant to X-rays and air there is a high degree of delocalisation making it less likely that the unpaired electrons will react with either other diradicals, intermolecularly, or with gases present in the ambient air. In the case of BDT-NN, the unpaired electrons are almost entirely located in the nitronyl nitroxide moieties, therefore lacking the chemically

stabilising influence of wider delocalisation.

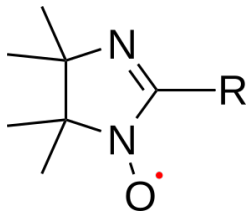

Figure 4.11.: Chemical structure of the imino nitroxide moiety that constitutes a major contribution to the degradation of the nitronyl nitroxide moiety.

The diNN-Blatter triradical represents the next step in this investigation with one more nitronyl nitroxide moiety than the NN-Blatter diradical, which has been proven to be a destabilising factor for the thin films examined here when compared to films of the Blatter radical at its core. While the films show a high degree of stability towards X-ray exposure during all measurements as well as towards UHV conditions, the same cannot be said for exposure to air. In the case of films deposited via OMBD the exposure to air leads to a drastic reduction in intensity in the regions attributed to both nitronyl nitroxide and Blatter moieties in the N 1s spectra even after only a few hours (appendix E). Coupled with the relative increase of intensity in the region associated with the undesired by-products (imino nitroxide and hydrogenated 1,2,4-benzotriazinyl) this leads to the conclusion that both types of radical sites appear to exhibit increased reactivity in these films when compared to their mono- and diradical counterparts.
Drop-coated films, with their greater thickness when compared to films deposited via OMBD (two orders of magnitude), show far less severe degradation in XPS measurements over longer periods of time. This can potentially be attributed to several factors not related to the actual stability of the triradicals in the films. Al-$K\alpha$ radiation with its photon energy of 1486.6 eV has a relatively large information depth. So while the triradicals in the uppermost layers of the drop-coated films might degrade in a similar fashion to that observed in the evaporated films, this information is not selectively probed with the available experimental set-up in our home lab. Photon energy-dependent measurements conducted at a synchrotron facility would be required to gain insight into the degradation process at different probing depths. In addition, film morphology can also play a role.
Having examined the stability of di- and triradical thin films obtained by evaporation in UHV conditions, the next section investigates the stability of an alternative system of monoradical monolayers prepared by self-assembly in a wet chemical process. In this the focus is again on the stability of the films towards exposure to air and long exposure to

X-ray radiation. In both cases the C 1s and Cl 2p spectra as well as the survey spectra are the focus of the analysis.

As for the former there is a marked increase in the C 1s intensity after prolonged exposure to air. Two fits conducted under two different assumptions (adsorption of environmental carbon contaminants and intramolecular cyclisation) result in plausible fits (figure 4.12 bottom). Close examination of the measured data reveals an increase in the C 1s intensity relative to the substrate signal but no significant change in line shape beyond that (figure 4.12 top). Furthermore neither the intensity of the Cl 2p signal nor the Cl 2p/Au 4f ratio change after prolonged exposure to air. The latter should decrease proportionally to the two chlorine atoms which are abstracted in the case that the cyclisation reaction takes place. This stoichiometric analysis strongly favours the possibility of carbon contamination from the air (appendix C).

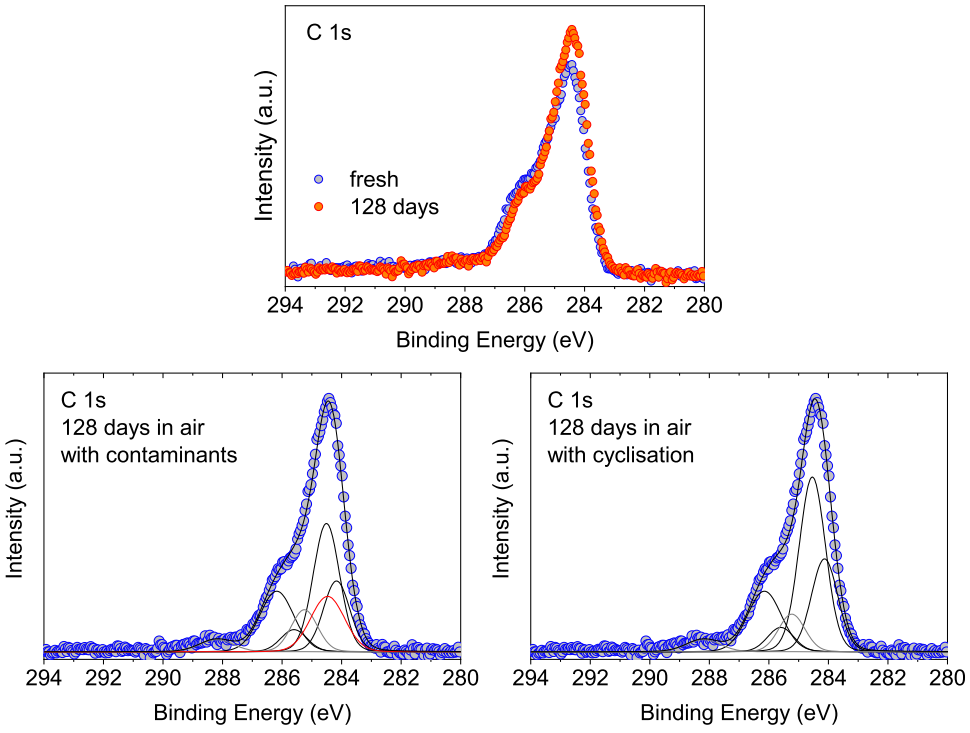

Figure 4.12.: C 1s spectra of the self-assembled monolayers showing the increase in intensity over 128 days of exposure to air (top) and fit results for both scenarios mentioned with the contaminant contribution highlighted in red (bottom).

X-ray exposure of up to eight hours during measurements leads to no observable change in the C 1s spectra. Longer measurements of over 50 hours result in an increase in

the substrate signal while the C 1*s* and Cl 2*p* intensities remain the same. This is an indication for changes in film morphology rather than chemical changes. Such post-growth processes, like ripening or desorption, are known for organic thin films, especially with physisorbed molecules.[18,21,67] Similar behaviour has been observed in gold-thiolate systems with a strong covalent bond between adsorbate and surface.[97]

5. Conclusions and Outlook

Using X-ray techniques we investigated the phenomena that govern sublimation, film formation, and stability of novel polyradical thin films as well as the properties of self-assembled monolayers of a modified PTM radical prepared closer to the reality of industrial device manufacture. The major results and conclusions of this investigation are as follows:

- We showed for the first time that the deposition of thin films formed from intact di- and triradicals via organic molecular beam deposition is possible. This has been considered an impossible task so far due to the high reactivity of these molecules. Furthermore X-ray photoelectron spectroscopy has once again proven to be an excellent method for the study of these films, showing the ability to verify the intactness of the radicals without the need for further methods.

- We gained insight into the parameters and processes that govern thermal deposition of di- and triradicals showing that film formation is not influenced by the magnetic ordering or the distance between the radical sites in the solid phase but purely by crystal formation thermodynamics and the onset of thermal decomposition.

- The morphology of the films is consistent with their monoradical counterparts in exhibiting Volmer-Weber-type Island growth. This phenomenon increases in severity from the mono- to triradicals.

- Film stability towards exposure to air and X-rays is correlated solely with the delocalisation of the unpaired electrons and the onset of thermal decomposition

- It was also possible to establish that monolayers of covalently bound PTM radicals on gold show a remarkable stability of the radical over a prolonged period of time (over four months) without showing any degradation. In this context the viability of XPS to distinguish between a diamagnetic molecule and its radical derivative could also be established, showing that what has been proven to be possible for

radical with unpaired electrons located in the nitrogen-containing moieties is also possible for purely carbon-based radical centres.

- Slight changes in binding energies in the core-level spectra under extremely long X-ray exposure hint at changes in film morphology caused by post-growth phenomena similar to those observed in gold-sulphur bonds in similar films and clusters.

The results on polyradical thin films presented in this work act as a starting point for further investigations into these kinds of systems. With them it is possible to synthesise and deposit new purely organic polyradicals or to vary different parameters, like substrate composition or temperature, in order to elucidate further aspects of the field as yet untested. Similarly, the results on self-assembled monolayers of the modified PTM radical grant insight into the phenomena present in these films that need to be adressed before a practical application can be achieved.
This present work carries the use of purely organic radicals in real-world applications one step closer to reality.

6. Symbols and Abbreviations

%	percent
$°C$	degrees Celsius
a.u.	arbitrary units
AFM (magnetism)	anti-ferromagnetic
AFM (method)	atomic force microscopy
Al	element symbol of aluminium
ArTOF	angular-resolved time of flight (electron analyser)
Au	element symbol of gold
mbar	millibar
BW	bandwidth
C	element symbol of carbon
CCD	charge-coupled device
Cl	element symbol of chlorine
cos	cosine
Cp^-	cyclopentadienyl anion ($C_5H_5{}^-$)
d (diffraction)	Abbe diffraction limit
d (film thickness)	nominal film thickness
D (e.g. 2D)	dimensional
E	energy
ESCA	Electron Spectroscopy for Chemical Analysis
et. al.	et alii/et aliae/et alia (lat.: and others)
eV	electron Volt
g	gramme
h (constant)	Planck constant
h (unit)	hour
H	element symbol of hydrogen
HZB	Helmholtz-Zentrum Berlin
K	Kelvin

λ	wavelength
λ_n	inelastic mean free path
ln	natural logarithm
m	metre
MBE	molecular beam epitaxy
Mg	element symbol of magnesium
n	refractive index
ν	frequency
N	element symbol of nitrogen
NEXAFS	near-edge x-ray absorption fine structure
NN	nitronyl nitroxide
O	element symbol of oxygen
OLED	organic light-emitting diode
PD	Privatdozent
PES	photoelectron spectroscopy
PTM	Perchlorotriphenylmethyl
rad	radian
s	second
σ	elemental sensitivity factor
S (element)	element symbol of sulphur
S (quantum number)	total spin angular momentum
Si	element symbol of silicon
sin	sine
SUMO	singly-occupied molecular orbital
θ	a specified angle
TGA	thermogravimetric analysis
UHV	ultra-high vacuum (approx. 10^{-8} mbar and below)
wL	Lorentzian width in a Voigt profile
XMCD	X-ray magnetic circular dichroism
XPS	X-ray photoelectron spectroscopy
XRD	X-ray diffraction

7. List of Publications

Accepted Publications

I

N. Gallagher, H. Zhang, T. Junghoefer, E. Giangrisostomi, R. Ovsyannikov, M. Pink, S. Rajca, M. B. Casu, A. Rajca, "Thermally and Magnetically Robust Triplet Ground State Diradical", *Journal of the American Chemical Society* **2019**, *141*, 4764–4774, DOI 10.1021/jacs.9b00558.

II

J. A. de Sousa, F. Bejarano, D. Gutiérrez, Y. Leroux, E.-M. Nowik Boltyk, T. Junghoefer, E. Giangrisostomi, R. Ovsyannikov, M. B. Casu, J. Veciana, M. Mas-Torrent, B. Fabre, C. Rovira, N. Crivillers, "Exploiting the Versatile Alkyne-based Chemistry for Expanding the Applications of a Stable Triphenylmethyl Organic Radical on Surfaces", *Chemical Science* **2019**, *11*, 516–524, DOI 10.1039/c9sc04499j.

III

T. Junghoefer, E. M. Nowik-Boltyk, J. A. de Sousa, E. Giangrisostomi, R. Ovsyannikov, T. Chassé, J. Veciana, M. Mas-Torrent, C. Rovira, N. Crivillers, M. B. Casu, "Stability of Radical-Functionalized Gold Surfaces by Self-Assembly and On-surface Chemistry", *Chemical Science* **2020**, *11*, 9162–9172, DOI 10.1039/d0sc03399e.

IV

T. Junghoefer, N. M. Gallagher, K. Kolanji, E. Giangrisostomi, R. Ovsyannikov, T. Chassé, M. Baumgarten, A. Rajca, A. Calzolari, M. B. Casu, "Challenges in Controlled Thermal Deposition of Organic Diradicals", *Chemistry of Materials* **2021**, *33*, 2019–2028, DOI 10.1021/acs.chemmater.0c03880.

V
C. Shu, M. Pink, T. Junghoefer, E. Nadler, S. Rajca, M. B. Casu, A. Rajca, "Synthesis and Thin Films of Thermally Robust Quartet (S = 3/2) Ground State Triradical", *Journal of the American Chemical Society* **2021**, *143*, 5508–5518, DOI 10.1021/jacs.1c01305.

Submitted Publications

VI
S. Zhang, M. Pink, T. Junghoefer, W. Zhao, S.-N. Hsu, S. Rajca, B. W. Boudouris, M. B. Casu, A. Rajca, "Conducting High-spin (S = 1) Organic Diradical with Robust Stability", **2020**, DOI 10.26434/chemrxiv.13027835.v1.

VII
T. Junghoefer, I. Baev, M. Glaser, F. Ciccullo, E. Giangrisostomi, R. Ovsyannikov, F. Kielgast, M. Nissen, J. Schwarz, N. M. Gallagher, A. Rajca, M. Martins, A. Calzolari, M. B. Casu, "Magnetic Behavior in Metal-free Radical Thin Films", **2021**, https://arxiv.org/abs/1911.02082.

Contributions

This work was conducted as part of the DFG project CA 852/11–1 “Interplay of structural and electronic properties and their impact on thin films of metal-free organic radicals.”.

Contributions by Co-Authors

The group of Professor Andrzej Rajca, which includes Nolan Gallagher, Hui Zhang, Suchada Rajca, and Shuyang Zhang, is responsible for the synthesis of the Pyrene-Blatter, NN-Blatter, diBlatter, and diNN-Blatter radicals as well as characterisation by nuclear magnetic resonance (NMR), electron paramagnetic resonance (EPR), and superconducting quantum interference device (SQUID) measurements. They also conducted single-molecule density functional theory (DFT) calculations (publications I and IV–VII).

Maren Pink performed X-ray diffraction (XRD) measurements and the subsequent structural calculations for the NN-Blatter, diBlatter, and diNN-Blatter radicals (publication I, V, and VI).

Arrigo Calzolari conducted the DFT calculations of the Pyrene-Blatter, NN-Blatter, and BDT-NN molecules (publications IV and VI).

The group of Professor Martin Baumgarten, including Kubandiran Kolanji, is responsible for the synthesis of the BDT-NN radical (publication IV).

The groups of Professor Jaume Veciana, Professor Concepció Rovira, Marta Mas-Torrent, and Núria Crivillers, including Jesús Alejandro de Sousa, Francesc Bejarano, and Diego Gutiérrez, as well as the Bruno Fabre and Yann R. Leroux synthesised and characterised the modified PTM radical. They also manufactured the self-assembled monolayers of the molecule and measured cyclic voltammerty (CV) and the transport properties of these films (publications II and III).

Ewa Małgorzata Nowik-Boltyk participated in all XPS and AFM measurements conducted while working on her Master-thesis on the topic of the self-assembled monolayers of the modified PTM radical in the group of Professor Dr Maria Benedetta Casu. During that time she also performed the evaluation of the measured data (publications II and III).

Elke Nadler is responsible for the measurement and processing of the SEM images taken of the diNN-Blatter films (publication V).

The group of Professor Wilfried Wurth († 2019) and Michael Martins, which includes Ivan Baev, Fridtjof Kielgast, Matz Nissen, and Julius Schwarz, designed and operated the removable ultra-low temperature X-ray circular magnetic dichroism (XMCD) end-station installed at the Variable Polarization XUV Beamline P04 at PETRAIII (Deutsches Elektronen-Synchrotron, Hamburg). They, as well as Mathias Glaser, participated in the beamtimes at PETRA III (publication VII).

Francesca Ciccullo of the group of Professor Dr Maria Benedetta Casu participated in the beamtimes at BESSYII (publication VII).

Professor Thomas Chassé took part in the photoelectron measurements conducted in his lab at the University of Tübingen (publications III and IV).

The group of Bryan W. Boudouris, including Wenchao Zhao and Sheng-Ning Hsu, performed the two-probe conductivity measurements of the diBlatter radical (publication VI).

Erika Giangrisostomi and Ruslan Ovsyannikov are the beamline scientists at the Low-DosePES end-station of the PM4 beamline at BESSYII and are thus responsible for technical and scientific support during the measurements conducted there (publications I–IV and VI).

Professor Dr Maria Benedetta Casu conceived and supervised the DFG-funded project as part of which this work and the appendant publications were written. She took part in the photoelectron measurements in the home lab and at the synchrotron facilities. She interpreted the data for the publications based on my analysis.

Own Contributions

I was hired within the DFG project CA 852/11–1 “Interplay of structural and electronic properties and their impact on thin films of metal-free organic radicals.” which provided the thematic framework for this dissertation. Within this framework, I was responsible for the following:

For all publications detailed above I conducted all depositions of the films via OMBD and drop-casting, the XPS measurements, both in the home lab as well as during beamtimes at the synchrotron facilities BESSYII and PETRAIII, AFM measurements, NEXAFS measurements the BESSYII synchrotron facility, and XMCD measurements at the PETRAIII synchrotron facility.

The corresponding data processing and analysis (unless stated otherwise in the preceding section and excluding publication VII) was also performed by me.

For the XPS measurements this constitutes the calibration and normalisation of the data, the calculation of film thickness and stoichiometry, determining the likely growth-mode of the film, and the fit analysis of the core-level spectra. Furthermore the comparison of the spectra of different measurements to identify trends based on deposition parameters and film thickness and other parameters.

For the NEXAFS measurements this is the averaging and normalisation of the data, identification of characteristic peaks and any dichroism present in the spectra, and calculation of molecular orientation.

Furthermore, I contributed to the scientific discussion with my supervisor Professor Dr Benedetta Casu on all publications.

Bibliography

[1] J. R. R. Tolkien, *The Two Towers*, George Allen & Unwin, London, **1954**.

[2] M. B. Casu, *Electronic Structure of Heterocyclic Organic Semiconductors*, Mensch & Buch Verl, Berlin, **2002**.

[3] T. Jackson, Y.-Y. Lin, D. Gundlach, H. Klauk, "Organic Thin-Film Transistors for Organic Light-Emitting Flat-panel Display Backplanes", *IEEE Journal of Selected Topics in Quantum Electronics* **1998**, *4*, 100–104, DOI 10.1109/2944.669475.

[4] J. Rivnay, S. C. B. Mannsfeld, C. E. Miller, A. Salleo, M. F. Toney, "Quantitative Determination of Organic Semiconductor Microstructure from the Molecular to Device Scale", *Chemical Reviews* **2012**, *112*, 5488–5519, DOI 10.1021/cr3001109.

[5] F. Vidor, T. Meyers, U. Hilleringmann, "Flexible Electronics: Integration Processes for Organic and Inorganic Semiconductor-Based Thin-Film Transistors", *Electronics* **2015**, *4*, 480–506, DOI 10.3390/electronics4030480.

[6] Y. Yu, G. Chen, Y. Zhou, Z. Han, "Recent Advances in Rare-Earth Elements Modification of Inorganic Semiconductor-Based Photocatalysts for Efficient Solar Energy Conversion: A Review", *Journal of Rare Earths* **2015**, *33*, 453–462, DOI 10.1016/s1002-0721(14)60440-3.

[7] G. P. Kini, S. J. Jeon, D. K. Moon, "Design Principles and Synergistic Effects of Chlorination on a Conjugated Backbone for Efficient Organic Photovoltaics: A Critical Review", *Advanced Materials* **2020**, *32*, 1906175, DOI 10.1002/adma.201906175.

[8] T. Tsujimura, *Oled Display Fundamentals and Applications*, John Wiley & Sons, **2017**, 320 pp.

[9] K. Sato, S. Nakazawa, R. Rahimi, T. Ise, S. Nishida, T. Yoshino, N. Mori, K. Toyota, D. Shiomi, Y. Yakiyama, Y. Morita, M. Kitagawa, K. Nakasuji, M. Nakahara, H. Hara, P. Carl, P. Höfer, T. Takui, "Molecular Electron-Spin Quantum Computers and Quantum Information Processing: Pulse-Based Electron Magnetic Resonance

Spin Technology Applied to Matter Spin-Qubits", *Journal of Materials Chemistry* **2009**, *19*, 3739, DOI 10.1039/b819556k.

[10] S. Nakazawa, S. Nishida, T. Ise, T. Yoshino, N. Mori, R. D. Rahimi, K. Sato, Y. Morita, K. Toyota, D. Shiomi, M. Kitagawa, H. Hara, P. Carl, P. Höfer, T. Takui, "A Synthetic Two-Spin Quantum Bit:g-Engineered Exchange-Coupled Biradical Designed for Controlled-NOT Gate Operations", *Angewandte Chemie International Edition* **2012**, *51*, 9860–9864, DOI 10.1002/anie.201204489.

[11] M. R. Wasielewski, M. D. E. Forbes, N. L. Frank, K. Kowalski, G. D. Scholes, J. Yuen-Zhou, M. A. Baldo, D. E. Freedman, R. H. Goldsmith, T. Goodson, M. L. Kirk, J. K. McCusker, J. P. Ogilvie, D. A. Shultz, S. Stoll, K. B. Whaley, "Exploiting Chemistry and Molecular Systems for Quantum Information Science", *Nature Reviews Chemistry* **2020**, *4*, 490–504, DOI 10.1038/s41570-020-0200-5.

[12] J. Lehmann, A. Gaita-Ariño, E. Coronado, D. Loss, "Quantum Computing with Molecular Spin Systems", *Journal of Materials Chemistry* **2009**, *19*, 1672–1677, DOI 10.1039/b810634g.

[13] A. Steane, "Quantum Computing", *Reports on Progress in Physics* **1998**, *61*, 117–173, DOI 10.1088/0034-4885/61/2/002.

[14] F. Troiani, M. Affronte, "Molecular Spins for Quantum Information Technologies", *Chemical Society Reviews* **2011**, *40*, 3119, DOI 10.1039/c0cs00158a.

[15] F. Ciccullo, A. Calzolari, K. Bader, P. Neugebauer, N. M. Gallagher, A. Rajca, J. van Slageren, M. B. Casu, "Interfacing a Potential Purely Organic Molecular Quantum Bit with a Real-Life Surface", *ACS Applied Materials & Interfaces* **2019**, *11*, 1571–1578, DOI 10.1021/acsami.8b16061.

[16] H. Guo, Q. Peng, X.-K. Chen, Q. Gu, S. Dong, E. W. Evans, A. J. Gillett, X. Ai, M. Zhang, D. Credgington, V. Coropceanu, R. H. Friend, J.-L. Brédas, F. Li, "High Stability and Luminescence Efficiency in Donor–acceptor Neutral Radicals Not Following the Aufbau Principle", *Nature Materials* **2019**, *18*, 977–984, DOI 10.1038/s41563-019-0433-1.

[17] X. Ai, E. W. Evans, S. Dong, A. J. Gillett, H. Guo, Y. Chen, T. J. H. Hele, R. H. Friend, F. Li, "Efficient Radical-Based Light-Bmitting Diodes with Doublet Emission", *Nature* **2018**, *563*, 536–540, DOI 10.1038/s41586-018-0695-9.

[18] M. B. Casu, "Nanoscale Studies of Organic Radicals: Surface, Interface, and Spinterface", *Accounts of Chemical Research* **2018**, *51*, 753–760, DOI 10.1021/acs.accounts.7b00612.

[19] R. Kakavandi, A. Calzolari, Y. B. Borozdina, P. Ravat, T. Chassé, M. Baumgarten, M. B. Casu, "Unraveling the Mark of Surface Defects on a Spinterface: The Nitronyl Nitroxide/TiO_2(110) Interface", *Nano Research* **2016**, *9*, 3515–3527, DOI 10.1007/s12274-016-1228-1.

[20] C. Arantes, E. T. Chernick, M. Gruber, M. L. M. Rocco, T. Chassé, R. R. Tykwinski, M. B. Casu, "Interplay between Solution Processing and Electronic Structure in Metal-free Organic Magnets Based on a Tempo Pentacene Derivative", *The Journal of Physical Chemistry C* **2016**, *120*, 3289–3294, DOI 10.1021/acs.jpcc.5b10028.

[21] F. Ciccullo, N. M. Gallagher, O. Geladari, T. Chassé, A. Rajca, M. B. Casu, "A Derivative of the Blatter Radical as a Potential Metal-Free Magnet for Stable Thin Films and Interfaces", *ACS Applied Materials & Interfaces* **2016**, *8*, 1805–1812, DOI 10.1021/acsami.5b09693.

[22] A. Caneschi, M. B. Casu, "Substrate-induced Effects in Thin Films of a Potential Magnet Composed of Metal-Free Organic Radicals Deposited on Si(111)", *Chemical Communications* **2014**, *50*, 13510–13513, DOI 10.1039/c4cc05990e.

[23] R. Kakavandi, S.-A. Savu, A. Caneschi, T. Chassé, M. B. Casu, "At the Interface between Organic Radicals and TiO_2(110) Single Crystals: Electronic Structure and Paramagnetic Character", *Chemical Communications* **2013**, *49*, 10103–10105, DOI 10.1039/c3cc45693e.

[24] R. Kakavandi, S.-A. Savu, A. Caneschi, M. B. Casu, "Paramagnetic Character in Thin Films of Metal-Free Organic Magnets Deposited on TiO_2(110) Single Crystals", *The Journal of Physical Chemistry C* **2013**, *117*, 26675–26679, DOI 10.1021/jp410038m.

[25] Z. Huang, Y. Zhang, Y. He, H. Song, C. Yin, K. Wu, "A Chemist's Overview of Surface Electron Spins", *Chemical Society Reviews* **2017**, *46*, 1955–1976, DOI 10.1039/c6cs00891g.

[26] H. M. Blatter, H. Lukaszewski, "A New Stable Free Radical", *Tetrahedron Letters* **1968**, *9*, 2701–2705, DOI 10.1016/S0040-4039(00)89678-1.

[27] F. A. Neugebauer, G. Rimmler, "ENDOR and Triple Resonance Studies of 1,4-dihydro-1,2,4-benzotriazinyl Radicals and 1,4-dihydro-1,2,4-benzotriazine Radical Cations", *Magnetic Resonance in Chemistry* **1988**, *26*, 595–600, DOI 10.1002/mrc.1260260712.

[28] K. Kolanji, L. Postulka, B. Wolf, M. Lang, D. Schollmeyer, M. Baumgarten, "Planar Benzo1,2- b:4,5- b'dithiophene Derivatives Decorated with Nitronyl and Imino Nitroxides", *The Journal of Organic Chemistry* **2019**, *84*, 140–149, DOI 10.1021/acs.joc.8b02499.

[29] J. P. Collman, N. K. Devaraj, C. E. D. Chidsey, "'Clicking' Functionality onto Electrode Surfaces", *Langmuir* **2004**, *20*, 1051–1053, DOI 10.1021/la0362977.

[30] T. Lummerstorfer, H. Hoffmann, "Click Chemistry on Surfaces: 1,3-Dipolar Cycloaddition Reactions of Azide-Terminated Monolayers on Silica", *The Journal of Physical Chemistry B* **2004**, *108*, 3963–3966, DOI 10.1021/jp049601t.

[31] L. Liang, D. Astruc, "The Copper(I)-Catalyzed Alkyne-azide Cycloaddition (CuAAC) 'Click' Reaction and Its Applications. An Overview", *Coordination Chemistry Reviews* **2011**, *255*, 2933–2945, DOI 10.1016/j.ccr.2011.06.028.

[32] E. A. Weiss, G. K. Kaufman, J. K. Kriebel, Z. Li, R. Schalek, G. M. Whitesides, "Si/SiO_2-Templated Formation of Ultraflat Metal Surfaces on Glass, Polymer, and Solder Supports: Their Use as Substrates for Self-Assembled Monolayers", *Langmuir* **2007**, *23*, 9686–9694, DOI 10.1021/la701919r.

[33] S. R. Forrest, "Ultrathin Organic Films Grown by Organic Molecular Beam Deposition and Related Techniques", *Chemical Reviews* **1997**, *97*, 1793–1896, DOI 10.1021/cr941014o.

[34] M. B. Casu, A. Schöll, K. R. Bauchspiess, D. Hübner, T. Schmidt, C. Heske, E. Umbach, "Nucleation in Organic Thin Film Growth: Perylene on Al_2O_3/Ni_3Al(111)", *The Journal of Physical Chemistry C* **2009**, *113*, 10990–10996, DOI 10.1021/jp809497h.

[35] M. B. Casu, X. Yu, S. Schmitt, C. Heske, E. Umbach, "Morphology of Perylene Thin Films on SiO_x/Si(100) and SiO_2/Si(100): A Spectroscopic and Microscopic Study of the Influence of the Preparation Parameters", *Chemical Physics Letters* **2009**, *479*, 76–80, DOI 10.1016/j.cplett.2009.08.015.

[36] J. R. Arthur, J. J. LePore, "GaAs, GaP, and $GaAs_xP_{1-x}$ Epitaxial Films Grown by Molecular Beam Deposition", *Journal of Vacuum Science and Technology* **1969**, *6*, 545–548, DOI 10.1116/1.1315677.

[37] E. Bauer, "Phänomenologische Theorie der Kristallabscheidung an Oberflächen. I", *Zeitschrift für Kristallographie* **1958**, *110*, 372–394, DOI 10.1524/zkri.1958.110.16.372.

[38] J. A. Venables, *Introduction to Surface and Thin Film Processes*, Cambridge University Press, **2000**, DOI 10.1017/cbo9780511755651.

[39] H. Hertz, "Ueber einen Einfluss des ultravioletten Lichtes auf die electrische Entladung", *Annalen der Physik und Chemie* **1887**, *267*, 983–1000, DOI 10.1002/andp.18872670827.

[40] W. Hallwachs, "Ueber den Einfluss des Lichtes auf electrostatisch geladene Körper", *Annalen der Physik und Chemie* **1888**, *269*, 301–312, DOI 10.1002/andp.18882690206.

[41] A. Einstein, "Über einen die Erzeugung und Verwandlung des Lichtes betreffenden heuristischen Gesichtspunkt", *Annalen der Physik und Chemie* **1905**, *322*, 132–148, DOI 10.1002/andp.19053220607.

[42] Nobel Media AB, Albert Einstein – Facts, https://www.nobelprize.org/prizes/physics/1921/einstein/facts/, retrieved: 07.05.2020.

[43] K. Siegbahn, K. Edvarson, "β-ray Spectroscopy in the Precision Range of 1: 105", *Nuclear Physics* **1956**, *1*, 137–159, DOI 10.1016/S0029-5582(56)80022-9.

[44] K. Siegbahn, C. Nordling, A. Fahlman, R. Nordberg, K. Hamrin, J. Hedman, G. Johansson, T. Bergmark, S.-E. Karlsson, I. Londgren, B. J. Lindberg, *ESCA: Atomic, Molecular and Solid State Structure Studied by Means of Electron Spectroscopy*, Almquist & Wiksell, Uppsala, **1967**.

[45] K. Siegbahn, C. Nordling, G. Johansson, J. Hedman, P. F. Hadén, K. Hamrin, U. Gelius, T. Bergmark, L. O. Werme, Manne R, Y. Baer, *ESCA Applied to Free Molecules*, North-Holland Publishing Company, Amsterdam, **1969**.

[46] H. Siegbahn, K. Siegbahn, "ESCA Applied to Liquids", *Journal of Electron Spectroscopy and Related Phenomena* **1973**, *2*, 319–325, DOI 10.1016/0368-2048(73)80023-4.

[47] Nobel Media AB, Kai M. Siegbahn – Facts, https://www.nobelprize.org/prizes/physics/1981/siegbahn/facts/, retrieved: 07.05.2020.

[48] M. P. Seah, W. A. Dench, "Quantitative Electron Spectroscopy of Surfaces: A Standard Data Base for Electron Inelastic Mean Free Paths in Solids", *Surface and Interface Analysis* **1979**, *1*, 2–11, DOI 10.1002/sia.740010103.

[49] S. Tanuma, C. J. Powell, D. R. Penn, "Calculations of Electorn Inelastic Mean Free Paths. Ii. Data for 27 Elements Over the 50-2000 Ev Range", *Surface and Interface Analysis* **1991**, *17*, 911–926, DOI 10.1002/sia.740171304.

[50] S. Tanuma, C. J. Powell, D. R. Penn, "Calculations of Electron Inelastic Mean Free Paths (IMFPS). IV. Evaluation of Calculated IMFPs and of the Predictive IMFP Formula TPP-2 for Electron Energies between 50 and 2000 Ev", *Surface and Interface Analysis* **1993**, *20*, 77–89, DOI 10.1002/sia.740200112.

[51] P. Willmott, *An Introduction to Synchrotron Radiation: Techniques and Applications*, John Wiley & Sons, Chichester, **2011**.

[52] W. Kossel, "Zum Bau der Röntgenspektren", *Zeitschrift für Physik* **1920**, *1*, 119–134, DOI 10.1007/BF01881031.

[53] W. Kossel, "Über die Ausbildung der Röntgenserien mit wachsender Ordnungszahl", *Zeitschrift für Physik* **1920**, *2*, 470–478, DOI 10.1007/BF01329979.

[54] R. d. L. Kronig, "Zur Theorie der Feinstruktur in den Rntgenabsorptionsspektren", *Zeitschrift für Physik* **1931**, *70*, 317–323, DOI 10.1007/BF01339581.

[55] R. d. L. Kronig, "Zur Theorie der Feinstruktur in den Rntgenabsorptionsspektren. III", *Zeitschrift für Physik* **1932**, *75*, 468–475, DOI 10.1007/BF01342238.

[56] G. Binnig, H. Rohrer, "The Scanning Tunneling Microscope", *Scientific American* **1985**, *253*, 50–58, DOI 10.1038/scientificamerican0885-50.

[57] Nobel Media AB, Gerd Binnig – Facts, https://www.nobelprize.org/prizes/physics/1986/binnig/facts/, retrieved: 04.11.2020.

[58] G. Binnig, C. F. Quate, C. Gerber, "Atomic Force Microscope", *Physical Review Letters* **1986**, *56*, 930–933, DOI 10.1103/PhysRevLett.56.930.

[59] G. Haugstad, *Atomic Force Microscopy*, John Wiley & Sons, **2012**, DOI 10.1002/9781118360668.

[60] E. Abbe, " Beiträge zur Theorie des Mikroskops und der mikroskopischen Wahrnehmung", *Archiv für Mikroskopische Anatomie* **1873**, *9*, 413–468, DOI 10.1007/bf02956173.

[61] In *Electron Microscopy*, John Wiley & Sons, **1997**, Chapter 2, pp. 305–497, DOI https://doi.org/10.1002/9783527614561.ch2.

[62] D. Necăs, P. Klapetek, "Gwyddion: An Open-source Software for Spm Data Analysis", *Central European Journal of Physics* **2012**, *1*, 181–188, DOI 10.2478/s11534-011-0096-2.

[63] E. Giangrisostomi, R. Ovsyannikov, F. Sorgenfrei, T. Zhang, A. Lindblad, Y. Sassa, U. B. Cappel, T. Leitner, R. Mitzner, S. Svensson, et al., "Low Dose Photoelectron Spectroscopy at BESSY II: Electronic structure of matter in its native state", *Journal of Electron Spectroscopy and Related Phenomena* **2018**, *224*, 68–78, DOI https://doi.org/10.1016/j.elspec.2017.05.011.

[64] A. Schöll, Y. Zou, M. Jung, T. Schmidt, R. Fink, E. Umbach, "Line Shapes and Satellites in High-resolution X-ray Photoelectron Spectra of Large Pi-conjugated Organic Molecules", *The Journal of Chemical Physics* **2004**, *121*, 10260–10267, DOI 10.1063/1.1807812.

[65] A. Schöll, Y. Zou, T. Schmidt, R. Fink, E. Umbach, "High-Resolution Photoemission Study of Different NTCDA Monolayers on Ag(111): Bonding and Screening Influences on the Line Shapes", *The Journal of Physical Chemistry B* **2004**, *108*, 14741–14748, DOI 10.1021/jp049005z.

[66] S.-A. Savu, M. B. Casu, S. Schundelmeier, S. Abb, C. Tönshoff, H. F. Bettinger, T. Chassé, "Nanoscale Assembly, Morphology and Screening Effects in Nanorods of Newly Synthesized Substituted Pentacenes", *RSC Advances* **2012**, *2*, 5112, DOI 10.1039/c2ra20168b.

[67] S.-A. Savu, I. Biswas, L. Sorace, M. Mannini, D. Rovai, A. Caneschi, T. Chassé, M. B. Casu, "Nanoscale Assembly of Paramagnetic Organic Radicals on Au(111) Single Crystals", *Chemistry – A European Journal* **2013**, *19*, 3445–3450, DOI https://doi.org/10.1002/chem.201203247.

[68] R. Nyholm, N. Mårtensson, "Evidence for $N_2N_3N_{45}$ Super Coster Kronig Processes in Metallic Nb, Mo, Ru and Rh", *Chemical Physics Letters* **1980**, *74*, 337–340, DOI 10.1016/0009-2614(80)85172-4.

[69] I. Cserny, L. Kövér, J. Tóth, M. F. Er, "Determination of Core Hole Lifetimes Using X-Ray Photoelectron Spectroscopy: Application and Use of Deconvolution Procedures", *Le Journal de Physique Colloques* **1987**, *48*, C9–1017–C9–1020, DOI 10.1051/jphyscol:19879182.

[70] O. Travnikova, R. F. Fink, A. Kivimäki, D. Céolin, Z. Bao, M. N. Piancastelli, "Disentangling the Complex Line Profiles in the Cl 2p Photoelectron Spectra of Cl_2", *Chemical Physics Letters* **2006**, *426*, 452–458, DOI 10.1016/j.cplett.2006.06.005.

[71] J. Hill, D. Royce, C. Fadley, L. Wagner, F. Grunthaner, "Properties of Oxidized Silicon As Determined by Angular-Dependent X-ray Photoelectron Spectroscopy", *Chemical Physics Letters* **1976**, *44*, 225–231, DOI 10.1016/0009-2614(76)80496-4.

[72] C. D. Wagner, L. E. Davis, M. V. Zeller, J. A. Taylor, R. H. Raymond, L. H. Gale, "Empirical Atomic Sensitivity Factors for Quantitative Analysis by Electron Spectroscopy for Chemical Analysis", *Surface and Interface Analysis* **1981**, *3*, 211–225, DOI 10.1002/sia.740030506.

[73] D. Briggs, M. P. Sheah, *Practical Surface Analysis*, John Wiley & Sons, Salle + Sauerländer, Chichester, New York, Brisbane, Toronto, Singapore, Aarau, Frankfurt am Main, Salzburg, **1990**.

[74] N. Koch, "Organic Electronic Devices and Their Functional Interfaces", *ChemPhysChem* **2007**, *8*, 1438–1455, DOI 10.1002/cphc.200700177.

[75] G. Heimel, I. Salzmann, S. Duhm, N. Koch, "Design of Organic Semiconductors from Molecular Electrostatics", *Chemistry of Materials* **2011**, *23*, 359–377, DOI 10.1021/cm1021257.

[76] N. Koch, "Electronic Structure of Interfaces with Conjugated Organic Materials", *Physica Status Solidi - Rapid Research Letters* **2012**, *6*, 277–293, DOI 10.1002/pssr.201206208.

[77] G. Heimel, S. Duhm, I. Salzmann, A. Gerlach, A. Strozecka, J. Niederhausen, C. Bürker, T. Hosokai, I. Fernandez-Torrente, G. Schulze, S. Winkler, A. Wilke, R. Schlesinger, J. Frisch, B. Bröker, A. Vollmer, B. Detlefs, J. Pflaum, S. Kera, K. J. Franke, N. Ueno, J. I. Pascual, F. Schreiber, N. Koch, "Charged and Metallic Molecular Monolayers through Surface-induced Aromatic Stabilization", *Nature Chemistry* **2013**, *5*, 187–194, DOI 10.1038/nchem.1572.

[78] N. Koch, N. Ueno, *The molecule-metal interface*, (Ed.: A. T. S. Wee), Wiley-VCH Verlag GmbH & Co. KGaA, Weinheim, **2013**.

[79] M. Hiramoto, M. Suezaki, M. Yokoyama, "Effect of Thin Gold Interstitial-layer on the Photovoltaic Properties of Tandem Organic Solar Cell", *Chemistry Letters* **1990**, *19*, 327–330, DOI 10.1246/cl.1990.327.

[80] M. Hiramoto, H. Fujiwara, M. Yokoyama, "Three-layered Organic Solar Cell with a Photoactive Interlayer of Codeposited Pigments", *Applied Physics Letters* **1991**, *58*, 1062–1064, DOI 10.1063/1.104423.

[81] A. F. Holleman, N. Wiberg, *Grundlagen und Hauptgruppenelemente*, De Gruyter, **2017**, DOI 10.1515/9783110495850.

[82] M. A. M. Leenen, V. Arning, H. Thiem, J. Steiger, R. Anselmann, "Printable Electronics: Flexibility for the Future", *Physica Status Solidi A* **2009**, *206*, 588–597, DOI 10.1002/pssa.200824428.

[83] M. Kaltenbrunner, M. S. White, E. D. Głowacki, T. Sekitani, T. Someya, N. S. Sariciftci, S. Bauer, "Ultrathin and Lightweight Organic Solar Cells with High Flexibility", *Nature Communications* **2012**, *3*, DOI 10.1038/ncomms1772.

[84] F. G. Brunetti, R. Kumar, F. Wudl, "Organic Electronics from Perylene to Organic Photovoltaics: Painting a Brief History with a Broad Brush", *Journal of Materials Chemistry* **2010**, *20*, 2934, DOI 10.1039/b921677d.

[85] M. Mas-Torrent, N. Crivillers, C. Rovira, J. Veciana, "Attaching Persistent Organic Free Radicals to Surfaces: How and Why", *Chemical Reviews* **2011**, *112*, 2506–2527, DOI 10.1021/cr200233g.

[86] S. Sanvito, "Molecular Spintronics", *Chemical Society Reviews* **2011**, *40*, 3336, DOI 10.1039/c1cs15047b.

[87] C. Herrmann, G. C. Solomon, M. A. Ratner, "Organic Radicals As Spin Filters", *Journal of the American Chemical Society* **2010**, *132*, 3682–3684, DOI 10.1021/ja910483b.

[88] K. Oyaizu, H. Nishide, "Radical Polymers for Organic Electronic Devices: A Radical Departure from Conjugated Polymers?", *Advanced Materials* **2009**, *21*, 2339–2344, DOI 10.1002/adma.200803554.

[89] L. Yuan, C. Franco, N. Crivillers, M. Mas-Torrent, L. Cao, C. S. S. Sangeeth, C. Rovira, J. Veciana, C. A. Nijhuis, "Chemical Control Over the Energy-Level Alignment in a Two-Terminal Junction", *Nature Communications* **2016**, *7*, DOI 10.1038/ncomms12066.

[90] V. Mugnaini, A. Calzolari, R. Ovsyannikov, A. Vollmer, M. Gonidec, I. Alcon, J. Veciana, M. Pedio, "Looking Inside the Perchlorinated Trityl Radical/Metal Spinterface through Spectroscopy", *The Journal of Physical Chemistry Letters* **2015**, *6*, 2101–2106, DOI 10.1021/acs.jpclett.5b00848.

[91] M. B. Casu, P. Cosseddu, D. Batchelor, A. Bonfiglio, E. Umbach, "A High-resolution Near-edge X-ray Absorption Fine Structure Investigation of the Molecular Orientation in the Pentacene/poly(3,4-ethylenedioxythiophene):poly(styrenesulfonate) Pentacene/system", *The Journal of Chemical Physics* **2008**, *128*, 14705, DOI 10.1063/1.2812649.

[92] M. Souto, V. Díez-Cabanes, L. Yuan, A. R. Kyvik, I. Ratera, C. A. Nijhuis, J. Cornil, J. Veciana, "Influence of the Donor Unit on the Rectification Ratio in Tunnel Junctions Based on Donor-Acceptor SAMs Using PTM Units As Acceptors", *Physical chemistry chemical physics : PCCP* **2018**, *20*, 25638–25647, DOI 10.1039/c8cp05488f.

[93] L. Yuan, N. Nerngchamnong, L. Cao, H. Hamoudi, E. del Barco, M. Roemer, R. K. Sriramula, D. Thompson, C. A. Nijhuis, "Controlling the Direction of Rectification in a Molecular Diode", *Nature Communications* **2015**, *6*, DOI 10.1038/ncomms7324.

[94] E. F. Ullman, L. Call, J. H. Osiecki, "Stable Free Radicals. VIII. New Imino, Amidino, and Carbamoyl Nitroxides", *The Journal of Organic Chemistry* **1970**, *35*, 3623–3631, DOI 10.1021/jo00836a008.

[95] E. F. Ullman, J. H. Osiecki, D. G. B. Boocock, R. Darcy, "Stable Free Radicals. X. Nitronyl Nitroxide Monoradicals and Biradicals As Possible Small Molecule Spin Labels", *Journal of the American Chemical Society* **1972**, *94*, 7049–7059, DOI 10.1021/ja00775a031.

[96] F. Ciccullo, M. Glaser, M. S. Sättele, S. Lenz, P. Neugebauer, Y. Rechkemmer, J. van Slageren, M. B. Casu, "Thin Film Properties and Stability of a Potential Molecular Quantum Bit Based on Copper(II)", *Journal of Materials Chemistry C* **2018**, *7*, 2074, DOI 10.1039/C8TC02610F.

[97] T. Bürgi, "Properties of the Gold-Sulphur Interface: From Self-assembled Monolayers to Clusters", *Nanoscale* **2015**, *7*, 15553–15567, DOI 10.1039/c5nr03497c.

Appendices

A. Thermally and Magnetically Robust Triplet Ground State Diradical

Reprinted with permission from
N. Gallagher, H. Zhang, T. Junghoefer, E. Giangrisostomi, R. Ovsyannikov, M. Pink, S. Rajca, M. B. Casu, A. Rajca, "Thermally and Magnetically Robust Triplet Ground State Diradical", *Journal of the American Chemical Society* **2019**, *141*, 4764–4774, DOI 10.1021/jacs.9b00558.

http://pubs.acs.org/articlesonrequest/AOR-w5JEhBGfUFbsQg2zvINV

JACS
JOURNAL OF THE AMERICAN CHEMICAL SOCIETY
Article
Cite This: J. Am. Chem. Soc. 2019, 141, 4764−4774
pubs.acs.org/JACS

Thermally and Magnetically Robust Triplet Ground State Diradical

Nolan Gallagher,[†] Hui Zhang,[†] Tobias Junghoefer,[§] Erika Giangrisostomi,[⊥] Ruslan Ovsyannikov,[⊥] Maren Pink,[‡] Suchada Rajca,[†] Maria Benedetta Casu,*[,§] and Andrzej Rajca*[,†]

[†]Department of Chemistry, University of Nebraska, Lincoln, Nebraska 68588-0304, United States
[§]Institute of Physical and Theoretical Chemistry, University of Tübingen, 72076 Tübingen, Germany
[‡]Department of Chemistry, Indiana University, Bloomington, Indiana 47405-7102, United States
[⊥]Helmholtz-Zentrum Berlin für Materialien und Energie (HZB), Albert-Einstein-Str 15, 12489 Berlin, Germany

Supporting Information

ABSTRACT: High spin (S = 1) organic diradicals may offer enhanced properties with respect to several emerging technologies, but typically exhibit low singlet triplet energy gaps and possess limited thermal stability. We report triplet ground state diradical **2** with a large singlet−triplet energy gap, $\Delta E_{ST} \geq 1.7$ kcal mol^{-1}, leading to nearly exclusive population of triplet ground state at room temperature, and good thermal stability with onset of decomposition at ∼160 °C under inert atmosphere. Magnetic properties of **2** and the previously prepared diradical **1** are characterized by SQUID magnetometry of polycrystalline powders, in polystyrene glass, and in other matrices. Polycrystalline diradical **2** forms a novel one-dimensional (1D) spin-1 (S = 1) chain of organic radicals with intrachain antiferromagnetic coupling of $J'/k = -14$ K, which is associated with the N···N and N···O intermolecular contacts. The intrachain antiferromagnetic coupling in **2** is by far strongest among all studied 1D S = 1 chains of organic radicals, which also makes 1D S = 1 chains of **2** most isotropic, and therefore an excellent system for studies of low-dimensional magnetism. In polystyrene glass and in frozen benzene or dibutyl phthalate solution, both **1** and **2** are monomeric. Diradical **2** is thermally robust and is evaporated under ultrahigh vacuum to form thin films of intact diradicals on silicon substrate, as demonstrated by X-ray photoelectron spectroscopy. Based on C−K NEXAFS spectra and AFM images of the ∼1.5 nm thick films, the diradical molecules form islands on the substrate with molecules stacked approximately along the crystallographic a-axis. The films are stable under ultrahigh vacuum for at least 60 h but show signs of decomposition when exposed to ambient conditions for 7 h.

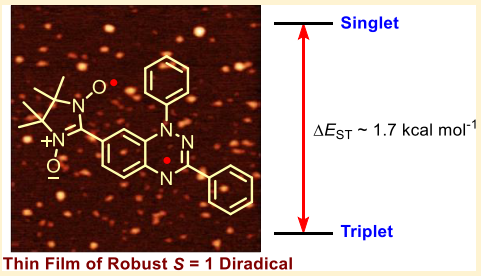

INTRODUCTION

Open-shell organic molecules with high-spin ground states and large energy gaps between the high-spin ground state and low-spin excited states possess unique, intriguing characteristics that are not only of fundamental interest but also have significant potential for numerous advanced technological applications. Notably, these molecules have long been considered the holey grail of purely organic magnets,[1−5] and recently have emerged as promising building blocks for organic spintronics,[6] spin filters,[7] sensors,[8] memory devices,[9] and probing quantum interference effects in molecular conductance.[10] Although the design principle has been well laid out,[11,12] such high-spin molecules with strong ferromagnetic interactions between unpaired electrons and persistence at room temperature remain highly uncommon,[13−16] and triplet ground state diradicals with robust thermal stabilities are especially rare.[17−19] The advancement in the design and synthesis of these exotic molecules will be crucial to the development of advanced organic magnetic materials and devices.

Recently, we reported triplet ground state diradicals with robust thermal stabilities, such as tetraazacyclophane diradical dication (TDD) and diradical **1** (Figure 1).[17,18] To our knowledge, these are the only two such diradicals that are well characterized with respect to stability by thermogravimetric analysis (TGA). Both TDD and **1** start decomposing at approximately 180 °C under nitrogen atmosphere and neutral diradical **1** could be sublimed under high vacuum at 140 °C without decomposition.

While these high-spin diradicals possess remarkable thermal properties, they are not fully populated in the high-spin state at room temperature. The singlet triplet energy gap, ΔE_{ST}, of both diradicals is only about 0.5 kcal mol^{-1}, as determined by quantitative EPR spectroscopy and SQUID magnetometry, which is similar to thermal energy at room temperature ($RT \approx$ 0.6 kcal mol^{-1}).[17,18] In such a case, there is a significant depopulation of the triplet ground state at room temperature and above, and thus the unique magnetic properties of the high-spin state with extra-large magnetic moment are compromised at ambient temperatures.

Received: January 16, 2019
Published: February 28, 2019

DOI: 10.1021/jacs.9b00558
J. Am. Chem. Soc. 2019, 141, 4764−4774

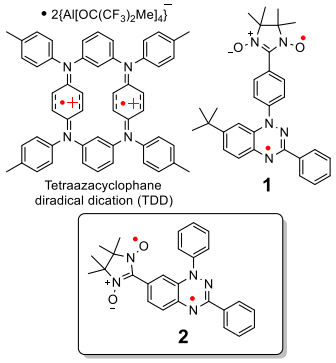

Figure 1. Thermally robust triplet ground state diradicals with onset of decomposition at $T \geq 160$ °C based upon TGA.

To rectify this deficiency, we designed diradical **2** (Figure 1) and preliminarily computed its magnetic properties. The DFT calculations suggested an increased ΔE_{ST} by a factor of ∼2.5, compared to **1**, and an estimated ∼95+% occupancy of the triplet ground state at room temperature.[17] We anticipated diradical **2** to possess both superior magnetic and excellent thermal properties, providing a novel high-spin diradical with robust high temperature stability and near-full occupation of the triplet ground state at ambient temperatures.

The potential of organic radicals in the development of organic electronics hinges upon their processability. The capacity of a molecule to form contacts or to evaporate onto a substrate without degradation is a critical prerequisite for device fabrication. In this regard, it is important to test the robustness of diradical **2** toward evaporation. Controlled evaporation of a diradical is considered very challenging, and to our knowledge, it has not been reported in literature. Achieving the first thin film of a high-spin diradical with nearly full-occupation of the triplet ground state at ambient temperature would be a significant step forward, providing exciting new avenues for the development of organic electronics.

Here we report the synthesis and study of high spin diradical **2** (Figure 1). As predicted, **2** has a large ΔE_{ST} of ≥1.7 kcal mol^{-1}, much larger than the thermal energy at room temperature, thus possessing a triplet ground state that is nearly exclusively populated (98+%) at room temperature. For comparison, we characterize both **1** and **2** by SQUID magnetometry in dilute matrices and as polycrystalline powders. Notably, polycrystalline diradical **2** forms a novel one-dimensional (1D) spin-1 ($S = 1$) chain consisting of close contacts between the heteroatoms (oxygens and nitrogens) of radical moieties with the largest spin densities. The 1D chain is distinctly different from those previously reported,[18,20] and it is the first observed 1D system consisting of nitronyl nitroxide and Blatter radicals. Importantly, the observed intrachain exchange coupling constant of $J'/k = -14$ K is much larger than the previously studied 1D $S = 1$ chains, with the next strongest $J'/k = -5.4$ K found in TDD.[18] Diradical **2** is thermally robust, with an onset of decomposition at ∼160 °C under inert atmosphere and is thermally evaporated under ultrahigh vacuum to form thin films on SiO_2/Si(111) wafers, with X-ray photoelectron spectroscopy suggesting the presence of intact **2**. The C−K NEXAFS spectra and AFM images of the films indicates the diradical molecules form islands on the substrate with molecules stacked approximately along the crystallographic *a*-axis. Diradical **2** possesses an unprecedented combination of a triplet ground state that is nearly exclusively populated at room temperature and a novel 1D $S = 1$ antiferromagnetic chain, with remarkable thermal stability and suitability for thin film deposition via thermal evaporation. The films are stable under ultrahigh vacuum for at least 60 h but show signs of decomposition when exposed to ambient conditions for 7 h. We present here the preparation and characterization of the first thin film of high spin organic diradical.

RESULTS AND DISCUSSION

Synthesis of 2. Our synthetic approach to **2**, follows closely the synthesis of diradical **1** and it takes advantage of the unusual stability of the Blatter radical, such that it may tolerate many common reaction conditions (Scheme 1).[21] Cyano-

Scheme 1. Synthesis of Diradical 2

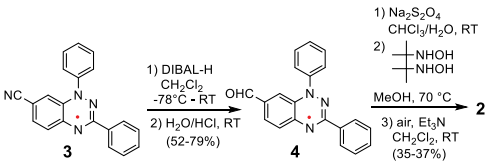

Blatter radical **3** is synthesized by adopting procedures available in the literature, as outlined in detail in the Supporting Information.[17,22−25] Treatment of **3** with DIBAL-H followed by hydrolysis of the imine group provides formyl-Blatter radical **4**. Radical **4** is initially reduced to the corresponding *leuco*-amine-aldehyde, or alternatively, it is directly condensed with 2,3-bis(hydroxyamino)-2,3-dimethyl-butane;[26] the resultant adduct is oxidized in air to provide diradical **2**, which is purified by normal phase chromatography (silica gel) at ambient conditions.

X-ray Crystallography. The structure of diradical **2** consists of two nonequivalent molecules, A and B, and one molecule of solvent (CH_2Cl_2). In molecule A, the nitronyl nitroxide radical moiety is nearly coplanar with the Blatter radical π-system with the corresponding N−C8A−C1A−C torsions in the −13−(−15)° range, while in molecule B, there is considerably greater out-of-plane twisting with the corresponding torsions in the 28−30° range (Figure S1, SI). In the crystal, molecules A and B pack in an alternating fashion into one-dimensional chains (along the crystallographic *a*-axis) with close intermolecular N···N and O···N contacts (Figure 2, bottom plot).

Within the π-conjugated pathway in the diradical, there are two dihedral angles of ∼49° and 30° connecting the 1,2,4-benzotriazinyl and nitronyl nitroxide moieties in **1**,[17] as opposed to one dihedral angle (or one torsion) in **2**. The radicals in **2** are then more coplanar than in **1**. The DFT geometry optimizations using UB3LYP/6-31G(d) level of theory[27] and starting from either conformation as observed in molecule A or B give more coplanar structures that are similar to molecule A, with N−C8−C1−C torsions in the ±13.7−(±13.8)° ranges (SI, Table S6).

EPR Spectroscopy. The EPR spectrum of **2** in glassy matrices shows exclusively a triplet diradical, without a trace of monoradical impurities (Figure 3 and Table 1). As expected,

DOI: 10.1021/jacs.9b00558
J. Am. Chem. Soc. 2019, 141, 4764−4774

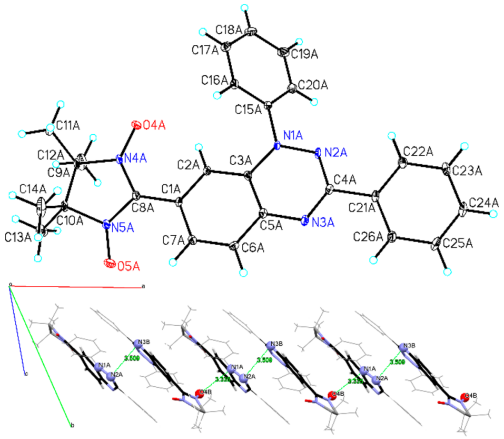

Figure 2. (Top) Single crystal X-ray structure of diradical **2** with molecule A shown only; carbon, nitrogen, and oxygen atoms are depicted with thermal ellipsoids set at the 50% probability level. (Bottom) Packing of molecules A and B into a one-dimensional $S = 1$ antiferromagnetic chain; nitrogens and oxygens with large positive spin densities and forming close intermolecular contacts, N2A···N3B = 3.509 Å and O4B···N1A = 3.335 Å, are emphasized as ball-and-stick. Additional information can be found in the Supporting Information (Figures S1–S3 and Table S1).

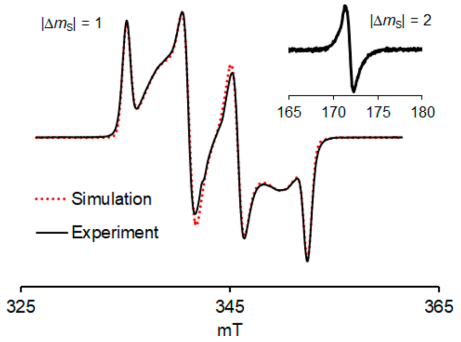

Figure 3. EPR (ν = 9.65 GHz) spectrum of 1.2 mM diradical **2** in 4:1 toluene/chloroform glass at 153 K. The $\Delta m_s = 2$ transition is shown as an inset. Simulation parameters: $g_{xx} = 2.0072$, $g_{yy} = 2.0026$, $g_{zz} = 2.0052$, $|D/hc| = 8.08 \times 10^{-3}$ cm^{-1}, $|E/hc| = 1.17 \times 10^{-3}$ cm^{-1}; line widths: $LW_x = 32.0$ MHz, $LW_y = 100.0$ MHz, $LW_z = 24.9$ MHz. For EPR spectra (with simulations) of **2** in polystyrene matrix at 295 K, see: SI, Figure S7.

the spectral simulation[28] reveals much greater spectral width, $2|D/hc| = 1.616 \times 10^{-2}$ for **2** vs $2|D/hc| = 4.64 \times 10^{-3}$ for **1**,[17] because of relative proximity of the unpaired electrons and the nearly coplanar nitronyl nitroxide and benzotriazinyl moieties in **2**. The B3LYP/EPR-II calculations estimate the relative values of D as $D/hc = +1.20 \times 10^{-2}$ cm^{-1} for **2** and $D/hc = -5.47 \times 10^{-3}$ cm^{-1} for **1**.[29] The computed D-tensor components are not only overestimated, as typical for these type of diradicals, but also the positive sign of D/hc in **2** is inconsistent with its experimental EPR spectrum (Supporting Information).[30,31]

SQUID magnetometry: triplet ground states of 1 and 2. We estimate singlet triplet energy gaps in polycrystalline **1** and **2** by fitting the χT vs T data in the T = 1.8–320 K and 70–320 K ranges, respectively, to the diradical model (eq 1).[4a]

$$\chi T = (1.118T/H)N\{2\sinh(a)/[1 + 2\cosh(a) + \exp((-2J/k)/T)]\} \quad (1)$$

where $a = 1.345(H/(T - \theta))$.

For **1**, an average of three fits (Figure 4 and SI, Figure S8) gives $2J/k = 252 \pm 10$ K, corresponding to $\Delta E_{ST} = 0.50 \pm 0.02$ kcal mol^{-1} (Table 1), which is in good agreement with $2J/k = 234 \pm 36$ K, obtained previously by quantitative EPR spectroscopy in dilute solutions/matrices.[17] For **2**, a much larger $2J/k = 876 \pm 36$ K is obtained as an average of four fits (Figure 5 and SI: Figure S9 and Table S2), corresponding to $\Delta E_{ST} = 1.74 \pm 0.07$ kcal mol^{-1} (Table 1). Although the measured values of $\chi T > 0.75$ emu K mol^{-1} and fitted values of $\Delta E_{ST} > 0$ would suggest triplet ground states for **1** and **2**, these results are dependent on an accurate weight of the SQUID

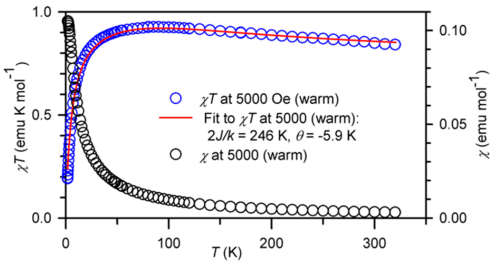

Figure 4. SQUID magnetometry of polycrystalline (solid) diradical **1**: plots of χT vs T and at χ vs T at H = 5000 Oe in the warming mode. χT vs T data, corrected for diamagnetism, are fit to a diradical model (eq 1), using two variable parameters: singlet triplet energy gap, $2J/k$, mean-field correction for intermolecular interactions between the radicals, θ. The values of standard error, *SE*, and parameter dependence, *DEP*, are provided; goodness of fit may be measured by standard error of estimate, *SEE*. Fitting parameters: $2J/k = 246$ K (SE = 8), $\theta = -5.89$ K (*SE* = 0.08), *DEP* = 0.0236, $R^2 = 0.9941$, *SEE* = 0.0175. Complete set of magnetic data (and fits) for solid diradical **1** may be found in the SI (Figure S8 and eq S1).

Table 1. Summary of Experimental and DFT-Computed Singlet–Triplet Energy Gaps and Selected EPR Parameters for Diradicals 1 and 2

	ΔE_{ST} (kcal mol^{-1})		D/hc (10^{-3} cm^{-1})		E/hc (10^{-3} cm^{-1})		g[a]	
	SQUID[b]	DFT[c]	EPR	DFT[d]	EPR	DFT[d]	EPR	DFT[d]
1	+0.50 ± 0.02	+1.4	2.32	−5.47	0.14	−1.56	2.0044	2.0053
2	+1.74 ± 0.07	+3.5	8.08	+12.0	1.17	+3.25	2.0050	2.0053

[a]Isotropic $g = (g_x + g_y + g_z)/3$. [b]ΔE_{ST} is determined by SQUID of solid diradicals **1** and **2**. [c]BS-DFT-computed ΔE_{ST} at the UB3LYP/6-31G(d,p) level.[17] [d]Computed at the B3LYP/EPR-II level using ORCA.

DOI: 10.1021/jacs.9b00558
J. Am. Chem. Soc. 2019, 141, 4764–4774

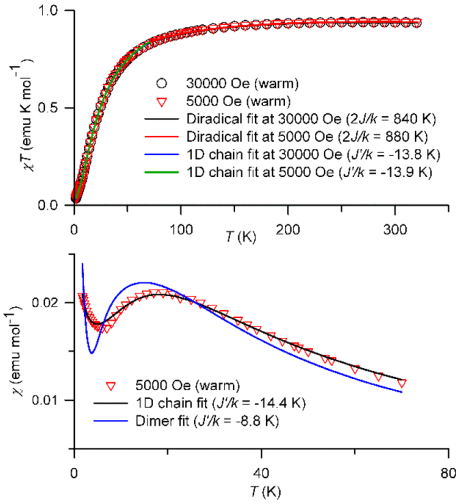

Figure 5. SQUID magnetometry of polycrystalline (solid) diradical **2**: plots of χT vs T and at χ vs T at various applied magnetic fields, H = 300 000 and 5000 Oe in the warming mode and H = 500 Oe in the cooling mode. Numerical fits to the diradical model (eq 1) for T = 70−320 K are carried out with two variable parameters: singlet triplet energy gap, $2J/k$ and mean-field correction for intermolecular interactions between the radicals, θ. Numerical fits to 1D chain (eq 2) or dimer (eq S2A,B, SI) models for T = 1.8−70 K are carried out with three variable parameters: intermolecular Heisenberg exchange coupling constant, J'/k, weight factor, N, and weight factor for isolated S = 1 diradical, N_{imp}. The results for numerical fits are summarized in Table 2 and in the Supporting Information (Table S3 and Figures S9 and S10).

sample. Also, the fitting of χT vs T for polycrystalline **1** and **2** require relatively large absolute values of negative mean-field parameters, $\theta \approx -6$ and -14 K, thus suggesting significant antiferromagnetic interactions between the S = 1 diradicals.

With such large values of $|\theta|$, magnetization data at low temperatures could not be fit adequately to Brillouin functions, thus sample-weight independent evidence for triplet ground state could not be obtained. Therefore, we prepare dilute diradicals in glassy matrices by dispersing **1** and **2** in polystyrene.

For the dilute samples of **1** and **2** in polystyrene, two-parameter fits to χT vs T data in the T = 1.8−370 and 1.8−360 K ranges give somewhat lower values of $2J/k$ = 165 ± 18 K and $2J/k$ = 838 ± 78 K (vs polycrystalline diradicals), as an average of two and three fits, respectively (Figure 6 and SI: Figures S11 and S12). Most importantly, these fits indicate that the value of θ is very small and practically negligible.

The magnetization (M) versus magnetic field (H) data, that is M versus $H/(T - \theta)$, at low temperatures (T = 1.8−5 K) provide excellent fits to the Brillouin functions with a small negative mean-field parameter, $|\theta| \leq 0.05$ K. Such fits have two variable parameters: total spin (S) and magnetization at saturation (M_{sat}); the mean-field parameter θ is adjusted until the M/M_{sat} versus $H/(T - \theta)$ plots overlap at all temperatures. The values of $S \approx 1.0$ (0.978−1.012), determined from the curvature of the Brillouin plots, unequivocally indicate the triplet (S = 1) ground state for both diradicals (Figure 6 and SI: Figures S11 and S12). Since the values of M_{sat} = 0.74 and

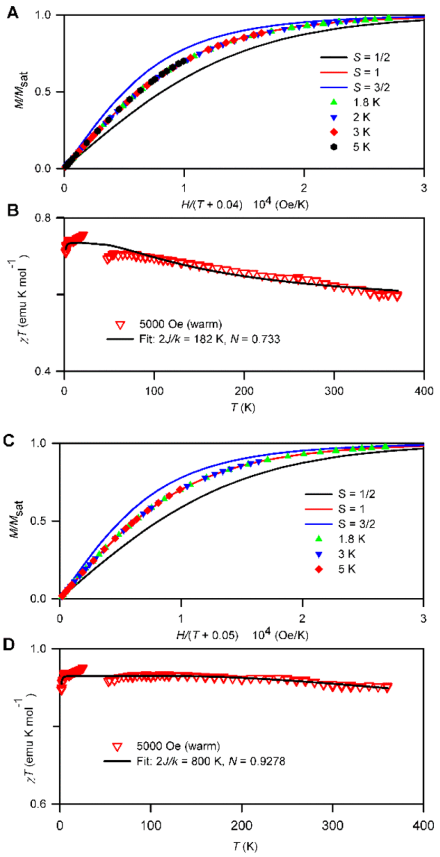

Figure 6. SQUID magnetometry of 30−40 mM diradicals **1** (A and B) and **2** (C and D) in polystyrene matrix. Plots A and C: M/M_{sat} vs $H/(T - \theta)$ plots, where θ = −0.04 or −0.05 K, at T = 1.8−5 K (symbols) and the Brillouin curves corresponding to S = 1/2−3/2 (lines). Plots B and D: χT vs T data at H = 5000 Oe in the warming mode were fit to a diradical model (eq 1), using two variable parameters: singlet−triplet energy gap, $2J/k$, mean-field correction for intermolecular interactions between the radicals, θ. The values of standard error, *SE*, and parameter dependence, *DEP*, coefficient of determination, R^2, and standard error of estimate, *SEE*. Fitting parameters: diradical **1**: $2J/k$ = 182 K (*SE* = 5), N = 0.733 (*SE* = 0.001), *DEP* = 0.5311, R^2 = 0.9441, *SEE* = 0.0109; diradical **2**: $2J/k$ = 800 K (SE = 20), N = 0.9278 (*SE* = 0.0008), *DEP* = 0.3336, R^2 = 0.746, *SEE* = 0.0066. Further details are reported in the SI: Table S3, Figures S11 and S12.

0.925 μ_B for **1** and **2**, respectively (μ_B = Bohr magneton) match well the corresponding values of N = 0.73 and 0.93 obtained from fits of χT vs T data to the diradical model, this implies that both diradicals are pure and N < 1.00 is obtained because of a "weighing error" of submilligram amounts of diradicals. The values of θ < 0 K and $|\theta| \approx 0$ K imply nearly negligible, and almost certainly intermolecular, antiferromagnetic coupling.

We also investigate dilute diradicals in benzene and dibutyl phthalate (DBP) matrices. Similar results are obtained for **1** and **2** in benzene and **2** in DBP; however, the fits to the Brillouin functions are less satisfactory because of much larger

DOI: 10.1021/jacs.9b00558
J. Am. Chem. Soc. 2019, 141, 4764−4774

Table 2. Fitting Parameters for SQUID Data for Polycrystalline Diradical 2

	T [K]	Fit	H [Oe]	2J/k or J′/k (SE, DEP)[a] [K]	θ (SE, DEP)[b] [K]	N (SE, DEP)[c]	SEE[d]	R²[e]
χT	70−320	Diradical	30000	844 (14, 0.178)	−14.05 (0.08, 0.178)	NA	0.0028	0.9933
			5000	878 (16, 0.172)	−13.87 (0.09, 0.172)	NA	0.0029	0.9926
	1.8−70	1D-chain	30000	−13.87 (0.06, 0.902)	0.48 (0.03, 0.701)	1.093 (0.002, 0.842)	0.0026	0.9999
			5000	−14.00 (0.07, 0.903)	0.48 (0.04, 0.700)	1.100 (0.003, 0.843)	0.0030	0.9999
		Dimer	30000	−9.329 (0.23, 0.767)	1.33 (0.03, 0.308)	0.97 (0.01, 0.725)	0.0240	0.9927
			5000	−9.590 (0.25, 0.757)	1.70 (0.01, 0.228)	0.97 (0.2, 0.733)	0.0269	0.9909
χ	1.8−70	1D-chain	5000	−14.32 (0.11, 0.926)	0.52 (0.01, 0.481)	1.116 (0.008, 0.918)	0.0003	0.9871
			500	−14.00 (0.10, 0.927)	0.41 (0.01, 0.532)	1.068 (0.007, 0.917)	0.0002	0.989
		Dimer	5000	−5.49 (0.25, 0.866)	1.56 (0.02, 0.749)	0.57 (0.04, 0.676)	0.0048	-
			500	−7.73 (0.59, 0.769)	1.97 (0.01, 0.608)	0.77 (0.10, 0.562)	0.0089	-
	T [K]	Fit	H [Oe]	J′/k (SE, DEP)[a] [K]	N (SE, DEP)[c]	N_{imp} (SE, DEP)[f]	SEE[d]	R²[e]
χT	1.8−70	1D-chain	30000	−13.82 (0.07, 0.9080)	1.086 (0.002, 0.8328)	0.0110 (0.0010, 0.832)	0.0028	0.9999
			5000	−13.85 (0.07, 0.8920)	1.094 (0.003, 0.8333)	0.0082 (0.0009, 0.752)	0.0032	0.9999
		Dimer	30000	−10.86 (0.07, 0.8817)	0.967 (0.003, 0.7830)	0.0696 (0.0014, 0.795)	0.0043	0.9998
			5000	−10.42 (0.10, 0.8542)	0.974 (0.005, 0.7751)	0.0537 (0.0018, 0.709)	0.0067	0.9994
χ	1.8−70	1D-chain	5000	−14.43 (0.11, 0.9194)	1.117 (0.007, 0.9079)	0.0108 (0.0002, 0.485)	0.0002	0.9899
			500	−14.03 (0.08, 0.9182)	1.067 (0.006, 0.9063)	0.0077 (0.0001, 0.504)	0.0002	0.9930
		Dimer	5000	−8.75 (0.26, 0.7387)	0.861 (0.028, 0.6951)	0.044 (0.001, 0.240)	0.0017	0.4916
			500	−8.36 (0.28, 0.7173)	0.814 (0.030, 0.6845)	0.038 (0.001, 0.175)	0.0018	0.3333

[a] J/k or J'/k, Heisenberg exchange coupling constant; $2J/k$ = singlet triplet energy gap in Kelvin; *SE*, standard error; *DEP*, parameter dependence. [b] θ, mean-field correction. [c] *N*, weight factor. [d] *SEE*, standard error of estimate. [e] R^2, coefficient of determination. [f] N_{imp}, weight factor for isolated $S = 1$ diradical.

$|\theta| = 0.6-0.8$ K observed in these matrices (SI, Table S3, Figures S13−S15).

SQUID Magnetometry: 1D Antiferromagnetic $S = 1$ Chain for Polycrystalline Diradical 2. For polycrystalline **1**, the χ vs T plot shows continuously increasing χ with decreasing T. For **2**, a broad maximum at about 19 K in χ vs T data is observed, thus suggesting relatively strong intermolecular coupling between $S = 1$ diradicals **2** (Figures 4 and 5). Two limiting models for such antiferromagnetic coupling are considered: (1) one-dimensional (1-D) Heisenberg chains of $S = 1$ diradicals (spin-1 chain) (eq 2) and (2) pairs of $S = 1$ diradicals (dimer) (eq S2, SI).[32,33] The numerical fits to these models are obtained at low temperatures, $T = 1.8-70$ K, to ensure that diradical **2** is almost completely in its $S = 1$ ground state at the highest temperature (70 K), which is significantly below $2J/k \approx 880$ K.

Initially, we fit χT vs T data in the low temperature range, $T = 1.8-70$ K, using eq 2 and eq S2B (Table 2, Figure 5). 3-Parameter fits with the following variable parameters, intermolecular Heisenberg exchange coupling constant, J'/k, weight factor, *N*, and weight factor for isolated $S = 1$ diradical, N_{imp}, are in excellent agreement with 1D-chain model (coefficient of determination, $R^2 = 0.9999$ and standard error of estimate, *SEE* = 0.0028 or 0.0032); fits to an $S = 1$ dimer model are less satisfactory ($R^2 = 0.9998$ or 0.9994 and *SEE* = 0.0043 or 0.0067). Even larger differences in fit quality between the two models are observed when the variable parameter N_{imp} is replaced with the mean-field parameter $\theta > 0$ (Table 2).

The χ versus T data provide a more sensitive measure of fit quality for different models. The fits to a 1D-chain (eq 2) provide *SEE* = 0.0002−0.0003, while the $S = 1$ dimer fits (SI, eq S2A) are much less satisfactory, with much larger *SEE* = 0.0017−0.0089 (Table 2, Figure 5).

$$\chi 1D = N\{[3/(2k(T-\theta))][(2 + a_1 \times K + a_2 \times K^2) /(3 + b_1 \times K + b_2 \times K^2 + b_3 \times K^3)]\} + N_{imp}(1.118/H)\{2\sinh(a)/[1 + 2\cosh(a)]\} \quad (2)$$

where $a_1 = 0.0194$, $a_2 = 0.777$, $b_1 = 4.346$, $b_2 = 3.232$, $b_3 = 5.634$, $K = -J'/kT$ and $a = 1.345(H/(T-\theta))$.

The 1D antiferromagnetic chain of weakly coupled $S = 1$ diradicals in polycrystalline **2** is consistent with the crystal packing, as discussed above (Figure 2). Two types of short N2A···N3B = 3.509 Å (dimer I) and O4B···N1A = 3.335 (dimer II) contacts between molecules A and B are identified. Because all nitrogens and oxygens in diradical **2** bear large positive spin densities, such contacts are anticipated to give rise to intermolecular antiferromagnetic coupling between pairs of molecules A and B within 1D chain

We carried out DFT calculations, based upon the broken symmetry approach, at the fixed X-ray geometry for molecules A and B forming dimers I (AB) and II (BA) as well as trimers (ABA and BAB),[18,34] to determine the values of J'/k. The computed J'/k are summarized in Table 3.

The agreement between the computed values of J'/k and the experimental $J'/k = -14$ K is reasonable, especially when accuracy of the DFT computations is considered.[35] Also, while the alternating chain of J'/k may not be excluded, it is

Table 3. B3LYP-Computed Values of Intrachain J'/k for 2[a]

	Dimer		Trimer	
	I (AB)	II (BA)	ABA	BAB
J'/k, 6-31G(d) [K]	−14.1	−12.7	−7.2	−12.0
J'/k, 6-311++G(d,p) [K]	−19.8	−9.2	–	–

[a] Broken symmetry triplets and quintets for dimers and trimers are used, respectively. Further details may be found in the SI (Table S8).

DOI: 10.1021/jacs.9b00558
J. Am. Chem. Soc. 2019, 141, 4764−4774

predicted by computation that the degree of alternation is relatively small and in agreement with the experiment.

Stability. Diradical **2** possesses excellent stability at ambient conditions, not only in air-saturated solution at ambient conditions (Figure S4, SI) but also on silica gel. Notably, solid **2** shows no signs of decomposition after storing on air at −20 °C for more than 2 years. In addition, solid **2** shows remarkable stability under vacuum annealing at 100 °C for 24 h, and we found that such condition effectively removes the solvent of crystallization (CH_2Cl_2) from the crystal lattice (SI, Figure S6). Thus, the annealed polycrystalline **2** is obtained for the EPR spectroscopy (Figure 3) and other studies, including TGA (Figure 7), as well as for thin films

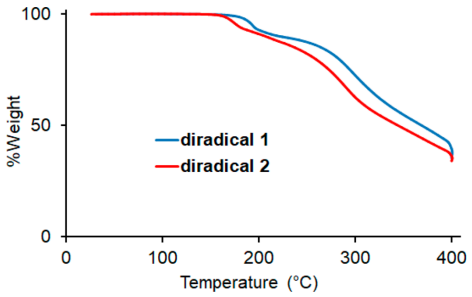

Figure 7. Thermogravimetric analysis (TGA) of diradicals **1** and **2** under N_2; heating rate = 5 °C min^{-1}. Further details may be found in the SI (Figures S4−S6).

(Figures 8−10). Thermogravimetric analysis data suggest that thermal decomposition of **2** starts at 160 °C, at a temperature that is about 15 °C lower than that for diradical **1** (Figure 7).

Thin Films of 2 on SiO_2/Si(111) Substrate. We test the robustness of diradical **2** toward evaporation. This aspect is important in view of the potential applications of this diradical in electronics. The ability to attach a molecule to a contact or to evaporate it onto a substrate, without degradation, is a requirement for device fabrication. Controlled evaporation of diradicals is considered very challenging, and not yet reported in literature. The presence of two radical sites, in particular the cross-conjugated diradicals with significant spin density within the π-system connecting two radical sites, such as in **2**, could potentially increase their instability during evaporation.[36]

We prepare thin films of diradical **2** on SiO_2/Si(111) wafers by using organic molecular beam deposition (OMBD) that allows for controlled evaporation and the consequent deposition of molecules onto a substrate, tuning the preparation conditions in ultrahigh vacuum (UHV).[37] We investigate the films by using X-ray photoelectron spectroscopy (XPS). XPS is an effective and powerful tool for investigation of organic and organic radical thin films.[38] Besides providing insight into the occupied states, it is element-sensitive, and it can also deliver quantitative information on the stoichiometric composition of the films,[39] due to the high sensitivity of the signal to the concentration of the emitting atoms. In addition, the features contributing to the spectroscopic lines are sensitive to the different chemical environment of the atoms of the same element. These assets are the basis for our analysis of core level spectra of a multilayer of **2** (Figure 8).

We focus on the C 1s and N 1s spectra, because the O 1s spectrum is a convolution of the substrate and the molecule

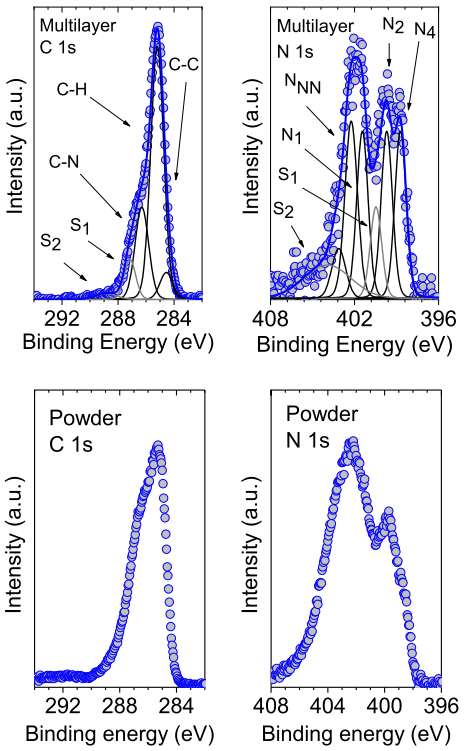

Figure 8. C 1s and N 1s core level XPS spectra of a multilayer of diradical **2** deposited on SiO_2/Si(111) wafers (top plots), compared to the powder spectra (bottom plots).

signal making the analysis less reliable. The film C 1s spectrum is characterized by a main line at around 285 eV due to photoelectrons emitted from the atoms in the aromatic ring and the carbon atoms bound to hydrogen atoms (C−C, C−H and CH_3). The shoulder at higher binding energy is due to contributions from the electrons emitted from carbon atoms bound also to nitrogen (C−N). Nitrogen atoms, because of their higher electronegativity, shift the electronic cloud. Thus, the carbon atoms bound to nitrogen atoms have smaller electron density and, consequently, the electrons are emitted with lower kinetic energy, i.e., higher binding energy. The N 1s core level spectrum shows contributions due to five nitrogen atoms: the three nitrogen atoms belonging to the Blatter radical have different chemical environment,[40,41] while the two nitrogen atoms belonging to the nitronyl nitroxide (NN) radical have an equivalent chemical environment. These differences are mirrored in the spectrum by the presence of two broad features, showing the highest intensity at around 402 eV. This binding energy corresponds to the line expected in the NN radical N 1s core level spectrum.[42]

A best fit procedure allows identifying the contributions from different atomic sites having slightly different binding energies due to variations in the chemical environment.[43] In calculating the best fit, we applied several constraints based on electronegativity, and bond strength[42,43] (see also Supporting Information for details). We used Voigt profiles, with fixed

DOI: 10.1021/jacs.9b00558
J. Am. Chem. Soc. 2019, 141, 4764−4774

constant Lorentzian width (0.08 and 0.10 eV, for C 1s and N 1s curves, respectively).[42−44] The Voigt profile takes into account both the finite core-hole lifetime (Lorentzian profile) and the broadening due to the finite experimental resolution and various inhomogeneities, e.g., molecular packing and local morphology[43,45] (Gaussian profile). To calculate the stoichiometry of the films, we also took into account the intensity of the satellites[43,44] typical features in photoemission that appear as an effect of the relaxation processes due to the creation of a core-hole.[46] Based on comparison of the film fit results (SI: Tables S4−S6) and the molecule stoichiometry, we can conclude that there was no degradation of the diradical molecules under our controlled evaporation condition.

This result is further supported by the XPS investigations performed on the powder samples, i.e., on molecules that did not undergo evaporation (Figure 8, bottom plots). Apart from a broadening of the lines and small energy shifts, due to typical charging effects occurring in organic crystals,[47] the film spectra are fully concomitant with the powder spectra. Thus, it is evident that diradical **2** is stable and robust to be evaporated under controlled conditions to form films of intact diradical molecules.

To shed light on the growth mode of diradical **2** under this preparation conditions, we follow the XPS core level signal of the substrate (Si 2p) by looking at its attenuation upon film deposition (Figure 9, top panel). The curve is characterized by a very slow decay. This intensity trend hints at a Volmer−Weber (VW) growth mode, i.e., island growth.[48,49] This result is consistent with the atomic force microscopy (AFM) ex situ images obtained on diradical **2** films (Figure 9 middle panel) clearly showing a film morphology dominated by islands. The VW growth mode occurs when the interaction between the deposited molecules is much stronger than between the molecules and the substrate. The VW growth of diradical **2** signifies the interacting molecules of diradical **2**, possibly resembling the 1D spin-1 chain in the solid state, on the inert SiO_2/Si(111) surfaces. The line profile (Figure 9, bottom panel), obtained averaging the AFM signal over all rows, evidence the formation of islands of different lateral size that for big assemblies ranges between 80 and 300 nm.

Near edge X-ray absorption fine structure (NEXAFS) spectroscopy offers the advantage to investigate in situ not only the electronic structure of a material, namely the unoccupied states, but also the structural properties of very thin films. Thus, we investigate diradical **2** thin films to determine the molecular orientation with respect to the substrate, by using two different polarization directions of the incident light, giving rise to NEXAFS dichroism (Figure 10).

We focus on the C−K edge spectra. In analogy with the NEXAFS spectra of carbon-based molecules, the spectra in Figure 10 are characterized by two main regions: the π^* region up to around 290 eV and the σ^* region in the photon energy range above 290 eV.[50] Several features are typically expected in the 286.0−287.4 eV photon range in the spectra of N-substituted aromatic carbon:[51] indeed, a strong resonance is visible at 286.2 eV. This resonance is due to transitions from C 1s levels, belonging to carbon atoms bound to nitrogen.[52−54] We also observe a very pronounced shoulder with two small knees at 284.4 and 285.2 eV. They have a C=C character, with the first shoulder mainly due to excitations along the molecular backbone and the intensity at around 285 eV within the phenyl groups.[50,55−57] The features show a strong dichroic behavior with the signal intensity at around 285 eV quenched

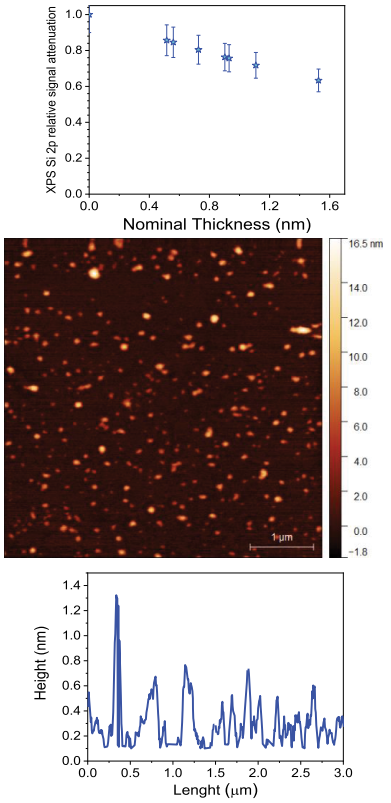

Figure 9. Attenuation of the Si 2p XPS signal, normalized to the corresponding saturation signal, as a function of film nominal thickness, deposition at room temperature (top panel). A typical AFM image of a 1.4 nm nominally thick film (middle panel) and its averaged height profile (bottom panel).

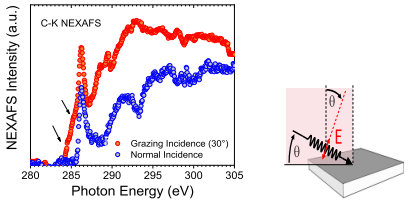

Figure 10. C−K NEXAFS spectra obtained from a 1.5 nm nominally thick film (left panel). The spectra were taken in grazing incidence and in normal incidence as indicated. Geometry of the experiment (right panel).

and the peak at 286.2 eV losing intensity in normal incidence. First, this clearly indicate that the island aggregation is not amorphous because in that case the signal for the two polarization directions would overlap. Second, this kind of NEXAFS dichroism agrees with an average orientation of the molecules in the film (note that the NEXAFS signal is averaged on the area spotted by the photon beam) similar to the one

DOI: 10.1021/jacs.9b00558
J. Am. Chem. Soc. 2019, 141, 4764−4774

adopted in the single crystals and with the crystallographic *a*-axis of the unit cell almost perpendicular to the substrate (see Figure 2).

Finally, we monitor the stability of the films in UHV (base pressure 2×10^{-10} mbar) by using XPS, focusing on the N 1s core level spectra that represent nitronyl nitroxide and Blatter radicals.[40−42] We observe no major changes in the spectra of the films after their exposure to UHV at room temperature for 17 and 60 h (Figure S20, SI). However, the films are much less robust in air, as we observed major changes in their XPS after 7 h of air exposure (Figure S21, SI). We note that the previously studied films of nitronyl nitroxide and the Blatter monoradical derivatives showed similar changes in their XPS after the films were kept for several weeks and several months at ambient conditions, respectively.[40−42,58] While we have demonstrated that it is possible to evaporate diradicals and deposit their thin films under controlled conditions without degradation, our results indicate that the diradical films are less stable when compared to the films of their monoradical analogues.

■ CONCLUSION

We have synthesized an organic diradical **2**, which, at room temperature, exists nearly exclusively in its high-spin, $S = 1$, ground state and it possesses a remarkable thermal stability to permit fabrication of intact diradical thin films on silicon substrate via evaporation under ultrahigh vacuum. The diradical molecules form islands on the substrate with molecules stacked approximately along the crystallographic *a*-axis. The diradical films were found to be stable under ultrahigh vacuum for at least 60 h, however, within few hours of exposure to air, XPS of the films showed major changes. While we have demonstrated that it is possible to evaporate diradicals and deposit their thin films under controlled conditions without degradation, our results indicate that the diradical films are less stable when compared to the films of nitronyl nitroxide or Blatter monoradicals. Polycrystalline diradical **2** consists of nearly isotropic 1-D antiferromagnetic $S = 1$ Heisenberg chains at low temperature. Notably, **2** possesses record intrachain antiferromagnetic coupling, $J'/k = -14$ K, among all to date studied $S = 1$ chains of organic radicals,[18,20] with a Haldane gap of $0.41 \times 2|J'/k| \approx 11.5$ K. The 1D chain of **2** is also most isotropic, with very weak local anisotropy, $|D/2J'| \approx 4 \times 10^{-4}$,[59] and thus is potentially an excellent system for studies of low dimensional magnetism.[60] Such diradical with an unprecedented combination of novel magnetic and thermal properties, suitable for thin film fabrication under ultrahigh vacuum, could facilitate the development of purely organic magnetic and electronic materials.

■ EXPERIMENTAL SECTION

Frozen solution EPR spectra were obtained using a Bruker EMX or EMX-plus X-band spectrometer and simulated with the EasySpin software.[28] The TGA/DSC or TGA instrument (TA Instruments TGA 550) was run either without or with IR attachment (Thermo NICOLET Is50 NIR). Variable temperature (from 1.8 K to up to 370 K) magnetic susceptibility measurements of **1** and **2** were performed using a Quantum Design SQUID magnetometer with applied magnetic fields of 30 000, 5000, and 500 Oe. Variable field (0−50 000 Oe) magnetization studies were carried out at temperatures of 1.8−5 K. Sample tubes for SQUID studies in dilute matrices are described in the SI.[61]

X-ray Crystallography. Crystals of **2** for X-ray studies was prepared by slow evaporation from solution in DCM/cyclohexane. Data collection was performed at the Advanced Photon Source, Argonne National Laboratory using $\lambda = 0.413\,28$ Å synchrotron radiation (silicon monochromators). Final cell constants were calculated from the xyz centroids of 9989 strong reflections from the actual data collection after integration (SAINT).[62] The intensity data were corrected for absorption (SADABS).[63] The space group $P\bar{1}$ was determined based on intensity statistics and the lack of systematic absences. The structure was solved and refined using the SHELX suite of programs.[64] All non-hydrogen atoms were refined with anisotropic displacement parameters. The hydrogen atoms were placed in ideal positions and refined as riding atoms with relative isotropic displacement parameters. Crystal and structure refinement data for **2** are in the Supporting Information and the accompanying file in CIF format.

Synthesis of 2. Standard techniques for synthesis under inert atmosphere (argon or nitrogen), using custom-made Schlenk glassware, custom-made double manifold high vacuum lines, argon-filled Vacuum Atmospheres gloveboxes, and nitrogen-filled glovebags. Chromatographic separations were carried out using normal phase silica gel. Multistep, efficient synthesis and characterization of the starting Blatter radical **3** is outlined in the Supporting Information (Scheme S1).

Blatter Radical ***4***. Starting 7-cyano Blatter radical **3** (1.605 g, 5.19 mmol) was dissolved in dichloromethane (100 mL) and cooled to −78 °C under a light N_2 flow. DIBAL-H (1 M in hexane, 12.0 mL, 12.0 mmol) was then added to the solution at −78 °C. The reaction was stirred at −78 °C for 1 h and then warmed to room temperature with stirring for 1 h. Then, 1 M HCl (100 mL) was added and the bilayer was stirred at room temperature for about 20 min. This caused a sizable amount of precipitate to collect on the walls of the round-bottom flask. The bilayer was decanted, separated, and the organic layer was shaken vigorously with aqueous KOH. The organic layer was then dried over Na_2SO_4 and evaporated (0.634 g); TLC indicated this solid to be radical **4** with only very minor impurities. The precipitate that was formed after HCl addition was then exposed to concentrated KOH and dichloromethane, causing it to dissolve in the organic layer upon mixing. TLC indicated a sizable amount of target material **4**, but with significantly more impurities. The solvent was evaporated and this residue purified on silica (dichloromethane eluent) to yield an additional 0.199 g of pure radical, to provide total of 0.833 g of **4** (52% yield). IR (powder, cm^{-1}): 3072, 3018, 2825, 2756, 2727, 1682, 1572, 1487, 1386, 1311, 1184, 1114, 1026, 829, 768. EPR (X-band, 9.65 GHz, benzene): $g = 2.0035$, $a_{N1} = 0.77$ mT, $a_{N2} = 0.48$ mT, $a_{N3} = 0.46$ mT. HR-ESI: 313.1229, 100%, $[M + H]^+$, calculated for $[M + H]^+$: 313.1215, also: 312.1136, 77%, M^+, calculated for M^+: 312.1137. Mp (DSC, 5 °C/min): 212−217 °C. To further characterize radical **4** by diamagnetic NMR spectroscopy, **4** (∼4 mg) was dissolved in DMSO-d_6 (∼0.5 mL), and then an excess of sodium dithionite was added to the NMR sample. Gently heating the NMR tube (to dissolve enough sodium dithionite to reduce the radical to *leuco*-triazine) caused a color change to the characteristic yellow of the reduced radical. This allowed for acquisition of ^{1}H NMR and ^{13}C NMR spectra for the *leuco*-triazine. ^{1}H NMR (400 MHz, DMSO-d_6): 9.56 (s, 1H), 9.34 (s, 1H), 7.82 (dd, 2H, $J_1 = 7.8$ Hz, $J_2 = 1.4$ Hz), 7.43−7.51 (m, 7H), 7.33 (dd, $J_1 = 7.8$ Hz $J_2 = 1.4$ Hz), 7.22−7.18 (m, 1H), 6.86 (d, 1H, 7.6 Hz), 6.68 (s, 1H). ^{13}C NMR (DMSO-d_6): $\delta = 190.6$, 146.4, 143.3, 140.5, 135.1, 132.2, 130.7, 130.4, 129.53, 129.34, 128.5, 125.9, 124.6, 122.2, 113.1, 107.9

Diradical ***2***. Note: in this procedure, the first step of reduction of radical **4** with $Na_2S_2O_4$ was omitted, that is, the second step (condensation with bis-hydroxyamine) was run directly on the radical. Blatter radical **4** (0.626 g, 0.46 mmol) was added to a Schlenk vessel followed by 2,3-bis(hydroxyamino)-2,3-dimethylbutane (0.503 g, 3.34 mmol). After purging the Schlenk vessel with nitrogen gas, MeOH (20 mL) was added. The suspension was heated to 70 °C in the Schlenk vessel overnight, during which time the mixture became homogeneous. Then the solution was cooled and diluted approximately 4-fold with ethyl acetate, and subsequently washed twice with brine, dried, and evaporated. The solid obtained was dissolved in dichloromethane (300 mL), and then triethylamine (2.0 mL, 14.28

DOI: 10.1021/jacs.9b00558
J. Am. Chem. Soc. 2019, 141, 4764−4774

mmol) was added. The solution was stirred overnight with a light air flow bubbling through the reaction. The resulatant purple/red colored solution was evaporated. The diradical was purified on silica eluting with 4:1 dichloromethane/EtOAc. Then, the solid diradical was washed sequentially with 10 mL of pentane, 10 mL of Et_2O, and finally 10 mL of MeOH; the solid was then dried under high vacuum at 100 °C in a chamber overnight, to remove any cocrystallized dichloromethane and other residual solvents (0.332 g, 38% yield). IR (powder, cm^{-1}): 3101, 3049, 2982, 2914, 1585, 1483, 1388, 1361, 1315, 1269, 1136, 823, 777, 733. HR-ESI: 439.2010, 100%, M^+, calculated for M^+: 439.2008.

Computational Details. All geometry optimizations were carried out at the UB3LYP/6-31G(d) level of theory, with obtained minima confirmed by frequency calculations. The broken-symmetry approach was applied for open-shell singlet calculations and spin contamination errors were corrected by approximate spin-projection method.[65] Computations of an intradimer coupling constant J'/k were carried out using dimers and trimers of **2** at X-ray geometry, using broken symmetry approach at the UB3LYP/6-31G(d) or UB3LYP/6-311+G(d,p) levels of theory.[34,66] All calculations were performed with the Gaussian 09 program suite.[27]

Thin Film Growth and XPS Measurements. Thin film growth and XPS measurements were performed in an UHV system comprising a substrate preparation chamber and a dedicated OMDB chamber connected to an analysis chamber (base pressure 2×10^{-10} mbar) equipped with a monochromatic Al Kα source (SPECS Focus 500) and a SPECS Phoibos 150 hemispherical electron analyzer. As a substrate, native SiO_2 grown on single-side-polished n-Si(111) wafers was used. The substrate was cleaned in an ultrasonic bath in acetone and ethanol (1 h each consecutive bath) and then annealed at around 500 K for 15 h. The cleanness was verified by XPS. Thin films of **2** were grown in situ by OMBD using a Knudsen cell keeping the substrate at room temperature. Powder samples were obtained embedding the powder in a passivated indium foil. The nominal thickness was determined by using the attenuation of the Si 2p XPS signal of the substrate. The spectra were measured at 20 eV pass energy, and the binding energy calibrated to the Si 2p signal at 99.8 eV. Because of the radiation-sensitivity of the diradical, beam exposure was minimized and a freshly prepared film was used for each set of spectra to prevent radiation damage. For the XPS measurements probing stability, the set of spectra was measured on the same films upon UHV or air exposure minimizing the acquisition time. The spectra have a slightly worse signal-to-noise ratio to preserve the intactness of the molecules in the films.

NEXAFS measurements were performed at the third-generation synchrotron radiation source Bessy II (Berlin) at the LowDose PES end-station, installed at the PM4 beamline ($E/\Delta E$ = 6000 at 400 eV) that included substrate preparation facilities like those described above for the XPS station. The measurements were carried out in multibunch hybrid mode (ring current in top up mode = 250 mA, c_{ff} = 1.6, 100 μm exit slit). The NEXAFS spectra, measured in total electron yield, were normalized by using the clean substrate signal and the ring current into account, and then scaling all spectra to give an equal edge jump.[50,57,67] Atomic force microscopy (AFM) studies were performed under ambient conditions in tapping mode with a Digital Instruments Nanoscope III Multimode AFM. No beam-induced degradation of the samples was observed on the time scale of all discussed experiments.

■ ASSOCIATED CONTENT

Supporting Information

The Supporting Information is available free of charge on the ACS Publications website at DOI: 10.1021/jacs.9b00558.

X-ray crystallographic files for **2** in CIF format (CIF)

General procedures and materials, additional experimental details, stoichiometry and integrated XPS experimental signal intensities for the thin films of radical, fit results for the energy positions and relative intensities of the photoemission lines in the C 1s and N 1s spectra (PDF)

■ AUTHOR INFORMATION

Corresponding Authors

*arajca1@unl.edu

*benedetta.casu@uni-tuebingen.de

ORCID

Suchada Rajca: 0000-0003-0904-8329

Maria Benedetta Casu: 0000-0002-5659-7040

Andrzej Rajca: 0000-0002-8856-1536

Notes

The authors declare no competing financial interest.

■ ACKNOWLEDGMENTS

We thank the National Science Foundation (NSF), Chemistry Division for support of this research under Grants No. CHE-1362454 (A.R.) and CHE-1665256 (A.R.) and the National Institutes of Health (NIGMS #R01GM124310-01 to S.R. and A.R.) for the upgrade of EPR spectrometer. NSF's ChemMatCARS Sector 15 is principally supported by the NSF/Department of Energy under grant number NSF/CHE-1346572. Use of the Advanced Photon Source was supported by the U.S. Department of Energy, Office of Science, Office of Basic Energy Sciences, under Contract No. DE-AC02-06CH11357. We also thank Thomas Chassé for accessing the photoelectron laboratory at the University of Tübingen, Hilmar Adler for technical support, and Helmholtz-Zentrum Berlin (HZB) for providing beamtime at BESSY II. Financial support from the German Research Foundation (DFG) under the contract CA852/11-1 and from Helmholtz-Zentrum Berlin is gratefully acknowledged. We thank Chan Shu for thermogravimetric studies of compounds **1** and **2**, and for determining stability of **2** in solution on air.

■ REFERENCES

(1) Rajca, A.; Wongsriratanakul, J.; Rajca, S. Magnetic ordering in an organic polymer. *Science* **2001**, *294*, 1503−1505.

(2) Ratera, L.; Veciana, J. Playing with organic radicals as building blocks for functional molecular materials. *Chem. Soc. Rev.* **2012**, *41*, 303−349.

(3) Wingate, A. J.; Boudouris, B. W. Recent advances in the syntheses of radical-containing macromolecules. *J. Polym. Sci., Part A: Polym. Chem.* **2016**, *54*, 1875−1894.

(4) (a) Rajca, A. Organic diradicals and polyradicals: from spin coupling to magnetism? *Chem. Rev.* **1994**, *94*, 871−893. (b) Rajca, A. The Physical Organic Chemistry of Very High-Spin Polyradicals. *Adv. Phys. Org. Chem.* **2005**, *40*, 153−199. (c) Gallagher, N. M.; Olankitwanit, A.; Rajca, A. High-Spin Organic Molecules. *J. Org. Chem.* **2015**, *80*, 1291−1298.

(5) (a) Rajca, A.; Lu, K.; Rajca, S. High-spin polyarylmethyl polyradical: Fragment of a macrocyclic 2-strand based upon calix[4]arene rings. *J. Am. Chem. Soc.* **1997**, *119*, 10335−10345. (b) Rajca, S.; Rajca, A.; Wongsriratanakul, J.; Butler, P.; Choi, S. Organic Spin Clusters. Dendritic-Macrocyclic Polyarylmethyl Polyradical with Very High-Spin of S = 10 and its Derivatives: Synthesis, Magnetic Studies, and Small Angle Neutron Scattering. *J. Am. Chem. Soc.* **2004**, *126*, 6972−6986. (c) Rajca, A.; Wongsriratanakul, J.; Rajca, S.; Cerny, R. L. Organic Spin Clusters: Annelated Macrocyclic Polyarylmethyl Polyradicals and Polymer with Very High-Spin S = 6 − 18. *Chem. - Eur. J.* **2004**, *10*, 3144−3157. (d) Rajca, A.; Wongsriratanakul, J.; Rajca, S. Organic Spin Clusters: Macrocyclic-Macrocyclic Polyarylmethyl Polyradicals with Very High-Spin S = 5 − 13. *J. Am. Chem. Soc.* **2004**, *126*, 6608−6626.

(6) Sanvito, S. Molecular spintronics. *Chem. Soc. Rev.* **2011**, *40*, 3336−3355.
(7) (a) Herrmann, C.; Solomon, G. C.; Ratner, M. A. Organic Radicals as Spin Filters. *J. Am. Chem. Soc.* **2010**, *132*, 3682−3684. (b) Hu, G.; Xie, S.; Wang, C.; Timm, C. Spin-dependent transport and functional design in organic ferromagnetic devices. *Beilstein J. Nanotechnol.* **2017**, *8*, 1919−1931.
(8) Gaudenzi, R.; Burzuri, E.; Reta, D.; Moreira, I. de P. R.; Bromley, S. T.; Rovira, C.; Veciana, J.; van der Zant, H. S. J. Exchange Coupling Inversion in a High-Spin Organic Triradical Molecule. *Nano Lett.* **2016**, *16*, 2066−2071.
(9) (a) Yonekuta, Y.; Susuki, K.; Oyaizu, K.; Honda, K.; Nishide, H. Battery-Inspired, Nonvolatile, and Rewritable Memory Architecture: a Radical Polymer-Based Organic Device. *J. Am. Chem. Soc.* **2007**, *129*, 14128−14129. (b) Oyaizu, K.; Nishide, H. Radical Polymers for Organic Electronic Devices: A Radical Departure from Conjugated Polymers? *Adv. Mater.* **2009**, *21*, 2339−2344. (c) Lee, J.; Lee, E.; Kim, S.; Bang, G. S.; Shultz, D. A.; Schmidt, R. D.; Forbes, M. D. E.; Lee, H. Nitronyl Nitroxide Radicals as Organic Memory Elements with Both n- and p-Type Properties. *Angew. Chem., Int. Ed.* **2011**, *50*, 4414−4418. (d) Gaudenzi, R.; de Bruijckere, J.; Reta, D.; Moreira, I. de P. R.; Rovira, C.; Veciana, J.; van der Zant, H. S. J.; Burzurí, E. Redox-Induced Gating of the Exchange Interactions in a Single Organic Diradical. *ACS Nano* **2017**, *11*, 5879−5883.
(10) Tsuji, Y.; Hoffmann, R.; Strange, M.; Solomon, G. C. Close relation between quantum interference in molecular conductance and diradical existence. *Proc. Natl. Acad. Sci. U. S. A.* **2016**, *113*, E413−E419.
(11) Borden, W. T.; Davidson, E. R. Effects of electron repulsion in conjugated hydrocarbon diradicals. *J. Am. Chem. Soc.* **1977**, *99*, 4587−4594.
(12) Ovchinnikov, A. A. Multiplicity of the ground state of large alternant organic molecules with conjugated bonds (do organic ferromagnets exist?). *Theor. Chim. Acta* **1978**, *47*, 297−304.
(13) (a) Boratyński, P. J.; Pink, M.; Rajca, S.; Rajca, A. Isolation of the Triplet Ground State Aminyl Diradical. *Angew. Chem., Int. Ed.* **2010**, *49*, 5459−5462. (b) Rajca, A.; Olankitwanit, A.; Wang, Y.; Boratynski, P. J.; Pink, M.; Rajca, S. High-Spin S = 2 Ground State Aminyl Tetraradicals. *J. Am. Chem. Soc.* **2013**, *135*, 18205−18215. (c) Shimizu, D.; Osuka, A. A Benzene-1,3,5-Triaminyl Radical Fused with Zn-II-Porphyrins: Remarkable Stability and a High-Spin Quartet Ground State. *Angew. Chem., Int. Ed.* **2018**, *57*, 3733−3736.
(14) Fukuzaki, E.; Nishide, H. Room-temperature high-spin organic single molecule: nanometer-sized and hyperbranched poly[1,2,(4)-phenylenevinyleneanisylaminium]. *J. Am. Chem. Soc.* **2006**, *128*, 996−1001.
(15) (a) Ishida, T.; Iwamura, H. Bis[3-tert-butyl-5-(N-oxy-tert-butylamino)phenyl] nitroxide in a quartet ground state: a prototype for persistent high-spin poly[(oxyimino)-1,3-phenylenes]. *J. Am. Chem. Soc.* **1991**, *113*, 4238−4241. (b) Veciana, J.; Rovira, C.; Crespo, M. I.; Armet, O.; Domingo, V. M.; Palacio, F. Stable polyradicals with high-spin ground states. 1. synthesis, separation, and magnetic characterization of the stereoisomers of 2,4,5,6-tetrachloro-α,α,α',α'-tetrakis(pentachloropheny1)-*m*-xylylene. *J. Am. Chem. Soc.* **1991**, *113*, 2552−2561. (c) Rajca, A.; Shiraishi, K.; Rajca, S. Stable diarylnitroxide diradical with triplet ground state. *Chem. Commun.* **2009**, 4372−4374.
(16) (a) Inoue, K.; Iwamura, H. 2-[*p*-(N-tert-butyl-N-oxyamino)-phenyl]-4,4,5,5-tetramethyl-4,5-dihydroimidazol-3-oxide-l-oxyl, a stable diradical with a triplet ground state. *Angew. Chem., Int. Ed. Engl.* **1995**, *34*, 927−928. (b) Shultz, D. A.; Fico, R. M.; Lee, H.; Kampf, J. W.; Kirschbaum, K.; Pinkerton, A. A.; Boyle, P. D. Mechanisms of exchange modulation in trimethylenemethane-type biradicals: The roles of conformation and spin density. *J. Am. Chem. Soc.* **2003**, *125*, 15426−15432. (c) Rajca, A.; Shiraishi, K.; Vale, M.; Han, H.; Rajca, S. Stable Hydrocarbon Diradical, an Analogue of Trimethylenemethane. *J. Am. Chem. Soc.* **2005**, *127*, 9014−9020. (d) Kato, K.; Furukawa, K.; Osuka, A. A Stable Trimethylenemethane Triplet Diradical Based on a Trimeric Porphyrin Fused π-System. *Angew. Chem., Int. Ed.* **2018**, *57*, 9491−9494.
(17) Gallagher, N. M.; Bauer, J. J.; Pink, M.; Rajca, S.; Rajca, A. High-spin organic diradical with robust stability. *J. Am. Chem. Soc.* **2016**, *138*, 9377−9380.
(18) Wang, W.; Chen, C.; Shu, C.; Rajca, S.; Wang, X.; Rajca, A. S = 1 Tetraazacyclophane Diradical Dication with Robust Stability: a Case of Low Temperature One-Dimensional Antiferromagnetic Chain. *J. Am. Chem. Soc.* **2018**, *140*, 7820−7826.
(19) Suzuki, S.; Furui, T.; Kuratsu, M.; Kozaki, M.; Shiomi, D.; Sato, K.; Takui, T.; Okada, K. Nitroxide-substituted nitronyl nitroxide and iminonitroxide. *J. Am. Chem. Soc.* **2010**, *132*, 15908−15910.
(20) Rajca, A.; Takahashi, M.; Pink, M.; Spagnol, G.; Rajca, S. Conformationally constrained, stable, triplet ground state (S = 1) nitroxide diradicals: antiferromagnetic chains of (S = 1) diradicals. *J. Am. Chem. Soc.* **2007**, *129*, 10159−10170.
(21) (a) Bodzioch, A.; Zheng, M.; Kaszyński, P.; Utecht, G. Functional Group Transformations in Derivatives of 1,4-Dihydrobenzo[1,2,4]triazinyl Radical. *J. Org. Chem.* **2014**, *79*, 7294−7310. (b) Constantinides, C. P.; Obijalska, E.; Kaszyński, P. P. Access to 1,4-Dihydrobenzo[*e*][1,2,4]triazin-4-yl Derivatives. *Org. Lett.* **2016**, *18*, 916−919.
(22) Savva, A. C.; Mirallai, S. I.; Zissimou, G. A.; Berezin, A. A.; Demetriades, M.; Kourtellaris, A.; Constantinides, C. P.; Nicolaides, C.; Trypiniotis, T.; Koutentis, P. A. Preparation of Blatter Radicals via Aza-Wittig Chemistry: The Reaction of N-Aryliminophosphoranes with 1-(Het)aroyl-2-aryldiazenes. *J. Org. Chem.* **2017**, *82*, 7564−7575.
(23) Constantinides, C. P.; Koutentis, P. A. Stable N- and N/S-Rich Heterocyclic Radicals: Synthesis and Applications. *Adv. Heterocycl. Chem.* **2016**, *119*, 173−207.
(24) Constantinides, C. P.; Berezin, A. A.; Zissimou, G. A.; Manoli, M.; Leitus, G. M.; Bendikov, M.; Probert, M. R.; Rawson, J. M.; Koutentis, P. A. A Magnetostructural Investigation of an Abrupt Spin Transition for 1-Phenyl-3-trifluoromethyl-1,4-dihydrobenzo[e]-[1,2,4]triazin-4-yl. *J. Am. Chem. Soc.* **2014**, *136*, 11906−11909.
(25) Berezin, A. A.; Zissimou, G. A.; Constantinides, C. P.; Beldjoudi, Y.; Rawson, J. M.; Koutentis, P. A. Route to Benzo- and Pyrido-Fused 1,2,4-Triazinyl Radicals via N′-(Het)aryl-N′-[2-nitro-(het)aryl]hydrazides. *J. Org. Chem.* **2014**, *79*, 314−327.
(26) Rajca, A.; Pink, M.; Mukherjee, S.; Rajca, S.; Das, K. 1,3-Alternate calix[4]arene nitronyl nitroxide tetraradical and diradical: synthesis, X-ray crystallography, paramagnetic NMR spectroscopy, EPR spectroscopy, and magnetic studies. *Tetrahedron* **2007**, *63*, 10731−10742.
(27) Frisch, M. J.; Trucks, G. W.; Schlegel, H. B.; Scuseria, G. E.; Robb, M. A.; Cheeseman, J. R.; Scalmani, G.; Barone, V.; Mennucci, B.; Petersson, G. A.; Nakatsuji, H.; Caricato, M.; Li, X.; Hratchian, H. P.; Izmaylov, A. F.; Bloino, J.; Zheng, G.; Sonnenberg, J. L.; Hada, M.; Ehara, M.; Toyota, K.; Fukuda, R.; Hasegawa, J.; Ishida, M.; Nakajima, T.; Honda, Y.; Kitao, O.; Nakai, H.; Vreven, T.; Montgomery, J. A., Jr.; Peralta, J. E.; Ogliaro, F.; Bearpark, M.; Heyd, J. J.; Brothers, E.; Kudin, K. N.; Staroverov, V. N.; Kobayashi, R.; Normand, J.; Raghavachari, K.; Rendell, A.; Burant, J. C.; Iyengar, S. S.; Tomasi, J.; Cossi, M.; Rega, N.; Millam, N. J.; Klene, M.; Knox, J. E.; Cross, J. B.; Bakken, V.; Adamo, C.; Jaramillo, J.; Gomperts, R.; Stratmann, R. E.; Yazyev, O.; Austin, A. J.; Cammi, R.; Pomelli, C.; Ochterski, J. W.; Martin, R. L.; Morokuma, K.; Zakrzewski, V. G.; Voth, G. A.; Salvador, P.; Dannenberg, J. J.; Dapprich, S.; Daniels, A. D.; Farkas, Ö.; Foresman, J. B.; Ortiz, J. V.; Cioslowski, J.; Fox, D. J. *Gaussian 09*, Revision A.1; Gaussian, Inc.: Wallingford, CT, 2009.
(28) Stoll, S.; Schweiger, A. EasySpin, a comprehensive software package for spectral simulation and analysis in EPR. *J. Magn. Reson.* **2006**, *178*, 42−55.
(29) Neese, F. *ORCA—An Ab Initio, Density Functional and Semiempirical Program Package*, version 3.0.1; University of Bonn, Germany, 2008.
(30) (a) Rajca, A.; Olankitwanit, A.; Rajca, S. Triplet Ground State Derivative of Aza-*m*-Xylylene Diradical with Large Singlet−Triplet Energy Gap. *J. Am. Chem. Soc.* **2011**, *133*, 4750−4753. (b) Olankit-

DOI: 10.1021/jacs.9b00558
J. Am. Chem. Soc. 2019, 141, 4764−4774

wanit, A.; Pink, M.; Rajca, S.; Rajca, A. Synthesis of Aza-*m*-Xylylene Diradicals with Large Singlet-Triplet Energy Gap and Statistical Analyses of their EPR Spectra. *J. Am. Chem. Soc.* **2014**, *136*, 14277−14288. (c) Olankitwanit, A.; Rajca, S.; Rajca, A. Aza-*m*-Xylylene Diradical with Increased Steric Protection of the Aminyl Radicals. *J. Org. Chem.* **2015**, *80*, 5035−5044.
(31) Sinnecker, S.; Neese, F. Spin−Spin Contributions to the Zero-Field Splitting Tensor in Organic Triplets, Carbenes and Biradicals - A Density Functional and Ab Initio Study. *J. Phys. Chem. A* **2006**, *110*, 12267−12275.
(32) Meyer, A.; Gleizes, A.; Girerd, J. J.; Verdaguer, M.; Kahn, O. Crystal structures, magnetic anisotropy properties, and orbital interactions in catena - (μ-nitrito) - bis (ethylenediamine) nickel(II) perchlorate and triiodide. *Inorg. Chem.* **1982**, *21*, 1729−1739.
(33) Belorizky, E.; Fries, P. H. Exact solutions for simple spin clusters with isotropic Heisenberg exchange interactions. *J. Chim. Phys. Phys.-Chim. Biol.* **1993**, *90*, 1077−1100.
(34) Sadhukhan, T.; Hansda, S.; Latif, I. A.; Datta, S. N. Metaphenylene-Based Nitroxide Diradicals: A Protocol to Calculate Intermolecular Coupling Constant in a One-Dimensional Chain. *J. Phys. Chem. A* **2013**, *117*, 13151−13160.
(35) Cho, Y.; Cho, W. J.; Youn, S.; Lee, G.; Singh, N. J.; Kim, K. S. Density Functional Theory Based Study of Molecular Interactions, Recognition, Engineering, and Quantum Transport in π Molecular Systems. *Acc. Chem. Res.* **2014**, *47*, 3321−3330.
(36) Huang, Z.; Zhang, Y.; He, Y.; Song, H.; Yin, C.; Wu, K. A chemist's overview of surface electron spins. *Chem. Soc. Rev.* **2017**, *46*, 1955−1976.
(37) Forrest, S. R. Ultrathin Organic Films Grown by Organic Molecular Beam Deposition and Related Techniques. *Chem. Rev.* **1997**, *97*, 1793−1896.
(38) Casu, M. B. Nanoscale Studies of Organic Radicals: Surface, Interface, and Spinterface. *Acc. Chem. Res.* **2018**, *51*, 753−760.
(39) Casu, M. B.; Chassé, T. *Photoelectron Spectroscopy Applications to Materials Science*, Second ed.; Wiley-VCH: Weinheim, 2014.
(40) Ciccullo, F.; Gallagher, N. M.; Geladari, O.; Chasse, T.; Rajca, A.; Casu, M. B. A Derivative of the Blatter Radical as a Potential Metal-Free Magnet for Stable Thin Films and Interfaces. *ACS Appl. Mater. Interfaces* **2016**, *8*, 1805−1812.
(41) Ciccullo, F.; Calzolari, A.; Bader, K.; Neugebauer, P.; Gallagher, N. M.; Rajca, A.; van Slageren, J.; Casu, M. B. Interfacing a Potential Purely Organic Molecular Quantum Bit with a Real-Life Surface. *ACS Appl. Mater. Interfaces* **2019**, *11*, 1571−1578.
(42) Savu, S.-A.; Biswas, I.; Sorace, L.; Mannini, M.; Rovai, D.; Caneschi, A.; Chassé, T.; Casu, M. B. Nanoscale Assembly of Paramagnetic Organic Radicals on Au(111) Single Crystals. *Chem. - Eur. J.* **2013**, *19*, 3445−3450.
(43) Savu, S.-A.; Casu, M. B.; Schundelmeier, S.; Abb, S.; Tonshoff, C.; Bettinger, H. F.; Chassé, T. Nanoscale assembly, morphology and screening effects in nanorods of newly synthesized substituted pentacenes. *RSC Adv.* **2012**, *2*, 5112−5118.
(44) Schöll, A.; Zou, Y.; Jung, M.; Schmidt, T.; Fink, R.; Umbach, E. Line Shapes and Satellites in High-Resolution X-Ray Photoelectron Spectra of Large Π-Conjugated Organic Molecules. *J. Chem. Phys.* **2004**, *121*, 10260−10267.
(45) Casu, M. B.; Schuster, B.-E.; Biswas, I.; Raisch, C.; Marchetto, H.; Schmidt, T.; Chassé, T. Locally Resolved Core-Hole Screening, Molecular Orientation, and Morphology in Thin Films of Diindenoperylene Deposited on Au(111) Single Crystals. *Adv. Mater.* **2010**, *22*, 3740−3744.
(46) Sjögren, B.; Svensson, S.; de Brito, A. N.; Correia, N.; Keane, M. P.; Enkvist, C.; Lunell, S. The C1s core shake-up spectra of alkene molecules: An experimental and theoretical study. *J. Chem. Phys.* **1992**, *96*, 6389−6398.
(47) Barth, G.; Linder, R.; Bryson, C. Advances in charge neutralization for XPS measurements of nonconducting materials. *Surf. Interface Anal.* **1988**, *11*, 307−311.
(48) Bauer, E. Phänomenologische Theorie Der Kristallabscheidung an Oberflächen. I. *Z. Kristallogr.* **1958**, *110*, 372−394.
(49) Venables, J. A. *Introduction to Surface and Thin Film Processes*; Cambridge University Press: Cambridge, 2000.
(50) Stöhr, J. *NEXAFS Spectroscopy*; Springer: 2003.
(51) Synchrotron-Based near-Edge X-Ray Spectroscopy of Natural Organic Matter in Soils and Sediments. In *Biophysico-Chemical Processes Involving Natural Nonliving Organic Matter in Environmental Systems*.
(52) Shen, C.; Haryono, M.; Grohmann, A.; Buck, M.; Weidner, T.; Ballav, N.; Zharnikov, M. Self-Assembled Monolayers of a Bis-(Pyrazol-1-Yl)Pyridine-Substituted Thiol on Au(111). *Langmuir* **2008**, *24*, 12883−12891.
(53) Zubavichus, Y.; Shaporenko, A.; Korolkov, V.; Grunze, M.; Zharnikov, M. X-Ray Absorption Spectroscopy of the Nucleotide Bases at the Carbon, Nitrogen, and Oxygen K-Edges. *J. Phys. Chem. B* **2008**, *112*, 13711−13716.
(54) Kelly, D. N.; Schwartz, C. P.; Uejio, J. S.; Duffin, A. M.; England, A. H.; Saykally, R. J. Communication: Near Edge X-Ray Absorption Fine Structure Spectroscopy of Aqueous Adenosine Triphosphate at the Carbon and Nitrogen K-Edges. *J. Chem. Phys.* **2010**, *133*, 101103.
(55) Käfer, D.; Ruppel, L.; Witte, G.; Wöll, C. Role of Molecular Conformations in Rubrene Thin Film Growth. *Phys. Rev. Lett.* **2005**, *95*, 166602.
(56) Casu, M. B.; Schuster, B.-E.; Biswas, I.; Raisch, C.; Marchetto, H.; Schmidt, T.; Chassé, T. Locally Resolved Core-Hole Screening, Molecular Orientation, and Morphology in Thin Films of Diindenoperylene Deposited on Au(111) Single Crystals. *Adv. Mater.* **2010**, *22*, 3740−3744.
(57) Casu, M. B. Nanoscale Order and Structure in Organic Materials: Diindenoperylene on Gold as a Model System. *Cryst. Growth Des.* **2011**, *11*, 3629−3635.
(58) Kakavandi, R.; Ravat, P.; Savu, S. A.; Borozdina, Y. B.; Baumgarten, M.; Casu, M. B. Electronic Structure and Stability of Fluorophore−Nitroxide Radicals from Ultrahigh Vacuum to Air Exposure. *ACS Appl. Mater. Interfaces* **2015**, *7*, 1685−1692.
(59) Zheludev, A.; Chen, Y.; Broholm, C. L.; Honda, Z.; Katsumata, K. Haldane-gap excitations in the low-Hcone-dimensional quantum antiferromagnet $Ni(C_5D_{14}N_2)_2N_3(PF_6)$. *Phys. Rev. B: Condens. Matter Mater. Phys.* **2001**, *63*, 104410.
(60) (a) Wierschem, K.; Sengupta, P. Quenching the haldane gap in spin-1 Heisenberg antiferromagnets. *Phys. Rev. Lett.* **2014**, *112*, 247203. (b) Blanc, N.; Trinh, J.; Dong, L.; Bai, X.; Aczel, A. A.; Mourigal, M.; Balents, L.; Siegrist, T.; Ramirez, A. P. Quantum criticality among entangled spin chains. *Nat. Phys.* **2018**, *14*, 273−276.
(61) Rajca, A.; Mukherjee, S.; Pink, M.; Rajca, S. Exchange Coupling Mediated Through-Bonds and Through-Space in Conformationally-Constrained Polyradical Scaffolds: Calix[4]arene Nitroxide Tetrarradicals and Diradical. *J. Am. Chem. Soc.* **2006**, *128*, 13497−13507.
(62) *SAINT*; Bruker Analytical X-Ray Systems: Madison, WI, current version.
(63) *SADABS*; Bruker Analytical X-Ray Systems: Madison, WI, current version.
(64) Sheldrick, G. M. A short history of *SHELX*. *Acta Crystallogr., Sect. A: Found. Crystallogr.* **2008**, *64*, 112−122.
(65) Trinquier, G.; Suaud, N.; Malrieu, J.-P. Theoretical Design of High-Spin Polycyclic Hydrocarbons. *Chem. - Eur. J.* **2010**, *16*, 8762−8772.
(66) Yamaguchi, K.; Jensen, F.; Dorigo, A.; Houk, K. N. A Spin Correction Procedure for Unrestricted Hartree−Fock and Møller−Plesset Wavefunctions for Singlet Diradicals and Polyradicals. *Chem. Phys. Lett.* **1988**, *149*, 537−542.
(67) Casu, M. B.; Cosseddu, P.; Batchelor, D.; Bonfiglio, A.; Umbach, E. A High-Resolution near-Edge X-Ray Absorption Fine Structure Investigation of the Molecular Orientation in the Pentacene/Poly(3,4-Ethylenedioxythiophene):Poly(Styrenesulfonate) Pentacene/System. *J. Chem. Phys.* **2008**, *128*, 014705.

DOI: 10.1021/jacs.9b00558
J. Am. Chem. Soc. 2019, 141, 4764−4774

Supporting Information

Thermally and Magnetically Robust Triplet Ground State Diradical.

Nolan Gallagher[†], Hui Zhang[†], Tobias Junghoefer[§], Erika Giangrisostomi,[⊥] Ruslan Ovsyannikov,[⊥]

Maren Pink[‡], Suchada Rajca[†], Maria Benedetta Casu*[§] and Andrzej Rajca*[†]

[†]*Department of Chemistry, University of Nebraska, Lincoln, Nebraska 68588-0304, USA.*

[§] *Institute of Physical and Theoretical Chemistry, University of Tübingen, 72076 Tübingen, Germany*

[‡]*Department of Chemistry, Indiana University, Bloomington, Indiana 47405-7102, USA.*

[⊥]*Helmholtz-Zentrum Berlin für Materialien und Energie (HZB), Albert-Einstein-Str 15, 12489 Berlin, Germany*

E-mail addresses: arajca1@unl.edu

benedetta.casu@uni-tuebingen.de

Table of Contents

1. Experimental Section: Synthesis and Measurements.

1.a General procedures and materials.

Throughout the following paragraphs labels "NG0893b" and alike correspond to sample or experiment codes directly traceable to the laboratory notebooks or raw data.

Tetrahydrofuran (THF) was freshly distilled from sodium/benzophenone prior to use or, like dichloromehtane (DCM), used directly from solvent purification system (LC Technology Solutions). Per-deuterated solvents for NMR spectroscopy were obtained from Cambridge Isotope Laboratories. All other commercially available chemicals were obtained from either Aldrich or Acros, unless indicated otherwise. Diradical **1** was synthesized according to the recently reported procedure.[S1] 2,3-Bis(hydroxyamino)-2,3-dimethylbutane (**BHDP**) was prepared according to the established procedure;[S1,S2] from 2.264 g of starting 2,3-dinitro-2,3-dimethylbutane, we obtained 1.273 g of target material (NG0908a, 73% yield). 3-Iodo-4-aminobenzonitrile (IAB) was synthesized according to a literature procedures,[S3,S4] as described in Section 1c. Benzoic acid *N*'-phenylhydrazide, compound **A**, was obtained according to the reported procedure,[S5,S6] as described in Section 1c. Standard techniques for synthesis under inert atmosphere, using vaccum lines and Schlenk glassware, were employed.

NMR spectra were obtained using Bruker spectrometer (^{1}H, 400 MHz) using chloroform-*d* ($CDCl_3$), acetone-d_6, or DMSO-d_6 as solvent. The chemical shift references were as follows: (^{1}H) chloroform-*h*, 7.26 ppm; (^{1}H) acetone-d_5, 2.05 ppm; (^{13}C) acetone-d_6, 30.23 ppm; (^{1}H) DMSO-d_5, 2.50 ppm; (^{13}C) DMSO-d_6, 39.51 ppm. Typical 1D FID was subjected to exponential multiplication with an exponent of 0.1 Hz (for ^{1}H) and 1.0 – 2.0 Hz (for ^{13}C). IR spectra were obtained using a commercial instrument, equipped with an ATR sampling accessory. MS analyses were carried out at local facilities for mass spectrometry.

1.b. X-ray crystallography.

The single crystal of diradical **2** was obtained by slow solvent evaporation from a solution of **2** in dichloromethane/cyclohexane.

The data collection for crystal of **2** was carried out using synchrotron radiation (λ = 0.41328 Å, E = 30 keV, silicon 111 and 113 monochromators, two mirrors to exclude higher harmonics) with a frame time of 0.3 seconds and a detector distance of 50 mm. A collection strategy was calculated and complete data to a resolution of 0.55 Å. Two major sections of frames were collected with 0.50º ϕ scans. The total exposure time was 0.12 hours. The frames were integrated with the Bruker SAINT software package[S7] using a narrow-frame algorithm. The integration of the data using a triclinic unit cell yielded a total of 70570 reflections to a maximum θ angle of 16.92° (0.71 Å resolution), of which 13333 were independent (average redundancy 5.293, completeness = 96.9%, R_{int} = 9.91%, R_{sig} = 7.35%) and 10227 (76.70%) were greater than 2σ(F2). The final cell constants of a = 10.9283(3) Å, b = 13.7142(4) Å, c = 17.0369(4) Å, α = 86.6245(8)°, β = 85.0011(8)°, γ = 67.4709(7)°, volume = 2348.64(11) Å^3, are based upon the refinement of the XYZ-centroids of 9989 reflections above 20 $\sigma(I)$ with 4.605° < 2θ < 33.79°. Data were corrected for absorption effects using the multi-scan method (SADABS[S8]). The ratio of minimum to maximum

apparent transmission was 0.884. The calculated minimum and maximum transmission coefficients (based on crystal size) were 0.9930 and 0.9980.

The space group *P*-1 was determined based on intensity statistics and systematic absences. The structure was solved and refined using the SHELX suite of programs.[S9] An intrinsic-methods solution was calculated, which provided most non-hydrogen atoms from the *E*-map. Full-matrix least squares / difference Fourier cycles were performed, which located the remaining non-hydrogen atoms. All non-hydrogen atoms were refined with anisotropic displacement parameters. The hydrogen atoms were placed in ideal positions and refined as riding atoms with relative isotropic displacement parameters. The final anisotropic full-matrix least-squares refinement on F2 with 626 variables converged at *R*1 = 5.55%, for the observed data and *wR*2 = 17.05% for all data. The goodness-of-fit was 1.060. The largest peak in the final difference electron density synthesis was 0.929 $e^-/Å^3$ and the largest hole was -1.238 $e^-/Å^3$ with an RMS deviation of 0.329 $e^-/Å^3$. On the basis of the final model, the calculated density was 1.363 g/cm^3 and *F*(000), 1012 e^-. Additional crystal and refinement information is summarized in Table S1.

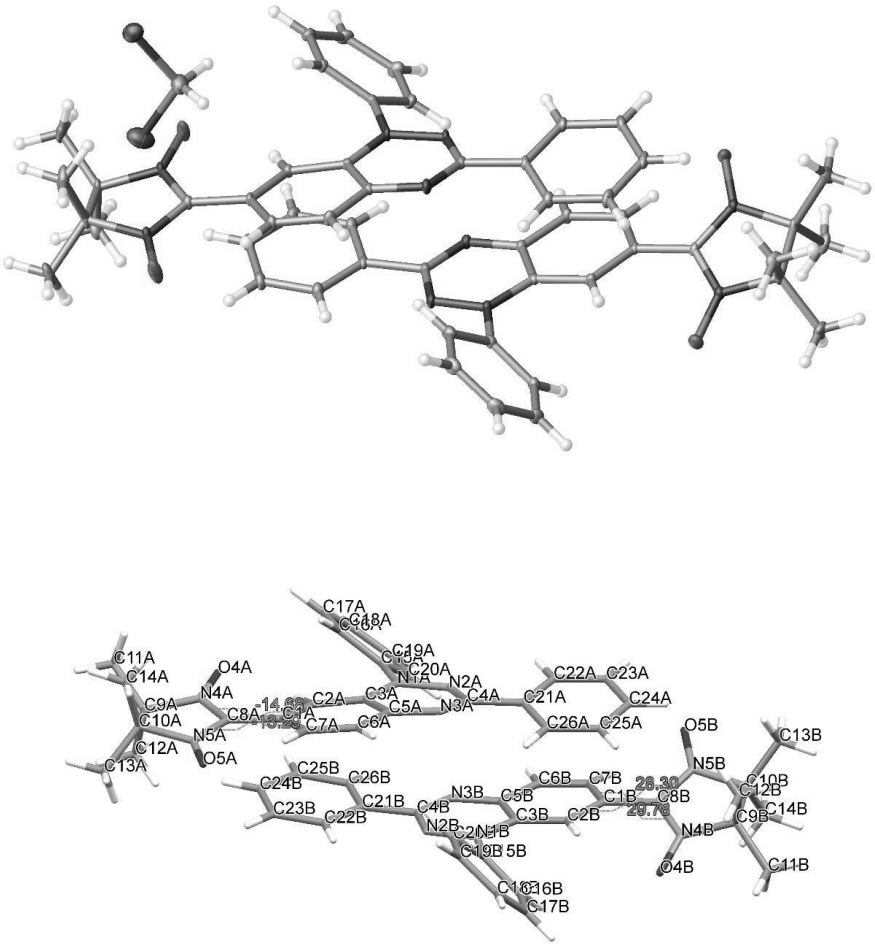

Fig. S1. X-ray crystallography of diradical **2** (label: s16009). Top plot: formula unit, showing molecule of solvent (CH_2Cl_2). Bottom plot: molecules A and B have their non-hydrogen atoms labeled and the following torsions are highlighted: for molecule A, C2A-C1A-C8A-N4A = –14.7(2) ° and C7A-C1A-C8A-N5A = –13.3(2) °, and for molecule B, C2B-C1B-C8B-N4B = 29.8(2) ° and C7B-C1B-C8B-N5B = 28.3(2) °.

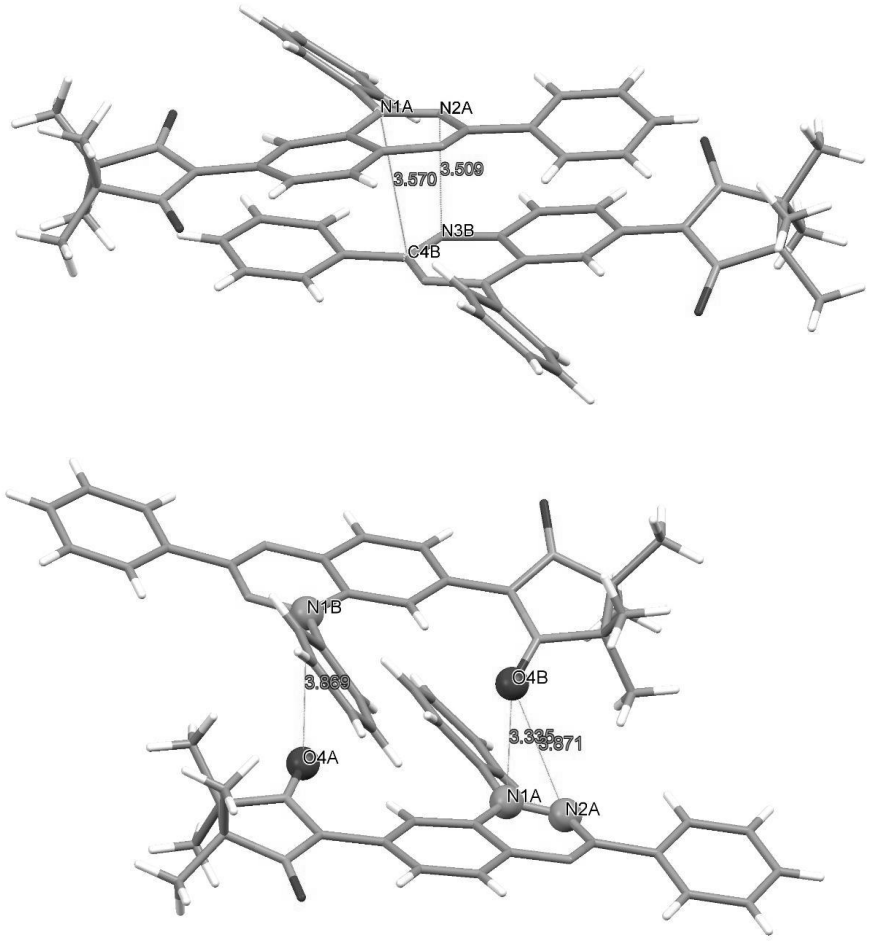

Fig. S2. X-ray crystallography of diradical **2** (label: s16009). Top plot: dimer I structure, highlighting the shortest intermolecular distances: N···N = 3.51 Å and N···C = 3.57 Å, corresponding to pairwise antiferromagnetic and ferromagnetic couplings, respectively. Because the positive spin densities on the N1 – N3 nitrogens of the triazinyl moiety are about the same but much greater than the relatively smaller and negative spin densities on the C4 carbons, the N2A···N3B = 3.509 Å contacts are expected to give rise to dominant antiferromagnetic coupling between $S = 1$ diradicals in the solid state. Bottom plot: dimer II structure, higlighting the shortest intermolecular distance, O···N = 3.335 Å. Because of the large positive spin densities on the N1 – N3 nitrogens of the triazinyl moiety and the O4 and O5 oxygens of the nitronyl nitroxide moiety, the O4B···N1A = 3.335 Å contacts, and to lesser extent, O4A···N1B = 3.869 Å and O4B···N2A = 3.871 Å contacts, are expected to lead to antiferromagnetic coupling between $S = 1$ diradicals in the solid state.

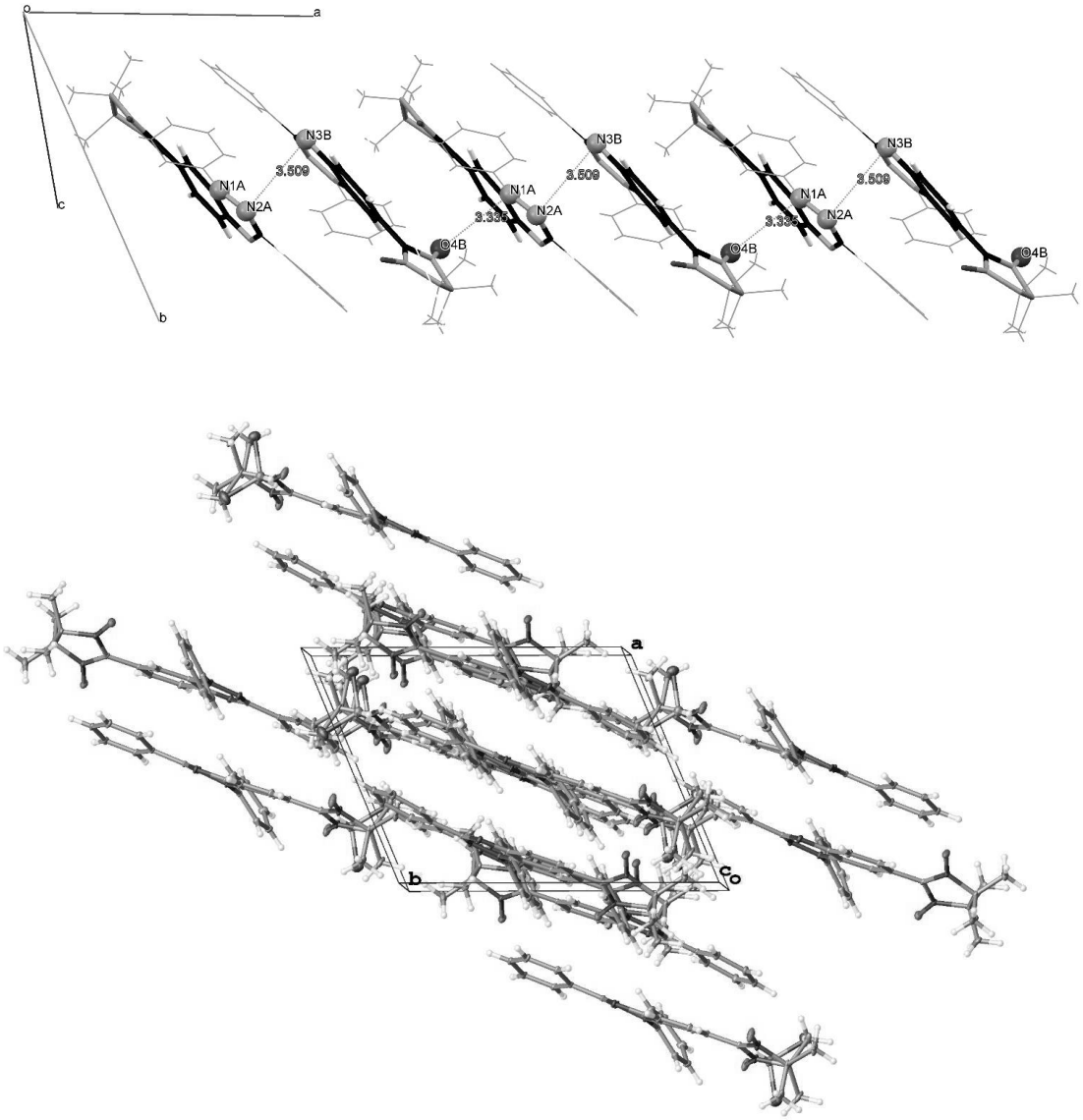

Fig. S3. Top plot: Hexamer of molecules **2**, showing packing of molecules A and B into one-dimensional $S = 1$ antiferromagnetic chain along crystallographic *a*-axis; nitrogens and oxygens with large positive spin densities and forming close intermolecular contacts, N2A···N3B = 3.509 Å and O4B···N1A = 3.335 Å, are emphasized in ball-and-stick. Bottom plot: Cell plot with a view along the *c*-axis.

Table S1. Crystal data and structure refinement for diradical **2** (label: s16009).

Empirical formula	C26.50 H26 Cl N5 O2	
Formula weight	481.97	
Crystal color, shape, size	black block, 0.123 × 0.056 × 0.040 mm^3	
Temperature	200(2) K	
Wavelength	0.41328 Å	
Crystal system, space group	Triclinic, *P*-1	
Unit cell dimensions	a = 10.9283(3) Å	α = 86.6245(8)°.
	b = 13.7142(4) Å	β = 85.0011(8)°.
	c = 17.0369(4) Å	γ = 67.4709(7)°.
Volume	2348.64(11) $Å^3$	
Z	4	
Density (calculated)	1.363 Mg/m^3	
Absorption coefficient	0.060 mm^{-1}	
F(000)	1012	
Data collection		
Diffractometer	APEX II on D8 Platform, Bruker, ChemMatCARS, APS	
Theta range for data collection	1.151 to 16.923°.	
Index ranges	-15<=h<=15, -19<=k<=19, -23<=l<=23	
Reflections collected	70570	
Independent reflections	13333 [R(int) = 0.0991]	
Observed Reflections	10227	
Completeness to theta = 14.357°	97.6 %	
Solution and Refinement		
Absorption correction	Semi-empirical from equivalents	
Max. and min. transmission	0.7403 and 0.6541	
Solution	Intrinsic methods	
Refinement method	Full-matrix least-squares on F^2	
Weighting scheme	$w = [\sigma^2 Fo^2 + AP^2]^{-1}$, with $P = (Fo^2 + 2\,Fc^2)/3$, A = 0.1003	
Data / restraints / parameters	13333 / 0 / 626	
Goodness-of-fit on F^2	1.060	
Final R indices [I > 2sigma(I)]	$R1$ = 0.0555, $wR2$ = 0.1493	
R indices (all data)	$R1$ = 0.0789, $wR2$ = 0.1705	
Largest diff. peak and hole	0.929 and -1.238 e.$Å^{-3}$	

Goodness-of-fit = $[\Sigma[w(F_o^2 - F_c^2)^2]/N_{observns} - N_{params})]^{1/2}$, all data.

$R1 = \Sigma(|F_o| - |F_c|) / \Sigma\,|F_o|$. $wR2 = [\Sigma[w(F_o^2 - F_c^2)^2] / \Sigma\,[w(F_o^2)^2]]^{1/2}$.

1.c Synthesis of diradical 2.

Scheme S1. Expanded synthetic scheme for diradical **2**.[a]

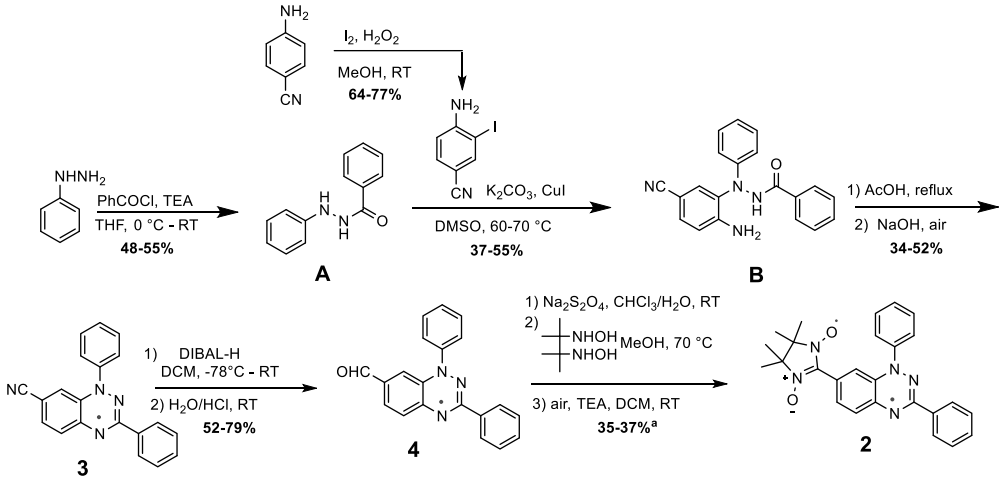

[a] In the transformation of **4** to **2**, when the first step (reduction of the radical with $Na_2S_2O_4$) was omitted for the last large-scale run and condensation was carried out directly on the Blatter radical, the yield of diradical **2** was 38%.

3-Iodo-4-aminobenzonitrile.

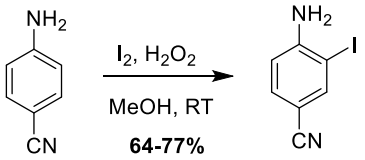

3-iodo-4-aminobenzonitrile = **IAB**

3-Iodo-4-aminobenzonitrile (IAB) was synthesized according to a modified literature procedure.[S3,S4] Briefly, to a solution of 4-aminobenzonitrile (2.03 g, 17.2 mmol) in methanol (13 mL) was added iodine (2.58 g, 10.2 mmol) followed by H_2O_2 (1.7 mL, 30% in H_2O). The reaction was then stirred overnight at room temperature covered in aluminum foil. The reaction was then quenched by addition of about 15 mL of saturated sodium metabisulfite, which caused a crystalline material to precipitate. This product was filtered and dried on the filter bed under air flow to yield a tan orange, crystalline powder (NG0893b, 2.69 g, 64%). Using the same procedure, from 10.03 g of 4-aminobenzonitrile, we obtained 15.90 g of target material (77% yield). ^{1}H NMR (NG0893b, 300 MHz, $CDCl_3$): 7.90 (d, 1H, J = 1.8 Hz), 7.40 (dd, 1H, J_1 = 8.4 Hz, J_2 = 1.8 Hz), 6.70 (d, 1H J = 8.4 Hz), 4.61 (br s, 2H). Lit.[S3]: ^{1}HNMR (300 MHz, $CDCl_3$): 7.88 (d, 1H, J = 1.8 Hz), 7.37 (dd, 1H, J = 1.8, 8.4 Hz), 6.68 (d, 1H, J = 8.4 Hz), 4.59 (br s, 2H).

Compound A: benzoic acid *N*'-phenylhydrazide.

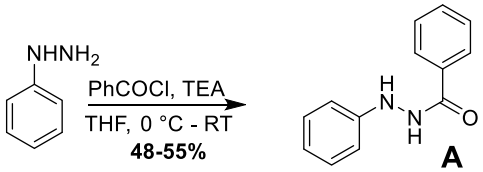

Benzoic acid *N*'-phenylhydrazide, compound A was synthesized according to a modified literature procedure.[S5,S6] Briefly, to a solution of phenylhydrazine (3.3 g, 30.5 mmol) in THF (40 mL) cooled to 0 °C was added triethylamine (4.8 mL, 34.6 mmol) followed by benzoyl chloride (3.8 mL, 32.7 mmol). The solution was allowed to warm to room temperature overnight with stirring. The reaction was quenched by addition of H_2O then sat. $NaHCO_3$ followed by dilution with EtOAc until the layers easily separated. The layers were separated and the organic layer washed twice with sat. $NaHCO_3$, dried over Na_2SO_4, and evaporated. The obtained solid was then recrystallized from ~ 50 mL of EtOH to obtain the target material **A** as white needles (NG0894a, 3.09 g, 48%). Later, using the same procedure with 6.6 g of phenylhydrazine, we obtained 7.13 g of target material (NG0899c, 55% yield). ^{1}H NMR (400 MHz, acetone-d_6, NG0894a) 9.68 (br s, 1H), 8.00 (d, J = 7.6 Hz, 2H), 7.49-7.58 (m, 3H), 7.16-7.20 (m, 3H), 6.95 (d, J = 8.2 Hz, 2H) 6.789 (t, J = 7.2 Hz, 1H). Lit.[S6]: ^{1}H NMR (400 MHz, $CDCl_3$): 4.01 d (1H), 6.66 m (1H), 7.18 q (2H), 7.44–7.46 m (J = 2 and 8 Hz, 2H), 7.51 t (1H), 7.95 m (2H), 8.00 m (1H).

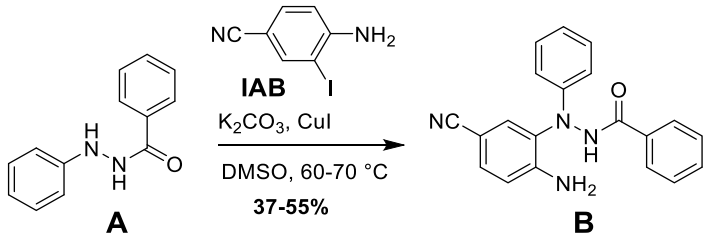

Run	SM (g/mmol)	**IAB** (g/mmol)	K_2CO_3 (g/mmol)	CuI (g/mmol)	DMSO (mL)	TM Mass (g)/mmol/yield
NG0894b	1.513/7.13	1.741/7.13	1.103/7.98	0.081/0.43	10	1.276/3.89/55%
NG08100b	6.032/28.43	6.914/28.32	4.42/31.98	0.320/1.70	40	3.42/10.41/37%

Compound **B** was prepared by adopting the Cu-catalyzed C–N coupling to the corresponding 2-iodoaniline, as previously reported.[S10,S11] Procedure for compound **B** (label: NG08100b): SM **A** (sample label: NG0899c, 6.032 g, 28.43 mmol) was added to a 250 mL RBF along with **IAB** (sample label: NG0899, 6.914 g, 28.32 mmol), CuI (0.320 g, 1.70 mmol) and K_2CO_3 (4.42 g, 31.98 mmol). DMSO (40 mL) was then added and the mixture was heated to 60–70 °C for 12 h under N_2 flow. At this time TLC indicated that most starting materials were consumed and the creation of a new spot. The reaction was

diluted with EtOAc and water, the layers were separated, and the organic layer washed 6x with brine. Following drying with Na_2SO_4 and evaporation of volatiles, the resulting dark semisolid was washed once with diethyl ether (15 mL), which caused complete solidification. The solid was then dispersed in benzene (50 mL) and filtered to yield the desired material, compund **B**, as a tan powder (3.421 g, 10.41 mmol, 37%). IR (NG08100b, powder, cm^{-1}): 3409, 3324, 3274, 3192, 3064, 3032, 2997, 2214, 1654, 1620, 1595, 1516, 1487, 1344, 1275, 1027, 895, 825, 744. ^{1}H NMR (400 MHz, acetone-d_6, NG08100b): 10.23 (br s, 1H), 8.01 (d, 2H, J = 7.6 Hz), 7.52-7.64 (m, 4H), 7.43 (dd, 1H, J_1 = 8.4 Hz, J_2 = 1.6 Hz), 7.36 (benzene**), 7.23 (t, 1H, J = 7.6 Hz) 6.99 (d, 1H, J = 8.4 Hz), 6.86 (t, 1H, J = 7.2 Hz), 6.76 (d, 2H, J = 8 Hz), 6.26 (br s, 2H). ^{13}C NMR (100 MHz, acetone-d_6, NG08100b): δ = 168.6, 152.8, 148.4, 135.0, 133.9, 133.64, 133.52, 131.2, 130.3, 130.0, 129.5, 128.8, 121.1, 120.5, 117.1, 114.5, 99.3. HR-ESI (NG08100b): 351.1228, 100%, M +Na^+, calculated for M+Na^+: 351.1222. M.p. (DSC, 5 °C/min): 209–215 °C.

** The benzene present in this sample of compound **B** appears to be very difficult to remove, and is still present by ^{1}H NMR spectroscopy even after drying the sample at 120 °C under high vacuum for several days. We confirmed that this peak corresponded to benzene by adding a drop of benzene in ~ 0.5 mL acetone-d_6, and then adding a few drops of this solution to the NMR sample – causing the peak at 7.36 to increase in intensity.

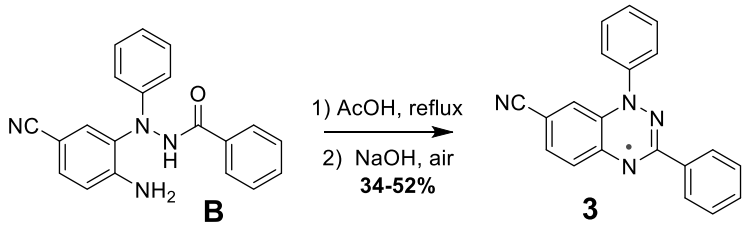

Run	SM (g/mmol)	AcOH (mL)	TM Mass (g)/mmol/yield
NG0895b	1.002/3.05	10	0.317/1.03/34%
NG0901b[a]	3.641/11.11	40	1.791/5.82/52%

[a] Although TM **3** (sample label: NG0901b) was pure enough for use in the next reaction, for characterization a small portion of **3** (NG0901b) was brought to analytical purity by column chromatrography (eluent: DCM), taking the most intensely colored portion of the radical band (sample label: NG0901c). From ~ 0.200 g, we obtained ~ 0.110 g.

Procedure for Blatter radical **3** (label: NG0895b). SM compound **B** (sample label: NG0894b, 1.002 g, 3.05 mmol) was dispersed in 10 mL of AcOH and heated to reflux (oil bath: 115 °C) during which time the mixture became dark brown. We examined the progress of this reaction by withdrawing small aliquots, diluting with EtOAc, and washing with concentrated NaOH. Contrary to literature reports of a very fast, quantitative yield reaction, we observe a more sluggish reaction with some starting material detectable even after 12 hours of reflux. As this process creates lower-R_f impurities with extended reflux times, we stopped the reaction after 12 hours by cooling to room temperature, diluting with EtOAc, and washing with NaOH with vigorous shaking in the separatory funnel. Following solvent drying (Na_2SO_4), evaporation of EtOAc *in vacuo*, the radical could be purified by washing with MeOH (~ 25 mL). IR

(NG0901c, powder, cm^{-1}): 3099, 3066, 3030, 2222, 1587, 1487, 1398, 1313, 1192, 1028, 885, 829, 752. EPR (X-band, 9.65 GHz, benzene, NG0901c): g = 2.0035, a_{N1} = 7.7 G, a_{N2} = 4.8 G, a_{N3} = 4.6 G. HR-ESI (NG0901c): 309.1137, 100%, M^+, calculated for M^+: 309.1140. mp (DSC, 5 °C/min): 217-221 °C.

To further characterize this radical by diamagnetic NMR spectroscopy, ~ 4-mg sample of **3** (sample label: NG0901c) was dissolved in ~ 0.5 mL of DMSO-d_6, and then an excess of sodium dithionite was added to the NMR sample. Gently heating the NMR tube (to dissolve enough sodium dithionite to reduce the radical) caused a color change to the characteristic yellow of the reduced radical. This allowed for acquisition of ^{1}H NMR and ^{13}C NMR spectra for this diamagnetic derivative of **3**. ^{1}H NMR (400 MHz, DMSO-d_6, NG0901c): 9.28 (s, 1H), 7.80 (d, 2H, 7.2 Hz) 7.46-7.50 (m, 7H), 7.19 (d, 2H, 7.2 Hz), 6.80 (d, 1H, 8.0 Hz), 6.41 (s, 1H). ^{13}C NMR (100 MHz, DMSO-d_6, NG0901c): δ = 147.8, 143.5, 139.3, 135.8, 131.4, 130.9, 130.2, 129.46, 129.30, 126.5, 125.7, 123.0, 119.8, 114.5, 113.0, 105.4.

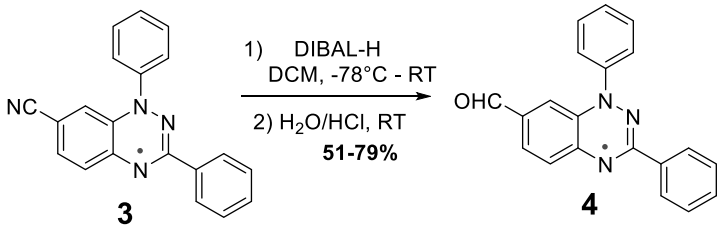

Run	SM (g/mmol)	DIBAL-H (1 M), (mL/mmol)	DCM (mL)	HCl (1 M) (mL/mmol)	TM Mass (g)/mmol/yield
NG0889b	0.120/ 0.39	0.90/0.90	12	20/20	0.095/0.30/79%
NG0896a	0.299/0.97	2.3/2.3	20	20/20	0.171/0.55/57%
NG0907	1.605/5.19	12.0/12.0	100	100	(0.634+0.199)/2.67/52%

Procedure for Blatter radical **4** (label: NG0907): Starting material **3** (sample label: NG0901b, 1.605 g, 5.19 mmol) was dissolved in DCM (100 mL) and cooled to –78 °C under a light N_2 flow. DIBAL-H (1 M in hexane**,** 12.0 mL, 12.0 mmol) was then added to solution at –78 °C. The reaction was stirred at –78 °C for one hour and then warmed to room temperature with stirring for one hour. Then, 100 mL of 1 M HCl was added and the bilayer was stirred at room temperature for ~ 20 min. This caused a sizeable amount of precipitate to collect on the walls of the round bottom flask. The bilayer was decanted, separated, and the organic layer was shaken vigorously with aqueous KOH. The organic layer was then dried over Na_2SO_4 and evaporated (0.634 g, NG0907a); TLC indicated this solid to be TM **4** with only very minor impurities. The precipitate that was formed after HCl addition was then exposed to concentrated KOH and DCM, causing it to dissolve in the organic layer upon mixing. TLC indicated a sizeable amount of TM **4**, but with significantly more impurities. The solvent was evaporated and this residue purified on silica (DCM eluent) to yield an additional 0.199 g (NG0907b) of pure radical **4** (NG0907a + NG0907b = 0.833 g, 2.67 mmol, 52% yield). IR (NG0907b, powder, cm^{-1}): 3072, 3018, 2825, 2756, 2727, 1682, 1572, 1487, 1386, 1311, 1184, 1114, 1026, 829, 768. EPR (X-band, 9.65 GHz, benzene, NG0907b): g = 2.0035,

a_{N1} = 7.7 G, a_{N2} = 4.8 G, a_{N3} = 4.6 G. HR-ESI (NG0907b): 313.1229, 100%, $[M+H]^+$, calculated for $[M+H]^+$: 313.1215, also: 312.1136, 77%, M^+, calculated for M^+: 312.1137, mp (DSC, 5 °C/min): 212–217°C.

To further characterize this radical by diamagnetic NMR spectroscopy, ~ 4-mg sample of **4** was dissolved in ~ 0.5 mL of DMSO-d_6, and then an excess of sodium dithionite was added to the NMR sample. Gently heating the NMR tube (to dissolve enough sodium dithionite to reduce the radical) caused a color change to the characteristic yellow of the reduced radical. This allowed for acquisition of ^{1}H NMR and ^{13}C NMR this diamagnetic derivative of **4**. ^{1}H NMR (400 MHz, DMSO-d_6, NG0907b): 9.56 (s, 1H), 9.34 (s, 1H), 7.82 (dd, 2H, J_1 = 7.8 Hz, J_2 = 1.4 Hz), 7.43-7.51 (m, 7H), 7.33 (dd, J_1 = 7.8 Hz J_2 = 1.4 Hz), 7.22-7.18 (m, 1H), 6.86 (d, 1H, 7.6 Hz), 6.68 (s, 1H). ^{13}C NMR (DMSO-d_6, NG0901c): δ = 190.6, 146.4, 143.3, 140.5, 135.1, 132.2, 130.7, 130.4, 129.53, 129.34, 128.5, 125.9, 124.6, 122.2, 113.1, 107.9

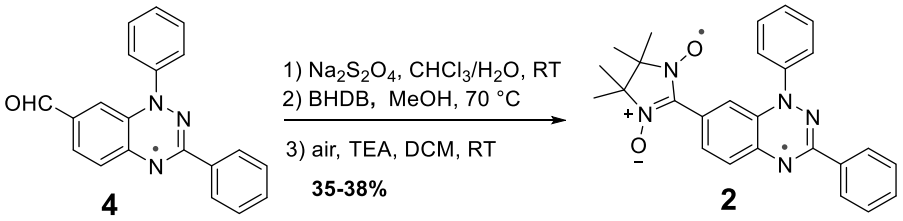

Run	SM (g/mmol)	BHDB (g/mmol)	MeOH (mL)	TEA (mL/mmol)	TM Mass (g)/mmol/yield (%)
NG0890	0.045/ 0.14	0.039/0.26	2.0	0.15/ 1.07	0.024/0.05/35
NG0896b	0.143/0.46	0.130/0.87	5.0	0.5/3.57	0.076/0.17/37
NG0908b*	0.626/2.01	0.503/3.34	20.0	2.0/14.28	0.332/0.76/38

*The first step (reduction of the radical with $Na_2S_2O_4$) was omitted in this procedure, and condensation was carried out directly on the radical **4**.

Procedure for diradical **2** (label: NG0908b): Blatter radical **4** (sample label: NG0907a, 0.626 g, 0.46 mmol) was added to Schlenk vessel followed by 2,3-bis(hydroxyamino)-2,3-dimethylbutane (**BHDP**) (sample label: NG0908a, 0.503 g, 3.34 mmol). After purging the Schlenk vessel with nitrogen gas, MeOH (20 mL) was added. The solution was heated to 70 °C in the Schlenk overnight, during which time the mixture became homogenous. Then the solution was cooled and diluted approximately fourfold with ethyl acetate, and subsequently washed twice with brine, dried, and evaporated. The solid obtained was dissolved in 300 mL DCM and TEA (2.0 mL, 14.28 mmol) was added. The solution was stirred overnight with a light air flow bubbling through the reaction. The obtained purple/red colored solution was evaporated. The diradical **2** was purified on silica eluting with 4:1 DCM:EtOAC. Then the solid was washed sequentially with 10 mL pentane, 10 mL Et_2O, and finally 10 mL MeOH; the solid was then dried under high vacuum at 100 °C in a chamber for 24 h, to remove any co-crystalized dichloromethane, see: Fig. S6 (NG0908b, 0.332 g, 0.76 mmol, 38% yield). IR (NG0896b, powder, cm^{-1}): 3101, 3049, 2982,

2914, 1585, 1483, 1388, 1361, 1315, 1269, 1136, 823, 777, 733. HR-ESI (NG0896b): 439.2010, 100%, M^+, calculated for M^+: 439.2008.

1.d Thermal stability of diradicals 1 and 2.

Thermal stability of diradicals was tested using two instruments: (1) TGA/DSC and (2) TGA instrument (TA Instruments TGA 550) that was run either without or with IR attachment (Thermo NICOLET Is50 NIR). A sample of polycrystalline diradical **1** or **2** was placed in the TGA instrument; thermogravimetric analysis was carried out under N_2 with heating at 5 ºC/min to 400 ºC and maintained for 10 minutes at 400 ºC. Two TGA/IR runs for each diradical were recorded (Fig. S4, top panel).

Stability of diradical **2** in air-saturated benzene was tested by EPR spectroscopy, using TEMPONE in benzene as an intensity reference. Three independent measurements of double integrated intensity (DI) were performed at each time point (Fig. S4, bottom panels).

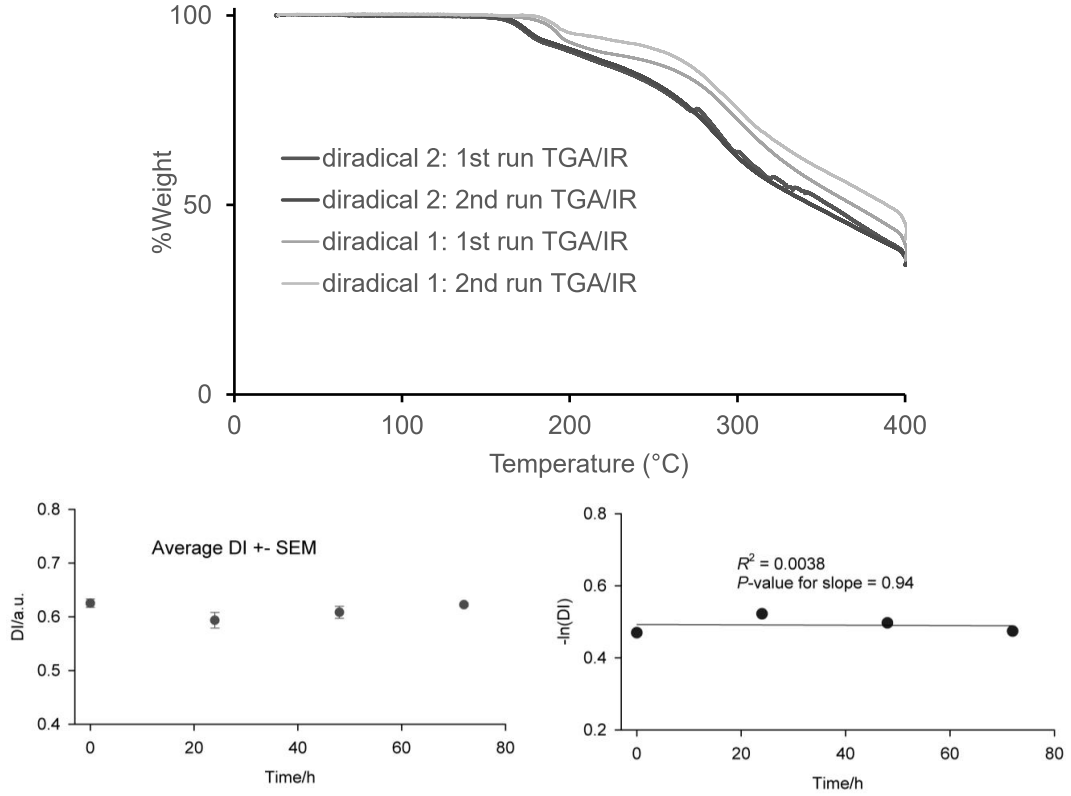

Fig. S4. Top panel: summary plots of TGA (with IR) runs for **1** and **2**. Diradical **2** was annealed at 100 °C for 24 h prior the TGA. IR spectra showed only significant increase of absorbtion at the wavenumbers corresponding to carbon dioxide, starting at about 175 and 160 °C for **1** and **2**, respectively. Bottom panels: stability of diradical **2** in benzene solution on air at room temperature (ambient conditions) by EPR spectroscopy, using TEMPONE in benzene as a reference.

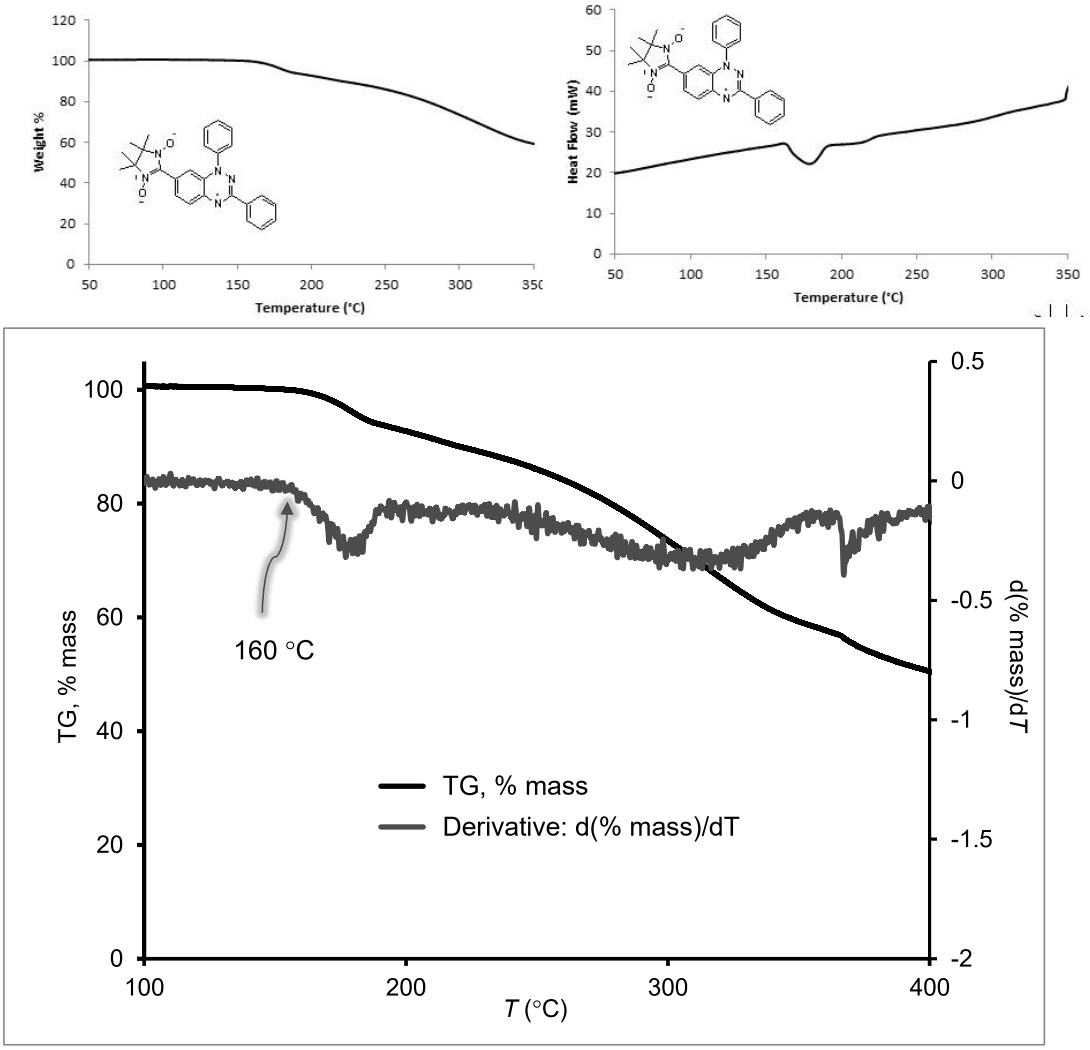

Fig. S5. Top left: TGA of diradical **2.** Top right: DSC of diradical **2**. Bottom: expanded plot of TGA of diradical **2**. Diradical **2** was annealed at 100 °C for 24 h prior the TGA/DSC.

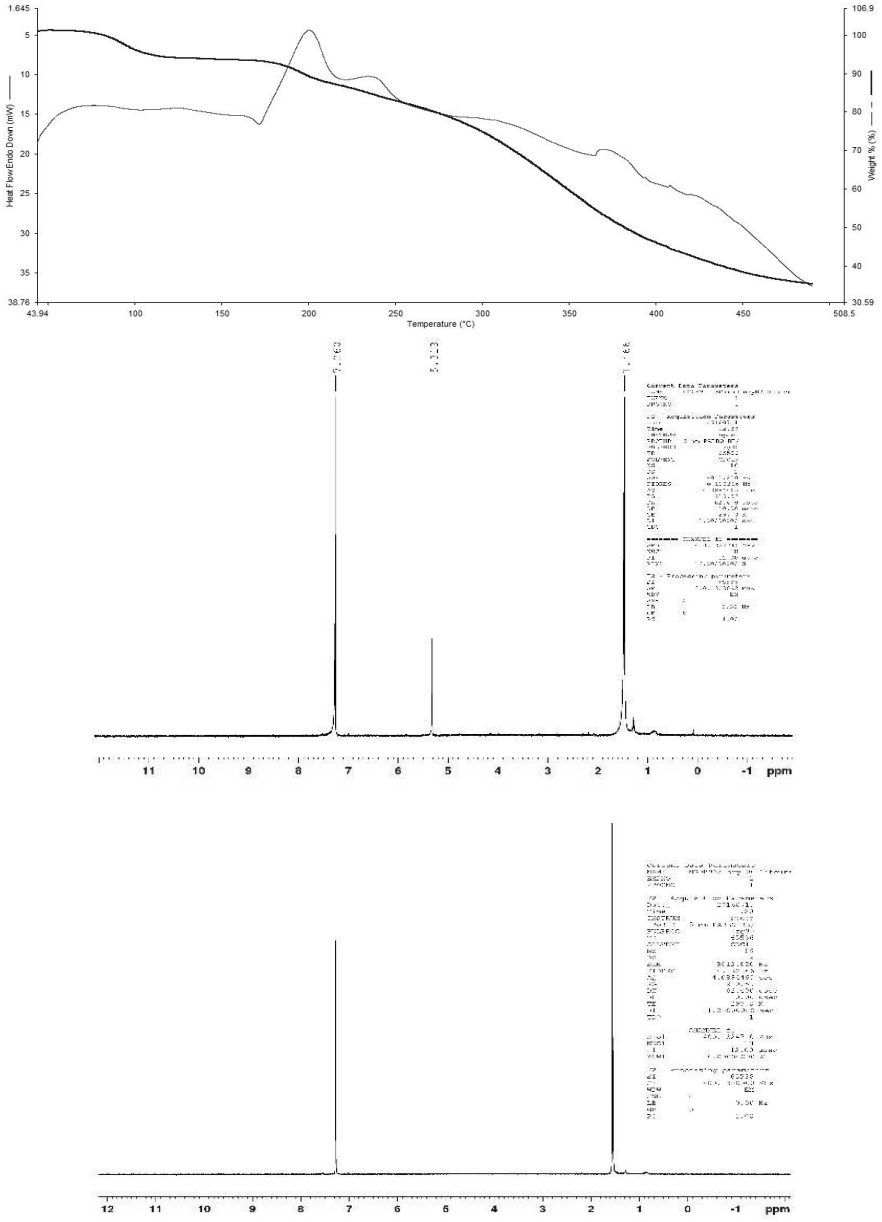

Fig. S6. Top plots: Thermogravimetric analysis (blue line) and differential scanning calorimetry (red line) of diradical **2** after drying under high vacuum at room temperature; note, a mass loss of ca. 10% at ~80 ºC. Middle plot: This mass loss is likely due to evaporation of tightly-bound dichloromethane, as indicated by ^{1}H NMR spectrum of the same sample. Bottom plot: After annealing at 100 ºC under high vacuum for 24 h, DCM is removed, as evidenced by ^{1}H NMR spectrum.

1.e EPR spectroscopy and SQUID magnetometry of diradicals 1 and 2.

EPR spectroscopy. CW X-band EPR spectra for radicals were acquired on Bruker EMX/EMX-plus instrument, equipped with a frequency counter and nitrogen flow temperature control (100–400 K). The spectra were obtained using a dual mode cavity, with an oscillating magnetic field perpendicular (TE_{102}) to the swept magnetic field; parallel mode (TE_{012}) was not used. Some spectra were obtained using TE_{102} high-sensitivity cavity, using Bruker EMX-plus instrument. Temperatures were verified using an independently calibrated thin wire thermocouple inserted into the EPR sample tube (containing the solvent) and positioned in the cavity at the same place as in the variable temperature studies. The samples were typically contained in 4-mm EPR sample tubes, equipped with high vacuum stopcocks (Kontes).

Typical parameters for EPR spectra of **1** and **2** in polystyrene at room temperature were: MW power = 0.0205 or 0.205 mW, modulation amplitude = 1 Gauss, conversion time = 40.96 ms, time constant = 10.24 ms, number of points = 1024 (Fig. S7). Selected EPR spectra of **2** were numerically simulated using EasySpin software. Notably, simulation of EPR spectrum of **2** in polystyrene glass gives significantly lower zero-field splitting parameters, D and E, compared to the spectra in toluene/chloroform glass; i.e., $|D/hc| = 7.76 \times 10^{-3}$ cm^{-1} vs. 8.08×10^{-3} cm^{-1} and $|E/hc| = 0.990 \times 10^{-3}$ cm^{-1} vs. 1.17×10^{-3} cm^{-1} (Fig. S7 vs Figure 3, main text).

Note that the experimental EPR spectra of **2** suggest that the second-largest principal value of the **D** tensor and the largest principal value of the **A** tensor are approximately parallel to the direction of the $2p_\pi$ orbitals on the nitrogens (y axis); this is because the spectral linewidth, LW_y, corresponding to the second-largest principal value of the **D** tensor (y-axis) is by a factor of 3 – 4 larger, compared to other linewidths, LW_x and LW_z. This situation is analogous to EPR spectrum of **1** and also planar nitroxide diradicals, indicating "prolate"-like spin density distribution with $D/hc < 0$. Thus, computed value of $D/hc > 0$ for **2** (Table S9) is inconsistent with its experimental EPR spectrum.

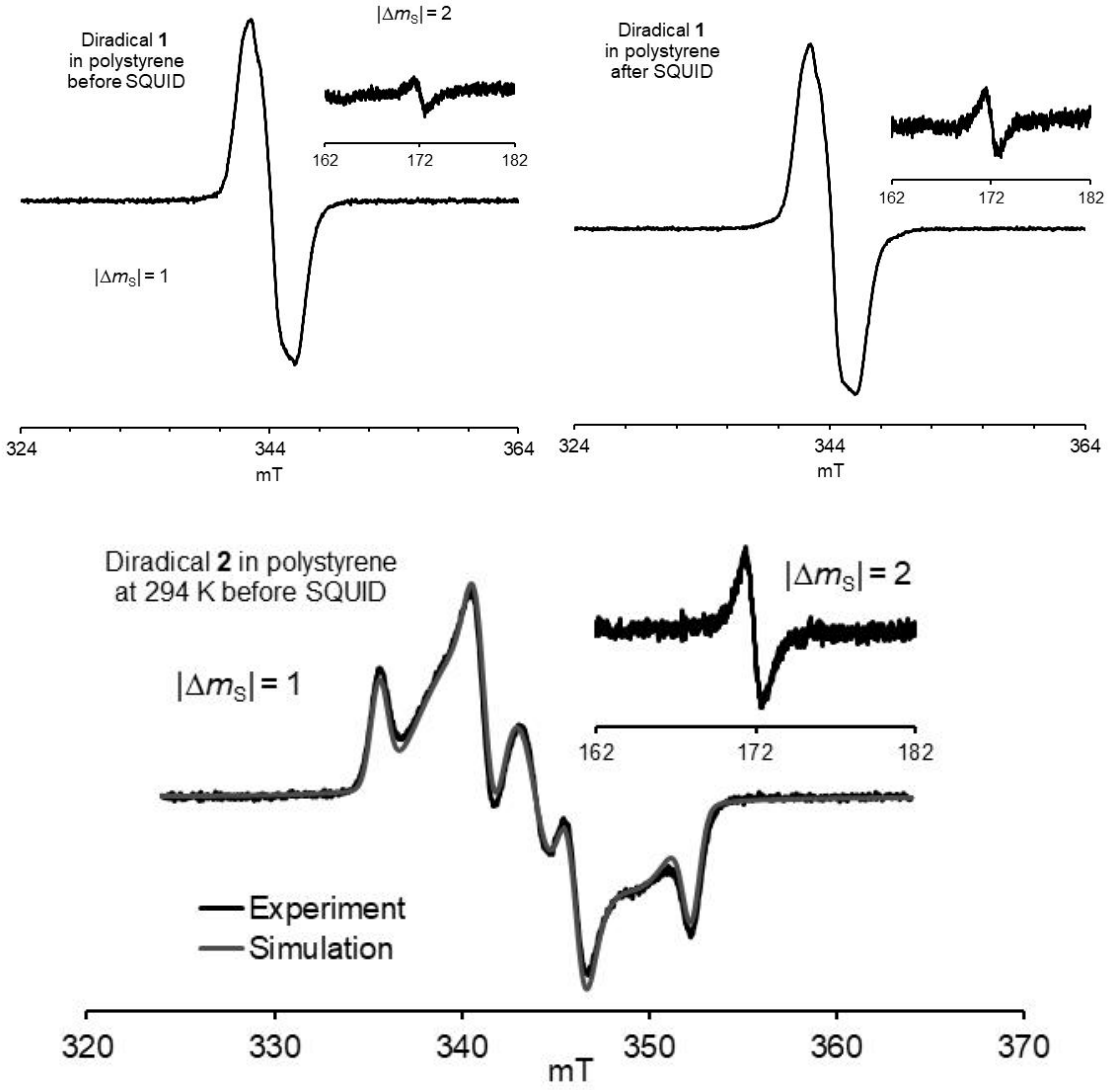

Fig. S7. Top panels: EPR (ν = 9.6564 – 9.6565 GHz, labels (Δm_s = 1): HZ838r3 & r7) spectra of diradical **1** in polystyrene glass at 294 K, before and after SQUID magnetometry. The Δm_s = 2 transitions are shown as insets (labels: HZ838r2 & r6). Bottom panel: EPR (ν = 9.6526 GHz, label: HZ804r1) spectra of diradical **2** in polystyrene glass at 294 K, prior to SQUID magnetometry. The Δm_s = 2 transition is shown as an inset (label: HZ804r3). Simulation parameters: g_{xx} = 2.0069, g_{yy} = 2.0027, g_{zz} = 2.0053, $|D/hc|$ = 232.68 MHz (7.76 × 10^{-3} cm^{-1}), $|E/hc|$ = 29.68 MHz (0.990 × 10^{-3} cm^{-1}); linewidths: LW_x = 33.0 MHz, LW_y = 94.4 MHz, LW_z = 29.2 MHz; center peak for exchange narrowed diradical **2**: g_{xx} = g_{yy} = g_{zz} = 2.0053, $|D|$ = 0.3 MHz (8.08 × 10^{-3} cm^{-1}), $|E|$ = 0.03 MHz, LW (homogenious) = 2.9 mT.

SQUID Magnetic Studies. Magnetic studies were carried out using 5-Tesla Quantum Design SQUID magnetometer at the applied mangetic fields H = 30000, 5000 and 500 Oe and at T = 1.80 – 370 K. The following samples were studied (temperature range):

(1) polycrystalline **1** and **2**; loaded to capsules and mounted in the colorless plastic straws (1.8 – 320 K),

(2) **1** and **2** in polystyrene matrix; prepared as described below (1.8 – 370 K),

(3) **1** and **2** in benzene and **2** in dibutylphthalate (DBP).

For polycrystalline and polystyrene samples, primary correction for diamagnetism was implemented by point-by-point background subtraction, together with Pascal constants correction, as described in detail in the following paragraphs.

Selected models for numerical fitting of magnetic data for diradicals 1 and 2.

Diradical Model. This model is used to fit χT *vs* T data, in order to obtain the singlet-triplet energy gap ($2J/k$ in Kelvin or ΔE_{ST} in kcal mol^{-1}). Where needed, impurities and inaccuracies in the mass balance are accounted for by the mass factor, N (eq. 1, main text); relatively weak inter-molecular interactions (compared to $2J/k$) between diradical molecules are described by mean-field parameter θ. Also, for some fits, such as polycrystalline **1**, **1** and **2** in polystyrene matrix or organic solvent matrix, another variable parameter, B, is used to account for a small residual background diamagnetism (eq. S1). These models (eq. 1 main text and eq. S1, SI) account for paramagnetic saturation.

$$\chi T = \{T^*[(1.118^*N^*\{2\sinh(a)/[1 + 2\cosh(a) + \exp((-2J/k)/T)]\}) + B]\}/H \quad \text{(S1)}$$
$$a = 1.345(H/(T - \theta))$$

***S* = 1 Dimer Model.** In this model, it is assumed that all S = 1 diradicals are involved in only one dominant pairwise intra-dimer antiferromagnetic exchange coupling (J'/k). Energy eigenvalues for Heisenberg Hamiltonian ($-2\sum_{i,j}J_{i,j}S_iS_j$) are obtained by vector decoupling technique.[S12,S13] Equations for the temperature dependence of magnetic susceptibility (χ vs. T or χT vs. T) are provided (eqs. S2A and eq. S2B). Also, impurities and inaccuracies in the mass balance are accounted for by the mass factor, N (eqs. S2A and S2B). Both equations account for paramagnetic saturation. Relatively weak inter-dimer interactions may be accounted by using the mean-field parameter θ (with N_{imp} set to zero) or alternatively with θ set to zero, small amount of free S = 1 diradical may be accounted by parameter N_{imp}.

$$\chi = (1.118/H)N[NOM/DEN] + N_{imp}(1.118/H)\{2\sinh(a)/[1 + 2\cosh(a)]\} \quad \text{(S2A)}$$
$$\chi T = (1.118T/H)N[NOM/DEN] + N_{imp}(1.118T/H)\{2\sinh(a)/[1 + 2\cosh(a)\} \quad \text{(S2B)}$$
$$NOM = \sinh(a) + 2\sinh(2a) + [(\sinh(a))\exp((-4J/k)/T)]$$
$$DEN = 1 + 2\cosh(a) + 2\cosh(2a) + \{[1 + 2\cosh(a)]\exp[(-4J/k)/T]\} + \exp((-6J/k)/T)$$
$$a = 1.345(H/(T - \theta))$$

Details of numerical fitting of SQUID magnetic data. SigmaPlot for Windows software package is used for numerical curve fitting of the magnetic data. Standard error (*SE*) for each variable parameter is provided. The reliability of a fit is measured by the parameter dependence (*DEP*), which is defined for each variable parameter as follows: *DEP = 1 – ((variance of the parameter, other parameters*

constant)/(variance of the parameter, other parameters changing)). Values close to 1 indicate an overparametrized fit.

The quality of fits may be measured by a coefficient of determination (R^2), which is defined for nonlinear numerical fits of the magnetic data as follows (eq. S3):

$$R^2 = 1 - [(\Sigma(y_i - Y_i)^2)/(\Sigma(y_i - \langle y \rangle)^2)] \quad \text{(S3)}$$

where y_i, Y_i , and $\langle y \rangle$ denote experimental values, fitted values, and the arithmetic mean of the experimental values. We list in figure captions and in Tables S2 and S3 values of R^2 that are statistically adjusted; values close to 1 indicate a fit of high quality.

The quality of fits is more reliably measured by standard error of estimate (*SEE*), which is defined as follows (eq. S4):

$$SEE = [\mathrm{SSE}/(n - 2)]^{1/2} \quad \text{(S4)}$$

where, SSE is the sum of squared errors and n is the number of points. The perfect fit would imply *SEE* = 0.0000.

SQUID magnetometry of diradicals 1 and 2 as polycrystalline powders. For diradicals **1** and **2**, initial SQUID run involved samples of 23.69 and 19.92 mg, respectively. For the background SQUID runs, a major portion of the sample was removed from the holder, to leave 11.34 and 5.04 mg samples of **1** and **2**, respectively. Following these runs, magnetization for the background, M_{bck}, was point-by-point subtracted from magnetization for the sample, M_{sample}, to provide corrected magnetization, M_{cr}, accounting for diamagnetism of sample holder. Thus, M_{cr} corresponded to mass of 12.35 and 14.88 mg for **1** and **2**, respectively. Subsequently, the M_{cr} were converted to corresponding molar magnetic susceptibilities for **1** and **2**:

$$\chi_{cor} = M_{cor}/(H^* n_{molsample}),$$

where, H is the applied magnetic field in Oe and $n_{molsample}$ is the number of moles of the sample of **1** or **2**. Final molar magnetic susceptibility, χ, was obtained by subtraction of Pascal constant-derived correction P:[S14]

$$\chi = \chi_{cor} - P$$

where, P = –0.00031328 emu/mol and P = –0.00026584 emu/mol for **1** and **2**, respectively.

While this procedure gave satisfactory χ for diradical **2**, an additional small correction for diamagnetic background (B) have to implemented when fitting the χT *vs* T data for polycrystalline **1** (eq. S1), as described in the following paragraph.

The χT *vs* T data for polycrystalline **1** in the T = 1.8 – 320 K range were fit with 3-parameter diradical model (eq. S1), with N set to 1.000. Three variable parameters were: J – intramolecular exchange coupling constant (in Kelvin); note that $2J$ = singlet-triplet energy gap (in Kelvin); N – mass factor (N = 1.00 for perfectly pure S = 1 diradical dication), and θ – the mean-field parameter to account for relatively weak (vs $2J/k$) inter-molecular interactions between diradicals, and B – correction for residual background diamgnetism. Subsequently, all χT *vs* T (and χ *vs* T) data were corrected for residual background diamagnetism using B, the χT *vs* T data were fit to diradical model (eq. 1, main text) with two variable parameters, J/k and θ (N was set to 1.00). Fits to the data at H = 30000 Oe in the warming and

cooling modes and H = 5000 Oe in the warming mode, gave $2J/k \approx 238 - 272$ K, i.e., $2J/k = 252 \pm 10$ K (or $\Delta E_{ST} \approx 0.5 \pm 0.02$ kcal mol^{-1}). These fits also gave $\theta \approx -5.9 - (-5.6)$ K suggesting presence of antiferromangetic interations between the diradical molecules; however, these interations were rather weak because the χ *vs* T data have not shown any maxima at low temperatures (Fig. S8).

In polycrystalline **2**, much stronger intermolecular antiferromagnetic interactions were found, compared to polycrystalline **1**. The χT *vs* T data, which were corrected point-by-point for diamagnetism, for polycrystalline **2** were fit in the T = 70 – 320 K range with 2-parameter diradical model (eq. 1, main text), with N set to 1.000. Two variable parameters were: J/k – intramolecular exchange coupling constant (in Kelvin); note that $2J/k$ = singlet-triplet energy gap (in Kelvin), and θ – the mean-field parameter to account for relatively weak (vs $2J/k$) inter-molecular interactions between diradicals. For diradical **2**, the magnetic data at low temperatures (T = 1.8 – 70 K) were fit using 3-parameter models. In the three-parameter models, three variable parameters were: J'/k – intra-chain or intra-dimer antiferromagnetic exchange coupling constant (in Kelvin), N – the mass factor (N = 1.00 for perfectly pure S = 1 diradical), and N_{imp} – the mass factor for a "free" S = 1 diradical; alternative fits replaced N_{imp} with θ - the mean-field parameter to account for relatively weak inter-chain or inter-dimer exchange couplings (in Kelvin). (Still another type of fit by using N_{imp} – the mass factor for an "impurity" S = ½ monoradical were found to be inferior, as expected because diradical **2** is nearly perfectly pure.) The results of the fits for diradical **2** are summarized in Table S2 (SI). Singlet-triplet energy gaps ($2J/k$ and ΔE_{ST}) for polycrystalline diradicals **1** and **2**, obtained from χT *vs* T diradical fits (Eq. 1, main text) at various magnetic fields (H) may be summarized as follows (mean ± SE):

for diradical **1**, $2J/k = 252 \pm 10$ K and $\Delta E_{ST} = 0.50 \pm 0.02$ kcal mol^{-1};

for diradical **2**, $2J/k = 876 \pm 36$ K and $\Delta E_{ST} = 1.75 \pm 0.07$ kcal mol^{-1}.

SQUID magnetometry of diradicals 1 and 2 in polystyrene matrix. Samples of **1** and **2** dispersed in polystyrene glass were prepared by dissolving diradical and polystyrene in THF, and the thoroughly evaporating the solvent. A similarly prepared sample of polystyrene glass was used for diamagnetic background correction. Detailed procedure for **2** may be found below; similar procedure was used for diradical **1**.

Diradical **2** (NG0896b, 2.48 mg) and polystyrene (MW = 29300 Da, 150.46 mg) were evacuated in a small vial for 30 min, and then charged with argon gas. Then, to the vial THF (0.6 mL, freshly distilled from benzophenone/sodium) was added and the mixture was sonicated and heated gently until polystyrene was completely dissolved to give a red-dark solution. Subsequently, the solution was evacuated gently at –30 °C to remove THF and then evacuated at p = ca. 1 mTorr for 1 h at RT. After that, the vial was transferred to a container and evacuated at 60 °C for 2 days at $p \approx 1$ mTorr. Then the solid was ground with plastic spatula, and the following samples were prepared: (1) for EPR spectroscopy (label: HZ804r…), (2) for ^{1}H NMR spectra (label: HZ804-solvent check), and (3) for SQUID, weight 43.40 mg (0.69 mg of diradical, label: HZ804s1…). After SQUID, the sample was recovered and ^{1}H NMR spectrum was obtained (label: HZ804-solvent check-after SQUID). Similar procedure was used diradical **1** (diradical weight = 0.75 mg, label: HZ838s1…).

The background sample without diradical was prepared using same procedure except the weight of polystyrene was 95.65 mg and volume of THF was 0.5 mL; evacuated at $p \approx 1$ mTorr overnight at 60 ^{o}C; two samples were prepared: (1) for ^{1}H NMR spectra (label: HZ804-polystyrene solvent check) and (2) for SQUID, weight 43.47 mg.

SQUID data were obtained for diamagnetic background sample using identical SQUID tube as for the diradical-containing sample. The SQUID tube, and its mounting to the sample holder, was similar to those used for solution samples (in benzene and DBP, described in the following paragraphs), except it was not flame sealed; the tube was open to the SQUID sample chamber atmosphere through two pinholes in the sample holder. Correction for diamagnetism was carried out analogously to those described in the preceding paragraphs for polycrystalline samples, with the final correction based on Eq. S1 (SI). After χT *vs* T data at 30000 Oe were corrected for diamagnetism, then raw magnetization data, M_r vs H at T = 1.8 – 5 K, were corrected to obtain final values of magnetization: $M = M_r + [(H^*B_{MH})/30000]$, where B_{MH} was obtained by a match between χT *vs* T data corrected previously using eq. S1 and χT_{cr} *vs* T obtained from M_r vs T at H = 30000 Oe; that is, $\chi T_{cr} = T * [(M_r - B_{MH})/(n^*30000)]$, where n = number of moles of diradical.

The resultant M vs H data were fit as M vs $H/(T + \theta)$ to the Brillouin functions with two variable parameters, S and M_{sat}, with θ adjusted incrementally, until the values of S at T = 1.8 – 5 K were within 0.004 or so. For diradicals **1** and **2**, θ-values were negative with $|\theta| \leq 0.05$ K, i.e., intermolecular interactions between the diradicals were antiferromagnetic and almost negligible. Nearly perfect fits were obtained with SEE = 0.0000 (see: figure captions in Figs. S11 and S12).

The χT *vs* T data for T = 1.8 – 360 K or 1.8 – 370 K, corrected for diamagnetism, were fit to diradical model (eq. 1, main text) using two variable parameters: singlet triplet gap ($2J/k$) and correction factor for the number of moles of diradical S = 1 (N). Notably, for both diradicals, fitted values of N = 0.729 – 0.730 and 0.923 – 0.928 were in a good agreement with the values of M_{sat} corresponding to 74.1% (0.741) and 92.5% (0.925) of theoretical values for 0.75 and 0.69 mg of S = 1 diradicals **1** and **2** (see: Table S3 and figure captions in Figs. S11 and S12). This indicated that the diradicals were pure and that $N < 1.000$ was because of the weighing error (number of moles of diradical in the SQUID sample). Singlet-triplet energy gaps ($2J/k$ and ΔE_{ST}) for diradicals **1** and **2** in polystyrene, obtained from χT *vs* T diradical fits (Eq. 1, main text) at various magnetic fields (H) may be summarized as follows (mean ± SE):
for **1** in polystyrene, $2J/k$ = 165 ± 18 K and ΔE_{ST} = 0.33 ± 0.04 kcal mol^{-1};
for **2** in polystyrene, $2J/k$ = 838 ± 78 K and ΔE_{ST} = 1.68 ± 0.16 kcal mol^{-1}.

EPR spectra at room temperature for **1** and **2** in polystyrene, before and/or after SQUID magnetometry, showed only minor center peaks, most likely due to exchange narrowing of a small fraction of aggregated diradicals (Fig. S7).[S15] This appears to account for slightly less than zero values of θ in M/M_{sat} vs. $H/(T - \theta)$ plots, as described in the preceding paragraphs.

SQUID magnetometry of diradicals 1 and 2 in frozen benzene and 2 in DBP. Weighed amount of diradical (0.80–2.53 mg) was transferred to a SQUID tube equipped with a 4-mm vacuum stopcock (Kontes),[S16,S17] and then placed under vacuum ($p \approx 1$ mTorr). The SQUID tube was described before in detail;[S18] briefly, it was made from 5-mm OD EPR quartz tube, which was open on both ends (overall

length of 22 – 25 cm) but it possessed an ultra thin quartz false bottom, ca. 5 – 7 cm from the end of the tube. Subsequently, a small amount of benzene was vacuum transferred to the tube (or DBP was added via syringe), to make ca. 0.8 cm height of the solution (ca. 100 μL). Homogenious, degassed solution of diradical (18 – 50 mM) was then frozen in liquid nitrogen and the quartz tube was flame sealed.

Because the values of θ obtained from Brillouin function fits M vs $H/(T - \theta)$ were non-negligible with 0.6 K < $|\theta| \leq$ 0.8 K, the χT vs T data (T = 1.8 – 250 K for benzene and T = 1.8 – 270 K for DBP) were fit to a diradical model (eq. 1, main text) with three variable parameters: singlet triplet gap ($2J/k$), correction factor for the number of moles of diradical S = 1 (N), and and θ – the mean-field parameter to account for relatively weak (vs $2J/k$) inter-molecular interactions between diradicals. Singlet-triplet energy gaps ($2J/k$ and ΔE_{ST}) for diradicals **1** and **2** in benzene, and **2** in DBP, obtained from χT *vs* T diradical fits (Eq. 1, main text) at various magnetic fields (H) may be summarized as follows (mean ± SE):
for **1** in benzene, $2J/k$ = 260 ± 1 K and ΔE_{ST} = 0.519 ± 0.002 kcal mol^{-1};
for **2** in benzene, $2J/k$ = 327 ± 7 K and ΔE_{ST} = 0.65 ± 0.01 kcal mol^{-1};
for **2** in DBP, $2J/k$ = 350 ± 10 K and ΔE_{ST} = 0.70 ± 0.02 kcal mol^{-1}.

Because of absence of point-by-point correction for diamagnetism and, in particular for samples in benzene and DBP, narrower temperature range by ca. 100 K, the values of $2J/k$ are much less reliable for diradical **2** with relatively large $2J/k$, compared to those obtained in polystyrene or polycrystalline diradicals.

Table S2. Complete set of fitting parameters for χT vs T and χ vs T data of polycrystalline diradical **2**.

χT or χ	T [K]	Fit	H [Oe]	J/k or J'/k (SE, DEP) [a] [K]	θ (SE, DEP) [b] [K]	N (SE, DEP) [c]	SEE [d]	R^2 [e]
χT	70-320	Diradical	30000 cool	488 (15, 0.219)	–13.6 (0.1, 0.219)	NA	0.0041	0.9838
			30000 warm	422 (7, 0.178)	–14.05 (0.08, 0.178)	NA	0.0028	0.9933
			5000 warm	439 (8, 0.172)	–13.87 (0.09, 0.172)	NA	0.0029	0.9926
			5000 cool	403 (6, 0.189)	–13.89 (0.09, 0.189)	NA	0.0028	0.9922
	1.8-70	1D-chain	30000 warm	–13.87 (0.06, 0.902)	0.48 (0.03, 0.701)	1.093 (0.002, 0.842)	0.0026	0.9999
			5000 warm	–14.00 (0.07, 0.903)	0.48 (0.04, 0.700)	1.100 (0.003, 0.843)	0.0030	0.9999
			500 cool	–13.84 (0.06, 0.892)	0.40 (0.03, 0.650)	1.058 (0.002, 0.837)	0.0024	0.9999
		Dimer	30000 warm	–9.33 (0.23, 0.767)	1.33 (0.03, 0.308)	0.97 (0.01, 0.725)	0.0240	0.9927
			5000 warm	–9.59 (0.25, 0.757)	1.70 (0.01, 0.228)	0.97 (0.2, 0.733)	0.0269	0.9909
			500 cool	–9.64 (0.27, 0.766)	1.781 (0.002, 0.344)	0.94 (0.02, 0.729)	0.0258	0.9917
χ	1.8-70	1D-chain	30000 warm	–13.87 (0.16, 0.923)	0.44 (0.02, 0.498)	1.093 (0.11, 0.912)	0.0004	0.9687
			5000 warm	–14.32 (0.11, 0.926)	0.52 (0.01, 0.481)	1.116 (0.008, 0.918)	0.0003	0.9871
			500 cool	–14.00 (0.10, 0.927)	0.41 (0.01, 0.532)	1.068 (0.007, 0.9171	0.0002	0.989
		Dimer	30000 warm	–6.14 (0.24, 0.910)	1.04 (0.04, 0.842)	0.67 (0.03, 0.706)	0.0034	-
			5000 warm	–5.49 (0.25, 0.866)	1.56 (0.02, 0.749)	0.57 (0.04, 0.676)	0.0048	-
			500 cool	–7.73 (0.59, 0.769)	1.97 (0.01, 0.608)	0.77 (0.10, 0.562)	0.0089	-
χT or χ	T [K]	Fit	H [Oe]	J'/k (SE, DEP) [a] [K]	N (SE, DEP) [c] [K]	N_{imp} (SE, DEP) [f]	SEE [d]	R^2 [e]
χT	1.8-70	1D-chain	30000 warm	–13.82 (0.07, 0.9080)	1.086 (0.002, 0.8328)	0.0110 (0.0010, 0.8320)	0.0028	0.9999
			5000 warm	–13.85 (0.07, 0.8920)	1.094 (0.003, 0.8333)	0.0082 (0.0009, 0.7524)	0.0032	0.9999
			500 cool	–13.72 (0.06, 0.8792)	1.053 (0.002, 0.8278)	0.0067 (0.0007, 0.6975)	0.0026	0.9999
		Dimer	30000 warm	–10.86 (0.07, 0.8817)	0.967 (0.003, 0.7830)	0.0696 (0.0014, 0.7950)	0.0043	0.9998
			5000 warm	–10.42 (0.10, 0.8542)	0.974 (0.005, 0.7751)	0.0537 (0.0018, 0.7087)	0.0067	0.9994
			500 cool	–10.18 (0.11, 0.8297)	0.940 (0.005, 0.7665)	0.0459 (0.0018, 0.6386)	0.0075	0.9993
χ	1.8-70	1D-chain	30000 warm	–14.33 (0.09, 0.9267)	1.106 (0.006, 0.9081)	0.0141 (0.0003, 0.6032)	0.0002	0.9929
			5000 warm	–14.43 (0.11, 0.9194)	1.117 (0.007, 0.9079)	0.0108 (0.0002, 0.4854)	0.0002	0.9899
			500 cool	–14.03 (0.08, 0.9182)	1.067 (0.006, 0.9063)	0.0077 (0.0001, 0.5036)	0.0002	0.9930
		Dimer	30000 warm	–10.06 (0.20, 0.7694)	0.915 (0.019, 0.7141)	0.064 (0.001, 0.3218)	0.0010	0.8129
			5000 warm	–8.75 (0.26, 0.7387)	0.861 (0.028, 0.6951)	0.044 (0.001, 0.2396)	0.0017	0.4916
			500 cool	–8.36 (0.28, 0.7173)	0.814 (0.030, 0.6845)	0.038 (0.001, 0.1748)	0.0018	0.3333

[a] J/k or J'/k, Heisenberg exchange coupling constant; note that $2J/k$ = singlet triplet energy gap in Kelvin, *SE*, standard error; *DEP*, parameter dependence. [b] θ, mean-field correction. [c] N, weight factor. [d] *SEE*, standard error of estimate. [e] R^2, coefficient of determination. .[f] N_{imp}, weight factor for isolated $S = 1$ diradical.

Table S3. Complete set of fitting parameters to the diradical model (eq. 1, main text) for χT vs. T data of diradicals **1** and **2** in polystyrene (PS), benzene, and dibutylphthalate (DBP).

Diradical	Matrix	*T* [K]	*H* [Oe]	2*J*/*k* (*SE*, *DEP*) [a] [K]	θ (*SE*, *DEP*) [b] [K]	*N* (*SE*, *DEP*) [c]	*SEE* [d]	R^2 [e]
1	PS	1.8-370	30000 warm,	147 (5, 0.684)	NA	0.731 (0.002, 0.684)	0.0099	0.9860
		1.8-370	5000 warm	182 (5, 0.531)	NA	0.733 (0.001, 0.531)	0.0109	0.9441
2	PS	1.8-360	30000 cool	990 (40, 0.302)	NA	0.923 (0.001, 0.302)	0.0070	0.9957
		1.8-360	5000 warm	800 (20, 0.334)	NA	0.9278 (0.0008, 0.334)	0.0066	0.7463
		1.8-360	5000 cool	730 (20, 0.303)	NA	0.923 (0.001, 0.303)	0.0084	0.6899
1	benzene	1.8-250	5000 cool	259 (21, 0.569)	–1.50 (0.05, 0.524)	0.760 (0.004, 0.718)	0.0165	0.9728
		1.8-250	5000 warm	258 (21, 0.568)	–1.60 (0.05, 0.532)	0.772 (0.004, 0.722)	0.0169	0.9697
		1.8-250	500 cool	262 (28, 0.584)	–1.46 (0.06, 0.503)	0.767 (0.006, 0.717)	0.0233	0.9520
2	benzene	1.8-260	30000 warm	338 (18, 0.532)	–2.83 (0.05, 0.577)	0.738 (0.002, 0.728)	0.0092	0.9966
		1.8-250	5000 cool	314 (31, 0.627)	–1.69 (0.06, 0.479)	0.702 (0.005, 0.733)	0.0198	0.9622
		1.8-250	5000 warm	329 (33, 0.611)	–1.83 (0.06, 0.489)	0.715 (0.005, 0.729)	0.0209	0.9558
2	DBP	1.8-270	30000 warm	359 (21, 0.521)	–2.88 (0.06, 0.567)	1.029 (0.004, 0.719)	0.0142	0.9959
		1.8-270	5000 warm	340 (32, 0.615)	–1.86 (0.07, 0.482)	0.997 (0.006, 0.728)	0.0291	0.9555

[a] 2*J*/*k*, singlet-triplet energy gap in Kelvins, related to Heisenberg exchange coupling constant, *J*/*k*; *SE*, standard error; *DEP*, parameter dependence. [b] θ, mean-field correction. [c] *N*, weight factor. [d] *SEE*, standard error of estimate. [e] R^2, coefficient of determination.

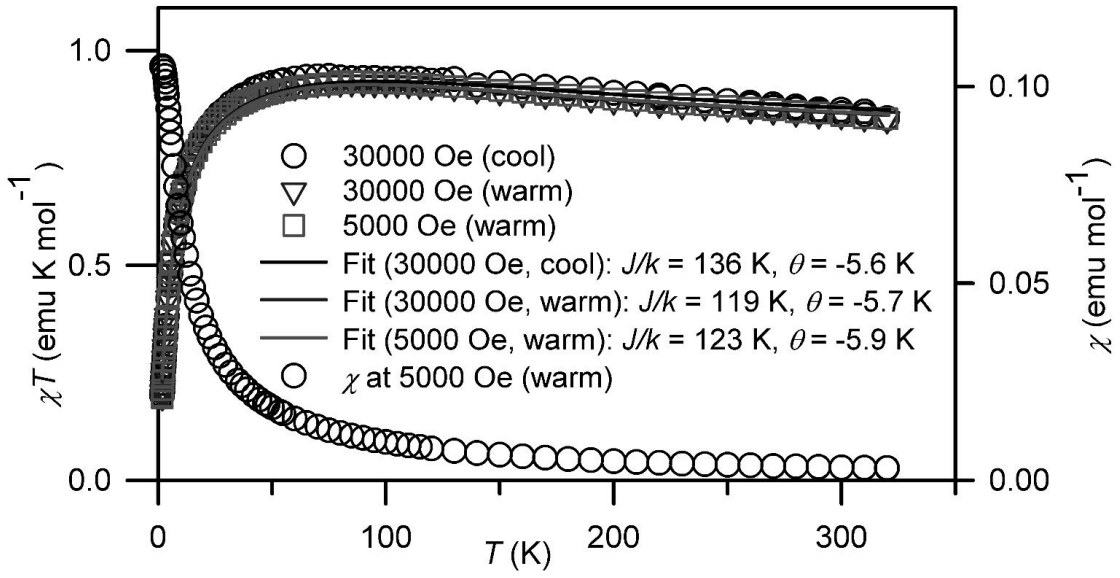

Fig. S8. SQUID magnetometry of polycrystalline (solid) diradical **1** (SQUID label: HZ723s1D_dir1_Figs). The χT vs T data corrected for diamagnetism at H = 30000 Oe in the cooling mode and H = 30000 and 5000 Oe in the warming modes were fit to a diradical model (eq. 1 main text), using two variable parameters: exchange coupling constant, J/k, mean-field correction for intermolecular interactions between the radicals, θ. The values of standard error, *SE*, and parameter dependence, *DEP*, are provided; goodness of fit may be measured by standard error of estimate, *SEE*. Fit for 30000 Oe cooling mode: J/k = 136 K (*SE* = 5), θ = –5.63 K (*SE* = 0.09), *DEP* = 0.0218, R^2 = 0.9940, *SEE* = 0.0193. Fit for 30000 Oe warming mode: J/k = 119 K (*SE* = 4), θ = –5.71 K (*SE* = 0.07), *DEP* = 0.0241, R^2 = 0.9958, *SEE* = 0.0164. Fit for 5000 Oe warming mode: J/k = 123 K (*SE* = 4), θ = –5.89 K (*SE* = 0.08), *DEP* = 0.0236, R^2 = 0.9941, *SEE* = 0.0175.

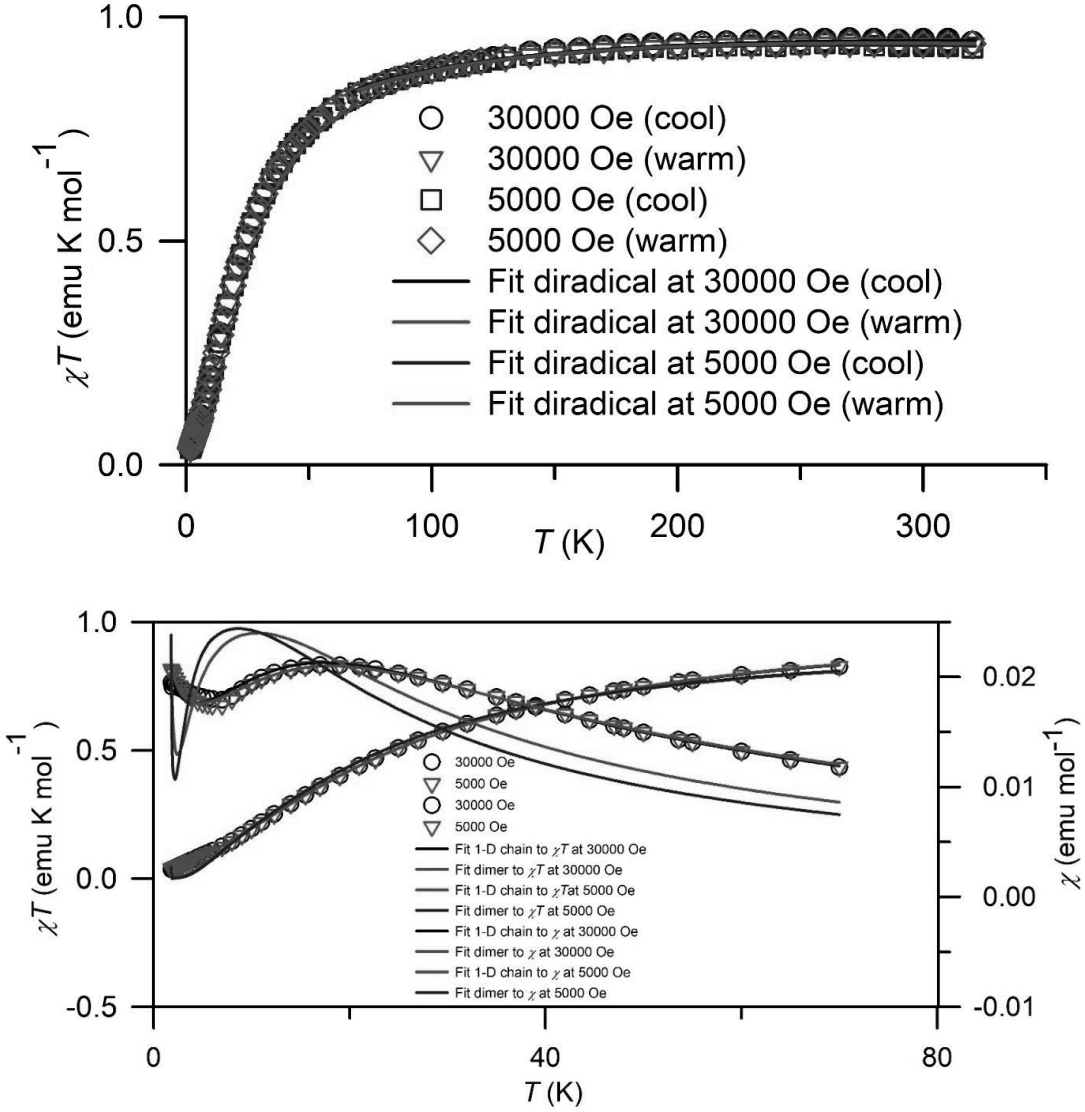

Fig. S9. SQUID magnetometry of polycrystalline (solid) diradical **2** (SQUID label: HZ7255s1C_bk_FigSI). All fitting parameters are summarized in Table S2 (upper rows). Top plot: χT vs T data corrected for diamagnetism at H = 30000 Oe and H = 5000 Oe in both cooling and warming modes were fit to diradical model in the temperature range, T = 70 – 320 K. Bottom plot: The χT vs T and χ vs T data corrected for diamagnetism at H = 30000 Oe and H = 5000 Oe in the warming modes were fit to 1-D chain or dimer models with the following three variable parameters: J'/k, θ, and N.

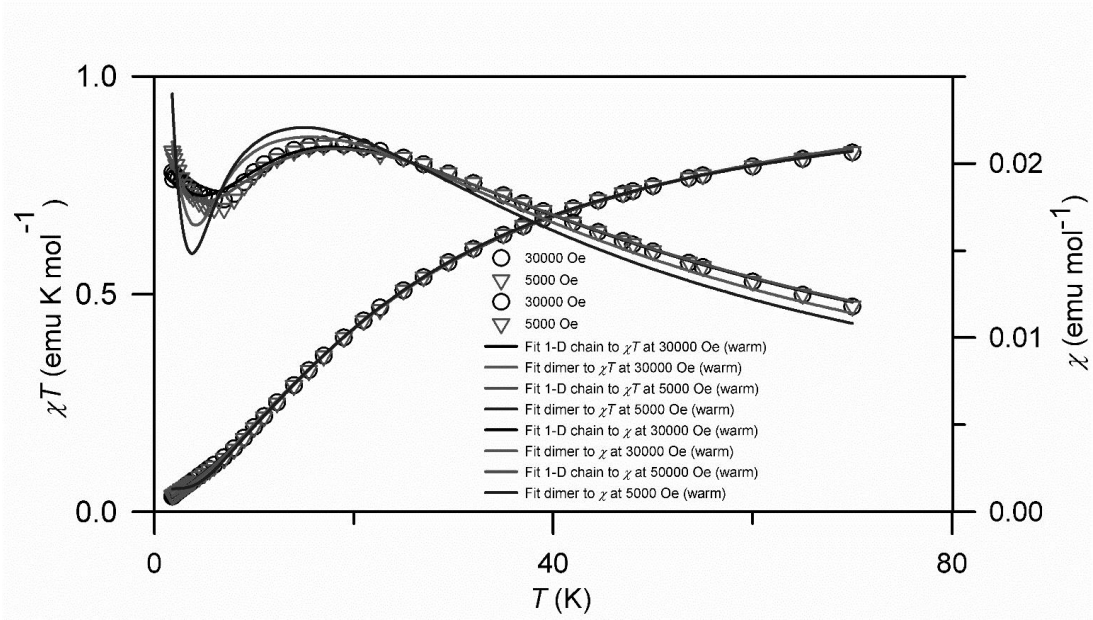

Fig. S10. SQUID magnetometry of polycrystalline (solid) diradical **2** (SQUID label: HZ7255s1C_bk_FigSI). All fitting parameters are summarized in Table S2 (lower rows). The χT vs T and χ vs T data corrected for diamagnetism at H = 30000 Oe and H = 5000 Oe in the warming modes were fit to 1-D chain or dimer models with the following three variable parameters: J'/k, N, and N_{imp}, where N_{imp} is the fraction of isolated S = 1 diradicals.

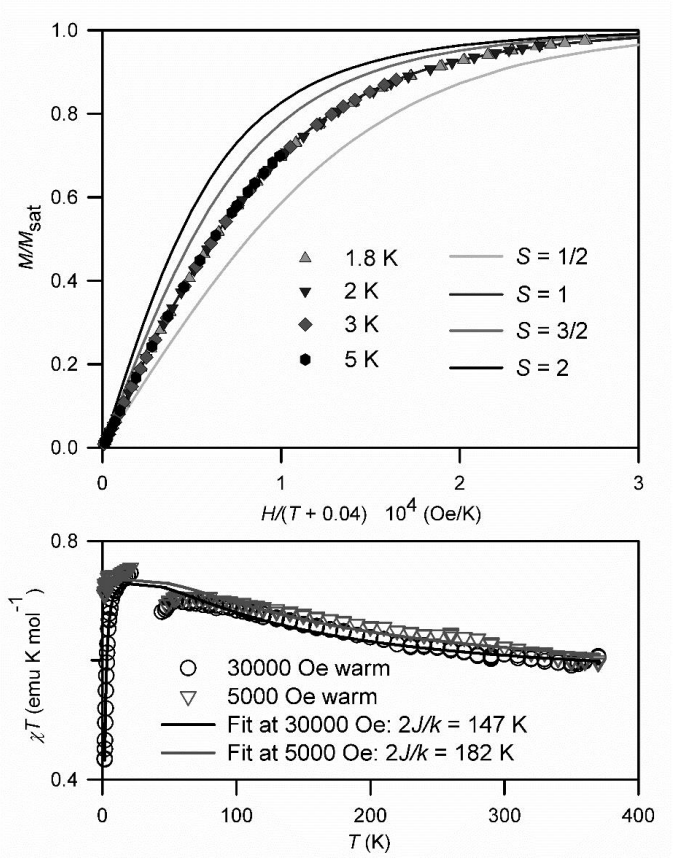

Fig. S11. SQUID magnetometry of diradical **1** (0.75 mg) in polystyrene matrix (total weight = 43.80 mg) (SQUID label: HZ833s1_PS_B). Top plots: M/M_{sat} vs $H/(T - \theta)$, where $\theta = -0.04$ K, plots at T = 1.8, 2, 3, and 5 K (symbols) and the Brillouin curves corresponding to S = ½ - 2 (lines). Numerical fits, M vs $H/(T + 0.04)$ and based on the Brillouin functions, with M corrected for diamagnetism, to the experimental data at T = 1.8, 2, 3, and 5 K gave the following values of the two variable parameters, S and M_{sat} (and parameter dependence): 1.8 K: $S = 0.979 \pm 0.002$, $M_{sat} = 0.01253 \pm 0.000004$ (0.534); 2 K: $S = 0.978 \pm 0.002$, $M_{sat} = 0.01254 \pm 0.000004$ (0.631); 3 K: $S = 0.982 \pm 0.001$, $M_{sat} = 0.01255 \pm 0.000004$ (0.824); 5 K: $S = 0.977 \pm 0.002$, $M_{sat} = 0.01262 \pm 0.000009$ (0.974). All fits were perfect with $R^2 = 1.0000$ and $SEE = 0.0000$. Bottom plots: following substraction for diamagnetism, the shown χT vs T data (T = 1.8 – 370 K) were fit to a diradical model (eq. 1, main text) using two variable parameters: $2J/k$ and N, as summarized in Table S3. Note: M_{sat} = 0.01253 emu at 1.8 K corresponds to 74.1% (0.741) of theoretical value for 0.75 mg of S = 1 diradical **1**, i.e., in an agreement with N = 0.731 – 0.733 obtained from χT vs T fits.

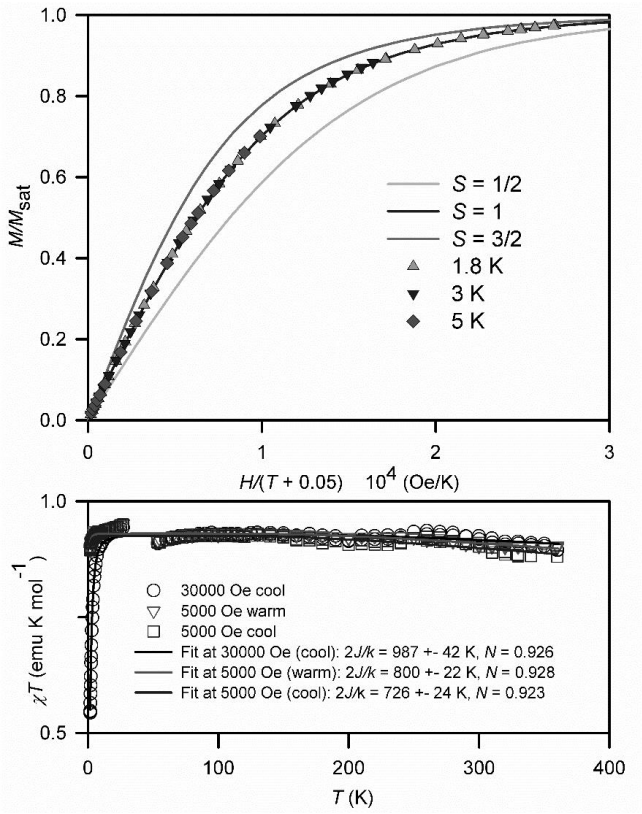

Fig. S12. SQUID magnetometry of diradical **2** in polystyrene matrix (SQUID label: HZ804s1_PS_B). Top plots: M/M_{sat} vs $H/(T-\theta)$, where $\theta = -0.05$ K, plots at $T = 1.8$, 3, and 5 K (symbols) and the Brillouin curves corresponding to $S = ½ – 3/2$ (lines). Numerical fits, M vs $H/(T + 0.05)$ based on the Brillouin functions, with M corrected for diamagnetism, to the experimental data at $T = 1.8$, 3, and 5 K gave the following values of the two variable parameters, S and M_{sat} (and parameter dependence): 1.8 K: $S = 1.008 \pm 0.002$, $M_{sat} = 0.01628 \pm 0.000005$ (0.479); 3 K: $S = 1.008 \pm 0.001$, $M_{sat} = 0.01630 \pm 0.000004$ (0.807); 5 K: $S = 1.012 \pm 0.002$, $M_{sat} = 0.01630 \pm 0.000011$ (0.968). Value $M_{sat} = 0.01628$ at 1.8 K corresponds to 0.925 μB, i.e., 92.5% of the expected value. All fits were perfect with $R^2 = 1.0000$ and SEE = 0.0000. Bottom plots: following substraction for diamagnetism, the shown χT vs T data ($T = 1.8 – 360$ K) were fit to a diradical model (eq. 1, main text) using two variable parameters: $2J/k$ and N, as summarized in Table S3. Note that $N = 0.923 – 0.928$, which is in a good agreement with the value of M_{sat} corresponding to 92.5% of the expected value.

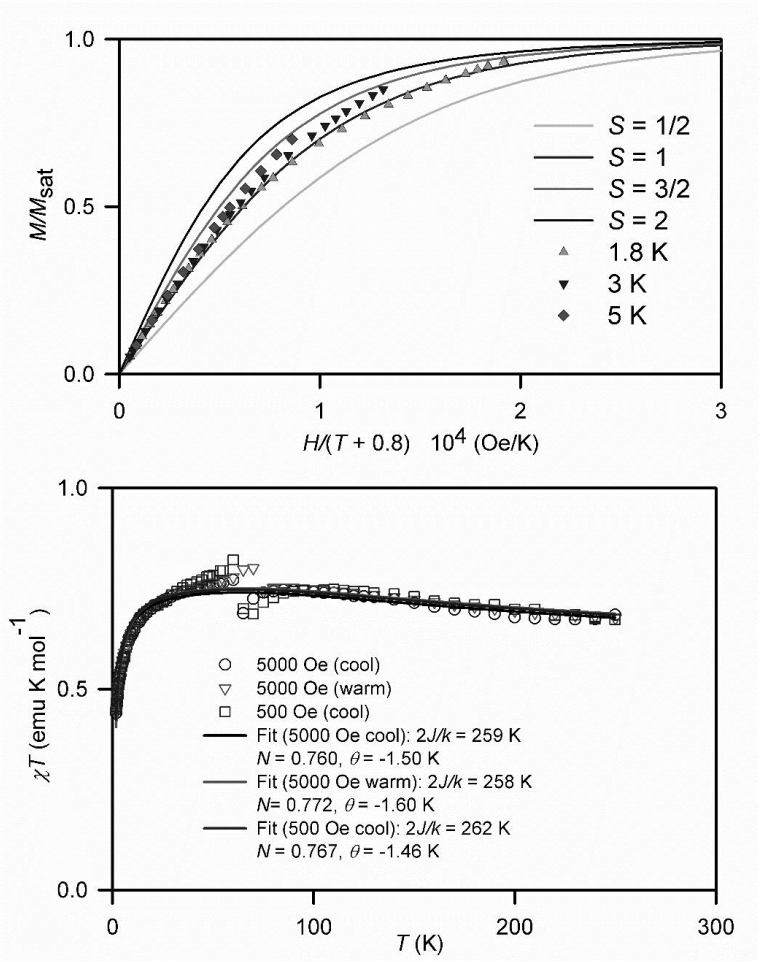

Fig. S13. SQUID magnetometry of ~50 mM diradical **1** (2.53 mg) in frozen benzene (SQUID label: HZ719s1D). Top plots: M/M_{sat} vs $H/(T - \theta)$, where $\theta = -0.8$ K, plots at $T = 1.8$, 3, and 5 K (symbols) and the Brillouin curves corresponding to $S = ½$ - 2 (lines). Numerical fits, M vs $H/(T + 0.8)$ and based on the Brillouin functions, with M corrected for diamagnetism, to the experimental data at $T = 1.8$, 3, and 5 K gave the following values of the two variable parameters, S and M_{sat} (and parameter dependence): 1.8 – 5 K: $S = 1.0$ and $M_{sat} = 0.0348 – 0.0382$ (0.71 – 0.98). Bottom plots: following substraction for diamagnetism, the shown χT vs T data ($T = 1.8 – 250$ K) were fit to a diradical model (eq. 1, main text) using three variable parameters: $2J/k$, N, and θ, as summarized in Table S3.

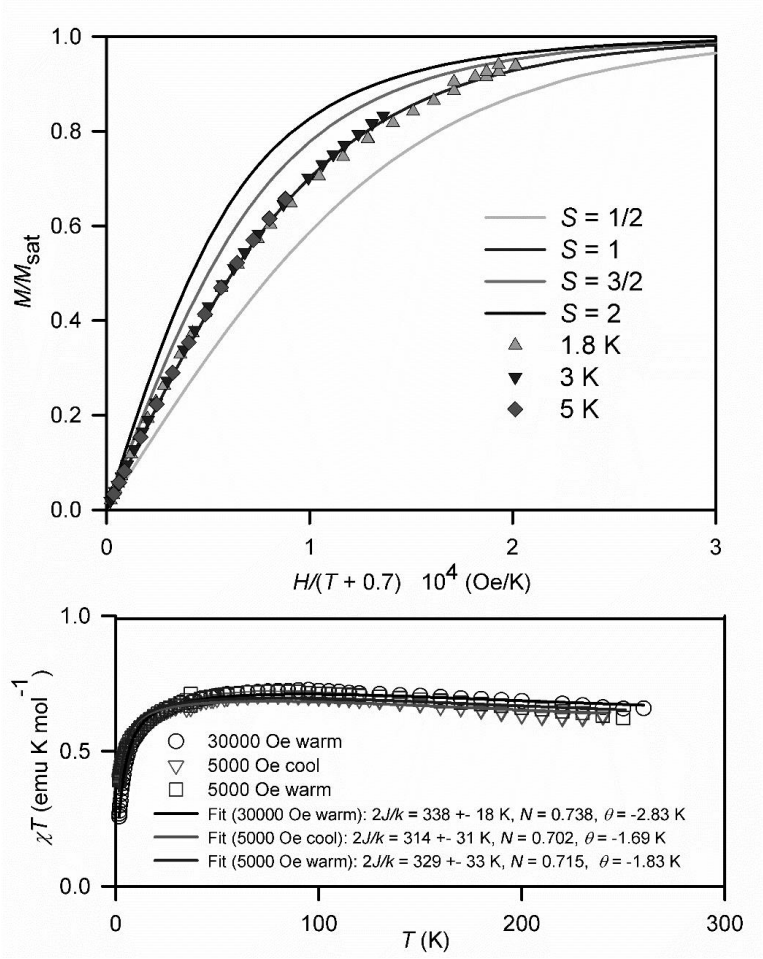

Fig. S14. SQUID magnetometry of ~25 mM diradical **2** (1.11 mg) in frozen benzene (SQUID label: HZ778s1B). Top plots: M/M_{sat} vs $H/(T - \theta)$, where $\theta = -0.7$ K, plots at $T = 1.8$, 3, and 5 K (symbols) and the Brillouin curves corresponding to $S = ½$ - 2 (lines). Numerical fits, M vs $H/(T + 0.7)$ and based on the Brillouin functions, with M corrected for diamagnetism, to the experimental data at $T = 1.8$, 3, and 5 K gave the following values of the two variable parameters, S and M_{sat} (and parameter dependence): 1.8 – 5 K: $S = 1.001 - 1.045$ and $M_{sat} = 0.0143 - 0.0148$ (0.69 – 0.98). Bottom plots: following substraction for diamagnetism, the shown χT vs T data ($T = 1.8 - 250$ K) were fit to a diradical model (eq. 1, main text) using three variable parameters: $2J/k$, N, and θ, as summarized in Table S3.

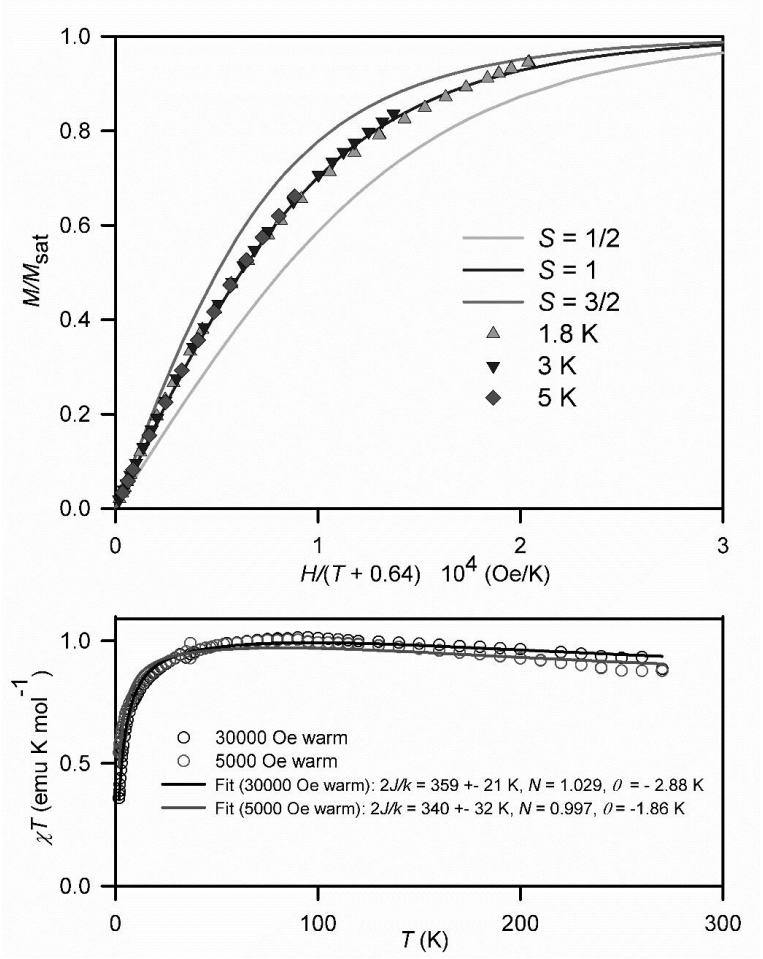

Fig. S15. SQUID magnetometry of 18 mM diradical **2** (0.80 mg) in DBP (SQUID label: HZ779s1B_FigSI). Top plots: M/M_{sat} vs $H/(T - \theta)$, where θ = –0.64 K, plots at T = 1.8, 3, and 5 K (symbols) and the Brillouin curves corresponding to S = ½ - 3/2 (lines). Numerical fits, M vs $H/(T + 0.64)$ and based on the Brillouin functions, with M corrected for diamagnetism, to the experimental data at T = 1.8, 3, and 5 K gave the following values of the two variable parameters, S and M_{sat} (and parameter dependence): 1.8 – 5 K: S = 1.013 – 1.050 and M_{sat} = 0.0140 – 0.0152 (0.67 – 0.98). Bottom plots: following substraction for diamagnetism, the shown χT vs T data (T = 1.8 – 270 K) were fit to a diradical model (eq. 1, main text) using three variable parameters: $2J/k$, N, and θ, as summarized in Table S3.

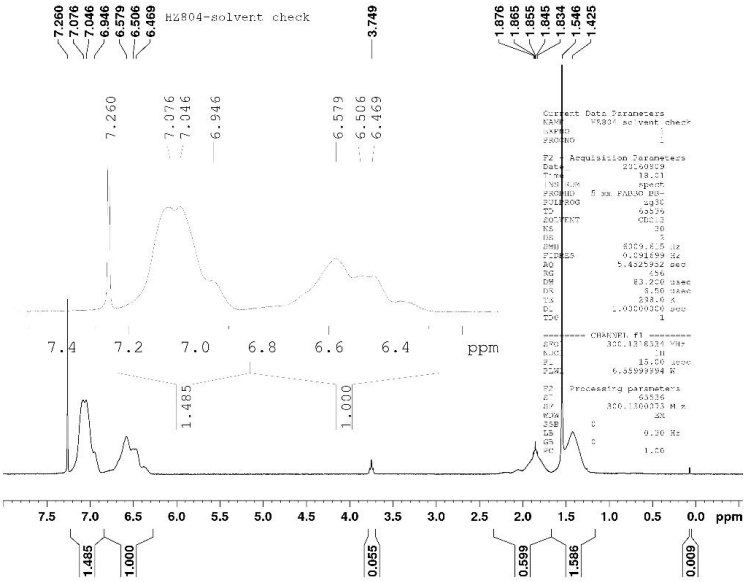

Fig. S16. ^{1}H NMR spectrum (300 MHz, chloroform-*d*) of the sample of diradical **2** in polystyrene prior to SQUID magnetometry; peak at ~3.75 ppm, integrating to 0.055 H corresponds to four protons in the CH_2-O moieties of residual THF.

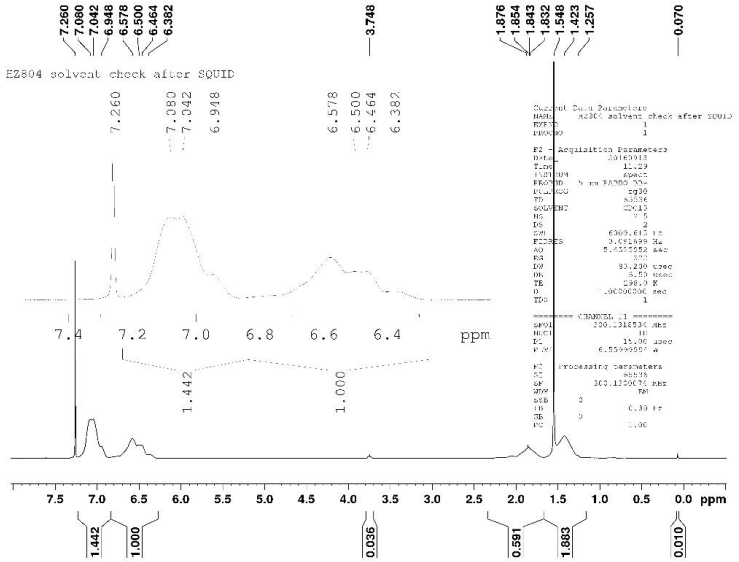

Fig. S17. ^{1}H NMR spectrum (300 MHz, chloroform-*d*) of the sample of diradical **2** in polystyrene after SQUID magnetometry; peak at ~3.75 ppm, integrating to 0.036 H corresponds to four protons in the CH_2-O moieties of residual THF.

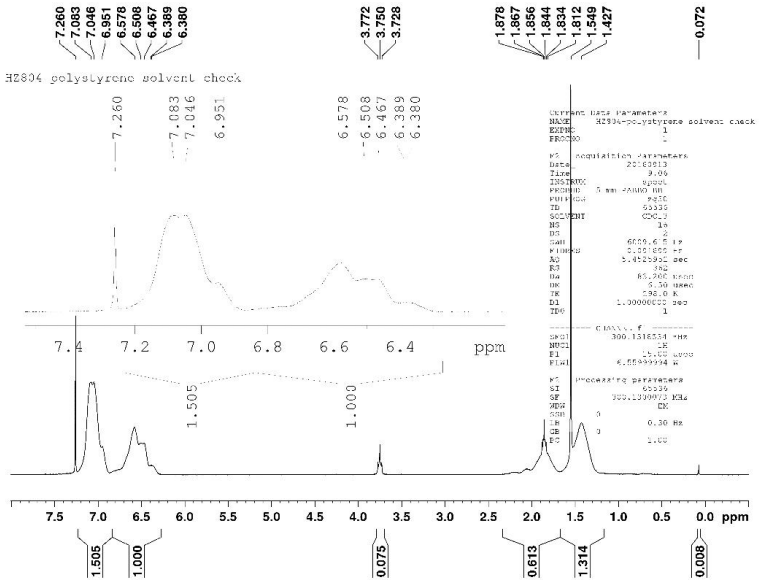

Fig. S18. ^{1}H NMR spectrum (300 MHz, chloroform-*d*) of the sample of polystyrene used for diamagnetic background prior to SQUID magnetometry; peak at ~3.75 ppm, integrating to 0.075 H corresponds to four protons in the CH_2-O moieties of residual THF.

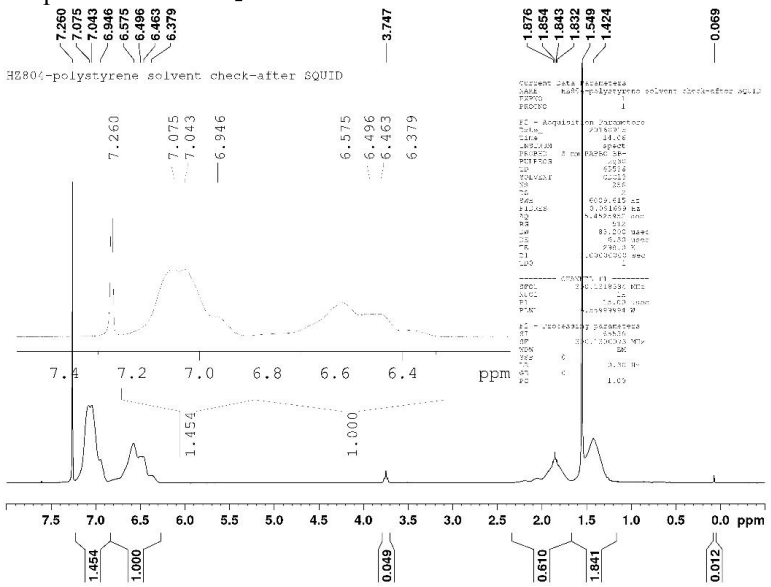

Fig. S19. ^{1}H NMR spectrum (300 MHz, chloroform-*d*) of the sample of polystyrene used for diamagnetic background after SQUID magnetometry; peak at ~3.75 ppm, integrating to 0.049 H corresponds to four protons in the CH_2-O moieties of residual THF.

2. Experimental Section: Films of Diradical 2 on Silicon.

2.a Stoichiometry and integrated XPS experimental signal intensities for the thin films of 2.

Table S4. Stoichiometric and experimental elemental ratios for diradical **2**.

	Theoretical value	Film
C	26.0	25.6
N	5.0	4.4
C/N	5.2	5.8

The sensitivity factors (σ) are: $\sigma_{C\ 1s} = 0.25$ and $\sigma_{N\ 1s} = 0.42$.[S19]

2.b Fit results for the energy positions and relative intensities of the photoemission lines in the C 1s and N 1s spectra.

We find that the integrated signal intensities obtained analyzing the XPS curves are in agreement with the theoretical elemental analyses. This means that the stoichiometry of the deposited thin films corresponds to the quantitative composition of the molecule, indicating deposition without degradation. The intensity ratio of the sum of the contributions to the C 1s main line are set to have an intensity ratio 65.3:7.7:27 (%) as in the molecule for C-H&CH_3:C-C:C-N (Table S5).

Similar considerations on stoichiometry and chemical environment also hold for the quantitative analysis of the N1s core level spectra. These spectra are the most important from the magnetic point of view since their signal depends on the photoelectrons emitted from the nitrogen atoms of the nitronyl nitroxide and the Blatter radical moieties that carry the unpaired electrons. The nitronyl nitroxide moiety has two atoms of oxygen which are spectroscopically equivalent because of resonance. Accordingly, the two nitrogen atoms are chemically equivalent and have consequently the same binding energy. Thus, we expect one peak (N_{NN}). The three nitrogen atoms in the Blatter radical moiety are assigned to the pyridine-like nitrogen (N_2) that has a carbon atom and a nitrogen atom as neighbors and to the nitrogen bound also to the phenyl ring (N_1) in agreement with previous works. Due to the delocalization of the unpaired electron, the peak at lower binding energy) can be related to photoelectron emitted from the nitrogen radical (N_{rad} or N_4). Thus, the intensity ratio of the sum of the contributions to the N 1s main line are set to have an intensity ratio 2:1:1:1 as in the molecule for N_{NN}:N_1:N_2:N_4 (Table S6).

Table S5. Fit results for the energy positions and relative intensities of the photoemission lines in the C 1s spectra.

	Energy (eV)	Lorentzian Width (eV)	Gaussian Width (eV)	Intensity (%)
C-C	284.6	0.08	1.05	6.4
C-H & CH_3	285.2	0.08	1.05	60.0
C-N	286.3	0.08	1.10	22.9
S_1	287.2	0.08	0.92	8.5
S_2	288.8	0.08	1.76	2.2

I(C-C+ C-H & CH_3+ S_1) = 74.9%
I(C-N+S_2) = 25.1%

Table S6. Fit results for the energy positions and relative intensities of the photoemission lines in the N 1s spectra.

	Energy (eV)	Lorentzian Width (eV)	Gaussian Width (eV)	Intensity (%)
N_4	398.7	0.10	0.90	17.0
N_2	399.7	0.10	0.90	17.0
N_1	401.4	0.10	0.90	17.0
N_{NN}	402.2	0.10	1.00	19.8
S_1	400.5	0.10	0.90	9.3
S_2	403.1	0.10	1.12	6.2
S_3	403.9	0.10	3.90	13.7

I(N_4+N_2+N_1+S_1) = 60.3%
I(N_{NN}+S_2+S_3) =39.7%

2.c Stabilty of fims under UHV and on air.

We have monitored the stability of the films in ultra-high vacuum (UHV, base pressure 2×10^{-10} mbar) by using XPS, focusing on the N 1s core level spectra, carrying the information on the radical state. Fig. S20 shows the N 1s core level spectra of ~1-nm films of diradical **2** kept 17 and 60 hours, respectively, in UHV at room temperature. The spectra show no major changes on the investigated time scale, indicating that the film of diradical **2** is stable under vacuum. Note that the spectra measured upon UHV storage have lower statistics than those measured on the freshly evaporated films to avoid artifacts due to long beam exposure.

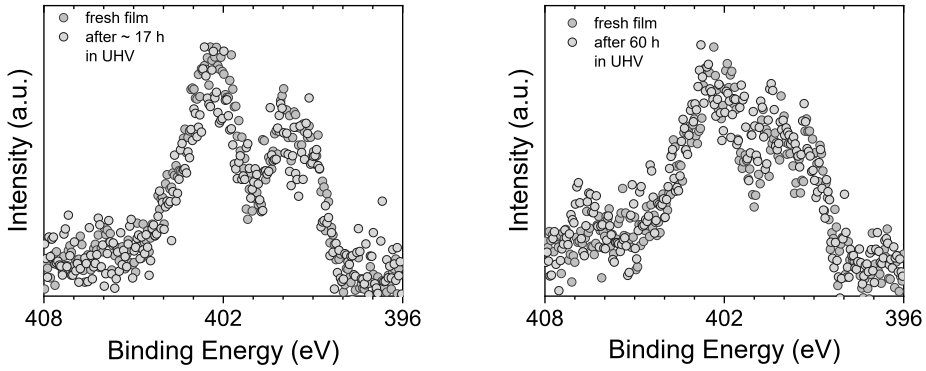

Fig. S20. Comparison of N 1s core level spectra of a freshly evaporated films while keeping the sample at room temperature in ultra-high vacuum conditions. Left plot: after 17 h. Right plot: after 60 h.

Using the same approach, we have investigated the film stability upon air exposure (Fig. S21). We have observed changes, already after 7 h of exposure to air. The major change is the increase of the intensity at around 401 eV. This intensity significantly grows with time exposure (see: arrows in Fig. S21).

In our previous work, we found changes in the intensity in the films of nitronyl nitroxide and the Blatter radical derivatives in the same binding energy range. These phenomena were related to a slow degradation of the films under ambient conditions due to changes impacting the radical part of the molecules, with the binding energy value hinting at a possible reduction (hydrogenation) of the Blatter radical,[S20,S21] and at the nitronyl nitroxide radical that underwent the release of an oxygen atom, converting to the imino nitroxide radical.[S22,S23] What is significantly different is the time scale: while the diradical films show clear changes on the time scale of few hours air exposure, the films of the single radicals were stable over several weeks in the case of the nitronyl nitroxide radical derivatives,[S22,S23] and over several months in the case of the Blatter radical derivative.[S20]

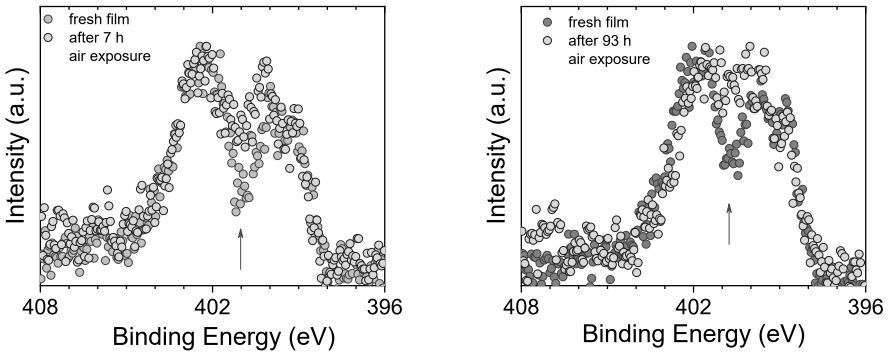

Fig. S21. Comparison of N 1s core level spectra of a freshly evaporated 1–1.4-nm films after exposure to air. Left plot: after 7 h. Right plot: after 93 h.

3. DFT computations.

DFT computations were performed using the Gaussian 09 program package (G09)[S24] running on a 4-cpu workstation under Linux operating system.

Geometry optimizations for diradical **2** were carried out at the UB3LYP/6-31G(d) level, using int=(grid=ultrafine) G09 keyword. For triplet state, optimizations were started from the X-ray determined geometries for Molecule A and Molecule B; both optimizations converged to the identical geometry. Geometry optimization for broken-symmetry singlet (BS) state started with the X-ray determined geometry for Molecule A, with the wavefunction optimized with stable=opt G09 keyword. Frequency calculations confirmed the minima on the potential energy surface (PES). Singlet-triplet energy gaps, ΔE_{ST}, for diradical **2** (Table S7) are computed using eq. S5, where $\Delta E_U = E_{BS} - E_T$, i.e., the energy difference between broken symmetry singlet and triplet states at their optimized geometries after ZPVE corrections at the UB3LYP/6-31G(d)+ZPVE theory level:[S25]

$$\Delta E_{ST} = \Delta E_U[<S^2_T>/(<S^2_T> - <S^2_{BS}>)] \qquad \text{(S5)}$$

DFT computations of intra-chain exchange coupling constant, *J'*, were carried out for dimers I and II, as well as for trimers ABA and BAB, of diradical **2** at the experimental X-ray geometry, obtained at 200 K (Table S8). All computations using 6-31G(d) and 6-311++G(d,p) basis sets employed int=(grid=ultrafine) and scf=tight keywords in Gaussian 09. Intramolecular coupling constants J_A and J_B for the monomers, molecules A and B, at the X-ray geometries were computed as well. Equations S6 – S9 were used to extract values of J_A, J_B, and *J'*,[S26] employing Yamaguchi spin contamination correction.[S27] Equation S6 refers to triplet (T) and broken symmetry singlet (BS) of the monomer **2**. Equations S7 and S8 refer to high-spin quintet (Q), broken symmetry triplet (BT), and broken symmetry singlet (BS) of the dimers of **2**.[S28] Equation S9 refers to high-spin septet (Sept) and broken symmetry quintet (BQ) of the trimers of **2**.

$$J_i = (E_{BS} - E_T)/(<S^2>_T - <S^2>_{BS}),\ i = \text{A or B} \qquad \text{(S6)}$$
$$J_i + 2J' = [(E_{BT} - E_Q)*3.0000]/(<S^2>_Q - <S^2>_{BT}),\ i = \text{A or B} \qquad \text{(S7)}$$
$$J_A + J_B + 4J' = [(E_{BS} - E_Q)*4.0000]/(<S^2>_Q - <S^2>_{BS}) \qquad \text{(S8)}$$
$$J_i + 4J' = [(E_{BQ} - E_{Sept})*5.0000]/(<S^2>_{Sept} - <S^2>_{BQ}),\ i = \text{A or B} \qquad \text{(S9)}$$

It was important to make sure that proper broken symmetry states of dimers and trimers were obtained by verifying their spin density distributions; for the BT state of dimer, effectively a combination of triplet and BS states for monomer, and for the BS state of dimer, effectively a combination of two BS states for monomer. For all broken symmetry states, proper convergence to the desired state was attained (and checked) by using stable=opt command in Gaussian 09 and various scf convergence commands (e.g., scf = Fermi).

EPR parameters (*D*-tensor and ^{14}N *A*-tensor) for diradical **2** (and **1**) were calculated using the B3LYP density functional (as implemented in ORCA[S29]) and the EPR-II basis set.[S30] All calculations used the previously optimized UB3LYP/6-31G(d,p) geometries for **1** and **2**.[S1] Input files were prepared using Gabedit.[S31] Quasi-restricted B3LYP density functional was used ("uno" option in ORCA). Calculations

of *D*-tensor employed spin-spin dipolar coupling only,[S30] with absolute values of *D* and *E* being significantly overestimated compared to the experiment (Table S9).[S1,S30,S32]

Table S7. Diradical **2** at optimized geometries: UB3LYP/6-31G(d)+ZPVE (in the gas phase) energies (hartree), zero point vibrational energies (hartree), lowest vibrational frequencies (cm^{-1}), RMS gradient norms (a.u.) in Cartesian coordinates, relative energies for triplet states (kcal mol^{-1}), and S-T splittings (kcal mol^{-1}). All computations listed in this Table were carried out with keyword int=(grid=ultrafine).[a]

State	Starting geometry	Spin densities	$E°$ (gas phase)	ZPVE	$E°$ + ZPVE	$\langle S^2 \rangle$	RMS gradient norm ($\times 10^{-6}$)[b]	Lowest vibrational frequencies	Dipole moment (D)	ΔE_U (S-T)	ΔE_{ST}
*Triplet	Molecule A	N1=+0.260 N2=+0.258 N3=+0.299 N4=+0.290 N6=+0.291	–1429.89104333	0.467248	–1429.423795	2.0799	0.34	16.0, 23.0, 33.3	5.02	0.00	**0.00**
*Triplet	Molecule B	N1=+0.260 N2=+0.258 N3=+0.299 N4=+0.290 N6=+0.291	–1429.89104332	-	-	2.0799	4.35	-	5.02	-	-
**BS-singlet	Molecule A	N1=+0.277 N2=+0.289 N3=+0.297 N4=-0.268 N6=-0.264	–1429.88835481	0.467234	–1429.421121	1.0643	6.89	15.8, 23.2, 33.4	5.16	1.68	**3.44**

[a] 1 Hartree = 627.51 kcal mol^{-1}. [b] In Cartesian coordinates. * For triplet state optimized geometries, starting from molecule A and B, the N(nitronyl nitroxide)–C–C–C torsional angles were: –13.7 – (–13.8)° and 13.7 – 13.8° respectively; analogous N(Blatter)-C-C-C torsional angles were 2.6 – 3.2° and –2.6 – (–3.2)°, respectively. Because of slight axial chirality, associated with these torsions, the two structures are mirror images, i.e., enantiomers. ** Wavefunction was tested for stability (stable=opt) and was found to be stable; the present value of ΔE_{ST} = 3.4 kcal mol^{-1} is similar to the previously computed value of ΔE_{ST} = 3.5 kcal mol^{-1} at UB3LYP/6-31G(d,p) level.[S1]

Table S8. Computed total energy (and $\langle S^2 \rangle$ in parentheses) in atomic units for diradical **2** and its dimers and trimers from single point calculations at the X-ray structure geometry using 6-31G(d) and 6-311++G(d,p) as the basis sets. Computed values of J and J' (i.e., J/k and J'/k in Kelvin) using equations S6 – S9. Note: all broken-symmetry states were checked for stability (stable=opt command in G09).

UB3LYP/ 6-31G(d)	$2S+1$	Energy ($<S^2>$)	J [K]	$J+2J'$ [K]	$2J+4J'$ [K]	$J+4J'$ [K]	J' [K]
Molecule A	3	-1429.56364914 (2.0772)	-	-	-		-
	1	-1429.56113872 (1.0644)	544.0	-	-		-
Molecule B	3	-1429.56316175 (2.0760)	-	-	-		-
	1	-1429.56086715 (1.0638)	497.5	-	-		-
Dimer I	5	-2859.12199567 (6.1487)	-	-	-		-
	3	-2859.11963692 (3.1383)	-	515.9	-		-14.1[a]
	1	-2859.11758853 (2.1279)	-	-	962.2		-19.8[b]
Dimer II	5	-2859.13189100 (6.1515)	-	-	-		
	3	-2859.12951820 (3.1393)	-	518.6	-		-12.7[a]
	1	-2859.12726076 (2.1268)	-	-	1010.0		-7.9[b]
Trimer ABA	7	-4288.69108320 (12.2242)	-	-	-	-	-
	5	-4288.68873014 (7.2140)	-	-	-	515. 4	-7.2[a]
Trimer BAB	7	-4288.69056370 (12.2228)	-	-	-	-	-
	5	-4288.68851224 (7.2129)	-	-	-	449.3	-12.0[c]
UB3LYP/ 6-311++G(d,p)	$2S+1$	Energy ($<S^2>$)	J [K]	$J+2J'$ [K]	$2J+4J'$ [K]		J' [K]
Molecule A	3	-1429.94894517 (2.0731)		-	-		
	1	-1429.94654415 (1.0612)	520.8	-	-		
Molecule B	3	-1429.94898684 (2.0720)					
	1	-1429.94677577 (1.0606)	479.8				
Dimer I	5	-2859.88786929 (6.1414)	-	-	-		
	3	-2859.88585694 (3.1319)	-	440.3	-		-19.8[c]
Dimer II	5	-2859.89794351 (6.1444)	-	-	-		
	3	-2859.89564522 (3.1325)	-	502.4	-		-9.2[a]

[a] Because the spin density distributions in the BT state of the dimer I and in the BQ state of the ABA trimer at the UB3LYP/6-31G(d) level, as well as BT state of the dimer II at the UB3LYP/6-311++G(d,p) level, indicated singlet state for molecule A and triplet state for other molecules, i = A was used in eq. S6, S7, and S9. [b] Spin density distribution in the BS state of the dimers indicate singlet state for both molecule A and B. [c] Because the spin density distribution in the BQ state of the BAB trimer at the UB3LYP/6-31G(d) and in the BT state of the dimer I at the UB3LYP/6-311++G(d,p) level indicated singlet state for molecule B and triplet state for other molecules, i = B was used in Eqs. S6, S7, and S9.

Table S9. B3LYP/EPR-II *D*-tensors and largest component of the ^{14}N *A*-tensors (for selected nitrogens). Coordinates x, y, z define molecule orientation in ORCA.[a]

				D-tensor (cm^{-1})			A_{ZZ} or A_{YY} (MHz)	
Diradical	*D* (cm^{-1})	*E* (cm^{-1})		D_{XX}	D_{ZZ}	D_{YY}	N (Blatter radical)	N (nitronyl nitroxide)
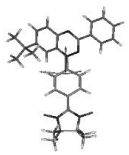 **1**^{S1}	-0.00547	-0.00156		–0.00365	+0.00027	+0.00338	+19.498	+23.828
			x	+0.9990	+0.0342	+0.0275	+0.1965	-0.0487
			y	+0.0432	-0.6643	-0.7462	+0.0325	-0.7552
			z	-0.0072	+0.7467	-0.6652	+0.9800	-0.6538
				D-tensor (cm^{-1})			A_{ZZ} (MHz)	
Diradical	*D* (cm^{-1})	*E* (cm^{-1})		D_{XX}	D_{YY}	D_{ZZ}	N (Blatter radical)	N (nitronyl nitroxide)
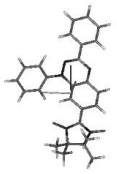 **2**	+0.01202	+0.00325		-0.00726	-0.00076	+0.00801	+18.434	+24.386
			x	-0.9952	+0.0868	+0.0449	-0.0314	-0.0034
			y	-0.0827	-0.9929	+0.0857	-0.1640	-0.1211
			z	+0.0520	+0.0816	+0.9953	+0.9860	+0.9926

[a] x, y, and z axes for **1** and **2** are shown in red, green, and blue, respectively.

4. ^{1}H NMR, ^{13}C NMR, IR, and EPR spectra of synthetic intermediates for diradical 2.

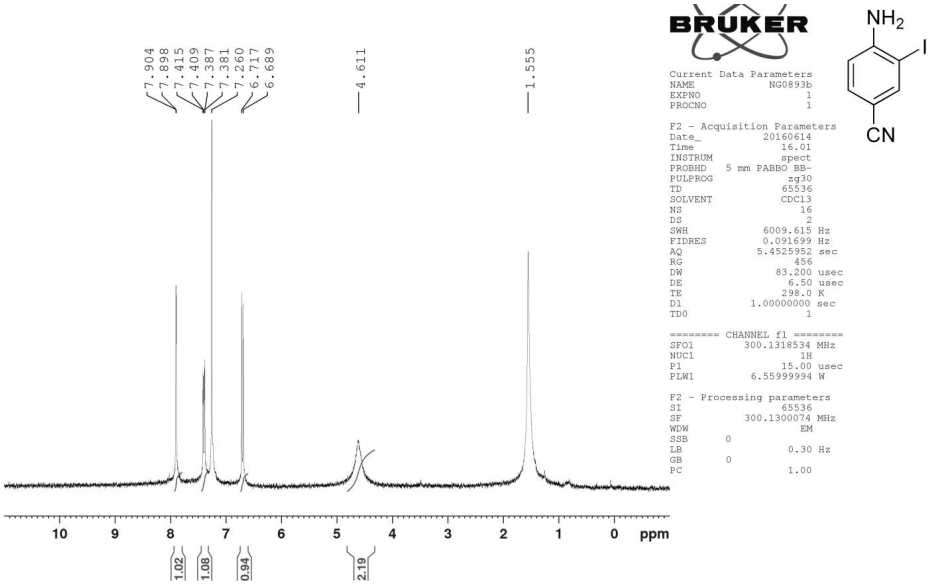

Fig. S22. ^{1}H NMR (300 MHz, $CDCl_3$) spectrum of 3-iodo-4-aminobenzonitrile, **IAB** (label: NG0894a).

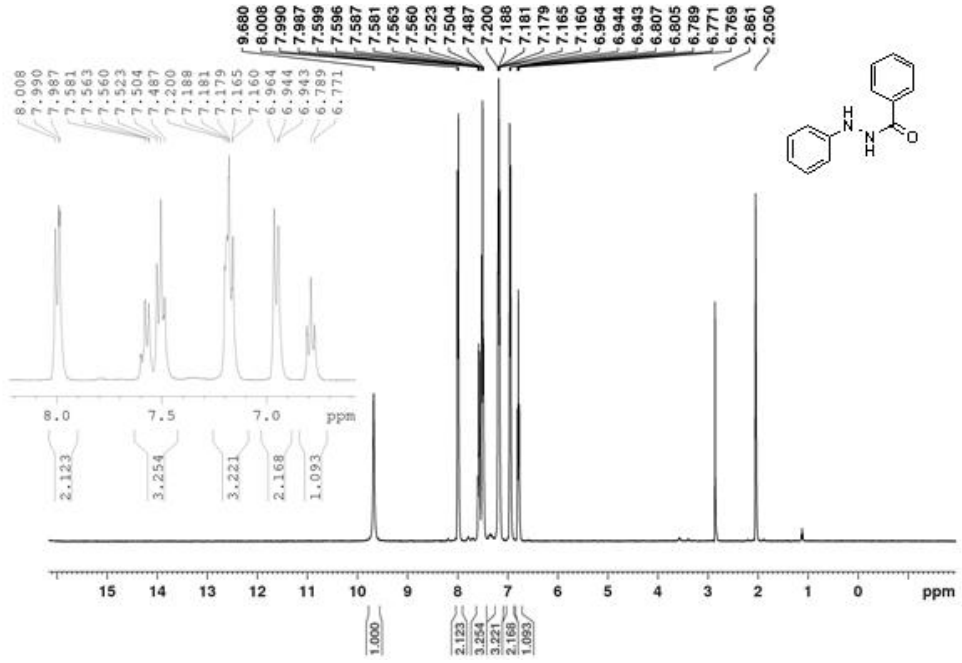

Fig. S23. ^{1}H NMR (400 MHz, acetone-d_6) spectrum of benzoic acid *N*'-phenylhydrazide (label: NG0894a).

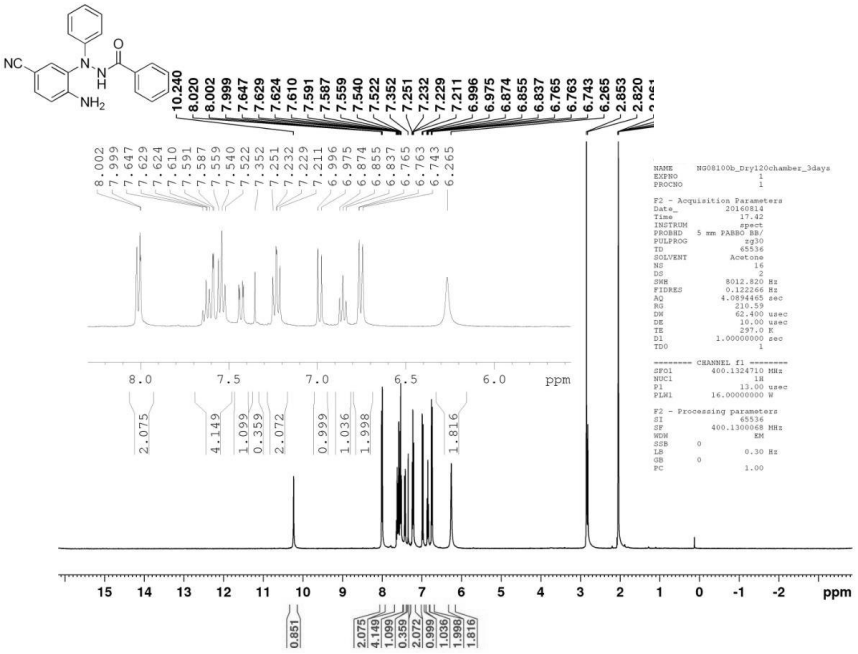

Fig. S24. ^{1}H NMR (400 MHz, acetone-d_6) spectrum of compound **B** (label: NG08100b).

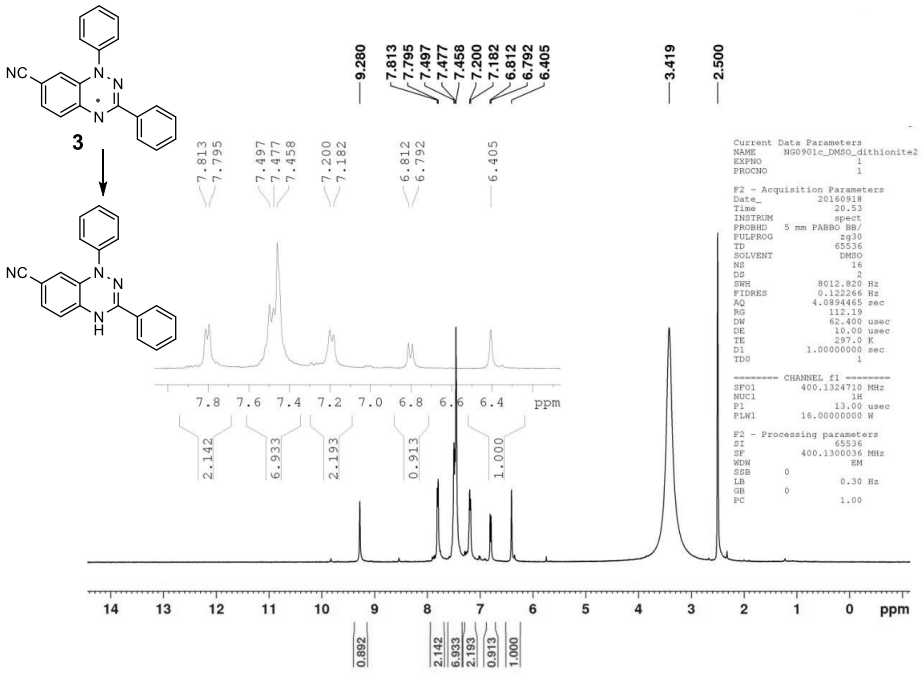

Fig. S25. ^{1}H NMR (400 MHz, DMSO-d_6) spectrum of reduced Blatter radical **3** (label: NG0901c).

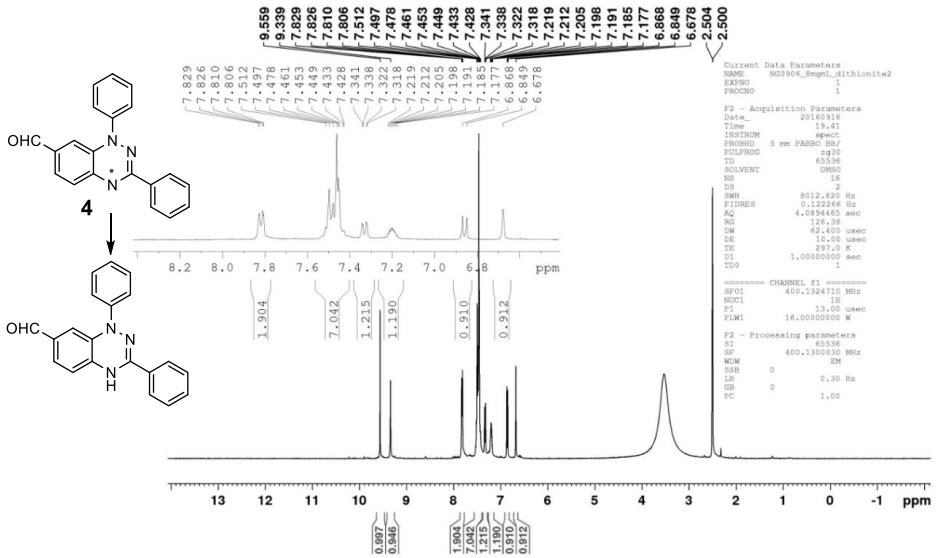

Fig. S26. ^{1}H NMR (400 MHz, DMSO-d_6) spectrum of reduced Blatter radical **4** (label: NG0907b).

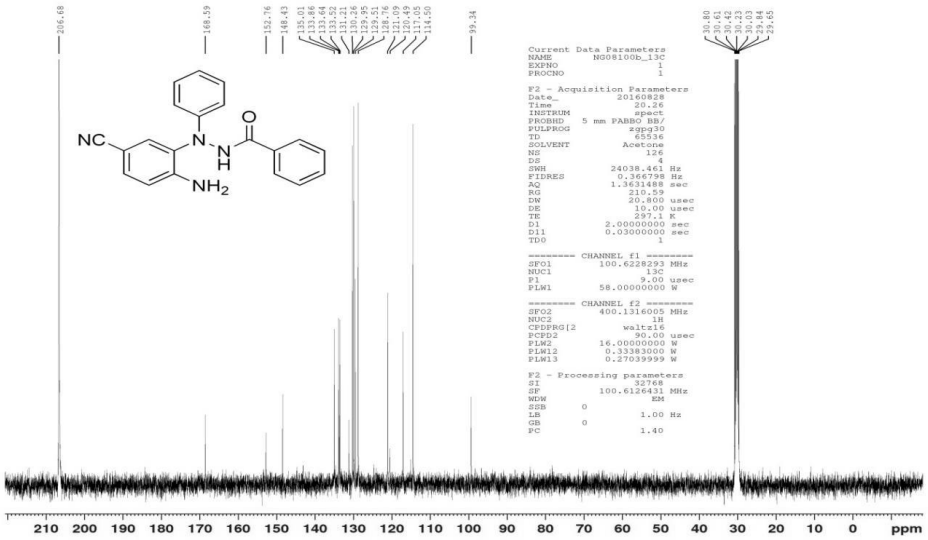

Fig. S27. ^{13}C NMR (400 MHz, acetone-d_6) spectrum of compound **B** (label: NG08100b).

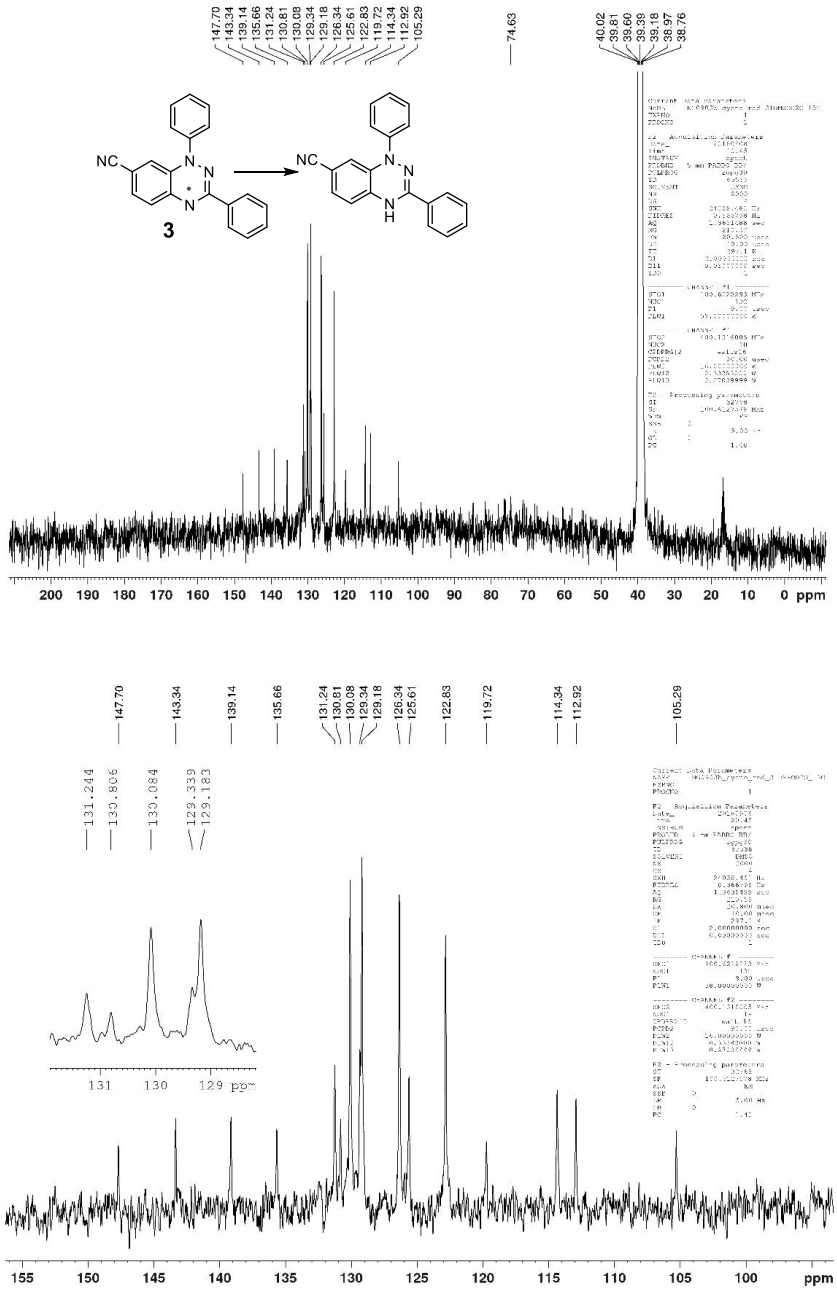

Fig. S28. ^{13}C NMR (DMSO-d_6) spectrum of reduced Blatter radical **3** (label: NG0901c).

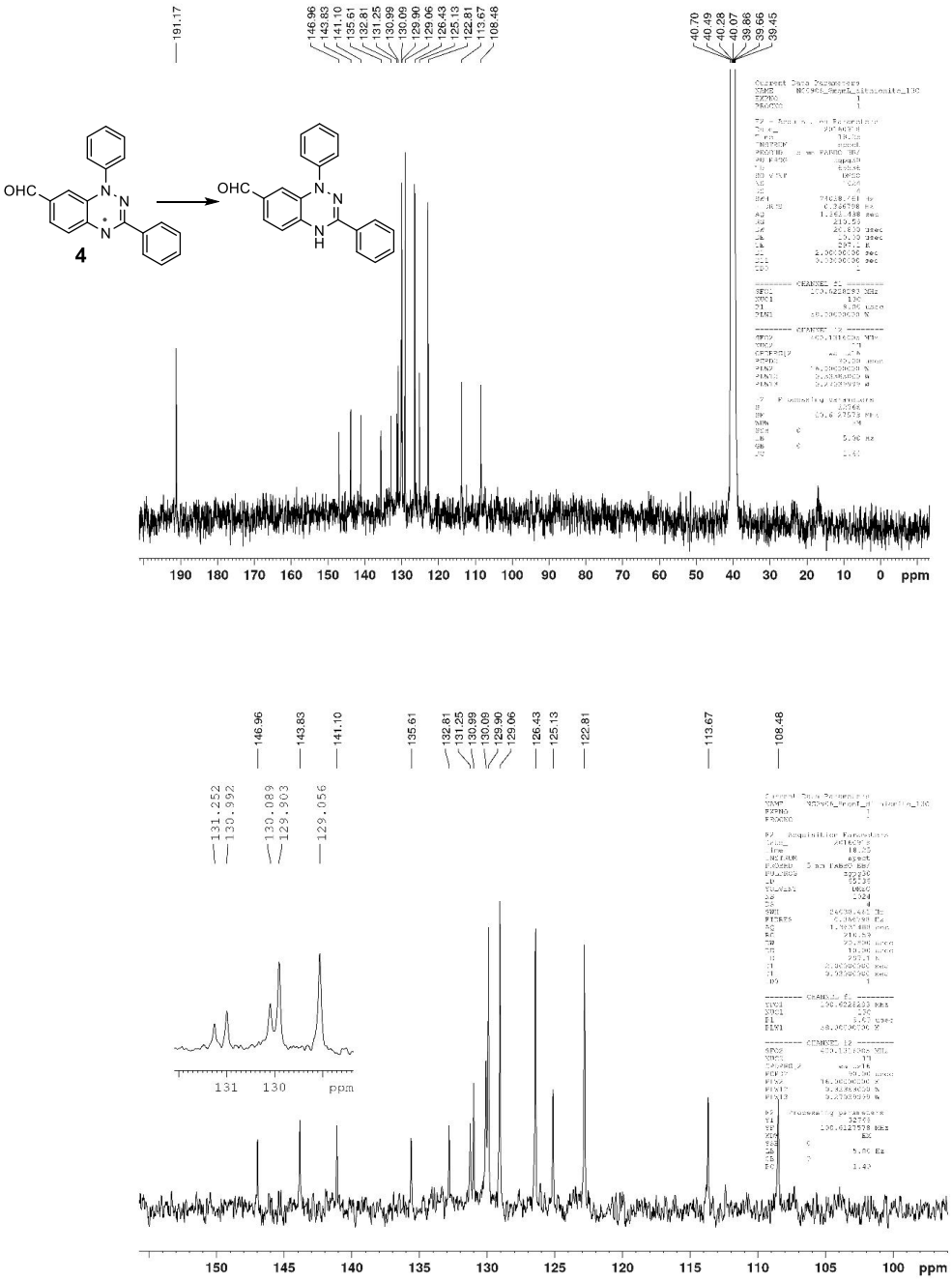

Fig. S29. ^{13}C NMR (DMSO-d_6) spectrum of reduced Blatter radical **4** (label: NG0907b).

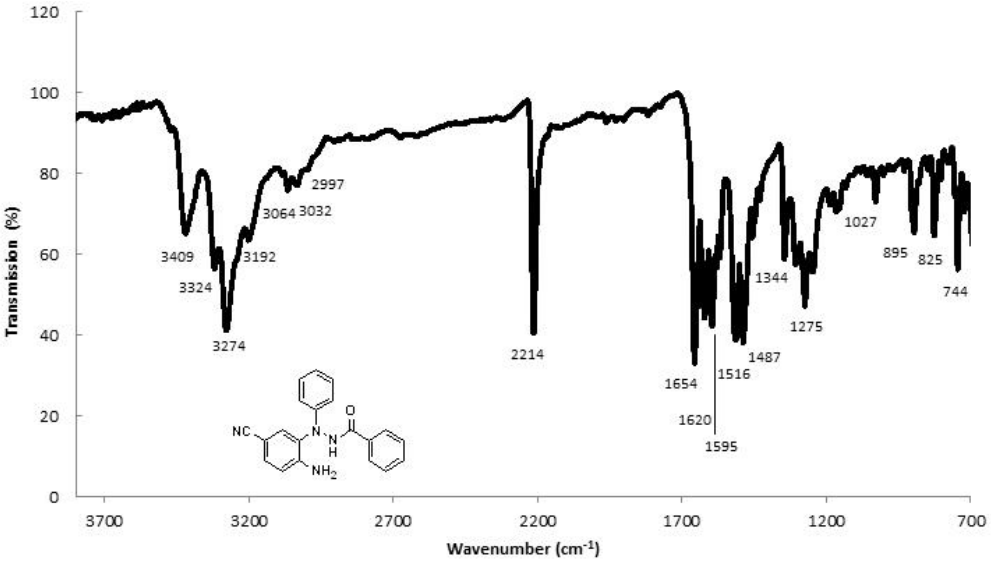

Fig. S30. FT-IR spectrum of compound **B** (label: NG08100b).

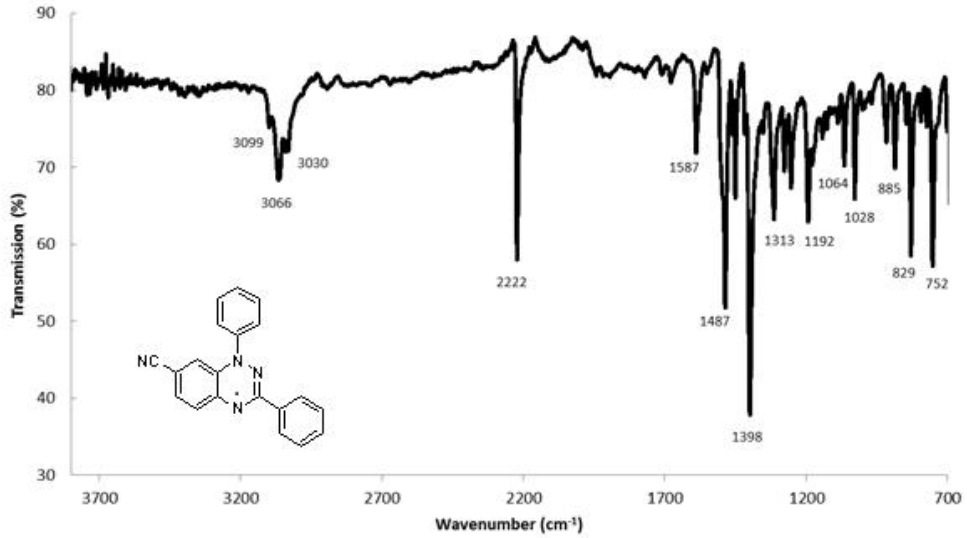

Fig. S31. FT-IR spectrum of Blatter radical **3** (label: NG0901c).

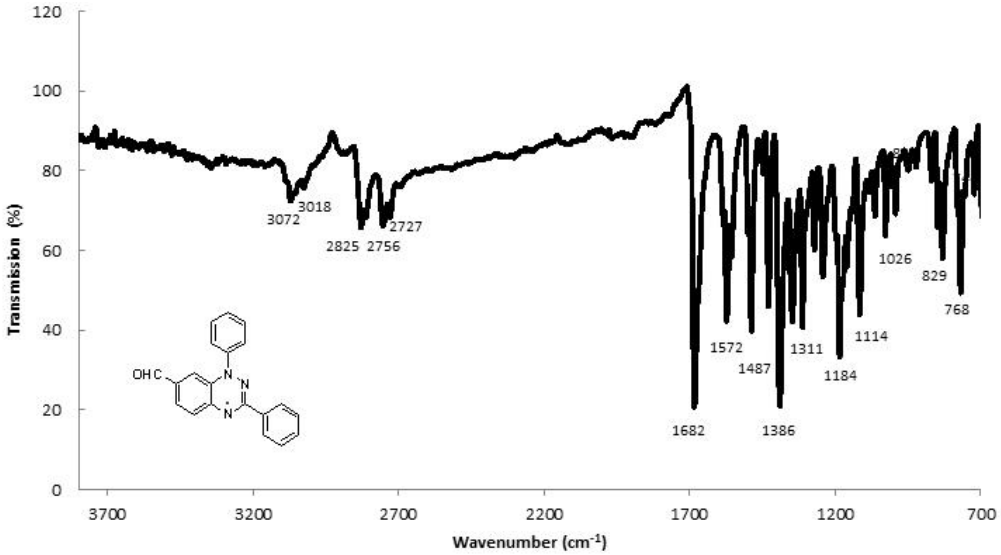

Fig. S32. FT-IR spectrum of Blatter radical **4** (label: NG0907b).

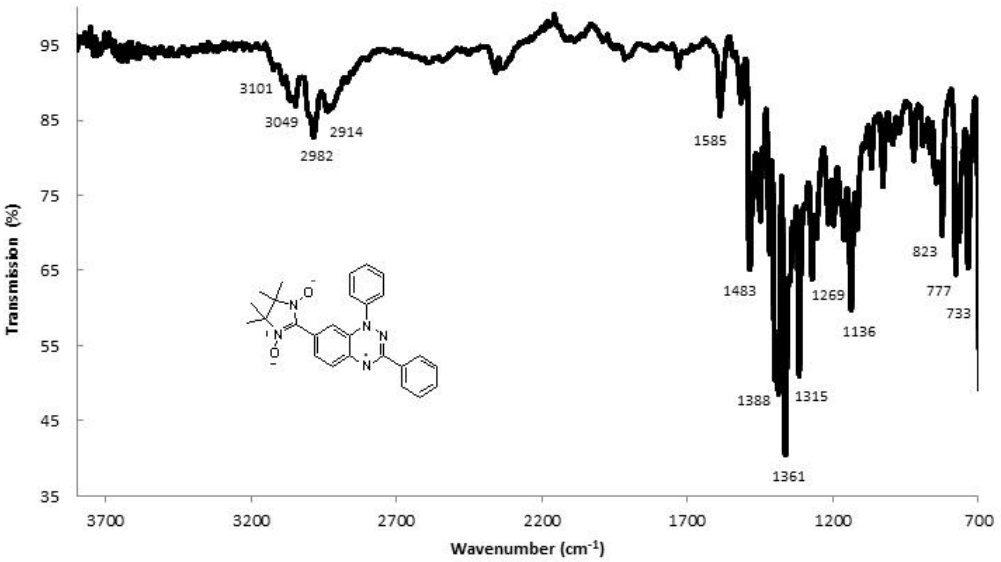

Fig. S33. FT-IR spectrum of diradical **2** (label: NG0896b).

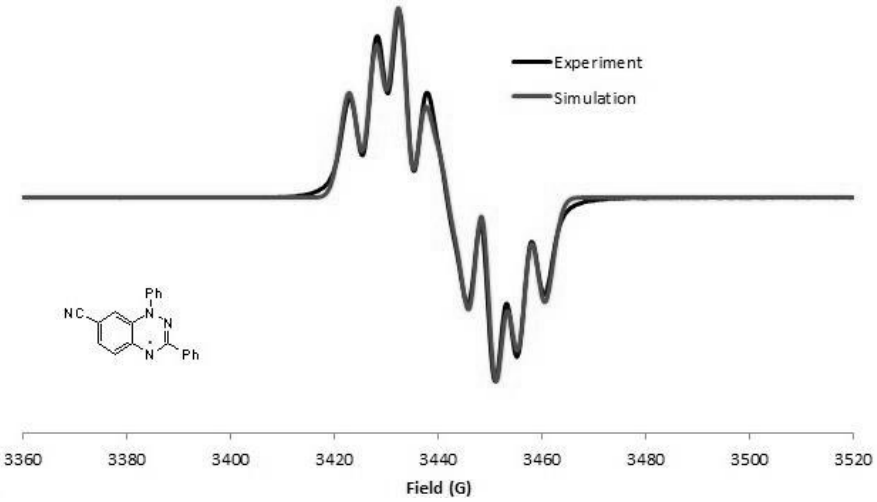

Fig. S34. EPR (X-band, 9.65 GHz) spectrum of Blatter radical **3** (sample label: NG0901c) in N_2-bubbled benzene. Simulation: g = 2.0035, a_{N1} = 7.7 G, a_{N2} = 4.8 G, a_{N3} = 4.6 G. ΔH_{pp} = 4.0 G

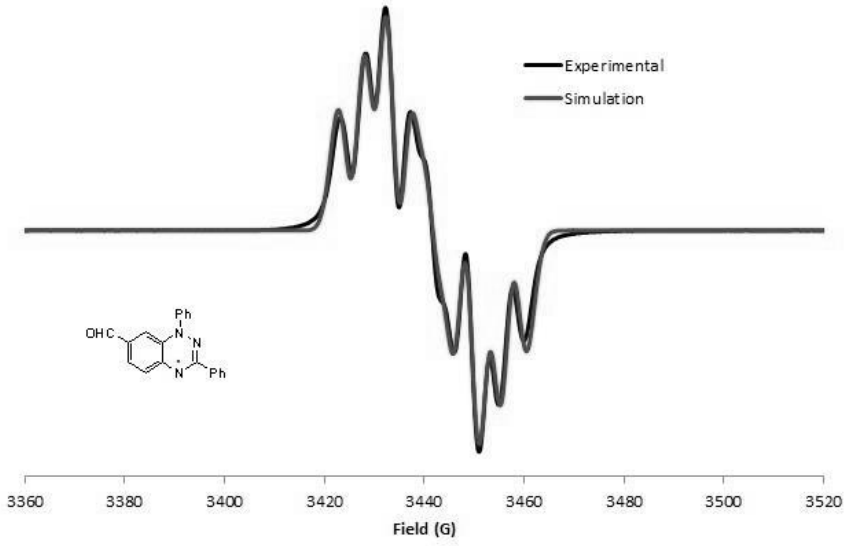

Fig. S35. EPR (X-band, 9.65 GHz) spectrum of Blatter radical **4** (sample label: NG0907b) in N_2-bubbled benzene. Simulation: g = 2.0035, a_{N1} = 7.7 G, a_{N2} = 4.8 G, a_{N3} = 4.6 G. ΔH_{pp} = 4.0 G

5. Optimized Geometries of Diradical 2 at the UB3LYP/6-31G(d)+ZPVE Level.

Triplet state of diradical 2: optimized geometry, starting from X-ray determined geometry of molecule A at the UB3LYP/6-31G(d) in the gas phase.

Stoichiometry C26H25N5O2(3)
Framework group C1[X(C26H25N5O2)]
Deg. of freedom 168
Full point group C1 NOp 1
Largest Abelian subgroup C1 NOp 1
Largest concise Abelian subgroup C1 NOp 1
Standard orientation:

Center Number	Atomic Number	Atomic Type	Coordinates (Angstroms) X	Y	Z
1	7	0	-1.828028	0.816598	-0.077371
2	7	0	-3.156654	0.527879	0.002833
3	7	0	-2.679655	-1.805494	-0.217920
4	7	0	3.461886	0.465653	-0.132819
5	8	0	2.901130	1.588661	-0.370724
6	7	0	3.840176	-1.685381	0.220121
7	8	0	3.695342	-2.937067	0.419289
8	6	0	1.434411	-1.012517	-0.062732
9	6	0	0.515820	0.055392	-0.004852
10	1	0	0.891590	1.060092	0.107696
11	6	0	-0.852402	-0.189784	-0.101729
12	6	0	-3.507938	-0.754784	-0.073130
13	6	0	-1.353088	-1.524719	-0.205513
14	6	0	-0.411474	-2.577484	-0.269660
15	1	0	-0.800423	-3.586561	-0.358856
16	6	0	0.944077	-2.338777	-0.201405
17	1	0	1.647375	-3.159017	-0.235627
18	6	0	2.861570	-0.753704	0.008242
19	6	0	4.930956	0.413213	0.200956
20	6	0	5.219003	-1.109182	0.017422
21	6	0	5.698046	1.348605	-0.733873
22	1	0	5.351297	2.372949	-0.582628
23	1	0	5.550488	1.096654	-1.785998
24	1	0	6.768822	1.304055	-0.508859
25	6	0	5.055514	0.910221	1.653311
26	1	0	4.629469	1.915611	1.713320
27	1	0	6.103954	0.955434	1.963184
28	1	0	4.512483	0.266083	2.351497
29	6	0	6.180892	-1.727546	1.032151
30	1	0	7.182459	-1.304234	0.902163
31	1	0	5.860863	-1.560632	2.062634
32	1	0	6.232926	-2.805885	0.868181
33	6	0	5.640652	-1.505695	-1.409702
34	1	0	6.659789	-1.170166	-1.624314
35	1	0	5.607174	-2.595752	-1.490531
36	1	0	4.968506	-1.085682	-2.164144
37	6	0	-1.538145	2.217350	-0.059849
38	6	0	-0.621653	2.773423	-0.959915
39	1	0	-0.103965	2.143089	-1.674012
40	6	0	-0.383929	4.147220	-0.938465
41	1	0	0.330132	4.572524	-1.637652
42	6	0	-1.062149	4.969526	-0.037737
43	1	0	-0.873942	6.039350	-0.026808
44	6	0	-1.987273	4.409846	0.846850
45	1	0	-2.521923	5.042367	1.550103
46	6	0	-2.228551	3.038337	0.840149
47	1	0	-2.948121	2.592030	1.516778
48	6	0	-4.966909	-1.031520	-0.001915
49	6	0	-5.902489	0.012146	0.082181
50	1	0	-5.550384	1.037602	0.087984
51	6	0	-7.264882	-0.268354	0.151258
52	1	0	-7.979467	0.548196	0.214408
53	6	0	-7.713412	-1.591668	0.136750
54	1	0	-8.777256	-1.808097	0.190290
55	6	0	-6.788172	-2.633873	0.051433
56	1	0	-7.129353	-3.665748	0.039027
57	6	0	-5.423883	-2.357916	-0.017764
58	1	0	-4.695899	-3.158320	-0.085028

Rotational constants (GHZ): 0.2370087 0.0678054 0.0546233
Standard basis: 6-31G(d) (6D, 7F)
SCF Done: E(UB3LYP) = -1429.89104333 A.U. after 4 cycles
Convg = 0.4244D-08 -V/T = 2.0095
<Sx>= 0.0000 <Sy>= 0.0000 <Sz>= 1.0000 <S**2>= 2.0799 S= 1.0264
<L.S>= 0.000000000000E+00
Annihilation of the first spin contaminant:
S**2 before annihilation 2.0799, after 2.0021

Item	Value	Threshold	Converged?
Maximum Force	0.000001	0.000015	YES
RMS Force	0.000000	0.000010	YES
Maximum Displacement	0.000024	0.000060	YES
RMS Displacement	0.000005	0.000040	YES

Predicted change in Energy=-6.912863D-12
Optimization completed.
-- Stationary point found.

Triplet state of diradical 2: optimized geometry, starting from X-ray determined geometry of molecule B at the UB3LYP/6-31G(d) in the gas phase.

Stoichiometry C26H25N5O2(3)
Framework group C1[X(C26H25N5O2)]
Deg. of freedom 168
Full point group C1 NOp 1
Largest Abelian subgroup C1 NOp 1
Largest concise Abelian subgroup C1 NOp 1
Standard orientation:

Center Number	Atomic Number	Atomic Type	Coordinates (Angstroms) X	Y	Z
1	7	0	1.828012	0.816588	-0.077293
2	7	0	3.156637	0.527873	0.002958
3	7	0	2.679674	-1.805490	-0.217848
4	7	0	-3.461844	0.465632	-0.132786
5	8	0	-2.901042	1.588636	-0.370542
6	7	0	-3.840181	-1.685410	0.220060
7	8	0	-3.695343	-2.937105	0.419145
8	6	0	-1.434410	-1.012549	-0.062756
9	6	0	-0.515835	0.055357	-0.004789
10	1	0	-0.891613	1.060063	0.107751
11	6	0	0.852391	-0.189809	-0.101650
12	6	0	3.507943	-0.754795	-0.072954
13	6	0	1.353088	-1.524728	-0.205462
14	6	0	0.411485	-2.577488	-0.269746
15	1	0	0.800410	-3.586570	-0.359016
16	6	0	-0.944076	-2.338790	-0.201517
17	1	0	-1.647358	-3.159046	-0.235836
18	6	0	-2.861574	-0.753733	0.008215
19	6	0	-4.930944	0.413210	0.200970
20	6	0	-5.219016	-1.109163	0.017451
21	6	0	-5.697961	1.348628	-0.733919
22	1	0	-6.768731	1.304252	-0.508830
23	1	0	-5.351028	2.372926	-0.582772
24	1	0	-5.550498	1.096556	-1.786029
25	6	0	-5.055509	0.910236	1.653325
26	1	0	-4.629528	1.915657	1.713306
27	1	0	-4.512431	0.266143	2.351517
28	1	0	-6.103959	0.955377	1.963193
29	6	0	-6.180835	-1.727543	1.032255
30	1	0	-6.232592	-2.805919	0.868438
31	1	0	-7.182486	-1.304467	0.902142
32	1	0	-5.860886	-1.560381	2.062723
33	6	0	-5.640783	-1.505647	-1.409663
34	1	0	-6.659924	-1.170071	-1.624194
35	1	0	-4.968663	-1.085636	-2.164131
36	1	0	-5.607337	-2.595705	-1.490503
37	6	0	1.538108	2.217334	-0.059845
38	6	0	0.621537	2.773314	-0.959883
39	1	0	0.103839	2.142913	-1.673918
40	6	0	0.383765	4.147105	-0.938512
41	1	0	-0.330369	4.572337	-1.637671
42	6	0	1.062031	4.969496	-0.037897
43	1	0	0.873774	6.039314	-0.027010
44	6	0	1.987255	4.409907	0.846645
45	1	0	2.521964	5.042501	1.549790
46	6	0	2.228573	3.038404	0.840032
47	1	0	2.948221	2.592175	1.516632
48	6	0	4.966942	-1.031499	-0.001848
49	6	0	5.902500	0.012176	0.082340
50	1	0	5.550379	1.037629	0.088265
51	6	0	7.264904	-0.268296	0.151367
52	1	0	7.979469	0.548269	0.214576
53	6	0	7.713470	-1.591594	0.136698
54	1	0	8.777319	-1.808005	0.190245
55	6	0	6.788255	-2.633811	0.051260
56	1	0	7.129467	-3.665674	0.038696
57	6	0	5.423955	-2.357880	-0.017882
58	1	0	4.695998	-3.158304	-0.085235

Rotational constants (GHZ): 0.2370118 0.0678053 0.0546233
Standard basis: 6-31G(d) (6D, 7F)
SCF Done: E(UB3LYP) = -1429.89104332 A.U. after 7 cycles
Convg = 0.6639D-08 -V/T = 2.0095
<Sx>= 0.0000 <Sy>= 0.0000 <Sz>= 1.0000 <S**2>= 2.0799 S= 1.0264
<L.S>= 0.000000000000E+00
Annihilation of the first spin contaminant:
S**2 before annihilation 2.0799, after 2.0021

Item	Value	Threshold	Converged?
Maximum Force	0.000014	0.000450	YES
RMS Force	0.000003	0.000300	YES
Maximum Displacement	0.000502	0.001800	YES
RMS Displacement	0.000125	0.001200	YES

Predicted change in Energy=-8.863434D-09
Optimization completed.
-- Stationary point found.

Broken-symmetry singlet state of diradical 2: optimized geometry, starting from X-ray determined geometry of molecule A at the UB3LYP/6-31G(d) in the gas phase.

Stoichiometry C26H25N5O2
Framework group C1[X(C26H25N5O2)]
Deg. of freedom 168
Full point group C1 NOp 1
Largest Abelian subgroup C1 NOp 1
Largest concise Abelian subgroup C1 NOp 1
Standard orientation:

Center Number	Atomic Number	Atomic Type	Coordinates (Angstroms) X	Y	Z
1	7	0	-1.823718	0.811746	-0.066325
2	7	0	-3.153869	0.529435	0.014973
3	7	0	-2.691380	-1.805595	-0.239423
4	7	0	3.458128	0.454464	-0.182122
5	8	0	2.895484	1.566028	-0.466145
6	7	0	3.832890	-1.678842	0.261267
7	8	0	3.680819	-2.922059	0.503671
8	6	0	1.428973	-1.023305	-0.074200
9	6	0	0.517239	0.043610	-0.001197
10	1	0	0.894079	1.046630	0.124262
11	6	0	-0.855470	-0.199364	-0.102921
12	6	0	-3.507985	-0.758872	-0.077331
13	6	0	-1.353380	-1.528817	-0.222480
14	6	0	-0.417643	-2.579727	-0.297120
15	1	0	-0.807640	-3.587591	-0.395540
16	6	0	0.942597	-2.344430	-0.228822
17	1	0	1.644492	-3.165569	-0.270622
18	6	0	2.863618	-0.756435	0.003392
19	6	0	4.926112	0.418202	0.163189
20	6	0	5.216016	-1.111972	0.056157
21	6	0	5.697959	1.308300	-0.811215
22	1	0	5.345559	2.337310	-0.714333
23	1	0	5.560510	1.003240	-1.850569
24	1	0	6.766922	1.279805	-0.575326
25	6	0	5.040114	0.986342	1.589989
26	1	0	4.615131	1.993889	1.596850
27	1	0	6.086303	1.045229	1.905083
28	1	0	4.490728	0.378107	2.314849
29	6	0	6.159191	-1.683653	1.114995
30	1	0	7.164792	-1.271551	0.980361
31	1	0	5.824190	-1.465526	2.131041
32	1	0	6.207888	-2.768925	1.004216
33	6	0	5.661169	-1.576102	-1.343103
34	1	0	6.683752	-1.250347	-1.556302
35	1	0	5.628685	-2.668738	-1.372137
36	1	0	5.001731	-1.193073	-2.127798
37	6	0	-1.526764	2.210932	-0.046215
38	6	0	-0.604642	2.764266	-0.942494
39	1	0	-0.087362	2.133598	-1.656562
40	6	0	-0.360401	4.136889	-0.917225
41	1	0	0.358128	4.559926	-1.613168
42	6	0	-1.038058	4.960639	-0.017471
43	1	0	-0.845127	6.029603	-0.004078
44	6	0	-1.969278	4.403715	0.862628
45	1	0	-2.503653	5.037532	1.564916
46	6	0	-2.217351	3.033570	0.852389
47	1	0	-2.941624	2.589146	1.525131
48	6	0	-4.969588	-1.024975	-0.004694
49	6	0	-5.897285	0.024634	0.088604
50	1	0	-5.537928	1.047434	0.100083
51	6	0	-7.261733	-0.246903	0.159156
52	1	0	-7.970561	0.574067	0.229425
53	6	0	-7.719161	-1.566779	0.136823
54	1	0	-8.784358	-1.776292	0.191534
55	6	0	-6.801372	-2.615149	0.042234
56	1	0	-7.149969	-3.644453	0.023915
57	6	0	-5.435667	-2.348133	-0.028317
58	1	0	-4.712712	-3.152542	-0.102545

Rotational constants (GHZ): 0.2376940 0.0678424 0.0547040
Standard basis: 6-31G(d) (6D, 7F)
SCF Done: E(UB3LYP) = -1429.88835481 A.U. after 8 cycles
Convg = 0.6514D-08 -V/T = 2.0095
<Sx>= 0.0000 <Sy>= 0.0000 <Sz>= 0.0000 <S**2>= 1.0643 S= 0.6464
<L.S>= 0.000000000000E+00
Annihilation of the first spin contaminant:
S**2 before annihilation 1.0643, after 0.5040

Item	Value	Threshold	Converged?
Maximum Force	0.000018	0.000450	YES
RMS Force	0.000004	0.000300	YES
Maximum Displacement	0.001236	0.001800	YES
RMS Displacement	0.000290	0.001200	YES

Predicted change in Energy=-1.445559D-08
Optimization completed.
-- Stationary point found.

6. References for Supporting Information.

S1 Gallagher, N. M.; Bauer, J. J.; Pink, M.; Rajca, S.; Rajca, A. High Spin Organic Diradical with Robust Stability. *J. Am. Chem. Soc.* **2016**, *138*, 9377–9380.

S2 Rajca, A.; Mukherjee, S.; Pink, M.; Rajca, S.; Das, K. 1,3-Alternate Calix[4]arene Nitronyl Nitroxide Tetraradical and Diradical: Synthesis, X-ray Crystallography, Paramagnetic NMR Spectroscopy, EPR Spectroscopy, and Magnetic Studies. *Tetrahedron* **2007**, *63*, 10731–10742.

S3 Li, F-N.; Kim, N-J.; Nam, Y-H.; Kim, S-H.; Seo, S-Y.; Jeong, Y-S.; Kim, S-Y.; Park, Y-H.; Suh, Y-G. Design, Synthesis, and Biological Evaluation of Phenylpropanamides as Novel Transient Receptor Potential Valnilloid 1 Antagonists. *Arch. Pharm. Res*. **2009**, *32*, 1201–1210.

S4 Waghmare, A. A.; Bose, P.; Pati, H. N. Direct nuclear halogenation of deactivated aryl and N-heteroaryl amines: An overview. *Der Pharma Chemica*, **2010**, *2*, 212 – 241.

S5 Thevis, M.; Schänzer, W.; Schmickler, H. Effect of the Location of Hydrogen Abstraction on the Fragmentation of Diuretics in Negative Electrospray Ionization Mass Spectrometry. *J. Am. Soc. Mass Spectrom.* **2003**, *14*, 658–670.

S6 Bazian, A.; Taheri, M.; Alavi, H. Synthesis of 4'-[3-Methyl-5-thioxo-1*H*-1,2,4-triazol-4(5*H*)-yl]-2',5'-diphenyl-2',4'-dihydro Spiro[indolin-3,3'[1,2,4]triazol]-2-one Derivatives. *Russ. J. Gen. Chem.* **2014**, *84*, 586–592.

S7 SAINT, Bruker Analytical X-Ray Systems, Madison, WI, current version.

S8 SADABS, Bruker Analytical X-Ray Systems, Madison, WI, current version.

S9 Sheldrick, G. M. A short history of *SHELX*. *Acta Cryst. A* **2008**, *64*, 112–122.

S10 Xiong, X.; Jiang, Y.; Ma, D. Assembly of *N*,*N*-Disubstituted Hydrazines and 1-Aryl-1*H*-indazoles via Copper-Catalyzed Coupling Reactions. *Org. Lett.* **2012**, *14*, 2552–2555.

S11 Takahashi, Y., Miura, Y. & Yoshioka, N. Synthesis and properties of the 3-*tert*-butyl-7-trifluoromethyl-1,4-dihydro-1-phenyl-1,2,4-benzotriazin-4-yl radical. *New J. Chem.* **2015**, *39*, 4783–4789.

S12. Beloritzky, E.; Fries, P. H. Exact solutions for simple spin clusters with isotropic Heisenberg exchange interactions. *J. Chim. Phys. (Paris)* **1993**, *90*, 1077–1100.

S13 Rajca, A.; Takahashi, M.; Pink, M.; Spagnol, G.; Rajca, S. Conformationally constrained, stable, triplet ground state (S = 1) nitroxide diradicals: antiferromagnetic chains of (S = 1) diradicals. *J. Am. Chem. Soc.* **2007**, *129*, 10159–10170.

S14 Carlin, R. L. Magnetochemistry. Springer: Berlin, **1986**, pp 2–4.

S15 Rajca, A.; Shiraishi, K.; Vale, M.; Han, H.; Rajca, S. Stable Hydrocarbon Diradical, an Analogue of Trimethylenemethane. *J. Am. Chem. Soc*. **2005**, *127*, 9014–9020.

S16 Rajca, S.; Rajca, A.; Wongsriratanakul, J.; Butler, P.; Choi, S. Organic Spin Clusters. Dendritic-Macrocyclic Polyarylmethyl Polyradical with Very High-Spin of S = 10 and its Derivatives: Synthesis, Magnetic Studies, and Small Angle Neutron Scattering. *J. Am. Chem. Soc.* **2004**, *126*, 6972–6986.

S17 Rajca, A.; Mukherjee, S.; Pink, M.; Rajca, S. Exchange Coupling Mediated Through-Bonds and Through-Space in Conformationally-Constrained Polyradical Scaffolds: Calix[4]arene Nitroxide Tetraradicals and Diradical. *J. Am. Chem. Soc.* **2006**, *128*, 13497–13507.
S18 Rajca, A. The Physical Organic Chemistry of Very High-Spin Polyradicals. *Adv. Phys. Org. Chem.* **2005**, *40*, 153-199.
S19 Wagner, C. D. Sensitivity factors for XPS analysis of surface atoms. *J. Electron Spectrosc. Relat. Phenom.* **1983**, *32*, 99-102.
S20 Ciccullo, F.; Gallagher, N. M.; Geladari, O.; Chasse, T.; Rajca, A.; Casu, M. B., A Derivative of the Blatter Radical as a Potential Metal-Free Magnet for Stable Thin Films and Interfaces. *ACS Appl. Mater. Interfaces* **2016**, *8*, 1805–1812.
S21 Ciccullo, F.; Calzolari, A.; Bader, K.; Neugebauer, P.; Gallagher, N. M.; Rajca, A.; van Slageren, J.; Casu, M. B., Interfacing a Potential Purely Organic Molecular Quantum Bit with a Real-Life Surface. *ACS Appl. Mater. Interfaces* **2019,** *11*, 1571–1578.
S22 Savu, S.-A.; Biswas, I.; Sorace, L.; Mannini, M.; Rovai, D.; Caneschi, A.; Chassé, T.; Casu, M. B., Nanoscale Assembly of Paramagnetic Organic Radicals on Au(111) Single Crystals. *Chem.-Eur. J.* **2013,** *19*, 3445–3450.
S23 Kakavandi, R.; Ravat, P.; Savu, S. A.; Borozdina, Y. B.; Baumgarten, M.; Casu, M. B., Electronic Structure and Stability of Fluorophore–Nitroxide Radicals from Ultrahigh Vacuum to Air Exposure. *ACS Appl. Mater. Interfaces* **2015,** *7*, 1685–1692.
S24 Frisch, M. J.; Trucks, G. W.; Schlegel, H. B.; Scuseria, G. E.; Robb, M. A.; Cheeseman, J. R.; Scalmani, G.; Barone, V.; Mennucci, B.; Petersson, G. A.; Nakatsuji, H.; Caricato, M.; Li, X.; Hratchian, H. P.; Izmaylov, A. F.; Bloino, J.; Zheng, G.; Sonnenberg, J. L.; Hada, M.; Ehara, M.; Toyota, K.; Fukuda, R.; Hasegawa, J.; Ishida, M.; Nakajima, T.; Honda, Y.; Kitao, O.; Nakai, H.; Vreven, T.; Montgomery, Jr., J. A.; Peralta, J. E.; Ogliaro, F.; Bearpark, M.; Heyd, J. J.; Brothers, E.; Kudin, K. N.; Staroverov, V. N.; Kobayashi, R.; Normand, J.; Raghavachari, K.; Rendell, A.; Burant, J. C.; Iyengar, S. S.; Tomasi, J.; Cossi, M.; Rega, N.; Millam, N. J.; Klene, M.; Knox, J. E.; Cross, J. B.; Bakken, V.; Adamo, C.; Jaramillo, J.; Gomperts, R.; Stratmann, R. E.; Yazyev, O.; Austin, A. J.; Cammi, R.; Pomelli, C.; Ochterski, J. W.; Martin, R. L.; Morokuma, K.; Zakrzewski, V. G.; Voth, G. A.; Salvador, P.; Dannenberg, J. J.; Dapprich, S.; Daniels, A. D.; Farkas, Ö.; Foresman, J. B.; Ortiz, J. V.; Cioslowski, J.; Fox, D. J. *Gaussian 09*, Revision A.1 (Gaussian, Inc., Wallingford CT, 2009).
S25 Trinquier, G.; Suaud, N.; Malrieu, J.-P. Theoretical Design of High-Spin Polycyclic Hydrocarbons. *Chem. Eur. J.* **2010**, *16*, 8762–8772.
S26 Sadhukhan, T.; Hansda, S.; Latif, I. A.; Datta, S. N. Metaphenylene-Based Nitroxide Diradicals: A Protocol To Calculate Intermolecular Coupling Constant in a One-Dimensional Chain. *J. Phys. Chem. A* **2013**, *117*, 13151−13160.
S27 Yamaguchi, K.; Jensen, F.; Dorigo, A.; Houk, K. N. A Spin Correction Procedure for Unrestricted Hartree−Fock and Møller−Plesset Wavefunctions for Singlet Diradicals and Polyradicals. *Chem. Phys. Lett.* **1988**, *149*, 537−542.

S28 Wang, W.; Chen, C.; Shu, C.; Rajca, S.; Wang, X.; Rajca, A. *S* = 1 Tetraazacyclophane Diradical Dication with Robust Stability: a Case of Low Temperature One-Dimensional Antiferromagnetic Chain. *J. Am. Chem. Soc.* **2018**, *140*, 7820–7826.
S29 Neese, F. ORCA – an ab initio, Density Functional and Semiempirical program package, Version 2.6. University of Bonn, **2008**.
S30 Sinnecker, S.; Neese, F. Spin−Spin Contributions to the Zero-Field Splitting Tensor in Organic Triplets, Carbenes and Biradicals − A Density Functional and Ab Initio Study. *J. Phys. Chem. A* **2006**, *110*, 12267–12275.
S31 Allouche, A.-R. Gabedit – A graphical user interface for computational chemistry softwares. *J. Comput. Chem.* **2011**, *32*, 174–182.
S32 Rajca, A.; Olankitwanit, A.; Rajca, S. Triplet Ground State Derivative of Aza-*m*-Xylylene Diradical with Large Singlet-Triplet Energy Gap. *J. Am. Chem. Soc.* **2011**, *133*, 4750–4753.

B. Exploiting the Versatile Alkyne-based Chemistry for Expanding the Applications of a Stable Triphenylmethyl Organic Radical on Surfaces

Reproduced from
J. A. de Sousa, F. Bejarano, D. Gutiérrez, Y. Leroux, E.-M. Nowik Boltyk, T. Junghoefer, E. Giangrisostomi, R. Ovsyannikov, M. B. Casu, J. Veciana, M. Mas-Torrent, B. Fabre, C. Rovira, N. Crivillers, "Exploiting the Versatile Alkyne-based Chemistry for Expanding the Applications of a Stable Triphenylmethyl Organic Radical on Surfaces", *Chemical Science* **2019**, *11*, 516–524, DOI 10.1039/c9sc04499j
with permission from the Royal Society of Chemistry.

Chemical Science

EDGE ARTICLE

View Article Online
View Journal | View Issue

Check for updates

Cite this: *Chem. Sci.*, 2020, **11**, 516

All publication charges for this article have been paid for by the Royal Society of Chemistry

Received 6th September 2019
Accepted 19th November 2019

DOI: 10.1039/c9sc04499j

rsc.li/chemical-science

Exploiting the versatile alkyne-based chemistry for expanding the applications of a stable triphenylmethyl organic radical on surfaces†

J. Alejandro de Sousa, ‡[ae] Francesc Bejarano,‡[a] Diego Gutiérrez,[a] Yann R. Leroux,[b] Ewa Malgorzata Nowik-Boltyk, [c] Tobias Junghoefer, [c] Erika Giangrisostomi,[d] Ruslan Ovsyannikov,[d] Maria Benedetta Casu, *[c] Jaume Veciana, [a] Marta Mas-Torrent, [a] Bruno Fabre, *[b] Concepció Rovira *[a] and Núria Crivillers *[a]

The incorporation of terminal alkynes into the chemical structure of persistent organic perchlorotriphenylmethyl (PTM) radicals provides new chemical tools to expand their potential applications. In this work, this is demonstrated by the chemical functionalization of two types of substrates, hydrogenated SiO_2-free silicon (Si–H) and gold, and, by exploiting the click chemistry, scarcely used with organic radicals, to synthesise multifunctional systems. On one hand, the one-step functionalization of Si–H allows a light-triggered capacitance switch to be successfully achieved under electrochemical conditions. On the other hand, the click reaction between the alkyne-terminated PTM radical and a ferrocene azide derivative, used here as a model azide system, leads to a multistate electrochemical switch. The successful post-surface modification makes the self-assembled monolayers reported here an appealing platform to synthesise multifunctional systems grafted on surfaces.

Introduction

The impact of (bio)molecular surface modification in different fields of research is supported by the wide variety of applications that derive from it. The goal of the functionalization can be either transferring specific molecular properties to the substrate, *i.e.* by grafting (multi)functional molecular systems, or generating novel interfaces, for example to promote cell-adhesion, (bio)sensing or to inhibit undesired reactions, among others.[1–7] The molecular modification of surfaces has also been a determining factor in the emerging field of molecular (spin)electronic devices.[8] In this context, among the extensive library of functional molecules investigated, optically-, redox- and magnetically-active stable organic radicals are very attractive.[9] Nowadays, these materials have attracted much interest and their exploitation as components of molecular functional materials is boosting a new generation of devices for applications in OLEDs,[10,11] energy storage and conversion,[12,13] molecular spintronics,[14] imaging,[15,16] sensors[17] and memory devices.[18–20] It has been shown that for the device implementation, in many cases their immobilization onto surfaces is needed.[21]

To this end, the formation of stable self-assembled monolayers (SAMs) on substrates typically employed for the fabrication of electronic components, such as silicon or gold, is a well-established strategy.[22,23] The hybrid system robustness, and hence its potential applicability, is equally dependent on the stability of the molecular entity as well as on the stability of the molecule–substrate interface. For this, beyond the search for transferring a specific molecular functionality to the surface (mainly magnetically-, redox- or optically-active), great efforts have been focused on: (i) the search for new robust anchoring groups and (ii) the post-grafting modification of SAMs. Terminal alkynes have appeared as an appealing alternative to the thiol group as they spontaneously and covalently react with gold.[24,25] Besides the stability of the C–Au bond, the high directionality of the σ-bonded C–Au has been demonstrated to provide higher conductance at the single-molecule level,[26] which makes terminal alkynes very attractive for molecular electronics. Interestingly, these functional groups can also be

[a]*Institut de Ciència de Materials de Barcelona (ICMAB-CSIC), Networking Research Center on Bioengineering Biomaterials and Nanomedicine (CIBER-BBN), Campus de la UAB, 08193 Bellaterra, Spain. E-mail: ncrivillers@icmab.es*

[b]*Univ Rennes, CNRS, ISCR (Institut des Sciences Chimiques de Rennes)-UMR 6226, F-35000 Rennes, France*

[c]*Institute of Physical and Theoretical Chemistry, University of Tübingen, 72076 Tübingen, Germany*

[d]*Helmholtz-Zentrum Berlin für Materialien und Energie (HZB), Albert-Einstein-Str 15, 12489 Berlin, Germany*

[e]*Laboratorio de Electroquímica, Departamento de Química, Facultad de Ciencias, Universidad de los Andes, 5101 Mérida, Venezuela*

† Electronic supplementary information (ESI) available: Synthetic details and characterization of the prepared compounds, details of the preparation of SAMs on Si–H and on Au, additional electrochemical characterization of SAMs, survey and XPS spectra of **SAM-3-Rad** and **SAM-2-Rad** together with their stoichiometric and experimental elemental ratios and instrumentation. See DOI: 10.1039/c9sc04499j

‡ These authors contributed equally.

View Article Online
Edge Article Chemical Science

used to covalently react with hydrogen-terminated silicon (Si–H) surfaces.[27–29] Concerning post-grafting modification, preparing monolayers with exposed functional end groups which can react with other (bio)molecular systems is of great importance to expand the applicability of these surfaces. Among the several chemical strategies reported to perform interfacial reactions on SAMs,[30] the so-called "click chemistry" has been one of the most employed, in particular the 1,3-dipolar cycloaddition of azides and alkynes to form 1,2,3 triazoles.[31–34] Hence, alkynes can be considered as very versatile groups to be employed for the modification and post-modification of substrates.

The functionalization of SiO_2-free silicon and gold substrates with electrical and/or light triggered molecules has been pursued with the aim of obtaining switchable surfaces. In the case of silicon, unlike metals, its electronic properties can be finely tuned by modifying the density and the nature of the charge carriers (electrons and holes) under light illumination, which can be used as a second gate for the tuning of the properties of the modified surface.[29]

In this work, by exploiting the rich chemistry offered by alkynes and the high chemical and thermal stability of perchlorotriphenylmethyl (PTM) radicals,[35] the redox properties of a PTM radical bearing one and two terminal alkyne groups (Fig. 1) have been dually exploited as: (i) a capacitance switch on Si–H triggered by light and, (ii) as an organic radical-based platform to be further modified by click chemistry giving rise to a multistate electrochemical switch. In both cases, a particular focus has been placed on the optimization of the experimental conditions to ensure the integrity of the radical and the terminal alkyne.

Results and discussion

Functionalization of Si–H surfaces with PTM radicals

Interfacing technologically important semiconducting surfaces, such as silicon, with high-quality, and stable redox-active films has appeared as a promising strategy toward functional devices for charge storage. Remarkably, by taking advantage of the fact that the charge transfer characteristics of silicon can be either inhibited or activated upon light illumination, this substrate constitutes a relevant platform for the development of photochemically switchable systems.[29,36,37] Then, silicon itself can be used as a light-controlled gate to turn ON/OFF the electronic communication with the grafted electroactive centers, in this case the PTM radicals. With this aim, we exploit herein the reactivity of the alkyne terminated PTM (**1-Rad**) to chemically modify SiO_2-free p-type Si–H substrates, forming robust Si–C═C bonds. To date, the functionalization of Si–H surfaces has been achieved with numerous electroactive molecules, among them are ferrocene, quinones, tetrathiafulvalenes (TTF) and metallic complexes.[29] However, to the best of our knowledge, before this work, only one example of an organic radical grafted on Si–H has been reported. In that case, the grafting was done through a two-step approach, to avoid the reactivity of the unpaired electron with the silicon surface bonds, thus leading to a loss of the radical character.[38] Herein, the Si–H functionalization was carried out in a single step by the hydrosilylation reaction of molecule **1-Rad** through the terminal acetylene group leading to the covalently bound PTM-terminated monolayer (**SAM-1-Rad-Si**) (Fig. 2a).

Although the hydrosilylation reaction between alkynes and Si–H can be performed by either thermal[39,40] or photochemical[41] activation, the instability in solution under light of the radical PTM moiety excluded the possibility of using in this work such a photochemical route. Several grafting attempts were carried out by varying the concentration of the PTM radical solution, solvent, temperature and immersion time (see the experimental details in the ESI and Table S1†). PTM radical monolayers with the highest surface coverage of PTM (estimated from the electrochemical measurements, *vide infra*) and the lowest oxidation level of underlying silicon were obtained at 145 °C for 20 h using 1,2-dichlorobenzene (DCB) as a high-boiling solvent and a *ca.* 7–10 mM concentration of **1-Rad**.

The **SAM-1-Rad-Si** monolayer was characterized by X-ray photoelectron spectroscopy, which, additionally to the chemical composition, provides information about the oxidation state of the underlying silicon (Fig. S1†). For the C 1s, two main peaks at, 285.0 and 286.6 eV, assigned to the C═C and the C–Cl bonds, respectively, were observed. The Cl 2p spectrum

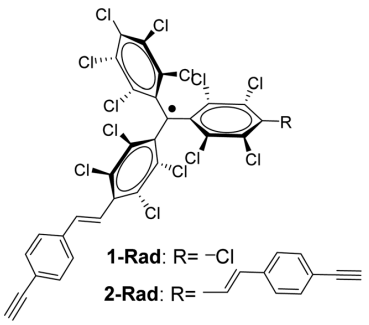

Fig. 1 Chemical structure of the PTM radicals employed in this work.

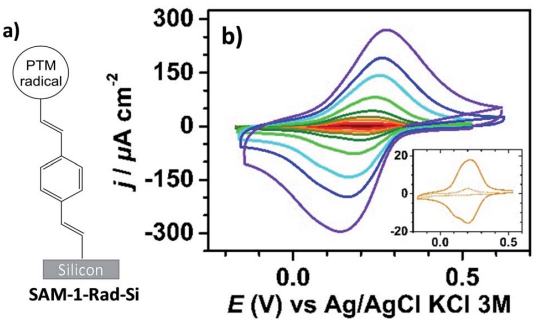

Fig. 2 (a) Sketch of SAM-1-Rad-Si. (b) Cyclic voltammograms under red light illumination of SAM-1-Rad-Si at different scan rates (0.1, 0.2, 0.4, 0.6, 1, 2, 4, 6 and 10 V s^{-1}, from brown to purple) in CH_3CN + 0.1 M Bu_4NClO_4. The inset shows comparative CVs at 0.4 V s^{-1} in the dark (dashed line) and under illumination (solid line).

displayed a typical doublet with both components at 200.8 ($2p_{3/2}$) and 202.5 ($2p_{1/2}$) eV, arising from the chlorinated phenyl rings of the PTM unit. Besides, the Si 2p spectrum was deconvoluted into two contributions at 99.2 and 99.8 eV assigned to bulk and interfacial silicon, respectively, in crystalline Si(111).[42,43] Additionally, a low intense peak appeared at 103 eV, which is attributed to the unavoidable oxidation of a certain content of remaining Si–H sites by water and atmospheric oxygen, indicating that, as expected, the surface is not fully passivated by the bulky radical **1-Rad**. Nevertheless, the low contribution of this peak was positively surprising considering the bulkiness of the PTM moiety.

SAM-1-Rad-Si was electrochemically characterized in the dark and under illumination through a red filter ($\lambda > 600$ nm) to avoid the possible degradation of the grafted PTM radical. As can be seen in Fig. 2b, the cyclic voltammograms (CVs) in the dark showed negligible oxidation and reduction currents (lower than 10 μA cm^{-2} at 10 V s^{-1}), as expected for a semiconductor under depletion conditions,[44] *i.e.*, when only a few majority charge carriers (holes in the case of p-type Si) are available for charge transfer (*vide infra*).

Upon illumination of **SAM-1-Rad-Si**, an intense reversible redox wave was observed at $E^{\circ\prime} = 0.21$ V *vs.* Ag/AgCl, KCl 3 M (average of the anodic E_{pa} and cathodic E_{pc} peak potentials) corresponding to the PTM(radical) ↔ PTM(anion) process promoted by captured photogenerated electrons (Fig. 2b). The redox response observed indicates that the radical character of the PTM remains unaltered upon grafting. Additionally, both the anodic and cathodic peak photocurrents I_{pa} and I_{pc}, corresponding to the reversible redox couple, were found to be proportional to the potential scan rate v, as expected for a surface-confined reversible redox species (Fig. S2a–c†).[45] The variation of E_{pa} and E_{pc} with v (Fig. S2b†) enabled us to determine the apparent rate constant for electron transfer at the bound PTM center, $k_{et,ap}$, using the recent theoretical model developed by Vogel *et al.* accounting for semiconductor diode effects.[46] A value of 90 ± 20 s^{-1} was estimated, in accordance with the literature data reported for other silicon electrodes modified with electrochemically reversible systems.[29,46]

The surface coverage of attached PTM moieties was electrochemically estimated from CVs of illuminated **SAM-1-Rad-Si** (eqn S1†). Indeed, anodic charge integration at several scan rates (between 0.4 and 1 V s^{-1}) resulted in an average value of (8.5 ± 0.3) × 10^{-11} mol cm^{-2}, very close to the analogous SAMs on Au (see Section 2.2.2).

To obtain further insights into the light dependence of the redox process in **SAM-1-Rad-Si**, differential capacitance measurements were performed in the same electrolytic medium (*i.e.* CH_3CN/Bu_4NClO_4). First, the flatband potential (E_{fb}), *i.e.* the electrode potential for which there is no space-charge region in the semiconductor, was estimated from the commonly used Mott–Schottky plot (C_{sc}^{-2} *vs.* E, eqn S(2)†) that gives the space-charge capacitance C_{sc} as a function of the electrode potential E under depletion conditions, *i.e.*, the depletion of valence band holes in the space charge region of the p-type surface.[47] In the dark, a linear C_{sc}^{-2}–E plot was obtained for potentials below 0.25 V *vs.* Ag/AgCl, KCl 3 M, in which the intercept and the slope of the curve enable E_{fb} and the dopant density N_D to be determined, respectively (Fig. S3†). The calculated N_D value (1.2 × 10^{15} boron atoms cm^{-3}) was consistent with the dopant density derived from the four-probe resistivity measurements of silicon samples, between 5 and 10 Ω cm. The extracted value of E_{fb} was 0.25 ± 0.02 V. Based on this parameter, it can be concluded that the PTM(radical) ↔ PTM(anion) redox process occurs in a potential range wherein the semiconductor is in weak depletion. The small potential difference between $E^{\circ\prime}$ and E_{fb} (around 50 mV) explains, however, why low (but not zero) oxidation currents are observed at **SAM-1-Rad-Si** in the dark (inset in Fig. 2b). Much higher currents were observed under illumination because the redox process could now occur with high rate thanks to the high concentration of photogenerated minority charge carriers (*i.e.* electrons).

In the dark, consistent with the current response, the measured capacitance values were small and did not exceed 1 μF cm^{-2}. In contrast, the capacitance curve under red light illumination was characterized by a much more intense capacitance peak (enhancement by a factor of ~10) at 0.18 V, close to the formal potential of bound PTM determined by CV (Fig. 3a). This capacitance peak was clearly attributed to the charging/discharging currents associated with the oxidation/reduction of the bound PTM centers,[48,49] in perfect line with previous reports on ferrocene-modified Si surfaces.[36,50]

This significant contrast between the two states (ON and OFF) permitted us to exploit this system as a capacitance switch and its cyclability was investigated by carrying out consecutive ON/OFF switching cycles by turning on and off the light along time (Fig. 3b). A ~30% decrease in the maximum

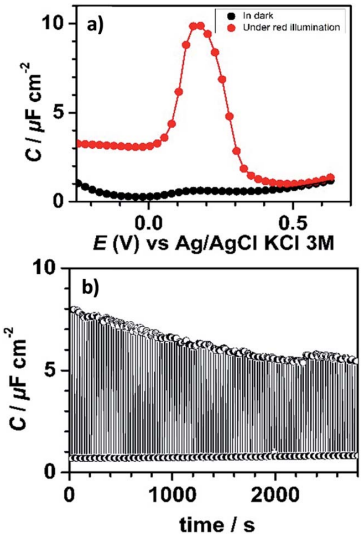

Fig. 3 (a) Capacitance–potential curves of SAM-1-Rad-Si measured at 50 Hz in the dark and under red light illumination. (b) Capacitance–time profile at 50 Hz measured at 0.18 V during dark (OFF state, 30 s)/illumination (ON state, 30 s) switching cycles. Electrolytic solution: CH_3CN + 0.1 M Bu_4NClO_4.

photocapacitance was observed along the first 30 minutes before reaching a situation of higher stability. This loss in the switching ability is believed to be caused by the gradual degradation of the electrical properties of the interface due to the oxidation of the underlying silicon. Indeed, owing to the moderately dense packing of the PTM monolayer (due to the bulky nature of the PTM head groups), traces of water and/or oxidizing species present in the electrolytic medium unavoidably penetrate through the molecular layer *via* defects or pinholes to react with remaining Si–H sites. Despite this, the functionalization was found to be remarkably stable.

Functionalization of PTM radical molecules *via* click chemistry, in solution and on the gold surface

In solution. The click chemistry is used in different fields of research, such as biomedical science, chemistry and materials science.[51,52] Remarkably, the functionalization of stable organic free radicals *via* this reaction has been only marginally explored. This is basically attributed to the low stability of the radical character under the most standard reductive "click" experimental conditions. In this work, we report for the first time the experimental conditions to achieve a click reaction between an alkyne-terminated PTM radical and an azide derivative (Scheme 1). The experimental conditions were first optimized in solution and then were used to engineer a radical-PTM-based SAM which acted as a platform to elaborate more complex multifunctional surfaces. In this work, the focus was placed on the reaction between the organic radical (**2-Rad**, Fig. 1), previously synthesized,[26] and an azidomethyl ferrocene (Fc–N_3) derivative leading to a donor–acceptor (D–A) SAM.

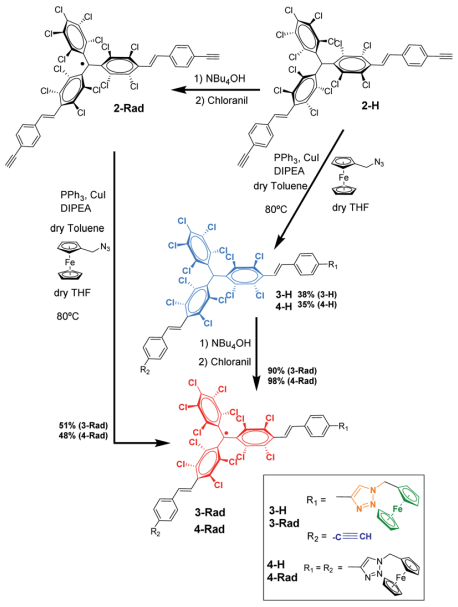

Scheme 1 Synthetic route to the preparation of the target radical PTM–Fc dyad **3-Rad**.

For the synthesis of the target radical PTM–Fc dyad (**3-Rad**) a copper-catalyzed azide–alkyne cycloaddition (CuAAC) click chemistry strategy was envisaged.[53–55] The standard conditions for the click reaction that generates *in situ* the copper(I) catalyst by reduction of $CuSO_4$ using ascorbic acid or ascorbate[56] could not be used here because the ascorbic acid reduces the radical to the anion that in turn is irreversibly protonated to the αH form.[57] Therefore, as mentioned above, before performing the reaction on the surface, the synthetic procedure was optimized in solution. The successful synthesis of the target molecule **3-Rad** with the highest reaction yield was obtained by using copper(I) iodide as a catalyst, and *N*-ethyldiisopropylamine (DIPEA) and triphenylphosphine as ligands (see ESI† for further details on the synthesis). As shown in Scheme 1, two routes were followed. First, the CuAAC reaction conditions starting with the non-radical precursor, αH-PTM molecules (**2-H**), were optimized. Both mono- and di-cycloaddition compounds, **3-H** and **4-H**, were obtained as products of the click reaction between the azidomethyl ferrocene and the PTM derivative with two acetylene-terminated groups (**2-H**) even when a 1 : 1 molar ratio of the azide and **2-H** was used. Next, the corresponding radicals **3-Rad** and **4-Rad** were prepared through treatment of the αH adducts, **3-H** and **4-H**, with tetra-*n*-butylammonium hydroxide (TBAOH), to generate the corresponding anions, and then the oxidation of these anions to the PTM radicals with *p*-chloranil. The second route consisted of directly coupling the open-shell compound, **2-Rad**, with the azidomethyl ferrocene to obtain also the two cycloaddition compounds **3-Rad** and **4-Rad** with better yield than in the case of the non-radical derivative. All the compounds were fully characterized by spectroscopic techniques (NMR, FT-IR, and UV/vis), cyclic voltammetry and electron paramagnetic resonance for the radicals (see ESI†).

On-surface PTM radical functionalization. PTM SAMs were prepared using a freshly template-stripped Au (Au^{TS}) surface as the substrate.[58] Its ultraflat topography makes it an ideal bottom electrode for the charge transport measurements, as well as for promoting the formation of higher quality monolayers.[59] Compounds **2-Rad**, **3-Rad**, **2-H** and **3-H** were used to generate **SAM-2-Rad**, **SAM-3-Rad**, **SAM-2-H** and **SAM-3-H**, respectively. These SAMs were prepared following a similar previously reported methodology,[26] working under inert conditions to avoid the oxidation of the alkyne (see ESI† for further details on the SAM preparation). All the SAMs were characterized by different electrochemical techniques: CV, square wave voltammetry (SWV) and electrochemical impedance spectroscopy (EIS). This allowed us to obtain information about the faradaic transfer process of the anchored molecules, the surface reaction yield and the capacitive behavior at different potentials.

SAM-5-Rad was obtained by the on-surface post-modification of **SAM-2-Rad**. The determination of the Fc/PTM ratio for the **SAM-5-Rad** by SWV and its control were essential to (i) estimate the yield of the on-surface click reaction, (ii) improve the faradaic-background current ratio, and (iii) decrease both capacitive currents and the double layer impact. It is important to mention that there is an intrinsic error in the estimation of the Fc/PTM ratio due to the different electron transfer rates of the electrochemical processes of both redox components but

the values were validated by comparison with those of **SAM-3-Rad** (Fig. S8†) in which the Fc/PTM ratio should be 1 : 1. Following the conditions used in solution, an ~30% reaction yield (Fc *vs.* PTM radical) was obtained (Fig. S4 and S5†). This value was enhanced to approximately 50% when a toluene–THF mixture was changed for acetonitrile as the solvent (Fig. S6 and S7†). This gain was attributed to both the better solubility of CuI and stability of Cu(I) in solution. Other parameters such as temperature and/or reaction time did not lead to a higher Fc surface coverage. The bulkiness of the PTM moieties, which can induce certain disorder of the layer, as was observed before by STM for a previously reported thiolated PTM SAM,[60] would be responsible for the yield decrease.

Fig. 4 shows the CV response of **SAM-3-H**, **SAM-2-Rad**, **SAM-3-Rad** and **SAM-5-Rad** at different scan rates. The stability of the different monolayers was demonstrated by performing consecutive voltammetric scans (Fig S9† to S14). Further, an I_{pa}/I_{pc} ratio very close to 1 and a I_{pa}, I_{pc} *vs.* scan rate linear relationship were determined, evidencing both the reversibility of the redox process and the confinement of the molecules on the surface (Fig. S15 and S16†). The reversible process observed at around −0.23 V (*vs.* Ag/AgCl, KCl 3 M) corresponds to the PTM(radical) ↔ PTM(anion) redox process while the redox signature of the Fc^+/Fc couple is clearly visible at +0.60 V (*vs.* Ag/AgCl, KCl 3 M). It is worth noting that the redox potential of the PTM radical bound to gold was *ca.* 400 mV lower than that observed for **SAM-1-Rad-Si** under illumination. This trend is not surprising and is usually observed for electroactive molecule-modified photoelectrodes.[29] In the case of silicon, the reduction of the PTM radical is easier owing to the photogenerated electron-induced activation of the redox process.[61] As expected, for **SAM-3-H** and **SAM-2-Rad**, only a single redox process attributed to either Fc or the PTM radical, respectively, was observed. In the case of **SAM-3-Rad** and **SAM-5-Rad**, two redox processes were present owing to the double functionality of the grafted monolayer.

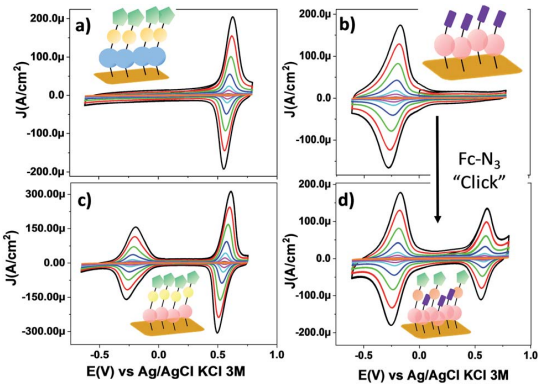

Fig. 4 CV curves of SAMs on gold: (a) **SAM-3-H**, (b) **SAM-2-Rad**, (c) **SAM-3-Rad** and (d) **SAM-5-Rad** in CH_2Cl_2 + 0.2 M Bu_4NPF_6 at different scan rates (0.05, 0.1, 0.25, 0.5, 1, 2, 3 and 4 V s^{-1}). The color code used for SAMs is the same as that used in Scheme 1. (Blue) PTM αH; (magenta) PTM radical; (yellow) triazole ring; (green) Fc and (violet) terminal alkyne moieties.

Interestingly, the PTM radical surface coverage estimated for the **SAM-3-Rad**, which was obtained by direct Au functionalization with the PTM–Fc dyad **3-Rad**, was very similar to that of the **SAM-2-Rad** (7.9 and 8.9 × 10^{-11} mol cm^{-2}, respectively) (Table S2†). Such a result denotes that the self-organization and the reactivity of the molecules for both SAMs were quite similar. These values further support that only one of the terminal alkynes of the **2-Rad** reacted with the Au surface.

To back up these findings, we investigated **SAM-2-Rad** and **SAM-3-Rad** by XPS[62] which is an effective tool for studying organic radical thin films.[63] It was found that the ratio of the integrated signal intensities of the different lines of the XPS curves agrees to a good extent with the theoretical percentages indicating that **SAM-2-Rad** and **SAM-3-Rad** were effectively obtained. The carbon concentration slightly exceeds the theoretical values (see Tables S3 and S4†). This is the usual case in samples prepared *ex situ* with wet-environment techniques. Molecular orbitals are highly directional and, consequently, they are perturbed if a different/new chemical interaction occurs. In this case, no deviation from the expected shapes was observed from the XPS main lines. Furthermore, a best fit procedure applied to the XPS spectra allows identifying the contributions from atomic sites having slightly different binding energies due to variations in the chemical environment.[62] Several constraints based on electronegativity and bond strength were applied[64,65](see ESI† for details). The comparison of the fitted results with the theoretical stoichiometry of the carbon atoms supports the successful preparation of **SAM-3-Rad** (Fig. S18† and Table S3†). In fact, any perturbation of the chemical environment of the carbon atoms that would hint at different chemical configurations would deliver a different best fit curve.

As depicted in the CVs shown in Fig. 4c and d, due to the presence of two electroactive moieties, an enhanced number of stable redox states can be realized, which is of interest for molecular memory devices. In particular, the PTM–Fc dyad displays two redox processes and hence, three distinct redox states, $[PTManion–Fc]^-$, PTMradical–Fc and $[PTMradical–Fc]^+$, in the −0.6 V to 0.8 V potential range. Such an electrochemical response prompted us to characterize **SAM-3-Rad** by EIS, using the applied potential as a perturbation signal and the capacitive real component as an output, characteristic of the interface at each redox state. This methodology was employed before in Fc-based and tetrathiafulvalene (TTF)-based SAMs by some of us.[66,67] It is important to emphasize that the three redox states are well differentiated in a narrow and stable potential window which makes the system very appealing.[68] The measurements were acquired in the frequency range from 100 kHz to 0.1 Hz with a 20 mV amplitude and the applied potentials were −0.5, 0.3 and 0.7 V. These values were chosen from the CV results to eliminate the contribution of the faradaic processes and thus to only consider the capacitive behaviour of the double layer. The Nyquist plots showed a common shape for a SAM-based interface with one semicircle without the diffusional process (Fig. S17†). The difference between the $[PTManion–Fc]^-$, PTMradical–Fc and $[PTMradical–Fc]^+$ species was evidenced in the Cole–Cole plot, where the imaginary capacitance (C_{im}) is

plotted *vs.* the real capacitance(C_{re})[48] (Fig. 5a). The obtained C_{re} values (indicated in the plot) were: C_{re1} (PTManion–Fc) = 6.5 μF cm^{-2}, C_{re2} (PTMradical–Fc) = 8.0 μF cm^{-2} and C_{re3} (PTMradical–Fc^{+}) = 12.8 μF cm^{-2}.

Clearly, the higher C_{re} value for the positively charged SAM (C_{re3}) is attributed to a well-defined charged double layer at the interface. The charged ferrocenium species are exposed to the top solid–electrolyte interface favoring the formation of a tight ion pair with the electrolyte anion (Fig. 5b, C_{re3}). In the case of the PTManion–Fc SAM, the negative charge of the PTM anion is located in the central carbon atom, which is shielded by the bulky chlorinated triphenyl rings. So, it forms a loose ion pair with the electrolyte cation.[69] Therefore, this ill-defined double layer generated at the PTManion–Fc SAM/electrolyte interface is expected to be very similar to that of the neutral PTM–Fc SAM (C_{re2}).

Charge transport measurements across PTM monolayers bound to gold

Charge transport measurements across the Au^{TS}/**SAM-N-rad**/liquid metal were performed in order to evaluate the SAMs as molecular wires, and to examine the influence of the D–A dyad. Moreover, the electrical output of the junction could be used to evaluate the second moiety introduced through the click chemistry on the PTM radicals (Fig. 6). The eutectic gallium indium alloy (EGaIn) was chosen as the top electrode,[70,71] since it has been successfully used previously to investigate different PTM-based SAMs and films.[72–74] The spontaneously formed oxide skin (mainly Ga_2O_3) allows the electrode to be shaped as a cone. In this work, the area of the GaO_x/EGaIn tip that was brought into contact with the sample surfaces was around 1000–2500 μm^2 in order to obtain stable measurements (see ESI† for details on the experimental setup).[75]

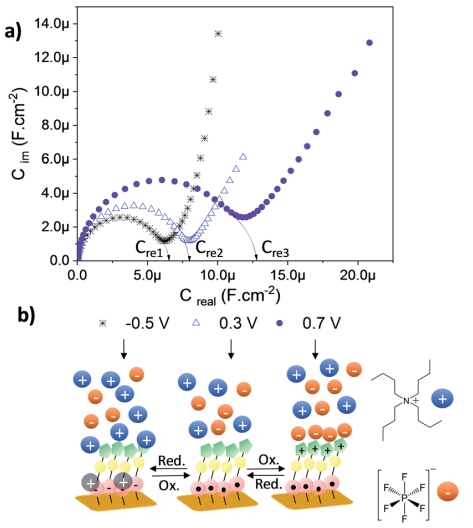

Fig. 5 (a) Cole–Cole plots recorded for the **SAM-3-rad** at different applied potentials to obtain three different redox states. The electrolytic medium (CH_2Cl_2 + 0.2 M Bu_4NPF_6) was used and the frequency was varied from 100 kHz to 0.1 Hz with a 20 mV amplitude. (b) Scheme of the three different interfaces at the specific applied voltage.

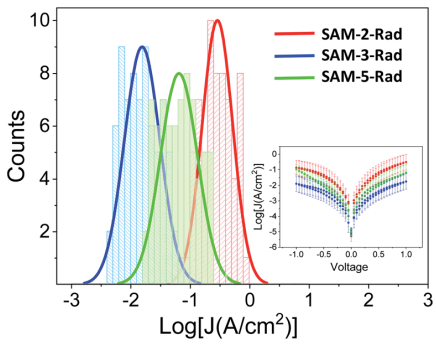

Fig. 6 Histograms and Gaussian fits of log|*J*| at 1 V for junctions Au^{TS}/**SAM-2,3** and **5-Rad**//GaO_x/EGaIn. Inset: Plots of mean log|*J*| *versus* *E*(*V*).

Fig. 6 shows that the three monolayers display a different molecular wire behaviour, in terms of the measured current through the junction, showing a current density (*J*) (**SAM-2-Rad**) > *J* (**SAM-5-Rad**) > *J* (**SAM-3-Rad**) (see ESI† for details on the statistical analysis). The differences between the three layers were mainly attributed to the different tunneling distances between the two electrodes arising from the thickness of the molecular layer. Taking into account that an approximately 50% of Fc incorporation was achieved to form **SAM-5-Rad** through the click reaction on **SAM-2-Rad**, the electrical response measured for this SAM was considered to be an average contribution of **SAM-2-Rad** and **SAM-3-Rad**. Current rectification was previously reported for SAMs incorporating Fc as the redox-active moiety.[73,76] Here, in the ±1 V range, we did not observe such a behaviour (inset in Fig. 6). This could be attributed to a poor molecular order within the layer and hence a poor directionality of the Fc moiety towards the top electrode, compared to well-ordered Fc-thiolated SAMs presenting a well-defined interface with the liquid-metal electrode.[76]

XPS and Near Edge X-ray Absorption Fine Structure (NEXAFS) measurements helped to confirm this interpretation. NEXAFS measurements of **SAM-5-Rad** show a clear Fe signal (Fig. 7d), however, the survey XPS and the Fe 2p core level spectra at 800 eV photon energy (Fi. S18 in ESI†) are characterized by a signal that is proportional to a lower concentration of iron atoms in comparison with the theoretical stoichiometry. These findings can be taken as an indication that **SAM-5-Rad** was obtained, however, the monolayer has a mixed nature: also molecules that do not carry the ferrocene unit are present, *i.e.*, **SAM-2-Rad**, and they contribute to the signal. NEXAFS measurements also allow determining the average molecular arrangement of the molecules in the films.[77] The C–K edge of **SAM-5-Rad** shows typical features due to transitions from the C 1s core levels to the unoccupied states, π* and σ* (Fig. 7b). In analogy with previous NEXAFS measurements of derivatives of the PTM radical, two main regions can be identified in the

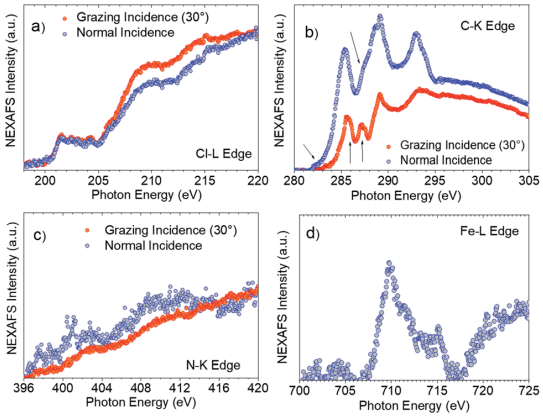

Fig. 7 **SAM-5-Rad** (a) Cl–L edge, (b) C–K edge (the arrows indicate the transitions as discussed in the text) and (c) N–K edge in grazing (30° to the substrate, red circles) and normal incidences (blue circles). (d) Fe–L edge NEXAFS spectrum at grazing incidence.

spectra in Fig. 7: the π* region up to around 290 eV and the σ* region in the photon energy range above 290 eV.[73,78,79] We can assign the feature at around 285.4 eV to contributions due to transitions from the C 1s core levels located in the carbon atoms of the aromatic rings and of the perchlorinated benzene rings to π* orbitals. The feature at 287.2 eV (see Fig. 7b, grazing incidence) is typical of ferrocene C–K NEXAFS spectra and is due to the C 1s to Fe 3d/π* transitions.[80–82] We observe a shoulder at 285.9 eV that is also assigned to contributions belonging to the ferrocene moiety.[80–82] The intensity at around 282.2 eV corresponds to transitions from the C 1s core levels to the singly unoccupied molecular orbital (SUMO).[60]

The determination of the average molecular orientation of **SAM-5-Rad** is very challenging, the Cl–L edge signal shows a very weak dichroism (Fig. 7a), and the resonances in the C–K edge spectra due to transitions from aromatic carbon atoms are all very close in energy (Fig. 7b). Thus, we have focused on the single building blocks. We have calculated an average molecular orientation of the ferrocene moiety of 22° with respect to the substrate using the intensities for the two polarizations at 285.9 eV and cross-checking with the intensities at 287.2 eV (21°).[77,83,84] The relative torsion of the component blocks in **SAM-5-Rad** together with the presence of **SAM-2-Rad** might hinder a good interaction with the top contact and, thus, contribute to the absence of a current rectification behaviour.

Conclusions

In summary, we have demonstrated that the functionalization of electro- and magnetically-active perchlorotriphenylmethyl radicals with terminal alkynes clearly permits us to expand their applicability. It has been shown that using the alkyne group as the grafting unit, chemically bonded self-assembled monolayers can be successfully prepared both on hydrogenated silicon and on gold in one step and preserving the radical character. The electronic properties of Si have allowed us to fabricate a light-triggered capacitance switch exploiting the redox properties of the grafted radicals. In the case of gold, not only the formation of the SAM but also its post-modification with other functional molecules through click chemistry has demonstrated the potential of such a versatile platform for achieving multifunctional layers displaying the fascinating properties of the attached organic radicals. In particular, here a radical donor–acceptor dyad has been on-surface synthesized following optimized conditions that enable the spin to be unaltered. For all this, we believe that the findings reported in this manuscript are a significant step forward in the implementation of organic radicals in molecular based devices with different properties and applications in fields such as energy storage and conversion, sensing, imaging, memory devices, and spintronics.

Conflicts of interest

There are no conflicts to declare.

Acknowledgements

S. Ababou-Girard and C. Meriadec (Institut de Physique de Rennes, UMR6251, France) are fully acknowledged for XPS measurements on the Si–H surfaces. Dr Vega Lloveras and Amable Bernabé are acknowledged for the EPR and MALDI-ToF measurements, respectively. We also would like to thank Thomas Chassé for allowing us to access the photoelectron laboratory at the University of Tübingen, Hilmar Adler for technical support, and Helmholtz-Zentrum Berlin (HZB) for providing beamtime at BESSY II. This work was funded by the Spanish Ministry project FANCYCTQ2016-80030-R, the Generalitat de Catalunya (2017SGR918) and the Spanish Ministry of Economy and Competitiveness, through the "Severo Ochoa" Programme for Centers of Excellence in R&D (SEV-2015-0496), the CSIC with the i-Link+ 2018 (Ref. LINKA20128) and CIBER-BBN. J. A. de S. is enrolled in the Materials Science PhD program of UAB. J.A. de S. thanks the Spanish Ministry for the FPI fellowship. Financial support from the German Research Foundation (DFG) under the contract CA852/11-1 and from Helmholtz-Zentrum Berlin is gratefully acknowledged.

Notes and references

1 K. T. Butler, G. Sai Gautam and P. Canepa, *npj Comput. Mater.*, 2019, **19**, DOI: 10.1038/s41524-019-0160-9.
2 M. S. Maglione, S. Casalini, S. Georgakopoulos, M. Barbalinardo, V. Parkula, N. Crivillers, C. Rovira, P. Greco and M. Mas-Torrent, *Small*, 2018, **14**, 1703344–1703351.
3 X. Su and T. A. Hatton, *Phys. Chem. Chem. Phys.*, 2017, **19**, 23570–23584.
4 C. Jia and X. Guo, *Chem. Soc. Rev.*, 2013, **42**, 5642–5660.
5 R. M. Arnold, N. E. Huddleston and J. Locklin, *J. Mater. Chem.*, 2012, **22**, 19357–19365.

6 G. A. Hudalla and W. L. Murphy, *Soft Matter*, 2011, **7**, 9561–9571.
7 S. Hosseinpour, M. Forslund, C. M. Johnson, J. Pan and C. Leygraf, *Surf. Sci.*, 2016, **648**, 170–176.
8 D. Xiang, X. Wang, C. Jia, T. Lee and X. Guo, *Chem. Rev.*, 2016, **116**, 4318–4440.
9 I. Ratera and J. Veciana, *Chem. Soc. Rev.*, 2012, **41**, 303–349.
10 X. Ai, E. W. Evans, S. Dong, A. J. Gillett, H. Guo, Y. Chen, T. J. H. Hele, R. H. Friend and F. Li, *Nature*, 2018, **563**, 536–540.
11 H. Guo, Q. Peng, X.-K. Chen, Q. Gu, S. Dong, E. W. Evans, A. J. Gillett, X. Ai, M. Zhang, D. Credgington, V. Coropceanu, R. H. Friend, J.-L. Brédas and F. Li, *Nat. Mater.*, 2019, **18**, 977–984.
12 D. A. Wilcox, V. Agarkar, S. Mukherjee and B. W. Boudouris, *Annu. Rev. Chem. Biomol. Eng.*, 2018, **9**, 83–103.
13 Y. Morita, S. Nishida, T. Murata, M. Moriguchi, A. Ueda, M. Satoh, K. Arifuku, K. Sato and T. Takui, *Nat. Mater.*, 2011, **10**, 947–951.
14 M. Mas-Torrent, N. Crivillers, V. Mugnaini, I. Ratera, C. Rovira and J. Veciana, *J. Mater. Chem.*, 2009, **19**, 1691–1695.
15 M. A. Sowers, J. R. Mccombs, Y. Wang, J. T. Paletta, S. W. Morton, E. C. Dreaden, M. D. Boska, M. Francesca Ottaviani, P. T. Hammond, A. Rajca and J. A. Johnson, *Nat. Commun.*, 2014, **5**, 1–9.
16 M. Hou, X. Lu, Z. Zhang, Q. Xia, C. Yan, Z. Yu, Y. Xu and R. Liu, *ACS Appl. Mater. Interfaces*, 2017, **9**, 44316–44323.
17 G. Seber, J. Muñoz, S. Sandoval, C. Rovira, G. Tobias, M. Mas-Torrent and N. Crivillers, *Adv. Mater. Interfaces*, 2018, **5**, 1701072.
18 C. Simão, M. Mas-Torrent, N. Crivillers, V. Lloveras, J. M. Artés, P. Gorostiza, J. Veciana and C. Rovira, *Nat. Chem.*, 2011, **3**, 359–364.
19 C. Simão, M. Mas-Torrent, J. Veciana and C. Rovira, *Nano Lett.*, 2011, **11**, 4382–4385.
20 J. Lee, E. Lee, S. Kim, G. S. Bang, D. A. Shultz, R. D. Schmidt, M. D. E. Forbes and H. Lee, *Angew. Chem., Int. Ed.*, 2011, **50**, 4414–4418.
21 M. Mas-Torrent, J. Veciana, N. Crivillers, C. Rovira and J. Veciana, *Chem. Rev.*, 2012, **112**, 2506–2527.
22 M. Halik and A. Hirsch, *Adv. Mater.*, 2011, **23**, 2689–2695.
23 M. Mas-Torrent, C. Rovira and J. Veciana, *Adv. Mater.*, 2013, **25**, 462–468.
24 T. Zaba, A. Noworolska, C. M. Bowers, B. Breiten, G. M. Whitesides and P. Cyganik, *J. Am. Chem. Soc.*, 2014, **136**, 11918–11921.
25 S. Zhang, K. L. Chandra and C. B. Gorman, *J. Am. Chem. Soc.*, 2007, **129**, 4876–4877.
26 F. Bejarano, I. J. Olavarria-Contreras, A. Droghetti, I. Rungger, A. Rudnev, D. Gutiérrez, M. Mas-Torrent, J. Veciana, H. S. J. Van Der Zant, C. Rovira, E. Burzurí and N. Crivillers, *J. Am. Chem. Soc.*, 2018, **140**, 1691–1696.
27 J. M. Buriak, *Chem. Rev.*, 2002, **102**, 1271–1308.
28 S. Ciampi, J. B. Harper and J. J. Gooding, *Chem. Soc. Rev.*, 2010, **39**, 2158–2183.
29 B. Fabre, *Chem. Rev.*, 2016, **116**, 4808–4849.
30 J. Li, P. S. Thiara and M. Mrksich, *Langmuir*, 2007, **23**, 11826–11835.
31 J. P. Collman, N. K. Devaraj and C. E. D. Chidsey, *Langmuir*, 2004, **20**, 1051–1053.
32 T. Klasen, T. Winkler, R. Chelmowski, A. Terfort, S. D. Köster, C. Wöll, N. Metzler-Nolte and D. Käfer, *Langmuir*, 2009, **25**, 11480–11485.
33 T. Lummerstorfer and H. Hoffmann, *J. Phys. Chem. B*, 2004, **108**, 3963–3966.
34 J. Mehlich and B. J. Ravoo, *Org. Biomol. Chem.*, 2011, **9**, 4108–4115.
35 M. Ballester, J. Riera, J. Castafier, C. Badía and J. M. Monsó, *J. Am. Chem. Soc.*, 1971, **93**, 2215–2225.
36 B. Fabre, Y. Li, L. Scheres, S. P. Pujari and H. Zuilhof, *Angew. Chem., Int. Ed.*, 2013, **52**, 12024–12027.
37 M. H. Choudhury, S. Ciampi, Y. Yang, R. Tavallaie, Y. Zhu, L. Zarei, V. R. Gonçales and J. J. Gooding, *Chem. Sci.*, 2015, **6**, 6769–6776.
38 L. Zhang, Y. B. Vogel, B. B. Noble, V. R. Gonçales, N. Darwish, A. Le Brun, J. J. Gooding, G. G. Wallace, M. L. Coote and S. Ciampi, *J. Am. Chem. Soc.*, 2016, **138**, 9611–9619.
39 D. Zigah, C. Herrier, L. Scheres, M. Giesbers, B. Fabre, P. Hapiot and H. Zuilhof, *Angew. Chem., Int. Ed.*, 2010, **49**, 3157–3160.
40 L. Scheres, J. Ter Maat, M. Giesbers and H. Zuilhof, *Small*, 2010, **6**, 642–650.
41 J. M. Buriak, *Chem. Mater.*, 2014, **26**, 763–772.
42 W. Peng, W. J. I. Debenedetti, S. Kim, M. A. Hines and Y. J. Chabal, *Appl. Phys. Lett.*, 2014, **104**, 241601.
43 K. Uno, A. Namiki, S. Zaima, T. Nakamura and N. Ohtake, *Surf. Sci.*, 1988, **193**, 321–335.
44 X. G. Zhang, *Electrochemistry of Silicon and Its Oxide*, 2004, Kluwer Acad., New York.
45 A. J. Bard and L. R. Faulkner, *Electrochemical Methods; Fundamentals and Applications*, John Wiley & Sons, Ltd, 2002.
46 Y. B. Vogel, A. Molina, J. Gonzalez and S. Ciampi, *Anal. Chem.*, 2019, **91**, 5929–5937.
47 A. W. Bott and D. Ph, *Curr. Sep.*, 1998, **17**, 87–91.
48 P. R. Bueno, F. Fabregat-Santiago and J. J. Davis, *Anal. Chem.*, 2013, **85**, 411–417.
49 J. Gonzalez and A. Molina, *J. Electroanal. Chem.*, 2003, **557**, 157–165.
50 B. Fabre, *Acc. Chem. Res.*, 2010, **43**, 1509–1518.
51 J. E. Moses and A. D. Moorhouse, *Chem. Soc. Rev.*, 2007, **36**, 1249–1262.
52 W. Xi, T. F. Scott, C. J. Kloxin and C. N. Bowman, *Adv. Funct. Mater.*, 2014, **24**, 2572–2590.
53 L. Zhu, C. J. Brassard, X. Zhang, P. M. Guha and R. J. Clark, *Chem. Rec.*, 2016, **16**, 1501–1517.
54 D. N. Barsoum, N. Okashah, X. Zhang and L. Zhu, *J. Org. Chem.*, 2015, **80**, 9542–9551.
55 B. T. Worrell, J. A. Malik and V. V. Fokin, *Science*, 2013, **340**, 457–460.
56 M. Meldal and C. W. Tomøe, *Chem. Rev.*, 2008, **108**, 2952–3015.
57 J. Castañer, M. Ballester and J. Riera, *Tetrahedron Lett.*, 1978, **20**, 643–644.

58 E. A. Weiss, G. K. Kaufman, J. K. Kriebel, Z. Li, R. Schalek and G. M. Whitesides, *Langmuir*, 2007, **23**, 9686–9694.
59 L. Yuan, L. Jiang, B. Zhang and C. A. Nijhuis, *Angew. Chem., Int. Ed.*, 2014, **53**, 3377–3381.
60 A. V Rudnev, C. Franco, N. Crivillers, G. Seber, A. Droghetti, I. Rungger, I. V Pobelov, J. Veciana, M. Mas-Torrent and C. Rovira, *Phys. Chem. Chem. Phys.*, 2016, **18**, 27733–27737.
61 P. G. Santangelo, G. M. Miskelly and N. S. Lewis, *J. Phys. Chem.*, 1988, **92**, 6359–6367.
62 K. Siegbahn, C. Nordling, A. Fahlman, R. Nordberg, K. Hamrin, J. Hedman, G. Johansson, T. Bergmark, S.-E. Karlsson, I. Lindgren and B. Lindberg, *ESCA: Atomic, Molecular, and Solid State Structured Studied by Means Electron Spectroscopy*, Almqvist and WiksellsBoktryckeri AB, Uppsala, 1967.
63 M. B. Casu, *Acc. Chem. Res.*, 2018, **51**, 753–760.
64 S. A. Savu, I. Biswas, L. Sorace, M. Mannini, D. Rovai, A. Caneschi, T. Chassé and M. B. Casu, *Chem.–Eur. J.*, 2013, **19**, 3445–3450.
65 S. A. Savu, M. B. Casu, S. Schundelmeier, S. Abb, C. Tönshoff, H. F. Bettinger and T. Chassé, *RSC Adv.*, 2012, **2**, 5112–5118.
66 E. Marchante, M. S. Maglione, N. Crivillers, C. Rovira and M. Mas-Torrent, *RSC Adv.*, 2017, **7**, 5636–5641.
67 E. Marchante, N. Crivillers, M. Buhl, J. Veciana and M. Mas-Torrent, *Angew. Chem., Int. Ed.*, 2016, **55**, 368–372.
68 J. Casado-Montenegro, E. Marchante, N. Crivillers, C. Rovira and M. Mas-Torrent, *ChemPhysChem*, 2016, **17**, 1810–1814.
69 J. Veciana, J. Riera, J. Castañer and N. Ferrer, *J. Organomet. Chem.*, 1985, **297**, 131–141.
70 W. F. Reus, M. M. Thuo, N. D. Shapiro, C. A. Nijhuis and G. M. Whitesides, *ACS Nano*, 2012, **6**, 4806–4822.
71 C. A. Nijhuis, W. F. Reus and G. M. Whitesides, *J. Am. Chem. Soc.*, 2009, **131**, 17814–17827.
72 L. Yuan, C. Franco, N. Crivillers, M. Mas-Torrent, L. Cao, C. S. S. Sangeeth, C. Rovira, J. Veciana and C. A. Nijhuis, *Nat. Commun.*, 2016, **7**, 12066–12075.
73 M. Souto, V. Díez-Cabanes, L. Yuan, A. R. Kyvik, I. Ratera, C. A. Nijhuis, J. Cornil and J. Veciana, *Phys. Chem. Chem. Phys.*, 2018, **20**, 25638–25647.
74 D. Gutiérrez, S. Riera-Galindo, M. R. Ajayakumar, J. Veciana, C. Rovira, M. Mas-Torrent and N. Crivillers, *J. Phys. Chem. C*, 2018, **122**, 17784–17791.
75 F. C. Simeone, H. J. Yoon, M. M. Thuo, J. R. Barber, B. Smith and G. M. Whitesides, *J. Am. Chem. Soc.*, 2013, **135**, 18131–18144.
76 L. Yuan, N. Nerngchamnong, L. Cao, H. Hamoudi, E. Del Barco, M. Roemer, R. K. Sriramula, D. Thompson and C. A. Nijhuis, *Nat. Commun.*, 2015, **6**, 6324–6334.
77 J. Stohr, *NEXAFS Spectroscopy*, Springer, 2003.
78 O. Shekhah, N. Roques, V. Mugnaini, C. Munuera, C. Ocal, J. Veciana and C. Wöll, *Langmuir*, 2008, **24**, 6640–6648.
79 V. Mugnaini, A. Calzolari, R. Ovsyannikov, A. Vollmer, M. Gonidec, I. Alcon, J. Veciana and M. Pedio, *J. Phys. Chem. Lett.*, 2015, **6**, 2101–2106.
80 E. Otero, R. G. Wilks, T. Regier, R. I. R. Blyth, A. Moewes and S. G. Urquhart, *J. Phys. Chem. A*, 2008, **112**, 624–634.
81 A. Shaporenko, K. Rössler, H. Lang and M. Zharnikov, *J. Phys. Chem. B*, 2006, **110**, 24621–24628.
82 S. Watcharinyanon, E. Moons and L. S. O. Johansson, *J. Phys. Chem. C*, 2009, **113**, 1972–1979.
83 M. B. Casu, A. Schöll, K. R. Bauchspiess, D. Hübner, T. Schmidt, C. Heske and E. Umbach, *J. Phys. Chem. C*, 2009, **113**, 10990–10996.
84 M. B. Casu, P. Cosseddu, D. Batchelor, A. Bonfiglio and E. Umbach, *J. Chem. Phys.*, 2008, **128**, 74702.

Electronic Supplementary Material (ESI) for Chemical Science.

Electronic supplementary information for:

Exploiting the versatile alkyne-based chemistry for expanding the applications of a stable triphenylmethyl organic radical on surfaces

J. Alejandro de Sousa, Francesc Bejarano, Diego Gutiérrez, Yann R. Leroux, Ewa-Malgorzata Nowik Boltyk, Tobias Junghoefer, Erika Giangrisostomi, Ruslan Ovsyannikov, Maria Benedetta Casu, Jaume Veciana, Marta Mas-Torrent, Bruno Fabre, Concepció Rovira, Núria Crivillers

Table of contents

1-Materials

All reagents used were of high quality. Ferrocenemethanol, glacial acetic acid, copper (I) iodide, aqueous 54-56% tetrabutylammonium hydroxide, tetrabutylammonium hexafluorophosphate 98% and *N*,*N*-diisopropylethylamine (DIPEA) were obtained from Sigma-Aldrich. Sodium azide and *p*-chloranil were obtained from Panreac.

All solvents were of HPLC grade. Toluene and THF were dried using sodium and benzophenone as indicator before use; acetonitrile and dichloromethane were dried using CaH_2 before use. The purification of the synthesised compounds was carried out using Carlo Erba silica gel (60, particle size 35-70).

2-Apparatus

2.1-Electrochemical measurements.

2.1.1-Silicon Surface

Cyclic voltammetry measurements were performed with an Autolab electrochemical analyzer (PGSTAT 30 potentiostat/galvanostat from Eco Chemie B.V.) equipped with the GPES and FRA softwares in a home-made three-electrode glass cell. The working electrode, modified Si(111), was pressed against an opening in the cell side using a Teflon circular piece and a FETFE (Aldrich) O-ring seal. An ohmic contact was made on the previously polished rear side of the sample by applying a drop of In-Ga eutectic (Alfa-Aesar, 99.99%). A steel piece was dropped on the eutectic-coated sample and then the assembly was screwed to the cell using a plastic cap screw. The electrochemically active area of the Si(111) surface (namely 0.3 cm^2) was estimated by measuring the charge under the voltammetric peak corresponding to the ferrocene oxidation on Si(111)-H and compared to that obtained with a 1 cm^2-Pt electrode under the same conditions. The counter electrode was a carbon rod and the system 10^{-2} M Ag^+ | Ag in acetonitrile was used as the reference electrode (+0.33 V versus aqueous Ag/AgCl, KCl 3M). All reported potentials are referred to Ag/AgCl, KCl 3M (uncertainty ± 5 mV). Tetra-n-butylammonium perchlorate Bu_4NClO_4 (Fluka, puriss, electrochemical grade) was used at 0.1 mol L^{-1} as supporting electrolyte in acetonitrile. The (CH_3CN + 0.1 M Bu_4NClO_4) electrolytic medium was dried over activated, neutral alumina (Merck) for 30 min, under stirring and under argon. About 20 mL of this solution was transferred with a syringe into the electrochemical cell prior to experiments. All electrochemical measurements were carried out inside a home-made Faraday cage, at room temperature (20 ± 2 ºC) under constant argon gas flow. The light was provided by a solar simulator with a fluence of 100 mW cm^{-2}

(LS0106, LOT Quantum Design) equipped with a AM 1.5G and red (Edmund Optics) filters. For impedance spectroscopy measurements, the amplitude of the alternating current (ac) signal was 10 mV. The differential capacitance C was determined from the imaginary part (Z") of the complex impedance Z″ ($C = -1/2\pi fZ''$) where f is the frequency. For Mott-Schottky experiments, the cell was in the dark and the potential was swept from positive to negative values at a frequency of 50 kHz (25 mV step potential).

2.1.2-Gold Surface

Cyclic voltammetry, square wave voltammetry and impedance spectroscopy characterizations were performed with an AUTOLAB 204 equipped with NOVA 2.3 software. A Pt mesh was used as the counter electrode, Ag/AgCl 3M KCl was used as reference electrode. Studies in solution were made using a glassy carbon as the working electrode (Area = 0.28 cm^2). For the electrochemical characterization of the SAMs, the modified Au^{TS} was used as the working electrode (area exposed of 1 cm^2). A 0.1M or 0.2M solution of $TBAPF_6$ in dry CH_2Cl_2 was used as the electrolytic medium, under argon atmosphere.

For impedance measurements, the frequency was scanned from 100 kHz to 0.1 Hz with a 20 mV amplitude. Four different potentials were applied: -0.5, 0, 0.3 and 0.7 V vs Ag/AgCl 3M KCl.

2.2-Electron Paramagnetic Resonance (EPR) spectroscopy.

EPR spectra were recorded at room temperature on a Bruker ESP 300 E spectrometer provided with a rectangular cavity T102 that works with an X band (9.5 GHz). The signal-to-noise ratio of spectra was increased by accumulation of scans using the F/Flock accessory to guarantee large field reproducibility. Precautions to avoid undesirable spectral distortion and line broadenings, such as those arising from microwave power saturation and magnetic field over modulation, were also taken into account to improve sensitivity.

2.3-UV-vis absorption spectroscopy.

UV-Vis spectra were obtained from a Varian Cary 5000 UV-Vis-NIR spectrophotometer. Quartz cuvettes with an optical path of 1 cm were used in all experiments.

2.4-MALDI-ToF mass spectroscopy.

The reported spectra were acquired with a Bruker Ultraflex mass spectrometer by operating at ion pulsed extraction in negative mode at high power. Ditranol was used as a matrix to improve the laser absorption.

2.5-Nuclear magnetic resonance spectroscopy (NMR).

The ^{1}H-NMR spectra were acquired with a Bruker Avance DPX (250 MHz) spectrometer and Bruker Avance-II+ (600MHz)), ^{13}C-NMR spectra were obtained from a Bruker Avance-III (400MHz) spectrometer. The calibration was made using residual nondeuterated chloroform (δ(1H) = 7.26 ppm; δ(13C) = 77.00 ppm) as internal references. The data analysis was carried out with MestReNova software (MestReLab Research S. L.). The following abbreviations were used to designate multiplicities: s = singlet, d = doublet, m = multiplet.

2.6-Infrared spectroscopy (IR).

The spectra were obtained from a FT-IR PerkinElmer spectrometer with a diamond ATR accessory.

2.7-X-ray photoelectron spectroscopy (XPS).

2.7.1-Silicon surface characterization.

XPS measurements were performed with an Mg K_{alpha} (hυ = 1254.6 eV) X-ray source and an Al source (hυ= 1486.6 eV) using a VSW HA100 photoelectron spectrometer with a hemispherical photoelectron analyzer, working at an energy pass of 20 eV for survey and resolved spectra. The experimental resolution was 1.0 eV. Unless specified, C1s set at 285.0 eV was used as the energy reference for all the analyses.

2.7.2-Gold surface characterization.

X-ray Photoelectron Spectroscopy (XPS) measurements were performed in an analysis chamber (base pressure 2 x 10^{-10} mbar) equipped with a monochromatic Al Kα source (SPECS XR 50 M plus SPECS Focus 500) and a SPECS Phoibos 150 hemispherical electron analyser. The detailed spectra were measured at 20 eV pass energy, the survey spectra at 50 eV pass energy, and their binding energy calibrated to the Au 4f signal at 84 eV. NEXAFS and photon dependent XPS measurements were performed at the third-generation synchrotron radiation source Bessy II (Berlin) at the LowDose PES end-station, at the PM4 beamline, equipped with a Scienta ArTOF-10k spectrometer. The measurements were carried out in multibunch hybrid mode (ring current in top up mode = 250 mA, cff = 1.6, 100-μm exit slit, estimated energy resolution = 340 meV at 640 eV). The NEXAFS spectra, measured in total electron yield, were normalized by using the clean substrate signal and the ring current into account, and then all spectra were scaled to give an equal edge jump.[1–3] No beam-induced degradation of the samples was observed on the time scale of all discussed experiments.

2.8-Transport measurements through Au^{TS}/SAM//GaOx/EGaIn junctions.

The "EGaIn measurements" were performed using a home-made measurement set-up. The *J-V* curves were acquired using a Keithley 2004B. The Keithley was controlled using in-house software developed with LabVIEW. During the measurements, the top-electrode GaOx/EGaIn was biased and the bottom electrode was grounded.

3. Synthesis and characterization of the synthesised compounds.

3.1-Synthesis of azidomethylferrocene.

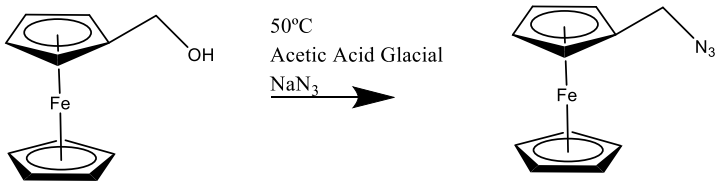

Scheme S 1. Synthesis of azidomethylferrocene.

Azidomethylferrocene was synthesized using the procedure reported by J.M. Casas-Solvas[4]. Ferrocenemethanol (133.0 mg, 0.6 mmol) and sodium azide (239.7 mg, 0.99 mmol) were mixed in glacial acetic acid (3 mL) and stirred at 50 ºC for 2 h. The resulting mixture was diluted in CH_2Cl_2 (50 mL) and the organic phase was washed with a saturated solution of $NaHCO_3$ (3 x 50 mL), dried (Mg_2SO_4), filtered and evaporated under vacuum. After column chromatography (silica gel, EtOAc:Hexane, 1:25) the desired compound was obtained as an orange oil (139 mg, 96%). **^{1}H-NMR** ($CDCl_3$, 250 MHz): δ(ppm)= 4.12 (s, 2H, **CH_2**); δ= 4.17 (s, 5H, Cp-**H**); δ= 4.20 (t, 2H, Cp-**H**); δ= 4.23 (t, 2H, Cp-**H**). ATR-IR: ν (cm^{-1}) = 3092 (Cp-H), 2923 (C-H), 2856(C-H), 2088 (ν_{as} $N=N^+-N^-$),1252 (ν_{as} $N=N^+-N^-$).

3.2-Synthesis of PTM-Fc alpha H compounds: 3-H and 4-H.

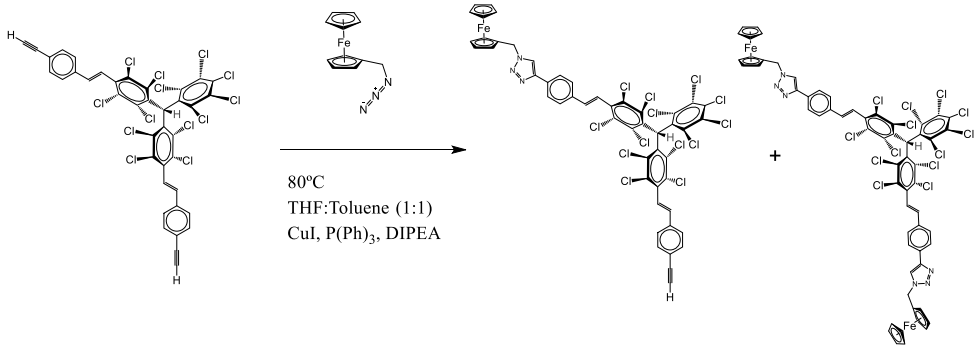

2-H 3-H 4-H

Scheme S2. Synthesis of compounds **3-H** and **4-H**.

Azidomethylferrocene (12.6 mg, 0.052 mmol) dissolved in 1 mL of dry THF was added to a mixture of diacetylene derivative **2-H** (50.4 mg, 0.053mmol) triphenylphosphine (8.1 mg, 0.031 mmol), CuI (6.4 mg, 0.0336 mmol) and *N*,*N*-diisopropylethylamine (DIPEA, 10.61 M; 50 μL, 0.265 mmol) in 1 mL of dry toluene. The mixture was stirred for 3 hours at 80°C under argon atmosphere. The resulting mixture was evaporated and the obtained solid dissolved in 20 mL of toluene. To remove the unreacted CuI, the resulting solution was vigorously washed (3 x 50mL) with a solution of 0.5 M of EDTA and 0.2M of NH_3 (the pH of the solution was adjusted to 9 with NaOH). This rinsing process consisted in stirring the organic phase for 3 hours with the washing aqueous solution. This was repeated three times. Finally, the organic phase was dried (Na_2SO_4), filtered and evaporated under vacuum. After evaporation of the solvent, the crude was purified by column chromatography with silica gel using as eluent CH_2Cl_2 to get pure αH-PTM-Fc (**3-H**) and then a gradient with $CHCl_3$ to have the αH-PTM-Fc2 (**4-H**). Both mono- and di- cycloaddition products were obtained as a yellow powder with a yield of 38 % (**3-H**) and 35% (**4-H**).

αH-PTM-Fc (3-H): ^{1}H NMR ($CDCl_3$, 600 MHz): δ(ppm) = 7.83 (d, 2H, *J*=8.18 Hz, Ar-**H**), 7.67 (s, 1H, N-**H**), 7.57 (d, 2H, *J*=8.21 Hz, Ar-**H**), 7.52 (d, 2H, *J*=8.21 Hz, Ar-**H**), 7.50 (d, 2H, *J*=8.26 Hz, Ar-**H**), 7.08-7.07 (m, 5H, **H**-C=C-**H and α H**), 5.36 (s, 2H, **CH_2**), 4.33 (m, 2H, **C_9-H**), 4.25 (m, 2H, **C_8-H**), 4.21 (s, 5H, **C_{10}-H**), 3.16 (s, 1H, C≡C-**H**); **^{13}C NMR** ($CDCl_3$, 101 MHz): δ =147.17 (**C-1**), 137.98, 137.58, 137.33, 136.99, 136.70, 136.45, 136.40, 135.73, 135.22, 135.18, 135.05, 134.96, 134.91, 134.04, 133.98, 133.49, 133.40, 132.62, 132.44, 132.26, 131.21, 128.59, 127.99, 127.44, 126.84, 126.06, 125.68, 124.19, 123.16, 122.51, 119.12

(**C-2**), 83.47 (**C≡C-H**), 80.74 (**C-7**), 78.55 (**C≡C-H**), 69.22 (**C-9**), 69.05 (**C-8**), 69.02 (**C-10**), 56.83 **(αH-C)**, 50.27 (**C-6**).

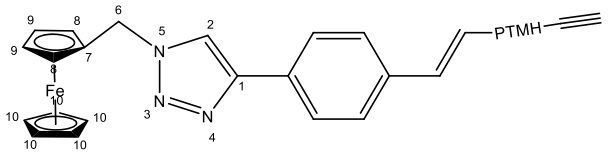

ATR-IR: ν (cm^{-1}) = 3298 (w) (CΞC-H), 3082 (w) (ArC-H), 3032 (w) (C=C-H), 2106 (w) (CΞC), 1632 (w) (C=C), 1611 (w), 1537 (w) (ArC-ArC), 1504 (w) (ArC-ArC),1454 (w) (N=N), 1413 (w) (Cl-ArC-ArC-Cl), 1360 (m) (Cl-ArC-ArC-Cl), 1334 (m) (Cl-ArC-ArC-Cl), 1291 (s), 1263 (m), 1230 (w), 1180 (w), 1138 (w), 1106 (w), 1041 (w) (C-N), 969 (w), 806 (ArC-Cl). **LDI-ToF** *m/z* $[M]^-$ calcd for $C_{50}H_{26}Cl_{13}FeN_3$, 1184.73; found, *1184.18* $[M-H]^+$; **UV/Vis (CH_2Cl_2):** λ (nm) (ε) 317.54 (60091), 434.36 (113). **CV** (0.1 M $TBAPF_6$ in CH_2Cl_2, vs Ag/AgCl KCl 3M): $E_{1/2}(Fc^+/Fc)$ = 0.60V

αH-PTM-Fc2 (4-H). ^{1}H NMR (CD_2Cl_2, 600 MHz): δ(ppm) = 7.83 (d, 4H, *J*=8.17 Hz, Ar-**H**), 7.67 (s, 1H, N-**H**), 7.57 (d, 4H, *J*=8.21 Hz, Ar-**H**), 7.08 (bs, 4H, **H**-C=C-**H**), 7.07 (s, 1H, **α H**), 5.36 (s, 4H, **CH_2**), 4.33 (m, 4H, **C_{p9}-H**), 4.25 (m, 4H, **C_{p8}-H**), 4.21 (s, 10H, **C_{p10}-H**); **^{13}C NMR ($CDCl_3$, 101 MHz):** δ(ppm)=147.16 (**C-1**), 137.95, 137.29, 137.27, 137.03, 136.45, 136.42, 135.73, 135.20, 134.99, 134.89, 134.05, 133.98, 133.96, 133.46, 133.40, 133.35, 132.40, 132.26, 132.22, 131.18, 127.43, 126.05, 123.17, 119.15 (**C-2**), 80.79 (**C-7**), 69.29 (**C-9**), 69.12 (**C-8**), 69.09 (**C-10**), 56.82 (**αH-C**), 50.29 (**C-6**).

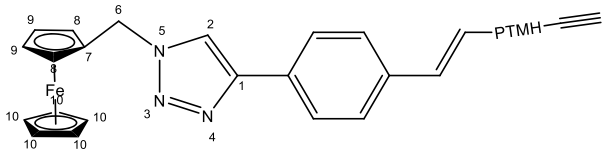

ATR-IR: ν (cm^{-1}) = 3090 (w) (ArC-H), 3037 (w) (C=C-H), 1632 (w) (C=C), 1610 (w) , 1537(w) (ArC-ArC), 1504 (w) (ArC-ArC), 1453 (w) (N=N), 1411 (w) (Cl-ArC-ArC-Cl), 1364 (m) (Cl-ArC-ArC-Cl), 1329 (m) (Cl-ArC-ArC-Cl), 1298 (s), 1272 (m), 1179 (w), 1141 (w), 1105 (w), 1068 (w), 1041 (w) (C-N), 966 (w), 806 (ArC-Cl); **LDI-ToF** (negative mode): *m/z* calcd. for $C_{61}H_{37}Cl_{13}Fe_2N_6$, 1425.76; found, 1425.21$[M]^+$; **UV/Vis (CH_2Cl_2):** λ (nm) (ε) 325.46 (76303), 432.38 (291). **CV** (0.1 M $TBAPF_6$ in CH_2Cl_2, vs Ag/AgCl KCl 3M): $E_{1/2}(Fc^+/Fc)$ = 0.61V.

3.3-Synthesis of PTM-Fc radicals compounds 3-Rad and 4-Rad

Two different synthetic routes (A and B) were followed to obtain **3-Rad** and **4-Rad**

Route A:

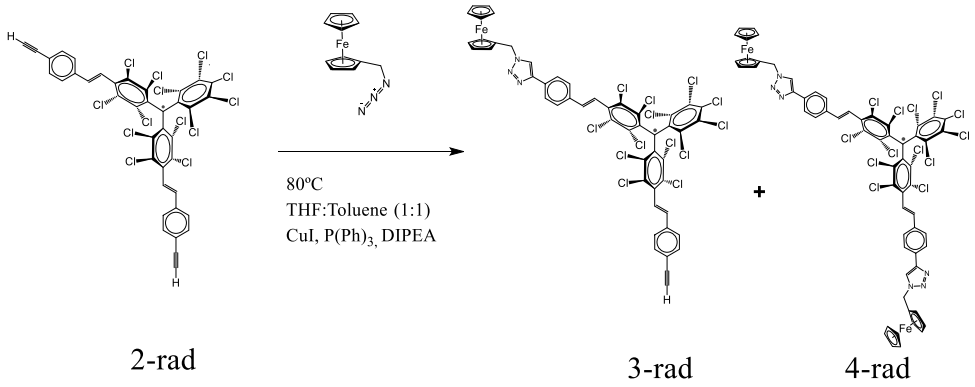

Scheme S3. Synthesis of compounds **3-Rad** and **4-Rad** by route A.

Route A: All the process was carried out in a laboratory equipped with red light to avoid the decomposition of the radical species in solution. Azidomethylferrocene (12.4 mg, 0.0515 mmol) dissolved in 1 mL of dry THF was added to a mixture of diacetylene derivative **2-Rad** (50.1 mg, 0.0530 mmol) triphenylphosphine (8 mg, 0.0305 mmol), CuI (6 mg, 0.0315 mmol) and *N*,*N*-diisopropylethylamine (DIPEA, 10.61 M; 50 μL, 0.26525 mmol) in 1 mL of dry toluene. The mixture was stirred for 3 hours at 80°C under argon atmosphere. The resulting mixture was evaporated and the obtained solid dissolved in 20 mL of toluene. To remove the unreacted CuI, the resulting solution was vigorously washed (3 x 50mL) with a solution of 0.5 M of EDTA and 0.2M of NH_3 (the pH of the solution was adjusted to 9 with NaOH). This rinsing process consisted in stirring the organic phase for 3 hours with the washing aqueous solution. This was repeated three times. Finally, the organic phase was dried (Na_2SO_4), filtered and evaporated under vacuum. After evaporation of the solvent, the crude was purified by column chromatography with silica gel using as eluent CH_2Cl_2 to the rad-PTM-Fc (**3-Rad**) and then a gradient with $CHCl_3$ to have the rad-PTM-Fc2 (**4-Rad**). Both mono- and di-cycloaddition products were obtained as a dark brown powder with a yield of 51% (**3-Rad**) and 48% (**4-Rad**).

Route B:

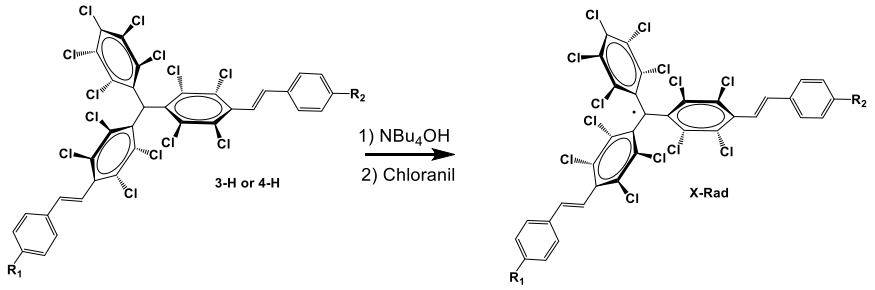

Scheme S4. Synthesis of compounds **3-Rad** and **4-Rad** by route B.

Route B

Synthesis of compound 3-Rad. All the process was carried out in a laboratory equipped with red light to avoid the decomposition of the radical species in solution. Tetrabutyl ammonium hydroxide 28 % aqueous (14 μL, 0.0151 mmol) was added to a solution of compound **3-H** (14.9 mg, 0.0126 mmol) in dry THF (5 mL) and the solution was stirred at room temperature. The formation of the perchlorotriphenylmethyl anion was monitored by UV/vis spectroscopy. When the deprotonation is complete (about 30 min), *p*-chloranil was added (3.9 mg, 0.0158 mmol) and the oxidation from the perchlorotriphenylmethyl anion to the radical was followed by UV/vis spectroscopy. When the oxidation was complete (about 180 min) the mixture was evaporated under vacuum and the crude was purified by column chromatography (silica gel, CH_2Cl_2). Compound **3-Rad** was obtained as a dark brown powder (13.5 mg, 90% yield).

ATR-IR: ν (cm^{-1}) = 3294 (w) (C≡C-H), 3078 (w) (ArC-H), 3032 (w) (ArC-H),2926 (w), 2854 (w), 2106 (w) (C≡C), 1681 (w) (C=C), 1609 (w), 1506 (w) (ArC-ArC), 1336 (m) (Cl-ArC-ArC-Cl), 1321 (m) (Cl-ArC-ArC-Cl), 1292 (w) (Cl-ArC-ArC-Cl), 1259 (w) (Cl-ArC-ArC-Cl), 1208 (w) (Cl-ArC-ArC-Cl), 1041 (m) (C-N), 970 (m), 817 (s) (C-Cl), **LDI-ToF** (negative mode) m/z: $[M]^-$ calcd for $C_{50}H_{25}Cl_{13}FeN_3$, 1183.73; found, 1183.18, **UV/Vis** (CH_2Cl_2): λ (nm) (ε)

308.96 (37809), 380.96 (17797), 442.28 (18400), 586.82 (2299); **CV** (0.1 M $TBAPF_6$ in CH_2Cl_2, vs Ag/AgCl KCl 3M): $E_{1/2}$(radical/anion) = -0.17V, $E_{1/2}(Fc^+/Fc)$ = 0.61; **EPR**: g = 2.0026, $a(^1H)$ = 1.9 G, ΔH_{pp} = 1.1 G, $a(^{13}CAr)$ = 12.6, 14.3 G, $a(^{13}C\alpha)$ = 29.4 G.

Synthesis of compound 4-Rad: Compound **4-H** (40.3 mg, 0.0282 mmol) was dissolved in dry THF (5 mL). 56 % aqueous tetrabutyl ammonium hydroxide (16 μL, 0.0339 mmol) was added and the solution was stirred at room temperature. The formation of the perchlorotriphenylmethyl anion was monitored by UV/vis spectroscopy. When the deprotonation is complete (about 20 min) *p*-chloranil (9.4 mg, 0.0382 mmol) was added and the oxidation to the radical was followed by UV/vis spectroscopy. When the oxidation was complete (about 180 min) the mixture was evaporated under vacuum and the crude was purified by column chromatography (silica gel, chloroform). Compound **4-Rad** was obtained as a dark brown powder (39.5 mg, 98% yield).

ATR-IR: ν (cm^{-1}) = 3139 (w) (ArC-H), 3085 (w) (ArC-H), 2924 (w), 2852 (w), 1625 (w) (C=C), 1497 (w) (ArC-ArC), 1325 (m) (Cl-ArC-ArC-Cl), 1294 (w) (Cl-ArC-ArC-Cl), 1258 (w) (Cl-ArC-ArC-Cl), 1224 (w) (Cl-ArC-ArC-Cl), 1177 (w), 1105 (w), 1040 (m) (C-N), 1000 (m), 817 (s) (C-Cl), **LDI-ToF** (negative mode): m/z calcd for $C_{61}H_{36}Cl_{13}Fe_2N_6$, 1424.76; found, 1424.07 $[M]^-$; **UV/Vis** (CH_2Cl_2): λ (nm) (ε) 316.22 (44431), 379.58 (24347), 448.88 (20665), 605.96 (2277); **CV** (0.1 M $TBAPF_6$ in CH_2Cl_2, vs Ag/AgCl KCl 3M): $E_{1/2}$(radical/anion) = -0.21V, $E_{1/2}(Fc^+/Fc)$ = 0.60; **EPR**: g = 2.0026, $a(^1H)$ = 1.9 G, ΔH_{pp} = 1.1 G, $a(^{13}CAr)$ = 12.6, 14.3 G, $a(^{13}C\alpha)$ = 29.4 G

4-General Procedures.

4.1- Templated stripped gold (Au^{TS}) substrates preparation.

Ultra-smooth template-striped gold substrates were prepared following a reported procedure[5] by thermal deposition of 200 nm of gold (99.999% purity) on a silicon (100) wafer with a native SiO_2 surface layer; the deposition parameters were 4 x 10^{-7} mTorr and rate 2A/s. After deposition, glass slides (1.5 cm^2) were glued onto the exposed gold using an epoxy resin (EpoTek, 353ND), the adhesive was cured at 80 °C for 12 hours in an oven. The glass/epoxy/metal substrate was cleaved from the Si wafer just before immersion into the desired solution, in order to minimize the contamination from air, and without any further cleaning procedure.

4.2-SAMs preparation.

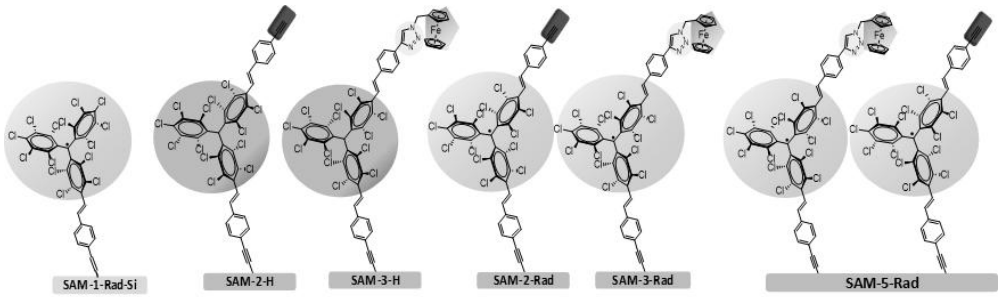

Scheme S5. SAMs prepared in this work.

4.2.1-Preparation of PTM radical-Modified Si(111) Surfaces (SAM-1-Rad-Si).

The chemicals used for cleaning and etching silicon wafer pieces (30% H_2O_2, 96-97% H_2SO_4 and 40% NH_4F solutions) were of VLSI semiconductor grade (Riedel-de-Haën). All Teflon vials used for cleaning of silicon were previously decontaminated in 3:1 v/v concentrated H_2SO_4/30% H_2O_2 at 100°C for 30 min, followed by copious rinsing with ultra-pure water.

***Caution**: The concentrated H_2SO_4:H_2O_2 (aq) piranha solution is very dangerous, particularly in contact with organic materials, and should be handled extremely carefully.*

All single side polished Si(111) samples (*p*-type, boron doped, 1-10 Ω cm, thickness = 525±25 μm, from Siltronix) were cut into 1.5 × ~4.0 cm^2 pieces from the same silicon wafer to ensure the maximum reproducibility of hydrogen-terminated and further molecular monolayer-modified surfaces. The sample was sonicated for 10 min successively in acetone (MOS semiconductor grade, Carlo Erba), ethanol (99.8%, VLSI semiconductor grade) and ultra-pure 18.2 MΩ cm water (Elga Purelab Classic UV, Veolia). It was then cleaned in 3:1 v/v concentrated H_2SO_4/30% H_2O_2 at 100°C for 30 min, followed by copious rinsing with ultra-pure water. The surface was etched with argon-degassed ppb grade 40% aqueous NH_4F for 20 min at room temperature[6]. The NH_4F solution was thoroughly degassed with argon for at least 30 min prior to the immersion of the piranha-treated surface. After etching, the Si-H sample was rinsed with argon-saturated water, blown dry with argon, and transferred immediately into a Pyrex Schlenk tube containing deoxygenated **1-Rad** dissolved in an aromatic solvent. An aluminum foil was put around the glassware to avoid the possible photochemical degradation of

the PTM radical. The hydrosilylation reaction was thermally activated and the alkyne solution was kept under a pressure of argon during the reaction.
The grafting conditions were optimized in order to produce the PTM radical-terminated monolayers with the highest PTM surface coverage and the lowest oxidation level of the underlying silicon surface. Toluene (99.8% from Sigma-Aldrich), mesitylene (99% extra-pure from Acros, passed through an activated neutral alumina column, then distilled over sodium) and 1,2-dichlorobenzene (DCB, 98% extra dry, from Acros) were tested as solvents since it has been demonstrated that the use of aromatic solvents with high boiling point was an efficient method for producing high-quality and well-ordered organic monolayers on silicon[7]. Moreover, different temperatures and concentrations of **1-Rad** were also tested. (Table S1). The optimal reaction conditions yielding the highest surface coverage of the PTM radical were as follows: 145°C for 20 h using DCB as the solvent and a **1-Rad** concentration higher than 7 mM. After reaction, the **SAM-1-Rad-Si** surface was thoroughly rinsed with toluene and dichloromethane, then dried under argon.

Table S1. Different experimental conditions used for the optimization of the thermal grafting of **1-Rad** on Si-H. The optimal conditions are highlighted in green.

Entry	**1-Rad** concentration / mM	Solvent	Temperature /°C	Time / h	Surface coverage of PTM radical / mol cm^{-2} [a]
1	2	Toluene	90	20	5×10^{-12}
2	2	Mesitylene	155	3	No grafting[b]
3	2.3	Mesitylene	115	20	No grafting[b]
4	2.3	DCB	130	20	7×10^{-12}
5	7	DCB	145	20	8.5×10^{-11}

[a] Determined electrochemically from the integration of the anodic voltammetric peak observed for illuminated **SAM-1-Rad-Si**.[b] Under these conditions, the radical is not stable and the solution changed colour over time.

4.2.2-Preparation of PTM Radical-Modified Gold Surfaces.

To form the SAMs, the freshly cleaved Au^{TS} substrates were introduced into a flat bottom flask containing a toluene (freshly distilled) solution containing 0.5 mM

of the desired compound and the flask was closed, filled with argon and sealed. The solution was heated for 6 hours at 40ºC and left 42 h at room temperature in dark. Then, the substrates were removed from the flask, thoroughly rinsed with toluene, dried with nitrogen stream. Compounds **2-H**, **3-H**, **2-Rad** and **3-Rad** were used to form **SAM-2-H**, **SAM-3-H**, **SAM-2-Rad** and **SAM-3-Rad**, respectively.

4.3-Click reaction on gold surface.

Two different methods were tested:

Methods 1 and 2:

To obtain the catalyst solution, two separated solutions were prepared: **solution 1** was prepared by 3 min sonication of CuI (10.1 mg) in 2 mL of dry acetonitrile and, **solution 2** consisted of $P(Ph)_3$ (16.4 mg) and 50 μL of *N*,*N*-diisopropylethylamine (10.61 M) in 2 mL of dry toluene.

In a flat bottom flask, **solution 1** (200 μL) and **solution 2** (200 μL) were added to a 2 mM solution of the azidomethylferrocene in 5 mL of dry toluene (**Method 1**) or 5 mL of dry acetonitrile (**Method 2**) and then **SAM-2-Rad** was introduced and the flask sealed. The flask was heated for 8 hours at 60ºC under argon atmosphere and dark and then left for 1 hour to cool down to room temperature. After removing the substrates from the flask, they were thoroughly rinsed with a solution of 0.5 M of EDTA and 0.2M of NH_3, acetonitrile, toluene, acetone and dichloromethane and finally dried under nitrogen stream.

The yield of the reaction was estimated from the cyclic voltammetry experiments (see Figures S4-S8) leading to an approximate yield of 30% and 50% for **Methods 1** and **2**, respectively.

4.4-Surface Coverage Calculation.

The surface coverage was calculated from the Equation S1[8,9]:

$$\Gamma = \frac{A_{peak}}{nFSv} \qquad \text{Equation S1}$$

where Γ is the surface coverage in mol cm^{-2}, A_{peak} is the integrated area of the anodic or cathodic voltammetry peak, n is the number of electrons transferred (in this case n = 1), F is Faraday's constant, S is the electrode surface area and v is the scan rate.

4.5-Charge transport measurements through the SAMs on gold.

The modified Au^{TS} substrates were top-contacted with the GaOx/EGaIn tips. These tips were prepared following the F.C. Simeone[10] procedure. After the formation of the tip, this was gently approached to a clean silicon surface (50 nm SiO_2 polished) that helped to flatten the irregularities and roughness generated during the tip preparation.

The GaOx/EGaIn tip area used to contact the samples surfaces was around 1000-2500 μm^2 as it is recommended to obtain stable measurements [11].The top-electrode was biased and the bottom electrode was grounded. The top electrode was biased from 0V →1 V→ 0V → -1 V→ 0V. For each sample, 12 traces on 24 junctions were collected, with a step size of 50 mV, integration time of 100 ms, and a delay of 50 ms, for acquiring the $J(V)$ curves. The tip was renewed every three junctions. Below, a schematic setup of the home made system for current vs. voltage measurements is shown.

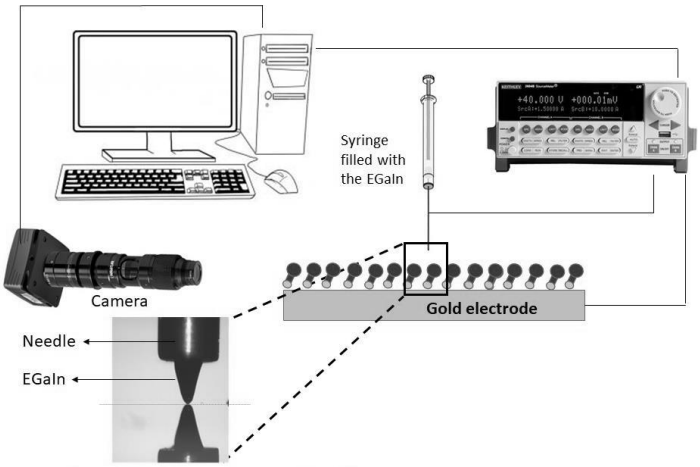

Real picture of the EGaIn cone contacting the monolayer on Au. The reflection of the cone can be seen.

4.6 Statistical Analysis of the measured IV curves.

For the statistical analysis of the I-V curves, we have employed the free R software. For doing so, we have taken into account that the trimmed mean values and standard deviations are robust estimators of central tendency. To compute a trimmed mean, a predetermined amount of observations is removed on each side of a distribution (remove outliers), and the remaining observations are averaged. Trimmed mean values provide a better estimation of the location of the bulk of the observations than a bare mean function when sampling from slightly asymmetric distributions. On the other hand, the bare standard deviation is dramatically affected by outliers and slightly asymmetries. More reliable results are obtained using the trimmed standard deviation. The trim argument can vary between 0 and 0.5. In this work, we have removed 10% of the total data, for which trim argument must be equal to 0.1. In this case, 5% of the upper part and 5% in the lower part is omitted.

To construct the histograms shown in Figure 6, we have considered two formulas to determine the number of bins in the histogram. We considered the Sturge's rule and the square root of the number of data ($\sqrt{N}$).

Sturge's rule is recommended when data is not skewed (as expected for Gaussian distribution). It should provide a good choice of bins in a histogram. In our data treatment, we follow roughly the Sturge's rule although for N $\leq$ 100 there is no big differences in the number of bins compared to ($\sqrt{N}$). Importantly, the histograms are normalized to their area in order to analyze the data correctly. For instance, the function of density line is applied only when the data is normalized. Density line can be used as an assessment of your best histogram.

ANNEX I: SAMs characterization: Cyclic–square wave voltammetry, Electrochemical impedance spectroscopy, EPR, XPS, NEXAFS and charge transport using the EGaIn technique.

I.1 SAM on silicon surface characterization.

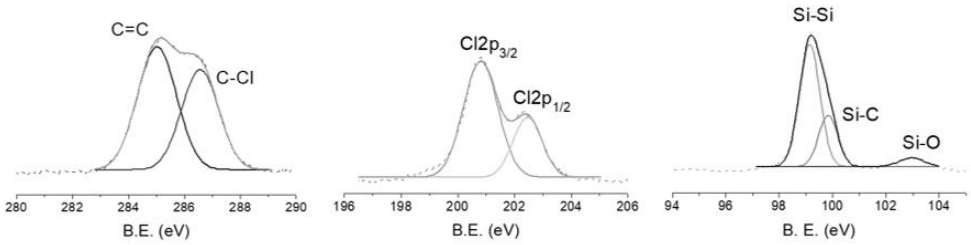

Figure S1: High-resolution XPS spectra deconvoluted peaks of **SAM-1-Rad-Si**: C 1s, Cl 2p and Si2p (from the left to the right).

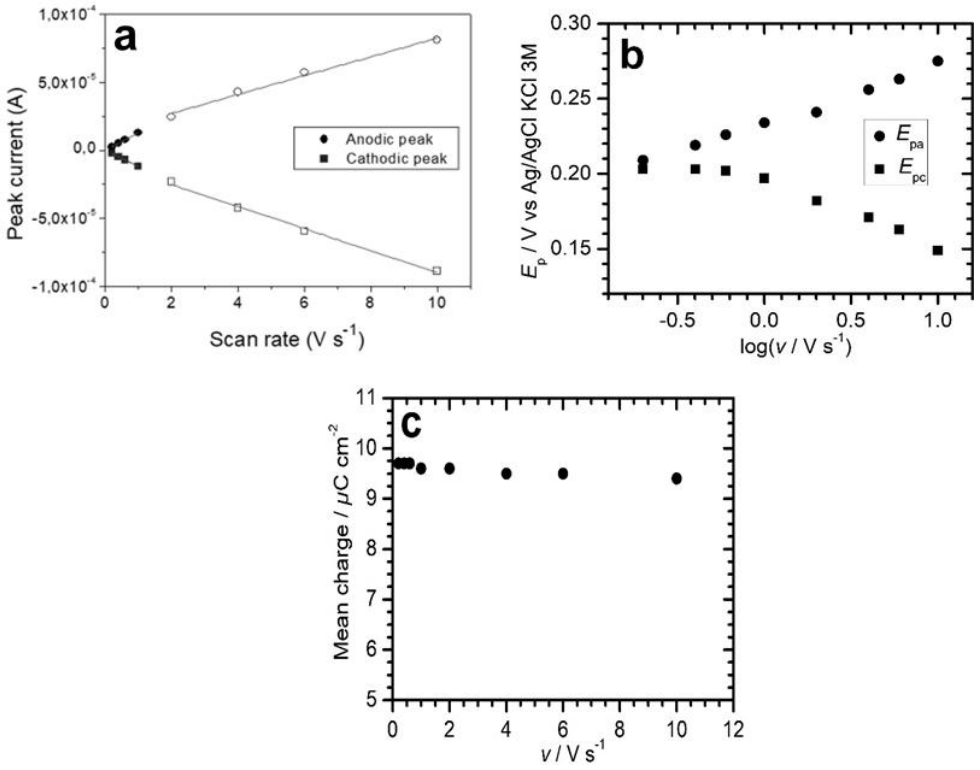

Figure S2: a) Anodic and cathodic peak photocurrent intensities plotted vs potential scan rate v under red-light illumination for **SAM-1-Rad-Si**, showing good linear relationships in the lower and higher scan rate ranges. b) Corresponding plots of the anodic E_{pa} and cathodic E_{pc} peak potentials as a function of log$v$. c) Mean charge (average of the anodic and cathodic charges calculated from the respective areas under the cyclic voltammetry peaks) vs v plot.

Mott-Schottky relationship (Equation S2):

$$\frac{1}{C_{sc}^2} = \frac{2}{eN_D A^2 \varepsilon_0 \varepsilon_r}\left(E - E_{fb} - \frac{kT}{e}\right) \qquad \text{Equation S2}$$

where:

- C_{SC} is the space charge capacitance;
- N_D is the the dopant density;
- E_{fb} is the flatband potential
- e is the electron charge (1.602×10^{-19} C);
- ε_r is the relative permittivity of Si (11.7);
- ε_0 is the vacuum permittivity (8.85×10^{-12} F m^{-1});
- A is the electrode surface area;
- E is the applied potential;
- k is the Boltzmann constant (1.38×10^{-23} m^2·kg·s^{-2}·K^{-1});
- T is temperature

N_D can be determined from the slope (b) of the linear part of the C_{SC}^{-2}-E plot (Figure S3) and E_{fb} is given by

$$E_{fb} = -\frac{a}{b} - \frac{kT}{e}$$

where a is the intercept of the linear part.

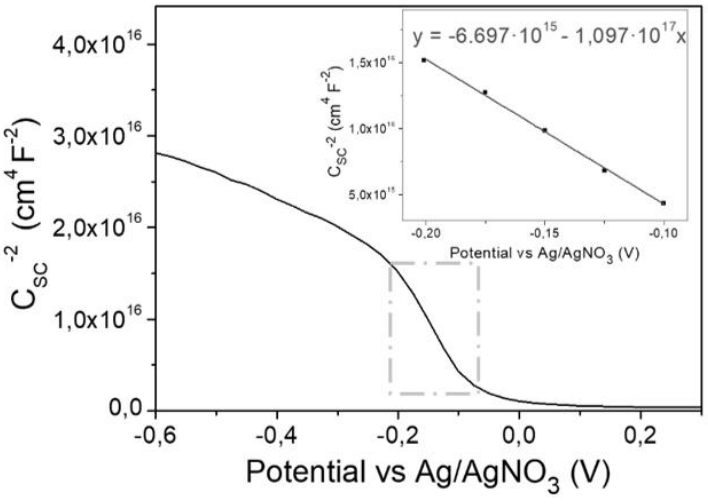

Figure S3: Mott-Schottky plot from impedance measurements at 50 kHz. The inset shows the linear fitting of the region indicated by the yellow rectangle.

I.2 SAM on gold surface characterization.

Figures S4 and S5 correspond to the on-surface modification of **SAM-2-Rad** using toluene as solvent. Figures S6 and S7 were obtained from the modification performed in acetonitrile. See above (page S14) for further details. Figure S8 corresponds to **SAM-3-Rad** and is used to extract a comparative Fc/PTM ratio.

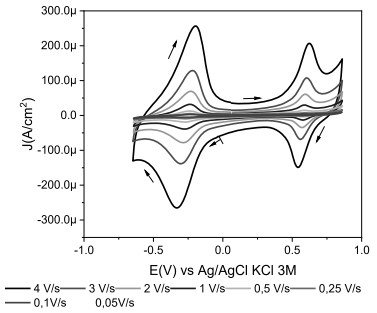

Figure S4: Cyclic voltammetry behaviour of **SAM-5-Rad**- using as electrolytic medium solution 0.1M $TBAPF_6$/ CH_2Cl_2, under argon atmosphere.

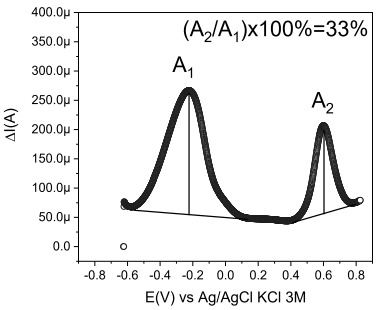

Figure S5: Square wave voltammetry behaviour of **SAM-5-Rad** using as electrolytic medium solution 0.1M $TBAPF_6$/ CH_2Cl_2, under argon atmosphere. Step=1mV, $E_{modulation}$=20mV and Frequency=100Hz

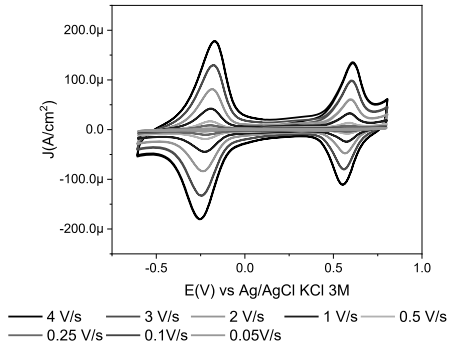

Figure S6: Cyclic voltammetry behaviour of **SAM-5-Rad** using as electrolytic medium solution 0.2M $TBAPF_6$/ CH_2Cl_2, under argon atmosphere.

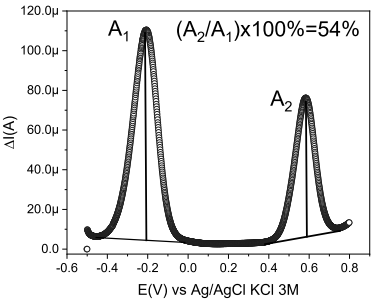

Figure S7: Square wave voltammetry behaviour of **SAM-5-Rad** using as electrolytic medium solution 0.2M $TBAPF_6$/ CH_2Cl_2, under argon atmosphere. Step=1mV, $E_{modulation}$=20mV and Frequency=40Hz

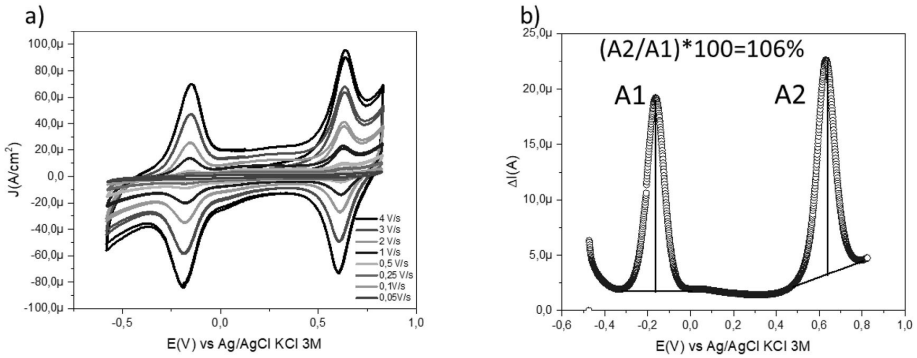

Figure S8: a) Cyclic voltammetry behaviour of **SAM-3-Rad** using as electrolytic medium solution 0.2M $TBAPF_6$/ CH_2Cl_2, under argon atmosphere, b) Square wave voltammetry behaviour of **SAM-3-Rad** using as electrolytic medium solution 0.2M $TBAPF_6$/ CH_2Cl_2, under argon atmosphere. Step=1mV, $E_{modulation}$=20mV and Frequency=40Hz

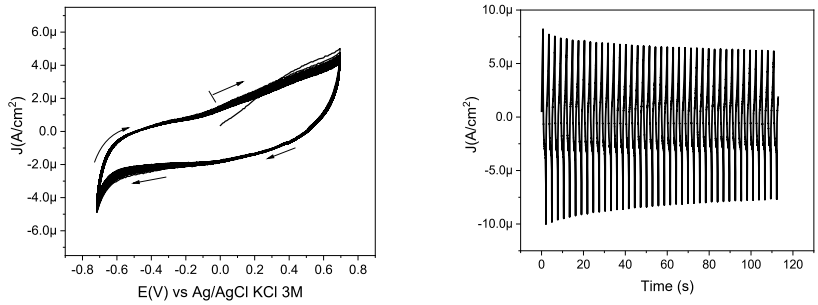

Figure S9: *Left:* Cyclic voltammetry (40 scans) of the blank Au ^{TS} (without the SAM) using as electrolytic medium solution 0.2M $TBAPF_6$/ CH_2Cl_2, under argon atmosphere and as scan rate 1V/s. *Right:* Current intensity stability over time.

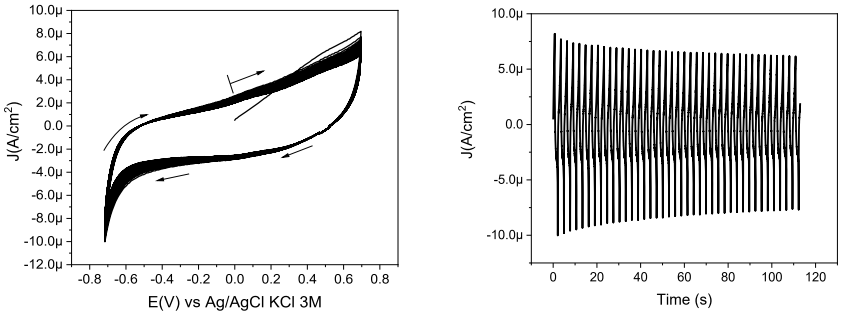

Figure S10: *Left:* Cyclic voltammetry (40 scans) of **SAM-2-H** using as electrolytic medium solution 0.2M $TBAPF_6$/ CH_2Cl_2, under argon atmosphere and as scan rate 1V/s. *Right:* Current density stability over time.

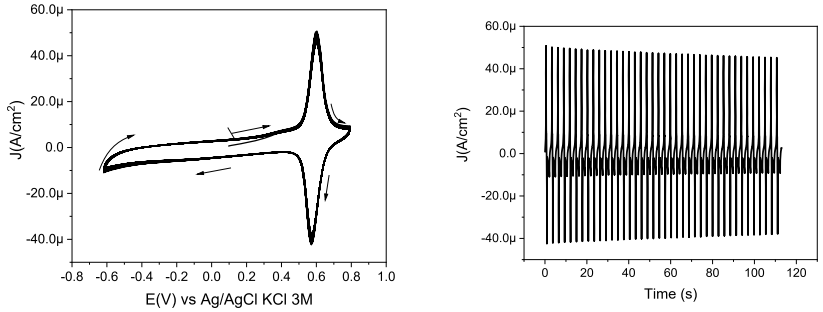

Figure S11 *Left:* Cyclic voltammetry (40 scans) of **SAM-3-H** using as electrolytic medium solution 0.2M $TBAPF_6$/ CH_2Cl_2, under argon atmosphere and as scan rate 1V/s. *Right:* Current density stability over time.

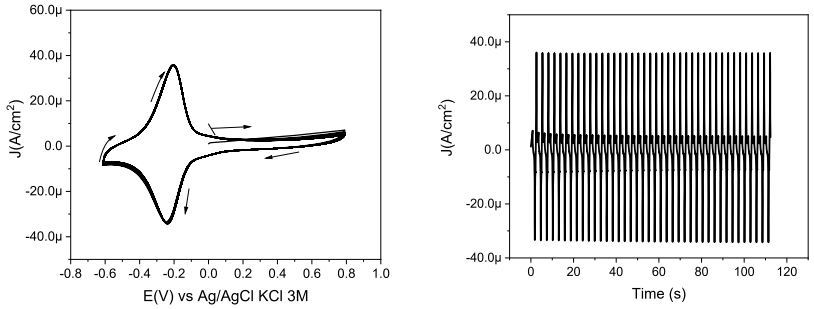

Figure S12: *Left:* Cyclic voltammetry (40 scans) of **SAM-2-Rad** using as electrolytic medium solution 0.2M $TBAPF_6$/ CH_2Cl_2, under argon atmosphere and as scan rate 1V/s. *Right:* Current density stability over time.

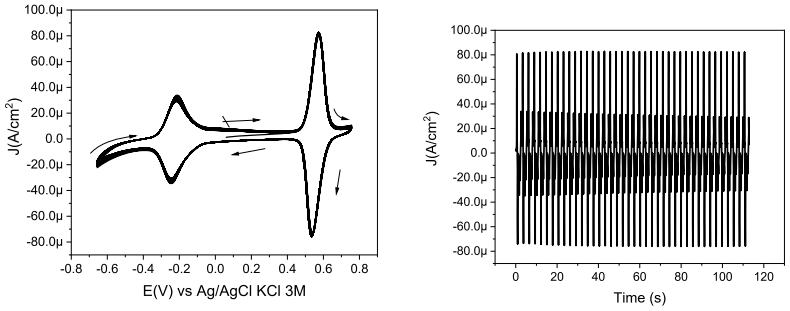

Figure S13: *Left:* Cyclic voltammetry behaviour (40 scans) of **SAM-3-Rad** using as electrolytic medium solution 0.2M $TBAPF_6$/ CH_2Cl_2, under argon atmosphere and as scan rate 1V/s. *Right:* Current density stability over time.

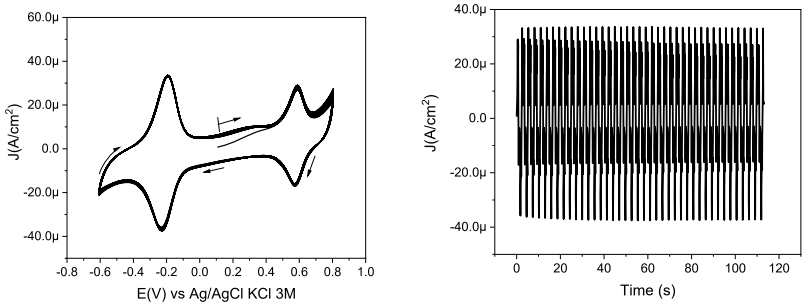

Figure S14: *Left:* Cyclic voltammetry (40 scans) of **SAM-5-Rad** using as electrolytic medium solution 0.2M $TBAPF_6/CH_2Cl_2$, under argon atmosphere and as scan rate 1V/s. *Right:* Current density stability over time.

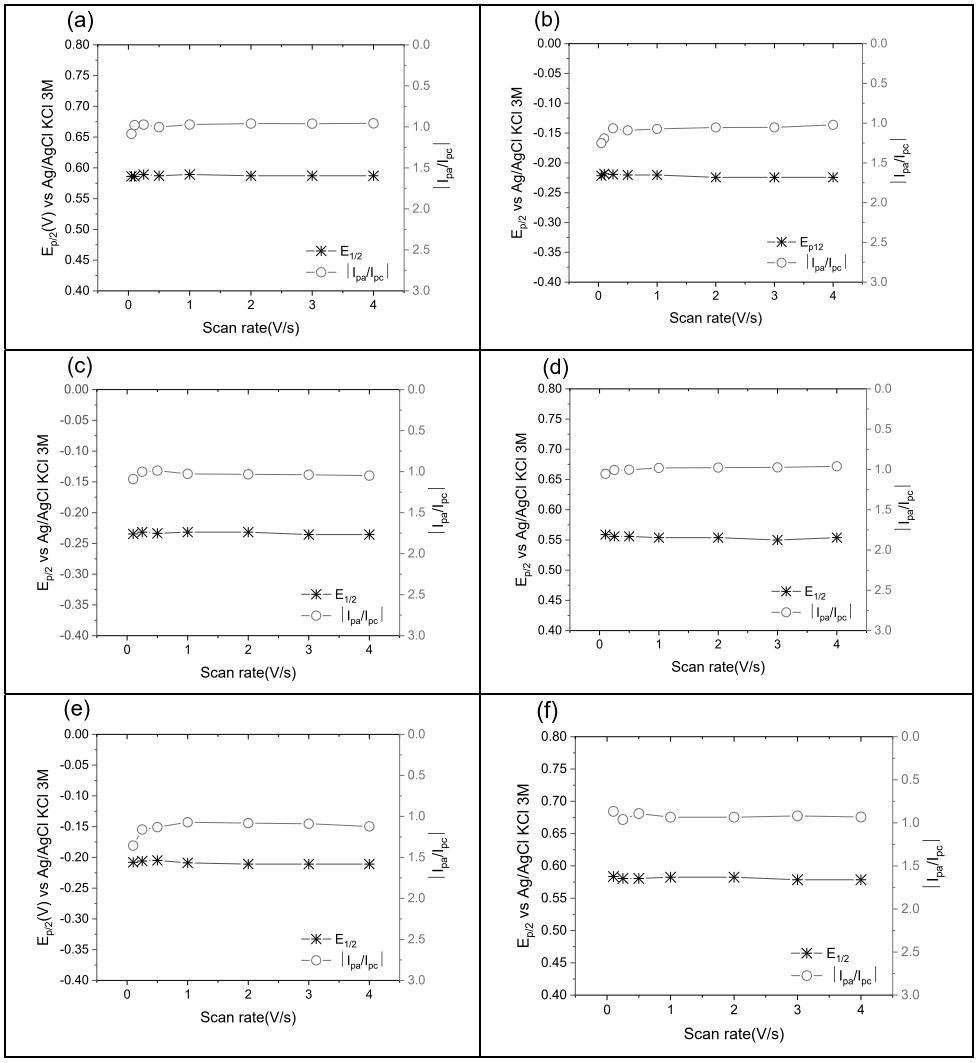

Figure S15: Plots of $E_{1/2}$ and $|I_{pa}/I_{pc}|$ versus scan rate for a) **SAM-3-H** d) **SAM-3-Rad** f) **SAM-5-Rad** (for the Fc peaks), and b) **SAM-2-Rad** c) **SAM-3-Rad** e) **SAM-5-Rad** (for the PTMs radical peaks).

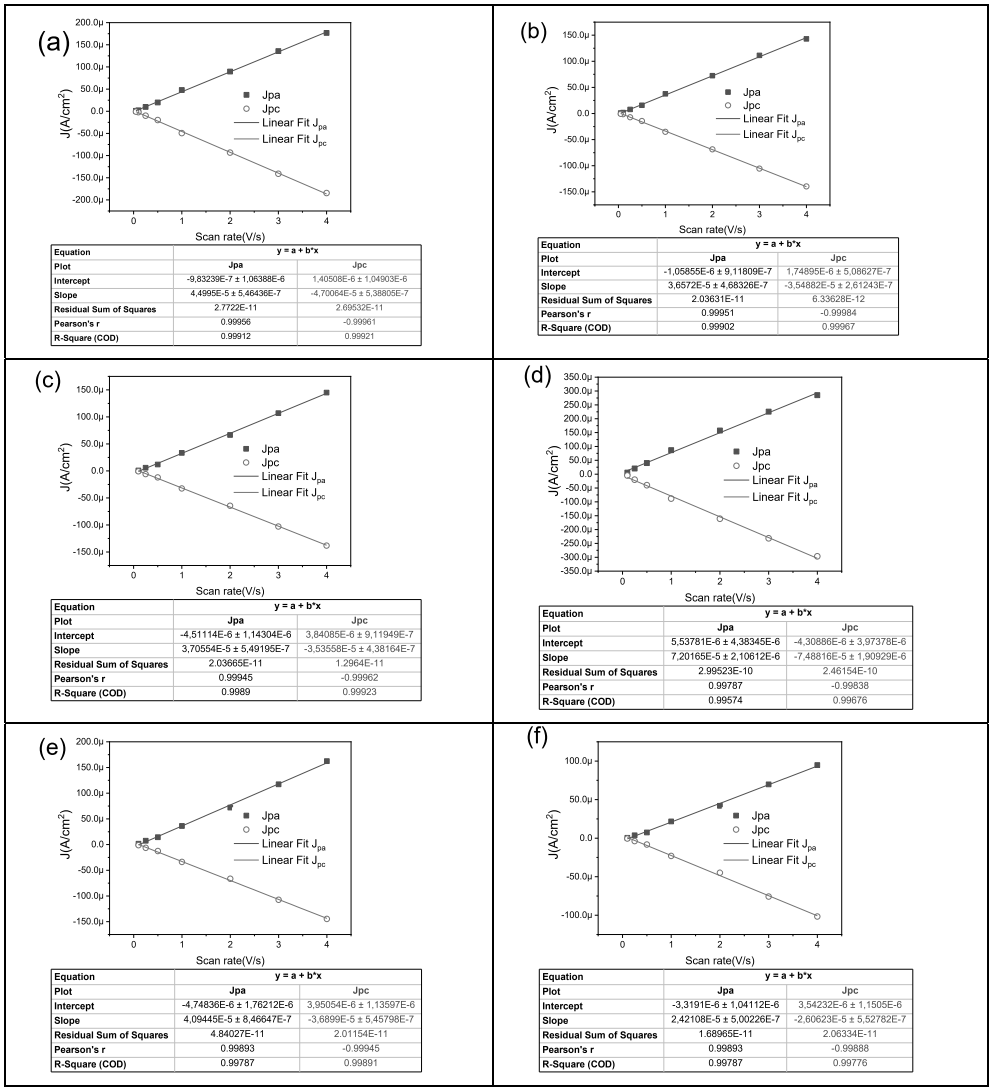

Equation	y = a + b*x	
Plot	Jpa	Jpc
Intercept	-9,83239E-7 ± 1,06388E-6	1,40508E-6 ± 1,04903E-6
Slope	4,4995E-5 ± 5,46436E-7	-4,70064E-5 ± 5,38805E-7
Residual Sum of Squares	2.7722E-11	2.69532E-11
Pearson's r	0.99956	-0.99961
R-Square (COD)	0.99912	0.99921

Equation	y = a + b*x	
Plot	Jpa	Jpc
Intercept	-1,05855E-6 ± 9,11809E-7	1,74895E-6 ± 5,08627E-7
Slope	3,6572E-5 ± 4,68326E-7	-3,54882E-5 ± 2,61243E-7
Residual Sum of Squares	2.03631E-11	6.33628E-12
Pearson's r	0.99951	-0.99984
R-Square (COD)	0.99902	0.99967

Equation	y = a + b*x	
Plot	Jpa	Jpc
Intercept	-4,51114E-6 ± 1,14304E-6	3,84085E-6 ± 9,11949E-7
Slope	3,70554E-5 ± 5,49195E-7	-3,53558E-5 ± 4,38164E-7
Residual Sum of Squares	2.03665E-11	1.2964E-11
Pearson's r	0.99945	-0.99962
R-Square (COD)	0.9989	0.99923

Equation	y = a + b*x	
Plot	Jpa	Jpc
Intercept	5,53781E-6 ± 4,38345E-6	-4,30886E-6 ± 3,97378E-6
Slope	7,20165E-5 ± 2,10612E-6	-7,48816E-5 ± 1,90929E-6
Residual Sum of Squares	2.99523E-10	2.46154E-10
Pearson's r	0.99787	-0.99838
R-Square (COD)	0.99574	0.99676

Equation	y = a + b*x	
Plot	Jpa	Jpc
Intercept	-4,74836E-6 ± 1,76212E-6	3,95054E-6 ± 1,13597E-6
Slope	4,09445E-5 ± 8,46647E-7	-3,6899E-5 ± 5,45798E-7
Residual Sum of Squares	4.84027E-11	2.01154E-11
Pearson's r	0.99893	-0.99945
R-Square (COD)	0.99787	0.99891

Equation	y = a + b*x	
Plot	Jpa	Jpc
Intercept	-3,3191E-6 ± 1,04112E-6	3,54232E-6 ± 1,1505E-6
Slope	2,42108E-5 ± 5,00226E-7	-2,60623E-5 ± 5,52782E-7
Residual Sum of Squares	1.68965E-11	2.06334E-11
Pearson's r	0.99893	-0.99888
R-Square (COD)	0.99787	0.99776

Figure S16: Plots of anodic and cathodic current densities versus scan rate. a) **SAM-3-H** d) **SAM-3-Rad** f) **SAM-5-Rad** (for the Fc peaks), and b) **SAM-2-Rad** c) **SAM-3-Rad** e) **SAM-5-Rad** (for the PTMs radical peaks).

Table S2. Surface coverage of SAMs calculated with Equation 1 for the different SAMs studied here.

Sample	*Γ (mol cm^{-2}) PTM Radical*	*Γ (mol cm^{-2}) Ferrocene*
SAM-3-H	--	5.8×10^{-11}
SAM-2-Rad	8.9×10^{-11}	--
SAM-3-Rad	7.9×10^{-11}	1.0×10^{-10}
SAM-5-Rad	8.6×10^{-11}	4.0×10^{-11}

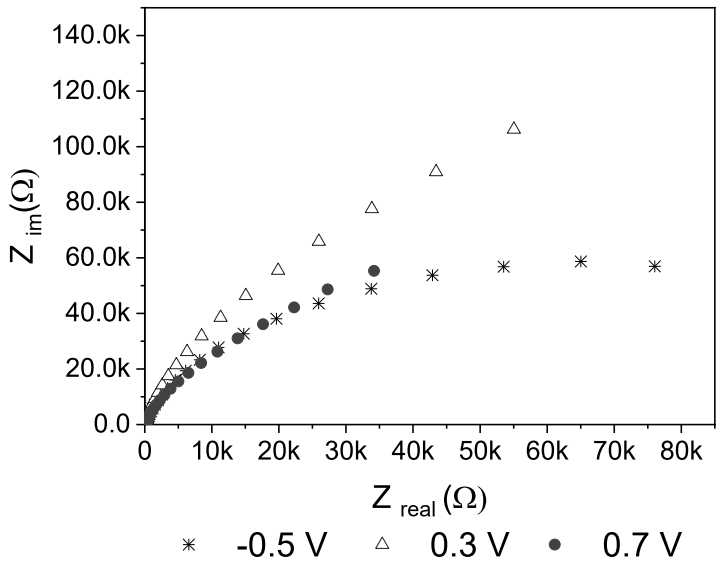

Figure S17: Impedance Nyquist plots for three applied potentials of the **SAM-3-Rad** using 0.1M $TBAPF_6/CH_2Cl_2$ as the electrolytic medium under argon atmosphere and a scan frequency from 100 kHz to 0.1 Hz with 20 mV amplitude.

XPS and NEXAFS Characterization of the SAMs

Stoichiometric and experimental elemental ratios for SAM-3-Rad. The values were obtained as discussed in reference[12].

Table S3. Stoichiometric and experimental elemental ratios for **SAM-3-Rad**.

	C	**N**	**Cl**	**Fe**
Sensitivity factor*	0.25	0.42	0.73	3
Number of atoms	50	3	13	1
Theoretical values (%)	75	4	19	2
SAM-3-Rad (%)	84.3	5.2	10.0	0.5

Stoichiometric and experimental elemental ratios for SAM-2-Rad.

Table S4. Stoichiometric and experimental elemental ratios for **SAM-2-Rad**.

	C	**Cl**
Sensitivity factor*	0.25	0.73
Number of atoms	39	13
Theoretical values (%)	75	25
SAM-2-Rad (%)	95	5

Stoichiometric and experimental elemental ratios for SAM-5-Rad.

Table S5. Stoichiometric and experimental elemental ratios for **SAM-5-Rad**.

	C	**N**	**Cl**	**Fe**
Sensitivity factor*	0.25	0.42	0.73	3
Number of atoms	50	3	13	1
Theoretical values (%)	75	4	19	2
SAM-5-Rad (%)	83.9	5.8	10.1	0.2

* C. D. Wagner, *J. Electron Spectrosc. Relat. Phenom.* **1983**, *32*, 99-102.

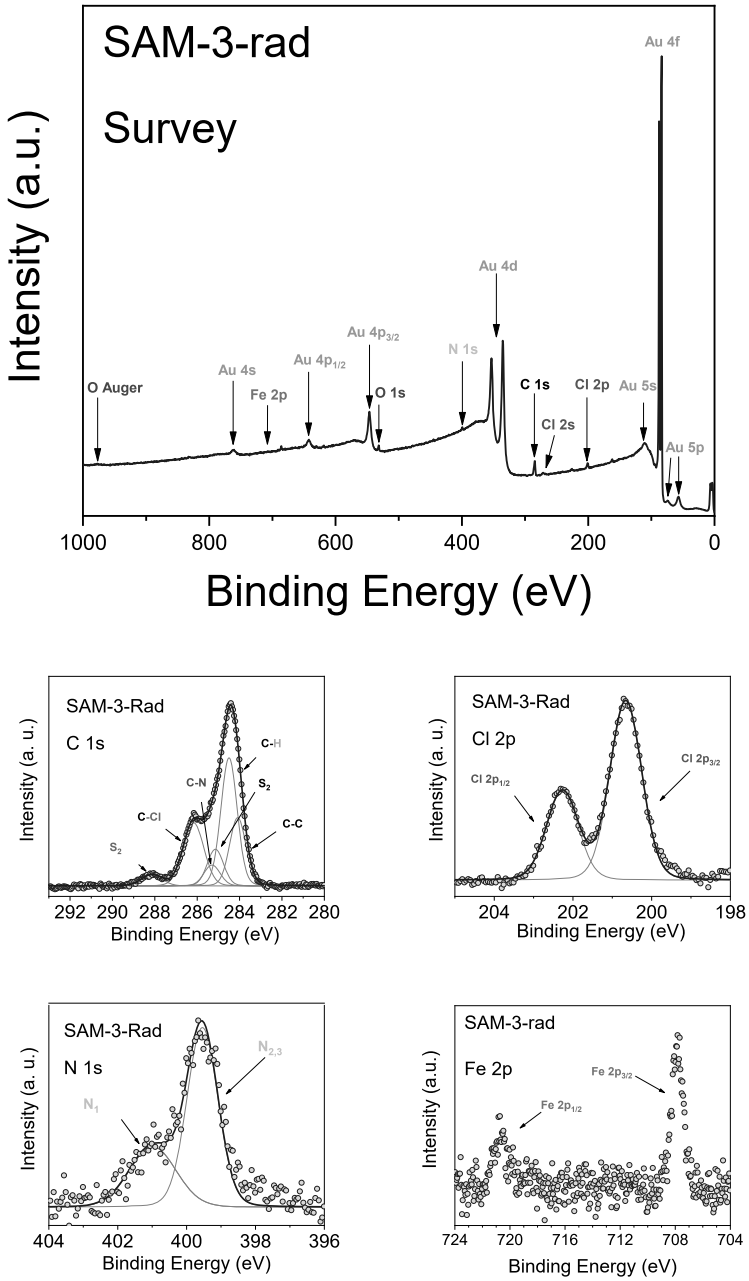

Figure S18: (upper panel) Survey and (lower panels) C 1s, Cl 2p, N 1s (together with their best fit) and Fe 2p XPS spectra of **SAM-3-Rad** (photon energy = 1486.6 eV).

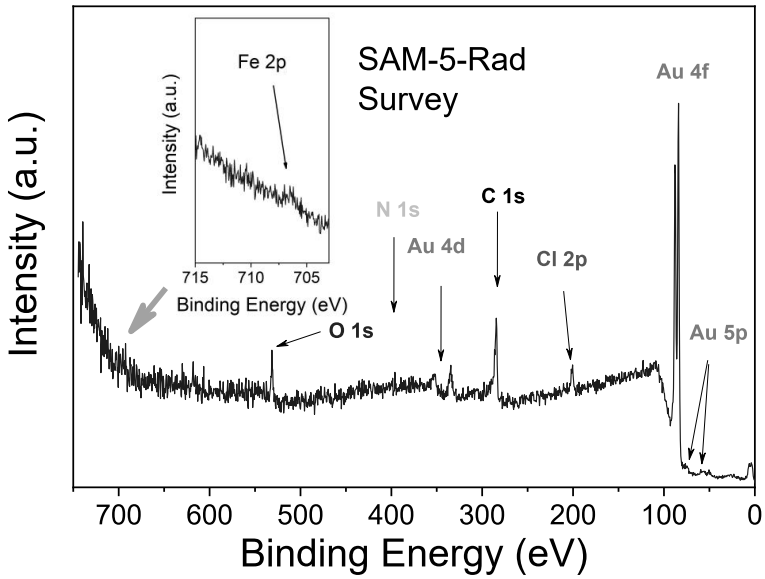

Figure S19: XPS survey spectrum of **SAM-5-Rad** together with the detailed Fe 2p core level spectrum (photon energy = 800 eV)

We used Voigt profiles, with fixed constant Lorentzian width. The Voigt profile considers both the finite core-hole lifetime (Lorentzian profile) and the broadening due to the finite experimental resolution and various inhomogeneities, e.g., molecular packing and local morphology[13,14] (Gaussian profile). To calculate the stoichiometry of the films, we also considered the intensity of the satellites[14,15], typical features in photoemission that appear as an effect of the relaxation processes due to the creation of a core-hole[16]. The fit that we use is based on the procedure adopted for closed-shell molecules[14]. The final fit is the result of several self-consistent interactions of sequential fits done considering all physical and chemical information and adding more constraints at each interaction, with the goal to keep the parameter dependency very low.

As we were more interested in the stoichiometry than in physical phenomena related to photoemission, we kept the number of satellites as low as possible to have a very simplified fit. However, satellite intensities cannot be neglected, especially in case of radicals because the simultaneous presence of a core-hole and a singly occupied molecular orbital on the time-scale of photoemission enhances the relaxation phenomena.[17,18]

The fit procedure systematically holds for all samples of a specific molecule, prepared and measured under the same conditions. In this way, we can also identify the samples that do not correspond to the expected stoichiometry. We work on sets of measured samples that are big enough to be statistically significant. We obtain an excellent agreement between the theoretical and the fit values that indicates that **SAM-3-Rad** is close to the theoretical stoichiometry, while this is not the case for **SAM-5-Rad**, as discussed in the paper.

Table S6. Fit results for the energy positions and relative intensities of the photoemission lines in the C 1s spectra.

	Energy (eV)	**Lorentzian Width (eV)**	**Gaussian Width (eV)**	**Intensity (%)**	**Theoretical values (%)**
C-C	284.1	0.08	0.86	19.6	22
C-H	284.5	0.08	0.86	36.9	46
S_1	285.1	0.08	0.86	10.6	
C-N	285.3	0.08	0.87	6.0	6
C-Cl	286.2	0.08	1.10	22.9	26
S_2	288.1	0.08	1.10	4.0	

I(C-C+ C-H + S_1) = 67.1 %

I(C-Cl+S_2) = 26.9 %

Table S7. Fit results for the energy positions and relative intensities of the photoemission lines in the Cl 2p spectra.

	Energy (eV)	**Lorentzian Width* (eV)**	**Gaussian Width (eV)**	**Intensity (%)**
Cl $2p_{3/2}$	200.7	0.1	0.9	66.3
Cl $2p_{3/2}$	202.3	0.1	0.9	33.7

*O. Travnikova et. al. *Chem. Phys. Lett.* **2006**, *426*, 452-458.

Table S8. Fit results for the energy positions and relative intensities of the photoemission lines in the N 1s spectra.

	Energy (eV)	Lorentzian Width (eV)	Gaussian Width (eV)	Intensity (%)
$N_{2,3}$	399.5	0.1	1,01	66.4
N_1	401.0	0.1	1.54	33.6

ANEX II: H^1-NMR, C^{13}-NMR, FT-IR, UV-Vis, LDI-TOF, EPR spectra and cyclic –square wave voltammetry of the synthesized molecules.

1) α-H-bisalkPTM-Fc_1 (3-H)

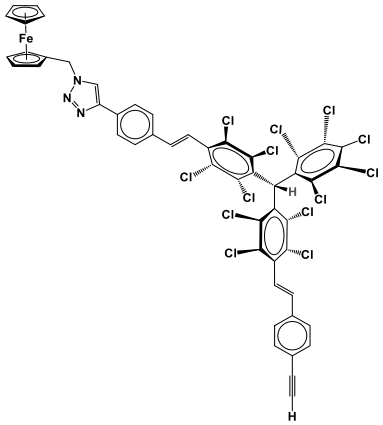

^{1}H-NMR, $CDCl_3$, 600 MHz

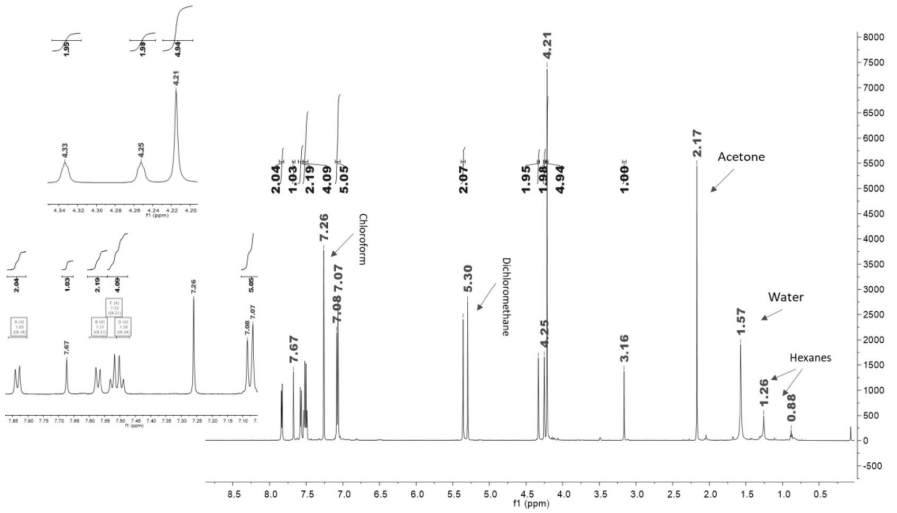

Figure S20: ^{1}H-NMR spectrum of **3-H** in $CDCl_3$.

^{13}C-NMR, $CDCl_3$, 101 MHz

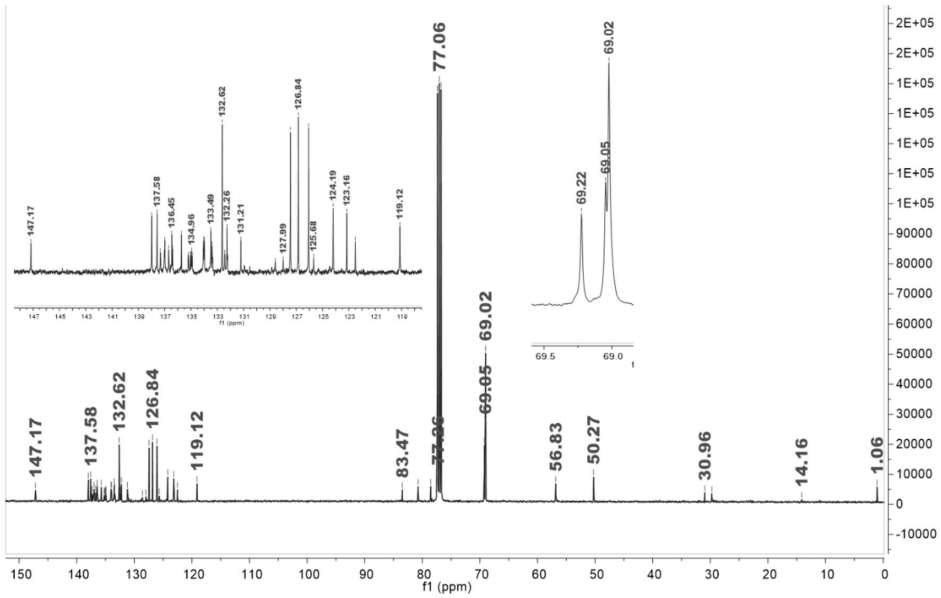

Figure S21: ^{13}C-NMR spectrum of **3-H** in $CDCl_3$

FT-IR

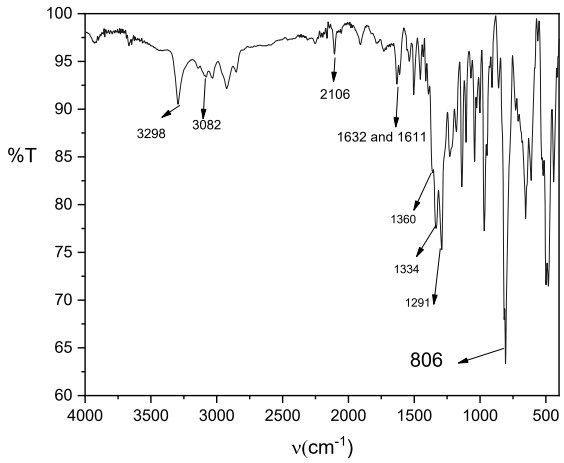

Figure S22: FT-IR spectrum of **3-H** in powder.

UV-Vis

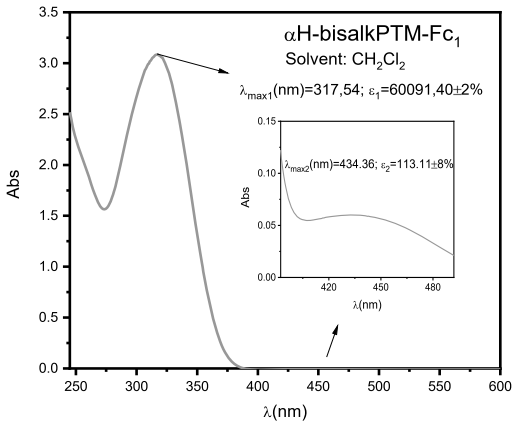

Figure S23: UV-Vis spectrum of **3-H** in CH_2Cl_2.

Cyclic voltammetry

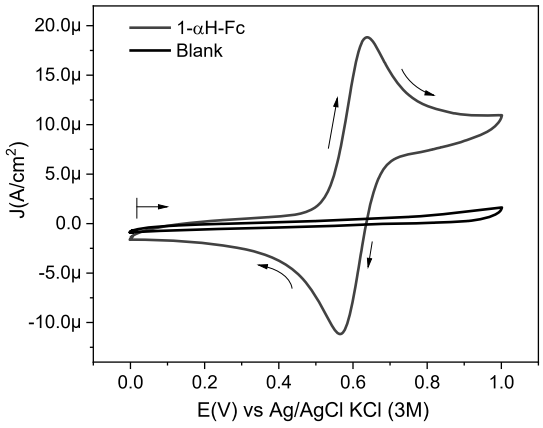

Figure S24: Cyclic Voltammetry of **3-H** at 0.5 mM over a glassy carbon electrode at 100mV/s, using as electrolytic medium a 0.1M solution of $TBAPF_6$ in CH_2Cl_2, under argon atmosphere.

MALDI-ToF

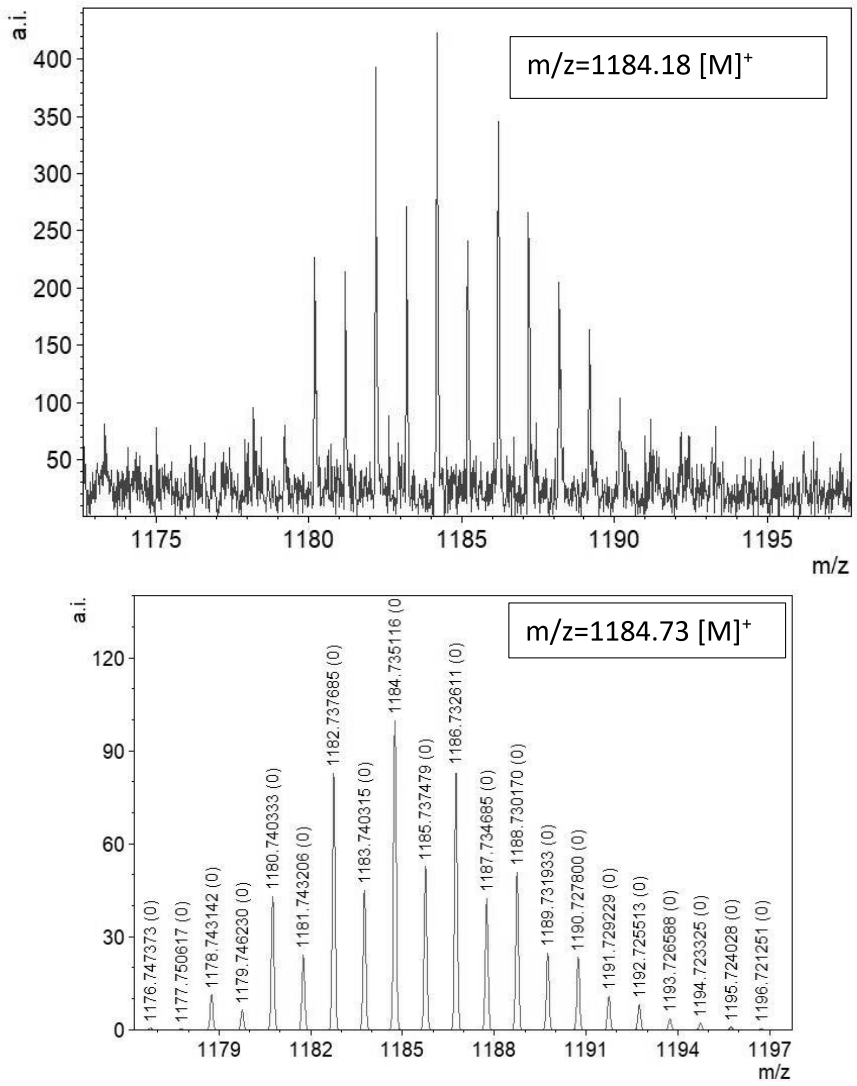

Figure S25: MALDI-ToF spectra of **3-H** experimental (top) and simulated (bottom)

α-H-bisalkPTM-Fc$_2$ (4-H)

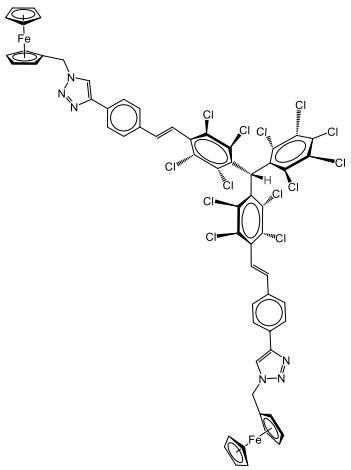

^{1}H-NMR, CDCl$_3$, 600 MHz

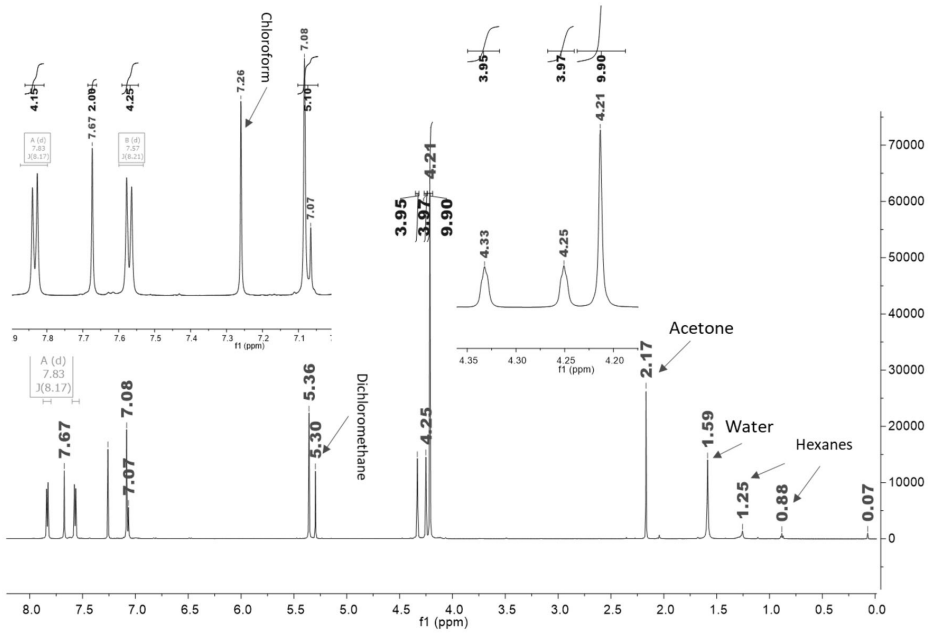

Figure S26: ^{1}H-NMR spectrum of **4-H** in CDCl$_3$.

^{13}C-NMR, $CDCl_3$, 101 MHz

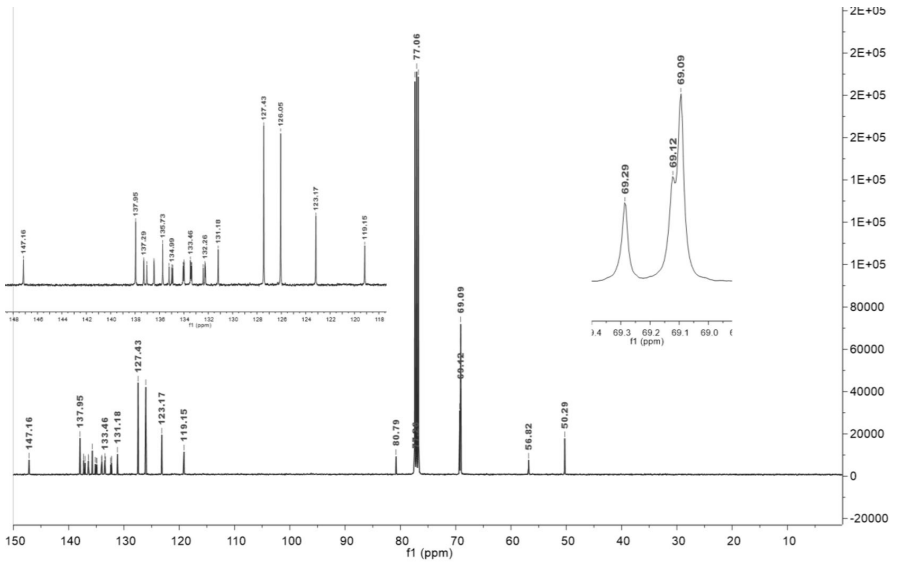

Figure S27: ^{13}C-NMR spectrum of **4-H** in $CDCl_3$.

FT-IR

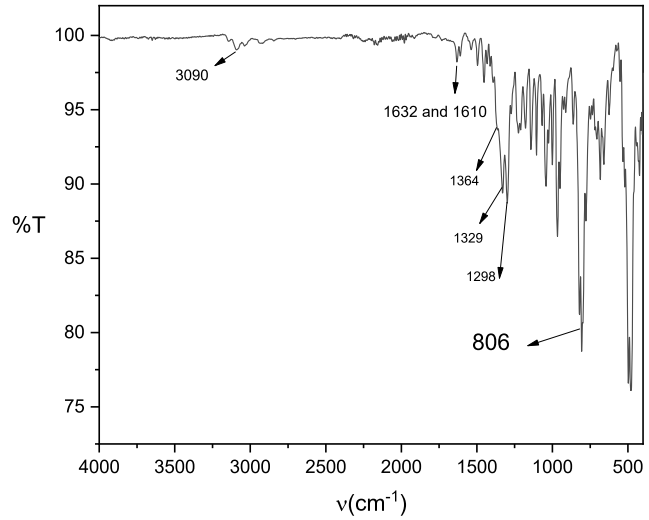

Figure S28: FT-IR spectrum of **4-H** in powder.

UV-Vis

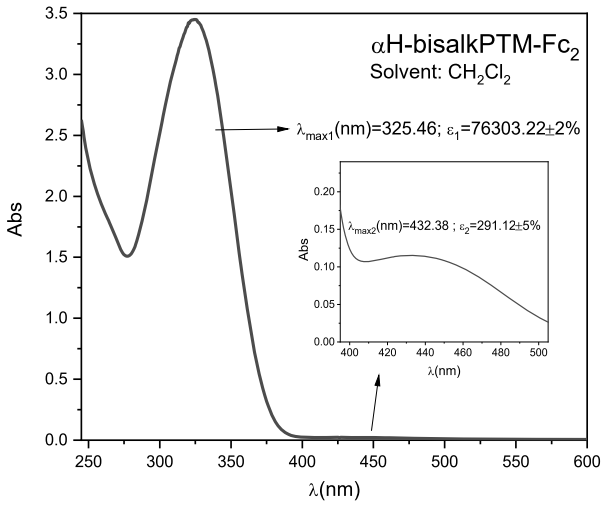

Figure S29: UV-Vis spectrum of **4-H** in CH_2Cl_2.

Cyclic voltammetry.

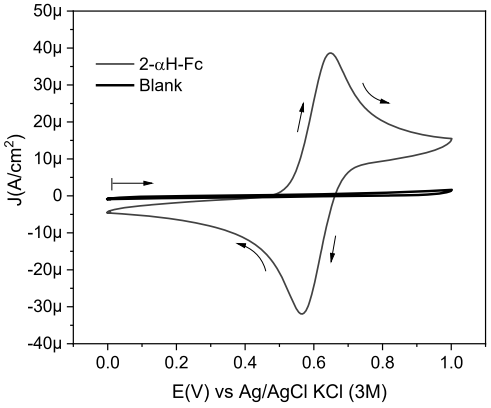

Figure S30: Cyclic Voltammetry of **4-H** at 0.46 mM over a glassy carbon electrode at 100mV/s, using as electrolytic medium a 0.1M solution of $TBAPF_6$ in CH_2Cl_2, under argon atmosphere.

MALDI-ToF

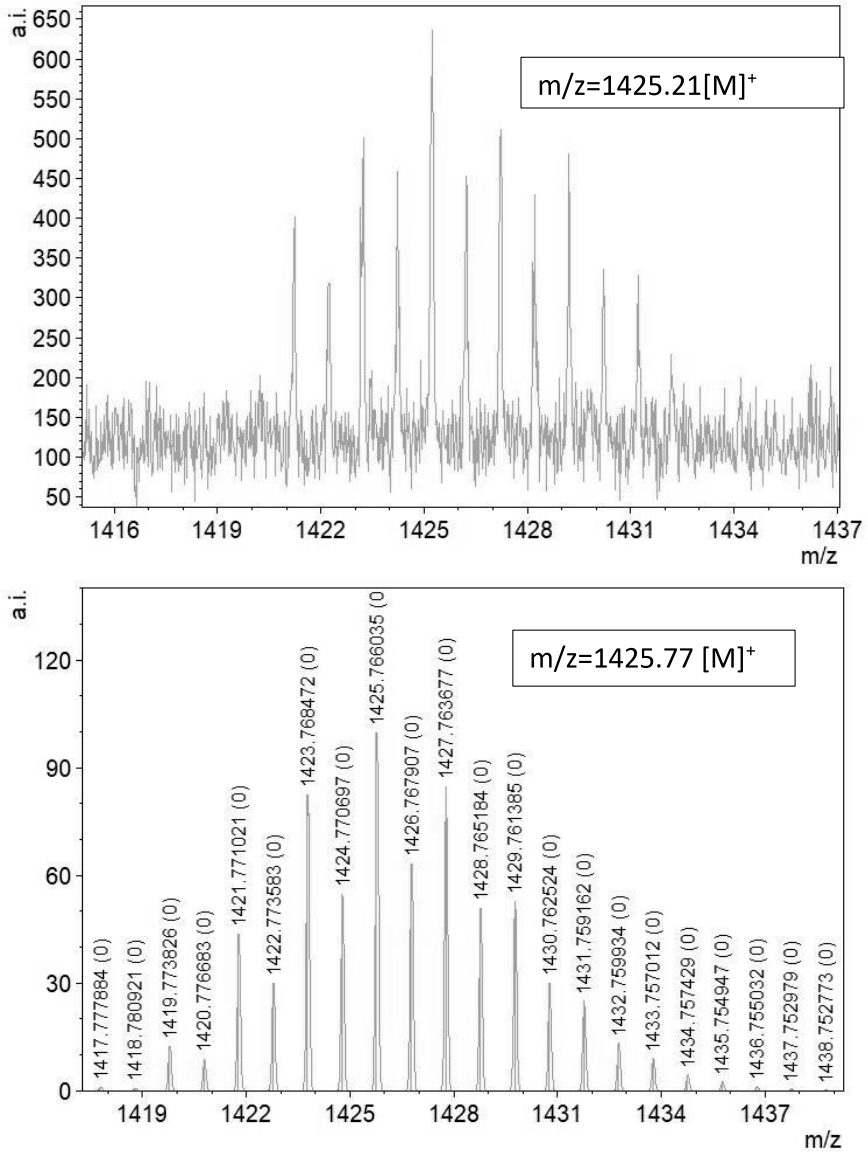

Figure S31: MALDI-ToF spectra of **4-H** experimental (top) and simulated (bottom).

rad-bisalkPTM-Fc$_1$ (3-Rad)

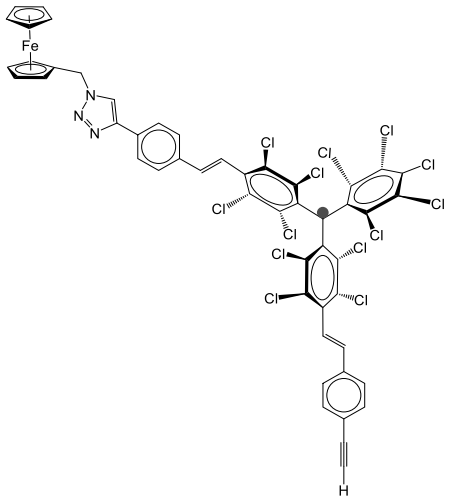

FT-IR

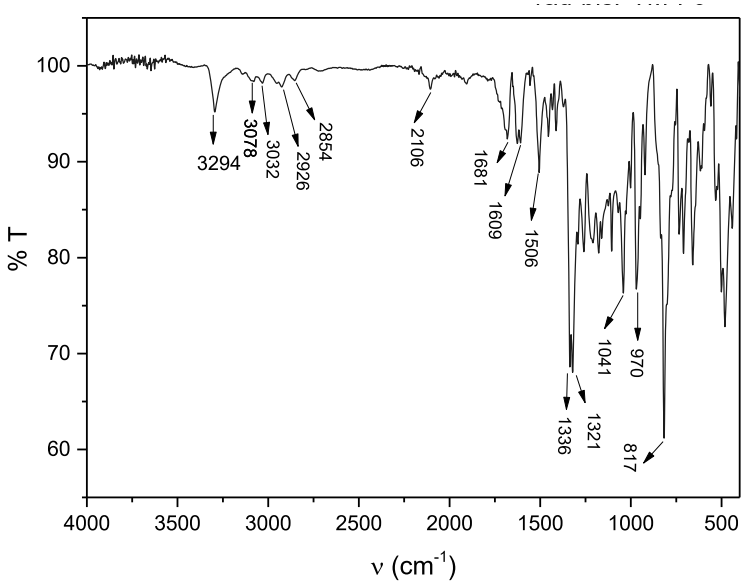

Figure S32: FT-IR spectrum of **3-Rad** in powder.

UV-Vis

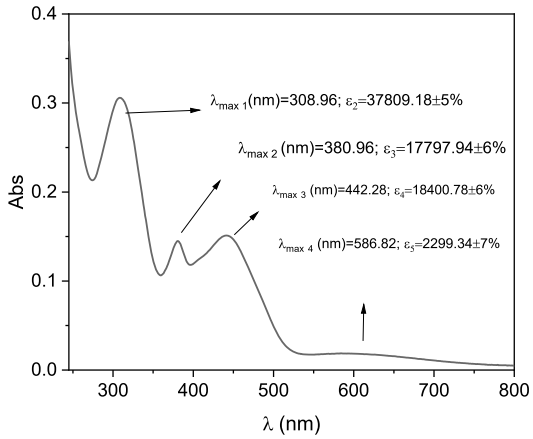

Figure S33: UV-Vis spectrum of **3-Rad** in CH_2Cl_2.
λ_{max} = maximum wavelength and ε= Molar absorptivity.

Electron paramagnetic resonance (EPR)

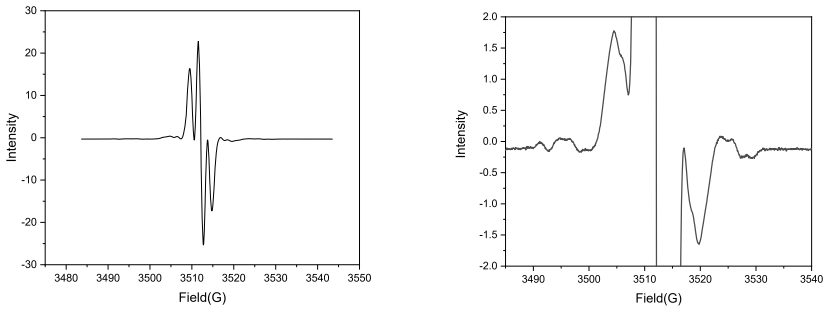

Figure S34: EPR spectra of **3-Rad** in dichloromethane at room temperature. The red spectrum (right) was recorded at higher power conditions.

MALDI-ToF

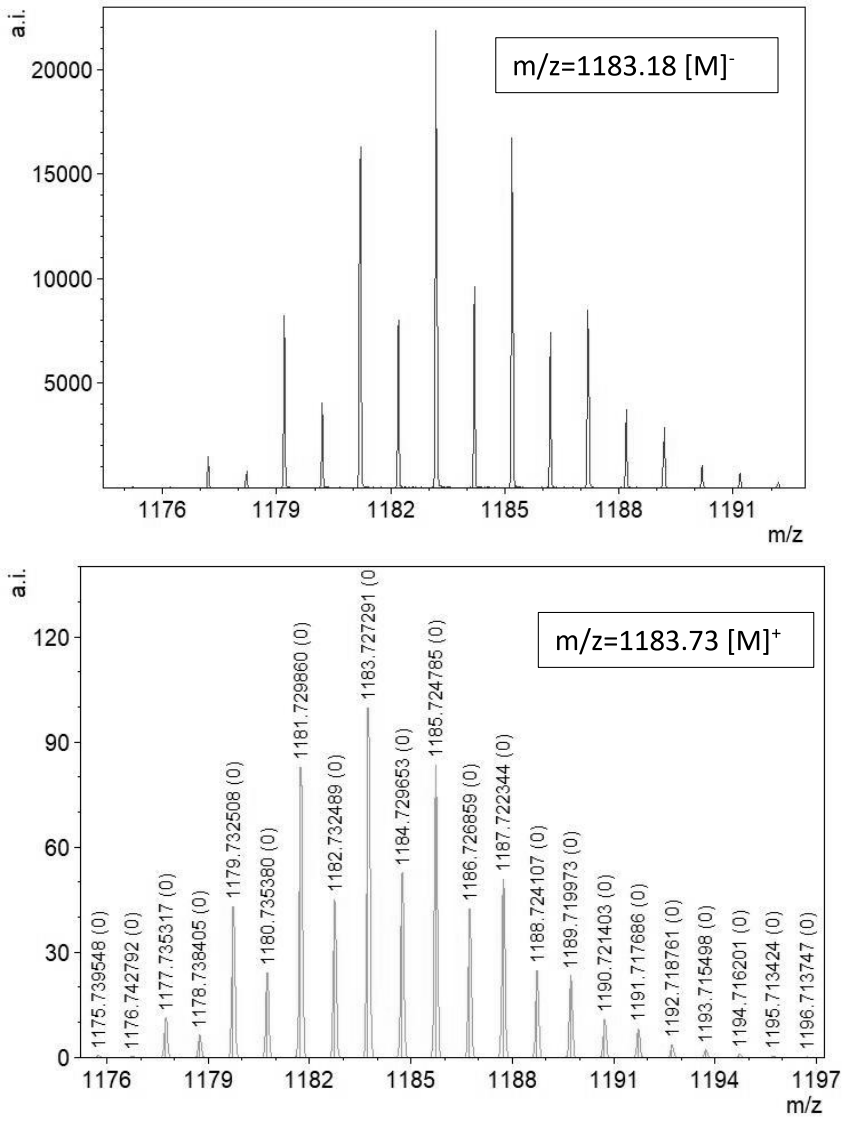

Figure S35: MALDI-ToF spectra of **3-Rad** experimental (top) and simulated (bottom), negative mode.

Cyclic voltammetry

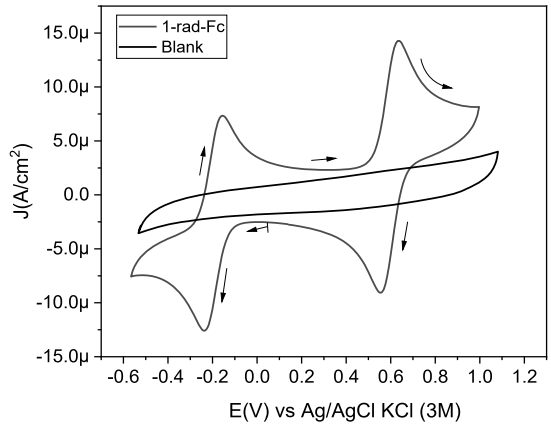

Figure S36: Cyclic voltammetry of **3-Rad** (0.35 mM) over a glassy carbon electrode using as electrolytic medium a 0.1M solution of $TBAPF_6$ in CH_2Cl_2, under argon atmosphere.

Square wave voltammetry

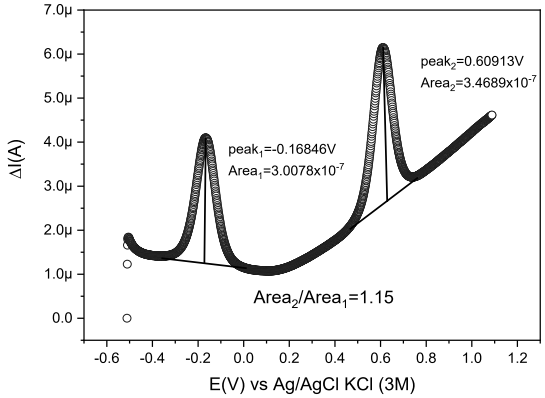

Figure S37: Square wave voltammetry of **3-Rad (**0.058 mM) over a glassy carbon electrode using as electrolytic medium a 0.1M solution of $TBAPF_6$ in CH_2Cl_2, under argon atmosphere. Step=1mV, $E_{modulation}$=20mV and Frequency=40Hz

rad-bisalkPTM-Fc$_2$ (4-Rad)

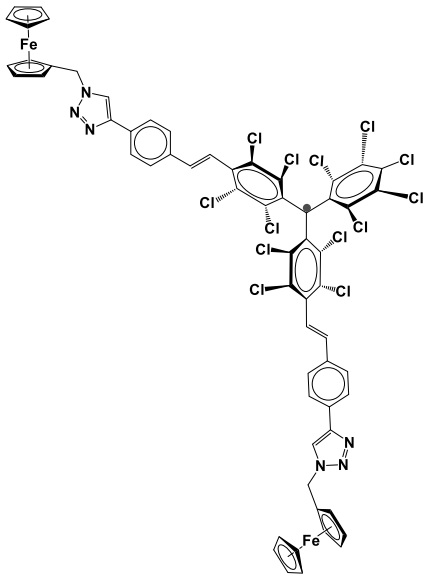

FT-IR

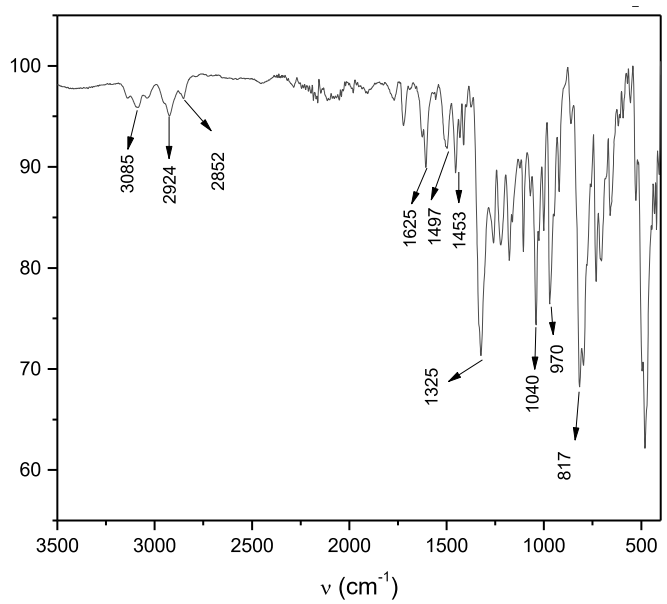

Figure S38: FT-IR spectrum of compound **4-Rad** in powder.

UV-Vis

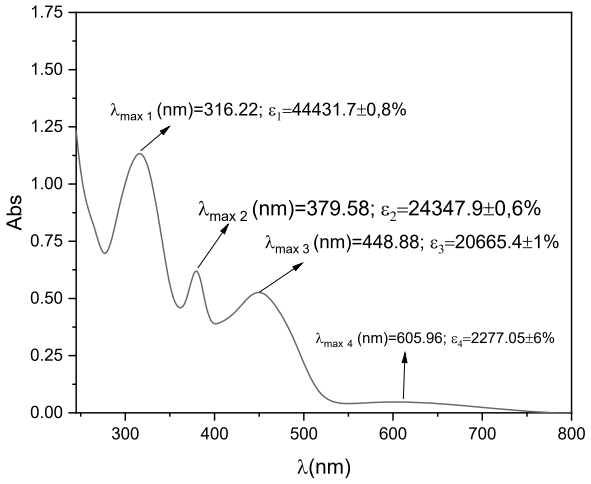

Figure S39: UV-Vis spectrum of **4-Rad** in CH_2Cl_2.
λ_{max} = maximum wavelength and ε= Molar absorptivity.

Electron paramagnetic resonance (EPR)

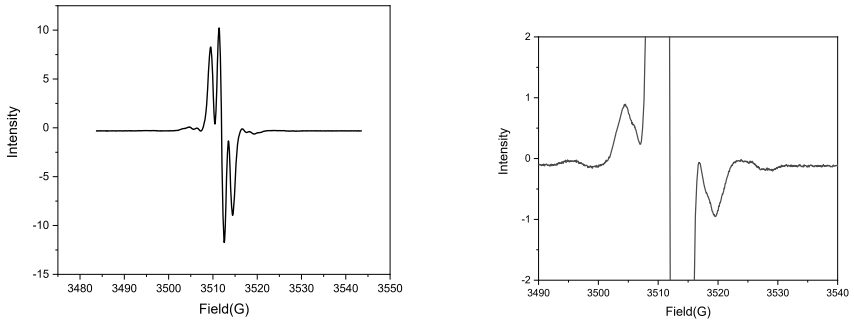

Figure S40: EPR spectra of **4-Rad** in dichloromethane at room temperature. The red spectrum (right) was recorded at higher power conditions.

MALDI-ToF

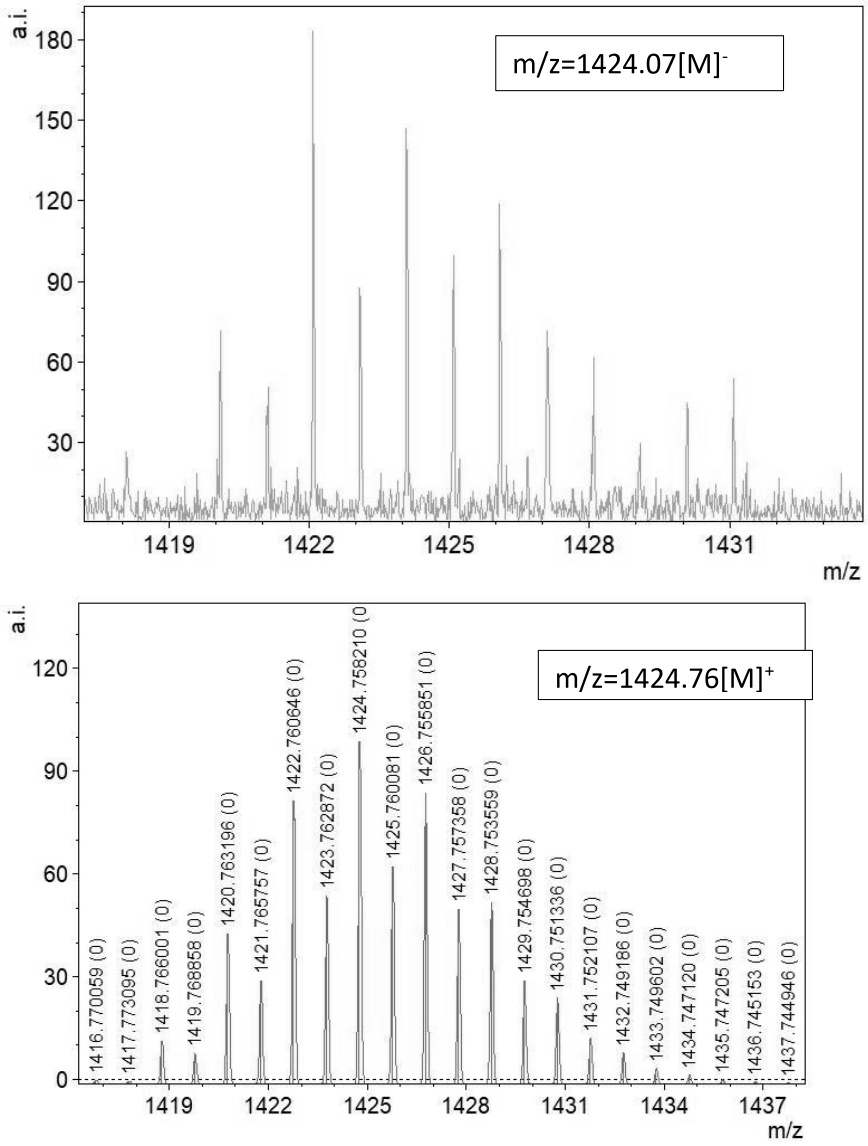

Figure S41: MALDI-ToF spectra of **4-Rad** experimental (top) and simulated (bottom), negative mode.

Cyclic voltammetry

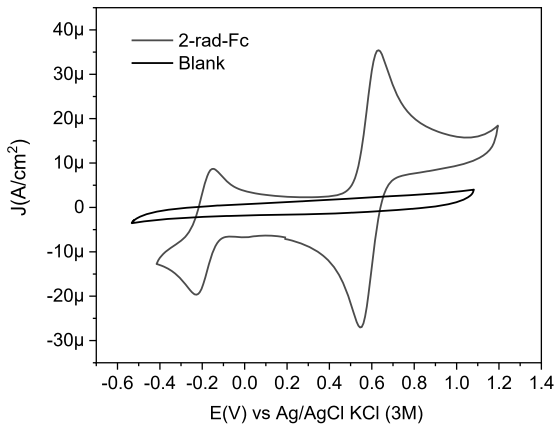

Figure S42: Cyclic Voltammetry of compound **4-Rad** (0.41 mM) over a glassy carbon electrode using as electrolytic medium a 0.1M solution of $TBAPF_6$ in CH_2Cl_2, under argon atmosphere.

Square wave voltammetry.

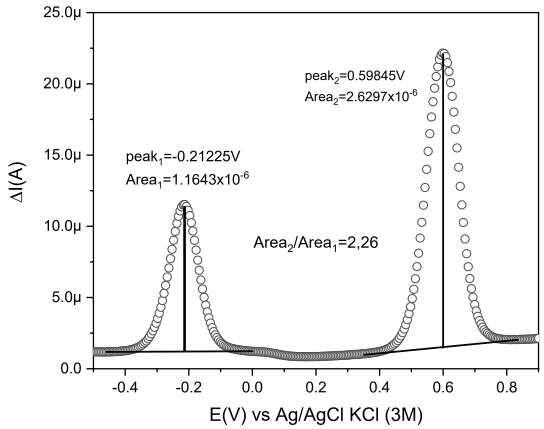

Figure S43: Square wave voltammetry of compound **4-Rad** (0.41 mM) over a glassy carbon electrode using as electrolytic medium a 0.1M solution of $TBAPF_6$ in CH_2Cl_2, under argon atmosphere. Step=5mV, $E_{modulation}$=20mV and Frequency=10Hz

References

(1) Stohr, J. *NEXAFS Spectroscopy*; Springer, 2003.

(2) Casu, M. B. Nanoscale Order and Structure in Organic Materials: Diindenoperylene on Gold as a Model System. *Cryst. Growth Des.* **2011**, *11*, 3629–3635.

(3) Casu, M. B.; Cosseddu, P.; Batchelor, D.; Bonfiglio, A.; Umbach, E. A High-Resolution near-Edge x-Ray Absorption Fine Structure Investigation of the Molecular Orientation in the Pentacene/Poly(3,4-Ethylenedioxythiophene): Poly(Styrenesulfonate) Pentacene/System. *J. Chem. Phys.* **2008**, *128*, 74702.

(4) Casas-Solvas, J. M.; Vargas-Berenguel, A.; Capitán-Vallvey, L. F.; Santoyo-González, F. Convenient Methods for the Synthesis of Ferrocene−Carbohydrate Conjugates. *Bioorg. Med. Chem. Lett* **1999**, *32*, 1–12.

(5) Park, K. M.; Thuo, M. M.; Whitesides, G. M.; Yoon, H. J.; Shapiro, N. D.; Soh, S. The Rate of Charge Tunneling through Self-Assembled Monolayers Is Insensitive to Many Functional Group Substitutions. *Angew. Chemie Int. Ed.* **2012**, *51*, 4658–4661.

(6) Wade, C. P.; Chidsey, C. E. D. Etch-Pit Initiation by Dissolved Oxygen on Terraces of H-Si(111). *Appl. Phys. Lett.* **1997**, *71*, 1679–1681.

(7) Alexander B. Sieval, Ralf Linke, Han Zuilhof, and E. J. R. S. High-Quality Alkyl Monolayers on Silicon Surfaces. *Adv. Mater.* **2000**, *12*, 1457–1460.

(8) Allen J. Bard Larry R. Faulkner. *Electrochemical Methods; Fundamentals and Applications*; John Wiley & Sons, Ltd, 2002.

(9) Eckermann, A. L.; Feld, D. J.; Shaw, J. A.; Meade, T. J. Electrochemistry of Redox-Active Self-Assembled Monolayers. *Coord. Chem. Rev.* **2010**, *254*, 1769–1802.

(10) Simeone, F. C.; Yoon, H. J.; Thuo, M. M.; Barber, J. R.; Smith, B.; Whitesides, G. M. Defining the Value of Injection Current and Effective Electrical Contact Area for EGaIn-Based Molecular Tunneling Junctions. *J. Am. Chem. Soc.* **2013**, *135*, 18131–18144.

(11) Reus, W. F.; Thuo, M. M.; Shapiro, N. D.; Nijhuis, C. A.; Whitesides, G. M. The SAM, Not the Electrodes, Dominates Charge Transport in Metal-Monolayer//Ga_2O_3/Gallium-Indium Eutectic Junctions. *ACS Nano* **2012**, *6*, 4806–4822.

(12) Savu, S. A.; Biswas, I.; Sorace, L.; Mannini, M.; Rovai, D.; Caneschi, A.; Chassé, T.; Casu, M. B. Nanoscale Assembly of Paramagnetic Organic

Radicals on Au(111) Single Crystals. *Chem. - A Eur. J.* **2013**, *19* (10), 3445–3450.

(13) Casu, M. B.; Schuster, B. E.; Biswas, I.; Raisch, C.; Marchetto, H.; Schmidt, T.; Chassé, T. Locally Resolved Core-Hole Screening, Molecular Orientation, and Morphology in Thin Films of Diindenoperylene Deposited on Au(111) Single Crystals. *Adv. Mater.* **2010**, *22*, 3740–3744.

(14) Savu, S. A.; Casu, M. B.; Schundelmeier, S.; Abb, S.; Tönshoff, C.; Bettinger, H. F.; Chassé, T. Nanoscale Assembly, Morphology and Screening Effects in Nanorods of Newly Synthesized Substituted Pentacenes. *RSC Adv.* **2012**, *2*, 5112–5118.

(15) Schöll, A.; Zou, Y.; Jung, M.; Schmidt, T.; Fink, R.; Umbach, E. Line Shapes and Satellites in High-Resolution x-Ray Photoelectron Spectra of Large π-Conjugated Organic Molecules. *J. Chem. Phys.* **2004**, *121*, 10260–10267.

(16) Sjögren, B.; Svensson, S.; Naves De Brito, A.; Correia, N.; Keane, M. P.; Enkvist, C.; Lunell, S. The C1s Core Shake-up Spectra of Alkene Molecules: An Experimental and Theoretical Study. *J. Chem. Phys.* **1992**, *96*, 6389–6398..

(17) Arantes, C.; Chernick, E. T.; Gruber, M.; Rocco, M. L. M.; Chassé, T.; Tykwinski, R. R.; Casu, M. B. Interplay between Solution Processing and Electronic Structure in Metal-Free Organic Magnets Based on a TEMPO Pentacene Derivative. *J. Phys. Chem. C* **2016**, *120*, 3289–3294.

(18) Kakavandi, R.; Savu, S. A.; Sorace, L.; Rovai, D.; Mannini, M.; Casu, M. B. Core-Hole Screening, Electronic Structure, and Paramagnetic Character in Thin Films of Organic Radicals Deposited on SiO_2/Si(111). *J. Phys. Chem. C* **2014**, *118*, 8044–8049.

C. Stability of Radical-functionalized Gold Surfaces by Self-assembly and On-surface Chemistry

Reproduced from
T. Junghoefer, E. M. Nowik-Boltyk, J. A. de Sousa, E. Giangrisostomi, R. Ovsyannikov, T. Chassé, J. Veciana, M. Mas-Torrent, C. Rovira, N. Crivillers, M. B. Casu, "Stability of Radical-Functionalized Gold Surfaces by Self-Assembly and On-surface Chemistry", *Chemical Science* **2020**, *11*, 9162–9172, DOI 10.1039/d0sc03399e
with permission from the Royal Society of Chemistry.

Chemical Science

ROYAL SOCIETY OF CHEMISTRY

EDGE ARTICLE

View Article Online
View Journal | View Issue

Cite this: *Chem. Sci.*, 2020, **11**, 9162

All publication charges for this article have been paid for by the Royal Society of Chemistry

Received 18th June 2020
Accepted 10th August 2020

DOI: 10.1039/d0sc03399e

rsc.li/chemical-science

Stability of radical-functionalized gold surfaces by self-assembly and on-surface chemistry†

Tobias Junghoefer, ‡[a] Ewa Malgorzata Nowik-Boltyk,‡[a] J. Alejandro de Sousa,[bd] Erika Giangrisostomi,[c] Ruslan Ovsyannikov,[c] Thomas Chassé,[a] Jaume Veciana,[b] Marta Mas-Torrent,[b] Concepció Rovira,[b] Núria Crivillers[b] and Maria Benedetta Casu *[a]

We have investigated the radical functionalization of gold surfaces with a derivative of the perchlorotriphenylmethyl (PTM) radical using two methods: by chemisorption from the radical solution and by on-surface chemical derivation from a precursor. We have investigated the obtained self-assembled monolayers by photon-energy dependent X-ray photoelectron spectroscopy. Our results show that the molecules were successfully anchored on the surfaces. We have used a robust method that can be applied to a variety of materials to assess the stability of the functionalized interface. The monolayers are characterized by air and X-ray beam stability unprecedented for films of organic radicals. Over very long X-ray beam exposure we observed a dynamic nature of the radical–Au complex. The results clearly indicate that (mono)layers of PTM radical derivatives have the necessary stability to withstand device applications.

Introduction

Molecular systems are materials that intersect with many different promising fields such as organic/molecular spintronics, electronics, and organic magnetism.[1–8] In this framework, organic radicals are exceptionally promising in various fields, and the research on radical thin films and interfaces has recently flourished, due to their potential use in applications from quantum computing to organic electronics and spintronics.[8–13]

We have recently demonstrated that a Blatter radical derivative is a potential quantum bit and we attached it to copper contacts to investigate the influence of a substrate on the radical magnetic moment.[9] Our work indicated the need for identifying strategies in order to attach the radical to the surface preserving its magnetic moment at the interface by using different methods ranging from evaporation to preparation in a wet environment. However, the radical functionalization of a substrate is eased by choosing a specific chemical group that has a high chemical affinity for the selected substrate. Usually thiols and disulfides are chosen to covalently modify gold surfaces, including gold nanoparticles, with organic radicals by adsorption from solution. More recently, alkyne terminated derivatives have started to play a role. Nitroxides (TEMPO),[14–17] nitronyl nitroxides[18–20] and tripheylmethyl[21–23] radicals have been successfully employed to prepare such paramagnetic hybrid materials. In this work, we capitalize our knowledge of radical thin films and interfaces by studying the functionalization of gold surfaces with derivatives of the perchlorotriphenylmethyl (PTM) radical. PTM is a very persistent and stable radical that shows a long coherence time at room temperature, being a strong potential candidate for quantum technologies.[24] Previously, self-assembled monolayers (SAMs) of PTM on gold substrates have been investigated to study their transport properties.[21–23,25] The radical character of the layers was proved by several techniques (UV-vis, cyclic voltammetry, EPR, NEXAFS and UPS); however, a careful and in-depth characterization of the stability of these radical SAMs has not been carried out so far. Such a stability is a necessary precondition to use radical-based SAMs for any practical application. Here, we used a ferrocene functionalized PTM derivative with an alkyne termination (Fig. 1) that covalently attaches to a gold substrate spontaneously.[26–31] The ferrocene functionalization makes the

[a]Institute of Physical and Theoretical Chemistry, University of Tübingen, 72076 Tübingen, Germany. E-mail: benedetta.casu@uni-tuebingen.de
[b]Institut de Ciència de Materials de Barcelona (ICMAB-CSIC), Networking Research Center on Bioengineering Biomaterials and Nanomedicine (CIBER-BBN), Campus de la UAB, 08193 Bellaterra, Spain
[c]Helmholtz-Zentrum Berlin für Materialien und Energie (HZB), 12489 Berlin, Germany
[d]Laboratorio de Electroquímica, Departamento de Química, Facultad de Ciencias, Universidad de los Andes, 5101 Mérida, Venezuela

† Electronic supplementary information (ESI) available: Survey spectra of SAM2A and fit results for the photoemission lines in the SAM2A C 1s spectra. SAM1 survey, stoichiometric analysis, and fit results for the photoemission lines in the SAM1 C 1s spectra. C 1s core level spectra at 460 and 640 eV. Fit results for SAM2 and SAM4 at 460 eV. Fit results for SAM2 and SAM4 at 640 eV. Electrochemical measurements, stability under air exposure, and stability under X-ray beam exposure. See DOI: 10.1039/d0sc03399e

‡ These authors contributed equally.

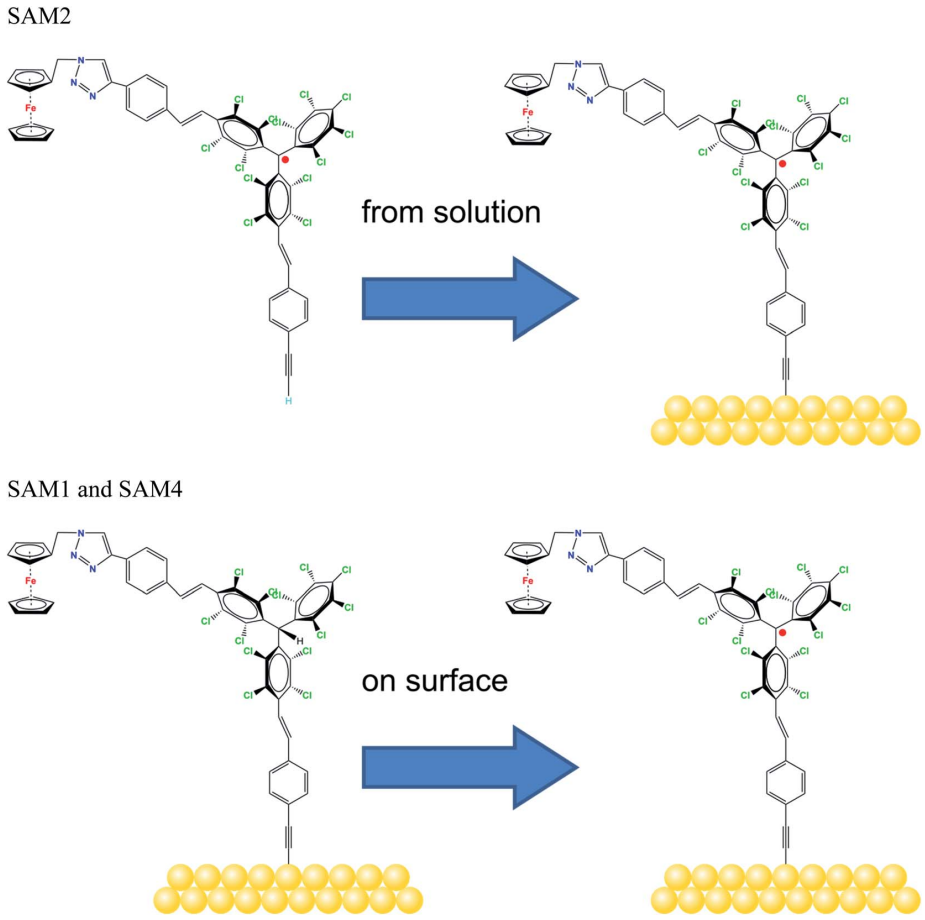

Fig. 1 Molecular structure of the radicals, as indicated, and the schematic sketch of the different SAM preparations.

molecules interesting for current rectification, as seen in SAMs incorporating ferrocene acting as a redox-active moiety.[32–34] We investigated also the formation of radical self-assembled monolayers (SAMs) obtained by using on-surface chemistry.

Our investigations were performed using X-ray photoelectron spectroscopy (XPS). While XPS is a well-established technique to investigate the electronic structure of materials, this is not the only aspect that can be examined.[35] Because of its high sensitivity, it is also possible to quantitatively calculate the stoichiometry of the investigated systems. Further aspects can be explored: it is very sensitive to the chemical environment of the elements, allowing the occurring chemical bonds and the charge transfer from/to surfaces to be revealed. It is possible to gain information on film stability (*e.g.*, under X-ray beam or air exposure) and on post-growth phenomena. It is extremely well suited to investigate radical thin films (including their radical character) when evaporated by using controlled conditions.[36] We proved in our previous work that XPS in combination with a careful and robust best fit procedure allows investigation of the radical character, with the results being in perfect agreement with electron paramagnetic resonance (EPR) measurements.[9,36–41] EPR is the technique typically used for radical characterization. However, its use for films is limited (1) by the fact that it is an *ex situ* technique. Radical thin films might not be stable enough outside the ultra-high vacuum environment where they are deposited or obtained by on-surface reaction.[42–44] (2) By the choice of the substrate that might contribute to the EPR signal.[41] (3) By the substrate dimensions that are often over-dimensioned for standard spectrometers. (4) By the fact that standard EPR spectrometers do not have the necessary sensitivity to measure (sub)monolayers. Conversely, XPS has a high sensitivity further beyond many other conventional chemical techniques, as it can detect less than 10^{13} atoms,[45] allowing investigations in the monolayer and submonolayer regime without requiring advanced "state-of-the-art" spectrometers, as it is the case for EPR, but a standard, commercially available, monochromatized laboratory XPS station is sufficient.

In this work, we investigate the chemistry of the SAM/gold interface, demonstrating that the SAMs were successfully

attached to the substrate, using also on-surface chemistry. We also show that it is possible to identify the spectroscopic lines associated with the radical character *versus* its diamagnetic counterpart. The work focuses on the SAM stability, under X-ray and air exposure, using a method that can be applied to any material to explore any kind of stability issue, such as gas exposure, humidity, aging, and temperature that are of paramount importance for technological applications.

Experimental section

SAM1 and SAM2 were prepared following the protocol thoroughly described in ref. 34. SAM4 was grown following a two-step reaction: (1) SAM1 was immersed in a 2 mM solution of Bu_4NOH/THF (freshly distilled) under an argon atmosphere. The solution was left with a gentle stirring for 8 h at room temperature in the dark. Then, the substrates were removed from the flask and thoroughly rinsed with THF (distilled). (2) Immediately afterwards, the substrates were immersed in a 4 mM *p*-chloranil/THF (distilled) solution under an argon atmosphere. The solution was left for 12 h at room temperature in the dark. Finally, the substrates were removed from the flask, thoroughly rinsed with THF (distilled) and dried with a nitrogen stream. Coverage and radical formation were checked with cyclic voltammetry.

An XPS Ultra High Vacuum (UHV) system (2×10^{-10} mbar base pressure) equipped with a monochromatic Al Kα source (SPECS Focus 500) and a SPECS Phoibos 150 hemispherical electron analyzer was used. Survey spectra were measured at 50 eV pass energy and individual core level spectra at 20 eV pass energy. Both were subsequently calibrated to the Au 4f signal at 84 eV. To minimize potential radiation damage, freshly prepared films were measured, and radiation exposure was minimized unless differently stated in the text (*i.e.*, stability measurements). For measurements probing air stability, X-ray beam exposure was further limited after air exposure to attribute the observed changes exclusively to the degradation by air exposure.

Photon-energy dependent XPS measurements were performed at the third-generation synchrotron radiation source BESSY II (Berlin, Germany) at the Low-Dose PES end station installed at the PM4 beamline ($E/\Delta E = 6000$ at 400 eV). They were carried out in multibunch hybrid mode with a SCIENTA ArTOF electron energy analyzer (ring current in top up mode = 300 mA).

Results and discussion

We examined two different layer preparations using the PTM radical derivative (SAM2 and SAM4) and we compared them with those obtained by depositing the diamagnetic counterpart, SAM1 (Fig. 1). The PTM radical and the diamagnetic derivative shown in Fig. 1 were synthesized as previously reported:[34] SAM2 is obtained by depositing the radical on a gold substrate from its solution. SAM4, in contrast, is obtained by first depositing the analogous diamagnetic molecules on gold and following a two-step synthesis (*i.e.*, anion generation and oxidation), and thus, the PTM radical is formed on the surface.[46]

Fig. 2 shows the SAM2 XPS spectra of the important core levels (for the survey and the stoichiometric analysis, see Fig. S1, Tables S1 and S2 in the ESI†). The spectra are characterized by the predominance of gold signals in agreement with the deposition of a monolayer. Apart from a carbon concentration that slightly exceeds the theoretical values, which is usual in samples prepared *ex situ* with wet-environment techniques, the films are remarkably clean, and no significant amounts of contaminants are visible. In XPS, the integrated area of the main lines corresponding to photoelectrons emitted from a given element, together with their satellites, is proportional to the concentration of that same element in the investigated system.[35,47,48] In highly resolved XPS spectra, the rich fine structure allows fitting the lines including contributions from different atomic sites of the same element which, due to a different chemical environment, are expected to show differences in their binding energies.[35,47,48]

The film stoichiometry agrees with the expected values, confirming that the radical derivative was indeed attached to the gold substrate. The C 1s spectroscopic line is characterized by a main peak at around 284.5 eV and a feature at around 286 eV. The C 1s intensity is due to photoelectrons emitted from the carbon atoms. The contributions mirror several different chemical environments. In fact, carbon atoms are not only bound to other carbon atoms, but to hydrogen, nitrogen, and chlorine atoms. Each different environment leads to a slightly different binding energy that can be identified by using a best fit procedure (Fig. 2a).[34,37,49] The fitting procedure in XPS is driven by specific and detailed chemical and physical arguments, and not by a mere mathematical approach. The curves are described using a Voigt profile, *i.e.*, a convolution of a Gaussian and a Lorentzian profile. This is because different contributions influence the line shape of the XPS main features: intrinsic lifetime broadening, vibronic and inhomogeneous broadening lead to a Lorentzian profile, while experimental contributions have a Gaussian profile. The lifetime of the core hole is determined basically using the Heisenberg uncertainty principle and consequently the intrinsic peak width is determined, too. For example, the Lorentzian width for the C 1s orbital is around 80 meV, and for the N 1s orbital it is around 100 meV in organic materials.[50] The experimental setup gives a contribution assumed to have a Gaussian lineshape due to the resolution of the analyser, the non-perfect monochromaticity of the X-rays, and inhomogeneities of different nature. The fit that we use is based on the procedure adopted for closed-shell molecules.[14] The final fit is the result of several self-consistent iteractions of sequential fits performed considering all physical and chemical information and adding more constraints at each iteraction, with the goal of keeping the parameter dependency very low (dependency values of the last fits in this work were very close to zero). The constraints in our fit are based on the element concentration, and the binding energy constraints must adhere to electronegativity and known values in the literature, so we use the published or measured core-hole lifetimes for each element. The fit procedure must systematically hold for all

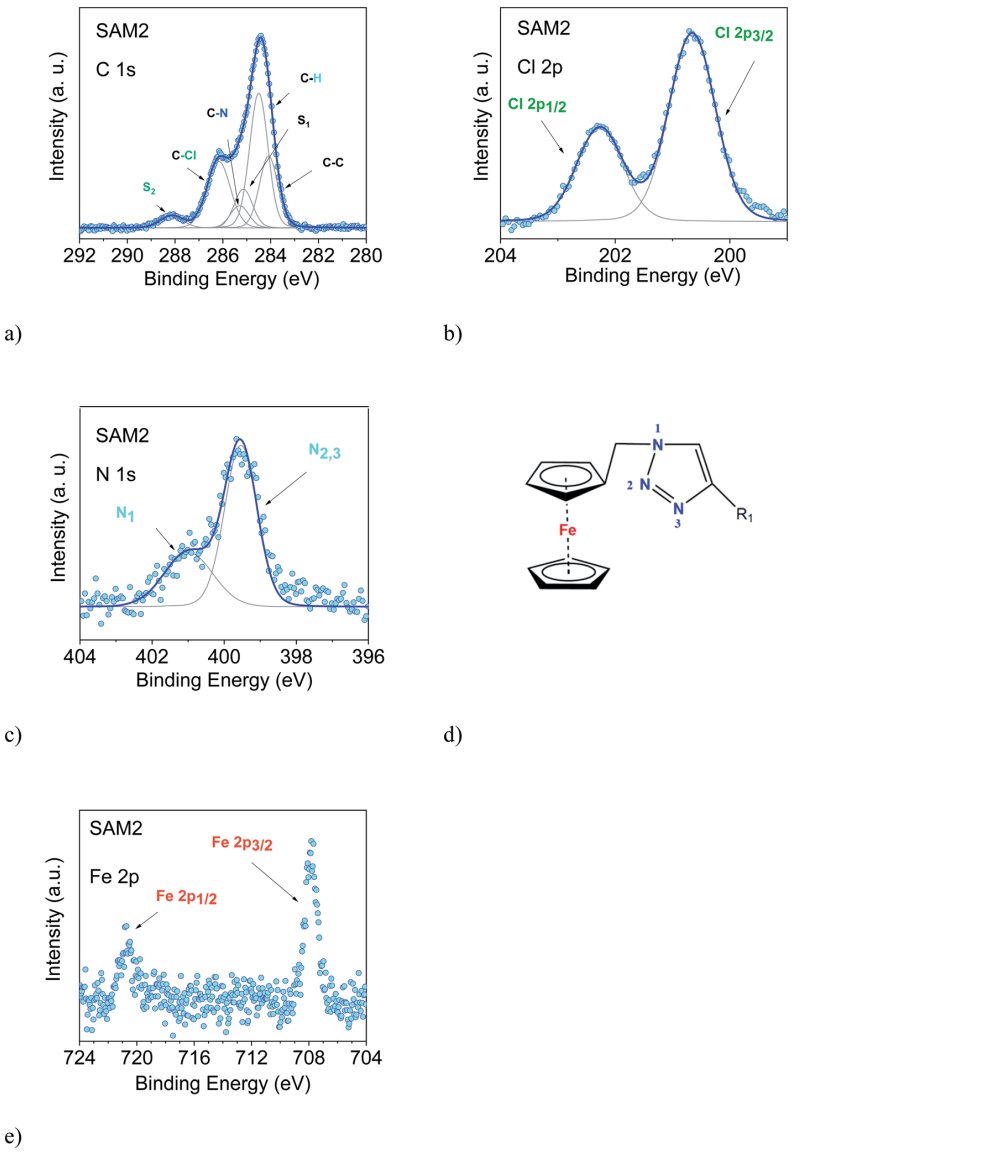

Fig. 2 SAM2. (a) C 1s, (b) Cl 2p, (c) N 1s (together with their best fit) and (e) Fe 2p XPS spectra (photon energy: 1486.6 eV). In (d) the chemical environment of the triazole derivative is shown in detail.

samples of a specific system, prepared and measured under the same conditions. Our procedure revealed to be extremely robust giving results in very good agreement with EPR and *ab initio* calculations, both for open-shell and closed-shell systems, as well.[9,36–41,51–55] To reach this result, we work on sets of samples that are large enough to be statistically significant. In this way, we can also identify the samples that do not correspond to the expected stoichiometry.[37,39,56,57]

In the spectra, we observe the presence of shake-up satellite intensities (Fig. 2). As a result of the core-hole formation, the symmetry is reduced, and a larger number of non-equivalent carbon atoms should be considered.[58,59] The ionization at different carbon sites may give different contributions to the shake-up spectra. The S_1 satellite can be related to the first HOMO–LUMO shake-up.[60] Its energy position with respect to the main line is lower than the optical gap, a typical effect in the HOMO–LUMO shake-up satellites of polyaromatic molecules caused by the enhanced screening of the core-hole due to its delocalization.[60–63] A large number of satellite features is expected upon a photoemission event. However, their assignment is very complicated, especially for large molecules because they are not completely described by theoretical models. Such

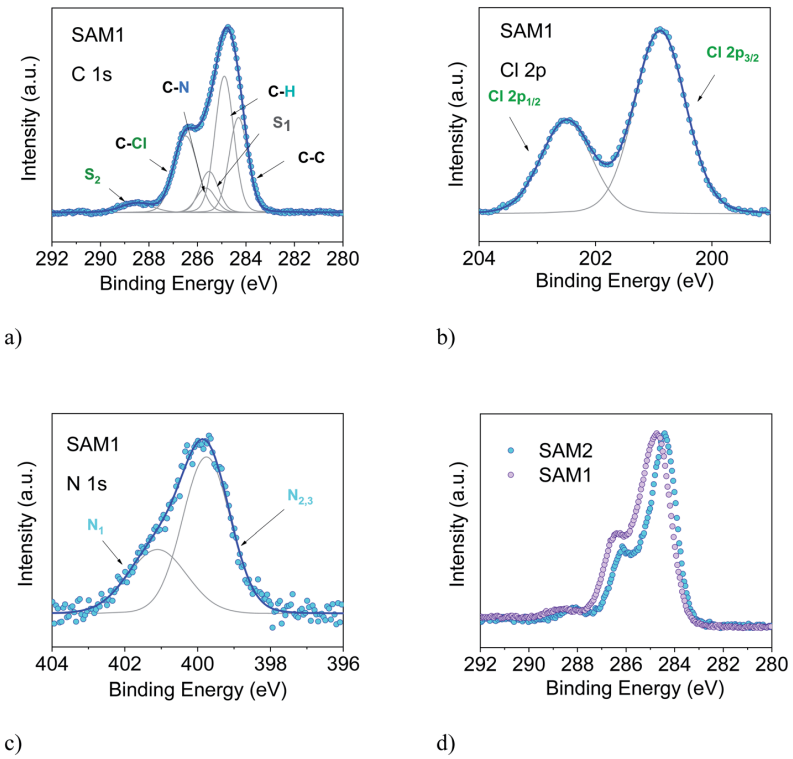

Fig. 3 SAM1. (a) C 1s, (b) Cl 2p, and (c) N 1s, together with their best XPS spectra (photon energy: 1486.6 eV). (d) Comparison of the C 1s XPS line of SAM1 (diamagnetic) and SAM2 (radical). Intensities are normalized to the peak maximum to allow comparison.

a detailed description is outside the goal of this work; therefore, we have identified most of the higher binding energy satellite intensities under a single component, S_2. This component is correlated with the C–Cl feature from a stoichiometric point of view. This assignment is further corroborated by the fact that the C–Cl feature and S_2 change simultaneously depending on the photon energy, as it can be easily seen in Fig. 2 and 3.

The intensities of the various contributions agree with the expected stoichiometry, confirming once more that the SAM2 carbon line corresponds to the radical derivative (Table S2 in the ESI†). The Cl 2p, N 1s and Fe 2p core level spectra are also shown. Their features confirm the presence of an intact molecule: Cl 2p core level lines show the typical doublet feature (spin–orbit splitting = 1.6 eV, as in the literature[64]), and the N 1s spectrum (Fig. 2c) is characterized by contributions due to photoelectrons emitted from three different chemical environments, confirming the intactness of the triazole derivative (Fig. 2c and d). The signal of the Fe 2p shows the expected doublet (spin–orbit splitting = 12.8 eV, concomitant with the values in the literature[64,65]), and the noteworthy absence of further intensities indicates that the signal is due to electrons emitted from iron atoms in the +2 oxidation state, as it is the case for ferrocene.[65–67] Note that, for the monolayers of clean ferrocene, the Fe 2p spectrum does not show any satellite intensity.[65–69] In fact, this intensity depends on the ligands and it varies with their electronegativity.[70] Additionally, in the case of monolayers on metal substrates, the image-charge formed at the interface[71] may further screen the satellite intensities. The XPS intensities and line shapes indicate that the radical was attached to the surface preserving the expected stoichiometry. Thus, we can confidently infer that the synthesis and the preparation of SAM2 were successful.

To support this conclusion and explore the use of XPS to identify the PTM radical, we investigated SAM1, *i.e.*, the SAM obtained from the diamagnetic counterpart of the PTM radical derivative (Fig. 1).

The essential core level spectra are shown in Fig. 3 (for the survey and the stoichiometric analysis, see Fig. S2, Tables S3 and S4 in the ESI†). In our discussion, we focus on the C 1s core level spectroscopic line. This is the line that is directly correlated with the radical character (see Fig. 1) because the unpaired electron mainly resides in the central radical carbon atom of the perchlorinated triphenylmethyl unit. The stoichiometry for SAM2 and SAM1 is different. In SAM1 the central methyl carbon atom of the PTM is bound to hydrogen. Therefore, we expect a different C 1s line broadening with respect to the radical spectra. Indeed, we observe a larger line for SAM1 (Full Width at Half Maximum (FWHM) = 1.8 eV *versus* 1.4 eV for SAM2, under the same experimental conditions). This difference is mirrored by a larger Gaussian width required in the fit procedure (see

Table S4 in the ESI†). We also observe a different binding energy. The SAM1 C 1s main line is at higher binding energy than the SAM2 main line. This indicates that the core-hole created upon photoemission is more efficiently screened in SAM2 than in the diamagnetic molecule. This can be explained considering the donor–acceptor character of SAM2 (ref. 34) where the simultaneous presence of the radical and the azidomethyl ferrocene unit stands for faster charge delocalization of the core-hole. These differences in the C 1s main line, binding energy and broadening between SAM1 and SAM2 allow using XPS to identify the radical character of the SAMs.

In an XPS experiment it is possible to probe different sampling depths:[72] when changing the photon energy, the materials emit electrons with different kinetic energy which is equivalent to emitting photoelectrons with different inelastic mean free path (λ). Thus, we performed a photon-energy-dependent experiment on SAM1, SAM2 and SAM4 using 460 and 640 eV photon energy, respectively. This corresponds to varying λ between 0.17 and 0.28 nm (ref. 73 and 74) (Fig. 4 and S3†). The experiment at 460 eV is very surface-sensitive (note that both experiments at 460 and 640 eV are very surface-sensitive with respect to the measurements so far discussed, which were performed at 1486.6 eV). We observe that, by varying the photon energy, the relative intensities of the main line and the line due to photoelectrons emitted from carbon atoms bound to the electronegative nitrogen and chlorine atoms change: the feature at higher binding energy has higher intensity at 640 eV. What is also important is that these changes are accompanied by changes in the S_2 satellite, indicating, as mentioned, that these two components are strongly correlated, corroborating our fit assignments. This change in the intensity depends on the photon energy and, thus, on the inelastic mean free path, and it is due to the surface core level shift effect,[75–78] *i.e.*, the difference of the core level photoemission between a surface atom/molecule and a bulk atom/molecule.[76,78,79] This effect is visible in organic thin films when the molecules are not planar and carry electronegative atoms.[49,80,81] In fact, electronegative atoms shift the electronic cloud, causing a different screening of the core-hole created upon photoemission. However, this screening is different when it occurs at different depths where structural differences are significant, for example, in the case of upright *versus* flat lying molecules.[80] In the present case, the C–Cl components are stronger at 640 eV when the experiment is less surface-sensitive. We can infer structural information from this dependence: the XPS results indicate that the PTM radical is closer to the substrate with respect to the azidomethyl-ferrocene unit (as sketched in Fig. 1); therefore, its contribution is stronger when λ is longer. For the photon energy of 1486.6 eV, λ is comparable with the dimensions of the molecule ($\lambda = 0.81$ nm (ref. 73)), in which case the stoichiometry information plays the major role against the structural information, as seen in closed-shell systems like phthalocyanines.[82]

Using the above results as a reference, we investigated SAM4 (Fig. 4, lower panel). This monolayer has the same theoretical stoichiometry as SAM2, but it has been obtained *via* on-surface radical formation from the diamagnetic molecule. We focused once more on the C 1s core level spectra. First, from the point of

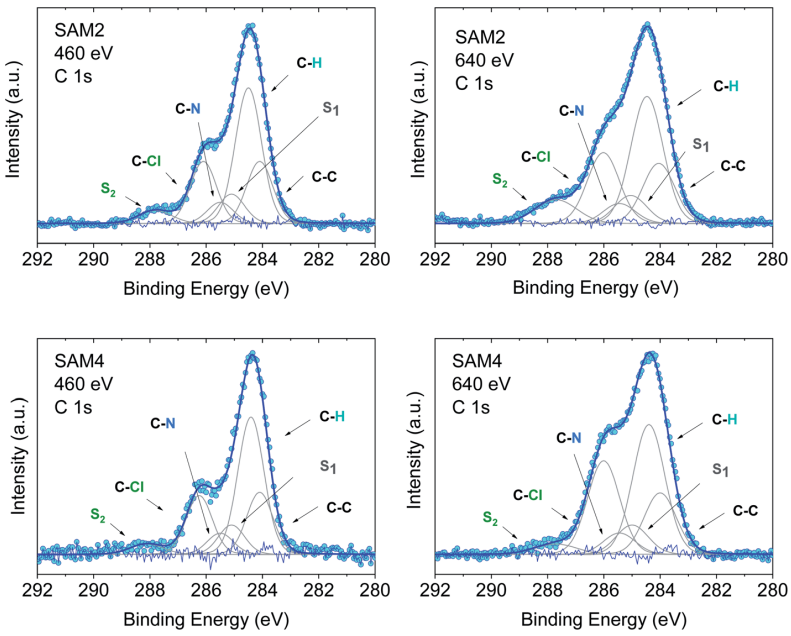

Fig. 4 C 1s core level spectra at 460 and 640 eV, as indicated, together with their best fit and residual. Upper panel: SAM2. Lower panel: SAM4. Intensities are normalized to the peak maximum to allow comparison. For the curve fits see the ESI.†

view of the stoichiometry, as previously performed for SAM2 and SAM1, we observe that the C 1s line shape has the same features as in the SAM2 core spectra. In this case also, we observe the same photon energy dependence at 460 and 640 eV, hinting at a similar structural adjustment of the molecule units with respect to the substrate. What is most important is that the FWHM of the C 1s line is narrower than in the case of the diamagnetic molecule, *i.e.*, SAM4 has a narrower main line than SAM1 (see Fig. S3†). Following our above discussion, this effect indicates a radical character of the film. Since the radical generation occurred on the surface, this result hints at and supports the successful on-surface preparation of the radical. A fit procedure backs these observations: the same best fit procedure leads to the same intensities and binding energies for the C 1s contributions of the spectra of SAM2 and SAM4 (Fig. 4 and Tables S5–S8 in the ESI†). Cyclic voltammetry experiments support the radical character of the layers, too (see Fig. S4 in the ESI†). The redox peaks corresponding to the PTM radical ↔ PTM anion and ferrocene ↔ ferrocenium redox process are clearly observed.

A change in photon energy as performed in the present XPS experiments also implies a change in the C 1s cross-section increasing the complexity of the screening effects. Looking at the fit results, we note that the S_1 intensity decreases with increasing the photon energy while the intensities of the S_2 satellite show the opposite behaviour (Tables S5–S8 in the ESI†). This gives a hint about the fact that the S_1 intensity is related to the dipole excitation of a core electron to the lowest unoccupied molecular orbital (LUMO) accompanied by the monopole ionization of the valence electron: this shake up contribution is near the ionization threshold region and decreases with the increase in energy,[83,84] as observed in our fits.

An important aspect that we intend to address here is the stability of the monolayer in the real environment. While the PTM radical is known to be chemically stable both in solution and in powder if visible light is avoided, there is no report on the chemical and structural stability of its films where single radical molecules are exposed to air. To tackle this issue, we kept SAM2 monolayers under air in darkness and measured them again 128 days later, always minimizing X-ray exposure during measurements. The results are shown in Fig. 5. The C 1s core level spectrum comparison between the fresh monolayer and the "aged" monolayer shows a small difference in the relative intensity of the main feature with respect to the feature at higher binding energy, while the Cl 2p spectra do not show major differences. Post-growth phenomena, such as desorption and ripening, are expected and well-known in the case of organic molecules, and expected also in radical films, especially

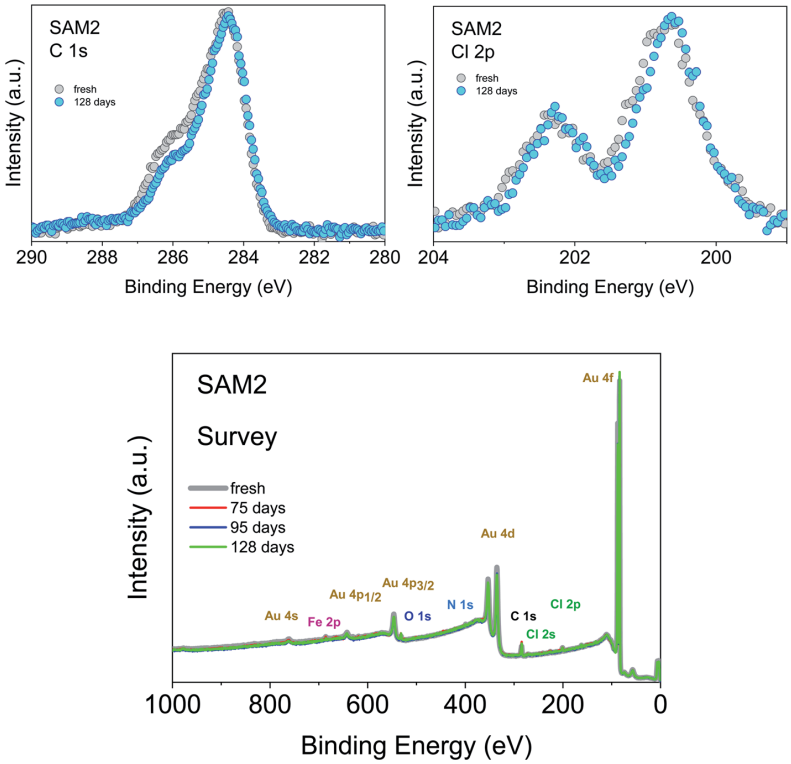

Fig. 5 Upper panel: (left) C 1s and (right) Cl 2p core level spectra of a freshly prepared monolayer and after 128 days of exposure to air and kept in darkness, as indicated (photon energy: 1486.6 eV). Intensities are normalized to the peak maximum to allow comparison. Lower panel: SAM2 survey XPS spectra under air exposure, as indicated (photon energy: 1486.6 eV).

for those systems having low vapor pressure at room temperature and physisorbed on surfaces.[36,37,40] To investigate the origin of the difference in the C 1s core level spectra we performed a best fit analysis, following two hypotheses. In one case, we performed the fit considering that PTM might switch to the perchlorophenylfluorenyl radical (PPF) (Fig. S5 and Table S9 in the ESI†). This is a known derivative of the PTM radical generated both by heating over 300 °C (ref. 85) and by photo-irradiation.[86] In the second case, we considered that the stoichiometry of the monolayer stays unchanged but the carbon intensity increases due to the adsorption of carbon impurities from the environment (Fig. S6 and Table S10 in the ESI†). Both fits are plausible. A closer inspection of the survey spectra helps to interpret the results (Fig. 5, lower panel). Initially, the gold signal is stronger, *i.e.*, its intensity decreases with time. Simultaneously the carbon signal increases, while the chlorine signal does not change. From the stoichiometric analysis of the spectra, we found that in the fresh monolayer the carbon to gold ratio (C/Au) and the chlorine to gold ratio (Cl/Au) are 0.37 and 0.04, respectively. After 128 days, they are 0.40 and 0.04, respectively. This clearly indicates that the chlorine content does not diminish and that the phenomenon playing the major role is carbon adsorption. This means that not only the PTM radical is chemically stable, but also its monolayers are stable under prolonged air exposure. This is a result of great significance because it fully supports the use in devices of the PTM radical and its derivatives grafted on surfaces.

We also studied the stability of SAM2 against X-rays. As previously, we focus our discussion on the PTM radical analysing the C 1s and the Cl 2p core level spectra (Fig. 6). We could observe first small changes in the spectroscopic lines after 18 hours of X-ray exposure, a 0.1 eV shift of the binding energy towards higher values and a difference in the satellite intensities. The fit analysis performed on the C 1s line confirms that these are not significant stoichiometric changes (Fig. S7, Tables S11 and S12 in the ESI†). We crosschecked this finding also using synchrotron radiation and monitoring the film in real-time over around 8 hours (Fig. 6, lower panel, photon energy: 640 eV, flux: 1×10^9 to 1×10^{10} photons per s). No changes were detected.

To understand what happens under very long X-ray exposure, we exposed the films to X-rays for 52 hours and we looked at the effects (Fig. 6d). After such a long exposure, the gold signal is more intense, while the C 1s and Cl 2p lines show no decrease in the intensity. This indicates that the gold substrate is more exposed with time. Usually this result hints at changes in the film morphology due to post-growth phenomena, such as desorption, dewetting or Ostwald ripening, which lead to the coalescence of small islands into big islands leaving a larger area of the substrate surface free. The result indicates, also in

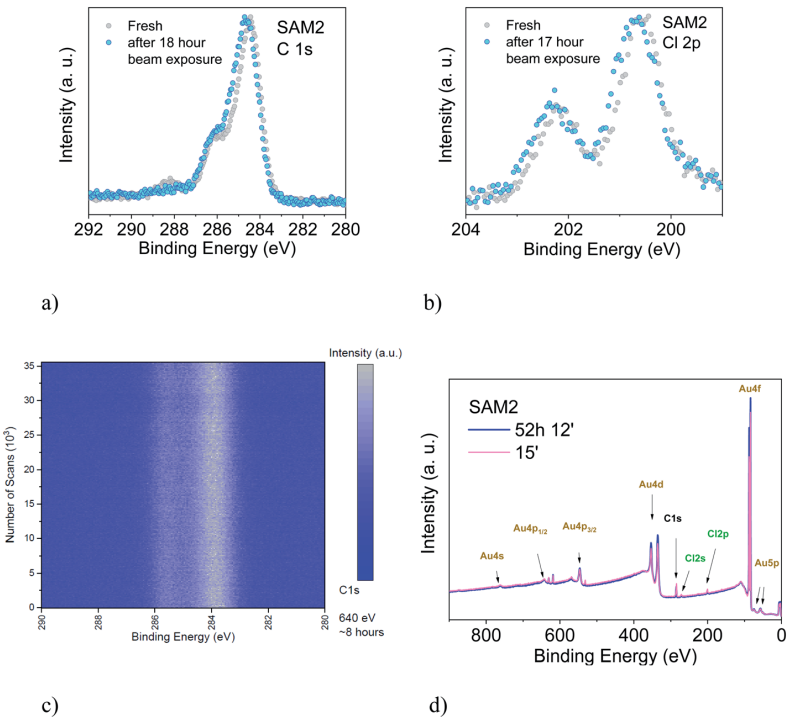

Fig. 6 Upper panel: (a) C 1s and (b) Cl 2p core level spectra of a freshly prepared monolayer and after 18 hours of X-ray exposure, as indicated (photon energy: 1486.6 eV). Intensities are normalized to the peak maximum to allow comparison. Lower panel: (c) time-dependent C 1s core level signal. Color scale: blue represents the background signal; white the initial peak intensity (photon energy: 640 eV). (d) Survey XPS spectra of a freshly prepared monolayer and after 52 hours of X-ray exposure, as indicated (photon energy: 1486.6 eV).

this case, some degree of dynamics, suggesting a change in the layer morphology. These experimental observations seem puzzling in the case of a strong adsorbate–substrate chemical bond. To help in understanding this phenomenon, we can look at one of the most investigated SAM systems: thiolates on gold. Investigations of thiolate–Au surfaces have demonstrated a clear dynamic nature of these surfaces, where the mobility of the adsorbate–Au complex plays an important role, both on flat surfaces as well as on nanoparticles, upon mild annealing and even at room temperature.[87] The mobility is explained in terms of the presence of defects on gold surfaces.[87–90] At defect sites, the interaction between a single gold atom and a covalently attached molecule is stronger than the interaction with the environment (gold atoms and surrounding molecules, respectively) causing the motion of the complete adsorbate + Au assembly on the surface, giving rise to ripening, and even to desorption. This is a very general mechanism of surface diffusion occurring when an adsorbate is strongly bound to coinage metals such as gold.[87,89] The behaviour of the PTM-based SAMs on gold and the resulting XPS spectra observed during prolonged X-ray beam exposure would hint at the fact that such a mechanism also occurs in the present case, favoured or induced by the prolonged X-ray exposure.

Conclusions

Once more, XPS has proved to be a very powerful tool to investigate radical films and radical/metal interfaces, uncovering phenomena not yet known. Furthermore, our XPS method to assess the stability of radical/inorganic interfaces can be applied to any system. In this work, we have investigated the stability of chemically functionalized gold surfaces with a PTM radical, either by preparing the self-assembled monolayers directly from the radical solution or, alternately, by chemical means obtaining the radical on the surface from its diamagnetic precursor. While the chemical stability of the PTM radical is well-known (PTM is considered an inert radical) here we show that the radical monolayers have unprecedented stability under ambient conditions and aggressive X-ray exposure. Extremely prolonged X-ray exposure indicates a dynamic nature of the radical–Au complex, analogously to the case of thiolate–Au surfaces. To our knowledge, this phenomenon has not yet been reported for this class of adsorbate–Au systems. Therefore, further investigations, including annealing experiments and theoretical modelling, are necessary to deepen the understanding of the dynamical aspects of this surface. We cannot exclude that similar phenomena might occur at room temperature also upon prolonged air exposure, with a reaction time of weeks, as seen for thiolate–Au nanoparticles.[87] Although further investigations on the long-term aging pattern of the PTM radical-based layers also depending on different parameters, such as temperature and visible light, are necessary, our results point out that carbon absorption from the ambient environment plays the major role when the monolayer is exposed to air for a long time.

The PTM radical and its derivatives form monolayers that have unprecedented stability properties, confirming that these systems are suitable candidates for market-oriented applications.

Conflicts of interest

There are no conflicts to declare.

Acknowledgements

The authors would like to thank Helmholtz-Zentrum Berlin (HZB) for providing beamtime at BESSY II (Berlin, Germany), and Hilmar Adler, Elke Nadler, and Sergio Naselli for technical support. J. A. de S. is enrolled in the Materials Science PhD program of UAB. J. A. de S. thanks the Spanish Ministry for an FPI fellowship. This work was funded by the Spanish Ministry project FANCYCTQ2016-80030-R and GENESIS PID2019-111682RB-100, the Generalitat de Catalunya (2017SGR918) and the Spanish Ministry of Economy and Competitiveness, through the "Severo Ochoa" Programme for Centers of Excellence in R&D (SEV-2015-0496), the CSIC with the i-Link+ 2018 (Ref. LINKA20128) and CIBERBBN. Financial support from HZB and German Research Foundation (DFG) under the contract CA852/11-1 is gratefully acknowledged.

References

1 F. Troiani and M. Affronte, *Chem. Soc. Rev.*, 2011, **40**, 3119–3129.
2 K. Bader, D. Dengler, S. Lenz, B. Endeward, S.-D. Jiang, P. Neugebauer and J. van Slageren, *Nat. Commun.*, 2014, **5**, 5304.
3 K. S. Pedersen, A.-M. Ariciu, S. McAdams, H. Weihe, J. Bendix, F. Tuna and S. Piligkos, *J. Am. Chem. Soc.*, 2016, **138**, 5801–5804.
4 A. Fernandez, E. Moreno Pineda, C. A. Muryn, S. Sproules, F. Moro, G. A. Timco, E. J. L. McInnes and R. E. P. Winpenny, *Angew. Chem., Int. Ed.*, 2015, **54**, 10858–10861.
5 A. Fernandez, J. Ferrando-Soria, E. M. Pineda, F. Tuna, I. J. Vitorica-Yrezabal, C. Knappke, J. Ujma, C. A. Muryn, G. A. Timco, P. E. Barran, A. Ardavan and R. E. P. Winpenny, *Nat. Commun.*, 2016, **7**, 10240.
6 M. Shiddiq, D. Komijani, Y. Duan, A. Gaita-Ariño, E. Coronado and S. Hill, *Nature*, 2016, **531**, 348.
7 J. M. Zadrozny, J. Niklas, O. G. Poluektov and D. E. Freedman, *ACS Cent. Sci.*, 2015, **1**, 488–492.
8 M. Mas-Torrent, N. Crivillers, C. Rovira and J. Veciana, *Chem. Rev.*, 2011, **112**, 2506–2527.
9 F. Ciccullo, A. Calzolari, K. Bader, P. Neugebauer, N. M. Gallagher, A. Rajca, J. van Slageren and M. B. Casu, *ACS Appl. Mater. Interfaces*, 2019, **11**, 1571–1578.
10 H. Guo, Q. Peng, X.-K. Chen, Q. Gu, S. Dong, E. W. Evans, A. J. Gillett, X. Ai, M. Zhang, D. Credgington, V. Coropceanu, R. H. Friend, J.-L. Brédas and F. Li, *Nat. Mater.*, 2019, **18**, 977–984.

11 X. Ai, E. W. Evans, S. Dong, A. J. Gillett, H. Guo, Y. Chen, T. J. H. Hele, R. H. Friend and F. Li, *Nature*, 2018, **563**, 536–540.
12 M. Mas-Torrent, N. Crivillers, V. Mugnaini, I. Ratera, C. Rovira and J. Veciana, *J. Mater. Chem.*, 2009, **19**, 1691–1695.
13 I. Ratera and J. Veciana, *Chem. Soc. Rev.*, 2012, **41**, 303–349.
14 O. Swiech, R. Bilewicz and E. Megiel, *RSC Adv.*, 2013, **3**, 5979–5986.
15 O. Swiech, N. Hrynkiewicz-Sudnik, B. Palys, A. Kaim and R. Bilewicz, *J. Phys. Chem. C*, 2011, **115**, 7347–7354.
16 A. Kaim, J. Szydłowska, P. Piotrowski and E. Megiel, *Polyhedron*, 2012, **46**, 119–123.
17 E. Megiel, *Adv. Colloid Interface Sci.*, 2017, **250**, 158–184.
18 M. Mannini, L. Sorace, L. Gorini, F. M. Piras, A. Caneschi, A. Magnani, S. Menichetti and D. Gatteschi, *Langmuir*, 2007, **23**, 2389–2397.
19 L. Poggini, G. Cucinotta, L. Sorace, A. Caneschi, D. Gatteschi, R. Sessoli and M. Mannini, *Rendiconti Lincei. Scienze Fisiche e Naturali*, 2018, **29**, 623–630.
20 V. Lloveras, E. Badetti, J. Veciana and J. Vidal-Gancedo, *Nanoscale*, 2016, **8**, 5049–5058.
21 N. Crivillers, C. Munuera, M. Mas-Torrent, C. Simão, S. T. Bromley, C. Ocal, C. Rovira and J. Veciana, *Adv. Mater.*, 2009, **21**, 1177–1181.
22 L. Yuan, C. Franco, N. Crivillers, M. Mas-Torrent, L. Cao, C. S. S. Sangeeth, C. Rovira, J. Veciana and C. A. Nijhuis, *Nat. Commun.*, 2016, **7**, 12066.
23 C. Simão, M. Mas-Torrent, J. Veciana and C. Rovira, *Nano Lett.*, 2011, **11**, 4382–4385.
24 Y.-Z. Dai, B.-W. Dong, Y. Kao, Z.-Y. Wang, H.-I. Un, Z. Liu, Z.-J. Lin, L. Li, F.-B. Xie, Y. Lu, M.-X. Xu, T. Lei, Y.-J. Sun, J.-Y. Wang, S. Gao, S.-D. Jiang and J. Pei, *ChemPhysChem*, 2018, **19**, 2972–2977.
25 M. R. Ajayakumar, I. Alcón, S. T. Bromley, J. Veciana, C. Rovira and M. Mas-Torrent, *RSC Adv.*, 2017, **7**, 20076–20083.
26 T. Heinrich, C. H. H. Traulsen, E. Darlatt, S. Richter, J. Poppenberg, N. L. Traulsen, I. Linder, A. Lippitz, P. M. Dietrich, B. Dib, W. E. S. Unger and C. A. Schalley, *RSC Adv.*, 2014, **4**, 17694–17702.
27 Y.-Q. Zhang, N. Kepčija, M. Kleinschrodt, K. Diller, S. Fischer, A. C. Papageorgiou, F. Allegretti, J. Björk, S. Klyatskaya, F. Klappenberger, M. Ruben and J. V. Barth, *Nat. Commun.*, 2012, **3**, 1286.
28 T. Zaba, A. Noworolska, C. M. Bowers, B. Breiten, G. M. Whitesides and P. Cyganik, *J. Am. Chem. Soc.*, 2014, **136**, 11918–11921.
29 N. J. Tao, *Nat. Nanotechnol.*, 2006, **1**, 173.
30 D. Fracasso, S. Kumar, P. Rudolf and R. C. Chiechi, *RSC Adv.*, 2014, **4**, 56026–56030.
31 F. Bejarano, I. J. Olavarria-Contreras, A. Droghetti, I. Rungger, A. Rudnev, D. Gutiérrez, M. Mas-Torrent, J. Veciana, H. S. J. van der Zant, C. Rovira, E. Burzurí and N. Crivillers, *J. Am. Chem. Soc.*, 2018, **140**, 1691–1696.
32 M. Souto, V. Díez-Cabanes, L. Yuan, A. R. Kyvik, I. Ratera, C. A. Nijhuis, J. Cornil and J. Veciana, *Phys. Chem. Chem. Phys.*, 2018, **20**, 25638–25647.
33 L. Yuan, N. Nerngchamnong, L. Cao, H. Hamoudi, E. del Barco, M. Roemer, R. K. Sriramula, D. Thompson and C. A. Nijhuis, *Nat. Commun.*, 2015, **6**, 6324.
34 J. A. de Sousa, F. Bejarano, D. Gutiérrez, Y. R. Leroux, E. M. Nowik-Boltyk, T. Junghoefer, E. Giangrisostomi, R. Ovsyannikov, M. B. Casu, J. Veciana, M. Mas-Torrent, B. Fabre, C. Rovira and N. Crivillers, *Chem. Sci.*, 2020, **11**, 516–524.
35 K. M. Siegbahn, *Nobel lecture: electron spectroscopy for atoms, molecules and condensed matter*, 2020, http://www.nobelprize.org/nobel_prizes/physics/laureates/1981/siegbahn-lecture.html, accessed 09 June 2020.
36 M. B. Casu, *Acc. Chem. Res.*, 2018, **51**, 753–760.
37 S.-A. Savu, I. Biswas, L. Sorace, M. Mannini, D. Rovai, A. Caneschi, T. Chassé and M. B. Casu, *Chem.–Eur. J.*, 2013, **19**, 3445–3450.
38 R. Kakavandi, S.-A. Savu, L. Sorace, D. Rovai, M. Mannini and M. B. Casu, *J. Phys. Chem. C*, 2014, **118**, 8044–8049.
39 R. Kakavandi, P. Ravat, S. A. Savu, Y. B. Borozdina, M. Baumgarten and M. B. Casu, *ACS Appl. Mater. Interfaces*, 2015, **7**, 1685–1692.
40 F. Ciccullo, N. M. Gallagher, O. Geladari, T. Chasse, A. Rajca and M. B. Casu, *ACS Appl. Mater. Interfaces*, 2016, **8**, 1805–1812.
41 F. Ciccullo, M. Glaser, M. S. Sättele, S. Lenz, P. Neugebauer, Y. Rechkemmer, J. van Slageren and M. B. Casu, *J. Mater. Chem. C*, 2018, **6**, 8028–8034.
42 N. Gallagher, H. Zhang, T. Junghoefer, E. Giangrisostomi, R. Ovsyannikov, M. Pink, S. Rajca, M. B. Casu and A. Rajca, *J. Am. Chem. Soc.*, 2019, **141**, 4764–4774.
43 S. Tebi, M. Paszkiewicz, H. Aldahhak, F. Allegretti, S. Gonglach, M. Haas, M. Waser, P. S. Deimel, P. C. Aguilar, Y.-Q. Zhang, A. C. Papageorgiou, D. A. Duncan, J. V. Barth, W. G. Schmidt, R. Koch, U. Gerstmann, E. Rauls, F. Klappenberger, W. Schöfberger and S. Müllegger, *ACS Nano*, 2017, **11**, 3383–3391.
44 M. R. Ajayakumar, C. Moreno, I. Alcón, F. Illas, C. Rovira, J. Veciana, S. T. Bromley, A. Mugarza and M. Mas-Torrent, *J. Phys. Chem. Lett.*, 2020, **11**, 3897–3904.
45 *Surface analysis – the principal techniques*, ed. J. C. Vickerman and I. S. Gilmore, Wiley, 2nd edn, 2009.
46 N. Crivillers, M. Mas-Torrent, S. Perruchas, N. Roques, J. Vidal-Gancedo, J. Veciana, C. Rovira, L. Basabe-Desmonts, B. J. Ravoo, M. Crego-Calama and D. N. Reinhoudt, *Angew. Chem., Int. Ed.*, 2007, **46**, 2215–2219.
47 O. Travnikova, K. J. Børve, M. Patanen, J. Söderström, C. Miron, L. J. Sæthre, N. Mårtensson and S. Svensson, *J. Electron Spectrosc. Relat. Phenom.*, 2012, **185**, 191–197.
48 K. Siegbahn, C. Nordling, A. Fahlman, R. Nordberg, K. Hamrin, J. Hedman, G. Johansson, T. Bergmark, S.-E. Karlsson, I. Lindgren and B. Lindberg, *ESCA, atomic, molecular and solid state structure studied by means of electron spectroscopy*, Almqvist and Wiksells, Uppsala, 1967.

49 S.-A. Savu, M. B. Casu, S. Schundelmeier, S. Abb, C. Tonshoff, H. F. Bettinger and T. Chassé, *RSC Adv.*, 2012, **2**, 5112–5118.
50 A. Schöll, Y. Zou, M. Jung, T. Schmidt, R. Fink and E. Umbach, *J. Chem. Phys.*, 2004, **121**, 10260–10267.
51 F. Ciccullo, A. Calzolari, I. Píš, S. A. Savu, M. Krieg, H. F. Bettinger, E. Magnano, T. Chassé and M. B. Casu, *J. Phys. Chem. C*, 2016, **120**, 17645–17651.
52 M. Glaser, F. Ciccullo, E. Giangrisostomi, R. Ovsyannikov, A. Calzolari and M. B. Casu, *J. Mater. Chem. C*, 2018, **6**, 2769–2777.
53 R. Kakavandi, A. Calzolari, Y. B. Borozdina, P. Ravat, T. Chassé, M. Baumgarten and M. B. Casu, *Nano Res.*, 2016, **9**, 3515–3527.
54 R. Kakavandi, S.-A. Savu, A. Caneschi and M. B. Casu, *J. Phys. Chem. C*, 2013, **117**, 26675–26679.
55 S. A. Savu, G. Biddau, L. Pardini, R. Bula, H. F. Bettinger, C. Draxl, T. Chasse and M. B. Casu, *J. Phys. Chem. C*, 2015, **119**, 12538–12544.
56 A. Caneschi and M. B. Casu, *Chem. Commun.*, 2014, **50**, 13510–13513.
57 R. Kakavandi, S.-A. Savu, A. Caneschi, T. Chasse and M. B. Casu, *Chem. Commun.*, 2013, **49**, 10103–10105.
58 C. Enkvist, S. Lunell, B. Sjögren, P. A. Brühwiler and S. Svensson, *J. Chem. Phys.*, 1995, **103**, 6333–6342.
59 B. Sjögren, S. Svensson, A. N. d. Brito, N. Correia, M. P. Keane, C. Enkvist and S. Lunell, *J. Chem. Phys.*, 1992, **96**, 6389–6398.
60 M. L. M. Rocco, M. Haeming, D. R. Batchelor, R. Fink, A. Schöll and E. Umbach, *J. Chem. Phys.*, 2008, **129**, 074702.
61 B.-E. Schuster, M. B. Casu, I. Biswas, A. Hinderhofer, A. Gerlach, F. Schreiber and T. Chassé, *Phys. Chem. Chem. Phys.*, 2009, **11**, 9000–9004.
62 M. B. Casu, S.-A. Savu, P. Hoffmann, B.-E. Schuster, T. O. Menteș, M. A. Niño, A. Locatelli and T. Chassé, *CrystEngComm*, 2011, **13**, 4139–4144.
63 M. B. Casu, B.-E. Schuster, I. Biswas, C. Raisch, H. Marchetto, T. Schmidt and T. Chassé, *Adv. Mater.*, 2010, **22**, 3740–3744.
64 *Handbook of X-ray photoelectron spectroscopy*, ed. J. Chastain, 1992.
65 A. W. Taylor and P. Licence, *ChemPhysChem*, 2012, **13**, 1917–1926.
66 M. C. Biesinger, B. P. Payne, A. P. Grosvenor, L. W. M. Lau, A. R. Gerson and R. S. C. Smart, *Appl. Surf. Sci.*, 2011, **257**, 2717–2730.
67 C. M. Woodbridge, D. L. Pugmire, R. C. Johnson, N. M. Boag and M. A. Langell, *J. Phys. Chem. B*, 2000, **104**, 3085–3093.
68 Y. Yokota, Y. Mino, Y. Kanai, T. Utsunomiya, A. Imanishi, M. A. Wolak, R. Schlaf and K.-i. Fukui, *J. Phys. Chem. C*, 2014, **118**, 10936–10943.
69 Y. Yokota, Y. Mino, Y. Kanai, T. Utsunomiya, A. Imanishi and K.-i. Fukui, *J. Phys. Chem. C*, 2015, **119**, 18467–18480.
70 A. P. Grosvenor, B. A. Kobe, M. C. Biesinger and N. S. McIntyre, *Surf. Interface Anal.*, 2004, **36**, 1564–1574.
71 H. Ishii, K. Sugiyama, E. Ito and K. Seki, *Adv. Mater.*, 1999, **11**, 605–625.
72 S. Hüfner, *Photoelectron spectroscopy*, Springer-Verlag, Berlin, Heidelberg, 3rd edn, 2003.
73 T. Graber, F. Forster, A. Schöll and F. Reinert, *Surf. Sci.*, 2011, **605**, 878–882.
74 S. Tanuma, C. J. Powell and D. R. Penn, *Surf. Interface Anal.*, 1991, **17**, 911–926.
75 S. F. Alvarado, M. Campagna and W. Gudat, *J. Electron Spectrosc. Relat. Phenom.*, 1980, **18**, 43–49.
76 D. E. Eastman, T. C. Chiang, P. Heimann and F. J. Himpsel, *Phys. Rev. Lett.*, 1980, **45**, 656–659.
77 R. E. Watson, J. W. Davenport, M. L. Perlman and T. K. Sham, *Phys. Rev. B: Condens. Matter Mater. Phys.*, 1981, **24**, 1791–1797.
78 W. F. Egelhoff Jr, *Surf. Sci. Rep.*, 1987, **6**, 253–415.
79 P. S. Bagus, C. J. Nelin, X. Zhao, S. V. Levchenko, E. Davis, X. Weng, F. Späth, C. Papp, H. Kuhlenbeck and H.-J. Freund, *Phys. Rev. B*, 2019, **100**, 115419.
80 M. B. Casu, Y. Zou, S. Kera, D. Batchelor, T. Schmidt and E. Umbach, *Phys. Rev. B: Condens. Matter Mater. Phys.*, 2007, **76**, 193311.
81 M. B. Casu, *Phys. Status Solidi RRL*, 2008, **2**, 40–42.
82 L. Zhang, H. Peisert, I. Biswas, M. Knupfer, D. Batchelor and T. Chassé, *Surf. Sci.*, 2005, **596**, 98–107.
83 E. E. Rennie, B. Kempgens, H. M. Köppe, U. Hergenhahn, J. Feldhaus, B. S. Itchkawitz, A. L. D. Kilcoyne, A. Kivimäki, K. Maier, M. N. Piancastelli, M. Polcik, A. Rüdel and A. M. Bradshaw, *J. Chem. Phys.*, 2000, **113**, 7362–7375.
84 K. Ueda, M. Hoshino, T. Tanaka, M. Kitajima, H. Tanaka, A. De Fanis, Y. Tamenori, M. Ehara, F. Oyagi, K. Kuramoto and H. Nakatsuji, *Phys. Rev. Lett.*, 2005, **94**, 243004.
85 M. Ballester, J. Castaner, J. Riera, J. Pujadas, O. Armet, C. Onrubia and J. A. Rio, *J. Org. Chem.*, 1984, **49**, 770–778.
86 M. A. Fox, E. Gaillard and C. C. Chen, *J. Am. Chem. Soc.*, 1987, **109**, 7088–7094.
87 T. Bürgi, *Nanoscale*, 2015, **7**, 15553–15567.
88 S. J. Stranick, A. N. Parikh, Y. T. Tao, D. L. Allara and P. S. Weiss, *J. Phys. Chem.*, 1994, **98**, 7636–7646.
89 S. J. Stranick, A. N. Parikh, D. L. Allara and P. S. Weiss, *J. Phys. Chem.*, 1994, **98**, 11136–11142.
90 R. K. Smith, S. M. Reed, P. A. Lewis, J. D. Monnell, R. S. Clegg, K. F. Kelly, L. A. Bumm, J. E. Hutchison and P. S. Weiss, *J. Phys. Chem. B*, 2001, **105**, 1119–1122.

Electronic Supplementary Material (ESI) for Chemical Science.

Stability of radical-functionalized gold surfaces by self-assembly and on-surface chemistry

Tobias Junghoefer,[a]‡ Ewa Malgorzata Nowik-Boltyk,[a]‡ J. Alejandro de Sousa,[b,d] Erika Giangrisostomi,[c] Ruslan Ovsyannikov,[c] Thomas Chassé,[a] Jaume Veciana,[b] Marta Mas-Torrent,[b] Concepció Rovira,[b] Núria Crivillers,[b] Maria Benedetta Casu* [a]

[a]Institute of Physical and Theoretical Chemistry, University of Tübingen, 72076 Tübingen, Germany

[b]Institut de Ciència de Materials de Barcelona (ICMAB-CSIC) and Networking Research Center on Bioengineering Biomaterials and Nanomedicine (CIBER-BBN) Campus de la UAB, 08193 Bellaterra, Spain

[c]Helmholtz-Zentrum Berlin für Materialien und Energie (HZB), 12489 Berlin, Germany.

[d]Laboratorio de Electroquímica, Departamento de Química, Facultad de Ciencias, Universidad de los Andes, 5101 Mérida, Venezuela

‡These authors contributed equally to this work

Contents:

1) SAM2 Survey.

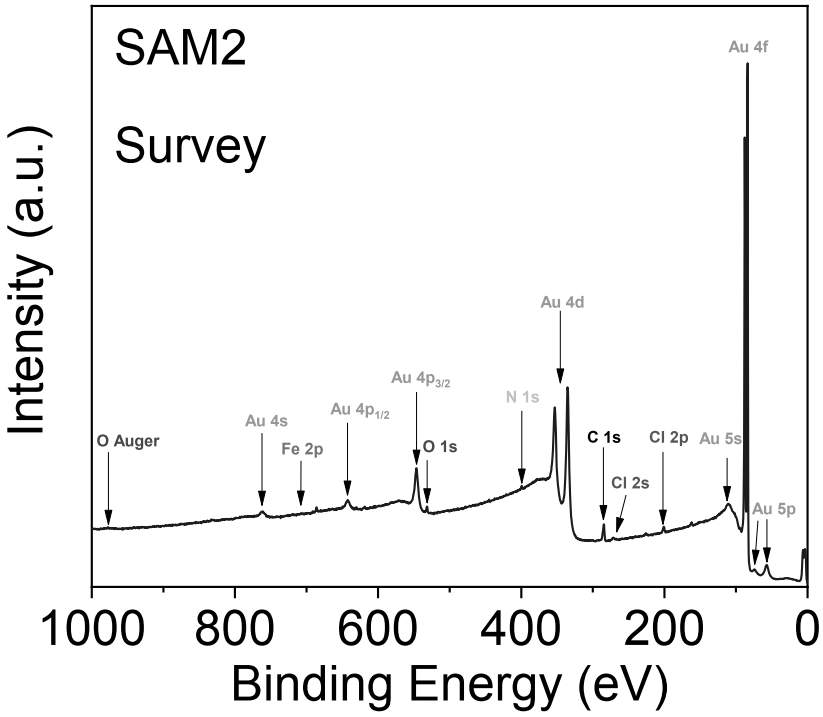

Figure S1. SAM2 XPS survey spectrum (photon energy: 1486.6 eV).

Stoichiometric and experimental elemental ratios for SAM2.

	C	**N**	**Cl**	**Fe**
Sensitivity factor*	0.25	0.42	0.73	3
Number of atoms	50	3	13	1
Theoretical values (%)	75	4	19	2
SAM2F (%)	84.3	5.2	10.0	0.5

Table S1. Stoichiometric and experimental elemental ratios for SAM2.

*C. D. Wagner, *J. Electron Spectrosc. Relat. Phenom.* **1983**, *32*, 99-102.

Table S2. Fit results for the energy positions and relative intensities of the photoemission lines in the SAM2 C 1s spectra.

	Energy (eV)	Lorentzian Width (eV)	Gaussian Width (eV)	Intensity (%)	Theoretical values (%)
C-C	284.2	0.08	1.00	19.9	22
C-H	284.6	0.08	1.00	36.5	46
S_1	285.3	0.08	1.00	11.9	
C-N	285.7	0.08	1.00	6.6	6
C-Cl	286.3	0.08	1.30	21.8	26
S_2	288.1	0.08	1.30	3.3	

C-C + C-H + S_1 = 68.3 %

C-Cl + S_2 = 25.1 %

2) SAM1 Survey.

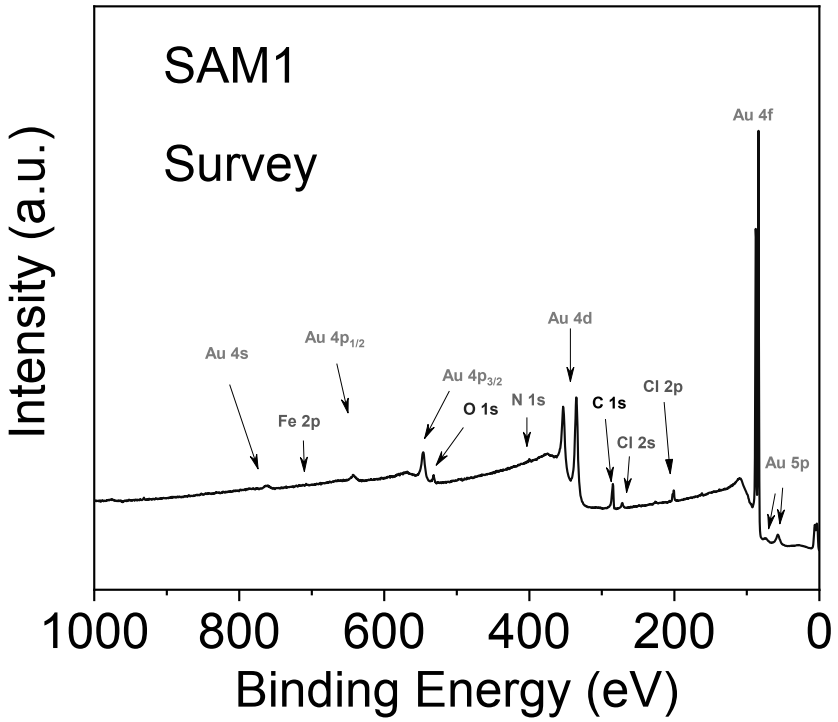

Figure S2. SAM1 XPS survey spectrum of (photon energy: 1486.6 eV).

	C	N	Cl	Fe
Sensitivity factor*	0.25	0.42	0.73	3
Number of atoms	50	3	13	1
Theoretical values (%)	75	4	19	2
SAM1 (%)	79	6	14	1

Table S3. Stoichiometric and experimental elemental ratios for SAM1.

*C. D. Wagner, *J. Electron Spectrosc. Relat. Phenom.* **1983**, *32*, 99-102.

Table S4. Fit results for the energy positions and relative intensities of the photoemission lines in the SAM1 C 1s spectra.

	Energy (eV)	Lorentzian Width (eV)	Gaussian Width (eV)	Intensity (%)	Theoretical values (%)
C-C	284.3	0.08	0.88	23.0	20
C-H	284.9	0.08	0.88	33.4	48
S_1	285.5	0.08	0.88	10.0	
C-N	285.7	0.08	0.89	6.1	6
C-Cl	286.5	0.08	1.10	23.4	26
S_2	288.5	0.08	1.50	4.1	

C-C + C-H + S_1 = 66.4 %

C-Cl + S_2 = 27.5 %

3) C 1s core level spectra at 460 and 640 eV.

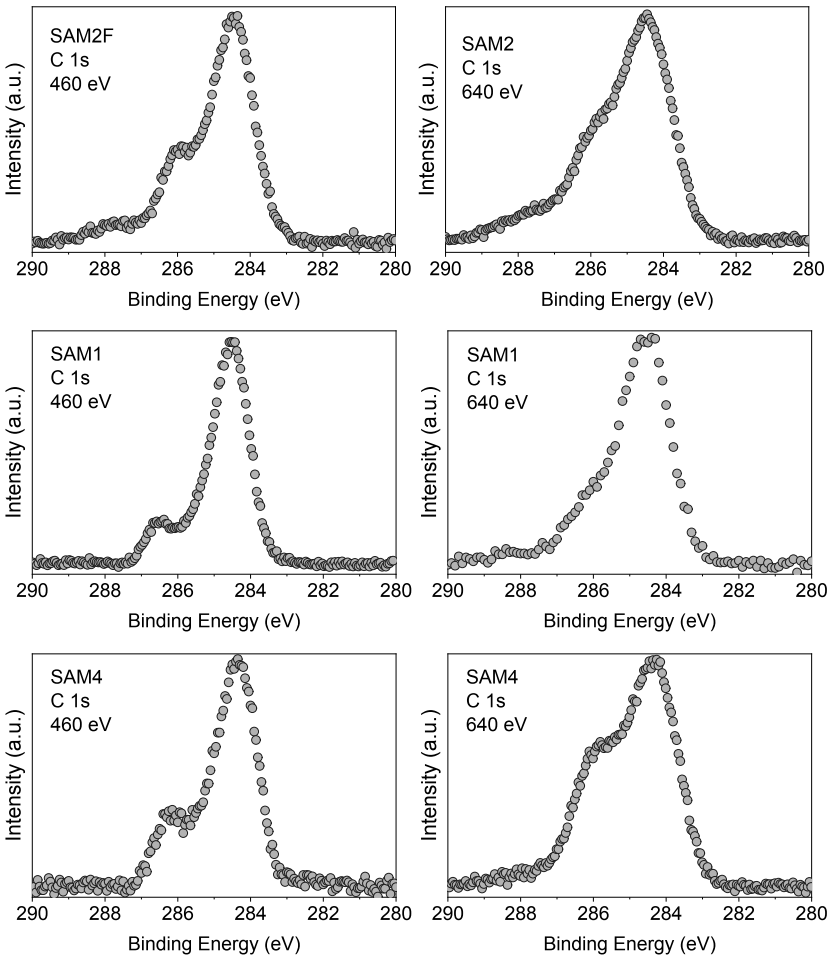

Figure S3. C 1s core level spectra at 460 and 640 eV, as indicated. Upper panel: SAM2. Middle panel: SAM1. Lower panel: SAM4. Intensities are normalized to the peak maximum to allow comparison.

4) Fit results for SAM2 and SAM4 at 460 eV.

Table S5. SAM2 C 1s at 460 eV. Fit results for the energy positions and relative intensities.

	Energy (eV)	Lorentzian Width (eV)	Gaussian Width (eV)	Intensity (%)	Theoretical values (%)
C-C	284.1	0.08	1.05	19.0	22
C-H	284.5	0.08	1.05	41.5	46
S_1	285.1	0.08	1.05	9.0	
C-N	285.5	0.08	1.05	6.5	6
C-Cl	286.1	0.08	1.05	19.0	26
S_2	287.8	0.08	1.35	5.0	

C-C + C-H + S_1 = 69.50 %

C-Cl + S2 = 24.00 %

Table S6. SAM4 C 1s at 460 eV. Fit results for the energy positions and relative intensities.

	Energy (eV)	Lorentzian Width (eV)	Gaussian Width (eV)	Intensity (%)	Theoretical values (%)
C-C	284.1	0.08	1.05	19.3	22
C-H	284.4	0.08	1.05	42.6	46
S_1	285.1	0.08	1.05	9.1	
C-N	285.5	0.08	1.05	6.6	6
C-Cl	286.3	0.08	1.05	18.3	26
S_2	288.1	0.08	1.35	4.1	

C-C + C-H + S_1 = 71 %

C-Cl + S2 = 22.4 %

5) Fit results for SAM2 and SAM4 at 640 eV.

Table S7. SAM2 C 1s at 640 eV. Fit results for the energy positions and relative intensities.

	Energy (eV)	Lorentzian Width (eV)	Gaussian Width (eV)	Intensity (%)	Theoretical values (%)
C-C	284.1	0.08	1.30	17.9	22
C-H	284.5	0.08	1.30	37.7	46
S_1	285.1	0.08	1.30	8.3	
C-N	285.5	0.08	1.30	6.0	6
C-Cl	286.0	0.08	1.30	21.0	26
S_2	287.7	0.08	1.70	9.1	

C-C + C-H + S_1 = 63.9 %

C-Cl + S2 = 30.1 %

Table S8. SAM4 C 1s at 640 eV. Fit results for the energy positions and relative intensities.

	Energy (eV)	Lorentzian Width (eV)	Gaussian Width (eV)	Intensity (%)	Theoretical values (%)
C-C	284.0	0.08	1.30	17.6	22
C-H	284.4	0.08	1.30	37.3	46
S_1	285.0	0.08	1.30	8.4	
C-N	285.5	0.08	1.30	6.1	6
C-Cl	286.0	0.08	1.30	26.8	26
S_2	287.7	0.08	1.70	3.8	

C-C + C-H + S_1 = 63.3 %

C-Cl + S2 = 30.6 %

6) Electrochemical measurements

Cyclic voltammetry experiments were performed with an AUTOLAB 204 potentiostat equipped with NOVA 2.3 software. A Pt mesh was used as the counter electrode, Ag/AgCl 3M KCl was used as reference electrode. For the electrochemical characterization of the SAMs, the modified Au was used as the working electrode (area exposed of 1 cm^2). A 0.2M solution of $TBAPF_6$ in dry CH_2Cl_2 was used as the electrolytic medium, under argon atmosphere.

The redox peaks corresponding to PTM radical ↔ PTM anion and ferrocene ↔ ferrocenium redox process are clearly observed.

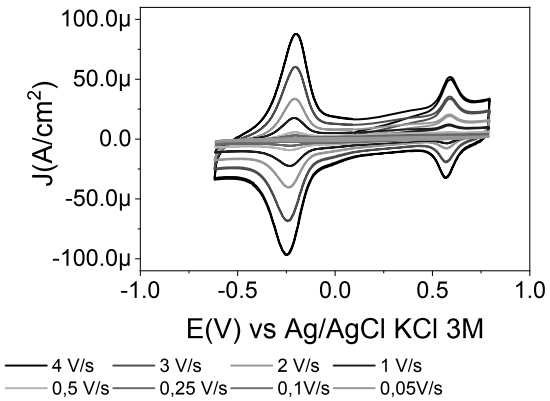

Figure S4. Cyclic voltammetry behavior of SAM4 using as electrolytic medium solution 0.2M $TBAPF_6$/ CH_2Cl_2, under argon atmosphere.

7) Stability under air exposure.

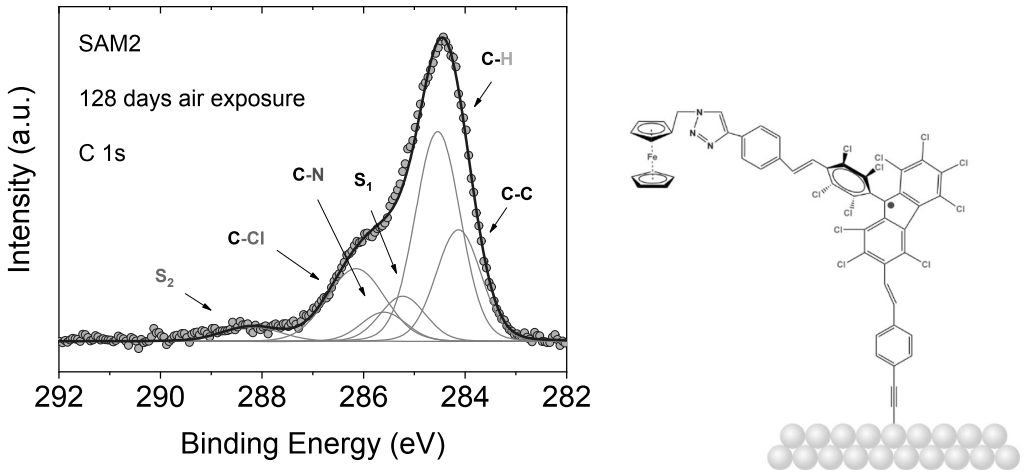

Figure S5. C1s core level spectrum together with its fit analysis after 128 days air exposure. The fit hypothesis was based on the switch to the PPF radical (chemical structure on the right, photon energy: 1486.6 eV).

Table S9. Fit results for the energy positions and relative intensities of the photoemission lines in the SAM2 C 1s spectra after 128 days air exposure, light-induced ring closure hypothesis.

	Energy (eV)	Lorentzian Width (eV)	Gaussian Width (eV)	Intensity (%)	Theoretical values (%)
C-C	284.1	0.08	1.0	22.0	26
C-H	284.5	0.08	1.0	41.3	46
S_1	285.2	0.08	1.0	8.9	
C-N	285.6	0.08	1.0	5.8	6
C-Cl	286.2	0.08	1.3	18.3	22
S_2	288.2	0.08	1.3	3.7	

C-C + C-H + S_1 = 72.2 %

C-Cl + S_2 = 22.0 %

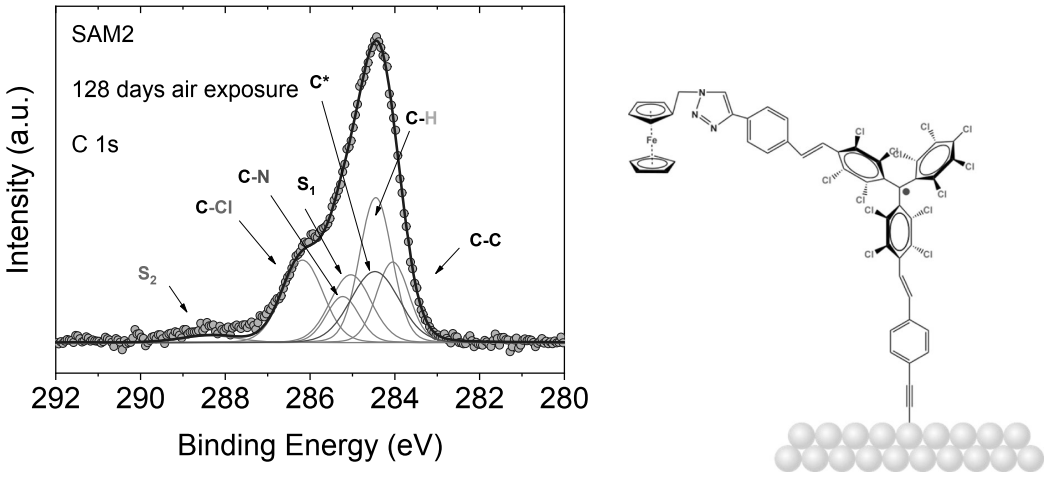

Figure S6. C1s core level spectrum together with its fit analysis after 128 days air exposure. The fit hypothesis was based on considering carbon contaminant adsorption, C*, on intact molecules (chemical structure on the right, see main text) (photon energy: 1486.6 eV).

Table S10. Fit results for the energy positions and relative intensities of the photoemission lines in the SAM2 C 1s spectra after 128 days air exposure, contaminant adsorption, C*; on intact molecules.

	Energy (eV)	Lorentzian Width (eV)	Gaussian Width (eV)	Intensity (%)	Theoretical values (%)
C-C	284.2	0.08	1.0	16.6	22
C-H	284.5	0.08	1.0	30.1	46
S_1	285.3	0.08	1.0	9.9	
C-N	285.6	0.08	1.0	5.2	6
C-Cl	286.2	0.08	1.3	18.1	26
S_2	288.2	0.08	1.3	3.6	
C*	284.5	0.08	1.3	16.5	

8) Stability under beam exposure.

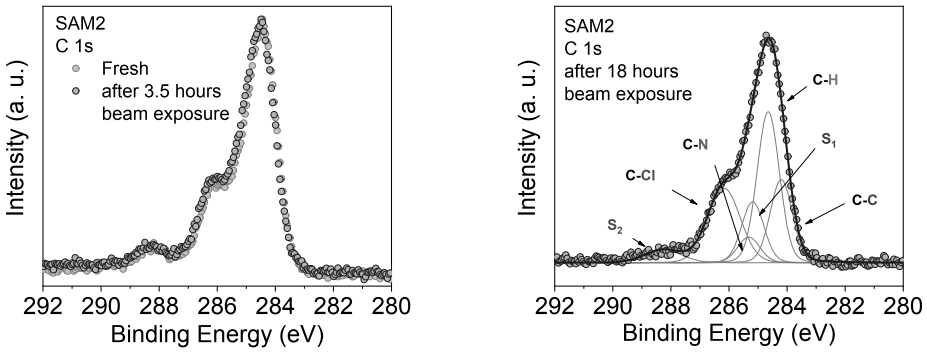

Figure S7. SAM2 C 1s spectra (left) after 3.5 hours beam exposure compared to the fresh film spectrum. No changes are detected. (right) After 18 hours beam exposure, together with its best fit (photon energy: 1486.6 eV).

Table S11. Fit results for the energy positions and relative intensities of the photoemission lines for the fresh film.

	Energy (eV)	Lorentzian Width (eV)	Gaussian Width (eV)	Intensity (%)	Theoretical values (%)
C-C	284.1	0.08	0.86	20.3	22
C-H	284.5	0.08	0.86	36.9	46
S_1	285.2	0.08	0.86	10.5	
C-N	285.3	0.08	0.87	6.1	6
C-Cl	286.2	0.08	1.07	19.8	26
S_2	288.2	0.08	1.40	6.4	

Table S12. Fit results for the energy positions and relative intensities of the photoemission lines after 18 hours X-ray (photon energy: 1486.6 eV).

	Energy (eV)	Lorentzian Width (eV)	Gaussian Width (eV)	Intensity (%)	Theoretical values (%)
C-C	284.2	0.08	0.86	20.5	22
C-H	284.7	0.08	0.86	36.0	46
S_1	285.3	0.08	0.86	11.1	
C-N	285.4	0.08	0.87	6.3	6
C-Cl	286.2	0.08	1.18	22.4	26
S_2	288.1	0.08	1.51	3.7	

D. Challenges in Controlled Thermal Deposition of Organic Diradicals

Reprinted with permission from
T. Junghoefer, N. M. Gallagher, K. Kolanji, E. Giangrisostomi, R. Ovsyannikov, T. Chassé, M. Baumgarten, A. Rajca, A. Calzolari, M. B. Casu, "Challenges in Controlled Thermal Deposition of Organic Diradicals", *Chemistry of Materials* **2021**, *33*, 2019–2028, DOI 10.1021/acs.chemmater.0c03880.

http://pubs.acs.org/articlesonrequest/AOR-QPYHVUYT85DIMPHHZJTM

CHEMISTRY OF MATERIALS

pubs.acs.org/cm

Article

Challenges in Controlled Thermal Deposition of Organic Diradicals

Tobias Junghoefer, Nolan M. Gallagher,[#] Kubandiran Kolanji,[#] Erika Giangrisostomi, Ruslan Ovsyannikov, Thomas Chassé, Martin Baumgarten, Andrzej Rajca, Arrigo Calzolari, and Maria Benedetta Casu*

Cite This: *Chem. Mater.* 2021, 33, 2019−2028

Read Online

ACCESS | Metrics & More | Article Recommendations | Supporting Information

ABSTRACT: We demonstrate that it is possible to evaporate diradicals in a controlled environment obtaining thin films in which the diradical character is preserved. However, evaporation represents a challenge. The presence of two radical sites makes the molecules more reactive also in the case of very stable single radicals. We have explored the parameters that play a role in this phenomenon. We found that the higher the formation energies of the crystal, the more difficult is the evaporation of intact radicals. Large delocalization of the unpaired electrons helps the diradical to stand evaporation. We have also investigated the lifetime of the films when exposed to X-rays or air. The onset of thermal degradation plays a role in the film lifetime. In fact, the lower the evaporation temperature with respect to the onset temperature, the longer is the film lifetime. The evaporation of different diradicals can be successfully addressed considering our findings.

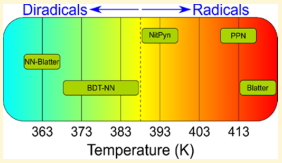

INTRODUCTION

Technology based on quantum phenomena, such as entanglement and superposition, is taking the lead in various fields. Its fast development involves a strong multidisciplinary approach including a new technological vision in terms of applications and devices, new algorithms, and materials. The latter implies not only the strategic use of materials but also their discovery and design.[1] Among the materials candidate to play a role in emerging quantum technologies, organic materials and, particularly, radicals have recently attracted much attention.[2−6] Inert organic radicals and their derivatives are metal-free carbon-based molecules with one unpaired electron that are demonstrated to be stable enough to match technical requirements, such as evaporation and film processing.[7−13] The restriction to a single spin per molecule constitutes a limitation for many spintronic applications,[2,4,5] so the synthesis and controlled growth of films of multi-spin radicals constitute a paramount step forward in the field. Diradicals have two unpaired electrons, each localized in a specific chemical group in the molecule. The singlet and triplet states in these molecules are in competition as a ground state. High spin diradicals with large energy gap between the triplet and singlet states are interesting because of their potential use in applications, such as sensors, memories, and quantum gates.[14−18] These technologies require a very high degree of control in attaching to a surface single or few spin systems in quantum gates or a larger number of spins for sensors.

However, the implementation of diradicals in real devices has been hampered by the fact that their controlled evaporation and deposition onto a substrate were considered practically impossible to achieve because of their high reactivity. Huang et al.[19] stated that the general rule of thumb is that the more unpaired electrons in a molecule has, the worse its thermal stability is. Thus, they excluded that diradicals could be evaporated because they would decompose during sublimation.[19]

Inspired by the promising technological opportunities offered by diradicals, we have tackled the problem of their evaporation. The nitronyl nitroxide (NN)[20] and Blatter single radicals[21] are stable against evaporation, and they have good film forming properties when fused to suitable substituents such as pyrene.[7,8,22] Controlled preparation techniques using Knudsen cell evaporation and electrospray deposition are a good choice for growing films of sensitive molecules or single-molecule magnets.[13,23,24] Thus, we chose organic molecular beam evaporation (OMBD), which allows to tune the preparation parameters to suit the film forming properties of the molecule.[25] The thin films were prepared in situ under ultrahigh vacuum (UHV) conditions by using opportunely calibrated Knudsen cells. Here, we report the successful controlled evaporation of a diradical obtained fusing the NN radical to a derivative of the Blatter radical ($C_{26}H_{25}N_5O_2$, NN-Blatter, Figure 1, S = 1)[12] and of a derivative of the benzodithiophene decorated with two NN radicals ($C_{26}H_{32}N_4O_6S_2$, BTD-NN, Figure 1, S = 1/2)[26] to identify the specific parameters that play a role for evaporation and film stability (Table 1). To fully investigate the problem of diradical

Received: October 2, 2020
Revised: January 8, 2021
Published: January 27, 2021

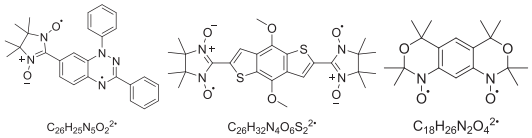

Figure 1. NN-Blatter (left), BTD-NN (middle), and dinitroxide (right) structures are shown.

evaporation, we have also evaporated a third diradical, a dinitroxide diradical with S = 1 ($C_{18}H_{26}N_2O_4$, Figure 1).[27]

Table 1. Main Properties of the Investigated Diradicals

parameter	BDT-NN	NN-Blatter	dinitroxide
formula	$C_{26}H_{32}N_4O_6S_2$	$C_{26}H_{25}N_5O_2$	$C_{18}H_{26}N_2O_4$
formula weight (g/mol)	560.67	481.97	334.41
density (g/cm^3)	1.332	1.363	1.297
spin	1/2	1	1
magnetic interaction	weak AFM	strong AFM	weak AFM
intramolecular ordering	dimer	1D chains	1D chains
evaporation temperature (K)	373−383	363	363

We have investigated the thin films (in the nanothickness regime) by using X-ray-based techniques and ab initio calculations, focusing on diradical film processes and the consequent challenges that must be addressed to successfully evaporate and grow diradical thin films. Furthermore, we investigated the film lifetime under X-ray and air exposure.

RESULTS AND DISCUSSION

We used X-ray photoelectron spectroscopy (XPS) to investigate the thin films because it is proven to be an efficient tool for the investigation of organic radical thin films.[13] The method is element-sensitive and allows insights into the stoichiometry of the film, and it is sensitive toward the different chemical environments of atoms of the same element.[28]

We focus on the C 1s and N 1s core level spectra (for NN-Blatter in Figure 2). The O 1s core level spectrum is the sum of the substrate (SiO_2/Si(111) wafers) and molecule signals, making the analysis less reliable. The important is that the spin densities are mainly localized in the nitrogen centres.[8,26,29,30] Therefore, the information on the radical is substantially delivered by the N 1s core level spectra. The NN-Blatter N 1s spectrum is composed of two main features. Two contributions originated by the photoelectrons emitted by the nitrogen atoms in the 2- and 4-positions of the 1,2,4-benzotriazinyl moiety are visible and are centered around 400 eV. At higher binding energies, the emitted photoelectrons from the two chemically equivalent nitrogen atoms of the nitronyl nitroxide moiety combine with those of the nitrogen atom in the 1-position of the 1,2,4-benzotriazinyl moiety to form a broad peak with its highest intensity above 402 eV. The C 1s core level spectrum shows a main line at around 285 eV and a pronounced shoulder at higher binding energies. The main line contains the contributions from the emission of photoelectrons in the aromatic rings, as well as the contributions from carbon atoms bound to other carbon atoms and hydrogen atoms (C−C, C−H, C−H_3). The shoulder is due to the signal of the

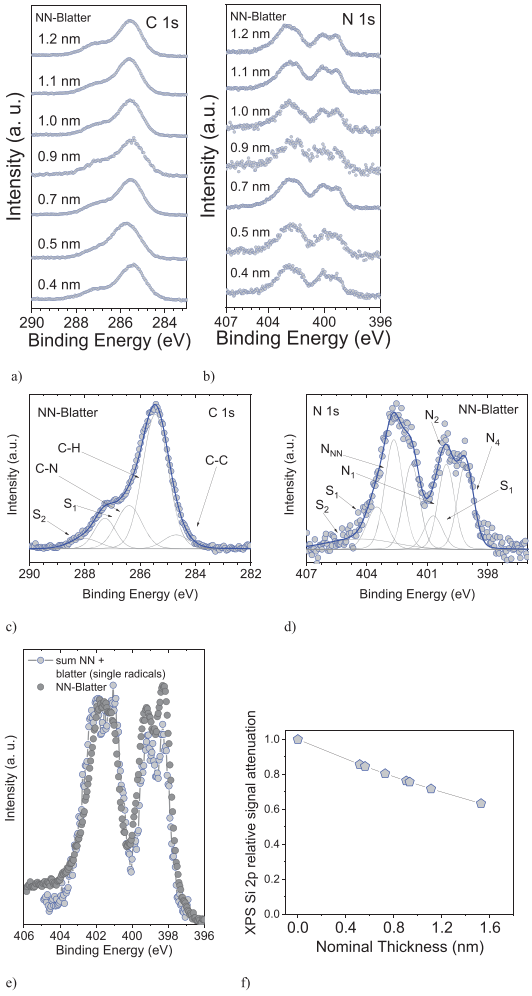

Figure 2. NN-Blatter (a) C 1s and (b) N 1s thickness-dependent core-level spectra of the NN-Blatter thin films, thickness as indicated. NN-Blatter (c) C 1s and (d) N 1s spectra with their best fit for the nominally 0.4 nm thick film. (e) N 1s core level spectrum obtained as a sum of the core level spectra of the single radicals (NN + Blatter radical[7,8]) compared to the NN-Blatter N1s core level spectrum as in (b). (f) Attenuation of the Si 2p XPS signal, normalized to the corresponding clean substrate signal, as a function of the film nominal thickness (the line is a guide to the eye).

photoelectrons emitted from carbon atoms bound to nitrogen atoms, which lie at higher binding energies due to the shift of charge toward the more electronegative nitrogen and resulting decrease in electron density on the carbon atoms.

Figure 2 shows the thickness-dependent C 1s and N 1s core level spectra, and it includes the typical best fit curves for the two core level spectra. The fit is forced by tight physical and chemical constraints (for details, see the Supporting Information and refs[7,12]31, and 32). The result indicates that the stoichiometry of the diradical film after evaporation and deposition corresponds to the theoretical values and, thus, that

https://dx.doi.org/10.1021/acs.chemmater.0c03880
Chem. Mater. 2021, 33, 2019−2028

the diradical character of the molecule is maintained throughout the complete process.[12]

We also observe that there is a difference in the binding energy of the emitted photoelectrons when adopting a stepwise evaporation instead of a direct evaporation. The stepwise evaporation leads to a shift of the N 1s and C 1s spectra toward lower binding energies (Figure 3). This shift may be understood in terms of a change in the film morphology.[33] In fact, the increase of the thickness in organic thin films (e.g., monolayer vs islands) leads to a less efficient screening of the core-hole created upon photoemission, by the corresponding substrate mirror charge.[33]

We explain our result considering that the NN-Blatter films grow following the Volmer–Weber (VW) growth mode,[12] i.e., purely island growth in case of direct evaporation, as it is also confirmed by the atomic force microscopy images of the films that clearly show island formation (Figure 3). Once the islands are formed during deposition, a successive evaporation adds molecules on the substrate left free from the first deposition. This leads to contributions in the XPS spectra due to photoelectrons coming from thinner regions of the assembly, that is, closer to the substrate and characterized by a more efficient screening of the core-hole (Figure 3). Note that the screening of the core-hole by an image charge is observable at the organic/metal-oxide interface; however, its effect is weaker than in metal substrates.[34] We also observe that the shift is nonrigid (0.4 eV for the N 1s and 0.2 eV for the C 1s main line, respectively). Nonrigid shifts may have different reasons: the image charge of the core-hole originates in elements at a different height from the substrate because the molecules are not completely planar or from a fractional charge transfer from the substrate to the adsorbate in physisorption.[35,36] To investigate this aspect, we performed an annealing experiment and we measured near-edge X-ray fine structure (NEXAFS) spectroscopy. In general, the island growth mode in thin films is driven by the intermolecular interaction being stronger than the interaction between adsorbate and substrate that cannot hence act as a template.[37] To evaluate the role played by the interaction with the substrate, an annealing experiment is very useful. The films were subsequently annealed at 323, 388, and 483 K, respectively, for 30 min at each temperature step (Figure 4). The complete desorption at 483 K indicates that the interaction with the substrate is very weak: the molecules are physisorbed on the SiO_2 surface. We also note that the films are remarkably stable up to 388 K (Figure 4). To investigate the orientation of the molecules on the substrate,

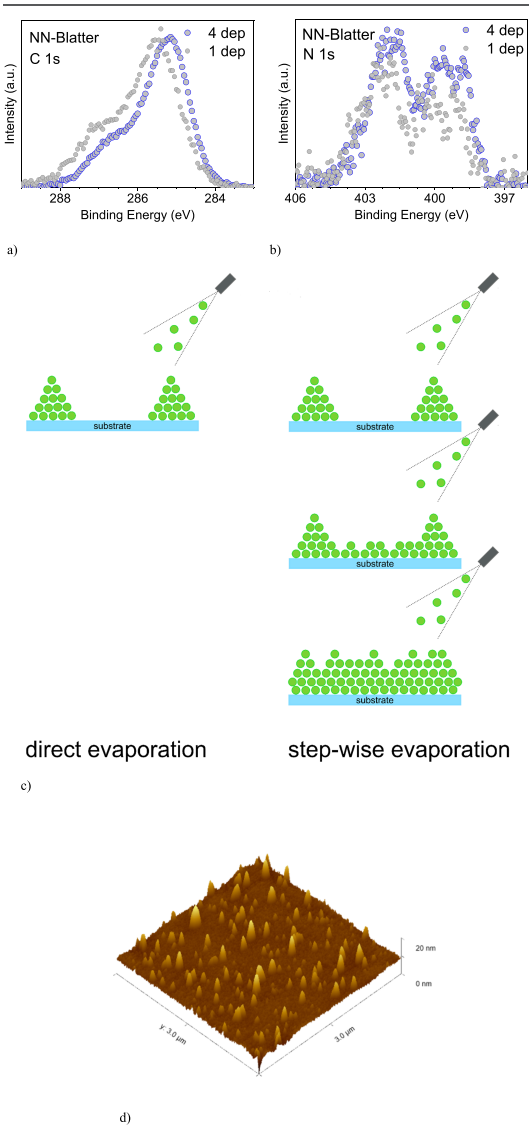

Figure 3. NN-Blatter (a) C 1s and (b) N 1s core level spectra: direct (grey dots) vs stepwise (blue dots) deposition (substrates kept at room temperature in both cases). (c) Sketch of the growth mode in the two cases. (d) A typical 3 μm × 3 μm atomic force microscopy image of a NN-Blatter thin film (direct evaporation).

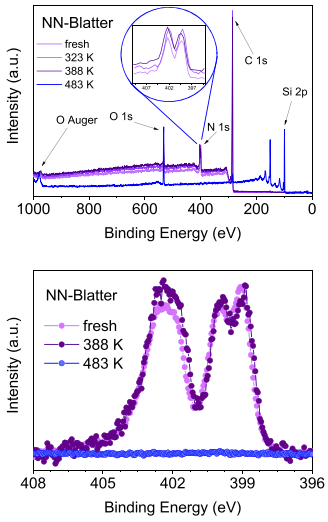

Figure 4. (Upper panel) NN-Blatter XPS survey spectra (lower panel) together with the detailed N 1s core level spectra at different annealing temperatures, as indicated.

https://dx.doi.org/10.1021/acs.chemmater.0c03880
Chem. Mater. 2021, 33, 2019−2028

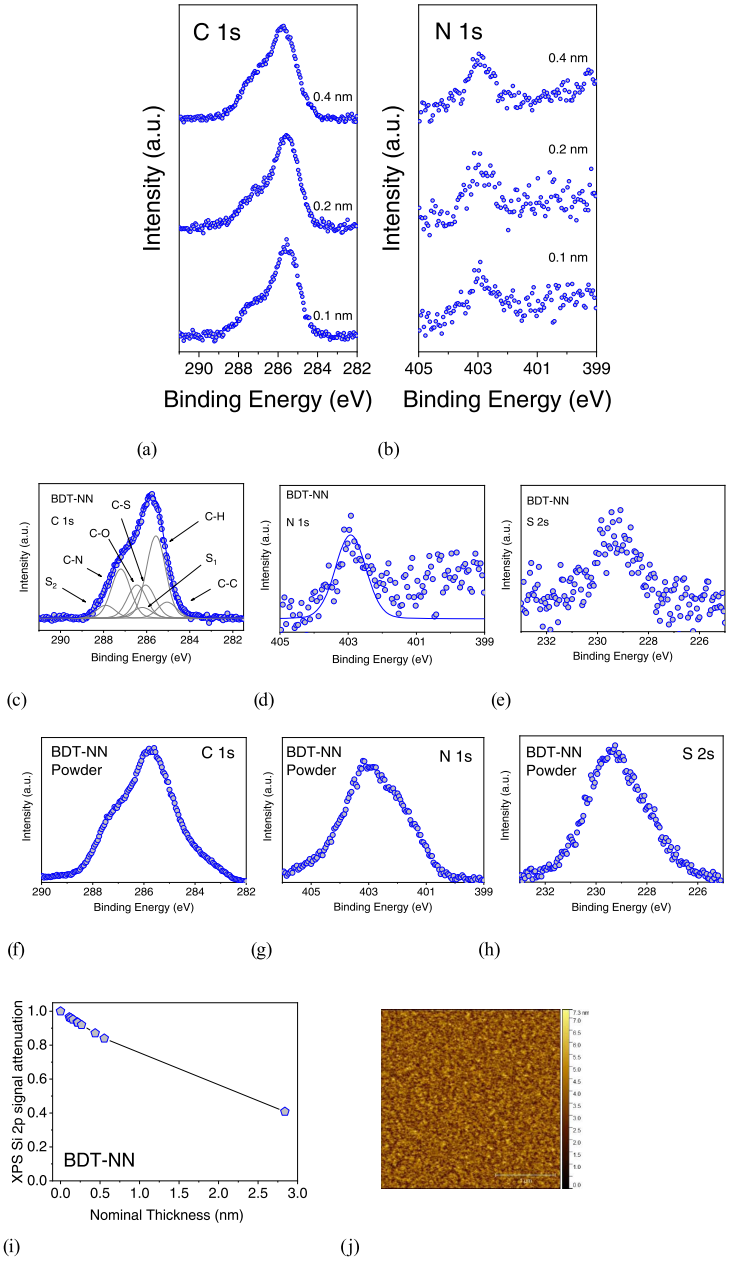

Figure 5. BTD-NN (a) C 1s and (b) N 1s thickness-dependent core-level spectra of the BTD-NN thin films, thickness as indicated. (c) C 1s, (d) N 1s, and (e) S 2s core-level spectra of the BTD-NN thin films (0.1 nm nominal thickness), compared to the correspondent spectra of the powder, (f)−(h), as indicated. (i) Attenuation of the Si 2p XPS signal, normalized to the corresponding saturation signal, as a function of film nominal thickness (the line is a guide to the eye). (j) A typical 5 μm × 5 μm atomic force microscopy image (2.9 nm nominal thickness).

we performed NEXAFS spectroscopy, which provides information on the unoccupied states and film structure (see the Supporting Information and Figure S1). We observe a NEXAFS dichroism that indicates that the molecules are not aligned with respect to the substrate,[38] generating a different image charge for carbon and nitrogen atoms because of the different distance from the substrate. This is reflected by and it is the reason for the XPS nonrigid shift.

The poor air stability of the NN-Blatter thin films[12] hinders ex situ investigations traditionally used to directly probe the

https://dx.doi.org/10.1021/acs.chemmater.0c03880
Chem. Mater. 2021, 33, 2019−2028

radical persistence, such as electron paramagnetic resonance spectroscopy. To dispel any doubts on the radical character in the films, besides using the fit procedure, we adopted several strategies as follows: (1) the comparison of the thin film core-level spectra with the same spectra obtained for the powder that show the same features, confirming the stoichiometry argument (see ref 12 and the Supporting Information). (2) The comparison of the N 1s core level spectra with N 1s core level spectra obtained as a stoichiometric sum of the single radical thin films, i.e., the NN and Blatter radical,[7] as shown in Figure 2, that prove the agreement between the NN-Blatter experimental N 1s core level spectrum and N 1s core level sum spectrum. (3) The use of ab initio calculations to further verify that the experimental occupied and unoccupied states correspond to intact diradicals (see below). This approach clearly shows that we evaporated the NN-Blatter without degradation.

To figure out which physical quantities play a role in growing diradical thin films by evaporation, we evaporated a second diradical (BTD-NN, Figure 1) adopting the same procedure as for the NN-Blatter thin films. We have chosen BTD-NN because it is a diradical that forms weakly antiferromagnetically coupled spin dimers of S = 1/2 moieties.[26] The distance between the two NN groups in the molecule is 0.7 nm (0.987 nm is the distance between the carbon atoms that are the radical centers). Its density is similar to and its molecular weight is slightly higher than NN-Blatter.[26] The idea behind this choice is to explore the influence of the magnetic coupling and the radical interaction on the film evaporation, growth, and stability (see also Table 1). The core level spectra are shown in Figure 5, together with the powder spectra.

Analogously to what we observed for NN-Blatter, we found that the BTD-NN film C 1s spectrum is characterized by a main line at 285.8 eV due to photoelectrons emitted from the atoms in the aromatic ring and carbon atoms bound to hydrogen atoms. The shoulder at higher binding energy is due to contributions from the electrons emitted from hetero-bound carbon atoms. The two nitrogen atoms belonging to the nitronyl nitroxide radical have an equivalent chemical environment; thus, we expect a single line in the N 1s spectrum. Indeed, this is the case with the main line at 403 eV. We also observe signal intensity at lower binding energy, indicating that a very small amount of nitronyl nitroxide radicals switched to the imino nitroxide radicals.[20,22,39] This switch is already present in the powder, as shown by the N1s line shape (Figure 5g). Note that, in this case, we do not observe any binding energy shift with thickness, although we have deposited also very (nominally) thin films (Figure 5a,b). This indicates that the diradicals are very weakly physisorbed on the SiO_2 wafer, without creating any image charge at the interface, similarly to the single radical NN derivative on inert substrates.[7] To shed light on the growth mode of the BTD-NN films, we followed the XPS core level signal of the substrate (Si 2p) by looking at its attenuation upon film deposition (Figure 5i). The curve is characterized by a very slow decay. This intensity trend is typical of the Volmer−Weber growth mode, i.e., island growth.[40] The atomic force microscopy ex situ images are consistent with this observation, clearly showing a film morphology dominated by islands (Figure 5j).

Following the same argument as for NN-Blatter, we can conclude that the evaporation of the BTD-NN films is successful because of (1) the agreement of the film stoichiometry with the theoretical values, (2) the agreement between film and powder spectra (see Tables S3 and S4 and Figure 5) the ab initio calculations (see the Supporting Information). Also in this case, the evaporation temperature (373−383 K) is lower than in the case of the single NN.[7] In the case of the BTD-NN films, we also observed an enhanced beam sensitivity with respect to the single NN radical derivatives that hinders the extensive use of X-ray techniques such as NEXAFS (Figure S3). The diradical samples were measured like the single radical derivative at room temperature using a monochromatized Al Kα lab source. The radiation damage occurs on a shorter time scale in comparison with the single radical derivative, and it does not depend on the sample thickness. (see also Table S5 in the Supporting Information).

To gain further insights, we carried out a first-principle study, based on density functional theory (DFT), of the structural, electronic, and magnetic properties of both diradicals in the isolated (i.e., single molecule) and aggregated (i.e., bulk-like) phases. DFT calculations cannot always assess the right exchange interaction and, thus, the magnetic character of the radical systems, also in the case of the Blatter radical.[30,41] On the contrary, our method shows a nice agreement with the experimentally determined magnetic character (see the Supporting Information for details).

Our results for the relative energetic stability are summarized in Figure 6. In the ground state, the NN-Blatter solid phase

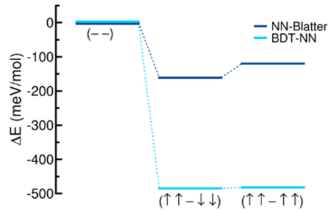

Figure 6. Total energy difference ΔE of the bulk crystals, as a function of the total magnetization, with respect to the nonmagnetic (− −) phase. Labels (↑↑−↓↓) and (↑↑−↑↑) correspond to AF and FM long-range (intermolecular) spin alignment and correspond to $M_T = 0$, and $8\mu_B$/cell, respectively.

exhibits a different short-range (intra-molecular) and long-range (inter-molecular) spin alignment distribution, which corresponds to a $M_T = 0 M_T = 0\mu_B$/cell and $M_A = 8.23$ cell, where M_T and M_A are the total and absolute magnetization, respectively (see Supporting Information for definitions and further details). The spins remain parallelly oriented (↑↑) within each single molecule, while they arrange in chains with AF order between next-neighbor molecules, (↑↑−↓↓), in agreement with the experimental evidence.[12,26] The fully parallelly oriented spin configuration, i.e., the FM state (↑↑−↑↑), is energetically less favored by 41 meV/mol than the AF phase.

BDT-NN crystal may be stabilized in both FM and AF phase at the same total energy, being the AF state only 2 meV/mol more stable than the FM one. In both cases, the absolute magnetization is $M_A = 8.5\mu_B$/cell, while $M_T = 8.0\mu_B$/cell and $M_T = 0$ $M_T = 0.0\mu_B$/cell, for the FM and AF state, respectively. The weak AF behavior detected in the experiments can be thus interpreted as a sequence of weak interacting S = 1/2 NN radicals. The different long-range spin arrangement also affects the DOS of the two bulk crystals and is shown in Figure S6.

https://dx.doi.org/10.1021/acs.chemmater.0c03880
Chem. Mater. 2021, 33, 2019−2028

To confirm this analysis, we simulated the N 1s XPS spectra for the two diradicals (Figure 7), in the single molecule

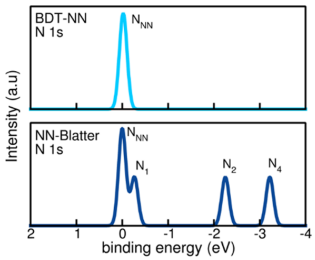

Figure 7. Simulated X-Ray N 1s core level spectra of BDT-NN (upper panel) and NN-Blatter (bottom panel) in the isolated molecule configuration. The NN peak is assumed as a zero energy reference for all spectra.

configuration. The XPS spectra of BDT-NN (top panel) are dominated by one-single peak relative to the N_{NN} atoms that result to be almost indistinguishable. Solid-state packing does not change this picture, in agreement with the experimental results. We conclude that each NN unit, both in the molecular and in the solid-state phase, remain intrinsically independent and weakly coupled to the rest of the molecule or to the environment (i.e., S = 1/2 single radicals). On the contrary, the intramolecular interactions affect the N 1s spectra of the NN-Blatter (bottom panel). Four peaks are clearly visible, the one at higher binding energy corresponds to the NN site; the other three (N_1, N_2, N_4) to the Blatter component, in very good agreement with the analysis of experimental data in Figure 2d.

The agreement between experiments and calculations that describes both the magnetic character and the electronic structure of the diradicals allows using the calculations to shed light on the complexity of the diradical evaporation.

A large variety of novel, chemically stable radicals under ambient conditions were synthesized in recent years.[20,21,42−48] It was found that, among them, the radicals that can stand evaporation are characterized either by protection of the unpaired spin centers with steric hindrance or by very large delocalization of the unpaired electron.[13,49] The controlled evaporation in UHV of a radical is more complicated than in the case of closed shell molecules: the temperature window available for a successful evaporation is very narrow, and it is difficult to keep the evaporation rate stable. In general, the Knudsen cell temperature for radical evaporation in UHV varies in the range between 390 and 420 K (Figure 8). Using higher evaporation temperatures damages the radical. This is a clear difference in comparison with closed shell systems that stand much higher temperatures.[50,51] In the case of NN-Blatter, the optimized evaporation temperature is significantly

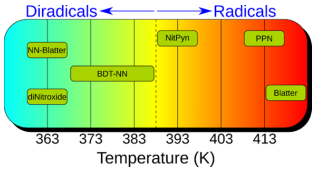

Figure 8. Schematic diagram of the evaporation temperature range for several diradicals and radicals.

lower than in the case of the NN and Blatter radicals taken separately (373 K vs 393 and 418 K, respectively[7,8]). The space of evaporation parameters, such as pressure, substrate temperature, evaporation temperature, is very limited: on the one hand, the evaporation temperature must be low enough to avoid damaging the radical (the upper limit is given by the onset of degradation in the thermal gravimetric analysis (TGA)); on the other hand, it must be high enough to overcome the intermolecular interaction, leading to sublimation. Similar arguments also apply for the substrate temperature and post-growth temperature treatments.

Thus, we investigated the thermodynamic stability of the two compounds, by evaluating the formation energies of the crystal bulk (E_{for}), with respect to the single molecule components: $E_{for} = (E_{cry} - 4E_{mol})/4.0$, where E_{cry} is the total energy of the crystalline bulk including 4 diradicals per cell and E_{mol} is the total energy of the isolated molecules. Both bulk structures are energetically very stable with $E_{for} = -1.6$ and -0.9 eV/mol, for BDT-NN and NN-Blatter, respectively. We further checked the effect of the dichloromethane units that stabilize the NN-Blatter crystal structure.[12] We prepared and reoptimized the atomic structure of a second crystal that does not included the CH_2Cl_2 molecules. Note that their presence has no effect on the magnetic order of the system but affect its stability. In fact, the formation energy of NN-Blatter reduces to -0.4 eV/mol when dichloromethane is not included in the system.

We have gained at this point a full picture of the systems that allows us to answer the initial question on why the diradicals are difficult to evaporate. Our results show that the strength of the antiferromagnetic interaction does not play a role since we observe a very similar behavior for both radicals that have different strength and sign of interactions. While NN-Blatter possesses a strong ferromagnetic interaction between the two radical sites with a weak antiferromagnetic intrachain formation, the BDT-NN has a medium-sized antiferromagnetic interaction between the spin centers. Other parameters that intuitively could play a role do not contribute either: in fact, the distance between the radical sites does not influence (in this case, 1.0 vs 0.7 nm) nor does the spin (1 vs two 1/5). Thermodynamics is the key. The two diradicals assemble in stable aggregates (high E_{for}), which includes both the initial powder (before evaporation) and the final films (after deposition). On the one hand, to evaporate the molecules, it is necessary to provide enough thermal energy (i.e., increasing the temperature) to release each molecule to its gas phase from the initial crystalline powder. On the other hand, temperature cannot be arbitrarily increased to avoid compromising the integrity of the molecules. Once the molecules reach the substrate, they easily tend to reaggregate growing in compact island rather than in ordered planar films (Figures 3 and 5). Kinetics most probably affects the morphology and size rather than the formation of the molecular islands.

Finally, we find that the diradical film stability in ambient air is extremely limited in comparison with the one observed for the NN and Blatter radical thin films[7,8] (Figure S2). Therefore, at this point, we intend to address the enhanced instability of the diradical films when exposed to X-rays and air. X-ray exposure is important not only to correctly perform the present experiments but it gives a direct comparison with standard closed shell organic molecules that are known to be stable under the soft X-rays.

https://dx.doi.org/10.1021/acs.chemmater.0c03880
Chem. Mater. 2021, 33, 2019−2028

The air stability is of special significance for investigations with ex situ techniques and for applications.

In both cases, the term stability indicates the film lifetime, i.e., how long the films can stand beam or air exposure at room temperature, without showing changes in the electronic structure that indicate radical degradation.

We observe that comparing, diradical to radical films, the number of radical sites makes a difference, also when comparing the same radical in single or diradical configuration, e.g., films of single NN derivatives are more stable than the BTD-NN films (see Table S5). However, the NN-Blatter thin films are more robust than the BTD-NN thin films. If we look at the molecular structure, BTD-NN carries two NN, with the two unpaired electrons delocalized over the two NO groups, one in each radical. NN-Blatter on the contrary carries only one NN radical and one Blatter radical. The delocalization of the unpaired electron in the present Blatter radical derivative is quite extended, as proved by the calculations (see the Supporting Information). In general, the films of the Blatter radical derivatives are more stable than those of the NN derivatives.[8,22] This difference is strongly enhanced when two NN radicals are present in the same molecule, as it is the case for BDT-NN that, for example, is very sensitive to X-ray exposure (see Figure S3). The onset of degradation in the TGA also plays a role on the film lifetime. We find a correlation between the film lifetime and TGA onset: the larger is the difference between the evaporation temperature and TGA onset temperature, the longer is the lifetime (Table S5). This correlation is not trivial because there is no thermal treatment involved since the samples are kept at room temperature in darkness. A new feature N* appears upon air exposure, and it grows with the duration of air exposure (Figure S2). A similar feature also appeared in the Blatter single radical films after long air exposure (several months) due to possible hydrogenation of the radical.[8] The longer film lifetime depending on the TGA onset suggests that the film degradation triggered by air exposure might have patterns similar to the degradation caused by annealing, as seen in the case of other organic thin films and nanoparticles.[52] These observations are fully backed up by the preliminary results obtained on a dinitroxide diradical (Figure S7). In this case, the very low TGA onset (∼ 103 °C) and the limited delocalization of the unpaired electrons over the N−O groups make the evaporation of the intact diradical very difficult and the film stability poor, forming films extremely sensitive also to short X-ray exposure.

CONCLUSIONS

We have demonstrated that it is possible to evaporate diradicals in a controlled environment obtaining thin films in which the diradical character is preserved. We have explored the parameters that might play a role in this phenomenon. We found that the strength of the antiferromagnetic interaction and the distance between the radical sites do not play a role nor does the spin. Bulk formation thermodynamics play the major role. The higher the formation energies of the crystal, the more difficult is the evaporation of intact radicals. The film lifetime under ambient air is correlated with the delocalization of the unpaired electrons and the onset of decomposition in TGA. The larger the delocalization and the higher the onset, the more stable are the films exposed to X-rays and air, making them attractive for applications. The evaporation of different diradicals can be successfully addressed considering our findings.

METHODS

Experimental Section. Thin films were prepared in situ under UHV conditions by OMBD using a Knudsen cell. Our measurements showed that the residual powder in the cell that underwent four evaporation cycles led to some minor degradation in the films; therefore, we grew the films using the same residual powder in the Knudsen cell for not more than three successive evaporation cycles.

Native SiO_2 grown on single-side polished n-Si(111) wafer was used as the substrate for all thin films. The wafers were cleaned in an ultrasonic bath by immersion in ethanol and acetone for 1 h each and annealed at around 500 K for several hours. Cleanness was verified by XPS. Nominal films thicknesses were calculated from the attenuation of the substrate signal. The NN-Blatter deposition rate was 0.03 nm/min. The substrate was kept at room temperature during deposition. The thin films were grown by direct deposition, unless specified differently in the text. The UHV system was composed of a dedicated OMDB chamber connected to an analysis chamber (2×10^{-10} mbar base pressure) in which the XPS measurements were conducted. It is equipped with a monochromatic Al Kα source (SPECS Focus 500) and a SPECS Phoibos 150 hemispherical electron analyzer. Survey spectra were measured at 50 eV pass energy and individual core level spectra at 20 eV pass energy. Both were subsequently calibrated to the Si 2p signal at 99.8 eV. To minimize potential radiation damage, only freshly prepared films were measured, and radiation exposure was limited. For measurements probing stability, beam exposure was further limited after air exposure to attribute the damage exclusively to the degradation by air exposure. This results in a worse signal-to-noise ratio in those spectra.

NEXAFS measurements were performed at the third-generation synchrotron radiation source BESSY II at the low-dose PES end station installed at the PM4 beamline ($E/\Delta E$ = 6000 at 400 eV). This end station was equipped with a similar setup as the one described above. The same calibrated Knudsen cells used to grow the films for the XPS measurements were mounted to a preparation chamber attached to the NEXAFS measuring chamber to reproduce the same preparation conditions, as for XPS. The measurements were carried out in multibunch hybrid mode (ring current in top up mode = 300 mA). The spectra were measured in a total electron yield and normalized with the clean substrate signal and ring current. Subsequently, they were scaled to give an equal absorption edge jump.

Atomic force microscopy was measured ex situ and under ambient conditions with a Digital Instruments Nanoscope III Multimode microscope using tapping mode. Note that while the XPS information on the decay of the substrate signal is obtained in situ without breaking the vacuum, the images are obtained after air exposure. The information obtained with the two techniques is correlated, but since the samples underwent a gradient of pressure from UHV to ambient conditions before microscopy, in this work, we use the images only to further support the XPS results on the Volmer−Weber (VW) growth mode without a quantitative evaluation.

Computational Section. Single molecules and crystalline systems have been simulated by using first-principle approaches based on DFT, as implemented in the Quantum-Espresso suite of codes.[53] Spin-unrestricted geometry optimizations were performed at the PBE-GGA level,[54] and van der Waals corrections were included within the semiempirical method proposed by Grimme (DFT-D2).[55] The electronic structure is described by using B3LYP hybrid-functional to correct the DFT deficiencies in reproducing the bandgap, without further atomic relaxation on the optimized PBE structures. Spin degrees of freedom are treated within the local spin density approximation. Atomic potentials are described by ultrasoft pseudopotential as available in the SSSP library.[56] Single-particle wavefunctions (charge) are expanded in plane waves up to a kinetic energy cutoff of 30 Ry (300 Ry), respectively. The first Brillouin zone of bulk systems is sampled with a $(2 \times 2 \times 2)$ k-point grid; center-zone Γ-point is used in the case of single molecules. All structures

https://dx.doi.org/10.1021/acs.chemmater.0c03880
Chem. Mater. 2021, 33, 2019−2028

were fully relaxed until forces on all atoms become lower than 0.03 eV/Å.

The N 1s core level spectra were calculated in the pseudopotential framework using the final state theory.[57] This approach provides only the relative shift between the core level binding energies of inequivalent atoms, while their absolute value is not defined. The choice of the reference does not change the analysis.

■ ASSOCIATED CONTENT

Supporting Information

The Supporting Information is available free of charge at https://pubs.acs.org/doi/10.1021/acs.chemmater.0c03880.

Stoichiometry: NN-Blatter, NEXAFS spectra: NN-Blatter; film stability upon air exposure: NN-Blatter; stoichiometry: BDT-NN, stability under X-rays; extended DFT results; temperature onset of degradation in thermal gravimetry analysis (TGA) for several radicals and diradicals and their film stability; and preliminary results obtained for dinitroxide (PDF)

■ AUTHOR INFORMATION

Corresponding Author

Maria Benedetta Casu − *Institute of Physical and Theoretical Chemistry, University of Tübingen, Tübingen 72076, Germany;* orcid.org/0000-0002-5659-7040; Email: benedetta. casu@uni-tuebingen.de

Authors

Tobias Junghoefer − *Institute of Physical and Theoretical Chemistry, University of Tübingen, Tübingen 72076, Germany*

Nolan M. Gallagher − *Department of Chemistry, University of Nebraska, Lincoln 68588-0304, United States*

Kubandiran Kolanji − *Max Planck Institute for Polymer Research, Mainz 55128, Germany*

Erika Giangrisostomi − *Helmholtz-Zentrum Berlin, Berlin 12489, Germany*

Ruslan Ovsyannikov − *Helmholtz-Zentrum Berlin, Berlin 12489, Germany*

Thomas Chassé − *Institute of Physical and Theoretical Chemistry, University of Tübingen, Tübingen 72076, Germany;* orcid.org/0000-0001-6442-8944

Martin Baumgarten − *Max Planck Institute for Polymer Research, Mainz 55128, Germany*

Andrzej Rajca − *Department of Chemistry, University of Nebraska, Lincoln 68588-0304, United States;* orcid.org/0000-0002-8856-1536

Arrigo Calzolari − *CNR-NANO Istituto Nanoscienze, Centro S3, Modena 41125, Italy;* orcid.org/0000-0002-0244-7717

Complete contact information is available at: https://pubs.acs.org/10.1021/acs.chemmater.0c03880

Author Contributions

#N.M.G. and K.K. contributed equally.

Notes

The authors declare no competing financial interest.

■ ACKNOWLEDGMENTS

The authors would like to thank Helmholtz-Zentrum Berlin (HZB) for providing beamtime at BESSY II (Berlin, Germany), Hilmar Adler, Elke Nadler, and Michael Pelzer for technical support, and Reza Kakavandi for the dinitroxide XPS measurements. Financial support from HZB and German Research Foundation (DFG) under the contract CA852/11-1 is gratefully acknowledged. We thank the National Science Foundation (NSF), Chemistry Division for support of this research under grant nos. CHE-1665256 (A.R.) and CHE-1955349 (A.R.).

■ REFERENCES

(1) Wasielewski, M. R.; Forbes, M. D. E.; Frank, N. L.; Kowalski, K.; Scholes, G. D.; Yuen-Zhou, J.; Baldo, M. A.; Freedman, D. E.; Goldsmith, R. H.; Goodson, T., III; Kirk, M. L.; McCusker, J. K.; Ogilvie, J. P.; Shultz, D. A.; Stoll, S.; Whaley, K. B. Exploiting chemistry and molecular systems for quantum information science. *Nat. Rev. Chem.* **2020**, 490−504.

(2) Nakazawa, S.; Nishida, S.; Ise, T.; Yoshino, T.; Mori, N.; Rahimi, R. D.; Sato, K.; Morita, Y.; Toyota, K.; Shiomi, D.; Kitagawa, M.; Hara, H.; Carl, P.; Höfer, P.; Takui, T. A Synthetic Two-Spin Quantum Bit: g-Engineered Exchange-Coupled Biradical Designed for CONTROLLED-NOT Gate Operations. *Angew. Chem., Int. Ed.* **2012**, *51*, 9860−9864.

(3) Ai, X.; Evans, E. W.; Dong, S.; Gillett, A. J.; Guo, H.; Chen, Y.; Hele, T. J. H.; Friend, R. H.; Li, F. Efficient radical-based light-emitting diodes with doublet emission. *Nature* **2018**, *563*, 536−540.

(4) Lehmann, J.; Gaita-Ariño, A.; Coronado, E.; Loss, D. Quantum computing with molecular spin systems. *J. Mater. Chem.* **2009**, *19*, 1672−1677.

(5) Sato, K.; Nakazawa, S.; Rahimi, R.; Ise, T.; Nishida, S.; Yoshino, T.; Mori, N.; Toyota, K.; Shiomi, D.; Yakiyama, Y.; Morita, Y.; Kitagawa, M.; Nakasuji, K.; Nakahara, M.; Hara, H.; Carl, P.; Hofer, P.; Takui, T. Molecular electron-spin quantum computers and quantum information processing: pulse-based electron magnetic resonance spin technology applied to matter spin-qubits. *J. Mater. Chem.* **2009**, *19*, 3739−3754.

(6) Ciccullo, F.; Calzolari, A.; Bader, K.; Neugebauer, P.; Gallagher, N. M.; Rajca, A.; van Slageren, J.; Casu, M. B. Interfacing a Potential Purely Organic Molecular Quantum Bit with a Real-Life Surface. *ACS Appl. Mater. Interfaces* **2018**, *11*, 1571−1578.

(7) Savu, S.-A.; Biswas, I.; Sorace, L.; Mannini, M.; Rovai, D.; Caneschi, A.; Chassé, T.; Casu, M. B. Nanoscale Assembly of Paramagnetic Organic Radicals on Au(111) Single Crystals. *Chem.-Eur. J.* **2013**, *19*, 3445−3450.

(8) Ciccullo, F.; Gallagher, N. M.; Geladari, O.; Chassé, T.; Rajca, A.; Casu, M. B. A Derivative of the Blatter Radical as a Potential Metal-Free Magnet for Stable Thin Films and Interfaces. *ACS Appl. Mater. Interfaces* **2016**, *8*, 1805−1812.

(9) Zhang, Y.; Zheng, Y.; Zhou, H.; Miao, M.-S.; Wudl, F.; Nguyen, T.-Q. Temperature Tunable Self-Doping in Stable Diradicaloid Thin-Film Devices. *Adv. Mater.* **2015**, *27*, 7412−7419.

(10) Low, J. Z.; Kladnik, G.; Patera, L. L.; Sokolov, S.; Lovat, G.; Kumarasamy, E.; Repp, J.; Campos, L. M.; Cvetko, D.; Morgante, A.; Venkataraman, L. The Environment-Dependent Behavior of the Blatter Radical at the Metal−Molecule Interface. *Nano Lett.* **2019**, *19*, 2543−2548.

(11) de Sousa, J. A.; Bejarano, F.; Gutiérrez, D.; Leroux, Y. R.; Nowik-Boltyk, E. M.; Junghoefer, T.; Giangrisostomi, E.; Ovsyannikov, R.; Casu, M. B.; Veciana, J.; Mas-Torrent, M.; Fabre, B.; Rovira, C.; Crivillers, N. Exploiting the versatile alkyne-based chemistry for expanding the applications of a stable triphenylmethyl organic radical on surfaces. *Chem. Sci.* **2020**, *11*, 516−524.

(12) Gallagher, N.; Zhang, H.; Junghoefer, T.; Giangrisostomi, E.; Ovsyannikov, R.; Pink, M.; Rajca, S.; Casu, M. B.; Rajca, A. Thermally and Magnetically Robust Triplet Ground State Diradical. *J. Am. Chem. Soc.* **2019**, *141*, 4764−4774.

(13) Casu, M. B. Nanoscale Studies of Organic Radicals: Surface, Interface, and Spinterface. *Acc. Chem. Res.* **2018**, *51*, 753−760.

(14) Lee, J.; Lee, E.; Kim, S.; Bang, G. S.; Shultz, D. A.; Schmidt, R. D.; Forbes, M. D. E.; Lee, H. Nitronyl Nitroxide Radicals as Organic

Memory Elements with Both n- and p-Type Properties. *Angew. Chem., Int. Ed.* **2011**, *50*, 4414−4418.
(15) Gaudenzi, R.; de Bruijckere, J.; Reta, D.; Moreira, I. D. P. R.; Rovira, C.; Veciana, J.; van der Zant, H. S. J.; Burzurí, E. Redox-Induced Gating of the Exchange Interactions in a Single Organic Diradical. *ACS Nano* **2017**, *11*, 5879−5883.
(16) Hu, G.; Xie, S.; Wang, C.; Timm, C. Spin-dependent transport and functional design in organic ferromagnetic devices. *Beilstein J. Nanotechnol.* **2017**, *8*, 1919−1931.
(17) Gaudenzi, R.; Burzurí, E.; Reta, D.; Moreira, I. D. P. R.; Bromley, S. T.; Rovira, C.; Veciana, J.; van der Zant, H. S. J. Exchange Coupling Inversion in a High-Spin Organic Triradical Molecule. *Nano Lett.* **2016**, *16*, 2066−2071.
(18) Sanvito, S. Molecular spintronics. *Chem. Soc. Rev.* **2011**, *40*, 3336−3355.
(19) Huang, Z.; Zhang, Y.; He, Y.; Song, H.; Yin, C.; Wu, K. A chemist's overview of surface electron spins. *Chem. Soc. Rev.* **2017**, *46*, 1955−1976.
(20) Ullman, E. F.; Call, L.; Osiecki, J. H. Stable Free radicals. VIII. New imino, Amidino, and Carbamoyl Nitroxides. *J. Org. Chem.* **1970**, *35*, 3623−3631.
(21) Blatter, H. M.; Lukaszewski, H. A new stable free radical. *Tetrahedron Lett.* **1968**, *9*, 2701−2705.
(22) Kakavandi, R.; Ravat, P.; Savu, S. A.; Borozdina, Y. B.; Baumgarten, M.; Casu, M. B. Electronic Structure and Stability of Fluorophore−Nitroxide Radicals from Ultrahigh Vacuum to Air Exposure. *ACS Appl. Mater. Interfaces* **2015**, *7*, 1685−1692.
(23) Rauschenbach, S.; Stadler, F. L.; Lunedei, E.; Malinowski, N.; Koltsov, S.; Costantini, G.; Kern, K. Electrospray Ion Beam Deposition of Clusters and Biomolecules. *Small* **2006**, *2*, 540−547.
(24) Erler, P.; Schmitt, P.; Barth, N.; Irmler, A.; Bouvron, S.; Huhn, T.; Groth, U.; Pauly, F.; Gragnaniello, L.; Fonin, M. Highly Ordered Surface Self-Assembly of Fe4 Single Molecule Magnets. *Nano Lett.* **2015**, *15*, 4546−4552.
(25) Forrest, S. R. Ultrathin Organic Films Grown by Organic Molecular Beam Deposition and Related Techniques. *Chem. Rev.* **1997**, *97*, 1793−1896.
(26) Kolanji, K.; Postulka, L.; Wolf, B.; Lang, M.; Schollmeyer, D.; Baumgarten, M. Planar Benzo[1,2-b,4,5-b′]dithiophene Derivatives Decorated with Nitronyl and Imino Nitroxides. *J. Org. Chem.* **2018**, *84*, 140−149.
(27) Rajca, A.; Takahashi, M.; Pink, M.; Spagnol, G.; Rajca, S. Conformationally Constrained, Stable, Triplet Ground State (S = 1) Nitroxide Diradicals. Antiferromagnetic Chains of S = 1 Diradicals. *J. Am. Chem. Soc.* **2007**, *129*, 10159−10170.
(28) Casu, M. B.; Chassé, T., Photoelectron Spectroscopy Applications to Materials Science. In *Handbook of spectroscopy*, Second, enlarged edition / edited by Günter Gauglitz and David S. Moore ed.; Gauglitz, G.; Moore, D. S., Eds. Wiley-VCH: Weinheim, Germany, 2014; Vol. *322*, pp. 1523−1556.
(29) Constantinides, C. P.; Koutentis, P. A.; Krassos, H.; Rawson, J. M.; Tasiopoulos, A. J. Characterization and Magnetic Properties of a "Super Stable" Radical 1,3-Diphenyl-7-trifluoromethyl-1,4-dihydro-1,2,4-benzotriazin-4-yl. *J. Org. Chem.* **2011**, *76*, 2798−2806.
(30) Zheng, Y.; Miao, M.-S.; Kemei, M. C.; Seshadri, R.; Wudl, F. The Pyreno-Triazinyl Radical − Magnetic and Sensor Properties. *Isr. J. Chem.* **2014**, *54*, 774−778.
(31) Junghoefer, T.; Nowik-Boltyk, E. M.; de Sousa, J. A.; Giangrisostomi, E.; Ovsyannikov, R.; Chassé, T.; Veciana, J.; Mas-Torrent, M.; Rovira, C.; Crivillers, N.; Casu, M. B. Stability of radical-functionalized gold surfaces by self-assembly and on-surface chemistry. *Chem. Sci.* **2020**, *11*, 9162−9172.
(32) Savu, S.-A.; Casu, M. B.; Schundelmeier, S.; Abb, S.; Tönshoff, C.; Bettinger, H. F.; Chassé, T. Nanoscale assembly, morphology and screening effects in nanorods of newly synthesized substituted pentacenes. *RSC Adv.* **2012**, *2*, 5112.
(33) Casu, M. B.; Schuster, B.-E.; Biswas, I.; Raisch, C.; Marchetto, H.; Schmidt, T.; Chassé, T. Locally Resolved Core-hole Screening, Molecular Orientation, and Morphology in Thin Films of Diindenoperylene Deposited on Au(111) Single Crystals. *Adv. Mater.* **2010**, *22*, 3740−3744.
(34) Winkler, S.; Frisch, J.; Amsalem, P.; Krause, S.; Timpel, M.; Stolte, M.; Würthner, F.; Koch, N. Impact of Molecular Dipole Moments on Fermi Level Pinning in Thin Films. *J. Phys. Chem. C* **2014**, *118*, 11731−11737.
(35) Savu, S.-A.; Biddau, G.; Pardini, L.; Bula, R.; Bettinger, H. F.; Draxl, C.; Chassé, T.; Casu, M. B. Fingerprint of Fractional Charge Transfer at the Metal/Organic Interface. *J. Phys. Chem. C* **2015**, *119*, 12538−12544.
(36) Peisert, H.; Petershans, A.; Chassé, T. Charge Transfer and Polarization Screening at Organic/Metal Interfaces: Distinguishing between the First Layer and Thin Films. *J. Phys. Chem. C* **2008**, *112*, 5703−5706.
(37) Venables, J. A., *Introduction to Surface and Thin Film Processes*; Cambridge University Press: Cambridge, 2000, DOI: 10.1017/CBO9780511755651.
(38) Stöhr, J.; Outka, D. A. Determination of molecular orientations on surfaces from the angular dependence of near-edge x-ray-absorption fine-structure spectra. *Phys. Rev. B* **1987**, *36*, 7891−7905.
(39) Caneschi, A.; Casu, M. B. Substrate-induced effects in thin films of a potential magnet composed of metal-free organic radicals deposited on Si(111). *Chem. Commun.* **2014**, *50*, 13510−13513.
(40) Bauer, E. Phänomenologische Theorie der Kristallabscheidung an Oberflächen. I. *Z. Kristallogr. Cryst. Mater.* **1958**, *110*, 372−394.
(41) Constantinides, C. P.; Koutentis, P. A.; Rawson, J. M. Antiferromagnetic Interactions in 1D Heisenberg Linear Chains of 7-(4-Fluorophenyl) and 7-Phenyl-Substituted 1,3-Diphenyl-1,4-dihydro- 1,2,4-benzotriazin-4-yl Radicals. *Chem. − Eur. J.* **2012**, *18*, 15433−15438.
(42) Rajca, A.; Shiraishi, K.; Pink, M.; Rajca, S. Triplet (S = 1) Ground State Aminyl Diradical. *J. Am. Chem. Soc.* **2007**, *129*, 7232−7233.
(43) Rajca, A.; Olankitwanit, A.; Wang, Y.; Boratyński, P. J.; Pink, M.; Rajca, S. High-Spin S = 2 Ground State Aminyl Tetraradicals. *J. Am. Chem. Soc.* **2013**, *135*, 18205−18215.
(44) Caneschi, A.; Gatteschi, D.; Sessoli, R.; Rey, P. Toward molecular magnets: the metal-radical approach. *Acc. Chem. Res.* **2002**, *22*, 392−398.
(45) Morgan, I. S.; Peuronen, A.; Hänninen, M. M.; Reed, R. W.; Clérac, R.; Tuononen, H. M. 1-Phenyl-3-(pyrid-2-yl)benzo[e][1,2,4]-triazinyl: The First "Blatter Radical" for Coordination Chemistry. *Inorg. Chem.* **2014**, *53*, 33−35.
(46) Demetriou, M.; Berezin, A. A.; Koutentis, P. A.; Krasia-Christoforou, T. Benzotriazinyl-mediated controlled radical polymerization of styrene. *Polym. Int.* **2014**, *63*, 674−679.
(47) Yan, B.; Cramen, J.; McDonald, R.; Frank, N. L. Ferromagnetic spin-delocalized electron donors for multifunctional materials: π-conjugated benzotriazinyl radicals. *Chem. Commun.* **2011**, *47*, 3201−3203.
(48) Veciana, J.; Rovira, C.; Crespo, M. I.; Armet, O.; Domingo, V. M.; Palacio, F. Stable polyradicals with high-spin ground states. 1. Synthesis, separation, and magnetic characterization of the stereoisomers of 2,4,5,6-tetrachloro-.alpha.,.alpha.,.alpha.',.alpha.'-tetrakis-(pentachlorophenyl)-m-xylylene biradical. *J. Am. Chem. Soc.* **1991**, *113*, 2552−2561.
(49) Mugnaini, V.; Calzolari, A.; Ovsyannikov, R.; Vollmer, A.; Gonidec, M.; Alcon, I.; Veciana, J.; Pedio, M. Looking Inside the Perchlorinated Trityl Radical/Metal Spinterface through Spectroscopy. *J. Phys. Chem. Lett.* **2015**, *6*, 2101−2106.
(50) Ciccullo, F.; Calzolari, A.; Pís, I.; Savu, S. A.; Krieg, M.; Bettinger, H. F.; Magnano, E.; Chassé, T.; Casu, M. B. A Quasi-Free-Standing Single Layer of a B3N3-Doped Nanographene Molecule Deposited on Au(111) Single Crystals. *J. Phys. Chem. C* **2016**, *120*, 17645−17651.
(51) Mattheus, C. C.; Dros, A. B.; Baas, J.; Oostergetel, G. T.; Meetsma, A.; de Boer, J. L.; Palstra, T. T. M. Identification of polymorphs of pentacene. *Synth. Met.* **2003**, *138*, 475−481.

(52) Bürgi, T. Properties of the gold−sulphur interface: from self-assembled monolayers to clusters. *Nanoscale* **2015**, *7*, 15553−15567.
(53) Giannozzi, P.; Baroni, S.; Bonini, N.; Calandra, M.; Car, R.; Cavazzoni, C.; Ceresoli, D.; Chiarotti, G. L.; Cococcioni, M.; Dabo, I.; Dal Corso, A.; de Gironcoli, S.; Fabris, S.; Fratesi, G.; Gebauer, R.; Gerstmann, U.; Gougoussis, C.; Kokalj, A.; Lazzeri, M.; Martin-Samos, L.; Marzari, N.; Mauri, F.; Mazzarello, R.; Paolini, S.; Pasquarello, A.; Paulatto, L.; Sbraccia, C.; Scandolo, S.; Sclauzero, G.; Seitsonen, A. P.; Smogunov, A.; Umari, P.; Wentzcovitch, R. M. QUANTUM ESPRESSO: a modular and open-source software project for quantum simulations of materials. *J. Phys.: Condens. Matter* **2009**, *21*, 395502.
(54) Perdew, J. P.; Burke, K.; Ernzerhof, M. Generalized Gradient Approximation Made Simple. *Phys. Rev. Lett.* **1996**, *77*, 3865−3868.
(55) Grimme, S. Semiempirical GGA-type density functional constructed with a long-range dispersion correction. *J. Comput. Chem.* **2006**, *27*, 1787−1799.
(56) Dal Corso, A. Pseudopotentials periodic table: From H to Pu. *Comput. Mater. Sci.* **2014**, *95*, 337−350.
(57) Pehlke, E.; Scheffler, M. Evidence for site-sensitive screening of core holes at the Si and Ge (001) surface. *Phys. Rev. Lett.* **1993**, *71*, 2338−2341.

https://dx.doi.org/10.1021/acs.chemmater.0c03880
Chem. Mater. 2021, 33, 2019−2028

Supporting Information

Challenges in controlled thermal deposition of organic diradicals

Tobias Junghoefer,[1] Nolan M. Gallagher,[2†] Kubandiran Kolanji,[3†] Erika Giangrisostomi,[4] Ruslan Ovsyannikov,[4] Thomas Chassé,[1] Martin Baumgarten,[3] Andrzej Rajca,[2] Arrigo Calzolari,[5] Maria Benedetta Casu[1*]

[1]Institute of Physical and Theoretical Chemistry, University of Tübingen, 72076 Tübingen, Germany

[2]Department of Chemistry, University of Nebraska, Lincoln, United States

[3]Max Planck Institute for Polymer Research, 55128 Mainz, Germany

[4]Helmholtz-Zentrum Berlin, 12489 Berlin, Germany

[5]CNR-NANO Istituto Nanoscienze, Centro S3, 41125 Modena, Italy

*Correspondence to: benedetta.casu@uni-tuebingen.de

†These authors contributed equally.

Contents

1) Stoichiometry: NN-Blatter.

The fitting procedure in XPS is driven by specific and detailed chemical and physical arguments that are described in detail in Ref. [1-3].

Table S1. NN-Blatter thin films. Fit results for the energy positions and relative intensities of the C 1s photoemission lines.

	Energy (eV)	Lorentzian Width (eV)	Gaussian Width (eV)	Intensity (%)	Theoretical values (%)
C-C	284.7	0.08	1.05	6.2	7.7
C-H & CH_3	285.5	0.08	1.05	58.9	65.3
C-N	286.4	0.08	1.05	19.0	27
S_1	287.3	0.08	0.80	10.8	
S_2	288.0	0.08	1.20	5.1	

$I(C\text{-}C+ C\text{-}H \& CH_3+ S_1) = 75.9\%$
$I(C\text{-}N+S_2) = 24.1\%$

Table S2. NN-Blatter thin films. Fit results for the energy positions and relative intensities of the N 1s photoemission lines.

	Energy (eV)	Lorentzian Width (eV)	Gaussian Width (eV)	Intensity (%)	Theoretical values (%)
N_4	399.1	0.10	0.90	17.3	20
N_2	400.1	0.10	0.90	17.3	20
N_1	401.7	0.10	0.90	17.3	20
N_{NN}	402.6	0.10	1.00	23.5	40
S_1	400.7	0.10	1.00	7.4	
S_2	403.5	0.10	1.14	8.6	
S_3	404.2	0.10	3.90	8.6	

$I(N_4+N_2+N_1+S_1) = 59.3\%$
$I(N_{NN}+S_2+S_3) = 40.7\%$

2) NEXAFS Spectra

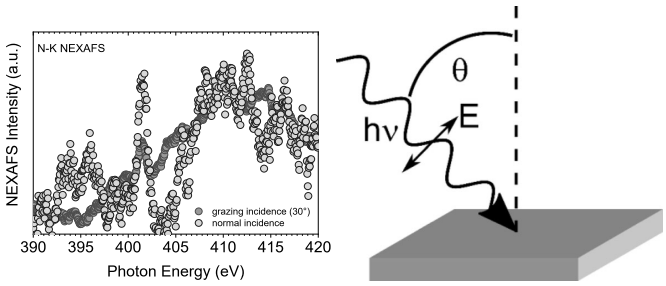

Figure S1. NN- Blatter N-K NEXAFS spectra with the geometry of the experiment.

The main peak at around 402 eV is typical for the nitronyl nitroxide NEXAFS spectrum.[4] Its dichroism indicates that the molecules are orientated in a fashion closely resembling the arrangement in the single crystal, however, identified by a specific orientation of the film unit cell, with the crystallographic *a*-axis almost perpendicular to the substrate.[2]

3) Film stability upon air exposure: NN-Blatter.

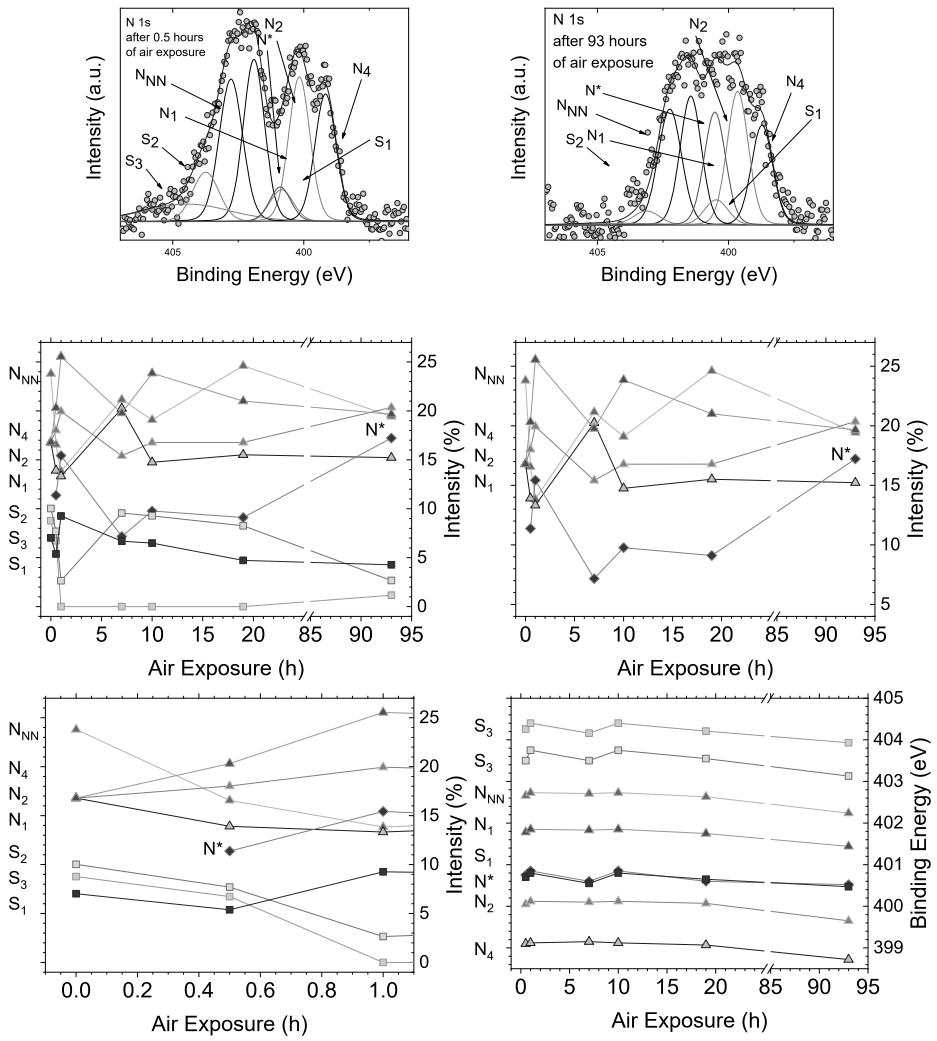

Figure S2. NN- Blatter. A new feature N* appears upon air exposure and it grows with the duration of air exposure. A similar feature also appeared in the Blatter single radical films after long air exposure (several months) due to possible hydrogenation of the radical.

4) Stoichiometry: BDT-NN.

Table S3. Comparison of the theoretical and experimental film elemental ratio.

	C 1s	N 1s	S 2s
Theoretical value.	26	4	2
film	27.9	3.3	0.8

The sensitivity factors (σ) are: $\sigma_{C\ 1s}$ = 0.25, $\sigma_{N\ 1s}$ =0.42 and $\sigma_{S\ 2s}$ 0.33=.[5]

Table S4. BDT-NN thin films. Fit results for the energy positions and relative intensities of the C 1s photoemission lines.

	Energy (eV)	Lorentzian Width (eV)	Gaussian Width (eV)	Intensity (%)	Theoretical values (%)
C-C	285.1	0.08	1.00	6.8	7.7
C-H	285.6	0.08	1.00	34.7	38.4
S_1	286.2	0.08	1.00	4.5	
C-S	286.1	0.08	1.00	14.0	15.4
C-O	286.5	0.08	1.00	14.0	15.4
C-N	287.2	0.08	1.00	20.6	23.1
S_2	287.9	0.08	1.00	5.4	

C-C + C-H + S_1 = 46.0 %
C-S + 1/3*S2 = 15.8 %
C-O + 1/3*S2 = 15.8 %
C-N + 1/3*S2 = 22.4 %

5) Stability under X-rays.

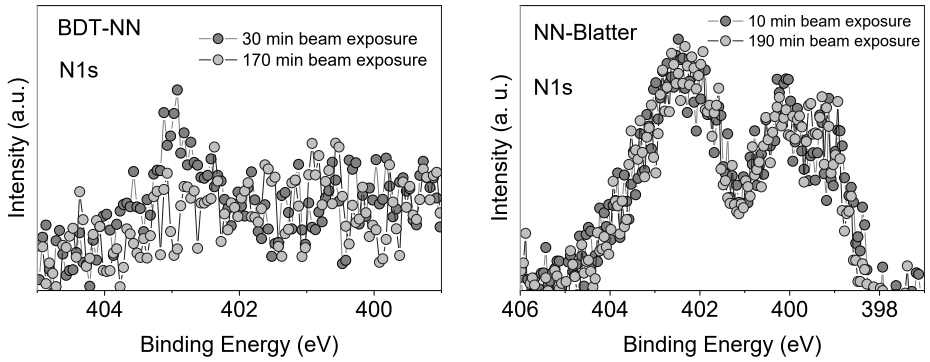

a) b)

Figure S3. Beam stability for a) BDT-NN, after 170 minutes the N 1s signal concomitant with the intact nitronyl nitroxide is not visible anymore and b) NN-Blatter. The N 1s signal does not show changes over a longer beam exposure (190 minutes) (photon energy: 1486.6 eV).

6) Extended DFT results.

Bulk crystals: Calculated Density of states.

We first investigated the stability and the magnetic order of the single molecules, by means of a set of total-energy-and-forces simulations at fixed values of total magnetization M_T=0,1,2 μ_B, where $M_T = \int(n_{up} - n_{dw})d^3r$ is the integral of the magnetization in the cell, and n_{up} and n_{dw} are the spin-up and the spin-down components of the electron charge density, described within the local spin density approximation. Thus, M_T=2 μ_B corresponds to two unpaired electrons with parallel spins (↑↑) and total spin S=1. In the case of M_T=0, we distinguish between non-magnetic spin unpolarized system (- -) and antiparallel (↑↓) spin arrangement, through the evaluation of the absolute magnetization $M_A = \int|n_{up} - n_{dw}|d^3r$. Non-magnetic systems have M_T= M_A=0 $_B$, while two antiparallel spin systems have M_T=0 μ_B and M_A=2 μ_B.

Figure S4a shows the total energy variation ΔE of the isolated molecules, as a function of the magnetic state M_T with respect to the non-magnetic state, assumed as the energy zero reference. For both diradicals all the magnetic phases $M_T \neq 0$ are energetically favoured, even though the case of a single unpaired electron M_T=1μ_B (↑ -) is the less stable one. This confirms the intrinsic diradical character (i.e., two unpaired electrons) of both molecules. Rather relevant differences hold for the spin alignment of the two systems. In the case of NN-Blatter (dark blue line), the parallel (↑↑) spin ordering is favoured by ~50 meV/mol with respect to the antiparallel (↑↓) one, indicating an intra-molecular spin coupling between the two unpaired electrons. On the contrary, for BDT-NN the parallel and antiparallel spin distributions are energetically equivalent (↑↑ is energetically more stable than ↑↓ only by 6 meV/mol). This corresponds to 2 uncorrelated spin radicals (S=1/2) allocated in the same molecule (one per NN unit).

The origin of this behaviour can be explained by the analysis of the electronic structure. Figure S5a shows the spin-polarized density of states (DOS) of the two diradicals in the parallel (↑↑) spin phase.

The magnetic character of the NN-Blatter derives from two single occupied molecular orbitals (labelled S_1 and S_2). S_1 and S_2 are π-like conjugated states: the former is mostly localized on the NN unit, the latter is centred on the Blatter part; but both wavefunctions have tails that extend over the phenyl ring connecting the two units. The corresponding spin-density plot (n_{up}-n_{dw}) in Figure S5b results to be extended on the entire core of the molecule. This is a fingerprint of the intra-molecular coupling between the two radical subsystems and the overall spin alignment of the diradical. On the contrary, in the case of BDT-NN, the magnetic character stems from two orbitals (labelled S) that are degenerate in energy but spatially centred in a separate NN unit. The corresponding spin density (Figure S5b) is localized on the O-N-C-N-O bonds, with no overlap in the central core. This corresponds to two unpaired S=1/2 radicals hosted in the same molecule, with no preference for their relative orientation. This justifies also the same total energy for the parallel and antiparallel distribution, shown in Figure S4a.

A similar analysis has been carried out for the bulk phases. In both cases, the initial structure has been taken from the experimental X-ray crystalline structure.[2, 6] Each crystal has a triclinic lattice symmetry and includes four diradical units in the original cell. The NN-Blatter crystal is further stabilized by two dichloromethane (CH_2Cl_2) molecules.[2] For both systems we optimized the atomic structure for different values of the total magnetization per cell, corresponding to non-magnetic, FM and AF long-range intermolecular orders.

BDT-NN crystal may be stabilized in both FM and AF phases at the same total energy, being the AF state only 2 meV/mol more stable than the FM one. In both cases, the absolute magnetization is M_A=~8.5 μ_B/cell, while M_T=8.0 μ_B/cell and M_T=0 μ_B/cell, for the FM and AF state, respectively. The weak AF behaviour detected in the experiments[2] can thus be interpreted as a sequence of weak interacting S=1/2 NN radicals. The different long-range spin arrangement also affects the DOS of the two bulk crystals as shown in Figure S6.

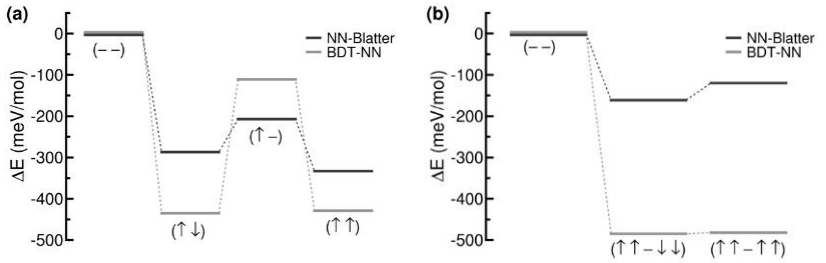

Figure S4. Total energy difference ΔE of (a) single molecules and (b) bulk crystals, as a function of the total magnetization, with respect to the non-magnetic (- -) phase. In panel (a) labels (↑↓), (↑ -), (↑↑) describe the single molecule (intra-molecular) spin alignment and correspond to M_T=0, 1, and 2μ_B/mol, respectively; in panel (b) (↑↑-↓↓) and (↑↑-↑↑) correspond to AF and FM long-range (inter-molecular) spin alignment, and correspond to M_T=0, and 8μ_B/cell, respectively.

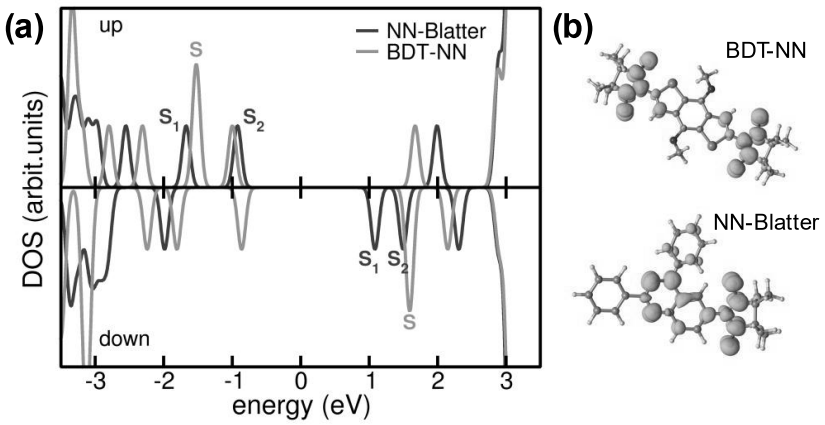

Figure S5. (a) Spin-polarized DOS plot for NN-Blatter (dark blue) and BDT-NN (light cyan) diradicals (single molecule). The corresponding spin-density isosurface plots are shown in panel (b).

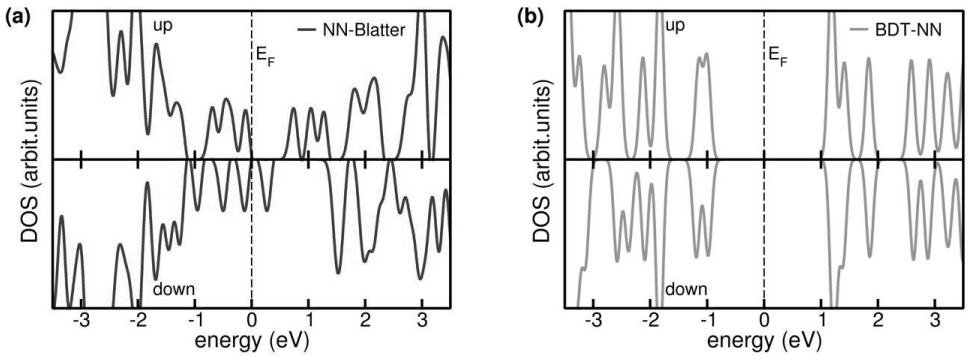

Figure S6. Spin-resolved DOS of (a) NN-Blatter and (b) BDT-NN in the crystalline phase and corresponding to the intermolecular AF long-range arrangement (↑↑ - ↓↓), with M_A=~8.5 μ_B/cell, while M_T=0.0 μ_B/cell. Vertical dashed lines mark the Fermi level, assumed as zero energy reference for both systems.

7) Temperature onset of degradation in thermal gravimetry analysis (TGA) for several radicals and diradicals and their film stability.

Table S5.

Diradicals	Onset TGA (K)	Film stability
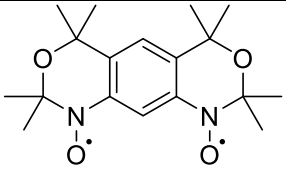 $C_{18}H_{26}N_2O_4^{2\bullet}$	376[7]	X-ray sensitive (~30 minutes under the beam without changes) UHV stable
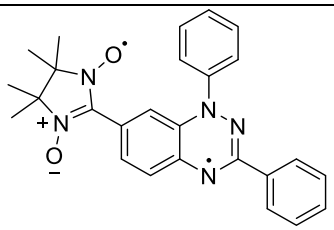 $C_{26}H_{25}N_5O_2^{2\bullet}$	433[2]	X-ray stable (see this work) UHV stable Stable few hours in air[2]
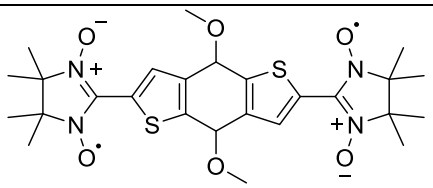 $C_{26}H_{34}N_4O_6S_2^{2\bullet}$	N/A	X-ray sensitive (see this work)

Radicals		
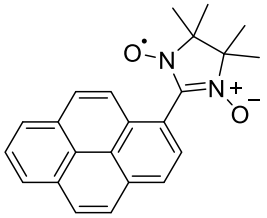 $C_{23}H_{21}N_2O_2^{\bullet}$	462[3]	X-ray stable[3] (several hours under the beam without changes) UHV stable Stable at least several weeks in air[3]

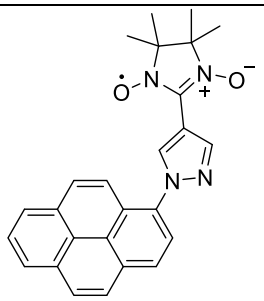 $C_{26}H_{23}N_4O_2^{\bullet}$	N/A	X-ray stable[8] (several hours under the beam without changes) UHV stable Stable at least several weeks in air[8]
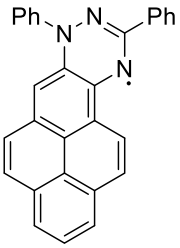 $C_{29}H_{18}N_3^{\bullet}$	(433) 523[9]	X-ray stable[9] (long exposure under the beam without changes) UHV stable Stable at least three months in air[9]
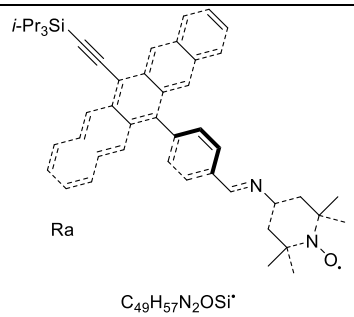 Ra $C_{49}H_{57}N_2OSi^{\bullet}$ 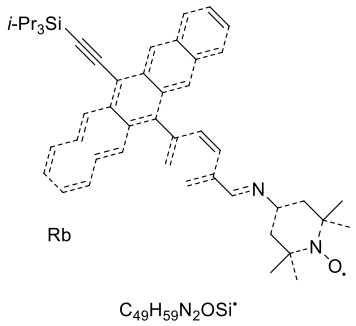 Rb $C_{49}H_{59}N_2OSi^{\bullet}$	N/A	X-ray sensitive[10] (~30 minutes under the beam without changes) Unstable in UHV and in air[10]

8) Preliminary results on diNitroxide.

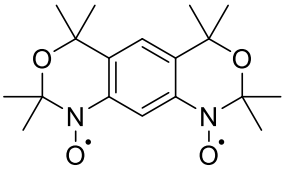

$C_{18}H_{26}N_2O_4^{2\bullet}$

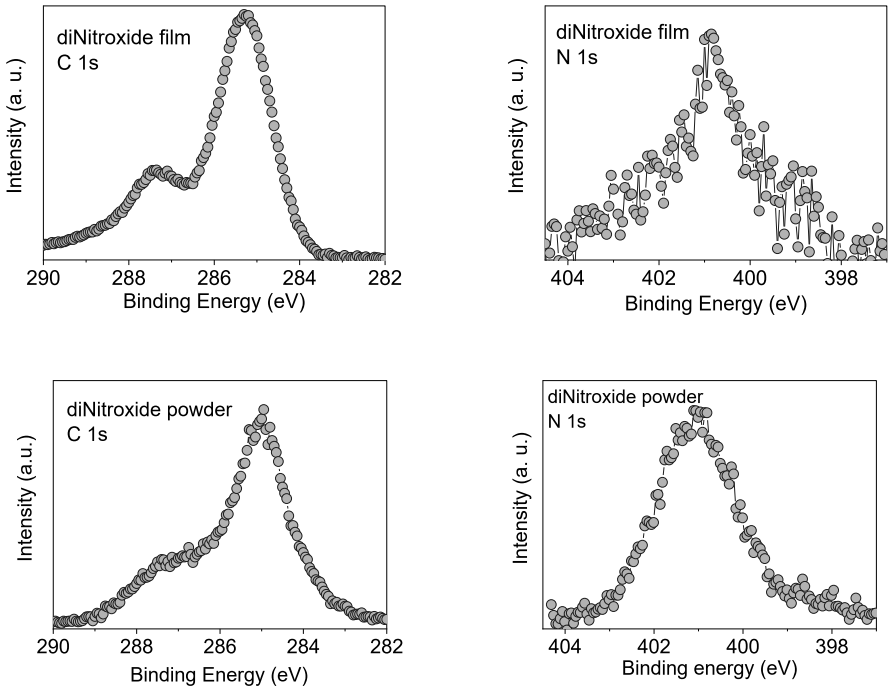

Figure S7. (upper panel) C 1s and N 1s core level XPS spectra of a multilayer, compared to the powder spectra (lower panel).

The integral intensity of the C1s and the N1s core level lines of the films is 10.7. The expected stoichiometric ratio is 9 The sensitivity factors (σ) are: $\sigma_{C\ 1s} = 0.25$, and $\sigma_{N\ 1s} = 0.42$[5].

9) REFERENCES

1. Junghoefer, T.; Nowik-Boltyk, E. M.; de Sousa, J. A.; Giangrisostomi, E.; Ovsyannikov, R.; Chassé, T.; Veciana, J.; Mas-Torrent, M.; Rovira, C.; Crivillers, N.; Casu, M. B., Stability of radical-functionalized gold surfaces by self-assembly and on-surface chemistry. *Chemical Science* **2020,** 11, 9162-9172.
2. Gallagher, N.; Zhang, H.; Junghoefer, T.; Giangrisostomi, E.; Ovsyannikov, R.; Pink, M.; Rajca, S.; Casu, M. B.; Rajca, A., Thermally and Magnetically Robust Triplet Ground State Diradical. *J. Am. Chem. Soc.* **2019,** 141, 4764-4774.
3. Savu, S.-A.; Biswas, I.; Sorace, L.; Mannini, M.; Rovai, D.; Caneschi, A.; Chassé, T.; Casu, M. B., Nanoscale Assembly of Paramagnetic Organic Radicals on Au(111) Single Crystals. *Chem.-Eur. J.* **2013,** 19, 3445-3450.
4. Kakavandi, R.; Savu, S.-A.; Caneschi, A.; Casu, M. B., Paramagnetic Character in Thin Films of Metal-Free Organic Magnets Deposited on TiO2(110) Single Crystals. *J. Phys. Chem. C* **2013,** 117, 26675-26679.
5. Wagner, C. D., Sensitivity factors for XPS analysis of surface atoms. *Journal of Electron Spectroscopy and Related Phenomena* **1983,** 32, 99-102.
6. Kolanji, K.; Postulka, L.; Wolf, B.; Lang, M.; Schollmeyer, D.; Baumgarten, M., Planar Benzo[1,2-b:4,5-b′]dithiophene Derivatives Decorated with Nitronyl and Imino Nitroxides. *J. Org. Chem.* **2019,** 84, 140-149.
7. Rajca, A.; Takahashi, M.; Pink, M.; Spagnol, G.; Rajca, S., Conformationally Constrained, Stable, Triplet Ground State (S = 1) Nitroxide Diradicals. Antiferromagnetic Chains of S = 1 Diradicals. *J. Am. Chem. Soc.* **2007,** 129, 10159-10170.
8. Kakavandi, R.; Ravat, P.; Savu, S. A.; Borozdina, Y. B.; Baumgarten, M.; Casu, M. B., Electronic Structure and Stability of Fluorophore–Nitroxide Radicals from Ultrahigh Vacuum to Air Exposure. *ACS Appl. Mater. Interfaces* **2015,** 7, 1685-1692.
9. Ciccullo, F.; Gallagher, N. M.; Geladari, O.; Chasse, T.; Rajca, A.; Casu, M. B., A Derivative of the Blatter Radical as a Potential Metal-Free Magnet for Stable Thin Films and Interfaces. *ACS Appl. Mater. Interfaces* **2016,** 8, 1805–1812.
10. Arantes, C.; Chernick, E. T.; Gruber, M.; Rocco, M. L. M.; Chasse, T.; Tykwinski, R. R.; Casu, M. B., Interplay between solution-processing and electronic structure in metal-free organic magnets based on a TEMPO pentacene derivative. *J. Phys. Chem. C.* **2016,** 120, 3289–3294.

E. Synthesis and Thin Films of Thermally Robust Quartet (S = 3/2) Ground State Triradical

Reprinted with permission from
C. Shu, M. Pink, T. Junghoefer, E. Nadler, S. Rajca, M. B. Casu, A. Rajca, "Synthesis and Thin Films of Thermally Robust Quartet (S = 3/2) Ground State Triradical", *Journal of the American Chemical Society* **2021**, *143*, 5508–5518, DOI 10.1021/jacs.1c01305.

http://pubs.acs.org/articlesonrequest/AOR-RNVWBHPGTNFWRJKTZIIG

JACS
JOURNAL OF THE AMERICAN CHEMICAL SOCIETY
pubs.acs.org/JACS
Article

Synthesis and Thin Films of Thermally Robust Quartet (S = 3/2) Ground State Triradical

Chan Shu, Maren Pink, Tobias Junghoefer, Elke Nadler, Suchada Rajca, Maria Benedetta Casu,* and Andrzej Rajca*

Cite This: J. Am. Chem. Soc. 2021, 143, 5508−5518
Read Online
ACCESS | Metrics & More | Article Recommendations | Supporting Information

ABSTRACT: High-spin (S = 3/2) organic triradicals may offer enhanced properties with respect to several emerging technologies, but those synthesized to date typically exhibit small doublet quartet energy gaps and/or possess limited thermal stability and processability. We report a quartet ground state triradical **3**, synthesized by a Pd(0)-catalyzed radical−radical cross-coupling reaction, which possesses two doublet−quartet energy gaps, $\Delta E_{DQ} \approx 0.2-0.3$ kcal mol^{-1} and $\Delta E_{DQ}2 \approx 1.2-1.8$ kcal mol^{-1}. The triradical has a 70+% population of the quartet ground state at room temperature and good thermal stability with onset of decomposition at >160 °C under an inert atmosphere. Magnetic properties of **3** are characterized by SQUID magnetometry in polystyrene glass and by quantitative EPR spectroscopy. Triradical **3** is evaporated under ultrahigh vacuum to form thin films of intact triradicals on silicon substrate, as confirmed by high-resolution X-ray photoelectron spectroscopy. AFM and SEM images of the ∼1 nm thick films indicate that the triradical molecules form islands on the substrate. The films are stable under ultrahigh vacuum for at least 17 h but show onset of decomposition after 4 h at ambient conditions. The drop-cast films are less prone to degradation in air and have a longer lifetime.

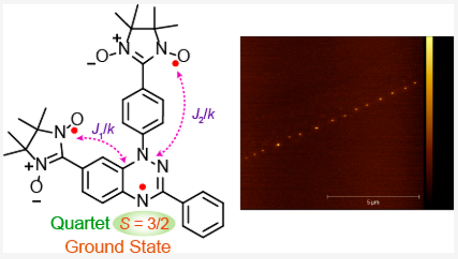

INTRODUCTION

Organic radicals with high-spin ground states and large energy gap between the high-spin ground state and low-spin excited state are promising building blocks for organic magnets,[1−10] spintronics,[11] spin filters,[12−14] sensors,[15] memory devices,[16−19] and exploration of quantum interference on molecular conductance.[20] Their potential use in organic electronics depends not only on intrinsic electronic properties and stability but also on processability. Albeit the design principles for high-spin radicals are clearly established[21,22] and a few triplet ground state diradicals with robust stability are prepared,[23−27] there are only a few reports of isolated high-spin triradicals that process both good thermal stability and an energy gap between the high-spin ground state and low-spin excited state on the order of the thermal energy (RT) at room temperature.[15,28−30]

Recently, we reported the robust triplet ground state diradicals **1** and **2** (Figure 1).[31,32] To our knowledge, these and the analogous oxoverdazyl-based diradicals[33] are the only neutral high-spin diradicals that are well characterized by thermogravimetric analysis (TGA) to establish firmly their robust thermal stability.[34] Diradicals **1** and **2** have an onset of decomposition at 175 and 160 °C, while the onset at 192 °C was reported for the oxoverdazyl-based diradical.[31−33] Diradical **2**, which has a 95+% thermal population of the triplet state at room temperature, can be evaporated under ultrahigh vacuum (UHV) to form thin films on silicon.[32]

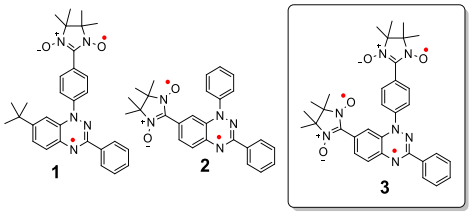

Figure 1. Thermally robust triplet ground state diradicals **1** and **2** and quartet ground state triradical **3**.

The next challenge is a high-spin triradical, with a significant population of the quartet ground state at room temperature, that is suitable for thin film fabrications. The design of triradicals involves another hurdle when an additional radical extends the molecular size. The triradical must possess not only excellent thermal stability but also a molecular mass that is still under the achievable limit of evaporation temperature.[35]

Received: February 2, 2021
Published: March 31, 2021

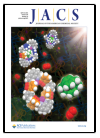

https://doi.org/10.1021/jacs.1c01305
J. Am. Chem. Soc. 2021, 143, 5508−5518

From our experience,[32,35] the controlled evaporation of diradicals is already very demanding. It would be unprecedented to successfully fabricate the first thin film of a high-spin triradical.[35−38]

Koutentis and co-workers recently reported the condensation-based synthesis of a Blatter-type triradical. The triradical is based on sequential connectivity of trimethylenemethane (TMM), *m*-phenylene, and TMM; thus, it is expected to possess nearly degenerate quartet and doublet states; that is, three $S = 1/2$ radicals are magnetically independent.[4] Their experimental finding of 300% spin concentration, corresponding to three $S = 1/2$ spins, means that the triradical is composed of three $S = 1/2$ spins that are magnetically independent at the temperature of measurement, in this case room temperature. Therefore, there is no experimental evidence for the claimed quartet ground state.[39]

The first pivotal step is the development of efficient synthetic methodologies for high-spin triradicals. Cross-couplings reactions are highly versatile and efficient methodologies in organic synthesis, relying on a metal catalyst to form a bond between two different starting materials that usually are enriched with an activating group. The development of the cross-coupling reactions in the synthesis of organic radicals has faced tremendous obstacles, largely due to the inherent reactivity of organic radicals which profoundly affect both the activation of the starting materials and the search for a suitable catalyst.[40] Okada and co-workers recently demonstrated the Pd(0)-catalyzed cross-coupling between the gold(I)−nitronyl nitroxide complex, such as **4** (Scheme 1),

Scheme 1. Synthesis of Triradical 3 and Diradicals 2 and 8

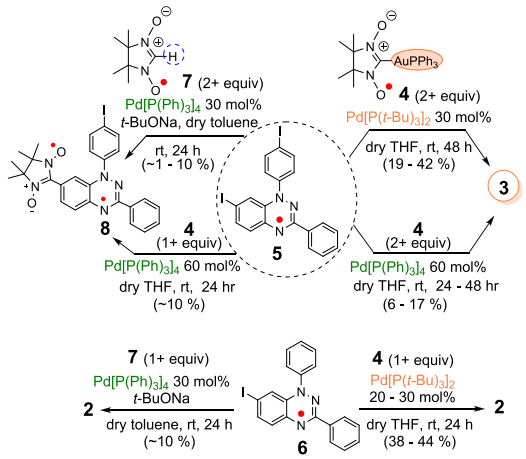

with diamagnetic iodo-substituted aromatic compounds.[41,42] Tretyakov and co-workers also utilized complex **4** for the Pd(0)-catalyzed cross-coupling with iodo-oxoverdazyls, which led to oxoverdazyl-nitronyl nitroxide diradicals in high yields.[33] These results provide valuable insight and motivation to further develop the cross-coupling methodology for a variety of stable organic radicals. We focus on the cross-coupling reactions between Blatter radicals and nitronyl nitroxide radicals (Scheme 1).

The Blatter moiety is considerably more electron-rich compared to typical diamagnetic π-systems or oxoverdazyl radicals (*vide infra*, Electrochemistry section). Thus, the common Pd(0) catalyst, such as $Pd(PPh_3)_4$ that was used by both Okada and Tretyakov,[33,41,42] may not be sufficiently powerful. In addition, spin delocalization in the Blatter radicals could be an impediment. The degree of spin density delocalization correlates with the strength of exchange coupling. The oxoverdazyl-nitronyl nitroxide diradicals have the smaller singlet−triplet energy gaps, $\Delta E_{ST} < 0.3$ kcal mol^{-1},[33] compared to $\Delta E_{ST} \approx 0.5$ kcal mol^{-1} for **1** and $\Delta E_{ST} \approx 1.7$ kcal mol^{-1} for **2**.[31,32] Thus, the spin density in the Blatter radicals is more delocalized than that in oxoverdazyls, leading to greater densities at the carbons of the C−I bonds in the starting Blatter radicals such as **5** and **6** (Scheme 1).

Here we report the synthesis and study of high-spin ($S = 3/2$) triradical **3** (Figure 1), in which we exploit the Pd(0)-catalyzed radical−radical cross-coupling reactions between di-iodo-substituted Blatter radical and nitronyl nitroxides. Triradical **3** has two doublet−quartet energy gaps, $\Delta E_{DQ} \approx 0.2-0.3$ kcal mol^{-1} and $\Delta E_{DQ}2 \approx 1.2-1.8$ kcal mol^{-1}, i.e., same order of magnitude as the thermal energy at room temperature, thus possessing a quartet ground state that is 70+% populated at room temperature. Triradical **3** is thermally robust, with an onset of decomposition at ∼160 °C under an inert atmosphere and is thermally evaporated under ultrahigh vacuum to form thin films on SiO_2/Si(111) wafers, with X-ray photoelectron spectroscopy indicating the presence of intact **3**. The AFM and SEM images of the evaporated films indicate the triradical molecules form isolated islands on the substrate, including preferential growth along a line defect of the substrate. We present here the preparation and characterization of the first thin film of high-spin ($S = 3/2$) organic triradical.

RESULTS AND DISCUSSION

Synthesis of 3. Syntheses of diradicals **1** and **2** start from the corresponding cyano-benzotriazinyl (cyano-Blatter) radicals, which are reduced to formyl-Blatter radicals and then condensed with 2,3-bis(hydroxyamino)-2,3-dimethylbutane.[31,32,43,44] Oxidation of the condensation products yields diradicals **1** and **2**, with isolated yields of 4−12% and 18−29%, respectively, for the multistep syntheses.[31,32] An analogous approach to triradical **3**, starting from the corresponding dicyano-Blatter radical, produces only miniscule quantities of triradical with ∼1% yield.

The cross-coupling of di-iodo-Blatter radical, such as **5**,[40,45−48] with 2+ equiv of **4** using the commonly used $Pd(PPh_3)_4$, with up to 60 mol % loading,[33,40−42] produces a low yield (6−17%) of triradical **3** while the coupling with 1+ equiv of **4** provides the monoiodo-substituted diradical **8** in ∼10% isolated yield (Supporting Information). Notably, the highly reactive Pd(0)-catalyst, $Pd[(t\text{-}Bu)_3P]_2$,[49] at a 30 mol % loading in the cross-coupling reaction of **4** with **5** allows for synthesis of triradical **3** in one step in good isolated yields (Scheme 1). This approach enables a routine preparation of **3** in 100+ mg batches (Supporting Information).

We explore the cross-coupling reaction of **4** with monoiodo-Blatter radical **6**[40,45−48] using the reactive catalyst, $Pd[(t\text{-}Bu)_3P]_2$,[49] which gives diradical **2** in 30−44% isolated yields (Scheme 1). We try the reactive Pd(II) catalyst,[41] such as [1,3-bis(2,6-diisopropylphenyl)imidazol-2-ylidene](3-chloropyridyl)palladium(II) dichloride, commonly abbreviated as Pd-PEPPSI-*i*-Pr, in the reaction of **4** with **6**, but the reaction mixtures fail to yield any detectable diradical **2**.

https://doi.org/10.1021/jacs.1c01305
J. Am. Chem. Soc. 2021, 143, 5508−5518

We also examine the recently developed Pd(0)-catalyzed cross-coupling between diamagnetic iodo-substituted aromatics and nitronyl nitroxide **7** in the presence of a strong base (*t*-BuONa).[50] Starting from **6**, this methodology provides diradical **2** in a low yield (∼10%). The cross-coupling of the diiodo-Blatter radical **5** with **7** produces only monoiodo-substituted diradical **8** in low yield (∼1−10%), while triradical **3** is not detectable under various conditions (Supporting Information).

X-ray Crystallography. The structure of triradical **3** is supported by single-crystal X-ray analysis. Two pseudo-polymorphs[51] are analyzed, triclinic (centrosymmetric *P*-1) and orthorhombic ($Pna2_1$), obtained by slow evaporation of solutions of **3** in toluene/heptane and chloroform/pentane, respectively. The orthorhombic structure is a solvent polymorph, containing one molecule of chloroform. The two pseudo-polymorphs have significantly different crystal packing with the triclinic structure containing C_i-symmetric dimers of triradical molecules, while in the orthorhombic crystal structure, one-dimensional π-stacks of triradical molecules are formed (see the Supporting Information).[32−34,52]

In molecules of triradical **3**, both nitronyl nitroxide radical moieties are nearly coplanar with the 1,2,4-benzotriazinyl (Blatter) radical π-system (Figure 2); in both pseudo-polymorphs, absolute values of N−C20−C5−C and N−C27−C11−C torsional angles are 19.8°−22.5° and 28.6°−34.1°, respectively. However, torsional angles between 1,4-phenylene rings (C8−C13) and the Blatter moiety are considerably greater, i.e., C9−C8−N1−C7 = 40.9°−49.7° and C13−C8−N1−N2 = 49.3°−51.4° (Figures S2 and S5). Consequently, the exchange coupling pathway from Blatter moiety to nitronyl nitroxide O1−N4−C20−N5−O2 (NNO1) is shorter and more coplanar than that to O3−N6−C27−N7−O4 (NNO2). Therefore, the exchange couplings associated with these two paths, J_1/k and J_2/k, are expected to be significantly different (Figure 2).

EPR Spectroscopy. The EPR spectra of **3** in glassy matrices show a quartet ($S = 3/2$) state, with a small admixture of thermally populated doublet ($S = 1/2$) state at $T = 110$ K (Figure 3). Because of relatively small value of zero-field splitting parameter, $D \approx 80$ MHz (Table 1), only a weak half-field ($|\Delta m_S| = 2$) transition can be observed, and no $|\Delta m_S| = 3$ signal can be detected.[53−55] Spectral simulations confirm the purity of the triradical,[56] that is, the absence of $S = 1$ or $S = 1/2$ impurities. The spectral width for $S = 3/2$ triradical **3** in toluene/chloroform glass is $4D \approx 320$ MHz, which is intermediate between $2D \approx 140$ MHz for $S = 1$ diradical **1** and $2D \approx 480$ MHz for **2**. This reflects the intermediate strength of magnetic dipole−dipole interactions in **3** that dominate the EPR spectra in glassy matrices. Similar to diradical **2**, the B3LYP/EPR-II calculations of **3** not only provide an overestimated value of $D = 160$ MHz but also indicate the positive sign of D, which is inconsistent with the experimental EPR spectrum (Supporting Information).[32,57−62]

We carry out variable temperature quantitative EPR spectroscopy on **3** in toluene/chloroform, 3:1.[31,63] At each temperature in the $T = 110$−331 K range, three independent measurements of the sample and the spin counting reference (Tempone in toluene/chloroform, 3:1) are obtained. The resultant average values of χT (mean ± SE, $n = 3$) are fit to the nonsymmetrical triradical model (Figure 2 and eq S1)[30,64] using two variable parameters, exchange coupling constants, J_1/k and J_2/k, and one fixed parameter, weight correction factor, $N = 0.99$ (Figure 3). The parameter N accounts for an inaccurate concentration of **3** due to the uncertainty in weighing about 1 mg of the triradical sample. The value of N is derived from the spectral simulations (fits) of EPR spectra at 110 K. These fits provide the relative content of $S = 3/2$ ground state and $S = 1/2$ excited state, which enables an estimation of the value of χT. The ratio of the measured χT = 1.632 ± 0.0058 emu K mol^{-1} ($n = 3$) to the estimated χT = 1.6479 ± 0.0003 emu K mol^{-1} ($n = 3$) provides the value of N = 0.99 (Figures S18 and S19).

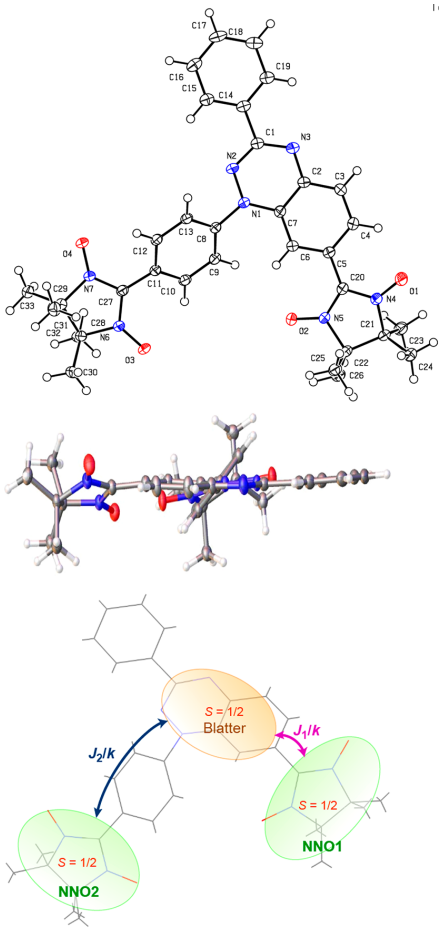

Figure 2. Single-crystal X-ray structure of triradical **3** (triclinic, centrosymmetric *P*-1 polymorph). (top) Top view, Ortep plot with carbon, nitrogen, and oxygen atoms depicted using thermal ellipsoids set at the 50% probability level. (middle) Side view of **3**. (bottom) Exchange coupling in **3**. Additional details may be found in the Supporting Information.

Values of $J_1/k = 280 \pm 17$ K and $J_2/k = 79 \pm 2.7$ K (mean ± SE) (Figure 4), obtained from a numerical fit to the nonsymmetrical trimer model (Figure 2 and eq S1), allow for the calculation of doublet−quartet energy gaps, $\Delta E_{DQ} \approx 0.2$ kcal mol^{-1}, for the lowest $S = 1/2$ excited state and $\Delta E_{DQ}2 \approx 1.2$ kcal mol^{-1}, the second lowest $S = 1/2$ excited state, by using eqs 1 and 2,[30] respectively (Table 1).

https://doi.org/10.1021/jacs.1c01305
J. Am. Chem. Soc. 2021, 143, 5508−5518

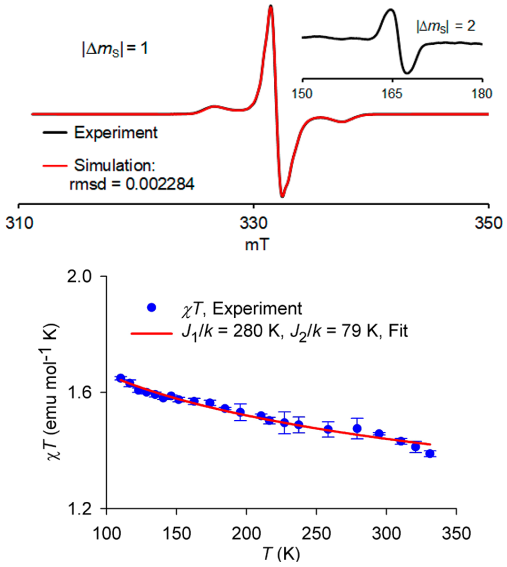

Figure 3. EPR spectroscopy of triradical **3**. (top) EPR (ν = 9.3245 GHz) spectrum of 2.32 mM triradical **3** in 2-MeTHF glass at 105 K. The $|\Delta m_S| = 2$ transition is shown as an inset. Simulation of the $|\Delta m_S| = 1$ region: S = 3/2, weight = 1.0000, D = 77.84 MHz, E = 22.70 MHz, g_{xx} = 2.0075, g_{yy} = 2.0047, g_{zz} = 2.0065; H-strain (MHz): H_x = 15.2, H_y = 79.3, H_z = 47.2; S = 1/2, weight = 0.17245, g_{xx} = 2.0018, g_{yy} = 2.0137, g_{zz} = 1.9968; H-strain (MHz): H_x = 10.2, H_y = 7.1, H_z = 17.8. (bottom) Quantitative EPR spectroscopy of 1.36 mM **3** in toluene/chloroform (3:1). Experimental values of χT (mean ± SE, n = 3) in the T = 110−331 K range and numerical two-parameter fit with two variable parameters, J_1/k = 280 ± 17 K and J_2/k = 79 ± 2.7 K (mean ± SE). Further details are reported in eq S1 and Figures S12−S18.

$$\Delta E_{DQ} = J_1 + J_2 - [J_1^2 + J_2^2 - (J_1 J_2)]^{1/2} \quad (1)$$

$$\Delta E_{DQ}2 = J_1 + J_2 + [J_1^2 + J_2^2 - (J_1 J_2)]^{1/2} \quad (2)$$

SQUID Magnetometry. The quartet ground state of **3** is confirmed by SQUID studies. The χT vs T and M/M_{sat} vs $H/(T - \theta)$ plots for a 19 mM sample of **3** in polystyrene are shown in Figure 4.

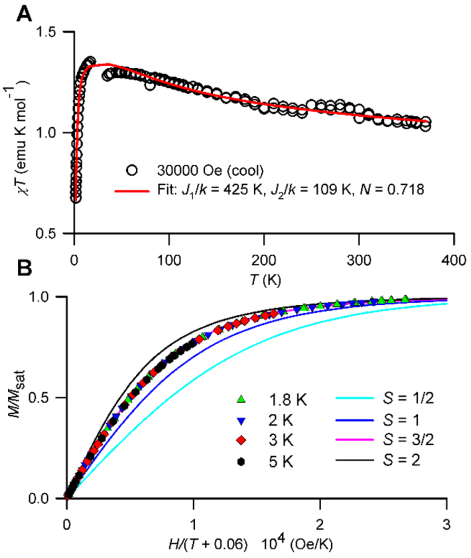

Figure 4. SQUID magnetometry of 19 mM triradical **3** in polystyrene matrix. (A) χT vs T data at H = 30000 Oe in the cooling mode were fit to a triradical model (eq S1) using three variable parameters: N = 0.718 ± 0.002, J_1/k = 425 ± 37 K, and J_2/k = 109 ± 4 K (mean ± SE), where N corresponds to weight correction factor. Downward turn in the χT vs T plot at low T is predominantly due to paramagnetic saturation. The gap in the data around 25 K corresponds to the passage through M = 0 for the entire sample. (B) M/M_{sat} vs $H/(T - \theta)$ plot, where θ = −0.06 K, at T = 1.8−5 K (symbols) and the Brillouin curves corresponding to S = 1/2 to 2 (lines). Further details are reported in Figures S20 and S21.

Using the nonsymmetrical triradical model, which includes the effects of paramagnetic saturation (Figure 2 and eq S1), the fits to the χT vs T data in the T = 1.8−370 K range give the following values of variable parameters: N = 0.718 ± 0.002, J_1/k = 425 ± 37 K, and J_2/k = 109 ± 4 K (mean ± SE), where N corresponds to weight correction factor (Figure 4A). The values of both J_1/k and J_2/k are greater than those obtained by EPR spectroscopy in toluene/chloroform. Consequently, larger $\Delta E_{DQ} \approx 0.30$ and $\Delta E_{DQ}2 \approx 1.83$ kcal mol^{-1} are obtained by using eqs 1 and 2 (Table 1). Also, these fits indicate that the

Table 1. Magnetic Characterization of Triradical 3 vs Diradicals 1 and 2

		matrix	|D| (MHz)	|E| (MHz)	J_1/k (K)	J_2/k (K)	ΔE_{DQ}[a]/ΔE_{ST} (kcal mol^{-1})
3	EPR	Tol/Chl[b]	80	23	280	79	+0.22[a]
	EPR	2-MeTHF	78	23			
	EPR	polystyrene	77	23			
	SQUID	polystyrene			425	109	+0.30[a]
	DFT	gas phase	160[c]	20[c]			+1.14[d]
2	SQUID	crystals[32]			438		+1.74 ± 0.07
	SQUID	polystyrene[32]			419		+1.68 ± 0.16
	EPR	Tol/Chl[b,32]	242	35.1			
1	SQUID	crystals[32]				126	+0.50 ± 0.02
	EPR	Tol/Chl[b,31]	69.6	4.2		117	+0.47

[a] ΔE_{DQ} (kcal mol^{-1}) determined experimentally by using eq 1. [b] Toluene/chloroform, 3:1. [c] D and E computed at the B3LYP/EPR-II level by using ORCA.[57] [d] BS-DFT-computed ΔEDQ at the UB3LYP/6-31G(d,p)+ZPVE level;[65] ΔEDQ2 = 1.22 (EPR) and 1.83 (SQUID) kcal mol^{-1} vs 2.59 (DFT) kcal mol^{-1}.

https://doi.org/10.1021/jacs.1c01305
J. Am. Chem. Soc. 2021, 143, 5508−5518

intermolecular exchange interactions between molecules of **3** are negligible; i.e., the value of mean-field parameter, θ, is near zero.

Using Brillouin functions with a small mean-field parameter, $\theta = -0.06$ K, two-parameter fits to the magnetization (M) vs magnetic field (H) data, i.e., the M vs $H/(T - \theta)$ data, at low temperatures (T = 1.8−5 K) provide the total spin, S = 1.5 and magnetization at saturation, M_{sat} = 0.736 μ_B (μ_B = Bohr magneton). These data unequivocally confirm a quartet (S = 3/2) ground state for **3**. In addition, the value of M_{sat} = 0.74 μ_B is comparable to N = 0.72, obtained from the fit to the χT vs T data, thus indicating that the triradical is pure. Both M_{sat} and N are less than 1.00 because of weighing errors of **3** in the submilligram range.

A sample of **3** in benzene is investigated, in which the fits to M vs $H/(T - \theta)$ data provide the total spin, S = 1.5, and indicate an S = 3/2 ground state (Figure S23). Because of the relatively large mean-field parameter, $\theta \approx -1$ K, indicating relatively strong intermolecular antiferromagnetic interactions, the four-parameter fits to the χT vs T data in the relatively narrow T = 1.8−260 K range are unreliable, and thus, ΔE_{DQ} could not be determined.

Electrochemistry and UV−Vis−NIR Spectroscopy. Cyclic voltammetry for diradical **2** and triradical **3** in 0.1 M tetrabutylammonium hexafluorophosphate in dichloromethane at room temperature shows the presence of reversible waves associated with the oxidation of Blatter radical moieties ($E^{+/0} \approx +0.4$ V) and nitronyl nitroxide moieties ($E^{2+/+} \approx +1.0$ V). A reversible wave corresponding to the reduction of either the Blatter radical or the nitronyl nitroxide moiety is also observed in the $E^{-/0} \approx -0.7$ to −0.9 V range (Table S5 and Figures S9−S11). (All redox potentials are reported versus SCE.) These values are comparable to those obtained for the parent Blatter radical (+0.10 and −0.96 V) and a derivative of nitronyl nitroxide (+0.81 and −0.75 V) in acetonitrile.[18,66] Notably, $E^{+/0}$ for the oxoverdazyl radicals is about 0.4 V more positive,[33,67] and therefore they are considerably more difficult to oxidize.

UV−vis−NIR spectra of diradical **2** and triradical **3** in dichloromethane have a similar spectral pattern, consisting of three major bands at 300, 370−380, and 510−550 nm (Figure S8). The peak intensity at 371 nm ($\varepsilon_{max} = 2.26 \times 10^4$ L mol^{-1} cm^{-1}) for **3** is about twice that at 381 nm ($\varepsilon_{max} = 1.3 \times 10^4$ L mol^{-1} cm^{-1}) for diradical **2**. The intense 371 nm peak is associated with the band originating from the phenyl-substituted nitronyl nitroxide, which usually appears at 362 nm ($\varepsilon_{max} = 1.77 \times 10^4$ L mol^{-1} cm^{-1}) in hexane or at 360 nm ($\varepsilon_{max} = 1.33 \times 10^4$ L mol^{-1} cm^{-1}) in ethanol.[43,68] Diradical **2** and triradical **3** have nearly identical absorption onsets in the 860−880 nm range, corresponding to an optical gap, E_g = 1.42 ± 0.01 eV (mean ± SE). The UV−vis−NIR spectrum for triradical **3** could be reproduced by the TD-DFT computation at the UCAM-B3LYP/6-31+G(d,p)/IEF-PCM-UFF level of theory employing a dichloromethane solvent model (Figure S26).

Thermal Stability. Triradical **3** possesses excellent stability at ambient conditions. It can be purified by chromatography using normal phase silica gel. Thermogravimetric analysis data suggest that thermal decomposition of **3** starts at 166 °C (1% mass loss), which is slightly higher than the onset temperature for diradical **2** (Figure 5) and lower than that for diradical **1**. The maximum rate of mass loss for **3** is at 180 °C.

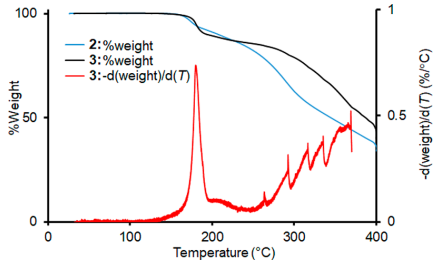

Figure 5. Thermogravimetric analysis (TGA) of triradical **3** under N_2; heating rate = 5 °C min^{-1}.

Thin Films of 3 on SiO_2/Si(111) Substrate. An important prerequisite of the technological applications foreseen for this class of materials requires attaching molecules to a substrate, to form either an interface or a film. A controlled and clean way to achieve this goal is by using controlled evaporation. We have previously focused our efforts on the evaporation of radicals and diradicals.[32,35−38,69−72]

Here, we extend our protocol to evaporate triradical **3**. We deposit thin films of triradical **3** on SiO_2/Si(111) wafers by organic molecular beam deposition (OMBD),[73] which has been proven to be a suitable method for growing radical and diradical thin films. However, increasing the number of radical sites implies an increased reactivity during evaporation, making it extremely challenging.[35,38] We investigate the obtained thin films by X-ray photoelectron spectroscopy (XPS), an effective and powerful tool for studies of organic and organic radical thin films.[38] We adopt the approach that was previously used for the diradical thin films to assess the intactness of triradical **3** in the films.[32,35] We also obtain the films by drop-casting deposition. Fabrication of films by the two growth methods allows exploring the differences due to preparation and thickness range. The C 1s and N 1s core level curves are shown in Figure 6 that also includes the fit components. In fact, XPS is sensitive to the stoichiometry of the films; identifying the contributions associated with each element in its chemical environment helps to gain information about the

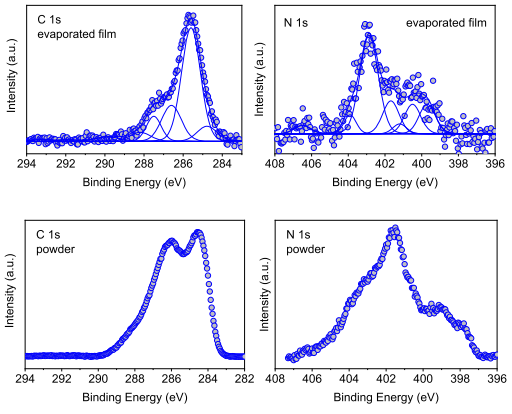

Figure 6. Typical C 1s and N 1s core level XPS spectra of triradical **3** deposited on SiO_2/Si(111) wafers (0.4 nm thick film, nominal thickness) (top plots) together with the fit analysis compared to the powder spectra (bottom plots).

https://doi.org/10.1021/jacs.1c01305
J. Am. Chem. Soc. 2021, 143, 5508−5518

chemical composition of the films after evaporation (the fit procedure is described step by step in refs 32 and 74). The elemental concentration of the films calculated from the XPS spectra agrees very well with the stoichiometry of the triradical (carbon 84.4% and nitrogen 16.6% as obtained from XPS versus the stoichiometric 82.5% and 17.5%, respectively). This agreement is further supported by the fit results of the single contributions due to photoelectrons emitted by atoms with different chemical environment that shows the expected intensities in the main line (Tables S6 and S7). Note that we do not consider the O 1s spectroscopic line because it is a superposition of the signal from the films and the substrate making its fit analysis speculative.

The C 1s spectrum of the evaporated films is characterized by a main line at around 285.5 eV due to photoelectrons emitted from the atoms in the aromatic ring and the carbon atoms bound to hydrogen atoms (C−C, C−H, and CH_3). The shoulder at higher binding energy is due to contributions from the electrons emitted from carbon atoms bound also to nitrogen (C−N).

Nitrogen atoms, because of their higher electronegativity, shift the electronic cloud; thus, the electrons are emitted with lower kinetic energy, i.e., higher binding energy. The N 1s core level spectrum shows contributions due to seven nitrogen atoms: the three nitrogen atoms belonging to the Blatter radical have different chemical environments, while the two nitrogen atoms belonging to the nitronyl nitroxide (NN) radical have equivalent chemical environments.[32,35,72,75] These differences give rise to a complex spectrum with two broad features, showing the highest intensity at around 402.5 eV that corresponds to the line expected in the NN radical N 1s core level spectrum.[72] We also observe the presence of satellites; they are typical features in photoemission that appear as an effect of the relaxation processes due to the creation of a core hole.[76,77] On the basis of the comparison of the film fit results (Tables S6 and S7) and the molecular stoichiometry, we can conclude that there is no degradation of the triradical molecules during evaporation and deposition, under the present conditions.

The comparison with the powder spectra also indicates that the evaporation and the deposition of the film are successful. We note that the XPS curves of the powder are affected by a strong charging effect. This effect is expected in organic crystals because of the absence of efficient screening of the core hole.[78] Here this effect is very strong, leading to a broadening of the features and changes in the line intensities. We noticed similarly strong charging effects also in the XPS curves of diradical **2** that may be viewed as a fusion of the Blatter radical with a single nitronyl nitroxide radical, therefore having two radical moieties in common with triradical **3**.[32]

XPS also offers the opportunity to identify *in situ* the thin film growth mode following the decay of the substrate signal during evaporation. We follow the XPS core level signal of the substrate (Si 2p) by looking at its attenuation upon film deposition (Figure 7). The curve is characterized by a very slow decay. This intensity trend hints at a Volmer−Weber (VW) growth mode, i.e., island growth.[79] This result is consistent with the *ex situ* atomic force microscopy (AFM) and the scanning electron microscope (SEM) images obtained for triradical **3** films (Figure 7), which are clearly showing a film morphology dominated by islands. The VW growth mode occurs when the interaction between the deposited molecules is much stronger than between the molecules and the substrate.[80] We have observed this growth mode for all thin films of radicals and diradicals that we have previously investigated, grown on SiO_2/Si(111) wafers, keeping the substrate at room temperature. However, the tendency to grow isolated islands increases from radicals to diradicals,[32,35] and now it is confirmed by the present results on triradical **3**.

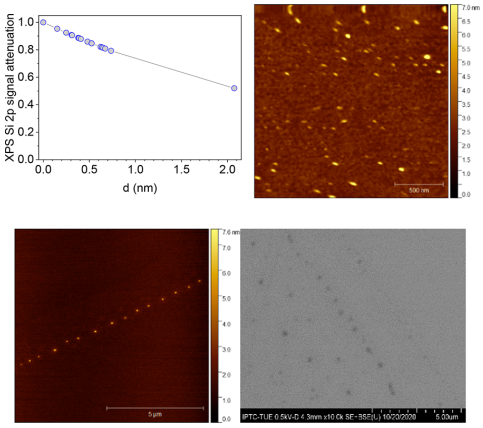

Figure 7. (upper panels) Attenuation of the Si 2p XPS signal, normalized to the corresponding saturation signal, as a function of film nominal thickness, deposition at room temperature (the line is a guide to the eye). A typical 2 μm × 2 μm AFM image of a film (0.4 nm nominally thick film, bottom panel). (lower panels) A 10 μm × 10 μm AFM image of a film (0.7 nm nominally thick film) showing the island decorating a line defect of the substrate, together with the corresponding SEM image.

We also observe that the nonstoichiometric films, resulting from failed evaporations of **3**, show a different island morphology. The microscopy investigations (Figure S24) suggest that different stoichiometry leads to different molecule−molecule interactions and plays a central role in the film morphology.

We investigate the drop-cast films using the same techniques. XPS spectra of the film (Figure 8) show the same features as those in the spectra of the evaporated samples. The results further affirm that the evaporation does not degrade the triradical. The fit procedure supports the expected result of films having elemental concentrations in agreement with the stoichiometry of the triradical (Tables S8 and S9). The AFM images as well as the SEM images are featureless and flat (over the examined field of view) as expected for the drop-cast preparation. The SEM images that comprise a larger area are characterized by distributed circular valleys, as typically observed in films obtained by using this processing method, due to the drying effects caused by the solvent evaporation (Figure 8).

Finally, we monitor the lifetime of the films in UHV (base pressure 2 × 10^{-10} mbar) by using XPS, focusing on the N 1s core level spectrum that is correlated to the nitronyl nitroxide and Blatter radicals.[38,72] We adopt the protocol previously applied to radical and diradical films.[32,35,74] We observe no major changes in the spectra of the evaporated films after their exposure to UHV at room temperature for around 17 h (Figure S25). However, after 4 h of air exposure, we observe major changes in their XPS spectra, indicating film degradation (Figure S25). Thus, the triradical thin films are much less

https://doi.org/10.1021/jacs.1c01305
J. Am. Chem. Soc. 2021, 143, 5508−5518

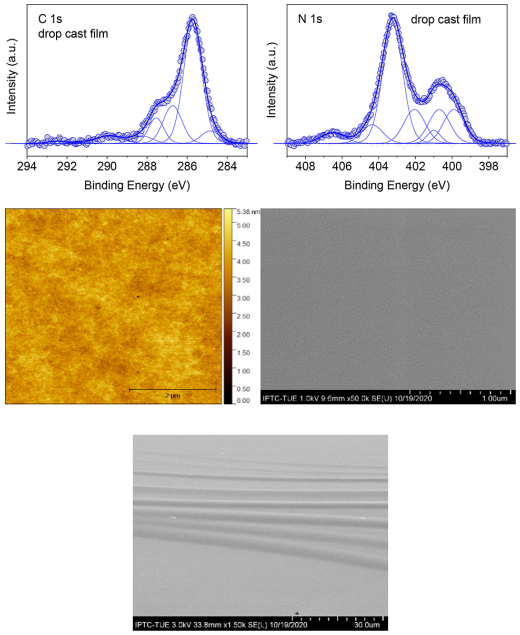

Figure 8. (upper panels) C 1s and N 1s core level XPS spectra of a drop-cast film of triradical **3** deposited on SiO_2/Si(111) wafers (top plots) together with the fit analysis. (middle panels) A typical featureless 5 μm × 5 μm AFM image of a drop-cast film with the corresponding SEM image. (lower panel) A typical SEM image showing the circular valleys due to the drying effects.

robust in air. We have found that diradical thin films have shorter lifetime in air than their monoradical analogues. (Nitronyl nitroxide and the Blatter monoradical derivatives showed changes in their XPS after the films were kept for several weeks/months at ambient conditions.[35,37,72]) This tendency is now also found for the evaporated triradical **3** films.

The drop-cast film N 1s core level spectra change on a longer time scale when exposed to air. These changes are different, however, rather than showing different line shapes as in the case of the evaporated films; there is a change in the relative intensities of the two broad features (Figure S25), which may be due to structural changes. We also observe changes in the intensity of the satellite features that would support this hypothesis.[81,82] In addition, the changes in N 1s core level spectra tend to saturate after 84 h. Also, the adsorption of ambient nitrogen may contribute to the changes of the core level line intensities. Because the drop-cast films are thicker by 2 orders of magnitude than the evaporated films (nanometers versus hundreds of nanometers), we may speculate that the changes in intensities originate from the degradation of the more superficial layers of the drop-cast films. These degraded layers then act as a protective buffer for the underneath material that keeps its properties.

CONCLUSION

We have synthesized a high-spin triradical **3** by the radical−radical cross-coupling reaction between di-iodo-substituted Blatter radical and nitronyl nitroxide derivative. We show that at room temperature 70+% of the triradical molecules populate the high-spin, $S = 3/2$, ground state. The triradical possesses a remarkable thermal stability to permit fabrication of intact triradical thin films on silicon substrate via evaporation under ultrahigh vacuum. The triradical molecules form isolated islands on the substrate with the tendency to decorate the substrate line defects, which might be useful for fabrication of nanostructured functionalized surfaces. The triradical films are stable under ultrahigh vacuum; however, within a few hours of exposure to air, XPS of the films show major changes. The drop-cast films show longer air lifetime. We have demonstrated that it is possible to evaporate triradicals and deposit their thin films under controlled conditions without degradation. The triradical films are less stable compared to the films of diradical **2** or nitronyl nitroxide and Blatter monoradicals. Our triradical, with an unprecedented combination of high-spin ground state and thermal properties, which is suitable for thin film fabrication under ultrahigh vacuum, could facilitate the development of purely organic magnetic and electronic materials.

EXPERIMENTAL SECTION

(Nitronyl nitroxide-2-ido)(triphenylphosphine)gold(I) (**4**) is synthesized by the reaction of nitronyl nitroxide (**7**) and $Au^I(PPh_3)Cl$ with NaOH in methanol/dichloromethane.[41,83,84] After purification by chromatography (deactivated Al_2O_3), the spin concentration of **4** is up to 99%. Di-iodo-Blatter radical **5** and its monoiodo analogue **6** are prepared according to previous literature.[45,46]

Frozen and liquid solution EPR spectra were obtained by using a Bruker EMX-plus X-band spectrometer and simulated with the EasySpin software.[56] The TGA instrument (TA Instruments TGA 550) was run either without or with IR attachment (Thermo NICOLET Is50 NIR). Variable temperature (from 1.8 up to 370 K) magnetic susceptibility measurements of **3** were performed by using a Quantum Design SQUID magnetometer with applied magnetic fields of 30000 and 5000 Oe. Variable field (0−50000 Oe) magnetization studies were performed at temperatures of 1.8−5 K. Sample tubes for SQUID studies in dilute matrices[85] are described in the Supporting Information.

X-ray Crystallography. Crystals of **3** for X-ray studies were prepared by slow evaporation from solution in in toluene/heptane and chloroform/pentane. Data collections were performed at 100 K at either the Advanced Photon Source, Argonne National Laboratory, by using $\lambda = 0.41328$ Å synchrotron radiation (silicon monochromators) or the Indiana University by using Mo Kα radiation. Following integration (SAINT),[86] the intensity data were corrected for absorption (SADABS).[87] The space groups for two polymorphs, *P*-1 and $Pna2_1$, were determined based on intensity statistics and the systematic absences. The structures were solved (SHELTX)[88] and then refined on *F*2 (SHELXL).[89] Crystal and structure refinement data for two polymorphs of **3** are in the Supporting Information and the deposited (CCDC #s: 2062663 and 2062664) files in CIF format.

Synthesis of Triradical 3. Standard techniques for synthesis under inert atmosphere (argon or nitrogen) using custom-made Schlenk glassware, custom-made double manifold high-vacuum lines, argon-filled MBraun glovebox, and nitrogen-filled glovebags. Chromatographic separations were performed by using either normal phase silica gel or neutral alumina.

Triradical **3**. A mixture of Blatter radical **5** (200.0 mg, 0.373 mmol, 1 equiv) and nitronyl nitroxide radical **4** (500.0 mg, 0.821 mmol, 2.2 equiv) was added to a Schlenk tube and evacuated on vacuum line for several minutes. The tube was kept under vacuum, and then it was transferred to the antichamber of the glovebox. Inside the argon-filled glovebox, palladium(0) catalyst ($Pd[P(t\text{-}Bu)_3]_2$, 57.0 mg, 30 mol %) was added into the tube. Freshly distilled, dry THF was added into the tube under an argon gas flow. The reaction mixture was stirred at room temperature for 48 h. The dark red solution was evaporated to

https://doi.org/10.1021/jacs.1c01305
J. Am. Chem. Soc. 2021, 143, 5508−5518

provide a dark solid, which was purified by silica gel column chromatography using dichloromethane, followed by 10% ethyl acetate in dichloromethane, as eluents. The resultant solid was washed with pentane to give 93.1 mg (42%) of product **3** as a dark solid. TLC (silica gel, ethyl acetate): R_f 0.43. HR-TOF-MS: m/z, $[M + Na]^+$ calcd for $C_{33}H_{36}N_7O_4Na$ 617.2726; found, 617.2728 (0.3 ppm, RA = 100%). IR (powder, cm^{-1}): 2981.51, 2937.11, 1599.50, 1518.83, 1480.79, 1448.57, 1419.16, 1392.11, 1363.07, 1310.84, 1271.29, 1254.60, 1194.33, 1130.93, 1069.11, 1025. 05, 1017.26, 952.98, 919.95, 863.37, 834.99, 823.22, 788.48, 699.98. 2981.51, 2937.11, 1599.50, 1518.83, 1480.79, 1448.57, 1419.16, 1392.11, 1363.07, 1310.84, 1271.29, 1254.60, 1194.33, 1130.93, 1069.11, 1025. 05, 1017.26, 952.98, 919.95, 863.37, 834.99, 823.22, 788.48, 699.98. The spin concentration was determined to be 378% (χT = 1.42 emu K mol^{-1}) in toluene/chloroform (4:1) fluid solution at 294 K and 435% (χT = 1.63 emu K mol^{-1}) at 110 K in toluene/chloroform (3:1) glass. For each measurement, TEMPONE in the identical solvent was used as a spin counting reference. Because we use S = 1/2 monoradical as reference (100% spin concentration), for an S = 3/2 triradical with perfectly populated quartet ground state spin concentration should be 100%$[3/2 \times (3/2 + 1)]/[1/2 \times (1/2 + 1)]$ = 500%; in other words, the signal intensity (or χT) should correspond to five independent monoradicals. Values of <500% reflect thermal population of the excited doublet states.

Computational Details. All geometry optimizations for **3** were performed at the UB3LYP/6-31G(d,p) level of theory in the gas phase or with Gaussian 16 default IEF-PCM solvent model for toluene, tetrahydrofuran, or ethanol (Table S10). Obtained minima were confirmed by frequency calculations. The broken-symmetry approach was applied for open-shell doublet calculations, and spin contamination errors were corrected by approximate spin-projection method.[90,91] Broken symmetry doublet wave functions ($\langle S^2 \rangle \approx 1.8$) at the UB3LYP/6-31G(d,p)+ZPVE level of theory were checked for stability. All calculations were performed with the Gaussian 16 program suite.[65]

Thin Film Growth, XPS, and Microscopy Measurements. Thin films were deposited on native SiO_2 grown on single-side polished n-Si(111) wafers. The films were evaporated via OMBD by using a Knudsen cell under UHV conditions. The UHV apparatus used for deposition and XPS measurements is composed of dedicated preparation and measurement (base pressure 3 × 10^{-10} mbar) chambers. The measurement chamber is equipped with a monochromatic Al Kα source (SPECS Focus 500) and a hemispherical electron analyzer (SPECS Phoibos 150). The wafers were cleaned by sonication for an hour each in ethanol and acetone and subsequent annealing at ca. 500 K in UHV and verification of cleanness by XPS. The nominal films thicknesses of the evaporated films were calculated from the attenuation of the substrate signal. Drop-cast films of triradical **3** from 50 μL of toluene solution with a concentration of 2–3 mg/mL were deposited on the substrates with an area of about 1 cm^2 under ambient conditions. Their thickness (100–250 nm) was estimated with a scratch test by using SEM images. For the preparation of powder samples indium foil was used into which the powder was firmly pressed to minimize the charging of the crystals. Pass energies of 50 and 20 eV were used for survey spectra and individual core level spectra, respectively. Spectra were calibrated to the Si 2p signal at 99.8 eV and the In 3d signal at 103.3 eV depending on the used substrate. Radiation damage was minimized by only measuring freshly prepared samples and limiting beam exposure. Beam exposure in measurements aimed to investigate the stability of the films was further reduced to attribute changes solely to the degradation by air or in UHV. This leads to a worse signal-to-noise ratio. Atomic force microscopy (AFM) was measured in air with a Digital Instruments Nanoscope III Multimode AFM using tapping mode and ScanAsyst mode. Scanning electron microscopy (SEM) was measured by using a HITACHI SU8030 ultrahigh resolution field emission scanning electron microscope.

■ ASSOCIATED CONTENT

Supporting Information

The Supporting Information is available free of charge at https://pubs.acs.org/doi/10.1021/jacs.1c01305.

General procedures and materials, additional experimental details, fit results for the energy positions and relative intensities of the photoemission lines in the C 1s and N 1s spectra; AFM and SEM microscopy of thin films; UHV and air film lifetime (PDF)

Accession Codes

CCDC 2062663–2062664 contain the supplementary crystallographic data for this paper. These data can be obtained free of charge via www.ccdc.cam.ac.uk/data_request/cif, or by emailing data_request@ccdc.cam.ac.uk, or by contacting The Cambridge Crystallographic Data Centre, 12 Union Road, Cambridge CB2 1EZ, UK; fax: +44 1223 336033.

■ AUTHOR INFORMATION

Corresponding Authors

Andrzej Rajca − *Department of Chemistry, University of Nebraska, Lincoln, Nebraska 68588-0304, United States;* orcid.org/0000-0002-8856-1536; Email: arajca1@unl.edu

Maria Benedetta Casu − *Institute of Physical and Theoretical Chemistry, University of Tübingen, 72076 Tübingen, Germany;* orcid.org/0000-0002-5659-7040; Email: benedetta.casu@uni-tuebingen.de

Authors

Chan Shu − *Department of Chemistry, University of Nebraska, Lincoln, Nebraska 68588-0304, United States*

Maren Pink − *Department of Chemistry, Indiana University, Bloomington, Indiana 47405-7102, United States*

Tobias Junghoefer − *Institute of Physical and Theoretical Chemistry, University of Tübingen, 72076 Tübingen, Germany*

Elke Nadler − *Institute of Physical and Theoretical Chemistry, University of Tübingen, 72076 Tübingen, Germany*

Suchada Rajca − *Department of Chemistry, University of Nebraska, Lincoln, Nebraska 68588-0304, United States;* orcid.org/0000-0003-0904-8329

Complete contact information is available at: https://pubs.acs.org/10.1021/jacs.1c01305

Notes

The authors declare no competing financial interest.

■ ACKNOWLEDGMENTS

We thank the National Science Foundation (NSF), Chemistry Division, for support of this research under Grants CHE-1665256 and CHE-1955349 (A.R.) and the National Institutes of Health (NIGMS #R01GM124310-01 to S.R. and A.R.) for the upgrade of EPR spectrometer. Support for the acquisition of the Bruker Venture D8 diffractometer through the Major Scientific Research Equipment Fund from the President of Indiana University and the Office of the Vice President for Research is gratefully acknowledged. NSF's ChemMatCARS Sector 15 is supported by the Divisions of Chemistry (CHE) and Materials Research (DMR), National Science Foundation, under Grant NSF/CHE-1834750. Use of the Advanced Photon Source, an Office of Science User Facility operated for the U.S. Department of Energy (DOE) Office of Science by

Argonne National Laboratory, was supported by the U.S. DOE under Contract DE-AC02-06CH11357. We also thank Thomas Chassé for accessing the photoelectron laboratory at the University of Tübingen. Financial support from the German Research Foundation (DFG) under Contract CA852/11-1 is gratefully acknowledged. We thank Dr. N. M. Gallagher for initial trials in the synthesis of triradical **3** by using the condensation method and Dr. Hui Zhang for sample preparations for SQUID measurements.

REFERENCES

(1) Rajca, A.; Wongsriratanakul, J.; Rajca, S. Magnetic ordering in an organic polymer. *Science* **2001**, *294*, 1503−1505.
(2) Ratera, L.; Veciana, J. Playing with organic radicals as building blocks for functional molecular materials. *Chem. Soc. Rev.* **2012**, *41*, 303−349.
(3) Wingate, A. J.; Boudouris, B. W. Recent advances in the syntheses of radical-containing macromolecules. *J. Polym. Sci., Part A: Polym. Chem.* **2016**, *54*, 1875−1894.
(4) Rajca, A. Organic diradicals and polyradicals: from spin coupling to magnetism? *Chem. Rev.* **1994**, *94*, 871−893.
(5) Rajca, A. The Physical Organic Chemistry of Very High-Spin Polyradicals. *Adv. Phys. Org. Chem.* **2005**, *40*, 153−199.
(6) Gallagher, N. M.; Olankitwanit, A.; Rajca, A. High-Spin Organic Molecules. *J. Org. Chem.* **2015**, *80*, 1291−1298.
(7) Rajca, A.; Lu, K.; Rajca, S. High-spin polyarylmethyl polyradical: Fragment of a macrocyclic 2-strand based upon calix[4]arene rings. *J. Am. Chem. Soc.* **1997**, *119*, 10335−10345.
(8) Rajca, S.; Rajca, A.; Wongsriratanakul, J.; Butler, P.; Choi, S. Organic Spin Clusters. Dendritic-Macrocyclic Polyarylmethyl Polyradical with Very High-Spin of *S* = 10 and its Derivatives: Synthesis, Magnetic Studies, and Small Angle Neutron Scattering. *J. Am. Chem. Soc.* **2004**, *126*, 6972−6986.
(9) Rajca, A.; Wongsriratanakul, J.; Rajca, S.; Cerny, R. L. Organic Spin Clusters: Annelated Macrocyclic Polyarylmethyl Polyradicals and Polymer with Very High-Spin *S* = 6−18. *Chem. - Eur. J.* **2004**, *10*, 3144−3157.
(10) Rajca, A.; Wongsriratanakul, J.; Rajca, S. Organic Spin Clusters: Macrocyclic-Macrocyclic Polyarylmethyl Polyradicals with Very High-Spin S = 5−13. *J. Am. Chem. Soc.* **2004**, *126*, 6608−6626.
(11) Sanvito, S. Molecular spintronics. *Chem. Soc. Rev.* **2011**, *40*, 3336−3355.
(12) Shil, S.; Bhattacharya, D.; Misra, A.; Klein, D. J. A high-spin organic diradical as a spin filter. *Phys. Chem. Chem. Phys.* **2015**, *17*, 23378−23383.
(13) Herrmann, C.; Solomon, G. C.; Ratner, M. A. Organic Radicals as Spin Filters. *J. Am. Chem. Soc.* **2010**, *132*, 3682−3684.
(14) Hu, G.; Xie, S.; Wang, C.; Timm, C. Spin-dependent transport and functional design in organic ferromagnetic devices. *Beilstein J. Nanotechnol.* **2017**, *8*, 1919−1931.
(15) Gaudenzi, R.; Burzuri, E.; Reta, D.; Moreira, I. d. P. R.; Bromley, S. T.; Rovira, C.; Veciana, J.; van der Zant, H. S. J. Exchange Coupling Inversion in a High-Spin Organic Triradical Molecule. *Nano Lett.* **2016**, *16*, 2066−2071.
(16) Yonekuta, Y.; Susuki, K.; Oyaizu, K.; Honda, K. Battery-Inspired, Nonvolatile, and Rewritable Memory Architecture: a Radical Polymer-Based Organic Device. *J. Am. Chem. Soc.* **2007**, *129*, 14128−14129.
(17) Oyaizu, K.; Nishide, H. Radical Polymers for Organic Electronic Devices: A Radical Departure from Conjugated Polymers? *Adv. Mater.* **2009**, *21*, 2339−2344.
(18) Lee, J.; Lee, E.; Kim, S.; Bang, G. S.; Shultz, D. A.; Schmidt, R. D.; Forbes, M. D. E.; Lee, H. Nitronyl Nitroxide Radicals as Organic Memory Elements with Both n- and p-Type Properties. *Angew. Chem., Int. Ed.* **2011**, *50*, 4414−4418.
(19) Gaudenzi, R.; de Bruijckere, J.; Reta, D.; Moreira, I. d. P. R.; Rovira, C.; Veciana, J.; van der Zant, H. S. J.; Burzuri, E. Redox-Induced Gating of the Exchange Interactions in a Single Organic Diradical. *ACS Nano* **2017**, *11*, 5879−5883.
(20) Tsuji, Y.; Hoffmann, R.; Strange, M.; Solomon, G. C. Close relation between quantum interference in molecular conductance and diradical existence. *Proc. Natl. Acad. Sci. U. S. A.* **2016**, *113*, E413−E419.
(21) Borden, W. T.; Davidson, E. R. Effects of electron repulsion in conjugated hydrocarbon diradicals. *J. Am. Chem. Soc.* **1977**, *99*, 4587−4594.
(22) Ovchinnikov, A. A. Multiplicity of the ground state of large alternant organic molecules with conjugated bonds (do organic ferromagnets exist?). *Theor. Chim. Acta* **1978**, *47*, 297−304.
(23) Inoue, K.; Iwamura, H. 2-[*p*-(*N*-tert-butyl-*N*-oxyamino)-phenyl]-4,4,5,5-tetramethyl-4,5-dihydroimidazol-3-oxide-l-oxyl, a stable diradical with a triplet ground state. *Angew. Chem., Int. Ed. Engl.* **1995**, *34*, 927−928.
(24) Shultz, D. A.; Fico, R. M.; Lee, H.; Kampf, J. W.; Kirschbaum, K.; Pinkerton, A. A.; Boyle, P. D. Mechanisms of exchange modulation in trimethylenemethane-type biradicals: The roles of conformation and spin density. *J. Am. Chem. Soc.* **2003**, *125*, 15426−15432.
(25) Rajca, A.; Shiraishi, K.; Vale, M.; Han, H.; Rajca, S. Stable Hydrocarbon Diradical, an Analogue of Trimethylenemethane. *J. Am. Chem. Soc.* **2005**, *127*, 9014−9020.
(26) Suzuki, S.; Furui, T.; Kuratsu, M.; Kozaki, M.; Shiomi, D.; Sato, K.; Takui, T.; Okada, K. Nitroxide-substituted nitronyl nitroxide and iminonitroxide. *J. Am. Chem. Soc.* **2010**, *132*, 15908−15910.
(27) Kato, K.; Furukawa, K.; Osuka, A. A Stable Trimethylenemethane Triplet Diradical Based on a Trimeric Porphyrin Fused π-System. *Angew. Chem., Int. Ed.* **2018**, *57*, 9491−9494.
(28) Shimizu, D.; Osuka, A. A Benzene-1,3,5-Triaminyl Radical Fused with Zn-II-Porphyrins: Remarkable Stability and a High-Spin Quartet Ground State. *Angew. Chem., Int. Ed.* **2018**, *57*, 3733−3736.
(29) Ishida, T.; Iwamura, H. Bis[3-tert-butyl-5-(*N*-oxy-*tert*-butylamino)phenyl] nitroxide in a quartet ground state: a prototype for persistent high-spin poly[(oxyimino)-1,3-phenylenes]. *J. Am. Chem. Soc.* **1991**, *113*, 4238−4241.
(30) Tanaka, M.; Matsuda, K.; Itoh, T.; Iwamura, H. Syntheses and Magnetic Properties of Stable Organic Triradicals with Quartet Ground States Consisting of Different Nitroxide Radicals. *J. Am. Chem. Soc.* **1998**, *120* (29), 7168−7173.
(31) Gallagher, N. M.; Bauer, J. J.; Pink, M.; Rajca, S.; Rajca, A. High-spin organic diradical with robust stability. *J. Am. Chem. Soc.* **2016**, *138*, 9377−9380.
(32) Gallagher, N.; Zhang, H.; Junghoefer, T.; Giangrisostomi, E.; Ovsyannikov, R.; Pink, M.; Rajca, S.; Casu, M. B.; Rajca, A. Thermally and Magnetically Robust Triplet Ground State Diradical. *J. Am. Chem. Soc.* **2019**, *141*, 4764−4774.
(33) Tretyakov, E. V.; Zhivetyeva, S. I.; Petunin, P. V.; Gorbunov, D. E.; Gritsan, N. P.; Bagryanskaya, I. Y.; Bogomyakov, A. S.; Postnikov, P. S.; Kazantsev, M. S.; Trusova, M. E.; Shundrina, I. K.; Zaytseva, E. V.; Parkhomenko, D. A.; Bagryanskaya, E. G.; Ovcharenko, V. I. Ferromagnetically Coupled S = 1 Chains in Crystals of Verdazyl-Nitronyl Nitroxide Diradicals. *Angew. Chem., Int. Ed.* **2020**, *59*, 20704−20710.
(34) Wang, W.; Chen, C.; Shu, C.; Rajca, S.; Wang, X.; Rajca, A. S = 1 Tetraazacyclophane Diradical Dication with Robust Stability: a Case of Low Temperature One-Dimensional Antiferromagnetic Chain. *J. Am. Chem. Soc.* **2018**, *140*, 7820−7826.
(35) Junghoefer, T.; Gallagher, N.; Kolanji, K.; Giangrisostomi, E.; Ovsyannikov, R.; Chassé, T.; Baumgarten, M.; Rajca, A.; Calzolari, A.; Casu, M. B. Challenges in controlled thermal deposition of organic diradicals. *Chem. Mater.* **2021**, *33*, 2019.
(36) Huang, Z.; Zhang, Y.; He, Y.; Song, H.; Yin, C.; Wu, K. A chemist's overview of surface electron spins. *Chem. Soc. Rev.* **2017**, *46* (7), 1955−1976.
(37) Ciccullo, F.; Gallagher, N. M.; Geladari, O.; Chasse, T.; Rajca, A.; Casu, M. B. A Derivative of the Blatter Radical as a Potential

https://doi.org/10.1021/jacs.1c01305
J. Am. Chem. Soc. 2021, 143, 5508−5518

Metal-Free Magnet for Stable Thin Films and Interfaces. *ACS Appl. Mater. Interfaces* **2016**, *8*, 1805−1812.
(38) Casu, M. B. Nanoscale Studies of Organic Radicals: Surface, Interface, and Spinterface. *Acc. Chem. Res.* **2018**, *51*, 753−760.
(39) Zissimou, G. A.; Berezin, A. A.; Manoli, M.; Nicolaides, C.; Trypiniotis, T.; Koutentis, P. A. 3,3′,3′′-(Benzene-1,3,5-triyl)tris(1-phenyl-1H-benzo[e][1,2,4]triazin-4-yl): A C_3 symmetrical Blatter-type triradical. *Tetrahedron* **2020**, *76*, 131077. Our additional concerns include EPR spectra simulation, thermal stability characterization, and DFT computations. We repeated the UB3LYP computations of doublet−quartet energy gap and obtained the broken-symmetry doublet with $\langle S^2 \rangle$ of 1.80, as expected, and the energy gap of only 0.17 kcal mol^{-1} (eq S2). Because this level of theory overestimates stability of high spin ground state (*vide infra*), this tridradical might turn out to be a low-spin (doublet) ground state, very close in energy to the excited quartet (ref 4).
(40) Constantinides, C. P.; Koutentis, P. A.; Loizou, G. Synthesis of 7-aryl/heteraryl-1,3-diphenyl-1,2,4-benzotriazinyls via palladium catalyzed Stille and Suzuki-Miyaura reactions. *Org. Biomol. Chem.* **2011**, *9*, 3122−3125.
(41) Tanimoto, R.; Suzuki, S.; Kozaki, M.; Okada, K. Nitronyl Nitroxide as a Coupling Partner: Pd-Mediated Cross-coupling of (Nitronyl nitroxide-2-ido)(triphenylphosphine)gold(I) with Aryl Halides. *Chem. Lett.* **2014**, *43*, 678−680.
(42) Tahara, T.; Suzuki, S.; Kozaki, M.; Shiomi, D.; Sugisaki, K.; Sato, K.; Takui, T.; Miyake, Y.; Hosokoshi, Y.; Nojiri, H.; Okada, K. Triplet Diradical-Cation Salts Consisting of the Phenothiazine Radical Cation and a Nitronyl Nitroxide. *Chem. - Eur. J.* **2019**, *25*, 7201−7209.
(43) Osiecki, J. H.; Ullman, E. F. Studies of free radicals. I. alpha.-Nitronyl nitroxides, a new class of stable radicals. *J. Am. Chem. Soc.* **1968**, *90*, 1078−1079.
(44) Rajca, A.; Pink, M.; Mukherjee, S.; Rajca, S.; Das, K. 1,3-Alternate calix[4]arene nitronyl nitroxide tetraradical and diradical: synthesis, X-ray crystallography, paramagnetic NMR spectroscopy, EPR spectroscopy, and magnetic studies. *Tetrahedron* **2007**, *63*, 10731−10742.
(45) Bodzioch, A.; Zheng, M.; Kaszyński, P.; Utecht, G. Functional Group Transformations in Derivatives of 1,4-Dihydrobenzo[1,2,4]-triazinyl Radical. *J. Org. Chem.* **2014**, *79*, 7294−7310.
(46) Koutentis, P. A.; Lo Re, D. Catalytic Oxidation of *N*-Phenylamidrazones to 1,3-Diphenyl-1,4-dihydro-1,2,4-benzotriazin-4-yls: An Improved Synthesis of Blatter's Radical. *Synthesis* **2010**, *2010*, 2075−2079.
(47) Constantinides, C. P.; Koutentis, P. A. Stable N- and N/S-Rich Heterocyclic Radicals: Synthesis and Applications. *Adv. Heterocycl. Chem.* **2016**, *119*, 173−207.
(48) Rogers, F. J. M.; Norcott, P. L.; Coote, M. L. Recent advances in the chemistry of benzo[e][1,2,4]triazinyl radicals. *Org. Biomol. Chem.* **2020**, *18*, 8255−8277.
(49) Fleckenstein, C. A.; Plenio, H. Sterically demanding trialkylphosphines for palladium-catalyzed cross coupling reactions—alternatives to $PtBu_3$. *Chem. Soc. Rev.* **2010**, *39*, 694−711.
(50) Suzuki, S.; Nakamura, F.; Naota, T. Environmentally Benign Strategy for Arylation of Nitronyl Nitroxide Using a Non-Transition Metal Nucleophile. *Org. Lett.* **2020**, *22* (4), 1350−1354.
(51) Constantinides, C. P.; Lawson, D. B.; Zissimou, G. A.; Berezin, A. A.; Mailman, A.; Manoli, M.; Kourtellaris, A.; Leitus, G. M.; Clérac, R.; Tuononen, H. M.; Koutentis, P. A. Polymorphism in a π stacked Blatter radical: structures and magnetic properties of 3-(phenyl)-1-(pyrid-2-yl)-1,4-dihydrobenzo[e][1,2,4]triazin-4-yl. *CrystEngComm* **2020**, *22*, 5453−5463.
(52) Rajca, A.; Takahashi, M.; Pink, M.; Spagnol, G.; Rajca, S. Conformationally constrained, stable, triplet ground state (S = 1) nitroxide diradicals: antiferromagnetic chains of S = 1 diradicals. *J. Am. Chem. Soc.* **2007**, *129*, 10159−10170.
(53) Rajca, A.; Utamapanya, S. Poly(arylmethyl) Quartet Triradicals and Quintet Tetraradicals. *J. Am. Chem. Soc.* **1993**, *115*, 2396−2401.
(54) Rajca, A.; Rajca, S.; Desai, S. R. Macrocyclic)-Conjugated Carbopolyanions and Polyradicals Based upon Calix[4]arene and Calix[3]arene Rings. *J. Am. Chem. Soc.* **1995**, *117*, 806−816.
(55) Rajca, S.; Rajca, A. Novel High-Spin Molecules: R-Conjugated Polyradical Polyanions. Ferromagnetic Spin Coupling and Electron Localization. *J. Am. Chem. Soc.* **1995**, *117*, 9172−9179.
(56) Stoll, S.; Schweiger, A. EasySpin, a comprehensive software package for spectral simulation and analysis in EPR. *J. Magn. Reson.* **2006**, *178*, 42−55.
(57) Neese, F. The ORCA program system. *Wiley Interdisciplinary Reviews: Comp. Mol. Sci.* **2012**, *2*, 73−78.
(58) Sinnecker, S.; Neese, F. Spin-Spin Contributions to the Zero-Field Splitting Tensor in Organic Triplets, Carbenes and Biradicals - A Density Functional and Ab Initio Study. *J. Phys. Chem. A* **2006**, *110*, 12267−12275.
(59) Rajca, A.; Olankitwanit, A.; Rajca, S. Triplet Ground State Derivative of Aza-*m*-Xylylene Diradical with Large Singlet-Triplet Energy Gap. *J. Am. Chem. Soc.* **2011**, *133*, 4750−4753.
(60) Olankitwanit, A.; Pink, M.; Rajca, S.; Rajca, A. Synthesis of Aza-*m*-Xylylene Diradicals with Large Singlet-Triplet Energy Gap and Statistical Analyses of their EPR Spectra. *J. Am. Chem. Soc.* **2014**, *136*, 14277−14288.
(61) Olankitwanit, A.; Rajca, S.; Rajca, A. Aza-*m*-Xylylene Diradical with Increased Steric Protection of the Aminyl Radicals. *J. Org. Chem.* **2015**, *80*, 5035−5044.
(62) Rajca, A.; Olankitwanit, A.; Wang, Y.; Boratynski, P. J.; Pink, M.; Rajca, S. High-Spin S = 2 Ground State Aminyl Tetraradicals. *J. Am. Chem. Soc.* **2013**, *135*, 18205−18215.
(63) Shu, C.; Zhang, H.; Olankitwanit, A.; Rajca, S.; Rajca, A. High-Spin Diradical Dication of Chiral π-Conjugated Double Helical Molecule. *J. Am. Chem. Soc.* **2019**, *141*, 17287−17294.
(64) Belorizky, E; Fries, P. Exact solutions for simple spin clusters with isotropic Heisenberg exchange interactions. *J. Chim. Phys. Phys.-Chim. Biol.* **1993**, *90*, 1077−1100.
(65) Frisch, M. J.; Trucks, G. W.; Schlegel, H. B.; Scuseria, G. E.; Robb, M. A.; Cheeseman, J. R.; Scalmani, G.; Barone, V.; Petersson, G. A.; Nakatsuji, H.; Li, X.; Caricato, M.; Marenich, A. V.; Bloino, J.; Janesko, B. G.; Gomperts, R.; Mennucci, B.; Hratchian, H. P.; Ortiz, J. V.; Izmaylov, A. F.; Sonnenberg, J. L.; Williams-Young, D.; Ding, F.; Lipparini, F.; Egidi, F.; Goings, J.; Peng, B.; Petrone, A.; Henderson, T.; Ranasinghe, D.; Zakrzewski, V. G.; Gao, J.; Rega, N.; Zheng, G.; Liang, W.; Hada, M.; Ehara, M.; Toyota, K.; Fukuda, R.; Hasegawa, J.; Ishida, M.; Nakajima, T.; Honda, Y.; Kitao, O.; Nakai, H.; Vreven, T.; Throssell, K.; Montgomery, J. A., Jr.; Peralta, J. E.; Ogliaro, F.; Bearpark, M. J.; Heyd, J. J.; Brothers, E. N.; Kudin, K. N.; Staroverov, V. N.; Keith, T. A.; Kobayashi, R.; Normand, J.; Raghavachari, R.; Rendell, A. P.; Burant, J. C.; Iyengar, S. S.; Tomasi, J.; Cossi, M.; Millam, J. M.; Klene, M.; Adamo, C.; Cammi, R.; Ochterski, J. W.; Martin, R. L.; Morokuma, K.; Farkas, O.; Foresman, J. B.; Fox, D. J. *Gaussian 16*, Revision A.03; Gaussian, Inc.: Wallingford, CT, 2016.
(66) Hutchison, K. A.; Srdanov, G.; Menon, R.; Gabriel, J.-C. P.; Knight, B.; Wudl, F. A Pressure Sensitive Two-Dimensional Tetracyanoquinodimethane (TCNQ) Salt of a Stable Free Radical. *J. Am. Chem. Soc.* **1996**, *118*, 13081−13082.
(67) Gilroy, J. B.; McKinnon, S. D. J.; Koivisto, B. D.; Hicks, R. G. Electrochemical Studies of Verdazyl Radicals. *Org. Lett.* **2007**, *9*, 4837−4840.
(68) Ullman, E. F.; Osiecki, J. H.; Boocock, D. G. B.; Darcy, R. Studies of Stable Free Radicals. X. Nitronyl Nitroxide Monoradicals and Biradicals as Possible Small Molecule Spin Labels. *J. Am. Chem. Soc.* **1972**, *94*, 7049−7059.
(69) Kakavandi, R.; Calzolari, A.; Borozdina, Y. B.; Ravat, P.; Chassé, T.; Baumgarten, M.; Casu, M. B. Unraveling the mark of surface defects on a spinterface: The nitronyl nitroxide/TiO_2(110) interface. *Nano Res.* **2016**, *9*, 3515−3527.
(70) Kakavandi, R.; Ravat, P.; Savu, S. A.; Borozdina, Y. B.; Baumgarten, M.; Casu, M. B. Electronic Structure and Stability of Fluorophore-Nitroxide Radicals from Ultrahigh Vacuum to Air Exposure. *ACS Appl. Mater. Interfaces* **2015**, *7* (3), 1685−1692.

https://doi.org/10.1021/jacs.1c01305
J. Am. Chem. Soc. 2021, 143, 5508−5518

(71) Caneschi, A.; Casu, M. B. Substrate-induced effects in thin films of a potential magnet composed of metal-free organic radicals deposited on Si(111). *Chem. Commun.* **2014**, *50* (88), 13510−13513.
(72) Savu, S.-A.; Biswas, I.; Sorace, L.; Mannini, M.; Rovai, D.; Caneschi, A.; Chassé, T.; Casu, M. B. Nanoscale Assembly of Paramagnetic Organic Radicals on Au(111) Single Crystals. *Chem. - Eur. J.* **2013**, *19* (10), 3445−3450.
(73) Forrest, S. R. Ultrathin Organic Films Grown by Organic Molecular Beam Deposition and Related Techniques. *Chem. Rev.* **1997**, *97* (6), 1793−1896.
(74) Junghoefer, T.; Nowik-Boltyk, E. M.; de Sousa, J. A.; Giangrisostomi, E.; Ovsyannikov, R.; Chassé, T.; Veciana, J.; Mas-Torrent, M.; Rovira, C.; Crivillers, N.; Casu, M. B. Stability of radical-functionalized gold surfaces by self-assembly and on-surface chemistry. *Chemical Science* **2020**, *11* (34), 9162−9172.
(75) Ciccullo, F.; Calzolari, A.; Bader, K.; Neugebauer, P.; Gallagher, N. M.; Rajca, A.; van Slageren, J.; Casu, M. B. Interfacing a Potential Purely Organic Molecular Quantum Bit with a Real-Life Surface. *ACS Appl. Mater. Interfaces* **2019**, *11* (1), 1571−1578.
(76) Enkvist, C.; Lunell, S.; Sjögren, B.; Brühwiler, P. A.; Svensson, S. The C1s shakeup spectra of Buckminsterfullerene, acenaphthylene, and naphthalene, studied by high resolution x-ray photoelectron spectroscopy and quantum mechanical calculations. *J. Chem. Phys.* **1995**, *103* (15), 6333−6342.
(77) Sjogren, B.; Svensson, S.; de Brito, A. N.; Correia, N.; Keane, M. P.; Enkvist, C.; Lunell, S. The C1s core shake-up spectra of alkene molecules: An experimental and theoretical study. *J. Chem. Phys.* **1992**, *96* (9), 6389−6398.
(78) Barth, G.; Linder, R.; Bryson, C. Advances in charge neutralization for XPS measurements of nonconducting materials. *Surf. Interface Anal.* **1988**, *11* (6−7), 307−311.
(79) Bauer, E. Phänomenologische Theorie der Kristallabscheidung an Oberflächen. *Z. Kristallogr.* **1958**, *110* (1−6), 372−394.
(80) Venables, J. A. *Introduction to Surface and Thin Film Processes.*; Cambridge University Press: Cambridge, 2000.
(81) Casu, M. B.; Schuster, B.-E.; Biswas, I.; Raisch, C.; Marchetto, H.; Schmidt, T.; Chassé, T. Locally Resolved Core-hole Screening, Molecular Orientation, and Morphology in Thin Films of Diindenoperylene Deposited on Au(111) Single Crystals. *Adv. Mater.* **2010**, *22* (33), 3740−3744.
(82) Arantes, C.; Chernick, E. T.; Gruber, M.; Rocco, M. L. M.; Chasse, T.; Tykwinski, R. R.; Casu, M. B. Interplay between solution-processing and electronic structure in metal-free organic magnets based on a TEMPO pentacene derivative. *J. Phys. Chem. C* **2016**, *120* (6), 3289−3294.
(83) Boocock, D. G. B.; Darcy, R.; Ullman, E. F. Studies of free radicals. II. Chemical properties of nitronylnitroxides. A unique radical anion. *J. Am. Chem. Soc.* **1968**, *90*, 5945−5946.
(84) Tretyakov, E. V.; Utepova, I. A.; Varaksin, M. V.; Tolstikov, S. E.; Romanenko, G. V.; Bogomyakov, A. S.; Stass, D. V.; Ovcharenko, V. I.; Chupakhin, O. N. New approach to synthesis of nitronyl and imino nitroxides based on S_NH methodology. *ARKIVOC* **2011**, *2011*, 76−98.
(85) Rajca, A.; Mukherjee, S.; Pink, M.; Rajca, S. Exchange Coupling Mediated Through-Bonds and Through-Space in Conformationally-Constrained Polyradical Scaffolds: Calix[4]arene Nitroxide Tetraradicals and Diradical. *J. Am. Chem. Soc.* **2006**, *128*, 13497−13507.
(86) *SAINT v. 2018.1*; Bruker AXS: Madison, WI, 2018.
(87) *SADABS v. 2018.1*; Bruker AXS: Madison, WI, 2018.
(88) Sheldrick, G. M. SHELXT - Integrated space-group and crystal structure determination. *Acta Crystallogr., Sect. A: Found. Adv.* **2015**, *71*, 3−8.
(89) Sheldrick, G. M. Crystal structure refinement with SHELXL. *Acta Crystallogr., Sect. C: Struct. Chem.* **2015**, *71*, 3−8.
(90) Trinquier, G.; Suaud, N.; Malrieu, J.-P. Theoretical Design of High-Spin Polycyclic Hydrocarbons. *Chem. - Eur. J.* **2010**, *16*, 8762−8772.
(91) Yamaguchi, K.; Jensen, F.; Dorigo, A.; Houk, K. N. A Spin Correction Procedure for Unrestricted Hartree-Fock and Møller-Plesset Wavefunctions for Singlet Diradicals and Polyradicals. *Chem. Phys. Lett.* **1988**, *149*, 537−542.

https://doi.org/10.1021/jacs.1c01305
J. Am. Chem. Soc. 2021, 143, 5508−5518

Supporting Information

Synthesis and Thin Films of Thermally Robust Quartet (S = 3/2) Ground State Triradical

Chan Shu[†], Maren Pink[‡], Tobias Junghoefer,[§] Elke Nadler[§], Suchada Rajca[†], Maria Benedetta Casu*[§], Andrzej Rajca*[†]

[†]Department of Chemistry, University of Nebraska, Lincoln, Nebraska 68588-0304.

[‡]Department of Chemistry, Indiana University, Bloomington, Indiana 47405-7102, USA.

[§]Institute of Physical and Theoretical Chemistry, University of Tübingen, 72076 Tübingen, Germany

E-mail address: arajca1@unl.edu

.

Table of Contents

1. Experimental Section: Synthesis, Measurements, and Computations.

1.a General procedures and materials.

Throughout the following paragraphs labels "CS447T" and alike correspond to sample or experiment codes directly traceable to the laboratory notebooks or raw data.

Tetrahydrofuran (THF) was kept with Na/K metal/benzophenone under nitrogen atmosphere. The distilled tetrahydrofuran was used immediately when the reaction was set up. Toluene was obtained from solvent purification system (LC Technology Solutions) and degassed. Chloroform ($CHCl_3$) was dried over CaH_2, then distilled to a Schlenk vessel, and subsequently degassed. All other commercially available chemicals were obtained from either Aldrich or Acros, unless indicated otherwise.

(Nitronyl nitroxide-2-ido)(triphenylphosphine) gold(I) **4** is synthesized by the reaction of nitronyl nitroxide **7** and $Au^{I}(PPh_3)Cl$ with NaOH in methanol/dichloromethane.[S1] After purification by chromatography (deactivated neutral alumina), the spin concentration of **4** is up to 99%. Nitronyl nitroxide **7** is obtained following the literature procedures, starting from formaldehyde and 2,3-bis(hydroxyamino)-2,3-dimethylbutane.[S2-S6] Di-iodo-Blatter radical **5** and its mono-iodo analogue **6** are prepared according to the previous literature.[S7]

Column chromatography (0 – 20 psig pressure) was conducted using normal-phase silica gel or neutral (deactivated) alumina. Standard techniques for synthesis under inert atmosphere (e.g. Schlenk glassware) were used as needed/described. IR spectra were obtained using a commercial instrument, equipped with an ATR sampling accessory. Triradical sample CS627 and diradical sample CS536 were used to obtain spectra; baseline for both spectra was corrected. Mass spectrometry analyses were conducted at a local mass spectrometry facility. Dichloromethane (DCM) was obtained from solvent purification system (LC Technology Solutions). DCM for electrochemistry and for generation of radical cation, was in addition dried over calcium hydride (CaH_2), and then distilled to a Schlenk vessel, and subsequently degassed by repeated freeze-and-thaw procedure. Per-deuterated solvents for NMR spectroscopy were obtained from Cambridge Isotope Laboratories. All other commercially available chemicals were obtained from either Aldrich or Acros, unless indicated otherwise.

1.b. X-ray crystallography.

Two cif files were deposited at CCDC with Deposition Numbers: 2062663 and 2062664.

The single crystals of triradical **3** were obtained by slow solvent evaporation from a solution of **3** in toluene/heptane (sample label: CS447T) or chloroform/pentane (sample label: CS442). The second crystal was a solvent polymorph, containing one molecule of chloroform.

The first crystal of **3** (sample label: CS447T and X-ray label: S19003) was investigated with synchrotron radiation at the ChemMatCARS[S8] 15IDD beamline at the Advanced Photon Source at Argonne National Laboratory, Chicago, utilizing the SCrAPS program.[S9] A black crystal (approximate dimensions 0.041 × 0.038 × 0.032 mm^3) was placed onto the tip of an glass rod and mounted on a Huber goniometer, equipped with a Pilatus 1M detector, and measured at 100(2) K.

The second crystal of **3** (sample label: CS442, X-ray label: 19114) was investigated at the University of Indiana. A black crystal (approximate dimensions 0.31 × 0.24 × 0.08 mm^3) was placed onto the tip of a 0.05 mm diameter glass capillary and mounted on a Bruker Venture D8 diffractometer equipped with a PhotonIII detector at 100(2) K.

The two pseudo polymorphs have significant differences in crystal packing with the first crystal (centrosymmetric P-1 space group) forming C_i-symmetric dimers of triradical molecules while the chloroform-containing crystal (non-centrosymmetric $Pna2_1$ space group) formed one-dimensional π-stacks of triradical molecules.

Data collection for the first crystal.

Data collection was carried out using synchrotron radiation (λ = 0.41328 Å, E = 30 keV, silicon 111 and 113 monochromators, two mirrors to exclude higher harmonics) with a frame time of 0.1 seconds and a detector distance of 15 cm. A randomly oriented region of reciprocal space was surveyed to the extent of two spheres with a detector position (2θ) at 0°, ω at -90°, κ at 0° and 30°, using φ scans. The total exposure time was 3 minutes. The frames were integrated with the Bruker SAINT software package[S10] using a narrow-frame algorithm. The integration of the data using a triclinic unit cell yielded a total of 30419 reflections to a maximum θ angle of 14.60° (0.82 Å resolution), of which 5295 were independent (average redundancy 5.745, completeness = 97.9%, R_{int} = 3.75%, R_{sig} = 2.49%) and 4652 (87.86%) were greater than $2\sigma(F^2)$. The final cell constants of a = 10.3155(5) Å, b = 12.2296(5) Å, c = 13.6485(6) Å, α = 113.7378(8)°, β = 103.2697(8)°, γ = 92.4892(9)°, volume = 1516.13(12) $Å^3$, are based upon the refinement of the XYZ-centroids of 9945 reflections above 20 σ(I) with 4.618° < 2θ < 29.17°. Data were corrected for absorption effects using the multi-scan method (SADABS).[S11] The ratio of minimum to maximum apparent transmission was 0.945. The calculated minimum and maximum transmission coefficients (based on crystal size) are 0.6892 and 0.7440. Please refer to Table S1 for additional crystal and refinement information.

Data collection for the second crystal (solvent polymorph).

The data collection was carried out using Mo Ka radiation (graphite monochromator) with a frame time of 4 or 2 seconds and a detector distance of 4.00 cm. A collection strategy was calculated and

complete data to a resolution of 0.71 Å with a redundancy of 19 were collected. Seven major sections of frames were collected with 0.50º w and f scans. A total of 1634 frames were collected. The total exposure time was 1.74 hours. The frames were integrated with the Bruker SAINT software package[S10] using a narrow-frame algorithm. The integration of the data using an orthorhombic unit cell yielded a total of 104889 reflections to a maximum θ angle of 30.07° (0.71 Å resolution), of which 9957 were independent (average redundancy 10.534, completeness = 99.8%, R_{int} = 4.21%, R_{sig} = 2.01%) and 9379 (94.20%) were greater than $2\sigma(F^2)$. The final cell constants of a = 22.0681(7) Å, b = 6.1421(2) Å, c = 25.0499(9) Å, volume = 3395.4(2) $Å^3$, are based upon the refinement of the XYZ-centroids of 9874 reflections above 20 σ(I) with 6.885° < 2θ < 60.02°. Data were corrected for absorption effects using the Multi-Scan method (SADABS).[S11] The ratio of minimum to maximum apparent transmission was 0.961. The calculated minimum and maximum transmission coefficients (based on crystal size) are 0.9070 and 0.9750. Please refer to Table S2 for additional crystal and refinement information.

Structure solution and refinement for the first crystal.

The space group P-1 was determined based on intensity statistics and the lack of systematic absences. The structure was solved and refined using the Shelx suite of programs.[S12] An intrinsic methods solution was calculated, which provided most non-hydrogen atoms from the E-map. Full-matrix least squares / difference Fourier cycles were performed, which located the remaining non-hydrogen atoms. All non-hydrogen atoms were refined with anisotropic displacement parameters. The hydrogen atoms were placed in ideal positions and refined as riding atoms with relative isotropic displacement parameters. The final anisotropic full-matrix least-squares refinement on F^2 with 405 variables converged at R1 = 3.73%, for the observed data and wR2 = 11.30% for all data. The goodness-of-fit was 1.089. The largest peak in the final difference electron density synthesis was 0.227 $e^-/Å^3$ and the largest hole was -0.221 $e^-/Å^3$ with an RMS deviation of 0.047 $e^-/Å^3$. On the basis of the final model, the calculated density was 1.303 g/cm^3 and F(000), 630 e^-. Hydrogen bonding was observed (see tables).

Structure solution and refinement for the second crystal (solvent polymorph).

The space group $Pna2_1$ was determined based on intensity statistics and systematic absences. The structure was solved and refined using the SHELX suite of programs.[S12] An intrinsic-methods solution was calculated, which provided most non-hydrogen atoms from the E-map. Full-matrix least squares / difference Fourier cycles were performed, which located the remaining non-hydrogen atoms. All non-hydrogen atoms were refined with anisotropic displacement parameters. The hydrogen atoms were placed in ideal positions and refined as riding atoms with relative isotropic displacement parameters. The final anisotropic full-matrix least-squares refinement on F^2 with 441 variables converged at R1 = 3.11%, for the observed data and wR2 = 8.61% for all data. The goodness-of-fit was 1.061. The largest peak in the final difference electron density synthesis was 0.332 $e^-/Å^3$ and the largest hole was -0.479 $e^-/Å^3$ with an RMS deviation of 0.049 $e^-/Å^3$. On the basis of the final model, the calculated density was 1.397 g/cm^3 and F(000), 1492 e^-. Hydrogen bonding was found and is listed in the tables. 19114 is a solvent polymorph of s19003.

Table S1. Crystal data and structure refinement for triradical **3** (X-ray label: s19003).

Empirical formula	C33 H36 N7 O4	
Formula weight	594.69	
Crystal color, shape, size	black block, 0.041 × 0.038 × 0.032 mm^3	
Temperature	100(2) K	
Wavelength	0.41328 Å	
Crystal system, space group	Triclinic, P-1	
Unit cell dimensions	a = 10.3155(5) Å	α = 113.7378(8)°.
	b = 12.2296(5) Å	β = 103.2697(8)°.
	c = 13.6485(6) Å	γ = 92.4892(9)°.
Volume	1516.13(12) $Å^3$	
Z	2	
Density (calculated)	1.303 Mg/m^3	
Absorption coefficient	0.038 mm^{-1}	
F(000)	630	
Data collection		
Diffractometer	Huber 6-circle, Huber	
Detector	Pilatus 1M, Dectris	
Theta range for data collection	0.984 to 14.597°.	
Index ranges	-12<=h<=12, -14<=k<=14, -16<=l<=16	
Reflections collected	30419	
Independent reflections	5295 [R_{int} = 0.0375]	
Observed Reflections	4652	
Completeness to theta = 14.357°	97.8 %	
Solution and Refinement		
Absorption correction	Semi-empirical from equivalents	
Max. and min. transmission	0.7440 and 0.6892	
Solution	Intrinsic methods	
Refinement method	Full-matrix least-squares on F^2	
Weighting scheme	$w = [\sigma^2 Fo^2 + AP^2 + BP]^{-1}$, with	
	$P = (Fo^2 + 2\,Fc^2)/3$, A = 0.0600, B = 0.4376	
Data / restraints / parameters	5295 / 0 / 405	
Goodness-of-fit on F^2	1.089	
Final R indices [I>2σ(I)]	R1 = 0.0373, wR2 = 0.1031	
R indices (all data)	R1 = 0.0428, wR2 = 0.1130	
Largest diff. peak and hole	0.227 and -0.221 $e.Å^{-3}$	

Goodness-of-fit = $[\Sigma[w(F_o^2 - F_c^2)^2]/N_{observns} - N_{params})]^{1/2}$, all data.

$R1 = \Sigma(|F_o| - |F_c|) / \Sigma |F_o|$. $wR2 = [\Sigma[w(F_o^2 - F_c^2)^2] / \Sigma [w(F_o^2)^2]]^{1/2}$.

Table S2. Crystal data and structure refinement for solvent polymorph of triradical **3** (X-ray label: 19114).

Empirical formula	$C_{34}H_{37}Cl_3N_7O_4$	
Formula weight	714.05	
Crystal color, shape, size	black plate, 0.31 × 0.24 × 0.08 mm^3	
Temperature	100(2) K	
Wavelength	0.71073 Å	
Crystal system, space group	Orthorhombic, $Pna2_1$	
Unit cell dimensions	a = 22.0681(7) Å	α = 90°.
	b = 6.1421(2) Å	β = 90°.
	c = 25.0499(9) Å	γ = 90°.
Volume	3395.4(2) $Å^3$	
Z	4	
Density (calculated)	1.397 Mg/m^3	
Absorption coefficient	0.320 mm^{-1}	
F(000)	1492	
Data collection		
Diffractometer	Venture D8, Bruker	
Source	IμS 3.0, Incoatec	
Detector	Photon III	
Theta range for data collection	2.460 to 30.067°.	
Index ranges	-31<=h<=31, -8<=k<=8, -35<=l<=35	
Reflections collected	104889	
Independent reflections	9957 [R_{int} = 0.0421]	
Observed Reflections	9379	
Completeness to theta = 25.242°	99.8 %	
Solution and Refinement		
Absorption correction	Semi-empirical from equivalents	
Max. and min. transmission	0.7460 and 0.7173	
Solution	Intrinsic methods	
Refinement method	Full-matrix least-squares on F^2	
Weighting scheme	$w = [\sigma^2 Fo^2 + AP^2 + BP]^{-1}$, with $P = (Fo^2 + 2\,Fc^2)/3$, A = 0.0515, B = 0.6926	
Data / restraints / parameters	9957 / 1 / 441	
Goodness-of-fit on F^2	1.061	
Final R indices [I>2σ(I)]	R1 = 0.0311, wR2 = 0.0820	
R indices (all data)	R1 = 0.0353, wR2 = 0.0861	
Absolute structure parameter	-0.007(9)	
Largest diff. peak and hole	0.332 and -0.479 e.$Å^{-3}$	

Goodness-of-fit = $[\Sigma[w(F_o^2 - F_c^2)^2]/N_{observns} - N_{params})]^{1/2}$, all data.
R1 = $\Sigma(|F_o| - |F_c|) / \Sigma |F_o|$. $wR2 = [\Sigma[w(F_o^2 - F_c^2)^2] / \Sigma [w(F_o^2)^2]]^{1/2}$.

Table S3. Hydrogen bonds for the first crystal of **3** (X-ray label: s19003) [Å and °].

D-H...A	d(D-H)	d(H...A)	d(D...A)	<(DHA)
C6-H6...O2	0.95	2.29	2.8499(17)	117.1
C24-H24B...O4#1	0.98	2.61	3.4446(18)	143.6
C25-H25B...N3#2	0.98	2.67	3.638(2)	167.4
C25-H25C...O4#1	0.98	2.50	3.4048(17)	152.9
C32-H32C...O3#3	0.98	2.56	3.5227(17)	167.0
C32-H32D...O2#3	0.98	2.58	3.4316(18)	145.2

Symmetry transformations used to generate equivalent atoms:
#1 x,y,z-1 #2 -x+2,-y+1,-z+1 #3 -x+1,-y,-z+1

Table S4. Hydrogen bonds for the solvent polymorph of **3** (X-ray label: 19114) [Å and °].

D-H...A	d(D-H)	d(H...A)	d(D...A)	<(DHA)
C6-H6...O2	0.95	2.24	2.867(2)	123.0
C26-H26A...Cl3#1	0.98	2.87	3.828(2)	165.6
C26-H26B...O3#2	0.98	2.40	3.324(3)	156.2
C30-H30C...O4#1	0.98	2.62	3.585(3)	167.6
C34-H34...O4	1.00	2.25	3.156(3)	149.6

Symmetry transformations used to generate equivalent atoms:
#1 x,y+1,z #2 x-1/2,-y+5/2,z

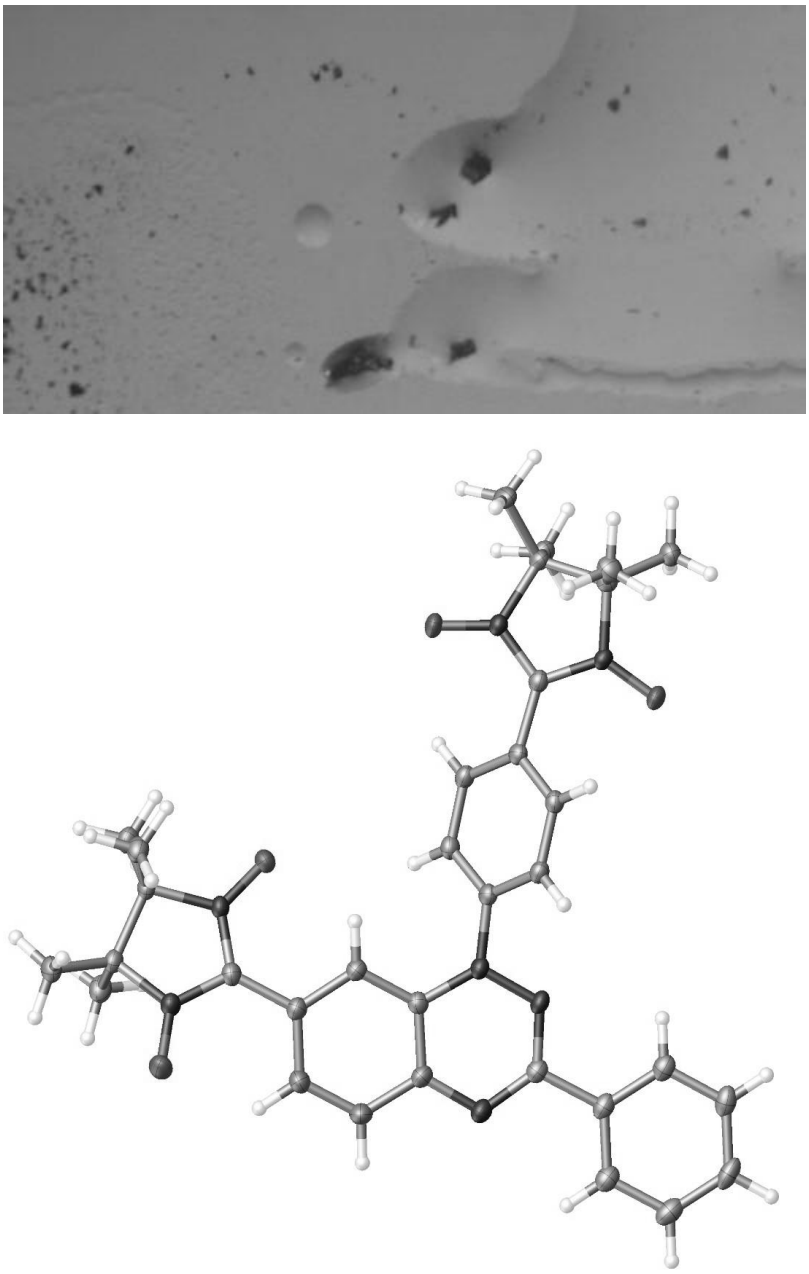

Fig. S1. X-ray crystallography of triradical **3** (first crystal, X-ray label: s19003). Top plot: bulk crystal sample. Bottom plot: formula unit.

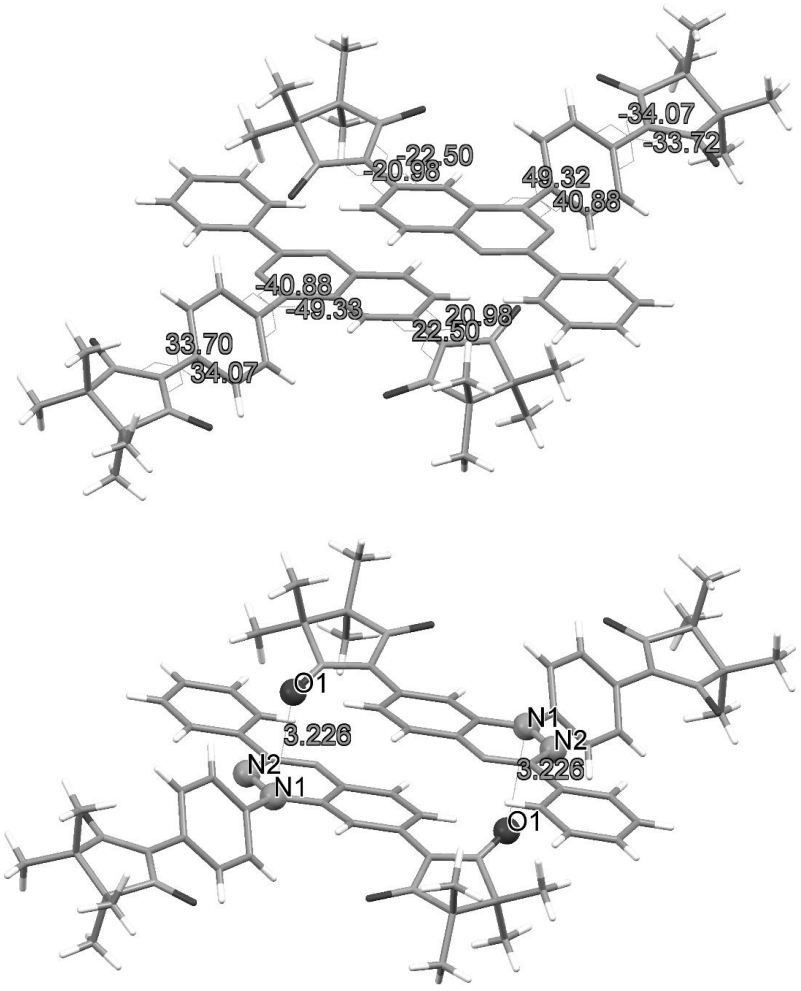

Fig. S2. X-ray crystallography of triradical **3** (first crystal, X-ray label: s19003). Top plot: racemic dimer structure, showing two (axially chiral) enantiomeric molecules of **3**; molecules are π-stacked along the crystallographic *a*-axis. Torsions between nitronyl nitroxides and phenyl rings, as well as between Blatter radical and phenyl rings are shown in green font. Bottom plot: racemic dimer structure, higlighting the shortest intermolecular distance, O1···N1 = 3.226 Å. The next shortest intra-dimer contact is O1···N2 = 3.431 Å. Because of the large positive spin densities at the N1 – N3 nitrogens of the triazinyl moiety and the O1 and O2 oxygens of the nitronyl nitroxide moiety, these short contacts are expected to lead to antiferromagnetic coupling between $S = 3/2$ triradicals (dimer-like) in the solid state. Formation of $S = 3/2$ 1-D antiferromagnetic chains is not likely because the shortest N···N or O···N contact between the dimers is relatively long O2···N1 = 4.122 Å.

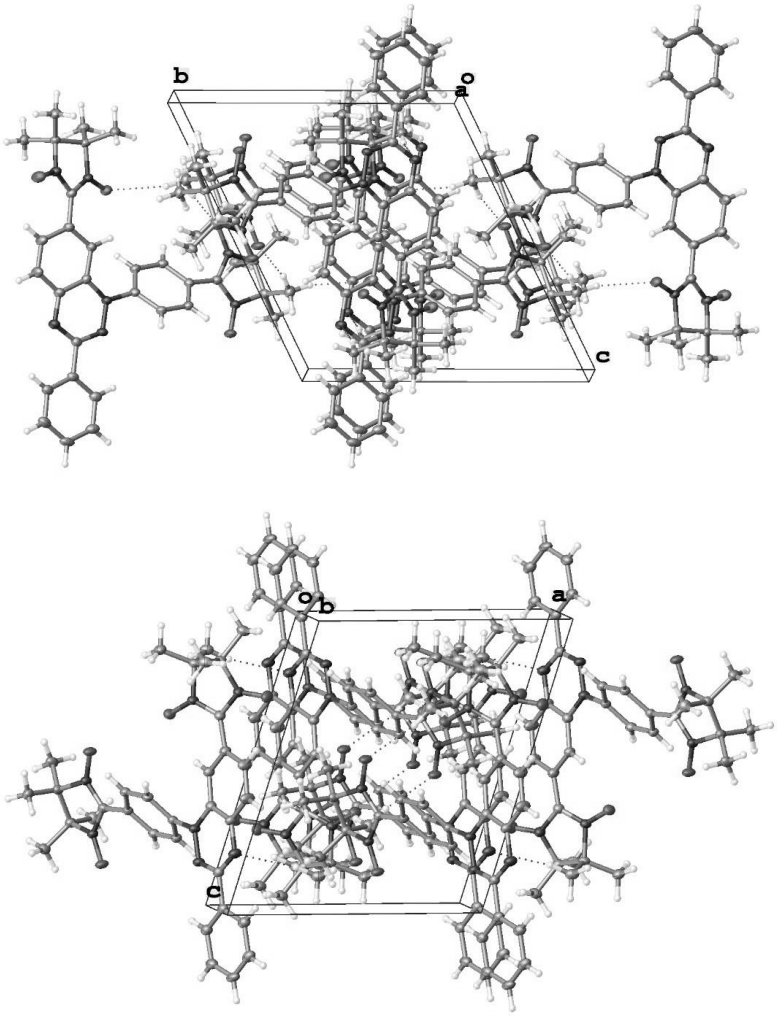

Fig. S3. X-ray crystallography of triradical **3** (first crystal, X-ray label: s19003). Top plot: cell plot with a view along the *a*-axis. Bottom plot: cell plot with a view along the *b*-axis.

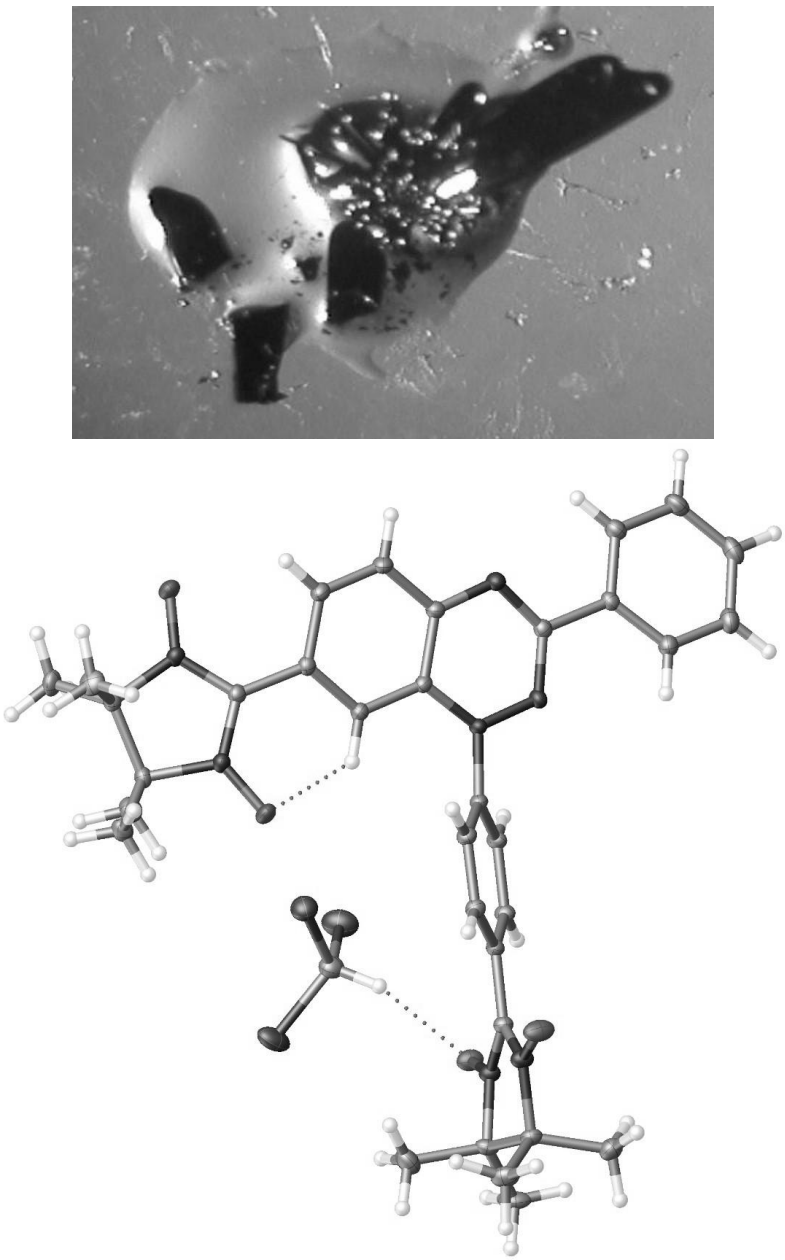

Fig. S4. X-ray crystallography of triradical **3**, solvent polymorph (X-ray label: 19114). Top plot: bulk crystal sample. Bottom plot: formula unit showing solvent molecule and close contacts (non-classical H-bonds).

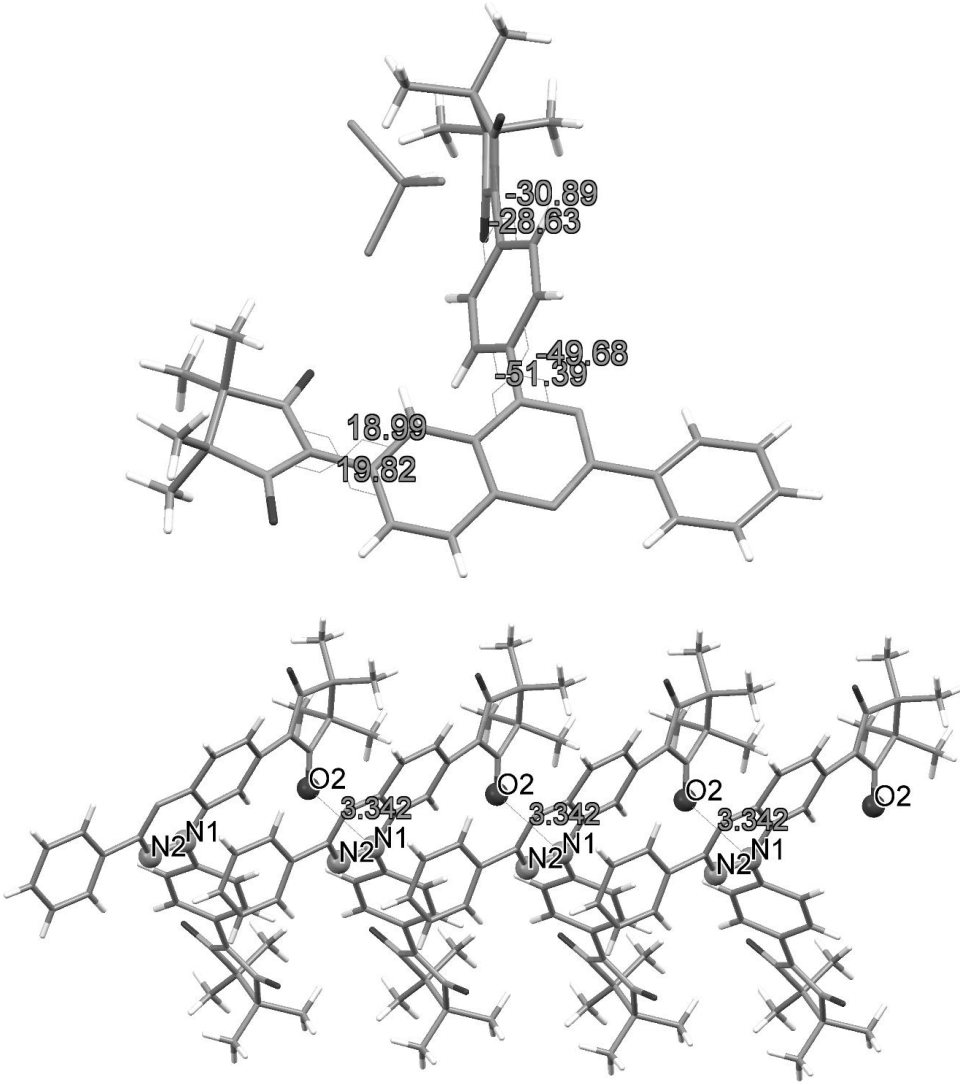

Fig. S5. X-ray crystallography of triradical **3**, solvent polymorph (X-ray label: 19114). Top plot: formula unit. Torsions between nitronyl nitroxides and phenyl rings, as well as between Blatter radical and phenyl rings are shown in green font. Bottom plot: tetramer of **3** π-stacked along crystallographic *b*-axis; short contacts O2···N1 = 3.342 Å and the next shortest contacts O2···N2 = 3.519 Å are highlighted with ball-and-stick atoms. Because of the large positive spin densities at the N1 – N3 nitrogens of the triazinyl moiety and the O1 and O2 oxygens of the nitronyl nitroxide moiety, these short contacts are expected to lead to antiferromagnetic coupling between $S = 3/2$ triradicals, and thus leading to the formation of $S = 3/2$ 1-D antiferromagnetic chains.

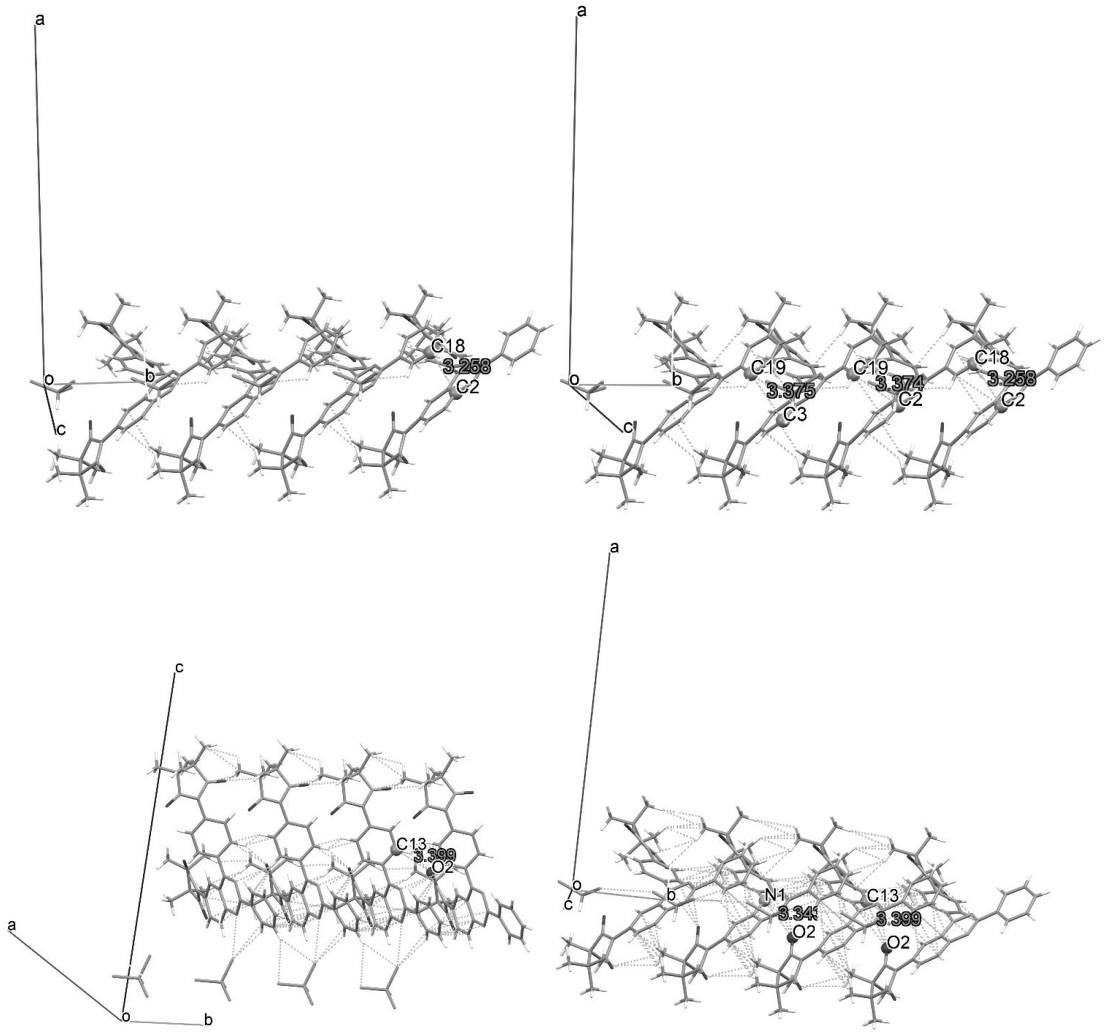

Fig. S6. X-ray crystallography of triradical **3**, solvent polymorph (X-ray label: 19114): tetramer of **3** π-stacked along crystallographic *b*-axis; all short contacts are shown using blue dash lines and selected contacts are highlighted with ball-and-stick atoms with distances shown in a green font. Most of the short contacts correspond to non-classical H-bonds (Table S4). Top left to bottom left clockwise: short contacts minus 0.1 Å, C2···C18 = 3.258 Å; short contacts minus 0 Å, C2···C18 = 3.258 Å, C2···C19 = 3.274 Å, C3···C19 = 3.375 Å; short contacts plus 0.2 Å, O2···C13 = 3.399 Å; short contacts plus 0.3 Å, O2···C13 = 3.399 Å, O2···N1 = 3.342 Å. The highlighted contacts, except for those involving C19, correspond to atoms with significant positive spin densities, and they are expected to lead to antiferromagnetic coupling between $S = 3/2$ triradicals, and thus leading to the formation of $S = 3/2$ 1-D antiferromagnetic chains.

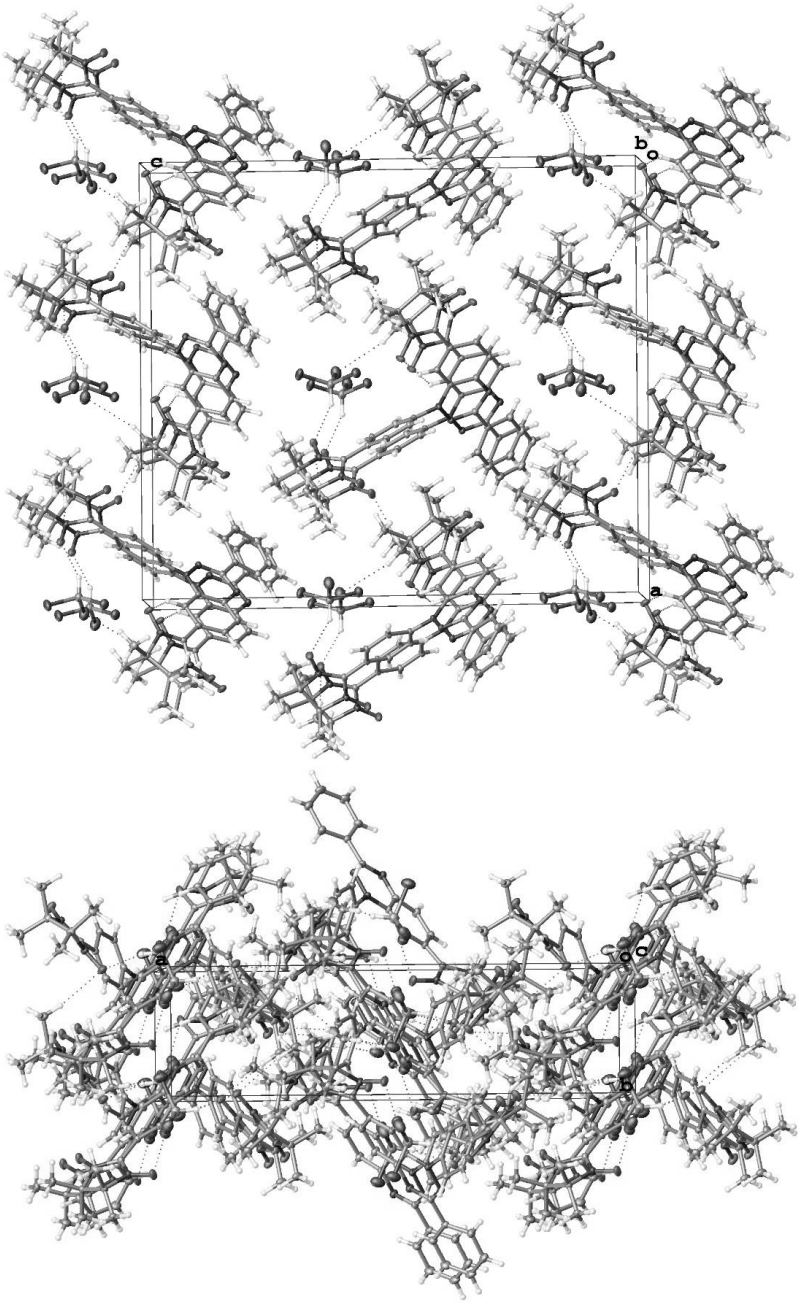

Fig. S7. X-ray crystallography of triradical **3**, solvent polymorph (X-ray label: 19114). Top plot: cell plot with a view along the *a*-axis. Bottom plot: cell plot with a view along the *b*-axis.

1.c Syntheses of triradical 3 and diradical 2 via Pd-catalyzed cross-couplings.

Triradical **3** (M_w = 594.6960)

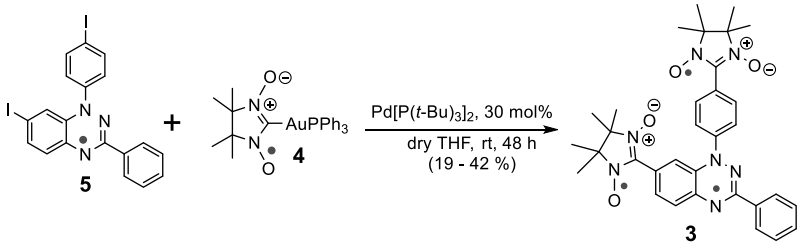

Run	Blatter radical **5** (mg/mmol/eq)	Nitronyl nitroxide **4** (mg/mmol/eq) spin conc.	$Pd[P(t\text{-}Bu)_3]_2$ (mg/eq)	THF (mL)	Time (h)	TM (mg, % yield)	TM spin conc.
CS3-80	1.8/0.00336/1	6.7/0.0109/3.2	1.0/60 mol%	0.5	28	[2]0.57mg	-
[1]CS3-90	10.0/0.0186/1	24.1/0.0391/2.1	0.48/ 5 mol%	2	23	no TM detected	-
[1]CS3-94	1.0/0.00186/1	2.4/0.00391/2.1	0.10/10 mol%	0.5	10	no TM detected	-
CS4-02	100/0.186/1	252/0.409/2.2	19.0/20 mol%	10	50	11.2 mg impure	327 % at rt in THF
[3]CS4-46	50.0/0.093/1	143/0.2325/2.5 spin conc. 78%	9.5/20 mol%	10	72	10.0, 18	370 % at RT in THF 432 % at 110 K in 2-MeTHF
CS4-54	50.0/0.093/1	143/0.2325/2.5 spin conc. 78%	9.5/20 mol%	10	48, 30 °C	[5]8.3 mg, impure	-
[4]CS4-92	50.0/0.093/1	125/0.203/2.2 spin conc. 88%	9.5/20 mol%	10	48	8.5 mg, impure	300 % at RT in THF
CS5-05	50.0/0.093/1	125/0.203/2.2 spin conc. ~100%	14.3/30 mol%	5	48	21.0, 38	Combined TMs: 378 % at rt in toluene/$CHCl_3$ (4:1) 435 % at 110 K in toluene/$CHCl_3$ (3:1)
CS5-09	200/0.373/1	500/0.821/2.2 spin conc. ~100%	57.0/30 mol%	20	48	93.1, 42	
CS5-96	180/0.335/1	450/0.73/2.2 spin conc. ~100%	51.3/30 mol%	20	48	37.3, 19	Combined TMs: 377 % at rt in toluene/$CHCl_3$ (4:1)
CS6-27	200/0.373/1	500/0.821/2.2 spin conc. ~100%	57.0/30 mol%	20	48	93.0, 42	

[1] $Pd[P(t\text{-}Bu)_3]_2$ was dissolved in THF then the solution was added into starting materials.
[2] Analytical TLC plate, with ethyl acetate as an eluent, was used.
[3] The reaction was monitored by TLC every 24 hours. After first 24 h, the triradical was a minor spot in the TLC.
[4] The reaction mixture was purified by column chromatography (regular silica gel, dichloromethane then 10% ethyl acetate in dichloromethane), and then by PTLC (regular silica gel, ethyl acetate as eluent).
[5] The reaction residue was purified by column (regular silica gel, dichloromethane then 10 % ethyl acetate in dichloromethane).

Run CS5-09: A mixture of Blatter radical **5** (200 mg, 0.373 mmol, 1 equiv) and nitronyl nitroxide radical **4** (500 mg, 0.821 mmol, 2.2 equiv) was added to a Schlenk tube and evacuated on vacuum line for several minutes. The tube was kept vacuum and transferred to the antechamber of glove box. Inside the argon-filled glove box, palladium(0) catalyst ($Pd[P(t\text{-}Bu)_3]_2$, 57 mg, 30 mol%) was added into tube. Fresh dry THF was added into tube under the argon gas flow. The reaction was stirred at room temperature for 48 hours. The dark red solution was evaporated by rotovap, to provide dark solid, which was purified by silica gel column chromatography using dichloromethane, followed by 10 % ethyl acetate in

dichloromethane, as eluents. The resultant solid was treated (washed) with pentane to give 93.1 mg (42 %) of product **3** as a dark solid. TLC (silica gel, ethyl acetate): R_f 0.43. HR-TOF-MS (Fig. S28): *m*/*z*, [M + Na]$^+$ calcd for $C_{33}H_{36}N_7O_4Na$ 617.2726; found, 617.2728 (0.3 ppm, RA = 100%); [M + 1 + Na]$^+$ calcd for $C_{32}{}^{13}C_1H_{36}N_7O_4Na$ 618.2760 (or [M + H + Na]$^+$ calcd for $C_{33}H_{37}N_7O_4Na$ 617.2805); found, 618.2755 (–0.8 ppm (or –8.1 ppm), RA = 61%). IR (powder, cm^{-1}) (Fig. S31): 2989, 2113*, 1733*, 1687*, 1596, 1515, 1482, 1449, 1420, 1387, 1362, 1313, 1270, 1251, 1216, 1166, 1132, 1068, 1044, 1026, 992, 967, 919, 868, 831, 781, 751, 739, 722, 695, 634, 617. (* = aromatic overtones or impurities.) The spin concentration was determined to be 378 % (χT = 1.42 emu K mol^{-1}) in toluene/chloroform (4:1) fluid solution at 294 K and 435 % (χT = 1.63 emu K mol^{-1}) at 110 K in toluene/chloroform (3:1) glass. For each measurement, TEMPONE in the identical solvent was used as a spin counting reference.

Diradical **2** (M_w = 439.5190).

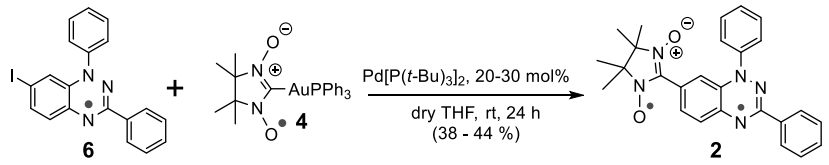

Run	Blatter radical **6** (mg/mmol/eq)	Nitronyl nitroxide **4** (mg/mmol/eq) spin conc.	Pd[P(*t*-Bu)$_3$]$_2$ (mg/eq)	THF (mL)	Time (h)	TM (mg, %yield)	TM spin conc.
CS3-87	10.0/0.0244/1	19.5/0.0317/1.3	1.3/10 mol%	2	28	[2]3.8 mg	-
[1]CS3-91	10.0/0.0244/1.1	13.7/0.0222/1	0.57/5 mol%	2	23	no TM detected	-
[1]CS3-95	1.0/0.00244/1.1	1.4/0.00222/1	0.11/10 mol%	0.5	24	no TM detected	-
CS4-59	20.0/0.0487/1	45.0/0.07305/1.5 spin conc. 78%	2.6/10 mol%	2	24	no TM detected	-
CS4-87	10.0/0.0244/1	16.5/0.0268/1.1 spin conc. 88%	2.6/20 mol%	2	24	3.1, 29	-
CS4-89	10.0/0.0244/1	16.5/0.0268/1.1 spin conc. 88%	2.6/20 mol%	2	24	3.8, 35	-
CS5-19	20.0/0.0488/1	33.0/0.0536/1.1 spin conc. ~100%	5.2/20 mol%	2	24	8.2, 38	-
CS5-36	20.0/0.0488/1	33.0/0.0536/1.1 spin conc. ~100%	7.5/30 mol%	1	24	9.5, 44	220% at 293 K in toluene/chloroform, 4:1
CS5-56	20.0/0.0488/1	33.0/0.0536/1.1 spin conc. ~100%	7.5/30 mol%	1	24	9.4, 44	224% at 293 K in toluene/chloroform, 4:1

[1] Pd[P(*t*-Bu)$_3$]$_2$ was dissolved in THF, and then the solution was added into starting materials.
[2] Column chromatography (regular silica gel) was used to purify crude mixture; 10% ethyl acetate in pentane, followed by 50% ethyl acetate in pentane were employed as eluents.

Run CS5-36: A mixture of Blatter radical **6** (20.0 mg, 0.0488 mmol, 1 equiv) and nitronyl nitroxide **4** (33.0 mg, 0.0536 mmol, 1.1 equiv) was added to a Schlenk tube and evacuated on vacuum line for several minutes. The tube was kept under vacuum, and then it was transferred to the antechamber of glovebox. Inside the argon-filled glovebox, palladium(0) catalyst (Pd[P(*t*-Bu)$_3$]$_2$, 7.5 mg, 30 mol%) was added to the tube. Fresh dry THF was added to the Schlenk tube under the argon gas flow. The reaction was stirred at room temperature for 24 h. The dark red solution was evaporated by

rotovap. The dark solid was purified by silica gel column chromatography using dichloromethane then 10% ethyl acetate in dichloromethane as eluent. The product **2** (9.5 mg, 44%) was isolated as a dark solid. TLC (silica gel, ethyl acetate/pentane, 1:1): R_f 0.35. HR-TOF-MS (Fig. S29): *m/z*, $[M + H]^+$ calcd for $C_{26}H_{26}N_5O_2$ 440.2087; found, 440.2077 (–2.3 ppm, RA = 100%); $[M + 1 + H]^+$ calcd for $C_{25}{}^{13}C_1H_{26}N_5O_2$ 440.2087; found, 441.2113 (–1.6 ppm, RA = 27%). IR (powder, cm^{-1}) (Fig. S32): 3070, 2984, 1588, 1525, 1487, 1450, 1424, 1400, 1384, 1361, 1315, 1272, 1252, 1199, 1168, 1141, 1120, 1068, 1026, 924, 878, 866, 851, 821, 775, 763, 688. The spin concentration was determined to be 220 % (χT = 0.83 emu K mol^{-1}) in toluene/chloroform (4:1) fluid solution at 293 K. For each measurement, TEMPONE in the identical solvent was used as a spin counting reference.

Attempted synthesis of triradical **3** using non-transition metal nucleophilic nitronyl nitroxide **7**: diradical **8** (M_w = 565.4155).

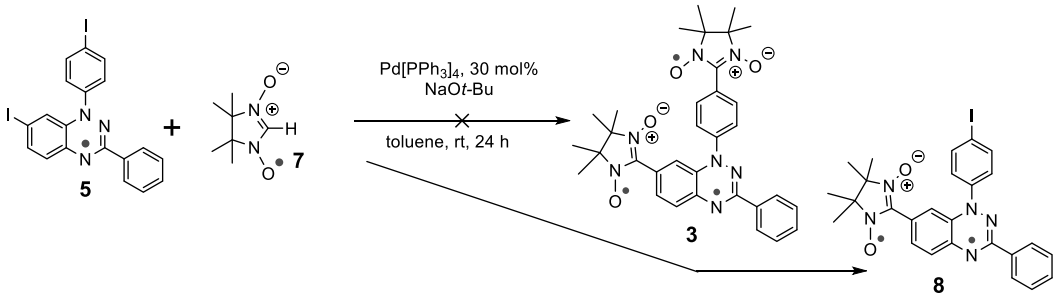

Run	Blatter radical **5** (mg/mmol/eq)	Nitronyl nitroxide **7** (mg/mmol/eq) spin conc.	$Pd[PPh_3]_4$ (mg, eq)	NaO*t*-Bu (mg/mmol/eq)	Toluene (mL)	Time (h)	Notes
CS5-64	10.0/0.0186/1	5.9/0.0372/3.2 spin conc. 99%	6.4/30 mol%	5.0/0.052/2.8	0.5	24	1.2 mg (11%) of **8** as dark solid isolated after PTLC. ESI-MS: *m/z* = 565.2
CS5-67	10.0/0.0186/1	5.9/0.0372/3.2 spin conc. 99%	6.4/30 mol% XPhos/60 mol%	5.0/0.052/2.8	0.5	24	Weak spot on TLC corresponding to TM; unable to isolate it by PTLC, ESI-MS: *m/z* = 578.9 (Fig. S37)
CS5-70	10.0/0.0186/1	5.9/0.0372/3.2 spin conc. 99%	6.4/30 mol% XPhos/60 mol%	5.0/0.052/2.8	0.5	2 (reflux)	Unable to detect any identifiable product or SM by TLC and ESI-MS (Fig. S37)
CS6-71	20/0.0372/1	11.8/0.0744/2	12.8/30 mol%	7.2/0.0744/2	1	120	0.30 mg (~1%) of **8** as dark solid isolated after column and PTLC. ESI-MS: *m/z* = 566.7

Run CS5-64: A mixture of Blatter radical **5** (10.0 mg, 0.0186 mmol, 1 equiv) and nitronyl nitroxide **7** (5.9 mg, 0.0372 mmol, 1 equiv) was added to a Schlenk tube and evacuated on vacuum line for several minutes. The tube was kept under vacuum, and then it was transferred to the antechamber of glove box. Inside the argon-filled glove box, NaO*t*-Bu (5.0 mg, 2.8 equiv) was added into tube. Then, in the nitrogen gas bag, palladium(0) catalyst ($Pd(PPh_3)_4$, 6.4 mg, 30 mol%) was added into tube. Dry toluene was added to the Schlenk tube under the argon gas flow. The reaction was stirred at room

temperature for 24 h. The dark red solution was evaporated by rotovap. The dark solid was purified by PTLC using ethyl acetate/pentane, 1:1 as eluent. TM **8** was isolated as dark solid (1.2 mg, 11%). TLC (silica gel, ethyl acetate/pentane, 1:1): R_f 0.43. LR-ESI-MS (0.1% HCOOH in MeOH): *m/z*, $[M]^+$, calcd for $C_{26}H_{24}IN_5O_2$: 565.0975; found: 565.1, RA = 100% (see: Figs. S34 – S36).

Repeat run CS6-71: A mixture of Blatter radical **5** (20.0 mg, 0.0372 mmol, 1 equiv) and nitronyl nitroxide **7** (11.8 mg, 0.0744 mmol, 2 equiv) was added to a Schlenk tube and evacuated on vacuum line for several minutes. The tube was kept vacuum and transferred to the antechamber of glove box. In the argon-filled glove box, NaO*t*-Bu (7.2 mg, 2 equiv) and $Pd(PPh_3)_4$ (12.8 mg, 30 mol%) were added into tube. Dry toluene was added into tube under the Ar flow. The reaction was stirred at room temperature and monitored by TLC (silica gel). Based on TLC analyses some of the Blatter radical **5** and nitronyl nitroxide **7** were left unreacted even after running reaction 5 days. The dark red solution was evaporated by rotovap. The dark residue was purified by silica gel column chromatography using 70 % ethyl acetate in pentane as eluent. The obtained dark solid was purified by PTLC using dichloromethane, and then ethyl acetate/dichloromethane, 1:1 as eluents. 0.3 mg dark solid were separated. TLC (silica gel, ethyl acetate/pentane= 1:1): R_f 0.43. LR-ESI-MS (0.1% HCOOH in MeOH): *m/z*, $[M+H]^+$, calcd for $C_{26}H_{25}IN_5O_2$: 566.105; found: 566.7, RA = 100% (see: Fig. S38). Spin concentration in toluene: chloroform, 4:1 solution were determined to 204 % at 293 K (label: CS674R1 to R6) and 213 % at 117 K (label: CS674R7 to R14). TEMPONE as reference in the same solution. The representative EPR spectra are shown in Fig. S18.

Run CS5-70: When the reaction was heated up to reflux, the Blatter radical **5** rapidly decomposed. Neither starting materials nor coupling products can be identified by ESI-MS and TLC.

Synthesis of diradical **8** using nitronyl nitroxide **4**:

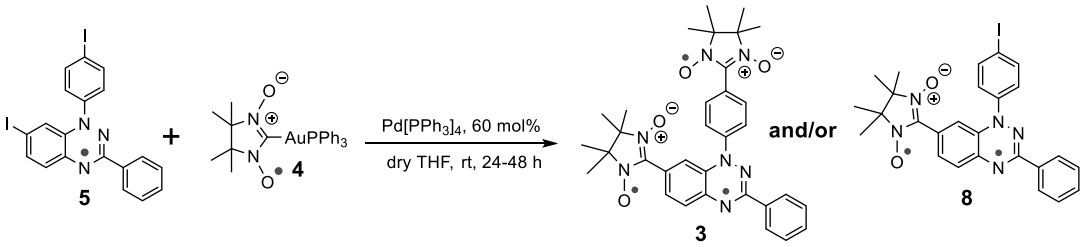

Run	Blatter radical **5** mg/mmol/eq	Nitronyl Nitroxide **4** mg/mmol/eq	$Pd(PPh_3)_4$ (mg, eq)	THF (mL)	Time[1] (h)	Notes
CS5-20	5/0.00932/1	6.3/0.0103/1.1	2.2/20 mol%	0.5	28	[2]1.1 mg of **8**, dark solid
CS5-25	12/0.0224/1	16.3/0.0265/1.1	15.5/60 mol%	1	24	-
CS5-33	10.0/0.0186/1	25.0/0.0409/2.2 spin conc. ~100%	13.0/60 mol%	0.5	48	3.3 mg of **3**, impure
CS5-35	20/0.0373/1	25/0.0406/1.1	26.0/60 mol%	1	24	[3]2.3 mg of **8**, impure
CS5-43	10/0.0186/1	12.5/0.0203/1.1	13.0/60 mol%	0.5	24	[3]2.0 mg of **8**, impure
CS5-46	10/0.0186/1	12.5/0.0203/1.1	2.9/30 mol% $Pd[P(t\text{-}Bu)_3]_2$	0.5	24	[4]1.4 mg of **8**; Spin conc. 177 % in THF at rt
CS6-82	20.0/0.0372/1	125.0/0.205/2.2 spin conc. ~100%	26.0/ 60 mol%	1.0	24	1.4 mg of **3** (6%); Spin conc. 359% in toluene/$CHCl_3$ (4:1) at rt
[5]CS6-83	20.0/0.0372/1	50.0/0.0818/2.2 spin conc. ~100%	26.0/60 mol%	1.0	24	1.60 mg of **3** (7%); Spin conc. 351% in toluene/$CHCl_3$ (4:1) at rt
CS6-84	50.0/0.0932/1	50.0/0.0818/2.2 spin conc. ~100%	65.0/60 mol%	2.5	48[1]	9.4 mg of **3** (17%); Spin conc. 386% in toluene/$CHCl_3$ (4:1) at rt

[1] With 2.2 equiv of **4**, further increasing the reaction time to 72 h lowers the isolated yield of **3**. [2] The residue was purified by column (regular silica gel, ethyl acetate/pentane, 1:1 as eluent). [3] Combine CS5-35 and CS5-43, to re-purify by PTLC; obtained 1.5 mg of dark solid, label: CS5-47p; spin conc. >200%, see: below description for CS5-35.
[4] The residue was purified by PTLC (regular silica gel, 100 mL DCM/pentane, 1:1, then add 100 mL ethyl acetate to continue the elution). [5] Crude mixture was purified after overnight. When TLC ws checked again, the diradical spot disappeared.

CS5-35: A mixture of di-iodo Blatter radical **5** (20.0 mg, 0.0373 mmol, 1 equiv) and nitronyl nitroxide **4** [Au^{I}(NN-2-ido)(PPh_3)] (25.0 mg, 0.0406 mmol, 1.1 equiv) was added to a Schlenk tube and evacuated on vacuum line for several minutes. Then, in the nitrogen-filled bag, $Pd(PPh_3)_4$ (0.020 g, 60 mol%) was added into tube. Fresh dry THF (1 mL) was added into tube under the argon gas flow. The reaction was stirred at room temperature for 24 hours. The dark red solution was evaporated by rotovap. The dark solid was purified by silica gel column chromatography using 50 % dichloromethane in pentane then 50 % ethyl acetate in pentane as eluent. Then the dark solid was combined with the CS543 product and purified again with PTLC using dichloromethane, and then 50 % ethyl acetate in dichloromethane as eluent. The dark solid, 1.5 mg of **8**, was labeled as CS5-47p. TLC (silica gel, ethyl acetate/pentane, 1:1): R_f 0.43. HR-TOF-MS (Fig. S30): *m/z*, $[M]^+$, calcd for $C_{26}H_{24}IN_5O_2$: 565.096923 found: 565.096429 (0.9 ppm, RA = 100% LR-ESI-MS: *m/z*, $[M]^+$, calcd for $C_{26}H_{24}IN_5O_2$: 565.097; found: 565.20, RA = 100% (Fig. S39). IR (powder, cm^{-1}) (Fig. S33): 2920, 2851, 1481, 1450, 1420, 1392, 1364, 1314, 1027, 1006, 850, 824, 695, 412. The spin concentration was determined to 208 % at 293 K in tetrahydrofuran and 213 % at 117 K in toluene/chloroform, 4:1 glass (TEMPONE as reference in the identical solvents). Representative EPR spectrum for **8** is shown in Fig. S17.

CS6-82: A mixture of di-iodo Blatter radical **5** (20 mg, 0.0373 mmol, 1 equiv) and nitronyl nitroxide radical **4** (50 mg, 0.0818 mmol, 2.2 equiv) was added to a Schlenk tube and evacuated on vacuum line for several minutes. The tube was kept vacuum and transferred to the nitrogen gas bag. Inside the nitrogen gas bag, palladium(0) catalyst ($Pd(PPh_3)_4$, 65 mg, 60 mol%) was added into tube. Fresh dry THF was added into tube under the argon gas flow. The reaction was stirred at room temperature for 24 hours. TLC shows that the reaction still have starting materials **5** and **4**. The dark red solution was evaporated by rotovap, to provide dark solid, which was purified by silica gel column chromatography using dichloromethane, followed by 10 % ethyl acetate in dichloromethane, as eluents. The resultant solid was purified again by silica gel column chromatography using the same eluents to

give 1.4 mg of product **3**. TLC (silica gel, ethyl acetate): R_f 0.43. LR-MSI-MS (0.1 % HCOOH in MeOH): m/z, $[M+H]^+$, calcd $C_{33}H_{37}N_7O_4$ 595.38, found 595.80, RA = 27%; $[3M + Na]^+$, calcd $C_{99}H_{111}N_{21}O_{12}Na_1$ 1805.8, found 1806.2, RA = 100% (Fig, S40). The spin concentration of **3** was determined to be 359 % in toluene/chloroform (4:1) fluid solution at 293 K (label: CS686R2 to R6 at 293 K, CS686R9 and R10 at 130 K). For each measurement, TEMPONE in the identical solvent was used as a spin counting reference.

CS6-83: This reaction was setup in the identical way as the preceding one (CS6-82); see: summary above. The reaction was stirred at room temperature for 24 hours. TLC shows that reaction mixture still have starting materials **5** and **4**. The dark red solution was evaporated by rotovap, to provide dark solid. The dark solid was dried under nitrogen gas overnight. When TLC ws checked again on the second day, the diradical spot disappeared. Crude mixture was purified by silica gel column chromatography using dichloromethane, followed by 10 % ethyl acetate in dichloromethane, as eluents. The resultant solid was purified again by silica gel column chromatography using the same eluents to give 1.60 mg of product **3**. 2.35 mg starting material **5** was recovered. LR-MSI-MS (0.1 % HCOOH in MeOH): m/z, $[M+H]^+$, calcd $C_{33}H_{37}N_7O_4$ 595.38, found 595.40, RA = 100% (Fig. S41). The spin concentration of **3** was determined to be 351% in toluene/chloroform (4:1) fluid solution at 293 K (label: CS687R1, R4 and R7 at 293 K, CS687R10 and R11 at 130 K). For each measurement, TEMPONE in the identical solvent was used as a spin counting reference.

CS6-84: A mixture of Blatter radical **5** (50 mg, 0.0932 mmol, 1 equiv) and nitronyl nitroxide radical **4** (125 mg, 0.205 mmol, 2.2 equiv) was added to a Schlenk tube and evacuated on vacuum line for several minutes. The tube was kept vacuum and transferred to the nitrogen gas bag. Inside the nitrogen gas bag, palladium(0) catalyst ($Pd(PPh_3)_4$, 65 mg, 60 mol%) was added into tube. Fresh dry THF was added into tube under the argon gas flow. The reaction was stirred at room temperature for 48 hours. TLC showed that SM **5** was almost consumed. The dark red solution was evaporated by rotovap, to provide dark solid, which was purified by silica gel column chromatography using dichloromethane, followed by 10 % ethyl acetate in dichloromethane, as eluents. The resultant solid was purified again by silica gel column chromatography using the same eluents. The resultant solid was treated (washed) with pentane to give 9.4 mg of product **3** as a dark solid. TLC (silica gel, ethyl acetate): R_f 0.43. LR-MSI-MS (0.1 % HCOOH in MeOH): m/z, $[M+H]^+$, calcd $C_{33}H_{37}N_7O_4$ 595.38, found 595.40, RA = 100% (Fig. S42). The spin concentration of **3** was determined to be 386 % in toluene/chloroform (4:1) fluid solution at 293 K (label: CS687R2, R5 and R8 at 293 K, CS687R12 and R13 at 130 K). For each measurement, TEMPONE in the identical solvent was used as a spin counting reference.

Synthesis of diradical **2** using non-transition metal nucleophilic nitronyl nitroxide **7**:

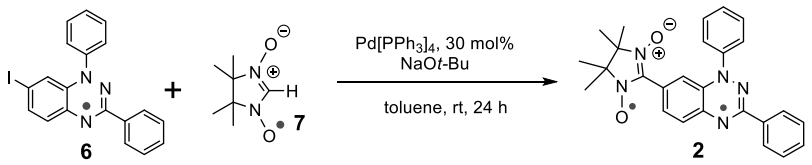

Run	Blatter radical **6** (mg/mmol/eq)	Nitronyl nitroxide **7** (mg/mmol/eq)	$Pd[PPh_3]_4$ (mg/eq)	NaO*t*-Bu (mg/mmol/eq)	Toluene (mL)	Time (h)	TM (mg, %yield)	Notes
CS5-63	10.0/0.0244/1	3.9/0.0244/1	8.5/30 mol%	3.0/0.0312/1.3	0.5	24	1.6, 12	brown solid after PTLC, ESI-MS: *m/z* = 439.3

Run CS5-63: A mixture of Blatter radical **6** (10.0 mg, 0.0244 mmol, 1 equiv) and nitronyl nitroxide **7** (3.9 mg, 0.0244 mmol, 1 equiv) was added to a Schlenk tube and evacuated on vacuum line for several minutes. The Schlenk tube was kept vacuum, and then it was transferred to the antechamber of glove box. Inside the argon-filled glove box, NaO*t*-Bu (3.0 mg, 1.3 equiv) was added into the tube. In the nitrogen gas bag, $Pd(PPh_3)_4$ (8.5 mg, 30 mol%) was added into the tube. Dry toluene was added into the Schlenk tube under the Ar flow. The reaction was stirred at room temperature for 24 h. The dark red solution was evaporated by rotovap. The dark solid was purified by PTLC using ethyl acetate/pentane, 1:1 as eluent. The product (1.6 mg, 12%) was obtained as a dark solid. TLC (silica gel, ethyl acetate/pentane,1:1): R_f 0.35. ESI-MS (0.1% HCOOH in MeOH): *m/z*, $[M]^+$, calcd for $C_{26}H_{25}N_5O_2$: 439.2008; found: 439.3, RA = 100% (see: Fig. S43).

1.c. UV-vis-NIR spectroscopy and electrochemistry

UV-vis-NIR spectroscopy of 3 and 2 in DCM at room temperature. UV-vis-NIR spectra of diradical **2** and triradical **3** were obtained using JASCO (model V-670) spectrophotometer in the λ = 250 – 2000 nm range, using dichloromethane (DCM) as a solvent. Two different samples of **3** were used to check for impurities and to verify extinction coefficients (ε): sample 1 (sample label: CS4-46, spectrum label: CS5-02) and sample 2 (sample label: CS6-27, spectrum label CS6-55). Spectral onsets were obtained by linear regression in the $\varepsilon \approx 0.010 - 0.003\ 10^4 \times$ L mol^{-1} cm^{-1} range (adjusted R^2 = 0.9949 – 0.9962, n = 91 – 241), followed by extrapolation (Fig. S8). For preliminary sample of **3** (sample label: CS4-02), onset at 876 nm was obtained (adjusted R^2 = 0.9870, n = 251). Thus, optical gap in diradical **2** and triradical **3** is E_g = 1.42 ± 0.01 eV (mean ± SE).

Cyclic and square wave voltammetry of 3 and 2 in DCM at room temperature. Voltammetry data for **3** and **2** were obtained in a glovebag under argon gas atmosphere, using procedures described for other π-conjugated compounds.[S13-S16] (The supply gas was a commercial ultra-high purity argon, certified to contain <1 ppm of O_2 and <1 ppm of H_2O.) The custom-made electrochemical cell, all solid reagents, syringes, needles, etc. were extensively evacuated in Schlenk vessels (typical pressure ≤ 1 mTorr, temperature 20–70 °C), prior to the transfer to the glovebag. Dichloromethane (DCM) was obtained from commercial solvent purification system, then distilled from calcium hydride under nitrogen, and stored in the absence of light in a Schlenk vessel on a vacuum line; just prior to the use, the solvent was vacuum transferred as needed. Commercial potentiostat/galvanostat was used. Three electrodes were employed: quasi-reference (Ag-wire), counter (Pt-foil), and working (100-μm Pt-disk). The concentration of an electroactive solute was about 0.8 – 0.9 mM. Concentration of the tetrabutylammonium hexafluorophosphate supporting electrolyte ($[n\text{-Bu}_4\text{N}]^+[\text{PF}_6]^-$) was about 0.1 M. The solution volume was about 2.4 mL. After a series of cyclic and square wave voltammograms with potential increments of 2 – 4 mV, a small amount (ca. 8 drops) of solution of decamethylferrocene (ca. 0.7 mg of Cp^*_2Fe, loaded to a Schlenk vessel in a glovebox under an argon atmosphere in the supporting electrolyte, ca. 0.8 mL) was added to the cell, to provide reference potentials (–0.130 V vs. SCE for $\text{Cp}^*_2\text{Fe}/\text{Cp}^*_2\text{Fe}^+$ in DCM).[S17,S18] Cyclic voltammograms with the scanning rates in the 50–1000 mV/s range and square wave voltammograms with frequencies in the 2 – 10 Hz range (pulse height 25 mV) were obtained.

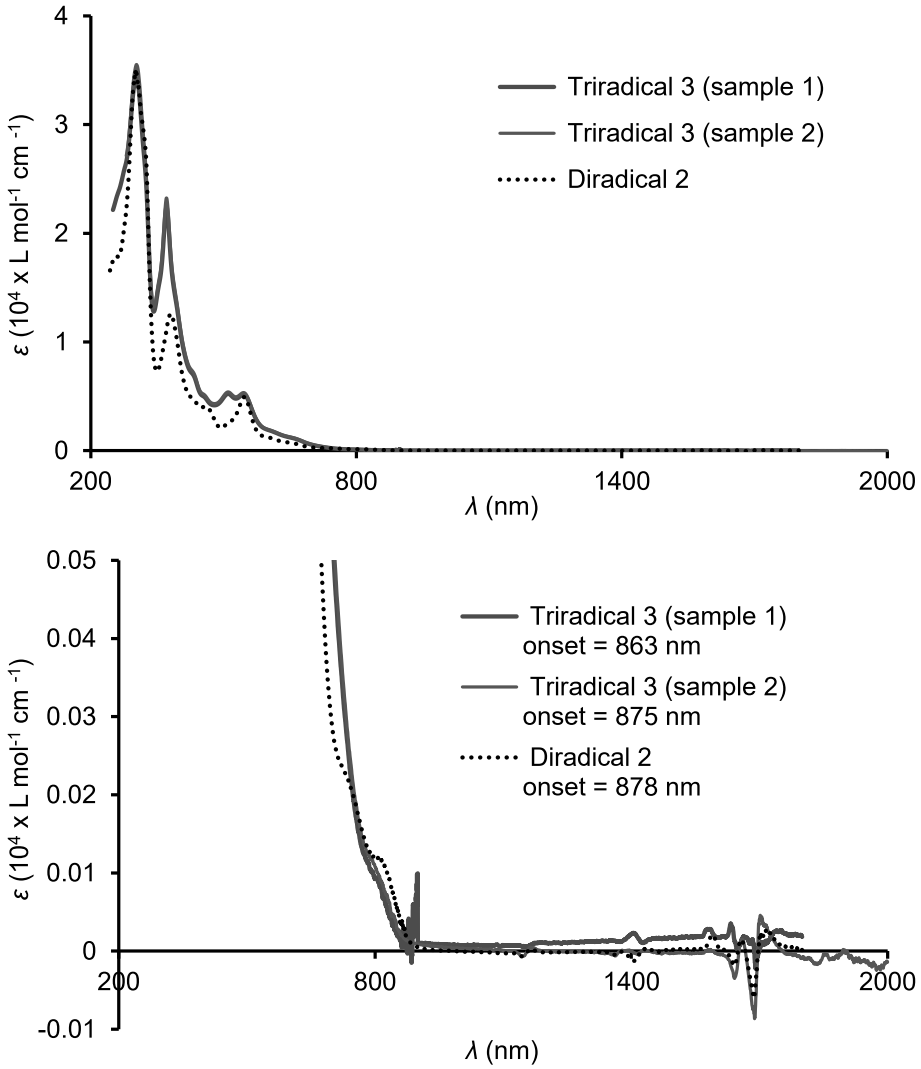

Fig. S8. UV-vis-NIR spectra of diradical **2** and triradical **3** in dichloromethane (λ = 250– 2000 nm range), with a vertical expansion. UV-vis-NIR, DCM, λ_{max}/nm (ε_{max}/L mol^{-1} cm^{-1}) triradical **3**: 303 (3.49 × 10^4), 371 (2.26 × 10^4), 510 (5.26 × 10^3), 545 (5.24 × 10^3); diradical **2**: 302 (3.5 × 10^4), 381 (1.3 × 10^4), 547 (4.9 × 10^3). For phenyl-substituted nitronyl nitroxide in ethanol the following spectra data were reported:[S19] λ_{max}/nm (ε_{max}/L mol^{-1} cm^{-1}), 238 (9400), 263 (12,200), 360 (13,300), and 588 (685).

Table S5. Summary of redox potentials for **3** and **2**.[a]

		Oxidation Potentials			Reduction Potentials		
Compound	Label	Oxidation step	CV $E_{1/2}^{ox}$ (V), n	SWV E_p^{ox} (V), n	Reduction step	CV $E_{1/2}^{red}$ (V), n	SWV E_p^{red} (V), n
Triradical **3**	CS6-01	$E^{+/0}$	0.413±0.006, 8	0.411±0.003, 9	$E^{-/0}$	–0.73±0.04, 2	–0.69±0.010, 4
		$E^{2+/+}$	0.972±0.006, 8	0.987±0.014, 9	$E^{2-/-}$	-	–1.43±0.014, 4
Triradical **3**	CS5-98	$E^{+/0}$	0.433±0.010, 12	0.407±0.006, 10	-	-	-
		$E^{2+/+}$	0.997±0.017, 12	0.936±0.015, 10	-	-	-
Diradical **2**	CS5-100	$E^{+/0}$	0.357±0.005, 13	0.352±0.006, 7	$E^{-/0}$	–0.85±0.02, 6	-
		$E^{2+/+}$	1.024±0.005, 12	1.022±0.010, 7	-	-	-

[a] Potentials from cyclic voltammetry (CV) and square wave voltammetry (SWV) are provided as mean ± 1 standard deviation, based on values from n voltammograms with scan rates of 50 – 1000 mV s^{-1} and with frequencies of 2 – 10 Hz, respectively. Supporting electrolyte: 0.1 M $[n\text{-Bu}_4\text{N}]^+[\text{PF}_6]^-$ in dichloromethane. 100-µm Pt-disk was a working electrode. The potentials were calibrated with decamethylferrocene as an internal standard: –0.130 V vs. SCE for $Cp^*_2Fe^{+/0}$ in dichloromethane.

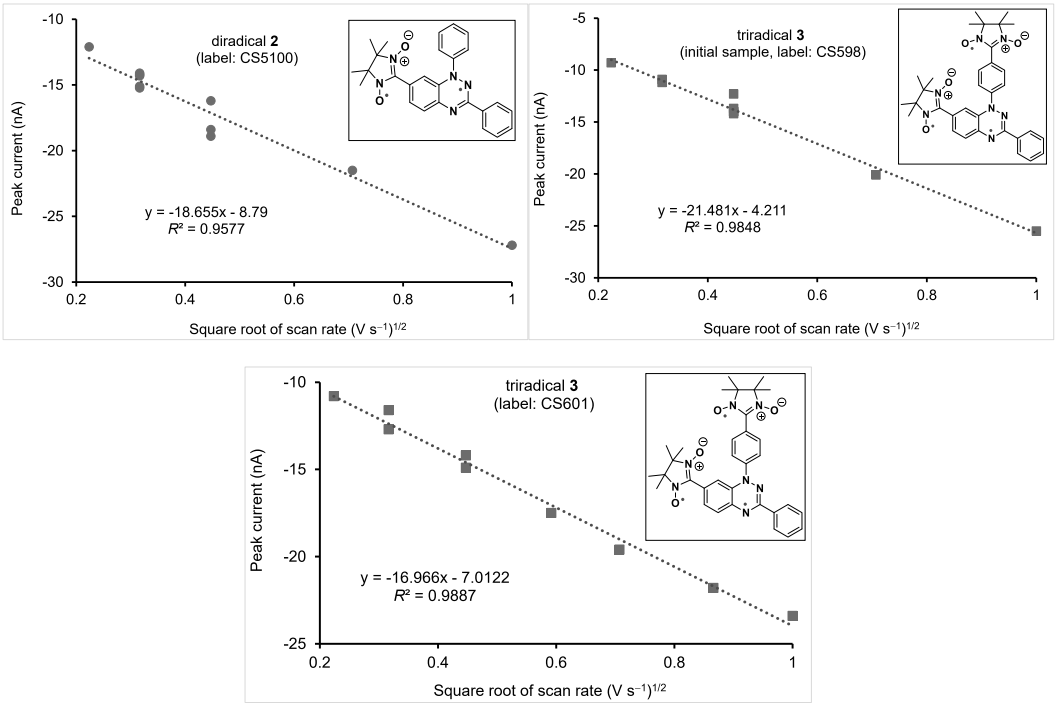

Fig. S9. Cyclic voltammetry of **2** and **3** in DCM: plots of peak current (nA) for the first oxidation wave at ~0.4 V (vs. SCE) vs. square root of scan rate $((V/s)^{1/2})$ (CV labels: CS5-98, CS5-100, and CS6-01).

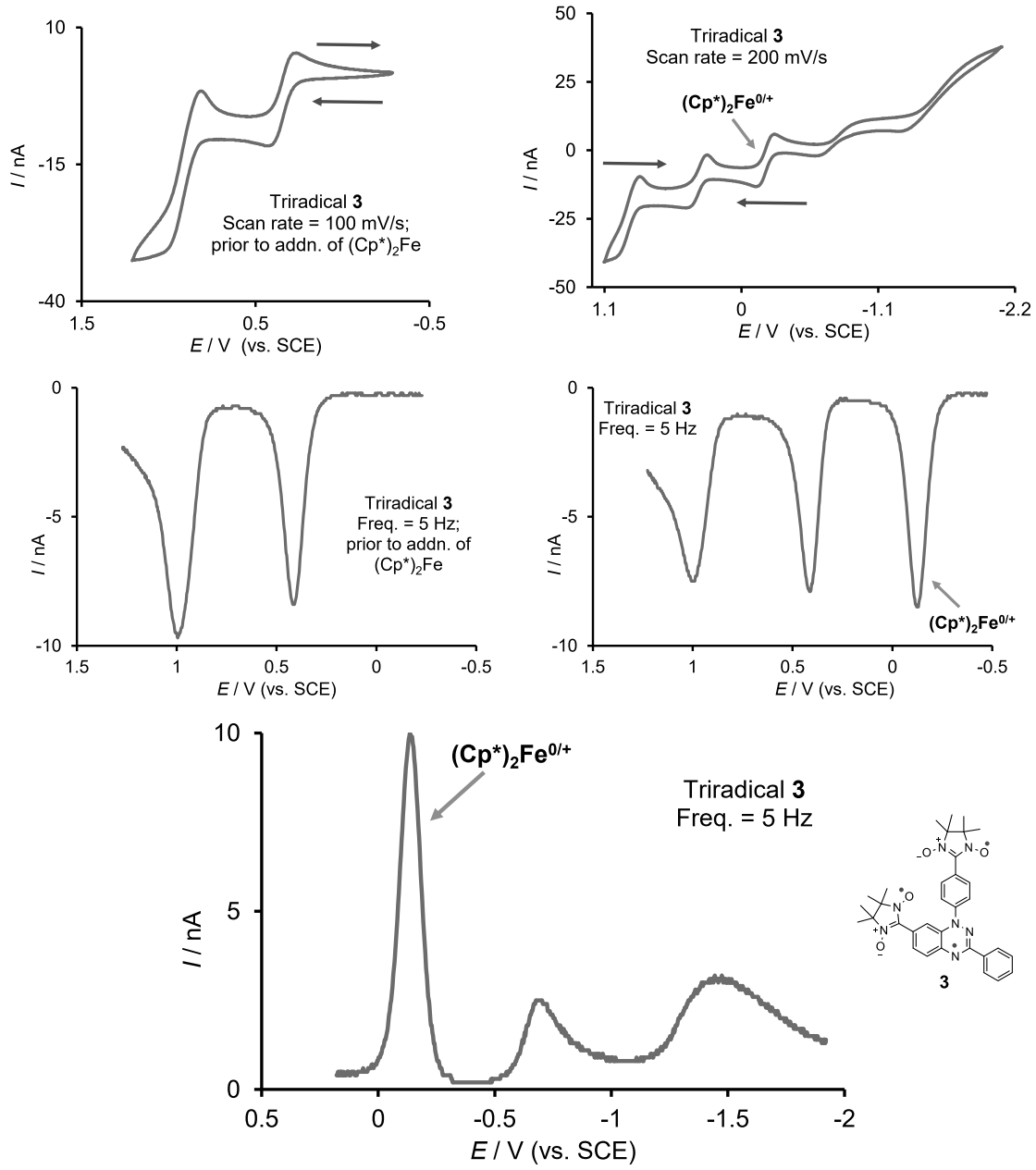

Fig. S10. Selected cyclic (CV) and square wave (SWV) voltammograms for triradical **3** in DCM without and with Cp^*_2Fe reference (CV and SWV labels, top-to-bottom: CS6-01C9 and CS6-01CC4, CS6-01S4 and CS6-01SS4, CS6-01SS13).

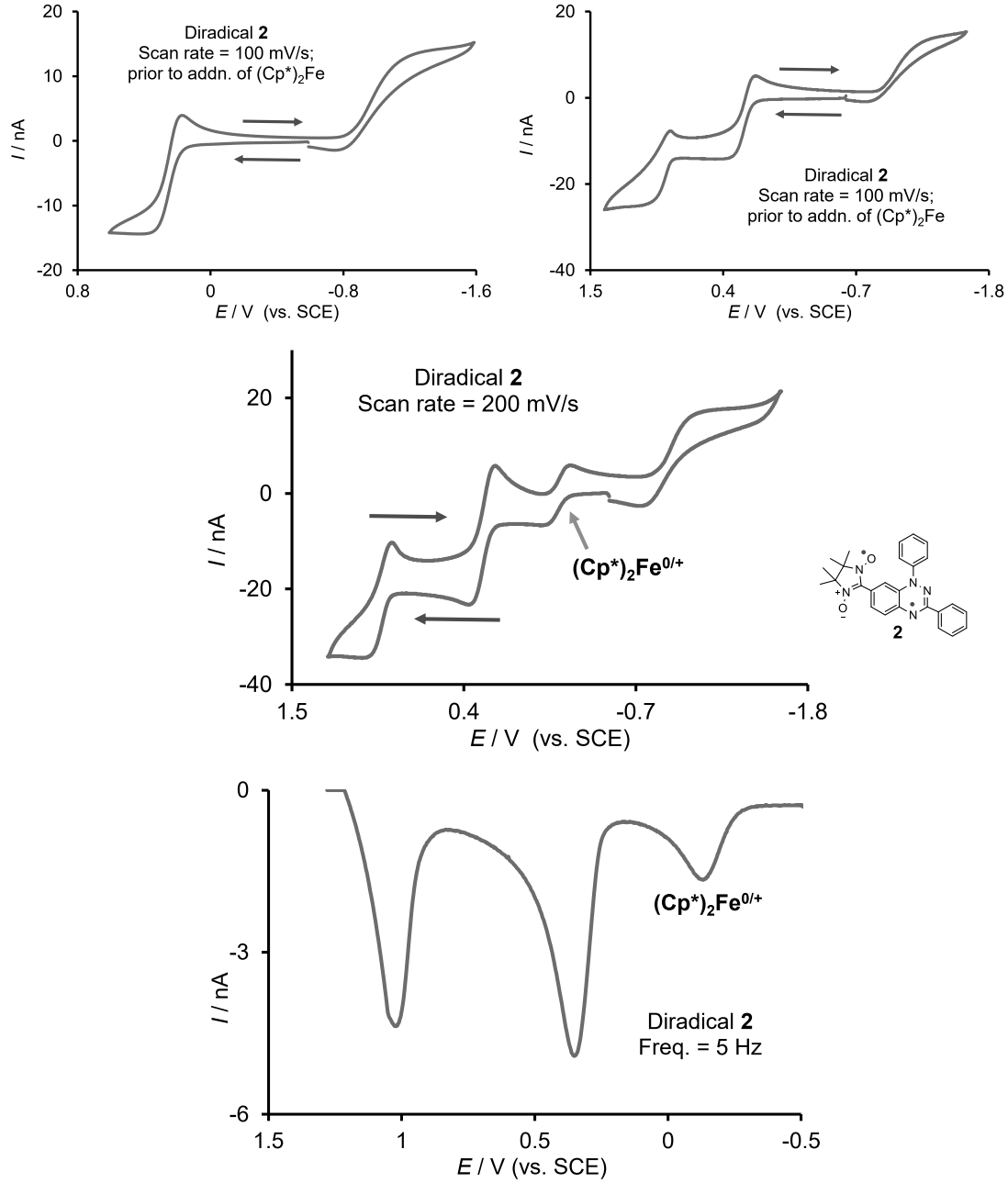

Fig. S11. Selected cyclic and square wave voltammograms for diradical **2** in DCM without and with Cp*$_2$Fe reference (CV and SWV labels, top-to-bottom: CS5-100C6 and CS5-100C7, CS5-100CC4, CS5-100SS3).

1.d EPR spectroscopy.

1.d1 General description and EPR microwave saturation plots. EPR spectra were obtained using Bruker CW EPR spectrometer (X-band EMXplus). For temperature control (400–95 K), EPR spectrometer was equipped with custom-made nitrogen flow system. Temperatures were calibrated using an additional thermocouple inserted to the EPR tube containing solvent.[S5,S16,S20] DPPH powder (g = 2.0037) was used as a g-value reference. EPR spectra were simulated using EasySpin.[S21] Simulations for triradical **3** (using pepper of EasySpin), including quartet (S = 3/2), with an admixture of thermally populated doublet (S = 1/2) state, are presented in Figs. S13 – S16 and S19 – S20; simulations for diradical **8** in Figs. S17 and S18 include triplet (S = 1) state and a small admixture of doublet (S = 1/2) impurity (<10%).

Simulations of the experimental EPR spectra of triradical **3** suggest that the second-largest principal value of the **D** tensor and the largest principal value of the **A** tensor are approximately parallel to the direction of the $2p_\pi$ orbitals on the nitrogens (y axis); this is because the spectral linewidth, H_y-strain, corresponding to the second-largest principal value of the **D** tensor (y-axis) is by a factor of 3 – 4 larger, compared to other line broadenings, H_x and H_z. This situation is analogous to EPR spectra of diradicals **1**, **2**, and also planar nitroxide diradicals, indicating "prolate"-like spin density distribution with $D/hc < 0$.[S22] Thus, computed value of $D/hc > 0$ for **3** (Table S11) is inconsistent with its experimental EPR spectrum.

Since at low temperatures required for quantitative EPR spectra obtained in the determination of doublet-quartet energy gap for triradical, slow electron spin relaxation rates may affect signal intensities, we have checked for microwave saturation at 110 K for both triradical and Tempone reference (Fig. S12).

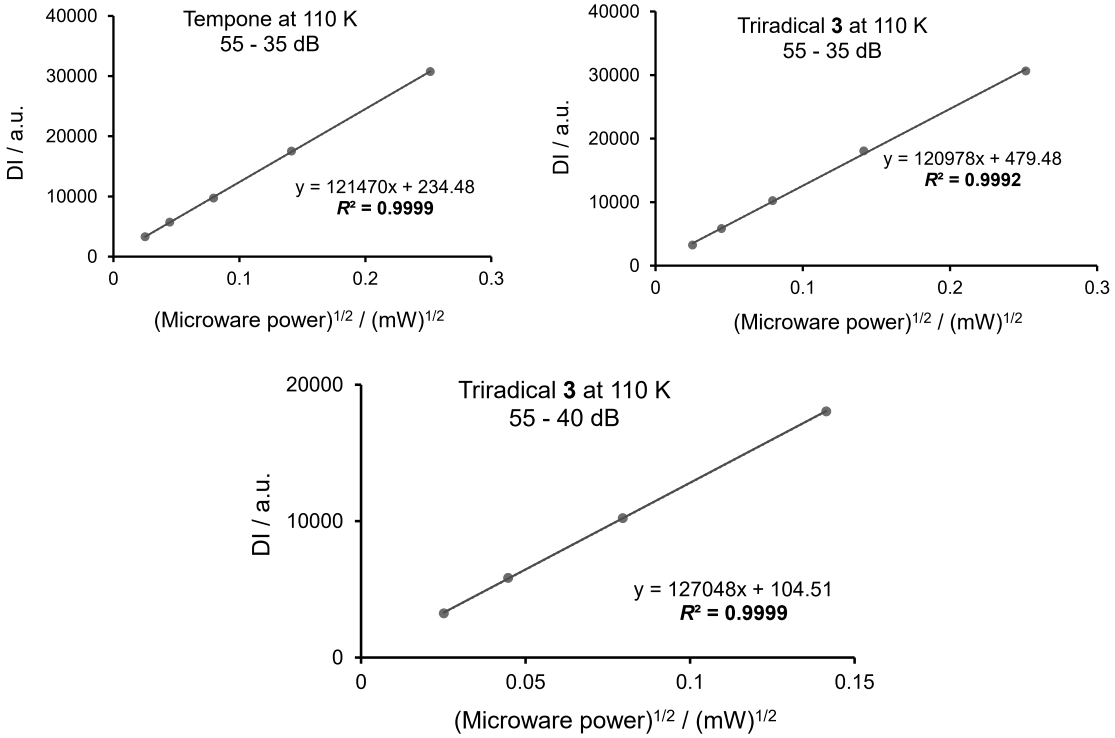

Fig. S12. Plots of EPR double integrated signal intensity (DI) versus the square root of microwave power in toluene/chloroform (3:1) at 110 K. Microwave power attenuation ranges were 55 – 35 dB for 1.36 mM triradical (sample label: CS529r#) and for 5.80 mM Tempone.

In Fig. S12 (above), absence of microwave saturation at 110 K is found down to attenuations of 40 dB and 35 dB (from 200 mW) for triradical and Tempone, respectively; therefore, the quantitative EPR can be carried out at attenuation of 40 dB – we have mostly used attenuation of 40 dB, and occasionally 50 dB. When the plots are extended to up to 15 dB, significant curvatures are observed.

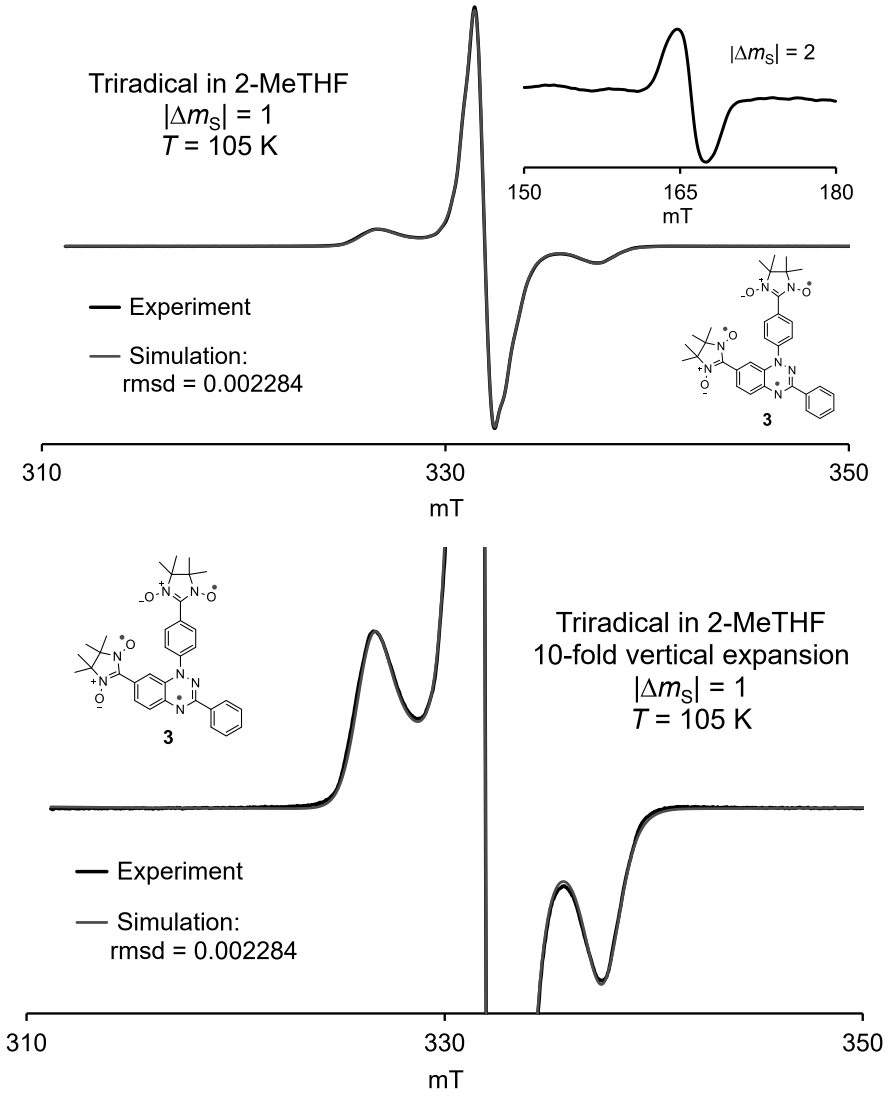

Fig. S13. Enlarged version of Figure 4 (top panel, main text). Top panel: EPR (ν = 9.3251 GHz, label: CS515r5) spectrum for 2.32 mM triradical **3** in 2-MeTHF at 105 K. Inset plot: the $|\Delta m_S| = 2$ transition at 105 K (ν = 9.3248 GHz, label: CS515r2). Simulation of the $|\Delta m_S| = 1$ region (label: try1363): rmsd = 0.0022841, S = 3/2, weight = 1.0000, D = 77.84 MHz, E = 22.70 MHz, g_{xx} = 2.0075, g_{yy} = 2.0047, g_{zz} = 2.0065; H-strain (MHz): H_x = 15.2, H_y = 79.3, H_z = 47.2; S = 1/2, weight = 0.17245, g_{xx} = 2.0018, g_{yy} = 2.0137, g_{zz} = 1.9968; H-strain (MHz): H_x = 10.2, H_y = 7.1, H_z = 17.8. Based on the above simulation χT = 1.6544 emu K mol^{-1} vs. measured χT = 1.582 ± 0.008 emu K mol^{-1}. Bottom panel: the 10-fold vertically expanded spectrum (with simulation), shown in the top panel.

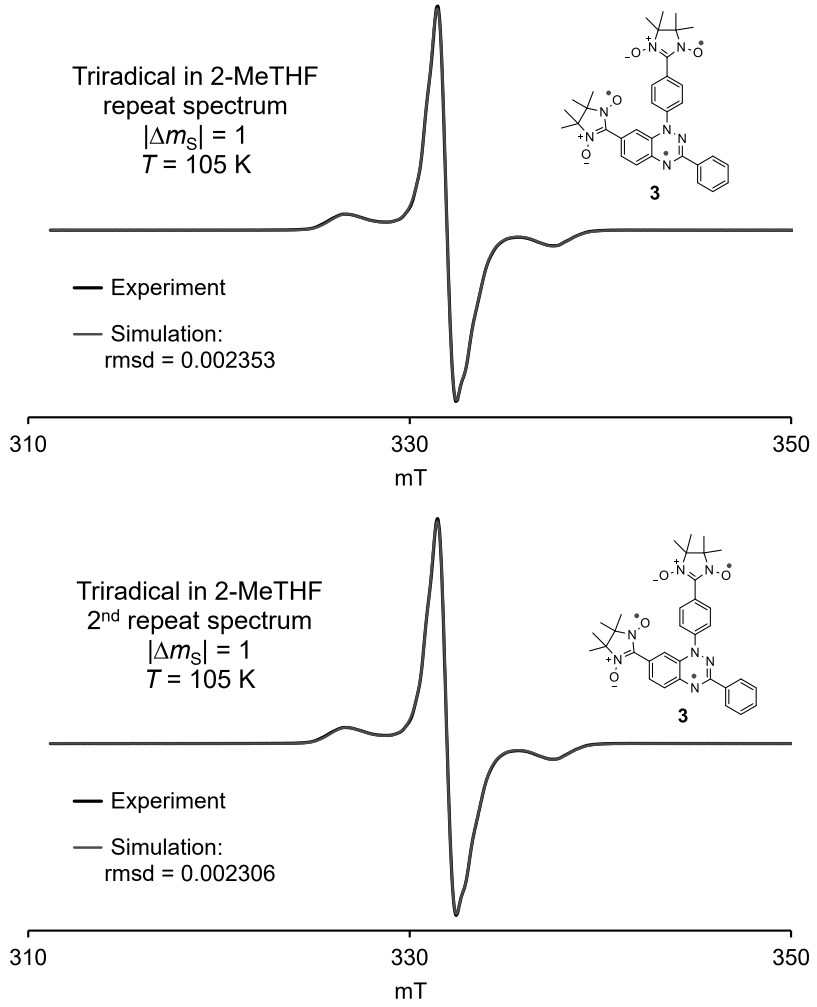

Fig. S14. Repeat EPR spectra for 2.32 mM triradical **3** in 2-MeTHF at 105 K. Top panel: EPR (ν = 9.3253 GHz, label: CS515r7) spectrum with simulation of the $|\Delta m_S| = 1$ region (label: try1365): rmsd = 0.0023531, S = 3/2, weight = 1.0000, D = 77.84 MHz, E = 22.70 MHz, g_{xx} = 2.0075, g_{yy} = 2.0048, g_{zz} = 2.0065; H-strain (MHz): H_x = 15.2, H_y = 79.2, H_z = 47.2; S = 1/2, weight = 0.17233, g_{xx} = 2.0018, g_{yy} = 2.0137, g_{zz} = 1.9968; H-strain (MHz): H_x = 10.2, H_y = 7.1, H_z = 17.8. Based on the above simulation χT = 1.6545 emu K mol^{-1} vs. measured χT = 1.582 ± 0.008 emu K mol^{-1}. Bottom panel: EPR (ν = 9.3253 GHz, label: CS515r9) spectrum with simulation of the $|\Delta m_S| = 1$ region (label: try1367): rmsd = 0.00230645, S = 3/2, weight = 1.0000, D = 77.82 MHz, E = 22.68 MHz, g_{xx} = 2.0074, g_{yy} = 2.0048, g_{zz} = 2.0065; H-strain (MHz): H_x = 15.1, H_y = 79.2, H_z = 47.3; S = 1/2, weight = 0.17301, g_{xx} = 2.0018, g_{yy} = 2.0137, g_{zz} = 1.9968; H-strain (MHz): H_x = 10.2, H_y = 7.1, H_z = 18.1. Based on the above simulation χT = 1.6538 emu K mol^{-1} vs. measured χT = 1.582 ± 0.008 emu K mol^{-1}.

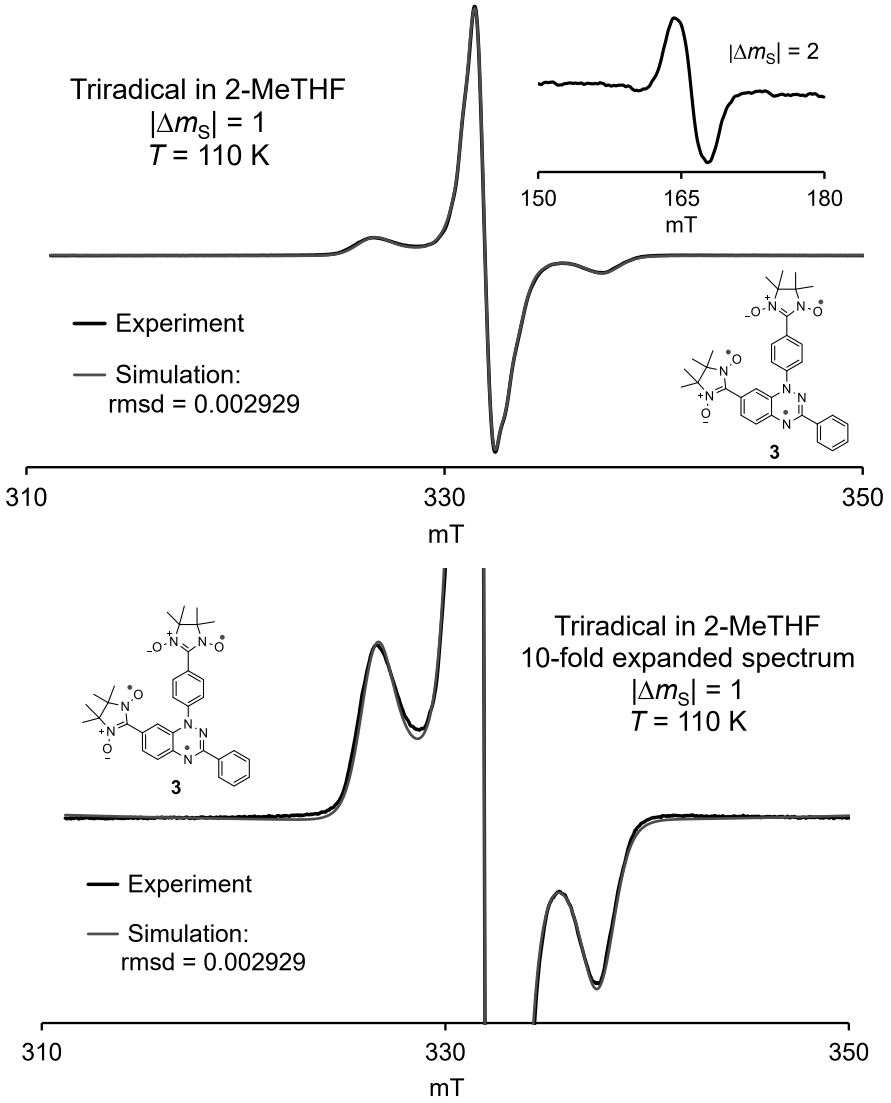

Fig. S15. Top panel: EPR (ν = 9.3245 GHz, label: CS508r11) spectrum for 2.32 mM triradical **3** in 2-MeTHF at 110 K. Inset plot: the $|\Delta m_S| = 2$ transition at 110 K (ν = 9.3229 GHz, label: CS508r8). Simulation of the $|\Delta m_S| = 1$ region (label: try1343): rmsd = 0.0029289, S = 3/2, weight = 1.0000, D = 77.85 MHz, E = 22.67 MHz, g_{xx} = 2.0074, g_{yy} = 2.0056, g_{zz} = 2.0062; H-strain (MHz): H_x = 14.7, H_y = 79.9, H_z = 46.3; S = 1/2, weight = 0.185815, g_{xx} = 2.0017, g_{yy} = 2.0136, g_{zz} = 1.9966; H-strain (MHz): H_x = 10.6, H_y = 7.2, H_z = 17.6. Based on the above simulation χT = 1.6400 emu K mol^{-1} vs. measured χT = 1.552 ± 0.008 emu K mol^{-1}. Bottom panel: the 10-fold vertically expanded spectrum (with simulation), shown in the top panel.

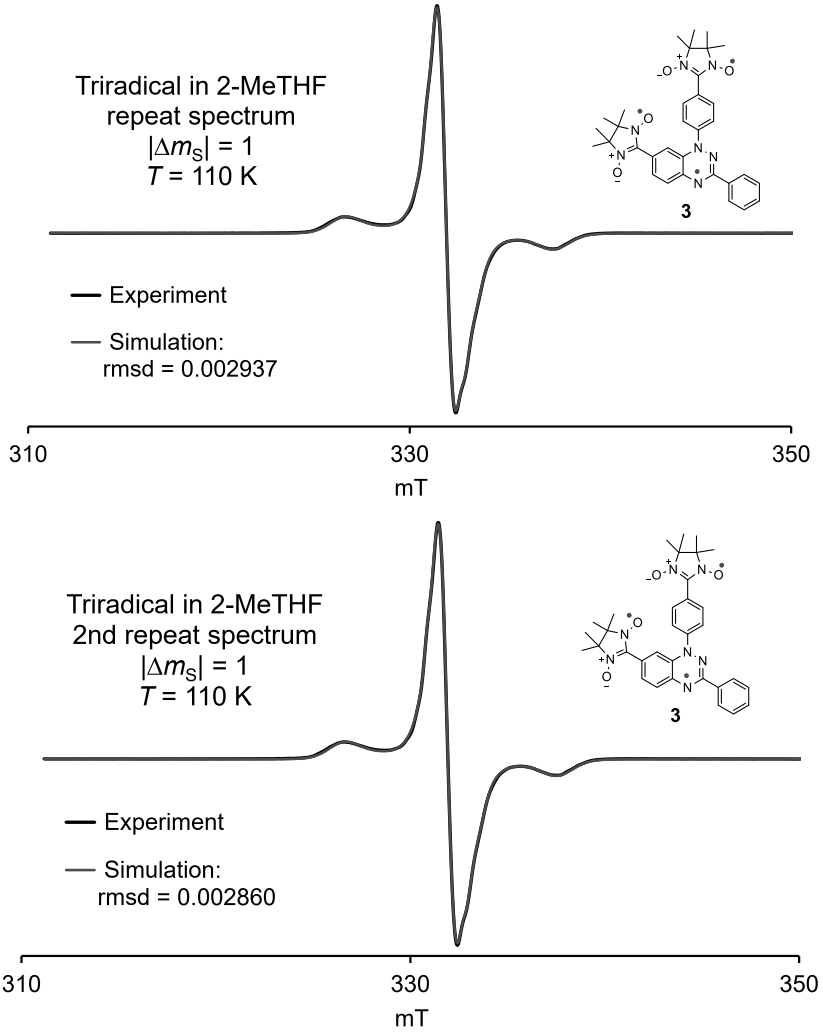

Fig. S16. Repeat EPR spectra for 2.32 mM triradical **3** in 2-MeTHF at 110 K. Top panel: EPR (ν = 9.3244 GHz, label: CS508r9) spectrum with simulation of the $|\Delta m_S| = 1$ region (label: try1348): rmsd = 0.0029370, S = 3/2, weight = 1.0000, D = 77.84 MHz, E = 22.67 MHz, g_{xx} = 2.0074, g_{yy} = 2.0057, g_{zz} = 2.0061; H-strain (MHz): H_x = 14.7, H_y = 80.0, H_z = 46.3; S = 1/2, weight = 0.18592, g_{xx} = 2.0017, g_{yy} = 2.0136, g_{zz} = 1.9966; H-strain (MHz): H_x = 10.7, H_y = 7.2, H_z = 17.6. Based on the above simulation χT = 1.6398 emu K mol^{-1}. Bottom panel: EPR (ν = 9.3245 GHz, label: CS508r7) spectrum with simulation of the $|\Delta m_S| = 1$ region (label: try1350): rmsd = 0.0028598, S = 3/2, weight = 1.0000, D = 77.87 MHz, E = 22.68 MHz, g_{xx} = 2.0074, g_{yy} = 2.0056, g_{zz} = 2.0062; H-strain (MHz): H_x = 14.7, H_y = 79.9, H_z = 46.4; S = 1/2, weight = 0.18398, g_{xx} = 2.0017, g_{yy} = 2.0136, g_{zz} = 1.9966; H-strain (MHz): H_x = 10.6, H_y = 7.2, H_z = 17.7. Based on the above simulation χT = 1.6419 emu K mol^{-1}.

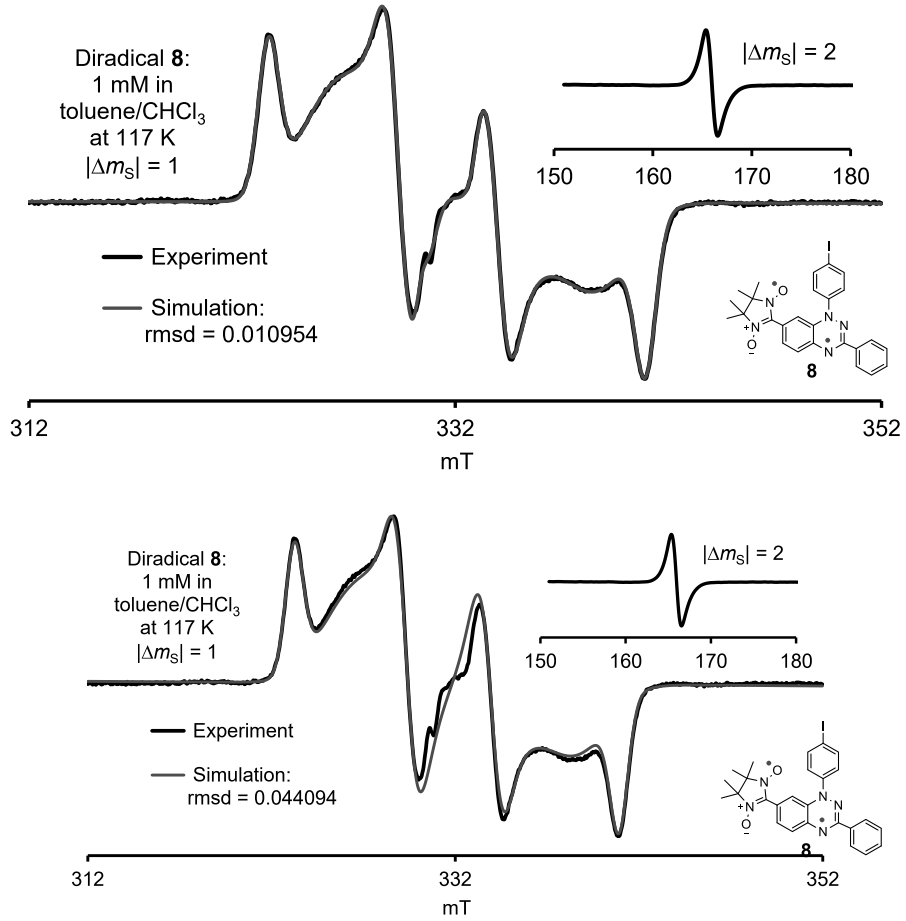

Fig. S17. EPR (ν = 9.3230 GHz, label: CS547R6) spectrum for ~1.0 mM diradical **8** in toluene/chloroform, 4:1 at 117 K. Inset plot: the $|\Delta m_S| = 2$ transition at 110 K (ν = 9.3238 GHz, label: CS547R12). The diradical was isolated from combined reactions (labels CS5-35 and CS5-46) of di-iodo-Blatter radical **5** with nitronyl nitroxide **4** (Au^I) in the presence of $(Ph_3P)_4Pd$. Top: Simulation of the $|\Delta m_S| = 1$ region (label: try1374): rmsd = 0.00109535, S = 1, weight = 1.0000, D = 247.39 MHz, E = 37.56 MHz, g_{xx} = 2.0083, g_{yy} = 2.0032, g_{zz} = 2.0058; H-strain (MHz): H_x = 36.5, H_y = 103.3, H_z = 32.3; impurity S = 1/2, weight = 0.04274, g_{xx} = 2.0071, g_{yy} = 2.0159, g_{zz} = 2.0015; H-strain (MHz): H_x = 33.1, H_y = 17.7, H_z = 23.9. Bottom: same data as above but simulation with S = 1 only (label: try1375): rmsd = 0.044094, D = 247.11 MHz, E = 36.69 MHz, g_{xx} = 2.0084, g_{yy} = 2.0030, g_{zz} = 2.0058; H-strain (MHz): H_x = 37.0, H_y = 110.1, H_z = 31.6. Measured $\chi T = 0.80 \pm 0.01$ emu K mol^{-1} at 117 K was significanlty lower than for diradical **2**, though the diradical is almost pure (<5% S = 1/2 impurities); this is most likely, because of large weighing error. (Only 0.30 mg of **8** was used to prepare the sample.) The simulation parameters for **8** are similar to those for **2**.[S23]

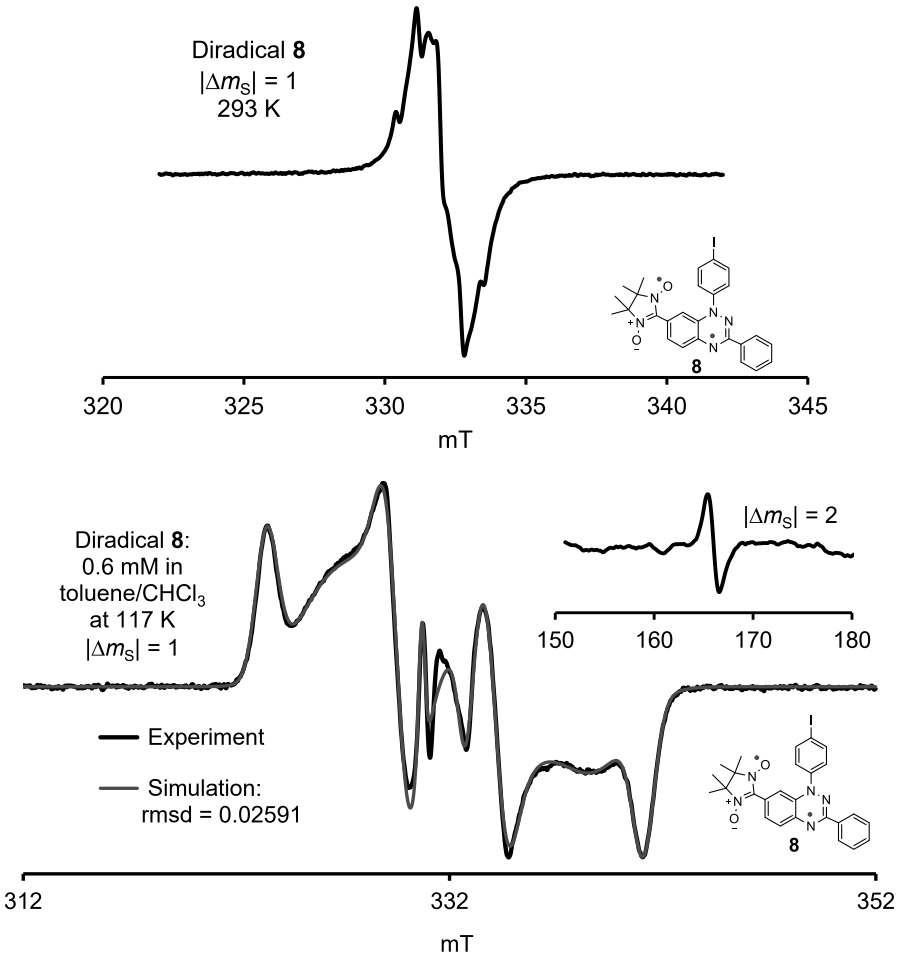

Fig. S18. EPR spectra for ~0.6 mM diradical **8** in toluene/chloroform, 4:1. The diradical was isolated from reaction (label CS6-71) of di-iodo-Blatter radical **5** with parent nitronyl nitroxide **7**. Top: EPR (ν = 9.3260 GHz, label: CS674R1) spectrum for **8** at 293 K. Bottom: EPR (ν = 9.3289 GHz, label: CS674R7) spectrum for **8** at 117 K. Inset plot: the |Δm_S| = 2 transition at 117 K (ν = 9.3255 GHz, label: CS674R11). Simulation of the |Δm_S| = 1 region (label: try1374): rmsd = 0.025913, S = 1, weight = 1.0000, D = 247.32 MHz, E = 37.08 MHz, g_{xx} = 2.0085, g_{yy} = 2.0034, g_{zz} = 2.0060; H-strain (MHz): H_x = 34.9, H_y = 107.6, H_z = 32.9; impurity S = 1/2, weight = 0.097443, g_{xx} = 2.0054, g_{yy} = 2.0151, g_{zz} = 2.0037; H-strain (MHz): H_x = 56.1, H_y = 8.7, H_z = 20.1. Measured χT = 0.76 ± 0.01 and 0.80 ± 0.01 emu K mol^{-1} at 293 and 117 K was significantly lower than for diradical **2**, though the diradical in not quite pure (~10% S = 1/2 impurities); because only 0.30 mg of diradical was available, the resultant weighing error is significant. The simulation parameters for **8** are similar to those for **2**[S23] and for **8**, prepared using nitronyl nitroxide **4** (preceding Figure).

1.d2 Quantitative EPR spectroscopy: determination of doublet-quartet energy gap (ΔE_{DQ}) for triradical 3 in toluene/chloroform. Quantitative variable temperature EPR spectroscopy for triradical in toluene/chloroform, 3:1 was carried out using tempone in toluene/chloroform, 3:1, as a reference.[S5,S16,S24] At each temperature, the triradical EPR tube was directly transferred from liquid nitrogen to the cavity and measured. Then, the reference EPR tube was directly transferred from liquid nitrogen to the cavity and measured. This process was repeated 3 times, alternating between the triradical and the reference.

EPR spectra were measured in the T = 110 – 331 K range. Average values of χT vs T were fit to the Equation S1, using either two-parameter (J_1/k and J_2/k = exchange coupling constants) fit or a three-parameter fit with J_1/k, J_2/k, and N, where N is weight correction factor. In a typical fit, mean-field parameter was set to $\theta = 0$, correction for diamagnetism, $B = 0$, and weight correction factor, $N = 0.99$. Factor $N = 0.99$ was obtained by comparing values of χT at T = 110 K: obtained by simulation of EPR spectra (Figs. S17 and S18) $\chi T = 1.6479 \pm 0.0003$ emu K mol^{-1} ($n = 3$) vs. measured $\chi T = 1.632 \pm 0.0058$ emu K mol^{-1} ($n = 3$).

In 2-MeTHF values of χT at 110 K and 105 K are as follows; at 110 K: obtained by simulation of EPR spectra (Figs. S13 and S14) $\chi T = 1.6406 \pm 0.0007$ emu K mol^{-1} ($n = 3$) vs. measured $\chi T = 1.552 \pm 0.0057$ emu K mol^{-1} ($n = 3$); at 105 K: obtained by simulation of EPR spectra (Figs. S15 and S16) $\chi T = 1.6542 \pm 0.0002$ emu K mol^{-1} ($n = 3$) vs. measured $\chi T = 1.582 \pm 0.0083$ emu K mol^{-1} ($n = 3$); thus, for this sample, the weight factor N is significantly smaller.

$$\chi T = T^*\{[N^*1.118^*(nom/den)] + B\}/H \quad \text{(S1A)}$$

$$nom = 0.5^*\sinh(0.5^*a)+1.5^*\sinh(1.5^*a)+0.5^*\sinh(0.5^*a)^*\{[1/\exp(\Delta E_{DQ}/T)]+[1/\exp(\Delta E_{DQ}2/T)]\} \quad \text{(S1B)}$$

$$den = \cosh(0.5^*a) + \cosh(1.5^*a) + \cosh(0.5^*a)^*\{[1/\exp(\Delta E_{DQ}/T)] + [1/\exp(\Delta E_{DQ}2/T)]\} \quad \text{(S1C)}$$

$$a = (1.345^*H)/(T - \theta) \quad \text{(S1D)}$$

$$\Delta E_{DQ} = J_1 + J_2 - [J_1^2 + J_2^2 - (J_1^*J_2)]^{1/2} \quad \text{(S1E)}$$

$$\Delta E_{DQ}2 = J_1 + J_2 + [J_1^2 + J_2^2 - (J_1^*J_2)]^{1/2} \quad \text{(S1F)}$$

Detailed procedure for sample and reference preparation. Triradical **3** (0.39 mg) was transferred into a 4-mm EPR tube by dichloromethane and the solvent was evaporated in high vacuum line overnight. Under argon gas flow, the solvent (toluene/chloroform, 2.7 : 1, previously degassed, 0.482 mL) was added into the tube to produce 1.36 mM solution of **3**, which was stirred with magnetic bar at –78 °C. After 20 min, the EPR tube was pumped in high vacuum line at –78 °C for 0.5 h. Then, the tube was frozen in liquid nitrogen and pumped again. The pump-freeze-thaw degassing process was repeated 3 times. Tempone (0.49 mg) was transferred to another 4-mm EPR tube and placed under vacuum for 3 min. Under argon gas flow, the solvent (toluene/chloroform, 2.7 : 1, previously degassed, 0.496 mL) was added into tube to produce 5.80 mM solution of tempone, which was stirred with magnetic bar at –78 °C. Then the solution was degassed using the identical procedure to that for the sample of triradical. The sample and reference EPR tubes were stored in the liquid nitrogen, with stopcock continuously pumped on a high vacuum line.

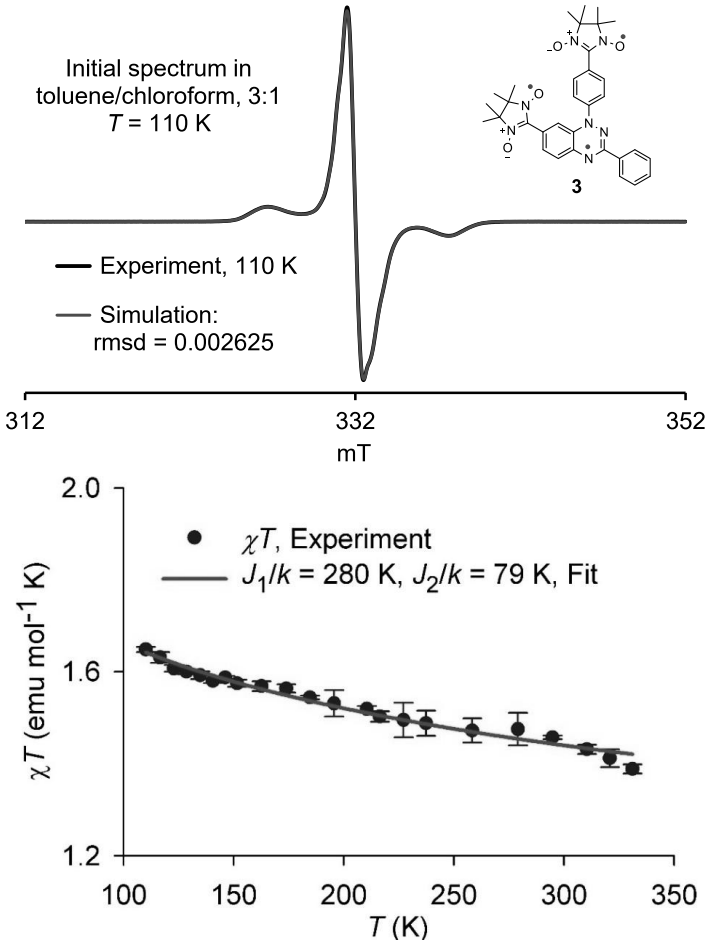

Fig. S19. Quantitative EPR spectroscopy in toluene/chloroform. Expanded version of Figure 4 (bottom panel, main text). Top panel: EPR (ν = 9.3256 GHz, label: CS529r7) spectrum for 1.36 mM triradical **3** in toluene/chloroform at 110 K obtained during quantitatitaive EPR spectroscopy. Simulation of the $|\Delta m_S| = 1$ region (label: try1342): rmsd = 0.00262546, $S = 3/2$, weight = 1.0000, $D = 79.69$ MHz, $E = 23.36$ MHz, $g_{xx} = 2.0072$, $g_{yy} = 2.0042$, $g_{zz} = 2.0066$; H-strain (MHz): $H_x = 14.4$, $H_y = 74.5$, $H_z = 54.4$; $S = 1/2$, weight = 0.17886, $g_{xx} = 2.0016$, $g_{yy} = 2.0137$, $g_{zz} = 1.9964$; H-strain (MHz): $H_x = 10.5$, $H_y = 7.5$, $H_z = 19.0$; $\chi T = 1.64742$ emu K mol^{-1}. Based on the above and simulations in Fig. S19, $\chi T = 1.6479 \pm 0.0003$ emu K mol^{-1} vs. measured $\chi T = 1.632 \pm 0.0058$ emu K mol^{-1}. Bottom panel: Experimental values of χT (mean ± SE) in the $T = 110 - 331$ K range and numerical two-parameter fit with two variable parameters, $J_1/k = 280 \pm 17$ K and $J_2/k = 79 \pm 2.7$ K (mean ± SE), following correction with weight factor $N = 0.99$ – obtained from simulation of EPR spectra at 110 K in the top panel and Fig. S18. Statistical parameters: parameter dependence = 0.704, adjusted $R^2 = 0.9724$, and standard error of estimate = 0.0120.

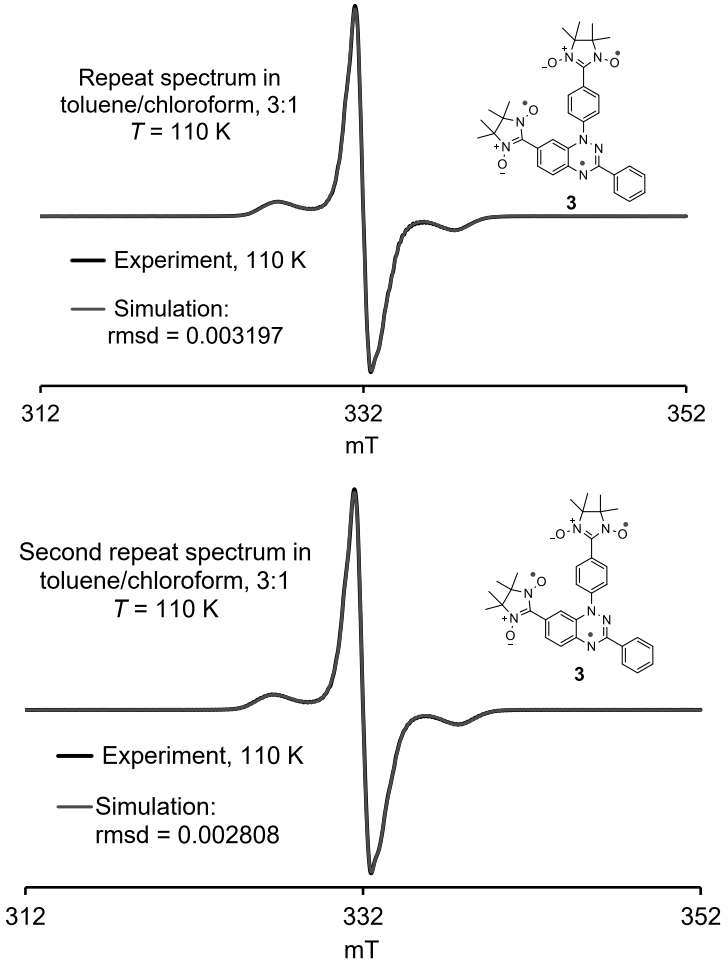

Fig. S20. Repeat EPR spectra for 1.36 mM triradical **3** at 110 K, obtained duirng quantitative EPR spectroscopy in toluene/chloroform, 3:1. Top panel: EPR (ν = 9.3255 GHz, label: CS529r9) spectrum. Simulation of the $|\Delta m_S| = 1$ region (label: try1354): rmsd = 0.0031972, $S = 3/2$, weight = 1.0000, D = 79.64 MHz, E = 23.36 MHz, g_{xx} = 2.0072, g_{yy} = 2.0042, g_{zz} = 2.0066; H-strain (MHz): H_x = 14.5, H_y = 74.4, H_z = 54.3; $S = 1/2$, weight = 0.17853, g_{xx} = 2.0016, g_{yy} = 2.0137, g_{zz} = 1.9964; H-strain (MHz): H_x = 10.5, H_y = 7.3, H_z = 18.8; χT = 1.64777 emu K mol^{-1}. Bottom panel: EPR (ν = 9.3255 GHz, label: CS529r11) spectrum. Simulation of the $|\Delta m_S| = 1$ region (label: try1356): rmsd = 0.0028079, $S = 3/2$, weight = 1.0000, D = 79.68 MHz, E = 23.33 MHz, g_{xx} = 2.0072, g_{yy} = 2.0042, g_{zz} = 2.0066; H-strain (MHz): H_x = 14.2, H_y = 74.4, H_z = 54.4; $S = 1/2$, weight = 0.17785, g_{xx} = 2.0016, g_{yy} = 2.0137, g_{zz} = 1.9965; H-strain (MHz): H_x = 10.5, H_y = 7.5, H_z = 18.8; χT = 1.64851 emu K mol^{-1}. Based on the above and simulation in Fig. S17, $\chi T = 1.6479 \pm 0.0003$ emu K mol^{-1} vs. measured $\chi T = 1.632 \pm 0.0058$ emu K mol^{-1}.

1.d3 SQUID magnetometry and EPR spectroscopy of triradical 3 in polystyrene matrix, and SQUID magnetometry in polycrystalline benzene matrix. Procedure for sample preparation and handling is analogous to that for diradicals **1** and **2**.[S23]

Polystyrene (MW = 29.30 kDa, 147.56 mg) was evacuated in a small vial for 30 min, and then charged with argon gas. Then, to the vial, triradical **3** (1.49 mg in 0.2 mL of THF) and THF (0.4 mL, freshly distilled from benzophenone/sodium) were added and the mixture was sonicated and heated gently until polystyrene was completely dissolved to give a red-dark solution. Subsequently, the solution was evacuated gently at –25 °C to remove THF and then evacuated at p = ca. 1 mTorr for 1 h at RT. After that, the vial was transferred to a container and evacuated at 60 °C for 2 days at $p \approx 1$ mTorr. Then the solid was ground with plastic spatula, and the following samples were prepared: (1) for EPR spectroscopy, (2) for ^{1}H NMR spectra, and (3) for SQUID, weight 43.63 mg (0.43 mg of triradical). After SQUID, the sample was recovered, and then ^{1}H NMR and EPR spectra were obtained.

Note that the sample was 19 mM in **3**, with relatively high concentration of **3** required to provide sufficient S/N ratio vs diamagnetic background of polystyrene in SQUID magnetometry. Consequently, in the simulations of the EPR spectra, S = ½ component corresponds to not only S = ½ excited state but also exchange-narrowed S = 3/2 state. (Similar, S = 1/2-like component, corresponding to exchange narrowed S = 1 state, was found in 30 – 40 mM samples of S = 1 diradicals **1** and **2** in polystyrene.[S23])

Sample of **3** for SQUID magnetometry in benzene was prepared as previously reported for diradical **2**.[S23] Because the highest usable temperature in benzene matrix is about 260 K and the presence of significant intermolecular antiferromagnetic interactions (as indicated by a mean-field parameter, $\theta \sim$ –1 K, the χT vs T could not be reliably fit to eq. S1. Therefore, in Fig. S23, only magnetization data are presented, showing unequivocally S = 3/2 ground state for triradical **3**.

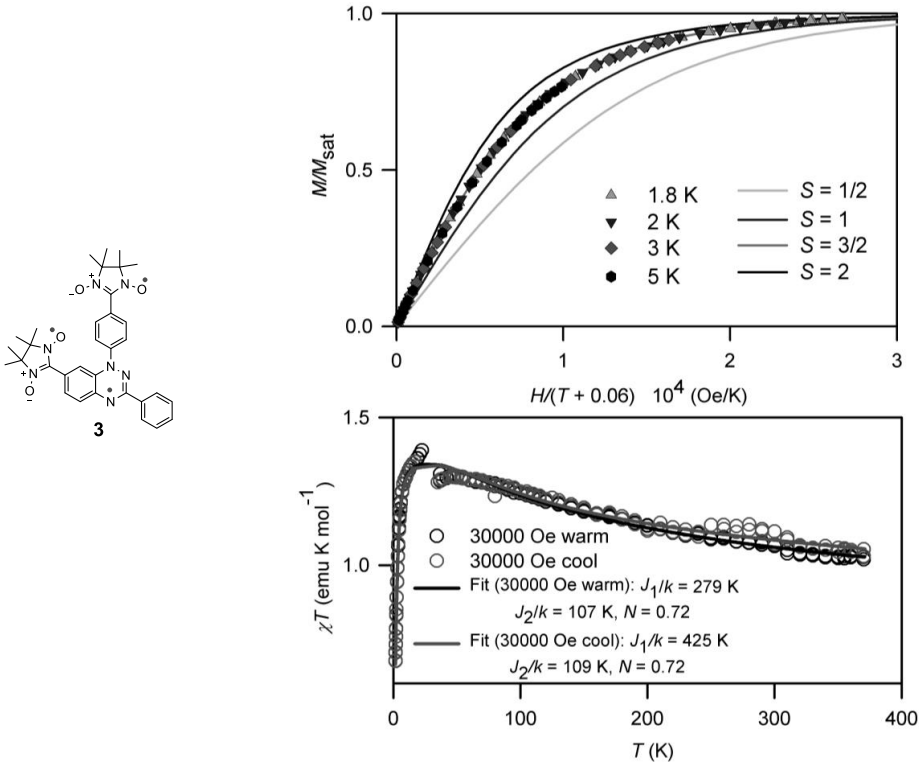

Fig. S21. SQUID magnetometry of 19 mM triradical **3** in polystyrene matrix. Top M/M_{sat} vs $H/(T - \theta)$ plot, where θ = −0.06 K (mean-field correction for interactions between triradicals), at T = 1.8–5 K (symbols) and the Brillouin curves corresponding to S = 1/2–2 (lines). Numerical fits, M vs $H/(T + 0.06)$ based on the Brillouin functions, with M corrected for diamagnetism, to the experimental data at T = 1.8, 2, 3, 5 K gave the following values of the two variable parameters, S and M_{sat} as mean ± SE (parameter dependence): 1.8 K: S = 1.501 ± 0.006, M_{sat} = 0.008926 ± 0.000007 (0.445); 2 K: S = 1.503 ± 0.006 M_{sat} = 0.008916 ± 0.000007 (0.525); 3 K: S = 1.509 ± 0.007, M_{sat} = 0.08882 ± 0.000011 (0.713); 5 K: S = 1.539 ± 0.016, M_{sat} = 0.008769 ± 0.000031 (0.933). Value M_{sat} = 0.008926 at 1.8 K corresponds to 0.736 μ_B, i.e., 73.6% of the expected value. All fits were near perfect with adjusted R^2 = 0.9999 and *SEE* = 0.0000. Bottom: χT vs T data at H = 30000 Oe in the warming and cooling modes were fit to a triradical model (eq S1, SI), using three variable parameters: weight correction factor, N = 0.718 ± 0.002, first exchange coupling constant, J_1/k, and second exchange coupling constant, J_2/k as mean ± SE (parameter dependence, *DEP*); the values of statistically adjusted coefficient of determination, adj. R^2, and standard error of estimate, *SEE*, are provided. Fitting parameters: cooling mode: N = 0.718 ± 0.002 (*DEP* = 0.744), J_1/k = 425 ± 37 K (*DEP* = 0.582), J_2/k = 109 ± 4 K (*DEP* = 0.792), adj. R^2 =0.9890, *SEE* = 0.0169; warming mode: N = 0.721 ± 0.001 (*DEP* = 0.711), J_1/k = 279 ± 14 K (*DEP* = 0.679), J_2/k = 107 ± 4 K (*DEP* = 0.813), adj. R^2 =0.9906, *SEE* = 0.0148. Note that N = 0.72, which is in a good agreement with the value of M_{sat} corresponding to 73.6% of the expected value.

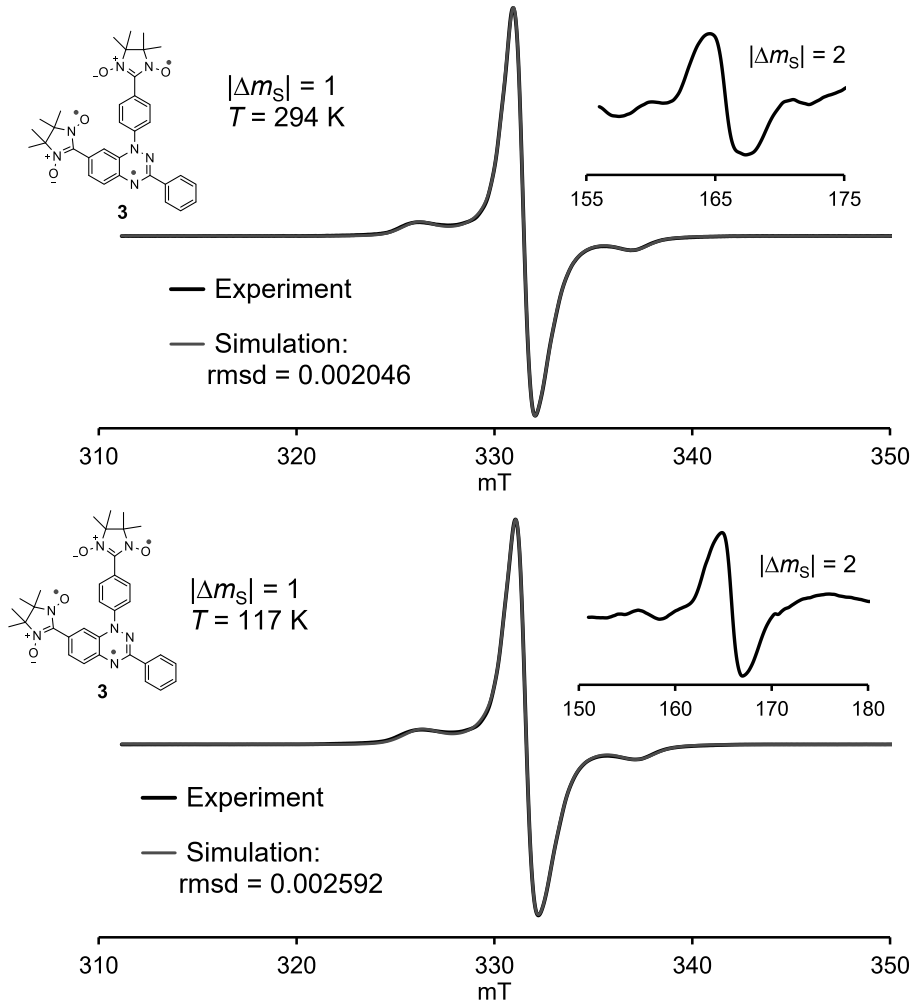

Fig. S22. EPR spectra for 19 mM triradical **3** in polystyrene following SQUID magnetometry. Top panel: EPR (ν = 9.3103 GHz, label: CS488r7) spectrum at 294 K. Inset plot: the $|\Delta m_S| = 2$ region at 294 K (label: CS488r2). Simulation of the $|\Delta m_S| = 1$ region (label: try1238): rmsd = 0.0020462, $S = 3/2$, weight = 1.0000, D = 76.34 MHz, E = 22.20 MHz, g_{xx} = 2.0071, g_{yy} = 2.0044, g_{zz} = 2.0062; H-strain (MHz): H_x = 11.5, H_y = 113.8, H_z = 49.1; "$S = ½$", weight = 1.3716, g_{xx} = 2.0044, g_{yy} = 2.0111, g_{zz} = 2.0001; H-strain (MHz): H_x = 48.3, H_y = 27.3, H_z = 28.3. Bottom panel: EPR (ν = 9.3141 GHz, label: CS488r8) spectrum at 117 K. Inset plot: the $|\Delta m_S| = 2$ region at 117 K (label: CS488r5). Simulation of the $|\Delta m_S| = 1$ region (label: try1340): rmsd = 0.0025923, $S = 3/2$, weight = 1.0000, D = 77.20 MHz, E = 22.85 MHz, g_{xx} = 2.0073, g_{yy} = 2.0041, g_{zz} = 2.0060; H-strain (MHz): H_x = 12.7, H_y = 111.0, H_z = 52.7; "$S = ½$", weight = 0.96305, g_{xx} = 2.0041, g_{yy} = 2.0119, g_{zz} = 1.9991; H-strain (MHz): H_x = 24.5, H_y = 23.1, H_z = 40.3.

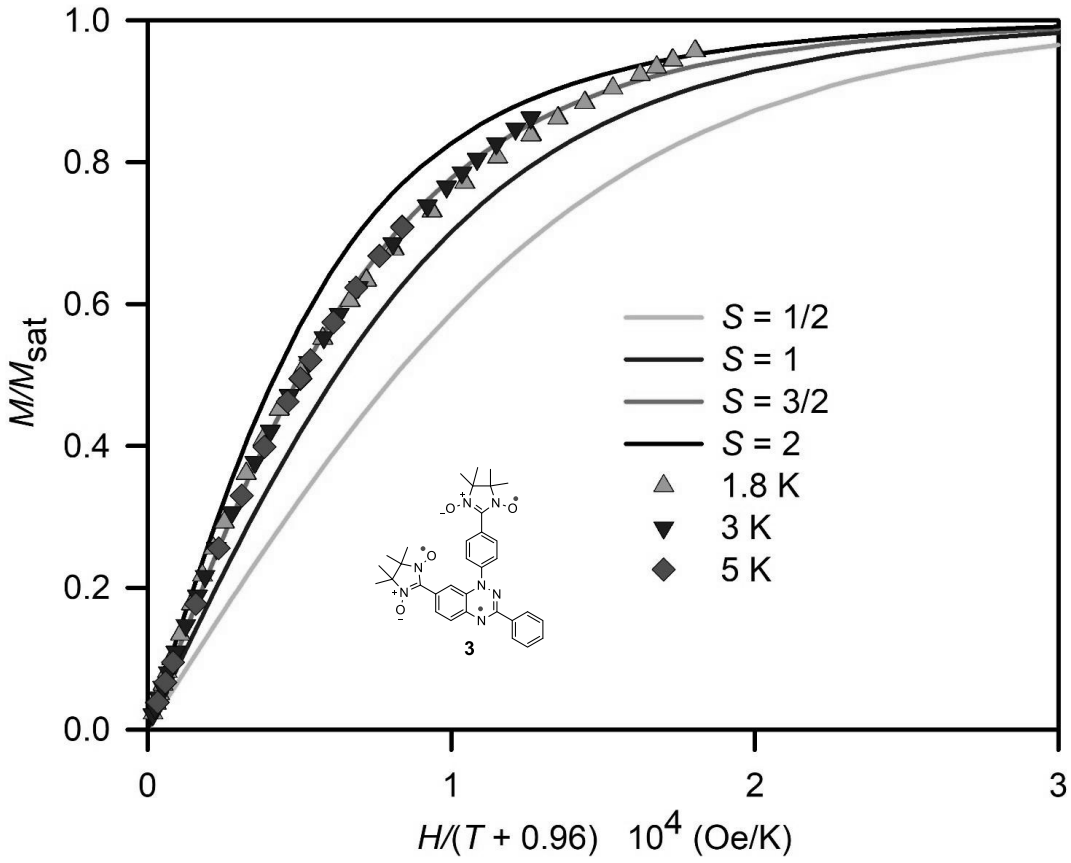

Fig. S23. SQUID magnetometry of 38 mM triradical **3** (1.69 mg) in polycrystalline benzene matrix. M/M_{sat} vs $H/(T - \theta)$ plot, where $\theta = -0.96$ K (mean-field correction for interactions between triradicals), at $T = 1.8$–5 K (symbols) and the Brillouin curves corresponding to $S = 1/2$–2 (lines). Numerical fits, M vs $H/(T + 0.96)$ based on the Brillouin functions, with M corrected for diamagnetism, to the experimental data at $T = 1.8$, 2, 3, 5 K gave the following values of the two variable parameters, S and M_{sat} as mean ± SE (parameter dependence): 1.8 K: $S = 1.488 \pm 0.031$, $M_{sat} = 0.02184 \pm 0.00010$ (0.660), SSE = 0.0003, adjusted $R^2 = 0.9983$; 3 K: $S = 1.493 \pm 0.019$, $M_{sat} = 0.02262 \pm 0.000086$ (0.844) SSE = 0.0001, adjusted $R^2 = 0.9996$; 5 K: $S = 1.467 \pm 0.015$, $M_{sat} = 0.02371 \pm 0.000095$ (0.961), SSE = 0.0000, adjusted $R^2 = 0.9999$. Value $M_{sat} = 0.02184$ at 1.8 K corresponds to 0.77 μ_B, i.e., 77% of the expected value.

1.e Thin films of triradical 3: stochiometry, microscopy and lifetime in UHV and air.

Fit results for the energy positions and relative intensities of the photoemission lines in the C 1s and N 1s spectra.

Table S6. Fit results for the energy positions and relative intensities of the photoemission lines in the C 1s spectra of the evaporated films.

	Energy (eV)	Lorentzian Width (eV)	Gaussian Width (eV)	Intensity (%)	Theory (%)
C-C	284.78	0.08	1.15	7.67	9.09
C-H	285.60	0.08	1.15	55.16	60.61
C-N	286.60	0.08	1.15	18.23	30.30
S1	287.50	0.08	0.85	9.59	
S2	288.20	0.08	1.20	4.80	
S3	289.85	0.08	1.50	2.88	
S4	291.90	0.08	1.00	0.72	
S5	292.30	0.08	1.00	0.96	

C-C + C-H + S1 = 72.42 %
C-N + S2 + S3 + S4 = 27.58 %

Table S7. Fit results for the energy positions and relative intensities of the photoemission lines in the N 1s spectra of the evaporated films.

	Energy (eV)	Lorentzian Width (eV)	Gaussian Width (eV)	Intensity (%)
Nrad	399.7	0.1	1.00	12.68
N2	400.5	0.1	1.00	12.68
N1	401.7	0.1	1.00	14.13
NNN	402.9	0.1	1.13	47.10
S1	401.2	0.1	0.83	3.62
S2	403.9	0.1	0.73	6.16
S3	406.5	0.1	1.00	3.62

Nrad + N2 + N1 + S1 = 43.12 % (42.86 % theo)
NNN + S2 + S3 = 56.88 % (57.14 % theo)

Table S8. Fit results for the energy positions and relative intensities of the photoemission lines in the C 1s spectra of the drop cast films.

Fit 1	Energy (ev)	Lorentzian Width (eV)	Gaussian Width (eV)	Intensity (%)	Theory (%)
C-C	285.60	0.08	1.10	7.47	9.09
C-H	286.00	0.08	1.10	60.80	60.61
C-N	287.43	0.08	1.10	19.73	30.30
S1	288.10	0.08	1.00	4.80	
S2	289.00	0.08	1.60	4.27	
S3	290.80	0.08	1.60	1.60	
S4	292.40	0.08	1.10	0.80	
S5	293.50	0.08	1.10	0.53	

C-C + C-H + S1 = 73.07 %
C-N + S2 + S3 + S4 = 26.93 %

Table S9. Fit results for the energy positions and relative intensities of the photoemission lines in the N 1s spectra of the drop cast films.

Fit 2	Energy (ev)	Lorentzian Width (eV)	Gaussian Width (eV)	Intensity (%)
Nrad	399.8	0.1	1.30	13.33
N2	400.6	0.1	1.30	13.33
N1	401.9	0.1	1.30	13.33
NNN	403.2	0.1	1.25	44.67
S1	400.8	0.1	0.8	3.33
S2	404.4	0.1	1.30	7.33
S3	406.6	0.1	1.30	3.67

Nrad + N2 + N1 + S1 = 43.33 % (43.12 % theo)
NNN + S2 + S3 = 56.67 % (57.14 % theo)

Morpholgy of a non-stochiometric film.

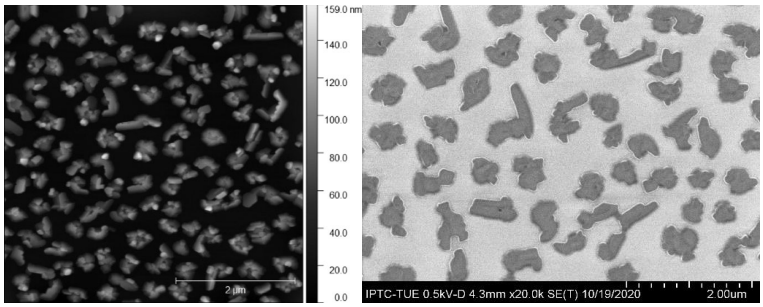

Figure S24. A 5 µm x 5 µm AFM image of a non-stochimetric film (2.1-nm nominally thick film,) together with the corresponding SEM image.

UHV and air film lifetime

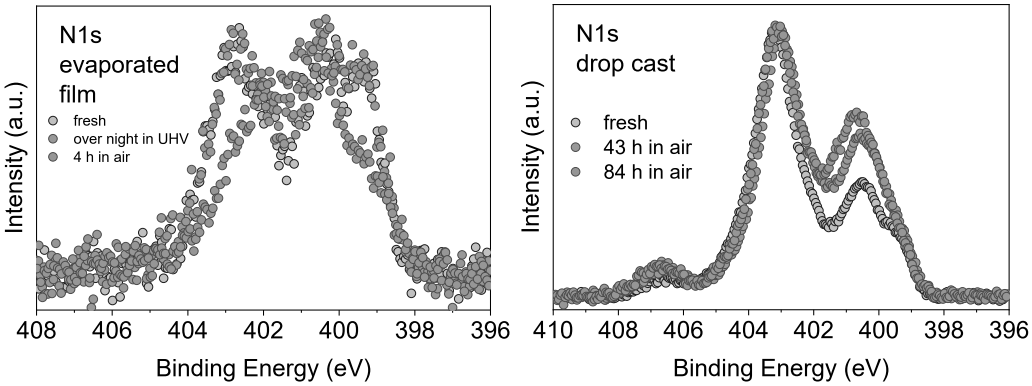

Figure S25. Left plot: Comparison of N 1s core level spectra of a freshly evaporated film while keeping the sample at room temperature in ultra-high vacuum conditions and in air (im darkness). Right plot: Comparison of N 1s core level spectra of a as preprared drop-cast film after 43 and 84 hours in air.

1.f DFT calculations.

Geometry optimizations and frequency calculations were performed using the Gaussian 16 program package[S25] running on a 16-cpu workstation under Linux operating system.

Geometries were fully optimized for triradical **3** at the UB3LYP/6-31G(d,p) level of theory in the gas phase and at the UB3LYP/6-31G(d,p)/IEF-PCM-UFF level of theory, using solvent model for toluene and teetrahydrofuran. Optimized geometries (C_1 point group) were determined to be minima (zero imaginary frequencies) on the potential energy surface. Broken symmetry wavefunctions were employed for doublet (S = 1/2) states of the triradical, and were checked for stability (stable=opt), following geometry optimization. Except for geometry optimization of the highest energy excited doublet state, all other optimized geometries have RMS forces in Cartesian coordinates less than 1×10^{-6} a.u. (and significantly lower in internal coordinates) that is typically better than the "tight" criterion for RMS forces in geometry optimization in Gaussian 16 (Table S10).

Using the UB3LYP/6-31G(d,p) geometry (gas phase) for quartet ground state of triradical **3**, the time-dependent density functional response theory (TD-DFT) calculations at the UCAM-B3LYP/6-31+G(d,p)/IEF-PCM-UFF level of theory in dichloromethane solvent model provided excitation energies and oscillator strengths (f) for electronic transitions for quartet state of **3**. For computed UV-vis-NIR absorption spectra, the electronic UV-vis-NIR data (f) data in the Gaussian 16 output files were converted to stick spectra in the text file format and then convoluted with the Gaussian functions with half-width of 0.15 eV, using graphical user interface Gabedit (version 2.5.0).[S26] The resultant computed UV-vis-NIR spectra of **3** were re-plotted with the wavelength (nm) axis using SigmaPlot program, with horizontal axes shifted by –0.15 eV. Vertical axes were scaled to fit the experimental spectra. Computed spectra for triradical **3** are plotted in Fig. S26. For calculation of electronic absorption spectra, up to 40 excited states were computed.

The doublet-quartet energy gaps (ΔE_{DQ}) between the quartet ground states and the open-shell doublet excited states for triradical were calculated using UB3LYP wave functions at the optimized geometries using ZPVE-corrected energies. The value of ΔE_{DQ} was obtained by correcting the calculated energy gap (ΔE_U) for spin contamination, using eq. S2.[S27-S29] In particular, the open-shell doublet excited states, which were calculated using broken-symmetry formalism, had a significant spin contamination as indicated by the mean values of S^2 operator, $\langle S^2_{BS}\rangle \approx 1.8$ (vs. expected value of $S(S + 1) = 0.75$), while the quartet ground states had $\langle S^2_Q\rangle \approx 3.9$ which is close to the expected value of $S(S + 1) = 3.75$. In eq. S2, it is assumed that the spin contamination of this doublet state originates from the high-spin (quartet) ground state only. The values of ΔE_{DQ} obtained using eq. S2 are expected to overestimate the actual doublet-quartet gaps for quartet ground state triradicals, analogously to singlet-triplet energy gaps in triplet ground state diradicals.[S30,S31] The calculated energy gaps, ΔE_{DQ}, are summarized in Table S10

$$\Delta E_{DQ} = \Delta E_U[\langle S^2_Q - 0.75\rangle/(\langle S^2_Q\rangle - \langle S^2_{BS}\rangle)] \quad \text{(S2)}$$

Spin density surfaces for radicals were calculated at the UB3LYP/6-31G(d,p) level. Cube files were obtained using "medium" setting in Gaussian 16, and surfaces were plotted with isodensity of 0.004 electron/Bohr^3 (Table S10).

EPR parameters (*D*-tensor and ^{14}N *A*-tensor) for triradical **3** were calculated using the B3LYP density functional (as implemented in ORCA[S32]) and the EPR-II basis set.[S33] All calculations used the previously optimized UB3LYP/6-31G(d,p) geometry for **3**. Input files were prepared using Gabedit.[S26] Quasi-restricted B3LYP density functional was used ("uno" option in ORCA). Calculations of *D*-tensor employed spin-spin dipolar coupling only,[S34] with absolute values of *D* and *E* being significantly overestimated compared to the experiment (Table S9).[S22-S24]

Table S10. Triradical **3**: UB3LYP/6-31G(d,p)+ZPVE (in the gas phase) and UB3LYP/6-31G(d,p)/IEF-PCM-UFF+ZPVE (in toluene and tetrahydrofuran) energies (hartree), zero point vibrational energies (hartree), lowest vibrational frequencies (cm^{-1}), RMS gradient norms (a.u.) in Cartesian coordinates, relative energies for triplet states (kcal mol^{-1}), and D-Q splittings (ΔE_{DQ} in kcal mol^{-1}, Eq. S2). Spin density maps for two lowest energy states in the gas phase are shown.[a]

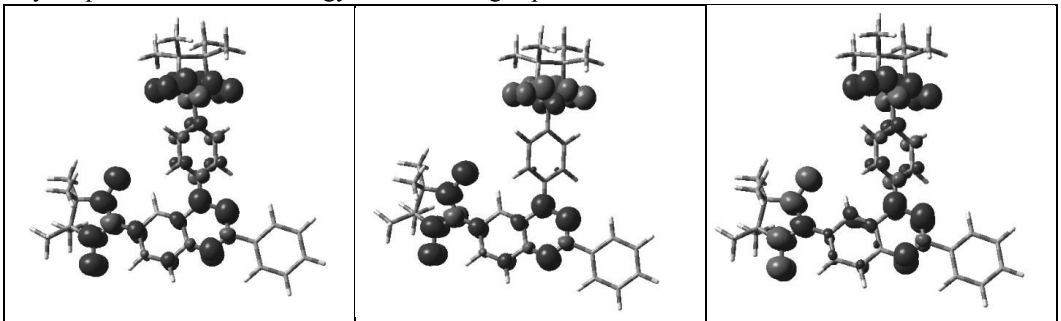

DFT	Medium	State	Geometry	Spin densities[b]	$E°$	ZPVE	$E°$ + ZPVE	$\langle S^2 \rangle$	RMS gradient norm ($\times 10^{-6}$)[c]	Lowest vibrational frequencies	ΔE_U(D-Q)	ΔE_{DQ}
UB3LYP	Gas ph.	Quartet	Quartet	+ + +	-1963.15717022	0.648594	-1962.508576	3.8995	0.07	6.7, 11.0, 15.6	0.000	**0.00**
		BS-doublet1	BS-doublet1	+ + –	-1963.15593037	0.688730	-1962.507418	1.8857	0.17	11.3, 11.7, 15.6	0.727	**1.14**
		BS-doublet2	BS-doublet2	– + +	-1963.15448777	0.648551	-1962.505936	1.8830	0.10	7.5, 11.2, 15.8	1.657	**2.59**
		BS-doublet3	BS-doublet3	– + –	-1963.15316900	0.648657	-1962.504512	1.8693	6.14	12.5, 13.8, 16.5	2.550	**3.96**
UB3LYP	toluene	Quartet	Quartet	+ + +	-1963.16585847	0.648354	-1962.517504	3.8953	0.28	11.2, 13.6, 16.6	0.000	**0.00**
		BS-doublet1*	BS-doublet1	+ + –	-1963.16471753	0.648315	-1962.516402	1.8824	0.33	9.4, 13.9, 17.6	0.692	**1.08**
		BS-doublet2*	BS-doublet2	– + +	-1963.16332617	0.648388	-1962.514938	1.8798	0.40	12.4, 14.3, 17.2	1.610	**2.51**
UB3LYP	tetrahydrofuran	Quartet	Quartet	+ + +	-1963.17279590	0.648177	-1962.524619	3.8922	0.52	13.9, 14.6, 16.7	0.000	**0.00**
		BS-doublet1*	BS-doublet1	+ + –	-1963.17175232	0.648057	-1962.523695	1.8797	0.44	12.4, 14.8, 18.5	0.580	**0.91**
		BS-doublet2*	BS-doublet2	– + +	-1963.17038415	0.648183	-1962.522201	1.8773	0.51	14.3, 15.2, 17.3	1.517	**2.37**
UB3LYP	ethanol	Quartet	Quartet	+ + +	-1963.17587157	0.648121	-1962.527751	3.8898	0.17	12.8, 16.2, 20.2	0.000	**0.00**
		BS-doublet1	BS-doublet1	+ + –	-1963.17485098	0.647934	-1962.526917	1.8784	0.50	12.9, 15.7, 18.3	0.523	**0.82**
		BS-doublet2*	BS-doublet2	– + +	-1963.17351951	0.648175	-1962.525345	1.8753	0.39	14.3, 17.0, 19.4	1.510	**2.35**

[a] 1 Hartree = 627.51 kcal mol^{-1}. [b] Relative signs of overall spin densities in the nitronyl nitroxide-Blatter-nitronyl nitroxide radical moieties, as illustrated by the spin density maps. [c] In Cartesian coordinates. * Wavefunction was tested for stability (stable=opt) and was found to be stable.

Table S11. B3LYP/EPR-II *D*-tensors and largest component of the ^{14}N *A*-tensors (for selected nitrogens). Coordinates x, y, z define molecule orientation in ORCA.[a]

			D-tensor (cm^{-1})				*A*ZZ (MHz)		
Triradical **3**	*D* (cm^{-1})	*E* (cm^{-1})		D_{YY}	D_{XX}	D_{ZZ}	N (Blatter radical)	N (nitronyl nitroxide)	N (nitronyl nitroxide)
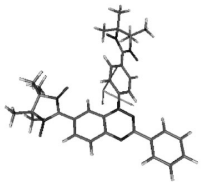	0.00532	0.00066		–0.00243	-0.00112	+0.00355	+11.992	+15.821	+16.215
			x	+0.9504	+0.3109	-0.0022	-0.2146	-0.3750	-0.0311
			y	+0.3108	-0.9501	+0.0270	+0.0164	-0.6754	-0.0118
			z	+0.0064	-0.0264	-0.9996	+0.9766	+0.6349	-0.9994

[a] x, y, and z axes for **1** and **2** are shown in red, green, and blue, respectively.

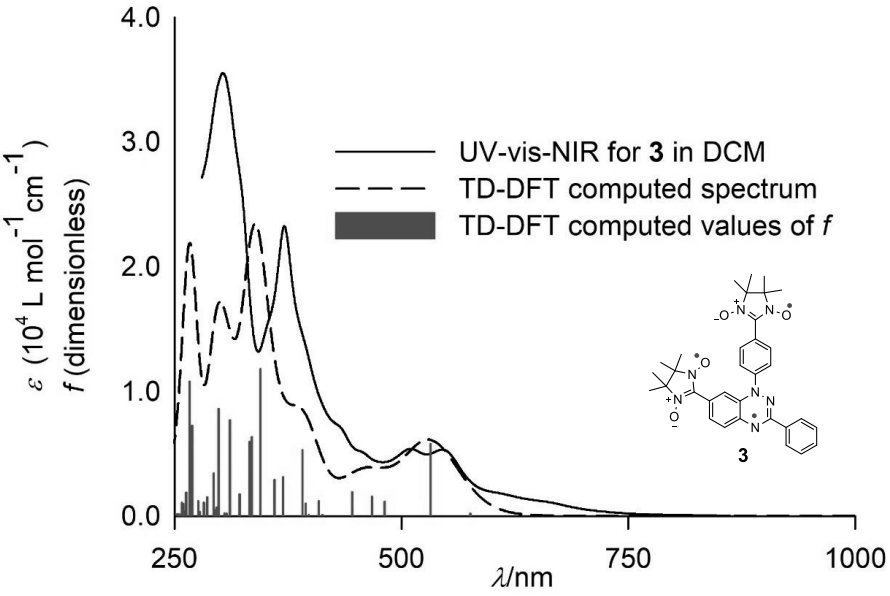

Fig. S26. UV-vis-NIR spectra of triradical **3** in dichloromethane (DCM) vs. TD-DFT computed spectrum; sticks correspond to computed oscillator strentghs (*f*).

Triradical **3**: α-orbitals	Triradical **3**: β-orbitals	Diradical **2**: α-orbitals	Diradical **2**: β-orbitals
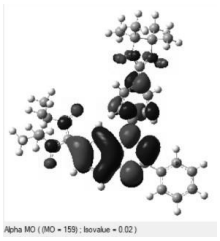 α-159, SOMO1, -0.1662	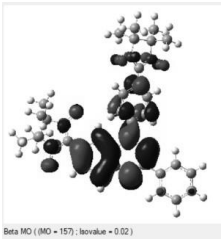 β-157, SOMO1, -0.0951	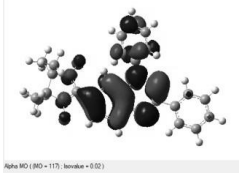 α-117, SOMO1, -0.1650	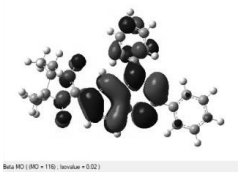 β-116, SOMO1, -0.0928
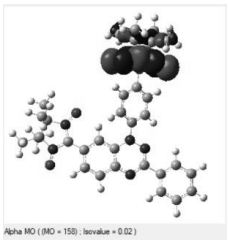 α-158, SOMO2, -0.1871	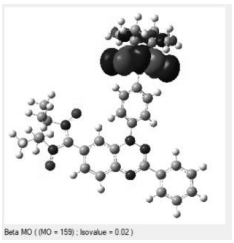 β-159, SOMO2, -0.0750	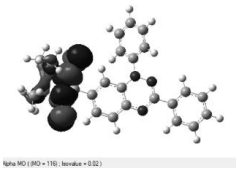 α-116, SOMO2, -0.1896	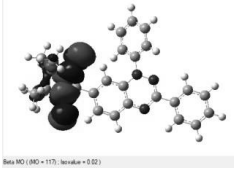 β-117, SOMO2, -0.0764
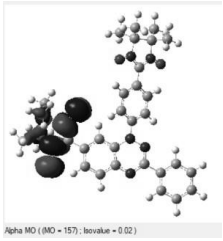 α-157, SOMO3, -0.1902	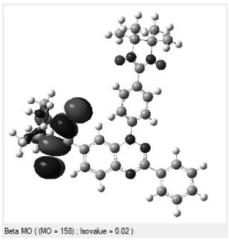 β-158, SOMO3, -0.0767	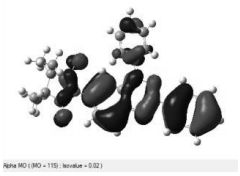 α-115, HOMO, -0.2272	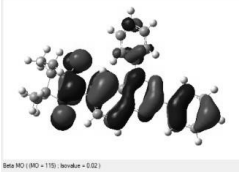 β-115, HOMO, -0.2066
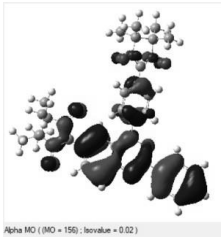 α-156, HOMO, -0.2262	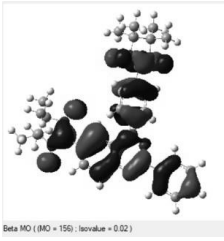 β-156, HOMO, -0.2034		

Fig. S27. SOMOs and HOMO surfaces for triradical **3** and diradical **2** at the UB3LYP/6-31G(d,p) level. Cube files were obtained using "course" setting in GaussView, and surfaces were plotted with isodensity of 0.02 electron/Bohr^3. Orbital energies in Hartrees. Please note that for **3**, SOMO1 – SOMO3 = 0.0240 ≈ SOMO1 – SOMO2 = 0.0246 Hartree for diradical **2** with with a relatively large ΔE_{ST}.

2. MS data and IR Spectra for 3, 2, and 8.

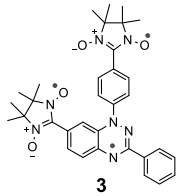

Multiple Mass Analysis: 4 mass(es) processed
Tolerance = 10.0 PPM / DBE: min = -1.5, max = 50.0
Element prediction: Off
Number of isotope peaks used for i-FIT = 3

Monoisotopic Mass, Odd and Even Electron Ions
1229873 formula(e) evaluated with 44 results within limits (up to 50 best isotopic matches for each mass)
Elements Used:
12C: 0-50 13C: 0-1 1H: 0-100 14N: 0-7 16O: 0-4 23Na: 1-1

Shu, Rajca CS505P
61573-1 1294 (2.674) Cm (916:1294)

XEVO-G2XSQTOF#YEB1443

13-Feb-2020 14:00:42
TOF MS ES+
1.62e+009

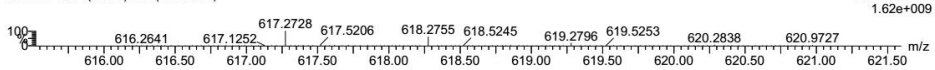

Minimum:	5.00				-1.5				
Maximum:	100.00		5.0	10.0	50.0				
Mass	RA	Calc. Mass	mDa	PPM	DBE	i-FIT	Norm	Conf(%)	Formula
617.2728	100.00	617.2726	0.2	0.3	19.0	-1.$	n/a	1.#R	12C33 1H36 14N7 16O4 23Na
		617.2722	0.6	1.0	23.5	-1.$	n/a	1.#R	12C37 13C 1H35 14N5 16O2 23Na
		617.2735	-0.7	-1.1	23.0	-1.$	n/a	1.#R	12C39 13C 1H37 14N2 16O3 23Na
		617.2695	3.3	5.3	27.0	-1.$	n/a	1.#R	12C44 1H36 14N 16O 23Na
		617.2762	-3.4	-5.5	27.5	-1.$	n/a	1.#R	12C42 13C 1H35 14N3 23Na
		617.2767	-3.9	-6.3	23.0	-1.$	n/a	1.#R	12C38 1H36 14N5 16O2 23Na
		617.2682	4.6	7.5	19.5	-1.$	n/a	1.#R	12C32 13C 1H35 14N7 16O4 23Na
		617.2681	4.7	7.6	27.5	-1.$	n/a	1.#R	12C42 1H34 14N4 23Na
		617.2776	-4.8	-7.8	27.0	-1.$	n/a	1.#R	12C44 13C 1H37 16O 23Na
		617.2780	-5.2	-8.4	22.5	-1.$	n/a	1.#R	12C40 1H38 14N2 16O3 23Na
		617.2668	6.0	9.7	22.5	-1.$	n/a	1.#R	12C41 1H38 16O4 23Na
617.5206	5.52	617.5202	0.4	0.6	8.0	-1.$	n/a	1.#R	12C36 13C 1H65 14N6 23Na
		617.5215	-0.9	-1.5	7.5	-1.$	n/a	1.#R	12C38 13C 1H67 14N3 16O 23Na
		617.5220	-1.4	-2.3	3.0	-1.$	n/a	1.#R	12C34 1H68 14N5 16O3 23Na
		617.5189	1.7	2.8	3.0	-1.$	n/a	1.#R	12C35 13C 1H69 14N2 16O4 23Na
		617.5229	-2.3	-3.7	7.0	-1.$	n/a	1.#R	12C40 13C 1H69 16O2 23Na
		617.5233	-2.7	-4.4	2.5	-1.$	n/a	1.#R	12C36 1H70 14N2 16O4 23Na
		617.5175	3.1	5.0	3.5	-1.$	n/a	1.#R	12C33 13C 1H67 14N5 16O3 23Na
		617.5247	-4.1	-6.6	7.5	-1.$	n/a	1.#R	12C37 1H66 14N6 23Na
		617.5260	-5.4	-8.7	7.0	-1.$	n/a	1.#R	12C39 1H68 14N3 16O 23Na
		617.5148	5.8	9.4	7.0	-1.$	n/a	1.#R	12C40 1H68 14N 16O2 23Na
618.2755	60.64	618.2759	-0.4	-0.6	27.0	-1.$	n/a	1.#R	12C42 1H35 14N4 23Na
		618.2760	-0.5	-0.8	19.0	-1.$	n/a	1.#R	12C32 13C 1H36 14N7 16O4 23Na
		618.2746	0.9	1.5	22.0	-1.$	n/a	1.#R	12C41 1H39 16O4 23Na
		618.2773	-1.8	-2.9	26.5	-1.$	n/a	1.#R	12C44 1H37 14N 16O 23Na
		618.2733	2.2	3.6	22.5	-1.$	n/a	1.#R	12C39 1H37 14N3 16O3 23Na
		618.2728	2.7	4.4	27.0	-1.$	n/a	1.#R	12C43 13C 1H36 14N 16O 23Na
		618.2719	3.6	5.8	23.0	-1.$	n/a	1.#R	12C37 1H35 14N6 16O2 23Na
		618.2715	4.0	6.5	27.5	-1.$	n/a	1.#R	12C41 13C 1H34 14N4 23Na
		618.2800	-4.5	-7.3	23.0	-1.$	n/a	1.#R	12C37 13C 1H36 14N5 16O2 23Na
		618.2805	-5.0	-8.1	18.5	-1.$	n/a	1.#R	12C33 1H37 14N7 16O4 23Na
		618.2701	5.4	8.7	22.5	-1.$	n/a	1.#R	12C40 13C 1H38 16O4 23Na
		618.2814	-5.9	-9.5	22.5	-1.$	n/a	1.#R	12C39 13C 1H38 14N2 16O3 23Na
619.2796	16.74	619.2797	-0.1	-0.2	22.5	-1.$	n/a	1.#R	12C37 1H36 14N6 16O2 23Na
		619.2793	0.3	0.5	27.0	-1.$	n/a	1.#R	12C41 13C 1H35 14N4 23Na
		619.2806	-1.0	-1.6	26.5	-1.$	n/a	1.#R	12C43 13C 1H37 14N 16O 23Na
		619.2811	-1.5	-2.4	22.0	-1.$	n/a	1.#R	12C39 1H38 14N3 16O3 23Na
		619.2780	1.6	2.6	22.0	-1.$	n/a	1.#R	12C40 13C 1H39 16O4 23Na
		619.2824	-2.8	-4.5	21.5	-1.$	n/a	1.#R	12C41 1H40 16O4 23Na
		619.2766	3.0	4.8	22.5	-1.$	n/a	1.#R	12C38 13C 1H37 14N3 16O3 23Na
		619.2838	-4.2	-6.8	18.5	-1.$	n/a	1.#R	12C32 13C 1H37 14N7 16O4 23Na
		619.2838	-4.2	-6.8	26.5	-1.$	n/a	1.#R	12C42 1H36 14N4 23Na
		619.2753	4.3	6.9	23.0	-1.$	n/a	1.#R	12C36 13C 1H35 14N6 16O2 23Na
		619.2851	-5.5	-8.9	26.0	-1.$	n/a	1.#R	12C44 1H38 14N 16O 23Na

Fig. S28. The HR-TOF-MS of triradical **3** (sample label: CS505p).

Multiple Mass Analysis: 5 mass(es) processed
Tolerance = 10.0 PPM / DBE: min = -1.5, max = 50.0
Element prediction: Off
Number of isotope peaks used for i-FIT = 3

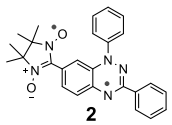

Monoisotopic Mass, Odd and Even Electron Ions
1266125 formula(e) evaluated with 47 results within limits (up to 50 best isotopic matches for each mass)
Elements Used:
12C: 0-50 13C: 0-1 1H: 0-100 14N: 0-5 16O: 0-3 23Na: 0-1
Shu, Rajca CS536P XEVO-G2XSQTOF#YEB1443 12-Feb-2020 13:16:20
61574 386 (0.785) Cm (41:392) TOF MS ES+
4.33e+008

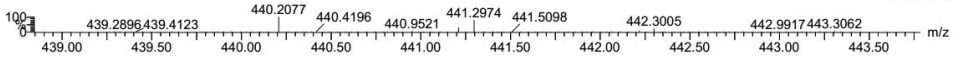

Minimum:	5.00				-1.5				
Maximum:	100.00		5.0	10.0	50.0				
Mass	RA	Calc. Mass	mDa	PPM	DBE	i-FIT	Norm	Conf(%)	Formula
440.2077	100.00	440.2076	0.1	0.2	13.0	-1.$	n/a	1.#R	12C26 1H29 14N2 16O3 23Na
		440.2082	-0.5	-1.1	21.0	-1.$	n/a	1.#R	12C30 13C 1H25 14N3
		440.2071	0.6	1.4	17.5	-1.$	n/a	1.#R	12C30 13C 1H28 16O 23Na
		440.2087	-1.0	-2.3	16.5	-1.$	n/a	1.#R	12C26 1H26 14N5 16O2
		440.2062	1.5	3.4	13.5	-1.$	n/a	1.#R	12C24 1H27 14N5 16O2 23Na
		440.2095	-1.8	-4.1	20.5	-1.$	n/a	1.#R	12C32 13C 1H27 16O
		440.2058	1.9	4.3	18.0	-1.$	n/a	1.#R	12C28 13C 1H26 14N3 23Na
		440.2055	2.2	5.0	16.5	-1.$	n/a	1.#R	12C27 13C 1H27 14N2 16O3
		440.2100	-2.3	-5.2	16.0	-1.$	n/a	1.#R	12C28 1H28 14N2 16O3
		440.2103	-2.6	-5.9	17.5	-1.$	n/a	1.#R	12C29 1H27 14N3 23Na
		440.2042	3.5	8.0	17.0	-1.$	n/a	1.#R	12C25 13C 1H25 14N5 16O2
		440.2116	-3.9	-8.9	17.0	-1.$	n/a	1.#R	12C31 1H29 16O 23Na
441.2113	27.25	441.2109	0.4	0.9	13.0	-1.$	n/a	1.#R	12C25 13C 1H29 14N2 16O3 23Na
		441.2120	-0.7	-1.6	16.5	-1.$	n/a	1.#R	12C25 13C 1H26 14N5 16O2
		441.2096	1.7	3.9	13.5	-1.$	n/a	1.#R	12C23 13C 1H27 14N5 16O2 23Na
		441.2133	-2.0	-4.5	16.0	-1.$	n/a	1.#R	12C27 13C 1H28 14N2 16O3
		441.2093	2.0	4.5	20.0	-1.$	n/a	1.#R	12C32 1H27 14N 16O
		441.2136	-2.3	-5.2	17.5	-1.$	n/a	1.#R	12C28 13C 1H27 14N3 23Na
		441.2141	-2.8	-6.3	13.0	-1.$	n/a	1.#R	12C24 1H28 14N5 16O2 23Na
		441.2079	3.4	7.7	20.5	-1.$	n/a	1.#R	12C30 1H25 14N4
		441.2150	-3.7	-8.4	17.0	-1.$	n/a	1.#R	12C30 13C 1H29 16O 23Na
		441.2154	-4.1	-9.3	12.5	-1.$	n/a	1.#R	12C26 1H30 14N2 16O3 23Na
441.2974	77.70	441.2974	0.0	0.0	14.0	-1.$	n/a	1.#R	12C28 13C 1H36 14N4
		441.2967	0.7	1.6	6.0	-1.$	n/a	1.#R	12C24 1H40 14N3 16O3 23Na
		441.2963	1.1	2.5	10.5	-1.$	n/a	1.#R	12C28 13C 1H39 14N 16O 23Na
		441.2987	-1.3	-2.9	13.5	-1.$	n/a	1.#R	12C30 13C 1H38 14N 16O
		441.2991	-1.7	-3.9	9.0	-1.$	n/a	1.#R	12C26 1H39 14N3 16O3
		441.2994	-2.0	-4.5	10.5	-1.$	n/a	1.#R	12C27 1H38 14N4 23Na
		441.2949	2.5	5.7	11.0	-1.$	n/a	1.#R	12C26 13C 1H37 14N4 23Na
		441.2947	2.7	6.1	9.5	-1.$	n/a	1.#R	12C25 13C 1H38 14N3 16O3
		441.3008	-3.4	-7.7	10.0	-1.$	n/a	1.#R	12C29 1H40 14N 16O 23Na
442.2181	6.16	442.2188	-0.7	-1.6	12.5	-1.$	n/a	1.#R	12C25 13C 1H30 14N2 16O3 23Na
		442.2174	0.7	1.6	13.0	-1.$	n/a	1.#R	12C23 13C 1H28 14N5 16O2 23Na
		442.2171	1.0	2.3	19.5	-1.$	n/a	1.#R	12C32 1H28 14N 16O
		442.2198	-1.7	-3.8	16.0	-1.$	n/a	1.#R	12C25 13C 1H27 14N5 16O2
		442.2157	2.4	5.4	20.0	-1.$	n/a	1.#R	12C30 1H26 14N4
		442.2212	-3.1	-7.0	15.5	-1.$	n/a	1.#R	12C27 13C 1H29 14N2 16O3
		442.2214	-3.3	-7.5	17.0	-1.$	n/a	1.#R	12C28 13C 1H28 14N3 23Na
		442.2147	3.4	7.7	16.5	-1.$	n/a	1.#R	12C30 1H29 14N 16O 23Na
		442.2219	-3.8	-8.6	12.5	-1.$	n/a	1.#R	12C24 1H29 14N5 16O2 23Na
442.3005	20.02	442.3001	0.4	0.9	6.0	-1.$	n/a	1.#R	12C23 13C 1H40 14N3 16O3 23Na
		442.3025	-2.0	-4.5	9.0	-1.$	n/a	1.#R	12C25 13C 1H39 14N3 16O3
		442.2984	2.1	4.7	13.0	-1.$	n/a	1.#R	12C30 1H38 14N2 16O
		442.3028	-2.3	-5.2	10.5	-1.$	n/a	1.#R	12C26 13C 1H38 14N4 23Na
		442.2971	3.4	7.7	13.5	-1.$	n/a	1.#R	12C28 1H36 14N5
		442.3041	-3.6	-8.1	10.0	-1.$	n/a	1.#R	12C28 13C 1H40 14N 16O 23Na
		442.3046	-4.1	-9.3	5.5	-1.$	n/a	1.#R	12C24 1H41 14N3 16O3 23Na

Fig. S29. The HR-TOF-MS of diradical **2** (sample label: CS536p).

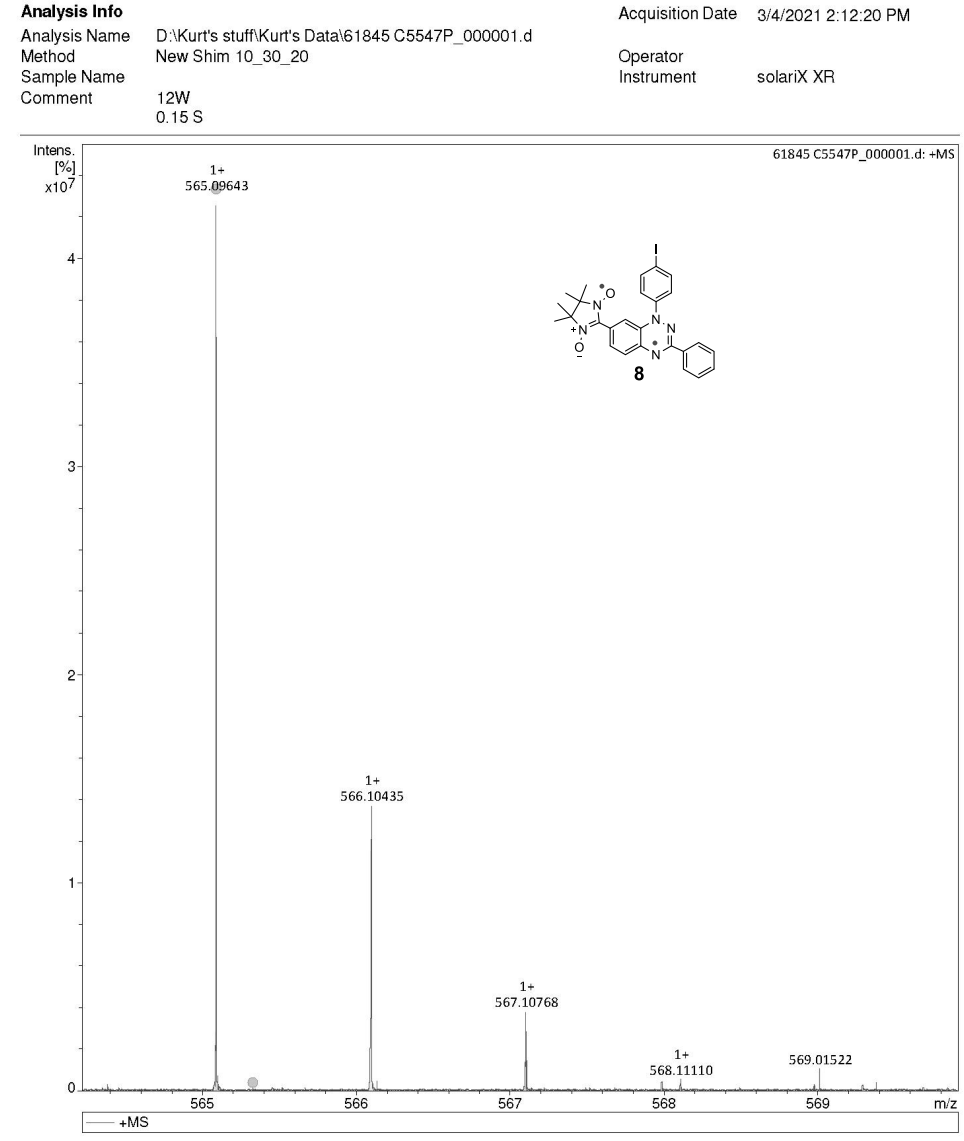

Meas. m/z	#	Ion Formula	Score	m/z	err [ppm]	Mean err [ppm]	mSigma	rdb	e⁻ Conf	N-Rule	
565.096429	1	C24H22IN8O	94.08	565.095581	-1.5	-1.9		3.6	21.0	even	ok
	2	C25H28INO6	63.29	565.095586	-1.5	-1.9		9.9	15.5	odd	ok
	3	C26H24IN5O2	100.00	565.096923	0.9	0.4		10.4	20.5	odd	ok
	4	C28H26IN2O3	34.11	565.098266	3.3	2.8		23.4	20.0	even	ok

Fig. S30. The HR-TOF-MS of diradical **8** (sample label: CS547p).

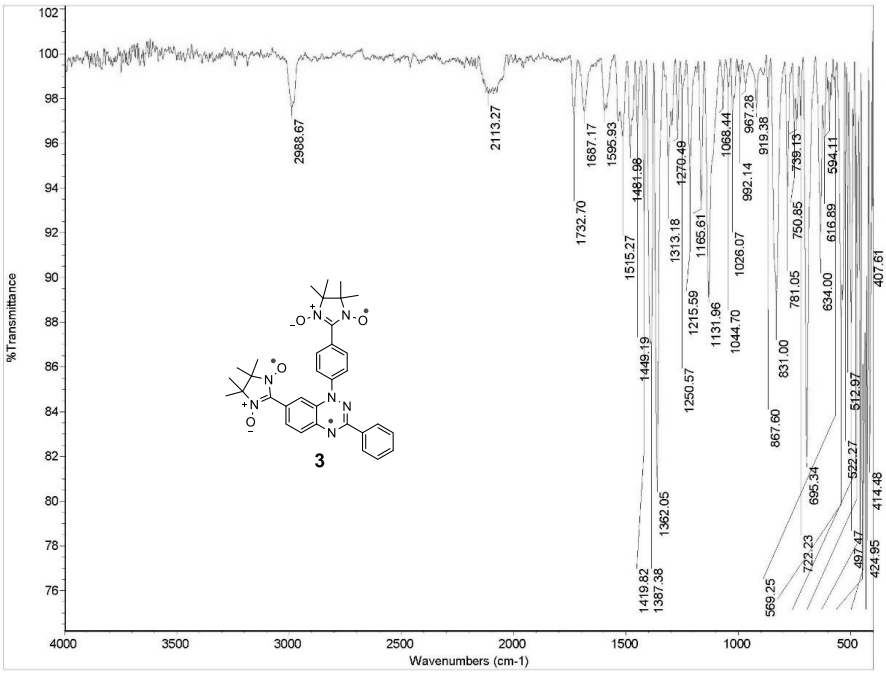

Fig. S31. IR (powder) spectrum of triradical **3** (sample label: CS567p).

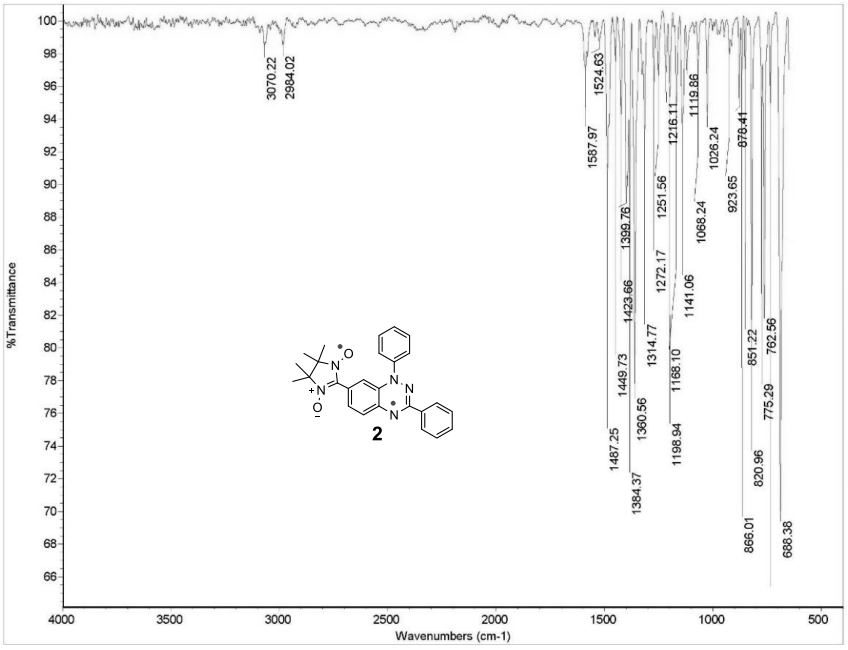

Fig. S32. IR (powder) spectrum of diradical **2** (sample label: CS536p_COR).

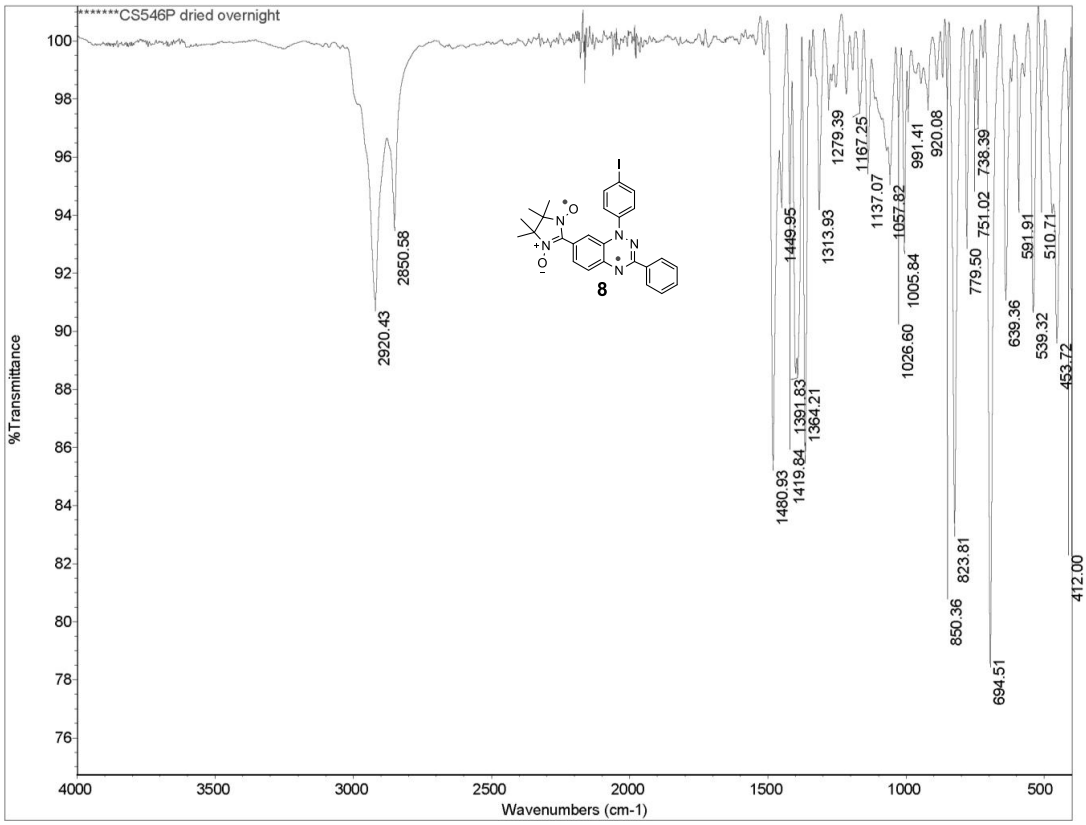

Fig. S33. IR (powder) spectrum of diradical **8** (sample label: CS547p_dried).

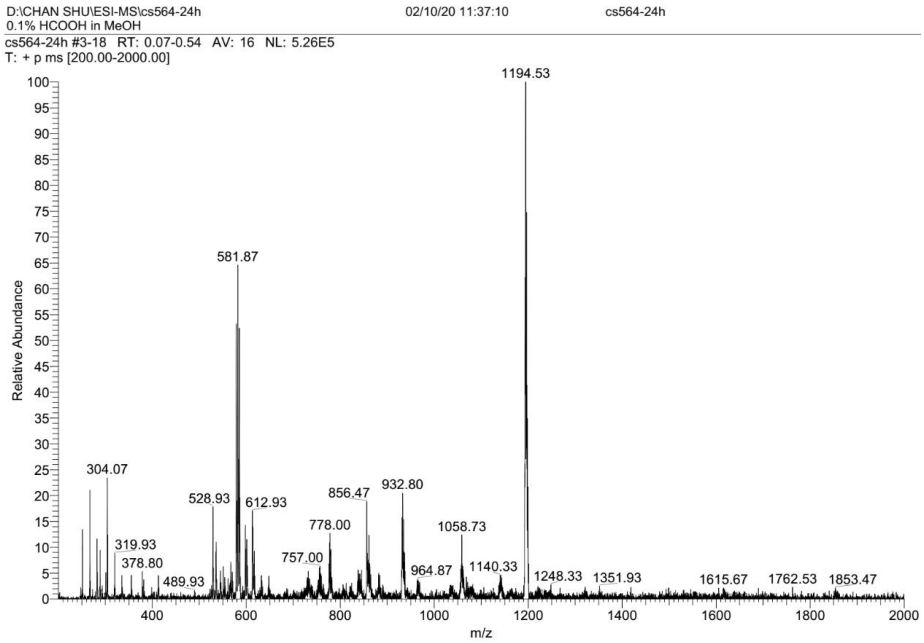

Fig. S34. LR-ESI-MS (0.1% HCOOH in MeOH, label: CS5-64) of crude mixture, obtained from reaction of di-iodo-Blatter radical **5** with nitronyl nitroxide **7**: full spectrum.

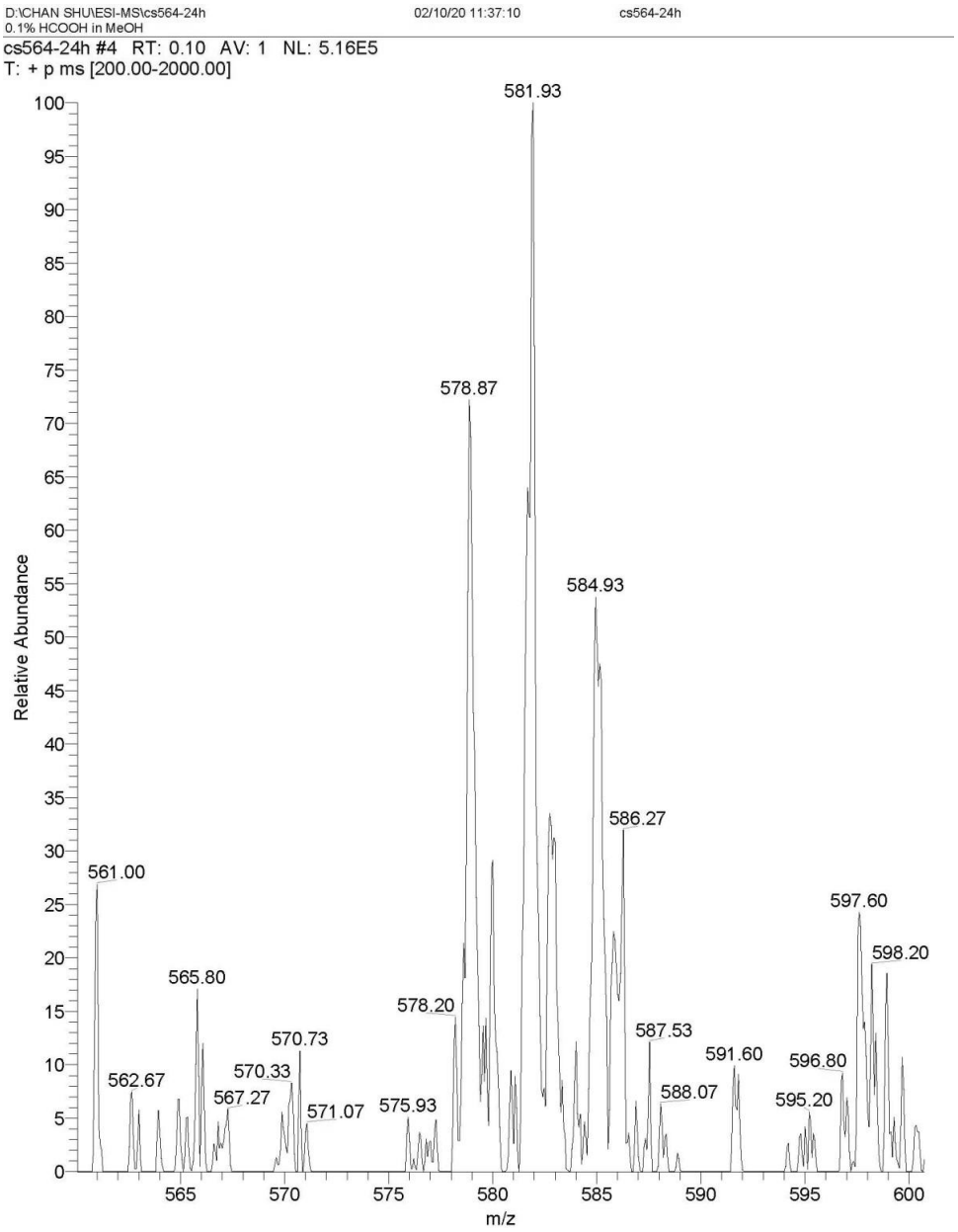

Fig. S35. LR-ESI-MS (0.1% HCOOH in MeOH, label: CS5-64) of crude mixture, obtained from reaction of di-iodo-Blatter radical **5** with nitronyl nitroxide **7**: expanded spectrum, *m/z* 550 – 600. Spectrum of purified diradical **8** is shown in the following Figure.

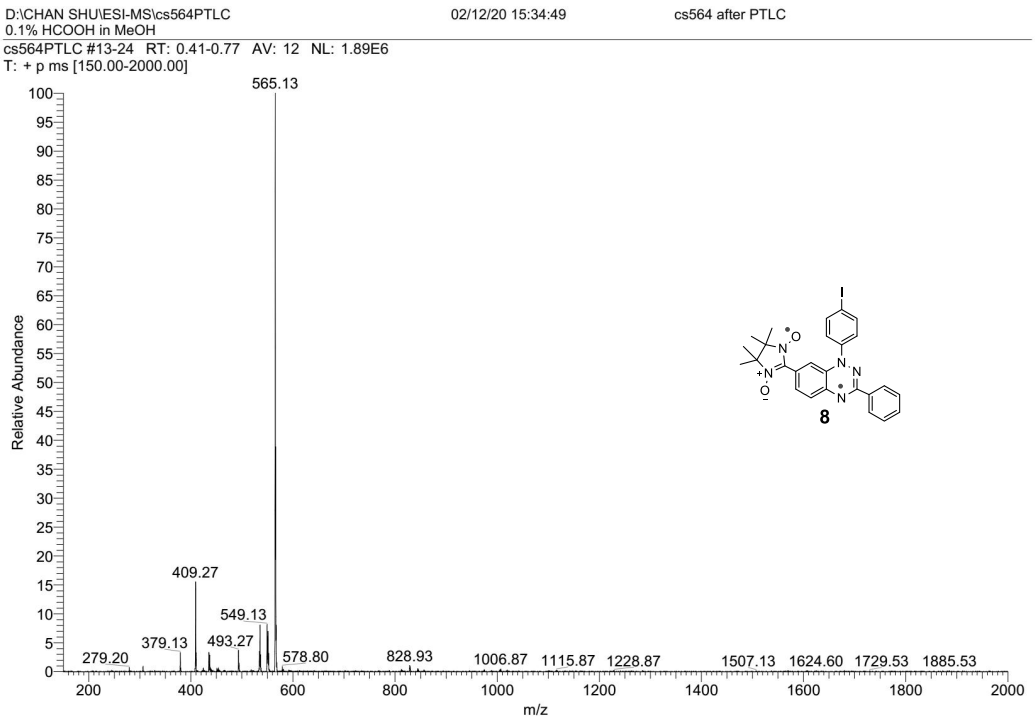

Fig. S36. LR-ESI-MS (0.1% HCOOH in MeOH, label: CS5-64) of purified diradical **8** (PTLC), obtained from reaction of di-iodo-Blatter radical **5** with nitronyl nitroxide **7**: *m/z*, $[M]^+$, calcd for $C_{26}H_{24}IN_5O_2$: 565.097; found: 565.13, RA = 100%. The crude mixture is shown in the two preceding Figures.

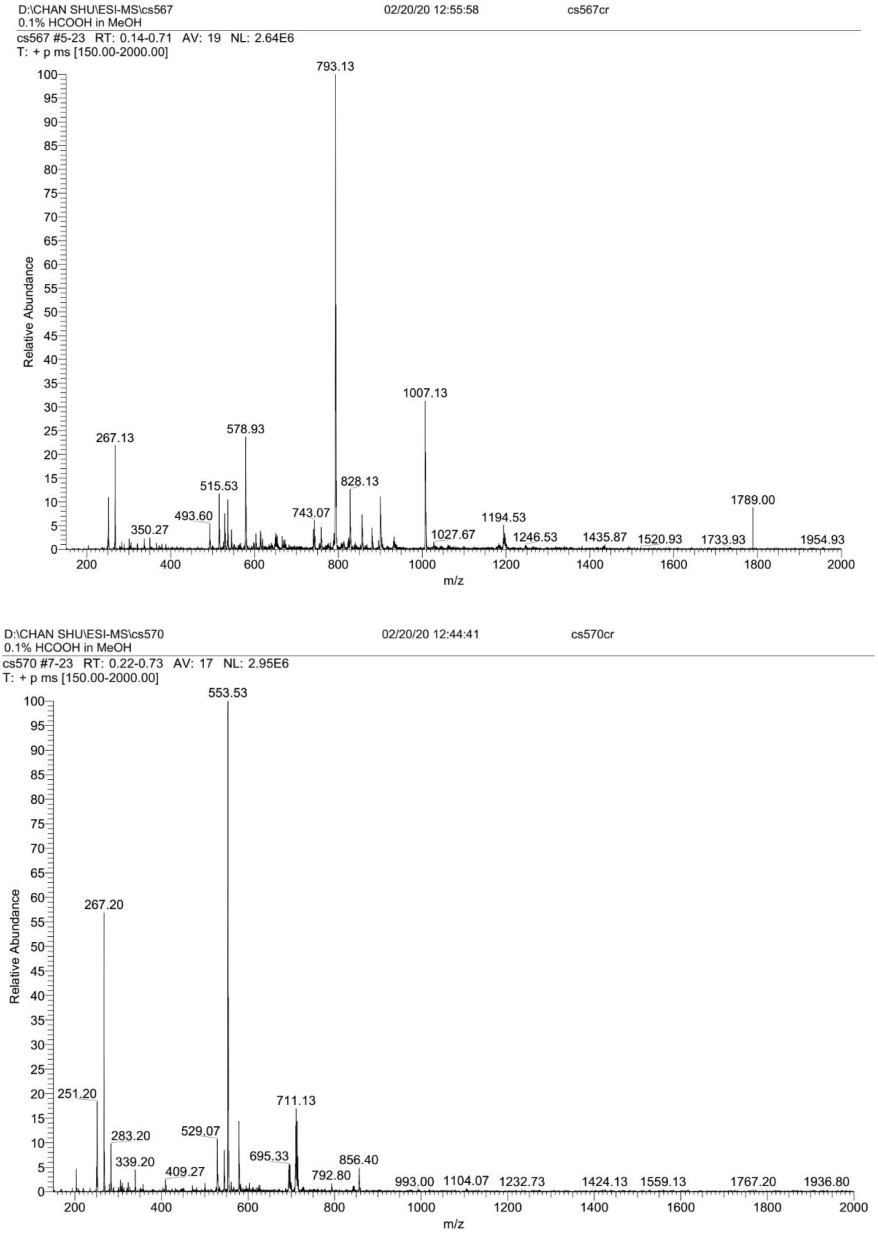

Fig. S37. LR-ESI-MS (0.1% HCOOH in MeOH), of crude reaction mixtures, showing a failure to obtain either diradical **8** or triradical **3**, from reaction of di-iodo-Blatter radical **5** with nitronyl nitroxide **7**. Top: label: CS5-67. The spectrum may show a small amount of "partially de-oxygenated" triradical **9** at *m/z* = 578.9.; compare to Fig. S35. Bottom: label: CS5-70.

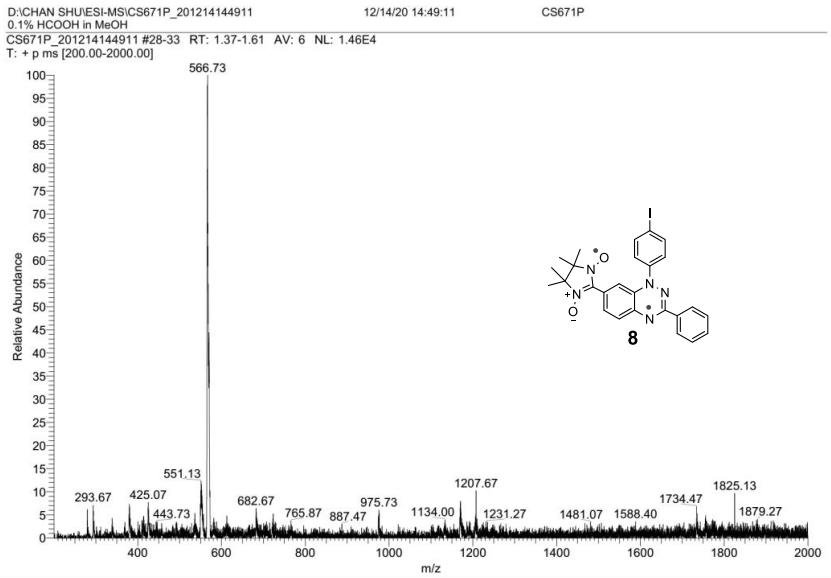

Fig. S38. LR-ESI-MS (0.1% HCOOH in MeOH, label: CS6-71) of purified diradical **8** (column and PTLC), obtained from repeat reaction of di-iodo-Blatter radical **5** with nitronyl nitroxide **7**: *m/z*, $[M+H]^+$, calcd for $C_{26}H_{25}IN_5O_2$: 566.105; found: 566.7, RA = 100%. EPR spectra for this sample of **8** are presented in Fig. S18.

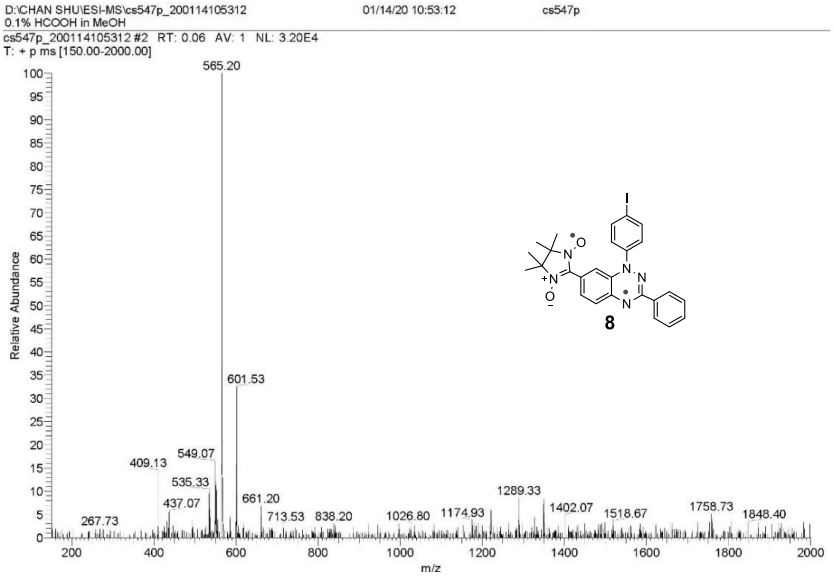

Fig. S39. LR-ESI-MS (0.1% HCOOH in MeOH, label: CS5-47p) of purified diradical **8** (PTLC), obtained from combined reactions (labels CS5-35 and CS5-46) of di-iodo-Blatter radical **5** with nitronyl nitroxide **4** (Au^I) in the presence of $(Ph_3P)_4Pd$: *m/z*, $[M]^+$, calcd for $C_{26}H_{24}IN_5O_2$: 565.097; found: 565.20, RA = 100%. EPR spectra for this sample of **8** are presented in Fig. S17.

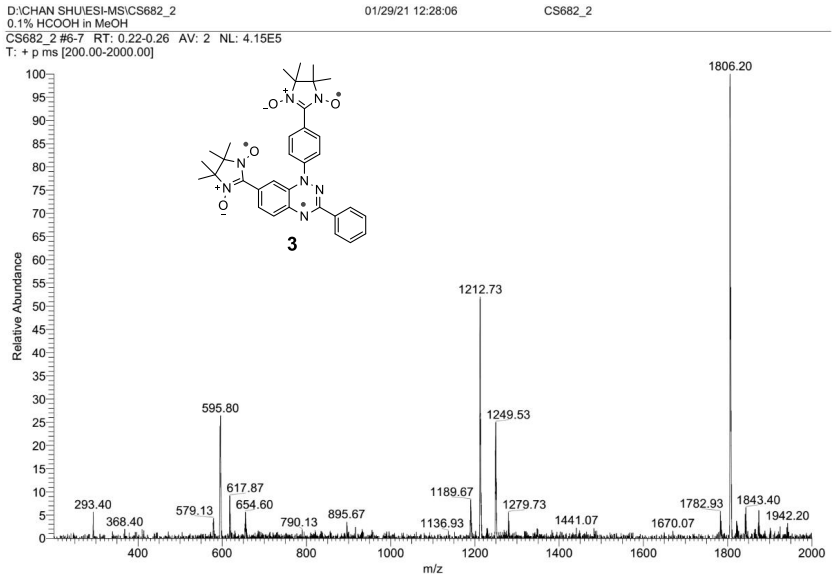

Fig. S40. ESI-MS (0.1% HCOOH in MeOH, label: CS682_2) for purified triradical **3**, obtained from reaction of di-iodo-Blatter radical **5** with nitronyl nitroxide **4**: *m/z*, $[M+H]^+$, calcd $C_{33}H_{37}N_7O_4$ 595.38, found 595.80, RA = 27%; $[3M + Na]^+$, calcd $C_{99}H_{108}N_{21}O_{12}Na_1$ 1805.8, found 1806.2, RA = 100%.

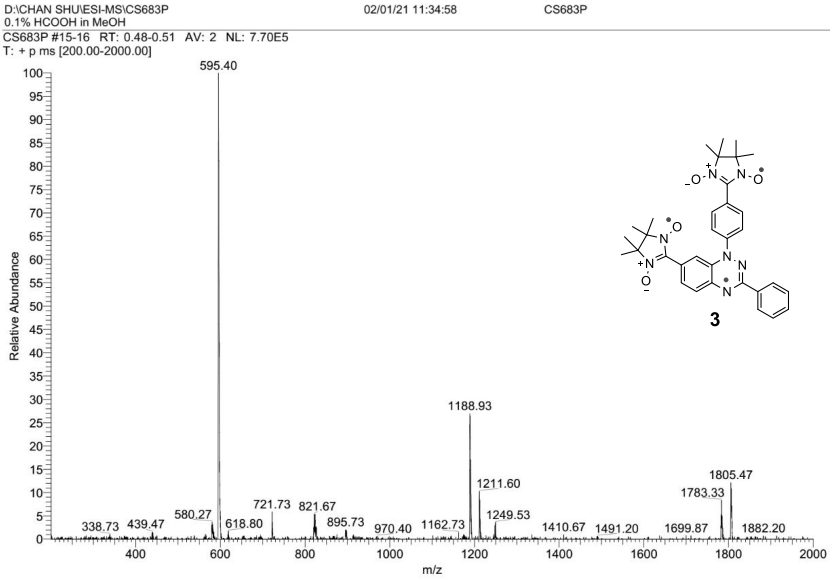

Fig. S41. ESI-MS (0.1% HCOOH in MeOH, label: CS683p) for purified triradical **3**, obtained from reaction of di-iodo-Blatter radical **5** with nitronyl nitroxide **4**: *m/z*, $[M+H]^+$, calcd $C_{33}H_{37}N_7O_4$ 595.38, found 595.40, RA = 100%; $[3M + Na]^+$, calcd $C_{99}H_{108}N_{21}O_{12}Na_1$ 1805.8, found 1805.5, RA = 15%.

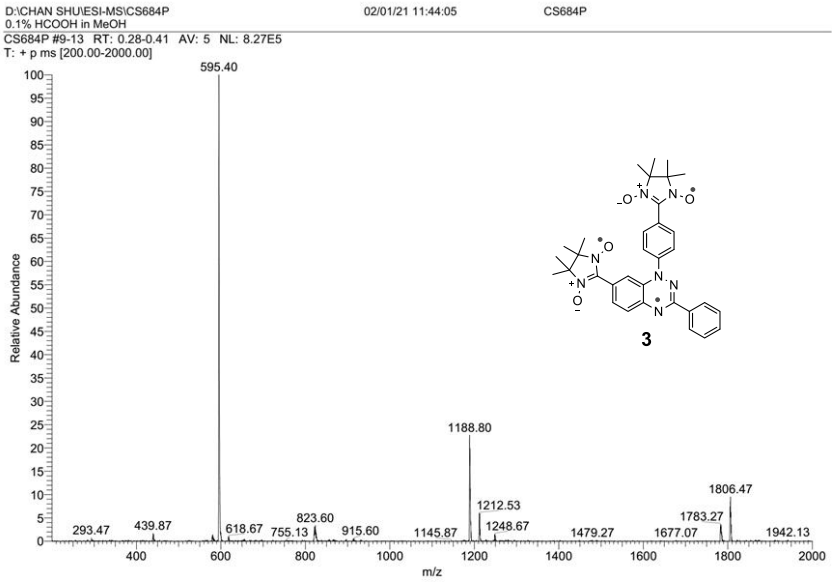

Fig. S42. ESI-MS (0.1% HCOOH in MeOH, label: CS684p) for purified triradical **3**, obtained from reaction of di-iodo-Blatter radical **5** with nitronyl nitroxide **4**: *m/z*, $[M+H]^+$, calcd $C_{33}H_{37}N_7O_4$ 595.38, found 595.40, RA = 100%; $[3M + Na]^+$, calcd $C_{99}H_{108}N_{21}O_{12}Na_1$ 1805.8, found 1806.5, RA = 10%.

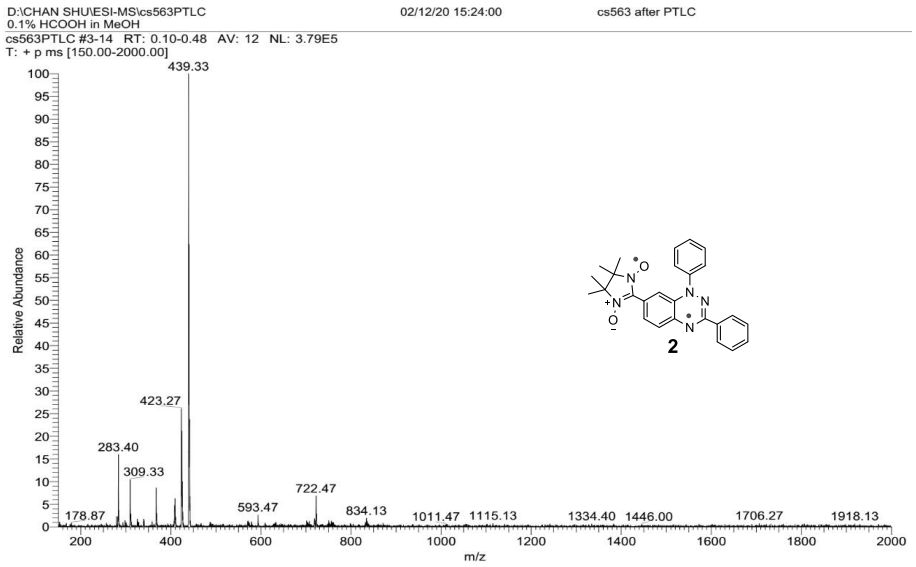

Fig. S43. ESI-MS (0.1% HCOOH in MeOH, label: CS5-63) for purified diradical **2**, obtained from reaction of mono-iodo-Blatter radical **6** with nitronyl nitroxide **7**: *m/z*, $[M]^+$, calcd for $C_{26}H_{25}N_5O_2$: 439.20; found: 439.33, RA = 100%.

3. Determination of diamagnetic impurities in triradical 3 and diradical 8 by quantitative ^{1}H NMR spectroscopy.

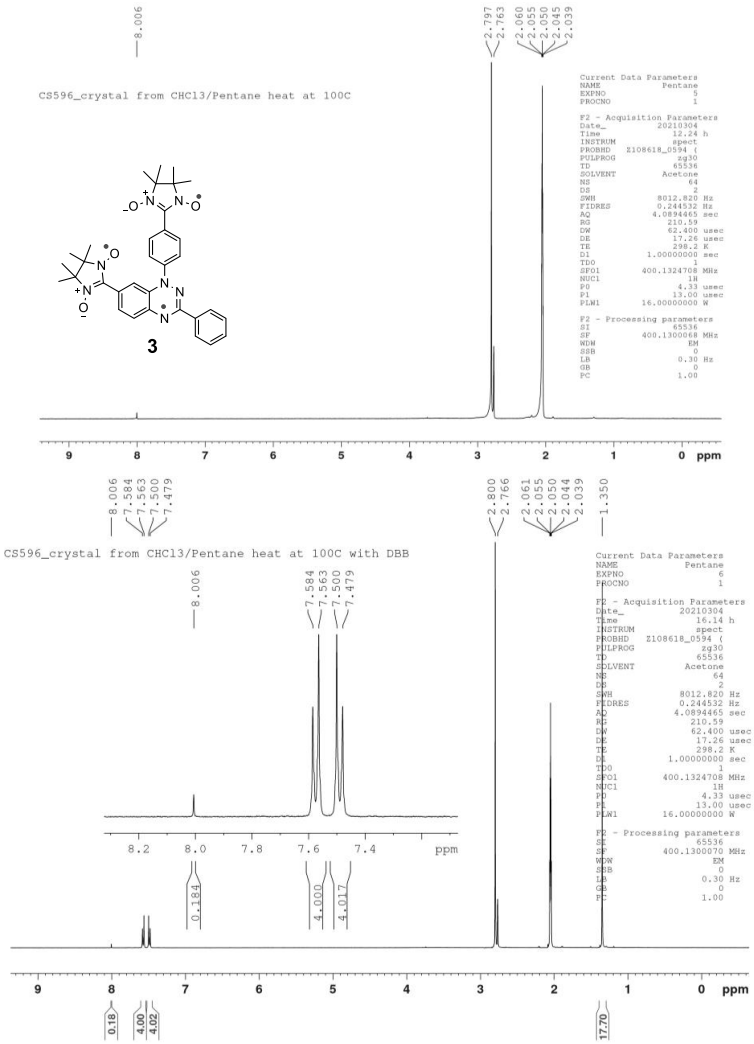

Fig. S44. ^{1}H NMR spectra (400 MHz, acetone-d_6) of triradical **3** (label: CS596_crystal from chloroform/pentane heat at 100 °C). Prior to the NMR spectrum the sample, which was crystalized from chloform/pentane, was heated overnight at 100 °C under 1 mTorr vacuum. The impurity was solvent included in the crystals, chloroform (8.01, s, 1H). Top: triradical **3**, 0.56 mg (0.94 µmol). Bottom: as above but 4,4'-di-*tert*-butylbiphenyl (0.34 mg, 1.28 µmol) was added to sample as standard. The molar ratio of chloroform to 4,4'-di-*tert*-butylbiphenyl is 0.18:1. Then, toluene content in triradical **3** was 0.230 µmol, which corresponds to 0.0275 mg and 4.9% content in triradical. Thus, **the purity of triradical 3 was 95.1%**. The H_2O/HDO peaks (2.80, s, 2H; 2.77, s, 1H) were from acetone-d_6.

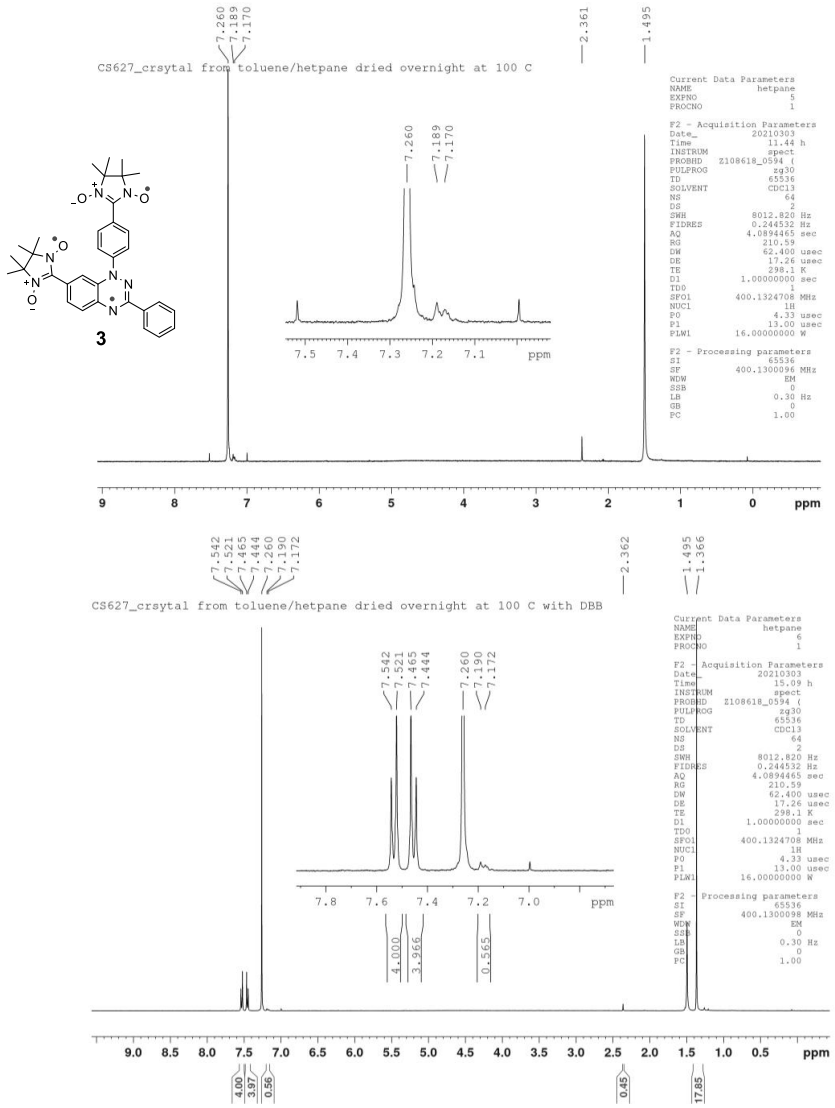

Fig. S45. ^{1}H NMR spectra (400 MHz, chloroform-*d*) of triradical **3** (label: CS627 _crystal from toluene/heptane heat at 100 °C). Prior to the NMR spectrum the sample, which was crystalized from toluene/heptane, was heated overnight at 100 °C under 1 mTorr vacuum. The impurity was solvent of crystallization, toluene (2.36, s, 3H; 7.17-7.19, m, 5H). Top: triradical **3**: 0.86 mg (1.01 µmol). Bottom: as above but 4,4'-di-*tert*-butylbiphenyl (0.29 mg, 1.09 µmol) was added to sample as standard. The molar ratio of toluene to 4,4'-di-*tert*-butylbiphenyl is 0.15 : 1. Then, toluene content in triradical **3** was 0.1635 µmol, which corresponds to 0.0151 mg and 1.8% content in triradical. Thus, **the purity of triradical 3 was 98.2%.** The H_2O peak (1.50, s, 2H) was from chloroform-*d*.

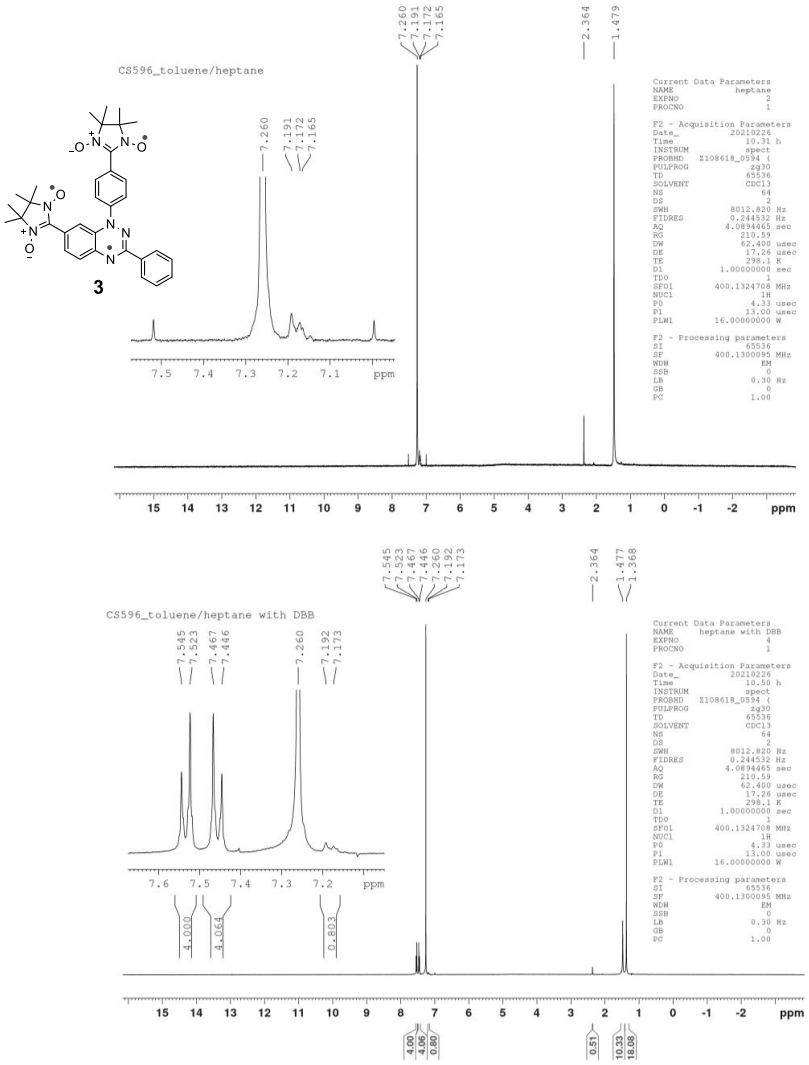

Fig. S46. Repeat sample of triradical **3**. ^{1}H NMR spectra (400 MHz, chloroform-*d*) of triradical **3** (label: CS596_crystal from toluene/heptane, 0.68 mg, 1.14 µmol). Prior to the NMR spectrum, the sample, which was crystalized from toluene/heptane, was heated overnight at room temperature under 1 mTorr vacuum. The impurity was solvent of crystallization, toluene (2.36, s, 3H; 7.17-7.19, m, 5H). Top: triradical **3**, 0.68 mg (1.14 µmol). Bottom: as above but 4,4'-di-*tert*-butylbiphenyl (0.31 mg, 1.16 µmol) was added to sample as standard. The molar ratio of toluene to 4,4'-di-*tert*-butylbiphenyl is 0.170 : 1. Then, toluene content in triradical **3** was 0.197 µmol, which corresponds to 0.0182 mg and 2.7% content in triradical. Thus, the **purity of triradical 3 was 97.3%**. The H_2O peak (1.48, s, 2H) was from chloroform-*d*.

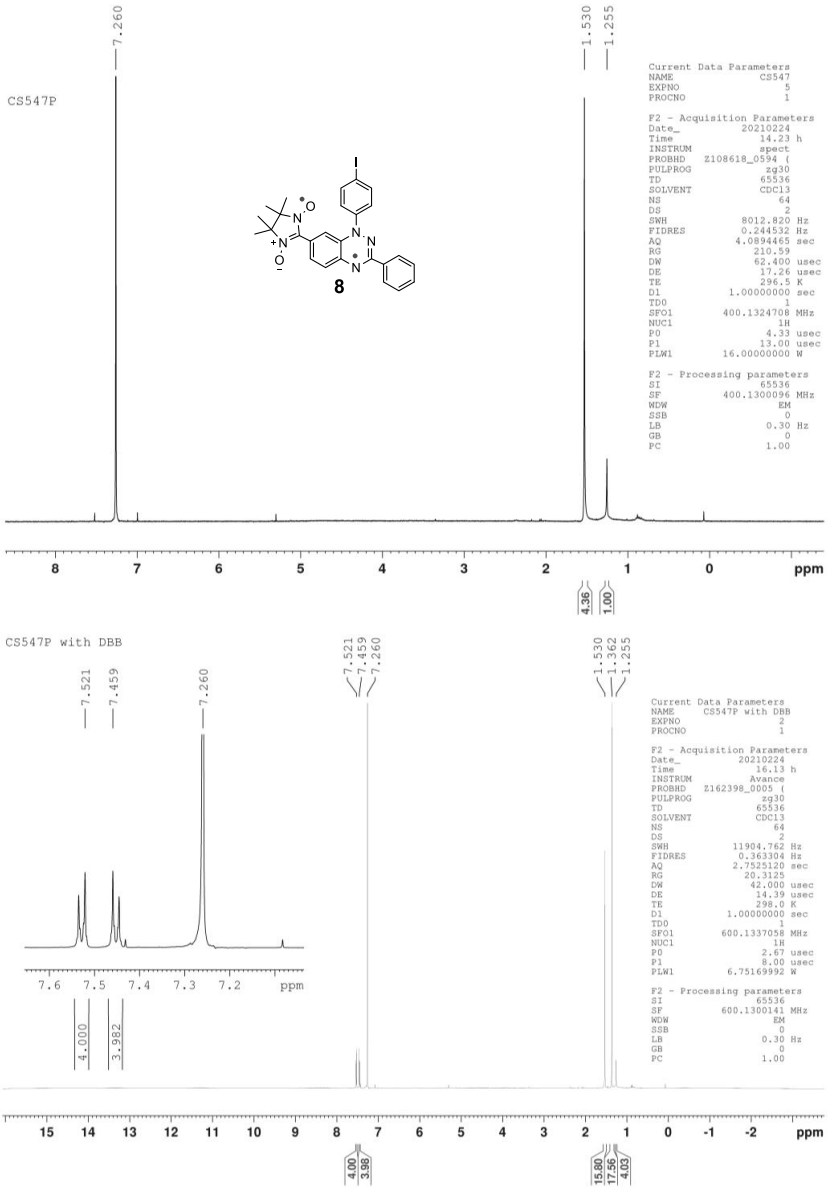

Fig. S47. ^{1}H NMR (chloroform-*d*) spectra of diradical **8** (label: CS547P). The impurity was hydrocarbon grease (1.26, s, CH_2). Top: 400 MHz, diradical **8**, 0.50 mg (0.88 µmol). Bottom: 600 MHz, diradical **8**, 0.50 mg (0.88 µmol) and 4,4'-di-*tert*-butylbiphenyl (0.17 mg, 0.64 µmol). The molar ratio of grease CH_2 groups to 4,4'-di-*tert*-butylbiphenyl was 2.0 : 1, which corresponds to 0.018 mg of grease and 3.6% content in diradical. Thus, **purity of diradical is 96.4%**. The H_2O peak (1.53, s, 2H) was from chloroform-*d*.

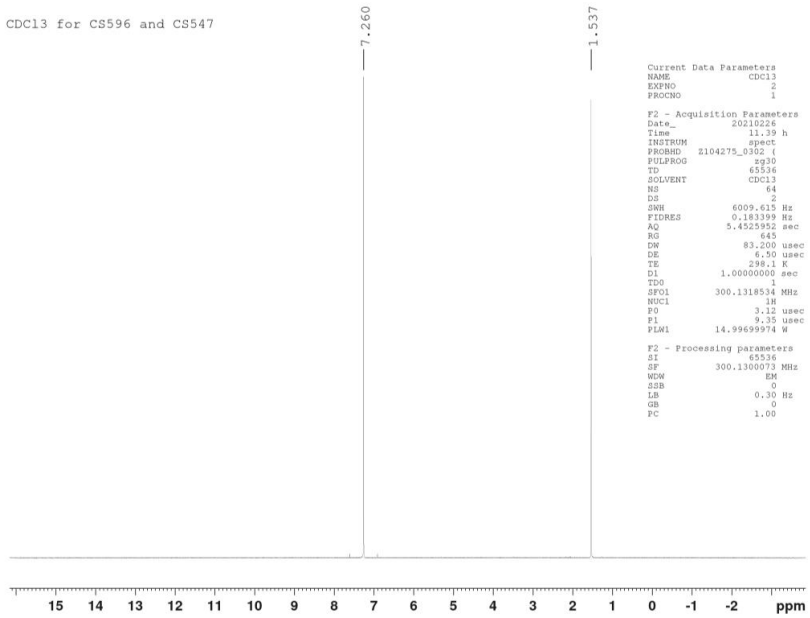

Fig. S48. ^{1}H NMR (300 MHz) spectrum of chloroform-*d* used in quantitative NMR experiments.

4. Outputs of DFT Calculations for Triradical 3.

Triradical quartet state at UB3LYP/6-31G(d,p) in the gas phase

Stoichiometry C33H36N7O4(4)
Framework group C1[X(C33H36N7O4)]
Deg. of freedom 234
Full point group C1 NOp 1
Largest Abelian subgroup C1 NOp 1
Largest concise Abelian subgroup C1 NOp 1
Standard orientation:

Center Number	Atomic Number	Atomic Type	Coordinates (Angstroms) X	Y	Z
1	6	0	-4.621976	-0.045555	-0.318954
2	6	0	-4.539865	1.324974	-0.425221
3	6	0	-3.303955	2.004119	-0.318104
4	6	0	-2.125714	1.214859	-0.143314
5	6	0	-2.206536	-0.168532	0.005425
6	6	0	-3.452452	-0.821502	-0.090409
7	1	0	-5.576597	-0.546153	-0.392821
8	1	0	-5.426655	1.930605	-0.575784
9	1	0	-1.325149	-0.759129	0.197148
10	6	0	-2.075146	3.927800	-0.140327
11	7	0	-3.275888	3.358897	-0.350487
12	7	0	-0.910137	3.295828	-0.009252
13	7	0	-0.921762	1.936053	-0.093797
14	6	0	-2.019024	5.411510	-0.062503
15	6	0	-0.796635	6.087391	0.078597
16	6	0	-3.206822	6.154896	-0.129430
17	6	0	-0.766813	7.477471	0.153822
18	1	0	0.121540	5.513409	0.122771
19	6	0	-3.171800	7.545754	-0.054145
20	1	0	-4.145470	5.625040	-0.240758
21	6	0	-1.953348	8.212029	0.088388
22	1	0	0.184992	7.989651	0.261515
23	1	0	-4.098199	8.110504	-0.106277
24	1	0	-1.927384	9.296439	0.146857
25	6	0	0.372566	1.345681	-0.069131
26	6	0	1.360811	1.903066	0.754476
27	6	0	0.698773	0.260828	-0.894583
28	6	0	2.641389	1.373253	0.774073
29	1	0	1.110222	2.752162	1.377924
30	6	0	1.982168	-0.267207	-0.884457
31	1	0	-0.040877	-0.164262	-1.561604
32	6	0	2.981963	0.272971	-0.045842
33	1	0	3.389599	1.794060	1.430231
34	1	0	2.227981	-1.091652	-1.537783
35	6	0	4.329041	-0.285231	-0.029814
36	6	0	6.167531	-1.746823	-0.440563
37	6	0	6.653095	-0.550311	0.433038
38	7	0	4.807077	-1.253466	-0.866506
39	7	0	5.334268	0.068593	0.824779
40	8	0	5.297004	0.930241	1.765487
41	8	0	4.191896	-1.842715	-1.816556
42	6	0	7.415229	0.535959	-0.347738
43	1	0	7.516113	1.414635	0.293545
44	1	0	8.413554	0.189049	-0.626706
45	1	0	6.882462	0.833556	-1.254682
46	6	0	7.430900	-0.923316	1.694693
47	1	0	8.388282	-1.376687	1.421525
48	1	0	7.623215	-0.020305	2.275925
49	1	0	6.881855	-1.619649	2.329898
50	6	0	7.008192	-2.045497	-1.681535
51	1	0	7.999221	-2.400194	-1.383546
52	1	0	6.517560	-2.824817	-2.266510
53	1	0	7.127077	-1.170815	-2.322313
54	6	0	5.918812	-3.046363	0.346756
55	1	0	5.381083	-3.743448	-0.300112
56	1	0	6.862747	-3.506479	0.650329
57	1	0	5.312439	-2.870597	1.239142
58	6	0	-3.534546	-2.266465	0.035890
59	6	0	-2.914505	-4.569402	-0.016332
60	6	0	-4.394976	-4.451044	0.458280
61	8	0	-5.884698	-2.579680	0.169611
62	8	0	-1.233661	-2.842767	-0.035068
63	7	0	-4.682159	-3.004954	0.138598
64	7	0	-2.474626	-3.129384	0.064031
65	6	0	-5.399328	-5.339670	-0.275415
66	1	0	-5.200240	-6.391671	-0.050972
67	1	0	-6.406977	-5.093586	0.063007
68	1	0	-5.365091	-5.199728	-1.356674
69	6	0	-4.586082	-4.594132	1.979307
70	1	0	-5.602152	-4.280864	2.229897
71	1	0	-4.451246	-5.632185	2.293920
72	1	0	-3.886973	-3.965874	2.537395
73	6	0	-2.752601	-4.980059	-1.491331
74	1	0	-1.711633	-4.819916	-1.781248
75	1	0	-2.997620	-6.035905	-1.632184
76	1	0	-3.387490	-4.382798	-2.151002
77	6	0	-2.002889	-5.425993	0.862387
78	1	0	-2.313237	-6.473793	0.812249
79	1	0	-0.977946	-5.345803	0.496922
80	1	0	-2.013093	-5.107158	1.905514

Rotational constants (GHZ): 0.0644821 0.0492485 0.0292104
Standard basis: 6-31G(d,p) (6D, 7F)
SCF Done: E(UB3LYP) = -1963.15717022 A.U. after 4 cycles
NFock= 4 Conv=0.28D-08 -V/T= 2.0094
<Sx>= 0.0000 <Sy>= 0.0000 <Sz>= 1.5000 <S**2>= 3.8995 S= 1.5370
<L.S>= 0.00000000000
Annihilation of the first spin contaminant:
S**2 before annihilation 3.8995, after 3.7586

Item	Value	Threshold	Converged?
Maximum Force	0.000000	0.000015	YES
RMS Force	0.000000	0.000010	YES
Maximum Displacement	0.000128	0.000060	NO
RMS Displacement	0.000026	0.000040	YES

Predicted change in Energy=-4.241407D-12
Optimization completed on the basis of negligible forces.
-- Stationary point found.

Triradical, broken symmetry doublet state (BSdoublet1, 1st excited state, the lowest energy) at UB3LYP/6-31G(d,p) in the gas phase

Stoichiometry C33H36N7O4(2)
Framework group C1[X(C33H36N7O4)]
Deg. of freedom 234
Full point group C1 NOp 1
Largest Abelian subgroup C1 NOp 1
Largest concise Abelian subgroup C1 NOp 1
Standard orientation:

Center Number	Atomic Number	Atomic Type	Coordinates (Angstroms) X	Y	Z
1	6	0	-4.623674	-0.104589	-0.248545
2	6	0	-4.566017	1.268637	-0.341977
3	6	0	-3.338737	1.965877	-0.264949
4	6	0	-2.144338	1.193562	-0.125262
5	6	0	-2.197556	-0.192892	0.002295
6	6	0	-3.436048	-0.864767	-0.066562
7	1	0	-5.572165	-0.619263	-0.300749
8	1	0	-5.466466	1.861133	-0.461866
9	1	0	-1.300659	-0.771207	0.156560
10	6	0	-2.130708	3.909200	-0.130257
11	7	0	-3.330044	3.321277	-0.297033
12	7	0	-0.954515	3.293887	-0.023408
13	7	0	-0.953575	1.933290	-0.092993
14	6	0	-2.092725	5.394205	-0.071227
15	6	0	-0.876364	6.087119	0.035835
16	6	0	-3.291114	6.121664	-0.122135
17	6	0	-0.862850	7.478277	0.093082
18	1	0	0.049646	5.525031	0.068739
19	6	0	-3.272325	7.513738	-0.064957
20	1	0	-4.225038	5.578698	-0.206827
21	6	0	-2.059826	8.197039	0.043426
22	1	0	0.084331	8.003711	0.174606
23	1	0	-4.206784	8.066100	-0.104604
24	1	0	-2.046549	9.282349	0.087784
25	6	0	0.352429	1.356555	-0.068509
26	6	0	1.310686	1.878660	0.807633
27	6	0	0.705718	0.322488	-0.942306
28	6	0	2.598543	1.362037	0.827662
29	1	0	1.035669	2.692048	1.467930
30	6	0	1.995016	-0.195322	-0.928826
31	1	0	-0.018118	-0.073322	-1.644418
32	6	0	2.966269	0.311477	-0.040699
33	1	0	3.327957	1.754295	1.521800
34	1	0	2.265688	-0.982464	-1.617613
35	6	0	4.323101	-0.234524	-0.023550
36	6	0	6.196051	-1.625736	-0.504285
37	6	0	6.626825	-0.522490	0.510359
38	7	0	4.845420	-1.106584	-0.932493
39	7	0	5.283763	0.041848	0.903917
40	8	0	5.192390	0.802243	1.924834
41	8	0	4.276268	-1.599924	-1.962661
42	6	0	7.408081	0.646238	-0.117356
43	1	0	7.468383	1.453720	0.615999
44	1	0	8.422449	0.339517	-0.385279
45	1	0	6.911809	1.032248	-1.011574
46	6	0	7.352276	-1.018210	1.760916
47	1	0	8.327786	-1.430475	1.486804
48	1	0	7.504325	-0.179235	2.441567
49	1	0	6.785718	-1.783034	2.293755
50	6	0	7.090202	-1.781567	-1.733973
51	1	0	8.073179	-2.156920	-1.434655
52	1	0	6.634133	-2.498323	-2.418473
53	1	0	7.222879	-0.842318	-2.272497
54	6	0	5.936450	-3.004264	0.130166
55	1	0	5.437017	-3.635031	-0.608877
56	1	0	6.874604	-3.482666	0.423122
57	1	0	5.291358	-2.931336	1.009611
58	6	0	-3.492272	-2.312395	0.040132
59	6	0	-2.836587	-4.604304	-0.056476
60	6	0	-4.308767	-4.516706	0.448829
61	8	0	-5.834399	-2.667536	0.214031
62	8	0	-1.183838	-2.851518	-0.081631
63	7	0	-4.625586	-3.071514	0.154519
64	7	0	-2.418214	-3.158714	0.036144
65	6	0	-5.312976	-5.412038	-0.276823
66	1	0	-5.091617	-6.463485	-0.071430
67	1	0	-6.317477	-5.187933	0.085352
68	1	0	-5.303251	-5.256522	-1.356454
69	6	0	-4.466865	-4.683047	1.971277
70	1	0	-5.482541	-4.389636	2.246322
71	1	0	-4.309198	-5.722845	2.269081
72	1	0	-3.766730	-4.050941	2.523715
73	6	0	-2.697700	-4.991371	-1.540216
74	1	0	-1.665351	-4.810496	-1.848213
75	1	0	-2.928876	-6.048885	-1.691611
76	1	0	-3.354859	-4.394972	-2.178509
77	6	0	-1.894172	-5.458571	0.791495
78	1	0	-2.188476	-6.510497	0.731728
79	1	0	-0.878046	-5.356227	0.407439
80	1	0	-1.888980	-5.155245	1.839276

Rotational constants (GHZ): 0.0643097 0.0493542 0.0293097
Standard basis: 6-31G(d,p) (6D, 7F)
SCF Done: E(UB3LYP) = -1963.15593037 a.u. after 2 cycles
Convg = 0.7097D-09 31 Fock formations.
S**2 = 1.8857 -V/T = 2.0094
<Sx>= 0.0000 <Sy>= 0.0000 <Sz>= 0.5000 <S**2>= 1.8857 S= 0.9614
<L.S>= 0.00000000000
Annihilation of the first spin contaminant:
S**2 before annihilation 1.8857, after 1.2452

Item	Value	Threshold	Converged?
Maximum Force	0.000000	0.000015	YES
RMS Force	0.000000	0.000010	YES
Maximum Displacement	0.000020	0.000060	YES
RMS Displacement	0.000003	0.000040	YES

Predicted change in Energy=-2.307452D-12

Optimization completed.
-- Stationary point found.

Triradical, broken symmetry doublet state (BSdoublet2, 2nd excited state) at UB3LYP/6-31G(d,p) in the gas phase

Stoichiometry C33H36N7O4(2)
Framework group C1[X(C33H36N7O4)]
Deg. of freedom 234
Full point group C1 NOp 1
Largest Abelian subgroup C1 NOp 1
Largest concise Abelian subgroup C1 NOp 1
Standard orientation:

Center Number	Atomic Number	Atomic Type	Coordinates (Angstroms) X	Y	Z
1	6	0	-4.624074	-0.083616	-0.321111
2	6	0	-4.552565	1.291516	-0.426375
3	6	0	-3.325798	1.977958	-0.323173
4	6	0	-2.142909	1.204919	-0.146766
5	6	0	-2.211200	-0.183451	0.002356
6	6	0	-3.448430	-0.842335	-0.094712
7	1	0	-5.574855	-0.592276	-0.389714
8	1	0	-5.445427	1.889074	-0.574680
9	1	0	-1.323825	-0.766147	0.191508
10	6	0	-2.116404	3.914395	-0.145226
11	7	0	-3.305882	3.342972	-0.360287
12	7	0	-0.939702	3.290716	-0.006595
13	7	0	-0.943513	1.931060	-0.092177
14	6	0	-2.064095	5.398966	-0.068651
15	6	0	-0.843755	6.078766	0.069230
16	6	0	-3.254717	6.138113	-0.133526
17	6	0	-0.818535	7.469294	0.143502
18	1	0	0.076327	5.507857	0.111404
19	6	0	-3.224429	7.528861	-0.059522
20	1	0	-4.191384	5.604112	-0.242157
21	6	0	-2.007620	8.199385	0.079992
22	1	0	0.131681	7.984916	0.248706
23	1	0	-4.152756	8.090582	-0.109962
24	1	0	-1.985370	9.283940	0.137656
25	6	0	0.353864	1.347794	-0.066718
26	6	0	1.338215	1.914127	0.755920
27	6	0	0.687299	0.262811	-0.889580
28	6	0	2.621658	1.391999	0.778339
29	1	0	1.081376	2.763326	1.376588
30	6	0	1.974101	-0.257044	-0.876616
31	1	0	-0.048204	-0.169586	-1.556454
32	6	0	2.969744	0.291741	-0.038713
33	1	0	3.366595	1.818824	1.434358
34	1	0	2.225405	-1.081389	-1.527989
35	6	0	4.320548	-0.256887	-0.020834
36	6	0	6.171703	-1.701758	-0.434278
37	6	0	6.644936	-0.506957	0.448592
38	7	0	4.808597	-1.216713	-0.861439
39	7	0	5.320057	0.099518	0.839389
40	8	0	5.272484	0.954639	1.785528
41	8	0	4.200706	-1.804584	-1.817006
42	6	0	7.401507	0.590052	-0.322542
43	1	0	7.493320	1.465382	0.324656
44	1	0	8.403488	0.252634	-0.600026
45	1	0	6.869764	0.889342	-1.229530
46	6	0	7.421032	-0.881903	1.710724
47	1	0	8.382825	-1.326238	1.438220
48	1	0	7.604366	0.018889	2.298268
49	1	0	6.875060	-1.586366	2.339578
50	6	0	7.018646	-1.985551	-1.674464
51	1	0	8.011509	-2.334331	-1.375613
52	1	0	6.536095	-2.764853	-2.266151
53	1	0	7.132611	-1.105745	-2.309082
54	6	0	5.931042	-3.008335	0.343821
55	1	0	5.401232	-3.705625	-0.309334
56	1	0	6.877705	-3.462642	0.647631
57	1	0	5.320295	-2.843309	1.235284
58	6	0	-3.508585	-2.297266	0.032963
59	6	0	-2.879177	-4.590288	-0.081480
60	6	0	-4.320212	-4.484428	0.507417
61	8	0	-5.833374	-2.611022	0.362974
62	8	0	-1.219946	-2.845595	-0.236573
63	7	0	-4.637785	-3.035731	0.227640
64	7	0	-2.445510	-3.145683	-0.036512
65	6	0	-5.375300	-5.369221	-0.156540
66	1	0	-5.159530	-6.422700	0.044179
67	1	0	-6.354863	-5.126491	0.258266
68	1	0	-5.422138	-5.220941	-1.236204
69	6	0	-4.394385	-4.644071	2.036884
70	1	0	-5.390044	-4.339259	2.367057
71	1	0	-4.230423	-5.684372	2.329477
72	1	0	-3.658406	-4.016986	2.546733
73	6	0	-2.827957	-4.999417	-1.564763
74	1	0	-1.813246	-4.832870	-1.933337
75	1	0	-3.076971	-6.056648	-1.686788
76	1	0	-3.514865	-4.405759	-2.173540
77	6	0	-1.893654	-5.438026	0.722979
78	1	0	-2.194359	-6.489389	0.693114
79	1	0	-0.900633	-5.344258	0.280617
80	1	0	-1.828128	-5.122030	1.764962

Rotational constants (GHZ): 0.0644097 0.0494293 0.0292858
Standard basis: 6-31G(d,p) (6D, 7F)
SCF Done: E(UB3LYP) = -1963.15448777 a.u. after 1 cycles
Convg = 0.7542D-09 1 Fock formations.
S**2 = 1.8830 -V/T = 2.0094
<Sx>= 0.0000 <Sy>= 0.0000 <Sz>= 0.5000 <S**2>= 1.8830 S= 0.9605
<L_S>= 0.00000000000
Annihilation of the first spin contaminant:
S**2 before annihilation 1.8830, after 1.2345

Item	Value	Threshold	Converged?
Maximum Force	0.000000	0.000015	YES
RMS Force	0.000000	0.000010	YES
Maximum Displacement	0.000049	0.000060	YES
RMS Displacement	0.000006	0.000040	YES

Predicted change in Energy=-4.607677D-12

Optimization completed.
-- Stationary point found.

Triradical, broken symmetry doublet state (BSdoublet3, highest energy) at UB3LYP/6-31G(d,p) in the gas phase

Symmetry turned off by external request.
Stoichiometry C33H36N7O4(2)
Framework group C1[X(C33H36N7O4)]
Deg. of freedom 234
Full point group C1 NOp 1
Z-Matrix orientation:

Center Number	Atomic Number	Atomic Type	Coordinates (Angstroms) X	Y	Z
1	6	0	-4.627919	-0.056514	-0.254229
2	6	0	-4.558608	1.319651	-0.358090
3	6	0	-3.330240	2.005657	-0.284604
4	6	0	-2.144522	1.232142	-0.131279
5	6	0	-2.208186	-0.156657	0.012805
6	6	0	-3.447571	-0.816533	-0.059314
7	1	0	-5.579962	-0.564701	-0.304220
8	1	0	-5.455048	1.916634	-0.485916
9	1	0	-1.315857	-0.738856	0.178325
10	6	0	-2.110281	3.942816	-0.161555
11	7	0	-3.307367	3.371205	-0.332193
12	7	0	-0.932003	3.317649	-0.041512
13	7	0	-0.945959	1.956661	-0.100632
14	6	0	-2.051792	5.428195	-0.112602
15	6	0	-0.825649	6.105844	-0.023653
16	6	0	-3.241523	6.170365	-0.154232
17	6	0	-0.793979	7.497350	0.025139
18	1	0	0.093378	5.532134	0.001795
19	6	0	-3.204746	7.562085	-0.105226
20	1	0	-4.182694	5.637906	-0.225136
21	6	0	-1.982193	8.230548	-0.014863
22	1	0	0.160563	8.011352	0.092483
23	1	0	-4.132466	8.126188	-0.137069
24	1	0	-1.954835	9.315864	0.023038
25	6	0	0.353420	1.364852	-0.073844
26	6	0	1.323183	1.891698	0.786928
27	6	0	0.689592	0.309738	-0.929233
28	6	0	2.604053	1.358233	0.811809
29	1	0	1.062376	2.721524	1.432267
30	6	0	1.971145	-0.226850	-0.908679
31	1	0	-0.041282	-0.091312	-1.620881
32	6	0	2.953689	0.283700	-0.035041
33	1	0	3.342256	1.756596	1.492915
34	1	0	2.226444	-1.033928	-1.579836
35	6	0	4.302013	-0.283853	-0.010797
36	6	0	6.141118	-1.737060	-0.438386
37	6	0	6.612025	-0.580136	0.494303
38	7	0	4.791120	-1.220978	-0.872708
39	7	0	5.286913	0.032258	0.878267
40	8	0	5.231654	0.858195	1.849603
41	8	0	4.193180	-1.770574	-1.857077
42	6	0	7.398957	0.530999	-0.224126
43	1	0	7.495831	1.380883	0.455357
44	1	0	8.398825	0.185700	-0.499425
45	1	0	6.885450	0.870889	-1.127174
46	6	0	7.355497	-1.006506	1.759846
47	1	0	8.322532	-1.444090	1.495027
48	1	0	7.526457	-0.128566	2.384519
49	1	0	6.791989	-1.731605	2.348386
50	6	0	7.005392	-1.987654	-1.674098
51	1	0	7.988492	-2.360749	-1.372420
52	1	0	6.521980	-2.738320	-2.301002
53	1	0	7.141217	-1.087614	-2.275224
54	6	0	5.870456	-3.067651	0.287346
55	1	0	5.345719	-3.734716	-0.400513
56	1	0	6.805775	-3.543800	0.592770
57	1	0	5.243989	-2.927378	1.172105
58	6	0	-3.502448	-2.272872	0.059042
59	6	0	-2.859387	-4.562839	-0.060802
60	6	0	-4.309762	-4.468431	0.506272
61	8	0	-5.830640	-2.603433	0.353907
62	8	0	-1.206862	-2.811756	-0.182048
63	7	0	-4.630244	-3.019105	0.233168
64	7	0	-2.434341	-3.116589	-0.000937
65	6	0	-5.349646	-5.352973	-0.181279
66	1	0	-5.132280	-6.406850	0.015470
67	1	0	-6.337040	-5.117381	0.218720
68	1	0	-5.379036	-5.197193	-1.260496
69	6	0	-4.406245	-4.640565	2.032974
70	1	0	-5.410067	-4.349320	2.350523
71	1	0	-4.235266	-5.681172	2.320432
72	1	0	-3.685119	-4.009332	2.558711
73	6	0	-2.781291	-4.963547	-1.545458
74	1	0	-1.762195	-4.785225	-1.895852
75	1	0	-3.018072	-6.022440	-1.677622
76	1	0	-3.463661	-4.373079	-2.162366
77	6	0	-1.881531	-5.409904	0.753991
78	1	0	-2.176474	-6.462561	0.713682
79	1	0	-0.882413	-5.308614	0.327302
80	1	0	-1.833466	-5.099418	1.798585

Rotational constants (GHZ): 0.0642017 0.0497322 0.0293805
Standard basis: 6-31G(d,p) (6D, 7F)
SCF Done: E(UB3LYP) = -1963.15316900 A.U. after 8 cycles
Convg = 0.7031D-08 -V/T = 2.0094
<Sx>= 0.0000 <Sy>= 0.0000 <Sz>= 0.5000 <S**2>= 1.8693 S= 0.9558
<L_S>= 0.000000000000E+00
Annihilation of the first spin contaminant:
S**2 before annihilation 1.8693, after 1.1806

Item	Value	Threshold	Converged?
Maximum Force	0.000027	0.000450	YES
RMS Force	0.000002	0.000300	YES
Maximum Displacement	0.001546	0.001800	YES
RMS Displacement	0.000174	0.001200	YES

Predicted change in Energy=-8.865129D-09
Optimization completed.
-- Stationary point found.

Triradical quartet state at UB3LYP/6-31G(d,p) in toluene

Stoichiometry C33H36N7O4(4)
Framework group C1[X(C33H36N7O4)]
Deg. of freedom 234
Full point group C1 NOp 1
Largest Abelian subgroup C1 NOp 1
Largest concise Abelian subgroup C1 NOp 1
Standard orientation:

Center Number	Atomic Number	Atomic Type	Coordinates (Angstroms) X	Y	Z
1	6	0	-4.617549	-0.085464	-0.326419
2	6	0	-4.549619	1.286611	-0.431203
3	6	0	-3.320564	1.976798	-0.323984
4	6	0	-2.134803	1.199022	-0.153177
5	6	0	-2.201219	-0.186137	-0.010972
6	6	0	-3.440687	-0.850213	-0.102581
7	1	0	-5.567927	-0.594053	-0.398329
8	1	0	-5.444252	1.881500	-0.580067
9	1	0	-1.312363	-0.768361	0.171358
10	6	0	-2.108459	3.912486	-0.142804
11	7	0	-3.304153	3.333492	-0.353182
12	7	0	-0.937545	3.290584	-0.013605
13	7	0	-0.938159	1.930895	-0.100263
14	6	0	-2.064730	5.397104	-0.062130
15	6	0	-0.848952	6.082201	0.094383
16	6	0	-3.256790	6.133055	-0.141523
17	6	0	-0.829567	7.472710	0.171617
18	1	0	0.073314	5.515904	0.150022
19	6	0	-3.232752	7.524426	-0.064619
20	1	0	-4.191673	5.598897	-0.263417
21	6	0	-2.020514	8.199389	0.092661
22	1	0	0.117288	7.991085	0.291608
23	1	0	-4.162524	8.082385	-0.126887
24	1	0	-2.002871	9.283759	0.152523
25	6	0	0.360916	1.349688	-0.072113
26	6	0	1.333373	1.893723	0.778335
27	6	0	0.703369	0.287937	-0.920402
28	6	0	2.617122	1.370430	0.801512
29	1	0	1.069486	2.724742	1.420607
30	6	0	1.991339	-0.229875	-0.907884
31	1	0	-0.026022	-0.124249	-1.606795
32	6	0	2.975018	0.295260	-0.042417
33	1	0	3.352472	1.777315	1.480692
34	1	0	2.252558	-1.032800	-1.581882
35	6	0	4.326709	-0.253477	-0.023924
36	6	0	6.201603	-1.641271	-0.514515
37	6	0	6.626946	-0.555585	0.523253
38	7	0	4.855091	-1.111285	-0.943766
39	7	0	5.281253	0.003781	0.916201
40	8	0	5.173483	0.737969	1.955196
41	8	0	4.291583	-1.573739	-1.991850
42	6	0	7.415943	0.620580	-0.080348
43	1	0	7.481844	1.414239	0.667425
44	1	0	8.428548	0.310980	-0.350458
45	1	0	6.925468	1.026309	-0.968946
46	6	0	7.343057	-1.078526	1.767937
47	1	0	8.310064	-1.504934	1.486798
48	1	0	7.514675	-0.251658	2.458701
49	1	0	6.763458	-1.840202	2.291113
50	6	0	7.108980	-1.774297	-1.737053
51	1	0	8.094909	-2.133233	-1.428460
52	1	0	6.676273	-2.497445	-2.429867
53	1	0	7.230970	-0.829485	-2.268256
54	6	0	5.936793	-3.030005	0.094817
55	1	0	5.446686	-3.650933	-0.658631
56	1	0	6.873681	-3.510650	0.387211
57	1	0	5.284178	-2.973297	0.969784
58	6	0	-3.509602	-2.296811	0.025501
59	6	0	-2.883596	-4.596928	-0.058689
60	6	0	-4.337452	-4.483606	0.496233
61	8	0	-5.845471	-2.610490	0.287451
62	8	0	-1.214639	-2.855290	-0.166735
63	7	0	-4.646507	-3.037749	0.191473
64	7	0	-2.446400	-3.153676	-0.003751
65	6	0	-5.374867	-5.378085	-0.181930
66	1	0	-5.150800	-6.428499	0.023866
67	1	0	-6.363113	-5.148331	0.219324
68	1	0	-5.406571	-5.232066	-1.262440
69	6	0	-4.442312	-4.626099	2.025572
70	1	0	-5.446008	-4.325040	2.333982
71	1	0	-4.279343	-5.662663	2.330480
72	1	0	-3.719260	-3.990973	2.543799
73	6	0	-2.802438	-5.009983	-1.539503
74	1	0	-1.778551	-4.854908	-1.887072
75	1	0	-3.056515	-6.065725	-1.661666
76	1	0	-3.471363	-4.414000	-2.165698
77	6	0	-1.925009	-5.450260	0.771683
78	1	0	-2.244310	-6.495940	0.748140
79	1	0	-0.923395	-5.382842	0.344334
80	1	0	-1.871844	-5.123525	1.811004

Rotational constants (GHZ): 0.0643755 0.0492088 0.0293039
Standard basis: 6-31G(d,p) (6D, 7F)
SCF Done: E(UB3LYP) = -1963.16585847 A.U. after 6 cycles
NFock= 6 Conv=0.60D-08 -V/T= 2.0094
<Sx>= 0.0000 <Sy>= 0.0000 <Sz>= 1.5000 <S**2>= 3.8953 S= 1.5360
<L.S>= 0.00000000000
Annihilation of the first spin contaminant:
S**2 before annihilation 3.8953, after 3.7582

Item	Value	Threshold	Converged?
Maximum Force	0.000000	0.000015	YES
RMS Force	0.000000	0.000010	YES
Maximum Displacement	0.000037	0.000060	YES
RMS Displacement	0.000008	0.000040	YES

Predicted change in Energy=-3.670778D-12
Optimization completed.

-- Stationary point found.

Triradical, broken symmetry doublet state (BSdoublet1, 1st excited state, the lowest energy) at UB3LYP/6-31G(d,p) in toluene

Stoichiometry C33H36N7O4(2)
Framework group C1[X(C33H36N7O4)]
Deg. of freedom 234
Full point group C1 NOp 1
Largest Abelian subgroup C1 NOp 1
Largest concise Abelian subgroup C1 NOp 1
Standard orientation:

Center Number	Atomic Number	Atomic Type	Coordinates (Angstroms) X	Y	Z
1	6	0	-4.616434	-0.161213	-0.253074
2	6	0	-4.579597	1.213605	-0.342877
3	6	0	-3.362407	1.927439	-0.266395
4	6	0	-2.157319	1.171937	-0.132966
5	6	0	-2.189586	-0.216252	-0.013988
6	6	0	-3.418163	-0.905085	-0.078512
7	1	0	-5.558200	-0.687991	-0.302721
8	1	0	-5.490415	1.791004	-0.458813
9	1	0	-1.282702	-0.781560	0.129455
10	6	0	-2.179567	3.887567	-0.128060
11	7	0	-3.371348	3.284600	-0.293910
12	7	0	-0.994856	3.287405	-0.024771
13	7	0	-0.977213	1.927186	-0.097450
14	6	0	-2.160074	5.373446	-0.065504
15	6	0	-0.953091	6.080825	0.056749
16	6	0	-3.365894	6.088227	-0.128288
17	6	0	-0.955873	7.472294	0.116675
18	1	0	-0.020438	5.530676	0.100299
19	6	0	-3.363999	7.480691	-0.068877
20	1	0	-4.293832	5.536926	-0.223789
21	6	0	-2.160454	8.177872	0.054247
22	1	0	-0.015693	8.007969	0.210364
23	1	0	-4.304282	8.022096	-0.118235
24	1	0	-2.160066	9.263054	0.100499
25	6	0	0.335545	1.364731	-0.070993
26	6	0	1.274139	1.869335	0.835830
27	6	0	0.710159	0.362558	-0.972543
28	6	0	2.567036	1.364300	0.857730
29	1	0	0.981161	2.657034	1.519346
30	6	0	2.005748	-0.140112	-0.957855
31	1	0	-0.001055	-0.017200	-1.696335
32	6	0	2.957193	0.348094	-0.039650
33	1	0	3.281084	1.739209	1.577166
34	1	0	2.295585	-0.899344	-1.670065
35	6	0	4.319715	-0.184309	-0.020299
36	6	0	6.233599	-1.487995	-0.575540
37	6	0	6.593641	-0.525033	0.600201
38	7	0	4.898096	-0.928395	-1.003323
39	7	0	5.223705	-0.019960	0.984545
40	8	0	5.056331	0.599789	2.088238
41	8	0	4.384896	-1.277459	-2.118992
42	6	0	7.399365	0.716951	0.178008
43	1	0	7.415841	1.419512	1.014406
44	1	0	8.428519	0.446401	-0.070661
45	1	0	6.951640	1.219422	-0.683248
46	6	0	7.250028	-1.182473	1.813967
47	1	0	8.236436	-1.586625	1.539353
48	1	0	7.373172	-0.438625	2.602534
49	1	0	6.653777	-2.003162	2.214886
50	6	0	7.195855	-1.468215	-1.762723
51	1	0	8.170419	-1.858258	-1.456012
52	1	0	6.800292	-2.104121	-2.556101
53	1	0	7.332229	-0.465803	-2.170491
54	6	0	5.964688	-2.941002	-0.144096
55	1	0	5.522556	-3.476387	-0.987450
56	1	0	6.894887	-3.440469	0.137669
57	1	0	5.269655	-2.993767	0.697792
58	6	0	-3.454445	-2.354597	0.027474
59	6	0	-2.780954	-4.639843	-0.100064
60	6	0	-4.228710	-4.566068	0.476275
61	8	0	-5.780054	-2.725085	0.313108
62	8	0	-1.150375	-2.862892	-0.201721
63	7	0	-4.572822	-3.123114	0.196950
64	7	0	-2.373736	-3.188672	-0.028545
65	6	0	-5.256006	-5.472924	-0.200899
66	1	0	-5.005323	-6.521124	-0.015607
67	1	0	-6.243082	-5.272241	0.218375
68	1	0	-5.307134	-5.310419	-1.278316
69	6	0	-4.309011	-4.732977	2.004714
70	1	0	-5.314370	-4.457853	2.331440
71	1	0	-4.120126	-5.770169	2.292113
72	1	0	-3.592179	-4.090277	2.522266
73	6	0	-2.711960	-5.028589	-1.588067
74	1	0	-1.696735	-4.845892	-1.947448
75	1	0	-2.944768	-6.087683	-1.722971
76	1	0	-3.402554	-4.438085	-2.195630
77	6	0	-1.793267	-5.485380	0.703817
78	1	0	-2.092282	-6.536792	0.670242
79	1	0	-0.799640	-5.392362	0.262871
80	1	0	-1.730922	-5.172100	1.746763

Rotational constants (GHZ): 0.0641734 0.0493736 0.0294195
Standard basis: 6-31G(d,p) (6D, 7F)
SCF Done: E(UB3LYP) = -1963.16471753 a.u. after 2 cycles
Convg = 0.1410D-08 23 Fock formations.
S**2 = 1.8824 -V/T = 2.0094
<Sx>= 0.0000 <Sy>= 0.0000 <Sz>= 0.5000 <S**2>= 1.8824 S= 0.9603
<L.S>= 0.00000000000
Annihilation of the first spin contaminant:
S**2 before annihilation 1.8824, after 1.2324

Item	Value	Threshold	Converged?
Maximum Force	0.000000	0.000015	YES
RMS Force	0.000000	0.000010	YES
Maximum Displacement	0.000045	0.000060	YES

RMS Displacement 0.000008 0.000040 YES
Predicted change in Energy=-8.319429D-12
Optimization completed.
-- Stationary point found.

Triradical, broken symmetry doublet state (BSdoublet2, 2nd excited state) at UB3LYP/6-31G(d,p) in toluene

Stoichiometry C33H36N7O4(2)
Framework group C1[X(C33H36N7O4)]
Deg. of freedom 234
Full point group C1 NOp 1
Largest Abelian subgroup C1 NOp 1
Largest concise Abelian subgroup C1 NOp 1
Standard orientation:

Center Number	Atomic Number	Atomic Type	Coordinates (Angstroms) X	Y	Z
1	6	0	-4.615872	-0.124930	-0.343261
2	6	0	-4.559442	1.251466	-0.447062
3	6	0	-3.340594	1.950152	-0.336108
4	6	0	-2.150764	1.189025	-0.157148
5	6	0	-2.204305	-0.200655	-0.012177
6	6	0	-3.434112	-0.871993	-0.111741
7	1	0	-5.561210	-0.642530	-0.417380
8	1	0	-5.459558	1.837205	-0.599442
9	1	0	-1.310408	-0.773798	0.175646
10	6	0	-2.149885	3.898901	-0.147062
11	7	0	-3.333096	3.316700	-0.368974
12	7	0	-0.967797	3.285964	-0.006580
13	7	0	-0.959587	1.926582	-0.095566
14	6	0	-2.111650	5.384221	-0.064581
15	6	0	-0.899155	6.073933	0.095290
16	6	0	-3.306795	6.115076	-0.145369
17	6	0	-0.885896	7.464681	0.174724
18	1	0	0.025300	5.511447	0.151536
19	6	0	-3.289016	7.506152	-0.066581
20	1	0	-4.238747	5.576314	-0.269680
21	6	0	-2.079680	8.186034	0.094301
22	1	0	0.058427	7.987025	0.297349
23	1	0	-4.220936	8.060387	-0.129842
24	1	0	-2.066926	9.270393	0.155843
25	6	0	0.342820	1.353214	-0.067882
26	6	0	1.311725	1.904292	0.782356
27	6	0	0.692150	0.293828	-0.916623
28	6	0	2.598500	1.388981	0.806059
29	1	0	1.042044	2.733749	1.424172
30	6	0	1.983363	-0.215857	-0.903321
31	1	0	-0.033834	-0.123181	-1.603706
32	6	0	2.963487	0.315818	-0.037738
33	1	0	3.331172	1.800687	1.485200
34	1	0	2.249760	-1.017116	-1.577242
35	6	0	4.318764	-0.223683	-0.019214
36	6	0	6.202799	-1.599781	-0.508428
37	6	0	6.621607	-0.508936	0.526621
38	7	0	4.852267	-1.079961	-0.937684
39	7	0	5.272446	0.042080	0.919549
40	8	0	5.160564	0.777426	1.957231
41	8	0	4.291157	-1.548380	-1.984289
42	6	0	7.402049	0.671276	-0.080177
43	1	0	7.463155	1.466974	0.665835
44	1	0	8.416531	0.367988	-0.350411
45	1	0	6.908154	1.071723	-0.969269
46	6	0	7.342291	-1.024305	1.771827
47	1	0	8.311717	-1.445153	1.490686
48	1	0	7.509329	-0.194737	2.460476
49	1	0	6.768130	-1.788458	2.297384
50	6	0	7.109910	-1.729288	-1.731531
51	1	0	8.098367	-2.081459	-1.423236
52	1	0	6.681114	-2.456408	-2.422619
53	1	0	7.225422	-0.784698	-2.264569
54	6	0	5.947981	-2.988945	0.104198
55	1	0	5.461547	-3.614946	-0.647429
56	1	0	6.888373	-3.462504	0.396897
57	1	0	5.295747	-2.934759	0.979607
58	6	0	-3.482185	-2.327576	0.022332
59	6	0	-2.841345	-4.617694	-0.092951
60	6	0	-4.270010	-4.516410	0.529019
61	8	0	-5.794942	-2.645891	0.409039
62	8	0	-1.197811	-2.857000	-0.293542
63	7	0	-4.601380	-3.069976	0.249545
64	7	0	-2.416206	-3.169149	-0.067790
65	6	0	-5.332642	-5.411813	-0.107964
66	1	0	-5.094589	-6.462392	0.080399
67	1	0	-6.302691	-5.189200	0.339161
68	1	0	-5.413989	-5.258946	-1.184914
69	6	0	-4.306235	-4.670274	2.060366
70	1	0	-5.297175	-4.377738	2.414735
71	1	0	-4.123806	-5.707961	2.350097
72	1	0	-3.565173	-4.034119	2.551049
73	6	0	-2.823457	-5.038488	-1.573589
74	1	0	-1.818012	-4.875483	-1.968072
75	1	0	-3.072389	-6.097345	-1.677988
76	1	0	-3.525887	-4.452743	-2.172054
77	6	0	-1.835845	-5.455712	0.696665
78	1	0	-2.145478	-6.504567	0.695187
79	1	0	-0.856309	-5.381484	0.221879
80	1	0	-1.736816	-5.121348	1.730183

Rotational constants (GHZ): 0.0643075 0.0493867 0.0293701
Standard basis: 6-31G(d,p) (6D, 7F)
SCF Done: E(UB3LYP) = -1963.16332617 A.U. after 4 cycles
NFock= 4 Conv=0.22D-08 -V/T= 2.0094
<Sx>= 0.0000 <Sy>= 0.0000 <Sz>= 0.5000 <S**2>= 1.8798 S= 0.9594
<L.S>= 0.00000000000
Annihilation of the first spin contaminant:
S**2 before annihilation 1.8798, after 1.2222

Item	Value	Threshold	Converged?
Maximum Force	0.000000	0.000015	YES
RMS Force	0.000000	0.000010	YES
Maximum Displacement	0.000050	0.000060	YES

RMS Displacement 0.000010 0.000040 YES
Predicted change in Energy=-7.125685D-13
Optimization completed.
-- Stationary point found.

Triradical quartet state at UB3LYP/6-31G(d,p) in tetrahydrofuran

Stoichiometry C33H36N7O4(4)
Framework group C1[X(C33H36N7O4)]
Deg. of freedom 234
Full point group C1 NOp 1
Largest Abelian subgroup C1 NOp 1
Largest concise Abelian subgroup C1 NOp 1
Standard orientation:

Center Number	Atomic Number	Atomic Type	Coordinates (Angstroms) X	Y	Z
1	6	0	-4.613938	-0.098904	-0.337133
2	6	0	-4.550745	1.273710	-0.443360
3	6	0	-3.324559	1.967580	-0.330861
4	6	0	-2.137145	1.194191	-0.155231
5	6	0	-2.199599	-0.191246	-0.011851
6	6	0	-3.436030	-0.859028	-0.106605
7	1	0	-5.562459	-0.610031	-0.414000
8	1	0	-5.447772	1.863610	-0.597980
9	1	0	-1.309084	-0.770094	0.172440
10	6	0	-2.118327	3.907725	-0.145441
11	7	0	-3.311589	3.325472	-0.360061
12	7	0	-0.945858	3.288828	-0.014267
13	7	0	-0.942975	1.929085	-0.099761
14	6	0	-2.078573	5.392830	-0.061967
15	6	0	-0.865805	6.080467	0.109439
16	6	0	-3.270941	6.127715	-0.152358
17	6	0	-0.849527	7.471134	0.189685
18	1	0	0.057669	5.517310	0.175526
19	6	0	-3.250398	7.519270	-0.072547
20	1	0	-4.204868	5.594355	-0.284639
21	6	0	-2.040927	8.196226	0.099126
22	1	0	0.095021	7.990595	0.321580
23	1	0	-4.180454	8.075501	-0.143609
24	1	0	-2.025822	9.280359	0.161427
25	6	0	0.357382	1.350416	-0.069952
26	6	0	1.325463	1.891006	0.787626
27	6	0	0.704067	0.294999	-0.924594
28	6	0	2.610571	1.370150	0.810455
29	1	0	1.058473	2.716419	1.435847
30	6	0	1.993399	-0.220076	-0.910809
31	1	0	-0.022408	-0.113089	-1.616584
32	6	0	2.973041	0.301842	-0.039380
33	1	0	3.342803	1.775250	1.494104
34	1	0	2.258328	-1.017670	-1.589804
35	6	0	4.326583	-0.243500	-0.021118
36	6	0	6.213617	-1.603799	-0.538770
37	6	0	6.617258	-0.562790	0.553463
38	7	0	4.873536	-1.056377	-0.968901
39	7	0	5.261601	-0.026227	0.946782
40	8	0	5.124874	0.655268	2.018325
41	8	0	4.328730	-1.463530	-2.049971
42	6	0	7.411102	0.640903	0.014041
43	1	0	7.467291	1.400431	0.797293
44	1	0	8.427287	0.343758	-0.255589
45	1	0	6.932279	1.085465	-0.862213
46	6	0	7.315058	-1.139150	1.784583
47	1	0	8.284903	-1.554418	1.497706
48	1	0	7.481020	-0.342714	2.511598
49	1	0	6.727867	-1.921841	2.266613
50	6	0	7.145627	-1.681741	-1.747113
51	1	0	8.126705	-2.046946	-1.431575
52	1	0	6.734204	-2.381072	-2.476487
53	1	0	7.272556	-0.715528	-2.237061
54	6	0	5.940494	-3.017416	0.006063
55	1	0	5.469611	-3.608795	-0.782633
56	1	0	6.873433	-3.506008	0.296843
57	1	0	5.270040	-2.999825	0.869049
58	6	0	-3.500979	-2.306389	0.023577
59	6	0	-2.877705	-4.606438	-0.081168
60	6	0	-4.317462	-4.493837	0.512384
61	8	0	-5.825862	-2.611820	0.357928
62	8	0	-1.213483	-2.858998	-0.233737
63	7	0	-4.632302	-3.045231	0.223337
64	7	0	-2.439622	-3.162189	-0.037618
65	6	0	-5.372074	-5.384036	-0.144671
66	1	0	-5.138554	-6.435243	0.044035
67	1	0	-6.348780	-5.163620	0.288922
68	1	0	-5.435358	-5.227511	-1.222312
69	6	0	-4.382454	-4.645136	2.043008
70	1	0	-5.378711	-4.349983	2.379914
71	1	0	-4.209634	-5.683392	2.335517
72	1	0	-3.647555	-4.012073	2.546723
73	6	0	-2.836508	-5.019608	-1.563496
74	1	0	-1.821348	-4.870457	-1.938166
75	1	0	-3.097783	-6.074323	-1.676684
76	1	0	-3.519167	-4.421832	-2.172796
77	6	0	-1.899013	-5.460503	0.724617
78	1	0	-2.225583	-6.503841	0.716023
79	1	0	-0.910580	-5.404076	0.266013
80	1	0	-1.812894	-5.128955	1.760192

Rotational constants (GHZ): 0.0643226 0.0491959 0.0293388
Standard basis: 6-31G(d,p) (6D, 7F)
SCF Done: E(UB3LYP) = -1963.17279590 A.U. after 2 cycles
NFock= 2 Conv=0.72D-08 -V/T= 2.0094
<Sx>= 0.0000 <Sy>= 0.0000 <Sz>= 1.5000 <S**2>= 3.8922 S= 1.5352
<L.S>= 0.00000000000
Annihilation of the first spin contaminant:
S**2 before annihilation 3.8922, after 3.7578

Item	Value	Threshold	Converged?
Maximum Force	0.000000	0.000015	YES
RMS Force	0.000000	0.000010	YES
Maximum Displacement	0.000045	0.000060	YES

RMS Displacement 0.000008 0.000040 YES
Predicted change in Energy=-4.986151D-12
Optimization completed.
-- Stationary point found.

Triradical, broken symmetry doublet state (BSdoublet1, 1st excited state, the lowest energy) at UB3LYP/6-31G(d,p) in tetrahydrofuran

Stoichiometry C33H36N7O4(2)
Framework group C1[X(C33H36N7O4)]
Deg. of freedom 234
Full point group C1 NOp 1
Largest Abelian subgroup C1 NOp 1
Largest concise Abelian subgroup C1 NOp 1
Standard orientation:

Center Number	Atomic Number	Atomic Type	Coordinates (Angstroms) X	Y	Z
1	6	0	-4.612062	-0.198401	-0.247837
2	6	0	-4.589072	1.177143	-0.338079
3	6	0	-3.378588	1.902024	-0.263868
4	6	0	-2.166273	1.158466	-0.133405
5	6	0	-2.185248	-0.230248	-0.014805
6	6	0	-3.406787	-0.930201	-0.075743
7	1	0	-5.549120	-0.733467	-0.296538
8	1	0	-5.506589	1.744055	-0.453401
9	1	0	-1.272332	-0.786720	0.123648
10	6	0	-2.212810	3.873768	-0.129740
11	7	0	-3.399672	3.260285	-0.291335
12	7	0	-1.022323	3.283931	-0.030937
13	7	0	-0.993104	1.923873	-0.101133
14	6	0	-2.205395	5.360270	-0.066400
15	6	0	-1.004017	6.077711	0.056844
16	6	0	-3.416660	6.066575	-0.128031
17	6	0	-1.017498	7.469343	0.118235
18	1	0	-0.066153	5.536581	0.101073
19	6	0	-3.425925	7.459229	-0.067144
20	1	0	-4.341601	5.510311	-0.223368
21	6	0	-2.227679	8.165879	0.056570
22	1	0	-0.081531	8.011946	0.212935
23	1	0	-4.370461	7.993050	-0.115627
24	1	0	-2.235752	9.250835	0.104116
25	6	0	0.324243	1.371682	-0.074356
26	6	0	1.255816	1.876889	0.839451
27	6	0	0.708188	0.378567	-0.982224
28	6	0	2.552049	1.379679	0.862188
29	1	0	0.955781	2.657060	1.528556
30	6	0	2.006959	-0.116438	-0.964818
31	1	0	0.002178	0.000459	-1.712028
32	6	0	2.951117	0.371228	-0.039301
33	1	0	3.260868	1.755579	1.586297
34	1	0	2.304266	-0.869010	-1.681117
35	6	0	4.316551	-0.154239	-0.016349
36	6	0	6.248523	-1.422648	-0.589161
37	6	0	6.580862	-0.504360	0.631176
38	7	0	4.916195	-0.853842	-1.017532
39	7	0	5.199381	-0.025918	1.010926
40	8	0	4.999411	0.540678	2.138091
41	8	0	4.422690	-1.152096	-2.157216
42	6	0	7.383235	0.759066	0.271297
43	1	0	7.384422	1.427764	1.135168
44	1	0	8.417243	0.503590	0.028026
45	1	0	6.945340	1.292899	-0.575972
46	6	0	7.222630	-1.206226	1.827349
47	1	0	8.213473	-1.575762	1.550025
48	1	0	7.335722	-0.493162	2.645406
49	1	0	6.624529	-2.044147	2.187842
50	6	0	7.232729	-1.348069	-1.755767
51	1	0	8.205289	-1.737523	-1.443174
52	1	0	6.862694	-1.961274	-2.578859
53	1	0	7.365003	-0.329859	-2.123845
54	6	0	5.983181	-2.893202	-0.219440
55	1	0	5.565176	-3.401239	-1.091568
56	1	0	6.912470	-3.393873	0.062352
57	1	0	5.271690	-2.984586	0.605145
58	6	0	-3.428625	-2.380927	0.028254
59	6	0	-2.746008	-4.660486	-0.140649
60	6	0	-4.170832	-4.600036	0.494629
61	8	0	-5.734490	-2.759452	0.419089
62	8	0	-1.134278	-2.866062	-0.299903
63	7	0	-4.533188	-3.155460	0.243954
64	7	0	-2.346304	-3.206014	-0.078424
65	6	0	-5.218330	-5.506499	-0.151636
66	1	0	-4.948584	-6.554205	0.005677
67	1	0	-6.187754	-5.325407	0.315200
68	1	0	-5.318223	-5.327968	-1.223065
69	6	0	-4.188767	-4.783977	2.022988
70	1	0	-5.182585	-4.522379	2.393243
71	1	0	-3.980966	-5.823074	2.288681
72	1	0	-3.456776	-4.142137	2.519803
73	6	0	-2.735745	-5.041819	-1.631997
74	1	0	-1.736419	-4.855660	-2.031828
75	1	0	-2.970012	-6.101138	-1.760146
76	1	0	-3.452426	-4.451825	-2.208955
77	6	0	-1.722414	-5.503789	0.619346
78	1	0	-2.023407	-6.554685	0.601276
79	1	0	-0.749950	-5.414693	0.132630
80	1	0	-1.613157	-5.188573	1.657827

Rotational constants (GHZ): 0.0640784 0.0494449 0.0294719
Standard basis: 6-31G(d,p) (6D, 7F)
SCF Done: E(UB3LYP) = -1963.17175232 a.u. after 2 cycles
Convg = 0.8527D-09 20 Fock formations.
S**2 = 1.8797 -V/T = 2.0094
<Sx>= 0.0000 <Sy>= 0.0000 <Sz>= 0.5000 <S**2>= 1.8797 S= 0.9593
<L.S>= 0.00000000000
Annihilation of the first spin contaminant:
S**2 before annihilation 1.8797, after 1.2217

Item	Value	Threshold	Converged?

Maximum Force	0.000000	0.000015	YES
RMS Force	0.000000	0.000010	YES
Maximum Displacement	0.000019	0.000060	YES
RMS Displacement	0.000003	0.000040	YES

Predicted change in Energy=-2.023398D-12
Optimization completed.
-- Stationary point found.

Triradical, broken symmetry doublet state (BSdoublet2, 2nd excited state) at UB3LYP/6-31G(d,p) in tetrahydrofuran

Stoichiometry C33H36N7O4(2)
Framework group C1[X(C33H36N7O4)]
Deg. of freedom 234
Full point group C1 NOp 1
Largest Abelian subgroup C1 NOp 1
Largest concise Abelian subgroup C1 NOp 1
Standard orientation:

Center Number	Atomic Number	Atomic Type	Coordinates (Angstroms) X	Y	Z
1	6	0	-4.611678	-0.139668	-0.353191
2	6	0	-4.560724	1.237198	-0.457633
3	6	0	-3.344934	1.940096	-0.340825
4	6	0	-2.153142	1.183602	-0.156737
5	6	0	-2.202195	-0.206259	-0.010814
6	6	0	-3.428641	-0.881770	-0.114728
7	1	0	-5.554893	-0.660212	-0.433144
8	1	0	-5.463344	1.817648	-0.615775
9	1	0	-1.306435	-0.775435	0.179793
10	6	0	-2.160507	3.893650	-0.148397
11	7	0	-3.341401	3.307516	-0.373682
12	7	0	-0.976984	3.284146	-0.006080
13	7	0	-0.964955	1.924690	-0.092667
14	6	0	-2.126699	5.379512	-0.064390
15	6	0	-0.917260	6.072201	0.108667
16	6	0	-3.322344	6.108969	-0.155903
17	6	0	-0.907366	7.463157	0.189700
18	1	0	0.008593	5.513166	0.175101
19	6	0	-3.308318	7.500302	-0.075612
20	1	0	-4.253368	5.570797	-0.289320
21	6	0	-2.101809	8.182593	0.097944
22	1	0	0.034624	7.986900	0.322861
23	1	0	-4.240686	8.052528	-0.147462
24	1	0	-2.091781	9.266765	0.160762
25	6	0	0.339032	1.354281	-0.063764
26	6	0	1.303214	1.901003	0.794484
27	6	0	0.692753	0.302622	-0.920329
28	6	0	2.591460	1.388352	0.817267
29	1	0	1.030197	2.723855	1.443395
30	6	0	1.985470	-0.203937	-0.906474
31	1	0	-0.030309	-0.109336	-1.613588
32	6	0	2.961194	0.323458	-0.033983
33	1	0	3.320833	1.797319	1.501661
34	1	0	2.255918	-0.998738	-1.586553
35	6	0	4.318362	-0.212534	-0.016241
36	6	0	6.215154	-1.558460	-0.536103
37	6	0	6.610813	-0.517541	0.559222
38	7	0	4.871472	-1.019348	-0.965690
39	7	0	5.251209	0.008828	0.952847
40	8	0	5.108874	0.686468	2.026022
41	8	0	4.330184	-1.427289	-2.048119
42	6	0	7.396816	0.692997	0.023687
43	1	0	7.447018	1.450809	0.809004
44	1	0	8.415281	0.403591	-0.245750
45	1	0	6.915739	1.136534	-0.851842
46	6	0	7.311407	-1.092321	1.789495
47	1	0	8.284243	-1.500379	1.502432
48	1	0	7.471451	-0.296605	2.518624
49	1	0	6.729032	-1.880100	2.269075
50	6	0	7.148343	-1.626649	-1.744123
51	1	0	8.131549	-1.986617	-1.429189
52	1	0	6.741759	-2.326321	-2.475882
53	1	0	7.269350	-0.658133	-2.231011
54	6	0	5.951591	-2.975410	0.004759
55	1	0	5.485462	-3.568018	-0.785835
56	1	0	6.887768	-3.458133	0.294911
57	1	0	5.280458	-2.964873	0.867330
58	6	0	-3.472504	-2.337742	0.020651
59	6	0	-2.834483	-4.627706	-0.115712
60	6	0	-4.248080	-4.527682	0.543150
61	8	0	-5.769987	-2.647892	0.480831
62	8	0	-1.199563	-2.860333	-0.362551
63	7	0	-4.584010	-3.078274	0.281805
64	7	0	-2.410085	-3.178061	-0.102772
65	6	0	-5.326511	-5.417703	-0.074748
66	1	0	-5.079691	-6.469293	0.093613
67	1	0	-6.283871	-5.205955	0.404022
68	1	0	-5.438589	-5.251797	-1.146975
69	6	0	-4.246333	-4.693189	2.073577
70	1	0	-5.229058	-4.407184	2.455105
71	1	0	-4.055397	-5.733113	2.348417
72	1	0	-3.494613	-4.060253	2.551879
73	6	0	-2.854462	-5.050602	-1.595668
74	1	0	-1.858568	-4.892898	-2.015699
75	1	0	-3.108484	-6.108948	-1.689942
76	1	0	-3.569918	-4.464750	-2.178228
77	6	0	-1.809919	-5.464780	0.650116
78	1	0	-2.125664	-6.511365	0.665488
79	1	0	-0.844747	-5.402239	0.145087
80	1	0	-1.678830	-5.123534	1.677782

Rotational constants (GHZ): 0.0642455 0.0493758 0.0294099
Standard basis: 6-31G(d,p) (6D, 7F)
SCF Done: E(UB3LYP) = -1963.17038415 A.U. after 4 cycles
NFock= 4 Conv=0.16D-08 -V/T= 2.0094
<Sx>= 0.0000 <Sy>= 0.0000 <Sz>= 0.5000 <S**2>= 1.8773 S= 0.9585
<L.S>= 0.00000000000

Annihilation of the first spin contaminant:
S**2 before annihilation 1.8773, after 1.2127

Item	Value	Threshold	Converged?
Maximum Force	0.000001	0.000015	YES
RMS Force	0.000000	0.000010	YES
Maximum Displacement	0.000039	0.000060	YES
RMS Displacement	0.000009	0.000040	YES

Predicted change in Energy=-4.396556D-12
Optimization completed.
-- Stationary point found.

Triradical quartet state at UB3LYP/6-31G(d,p) in ethanol

Stoichiometry C33H36N7O4(4)
Framework group C1[X(C33H36N7O4)]
Deg. of freedom 234
Full point group C1 NOp 1
Largest Abelian subgroup C1 NOp 1
Largest concise Abelian subgroup C1 NOp 1
Standard orientation:

Center Number	Atomic Number	Atomic Type	Coordinates (Angstroms) X	Y	Z
1	6	0	-4.608084	-0.160998	-0.329543
2	6	0	-4.567935	1.213100	-0.431959
3	6	0	-3.352504	1.926037	-0.324311
4	6	0	-2.152231	1.171221	-0.157991
5	6	0	-2.190897	-0.215704	-0.020836
6	6	0	-3.416876	-0.902672	-0.109079
7	1	0	-5.548906	-0.686662	-0.402525
8	1	0	-5.475758	1.787998	-0.580064
9	1	0	-1.289335	-0.780289	0.153809
10	6	0	-2.174567	3.884837	-0.141750
11	7	0	-3.360178	3.284700	-0.349989
12	7	0	-0.992041	3.283475	-0.017264
13	7	0	-0.970051	1.924222	-0.104471
14	6	0	-2.156086	5.370548	-0.057578
15	6	0	-0.952729	6.075681	0.110824
16	6	0	-3.358947	6.088881	-0.144389
17	6	0	-0.955931	7.466554	0.191249
18	1	0	-0.020690	5.526561	0.175043
19	6	0	-3.358065	7.480705	-0.064415
20	1	0	-4.286180	5.543401	-0.274060
21	6	0	-2.157791	8.174828	0.104021
22	1	0	-0.018516	7.999226	0.320878
23	1	0	-4.296130	8.023566	-0.132809
24	1	0	-2.157890	9.258991	0.166442
25	6	0	0.338326	1.362541	-0.075523
26	6	0	1.290359	1.894439	0.804654
27	6	0	0.704152	0.332207	-0.952241
28	6	0	2.580867	1.386091	0.828913
29	1	0	1.007324	2.701340	1.469340
30	6	0	1.999605	0.168008	-0.937980
31	1	0	-0.012519	-0.066432	-1.660022
32	6	0	2.962190	0.343190	-0.042581
33	1	0	3.301466	1.781580	1.530616
34	1	0	2.281455	-0.944941	-1.634280
35	6	0	4.321065	-0.189371	-0.020704
36	6	0	6.242139	-1.482120	-0.583587
37	6	0	6.591706	-0.537481	0.612484
38	7	0	4.907162	-0.918344	-1.010244
39	7	0	5.217073	-0.041136	0.993909
40	8	0	5.029117	0.551399	2.109885
41	8	0	4.398964	-1.239385	-2.137442
42	6	0	7.399458	0.711561	0.216186
43	1	0	7.415985	1.398988	1.065118
44	1	0	8.428573	0.442261	-0.032310
45	1	0	6.956550	1.230304	-0.637770
46	6	0	7.239898	-1.216837	1.818292
47	1	0	8.223558	-1.603218	1.538959
48	1	0	7.370511	-0.485339	2.617286
49	1	0	6.637545	-2.039720	2.205443
50	6	0	7.214278	-1.436311	-1.761845
51	1	0	8.190307	-1.816220	-1.448875
52	1	0	6.837813	-2.071759	-2.564963
53	1	0	7.341407	-0.427614	-2.157004
54	6	0	5.976962	-2.943171	-0.178198
55	1	0	5.549148	-3.469810	-1.034410
56	1	0	6.908248	-3.439324	0.104560
57	1	0	5.274071	-3.014590	0.655626
58	6	0	-3.457686	-2.351466	0.018541
59	6	0	-2.802704	-4.641795	-0.104374
60	6	0	-4.232125	-4.551809	0.518679
61	8	0	-5.768634	-2.687920	0.406243
62	8	0	-1.169008	-2.867182	-0.290147
63	7	0	-4.573115	-3.106309	0.242433
64	7	0	-2.385681	-3.190809	-0.068184
65	6	0	-5.286376	-5.454476	-0.121875
66	1	0	-5.030679	-6.502708	0.053192
67	1	0	-6.256644	-5.255117	0.335784
68	1	0	-5.376212	-5.290945	-1.196591
69	6	0	-4.264503	-4.711144	2.049505
70	1	0	-5.258365	-4.433406	2.407683
71	1	0	-4.070723	-5.748260	2.332382
72	1	0	-3.529360	-4.069911	2.542344
73	6	0	-2.785924	-5.053264	-1.587582
74	1	0	-1.780588	-4.891078	-1.982785
75	1	0	-3.035310	-6.111269	-1.695528
76	1	0	-3.488781	-4.464556	-2.182505
77	6	0	-1.795504	-5.481767	0.680894
78	1	0	-2.109377	-6.528876	0.681532
79	1	0	-0.818441	-5.415222	0.199725
80	1	0	-1.690500	-5.146989	1.713689

Rotational constants (GHZ): 0.0642037 0.0493058 0.0294331
Standard basis: 6-31G(d,p) (6D, 7F)
SCF Done: E(UB3LYP) = -1963.17587157 A.U. after 4 cycles
NFock= 4 Conv=0.18D-08 -V/T= 2.0094
<Sx>= 0.0000 <Sy>= 0.0000 <Sz>= 1.5000 <S**2>= 3.8898 S= 1.5346

<L.S>= 0.00000000000
Annihilation of the first spin contaminant:
S**2 before annihilation 3.8898, after 3.7576

Item	Value	Threshold	Converged?
Maximum Force	0.000000	0.000015	YES
RMS Force	0.000000	0.000010	YES
Maximum Displacement	0.000049	0.000060	YES
RMS Displacement	0.000009	0.000040	YES

Predicted change in Energy=-3.425909D-12
Optimization completed.
-- Stationary point found.

Triradical, broken symmetry doublet state (BSdoublet1, 1st excited state, the lowest energy) at UB3LYP/6-31G(d,p) in ethanol

Stoichiometry C33H36N7O4(2)
Framework group C1[X(C33H36N7O4)]
Deg. of freedom 234
Full point group C1 NOp 1
Largest Abelian subgroup C1 NOp 1
Largest concise Abelian subgroup C1 NOp 1
Standard orientation:

Center Number	Atomic Number	Atomic Type	Coordinates (Angstroms) X	Y	Z
1	6	0	-4.611244	-0.200950	-0.251389
2	6	0	-4.589177	1.174793	-0.342126
3	6	0	-3.379244	1.900153	-0.265358
4	6	0	-2.166798	1.157623	-0.132578
5	6	0	-2.185292	-0.231127	-0.013285
6	6	0	-3.406003	-0.931413	-0.076108
7	1	0	-5.547937	-0.736422	-0.302772
8	1	0	-5.507155	1.740396	-0.460452
9	1	0	-1.272172	-0.786878	0.126222
10	6	0	-2.214210	3.872838	-0.130421
11	7	0	-3.400617	3.258924	-0.293129
12	7	0	-1.023549	3.283276	-0.030685
13	7	0	-0.994048	1.923169	-0.099301
14	6	0	-2.207033	5.359585	-0.067003
15	6	0	-1.005747	6.077354	0.057403
16	6	0	-3.418224	6.066354	-0.129221
17	6	0	-1.019141	7.469102	0.118935
18	1	0	-0.067442	5.537103	0.102950
19	6	0	-3.427574	7.459123	-0.068077
20	1	0	-4.343822	5.511237	-0.224998
21	6	0	-2.229312	8.165813	0.056515
22	1	0	-0.083233	8.011525	0.214599
23	1	0	-4.372062	7.992887	-0.116984
24	1	0	-2.237370	9.250692	0.104272
25	6	0	0.323204	1.370758	-0.071536
26	6	0	1.253648	1.874026	0.844552
27	6	0	0.707792	0.379386	-0.981196
28	6	0	2.549982	1.376713	0.867206
29	1	0	0.953246	2.652381	1.535555
30	6	0	2.006588	-0.115880	-0.963006
31	1	0	0.002604	0.003418	-1.712914
32	6	0	2.949748	0.370089	-0.035736
33	1	0	3.258185	1.752111	1.592216
34	1	0	2.304536	-0.866976	-1.680651
35	6	0	4.315620	-0.154581	-0.013057
36	6	0	6.253135	-1.410095	-0.595487
37	6	0	6.577180	-0.509627	0.640979
38	7	0	4.921053	-0.837840	-1.021287
39	7	0	5.192189	-0.040440	1.020689
40	8	0	4.981748	0.505931	2.156151
41	8	0	4.432542	-1.116837	-2.168308
42	6	0	7.378414	0.760757	0.304018
43	1	0	7.377137	1.415567	1.178490
44	1	0	8.413154	0.509823	0.059767
45	1	0	6.942403	1.307667	-0.535822
46	6	0	7.214621	-1.228831	1.829013
47	1	0	8.206511	-1.593469	1.549588
48	1	0	7.325380	-0.527820	2.657787
49	1	0	6.615817	-2.072516	2.174606
50	6	0	7.242973	-1.314271	-1.755715
51	1	0	8.215382	-1.703791	-1.443295
52	1	0	6.880864	-1.918173	-2.589198
53	1	0	7.372766	-0.290258	-2.108319
54	6	0	5.990576	-2.886848	-0.249403
55	1	0	5.580937	-3.384082	-1.131689
56	1	0	6.920193	-3.387488	0.030950
57	1	0	5.274225	-2.993388	0.569116
58	6	0	-3.426832	-2.382435	0.027789
59	6	0	-2.749233	-4.662114	-0.156906
60	6	0	-4.163605	-4.601577	0.502818
61	8	0	-5.723316	-2.754492	0.467347
62	8	0	-1.140358	-2.865890	-0.345537
63	7	0	-4.527550	-3.154955	0.264831
64	7	0	-2.347712	-3.207523	-0.101051
65	6	0	-5.222807	-5.503621	-0.130517
66	1	0	-4.949180	-6.551990	0.014109
67	1	0	-6.183341	-5.327656	0.356328
68	1	0	-5.342595	-5.317387	-1.198593
69	6	0	-4.156483	-4.792926	2.030264
70	1	0	-5.144017	-4.533096	2.418167
71	1	0	-3.945491	-5.833665	2.286358
72	1	0	-3.415932	-4.154468	2.518593
73	6	0	-2.764750	-5.042936	-1.648327
74	1	0	-1.771647	-4.860050	-2.064846
75	1	0	-3.003889	-6.101574	-1.771986
76	1	0	-3.489368	-4.451150	-2.213335
77	6	0	-1.713668	-5.506391	0.585614
78	1	0	-2.017485	-6.556404	0.574493
79	1	0	-0.750198	-5.421139	0.080553
80	1	0	-1.584925	-5.190013	1.621516

Rotational constants (GHZ): 0.0640584 0.0494426 0.0294859
Standard basis: 6-31G(d,p) (6D, 7F)

SCF Done: E(UB3LYP) = -1963.17485098 a.u. after 2 cycles
Convg = 0.8166D-09 20 Fock formations.
S**2 = 1.8784 -V/T = 2.0094
<Sx>= 0.0000 <Sy>= 0.0000 <Sz>= 0.5000 <S**2>= 1.8784 S= 0.9589
<L.S>= 0.00000000000
Annihilation of the first spin contaminant:
S**2 before annihilation 1.8784, after 1.2166

Item	Value	Threshold	Converged?
Maximum Force	0.000000	0.000015	YES
RMS Force	0.000000	0.000010	YES
Maximum Displacement	0.000015	0.000060	YES
RMS Displacement	0.000003	0.000040	YES

Predicted change in Energy=-2.381586D-12
Optimization completed.
-- Stationary point found.

Triradical, broken symmetry doublet state (BSdoublet2, 2nd excited state) at UB3LYP/6-31G(d,p) in ethanol

Stoichiometry C33H36N7O4(2)
Framework group C1[X(C33H36N7O4)]
Deg. of freedom 234
Full point group C1 NOp 1
Largest Abelian subgroup C1 NOp 1
Largest concise Abelian subgroup C1 NOp 1
Standard orientation:

Center Number	Atomic Number	Atomic Type	Coordinates (Angstroms) X	Y	Z
1	6	0	-4.605868	-0.201425	-0.346712
2	6	0	-4.577700	1.176695	-0.447096
3	6	0	-3.372596	1.898230	-0.334082
4	6	0	-2.168310	1.160116	-0.158196
5	6	0	-2.194013	-0.230930	-0.018377
6	6	0	-3.410002	-0.925081	-0.117270
7	1	0	-5.541250	-0.736403	-0.423822
8	1	0	-5.490663	1.742366	-0.599449
9	1	0	-1.287662	-0.785966	0.163698
10	6	0	-2.216139	3.869859	-0.144558
11	7	0	-3.389557	3.286157	-0.363662
12	7	0	-1.022949	3.277819	-0.008289
13	7	0	-0.992090	1.918903	-0.095676
14	6	0	-2.203281	5.356283	-0.060650
15	6	0	-1.002768	6.066367	0.105711
16	6	0	-3.409489	6.069255	-0.145695
17	6	0	-1.011943	7.457485	0.186074
18	1	0	-0.068305	5.521320	0.167978
19	6	0	-3.414715	7.460813	-0.066016
20	1	0	-4.334225	5.519105	-0.273615
21	6	0	-2.216916	8.160168	0.100553
22	1	0	-0.076706	7.994357	0.313990
23	1	0	-4.355156	7.999718	-0.132874
24	1	0	-2.221771	9.244338	0.162824
25	6	0	0.319758	1.365354	-0.067447
26	6	0	1.268736	1.904847	0.811557
27	6	0	0.691736	0.337201	-0.944291
28	6	0	2.562365	1.404897	0.835504
29	1	0	0.980437	2.710280	1.475692
30	6	0	1.990536	-0.154261	-0.930304
31	1	0	-0.022150	-0.066651	-1.651892
32	6	0	2.950201	0.364014	-0.035850
33	1	0	3.280771	1.805633	1.536441
34	1	0	2.277186	-0.929517	-1.626467
35	6	0	4.312722	-0.158946	-0.015109
36	6	0	6.241760	-1.439912	-0.578097
37	6	0	6.586934	-0.489724	0.614794
38	7	0	4.902170	-0.886473	-1.003871
39	7	0	5.209593	-0.001901	0.997513
40	8	0	5.019657	0.592042	2.112320
41	8	0	4.394377	-1.213972	-2.129305
42	6	0	7.385088	0.763912	0.213585
43	1	0	7.398590	1.453648	1.060691
44	1	0	8.415517	0.501147	-0.036411
45	1	0	6.936750	1.277282	-0.640779
46	6	0	7.242094	-1.161326	1.821163
47	1	0	8.227744	-1.541894	1.540885
48	1	0	7.369418	-0.426740	2.617846
49	1	0	6.646059	-1.987155	2.211791
50	6	0	7.211642	-1.390562	-1.758077
51	1	0	8.190953	-1.762163	-1.445349
52	1	0	6.838784	-2.031334	-2.558639
53	1	0	7.330669	-0.382190	-2.156572
54	6	0	5.987257	-2.901661	-0.168415
55	1	0	5.561340	-3.433377	-1.022431
56	1	0	6.922466	-3.390733	0.113717
57	1	0	5.286508	-2.975713	0.666983
58	6	0	-3.429767	-2.381918	0.015188
59	6	0	-2.762147	-4.661974	-0.141309
60	6	0	-4.161457	-4.583493	0.551594
61	8	0	-5.708728	-2.721349	0.535386
62	8	0	-1.160591	-2.867856	-0.426558
63	7	0	-4.523359	-3.137685	0.303705
64	7	0	-2.358987	-3.205936	-0.136991
65	6	0	-5.241092	-5.486872	-0.044452
66	1	0	-4.972533	-6.535034	0.110541
67	1	0	-6.189050	-5.295117	0.460812
68	1	0	-5.383230	-5.316179	-1.112366
69	6	0	-4.120823	-4.754549	2.080829
70	1	0	-5.098500	-4.485462	2.486883
71	1	0	-3.908110	-5.792675	2.345876
72	1	0	-3.367473	-4.112524	2.544142
73	6	0	-2.811479	-5.084000	-1.620812
74	1	0	-1.827822	-4.913684	-2.064151
75	1	0	-3.053565	-6.145484	-1.709458
76	1	0	-3.548102	-4.507434	-2.185902
77	6	0	-1.707952	-5.484764	0.599410
78	1	0	-2.010653	-6.534878	0.624406
79	1	0	-0.756925	-5.412482	0.069342
80	1	0	-1.555041	-5.140093	1.622921

Rotational constants (GHZ): 0.0641368 0.0494817 0.0295031
Standard basis: 6-31G(d,p) (6D, 7F)

```
SCF Done:  E(UB3LYP) =  -1963.17351951     a.u. after    2 cycles
             Convg  =    0.8070D-09                    21 Fock formations.
           S**2 =   1.8753                  -V/T =   2.0094
 <Sx>= 0.0000 <Sy>= 0.0000 <Sz>= 0.5000 <S**2>= 1.8753 S= 0.9579
 <L.S>=   0.00000000000
 Annihilation of the first spin contaminant:
 S**2 before annihilation     1.8753,    after      1.2050
Item                 Value     Threshold  Converged?
 Maximum Force            0.000000     0.000015     YES
 RMS     Force            0.000000     0.000010     YES
 Maximum Displacement     0.000057     0.000060     YES
 RMS     Displacement     0.000009     0.000040     YES
 Predicted change in Energy=-1.664481D-11
 Optimization completed.
    -- Stationary point found.
```

6. Supporting References

S1. Tanimoto, R.; Suzuki, S.; Kozaki, M.; Okada, K. Nitronyl Nitroxide as a Coupling Partner: Pd-Mediated Cross-coupling of (Nitronyl nitroxide-2-ido)(triphenylphosphine)gold(I) with Aryl Halides. *Chem. Lett.* **2014**, *43*, 678–680.

S2. Suzuki, S.; Nakamura, F.; Naota, T. Environmentally Benign Strategy for Arylation of Nitronyl Nitroxide Using a Non-Transition Metal Nucleophile. *Org. Lett.* **2020**, *22*, 1350−1354.

S3. Bi, W.; Wang, F.; Bi, Y.; Wang, T.; Xue, P.; Zhang, Y.; Gao, X.; Liu, S.; Wang, Z.; Li, M.; Baudy-Floc'h, M.; Robinson, S. C.; Ngerebara, N.; Bi, L. Renal ischemia/reperfusion injury in rats is attenuated by a synthetic glycine derivative. *Eur. J. Pharmacology*, **2009**, *616*, 256–264.

S4. (a) Boocock, D. G. B.; Darcy, R.; Ullman, E. F. Studies of free radicals. II. Chemical properties of nitronylnitroxides. A unique radical anion. *J. Am. Chem. Soc.* **1968**, *90*, 5945–5946. (b) Tretyakov, E. V.; Utepova, I. A.; Varaksin, M. V.; Tolstikov, S. E.; Romanenko, G. V.; Bogomyakov, A. S.; Stass, D. V.; Ovcharenko, V. I.; Chupakhin, O. N. New approach to synthesis of nitronyl and imino nitroxides based on S_NH methodology. *Arkivoc* **2011**, 76–98.

DOI: http://dx.doi.org/10.3998/ark.5550190.0012.806 (c) Chupakhin, O. N.; Utepova, I. A.; Varaksin, M. V.; Tretyakov, E. V.; Romanenko, G. V.; Stass, D. V.; Ovcharenko, V. I. S_N^H Approach in the Synthesis of Nitronyl Nitroxides. *J. Org. Chem*. **2009**, *74*, 2870–2872.

S5. Gallagher, N. M.; Bauer, J. J.; Pink, M.; Rajca, S.; Rajca, A. High Spin Organic Diradical with Robust Stability. *J. Am. Chem. Soc.* **2016**, *138*, 9377–9380.

S6. Rajca, A.; Mukherjee, S.; Pink, M.; Rajca, S.; Das, K. 1,3-Alternate Calix[4]arene Nitronyl Nitroxide Tetraradical and Diradical: Synthesis, X-ray Crystallography, Paramagnetic NMR Spectroscopy, EPR Spectroscopy, and Magnetic Studies. *Tetrahedron* **2007**, *63*, 10731–10742.

S7. Bodzioch, A.; Zheng, M.; Kaszyński, P.; Utecht, G. Functional Group Transformations in Derivatives of 1,4-Dihydrobenzo[1,2,4]triazinyl Radical. *J. Org. Chem.* **2014**, 79, 7294– 7310

S8. http://chemmatcars.uchicago.edu/

S9. http://www.iumsc.indiana.edu/projects/SCrAPS/index.html

S10. SAINT, Bruker Analytical X-Ray Systems, Madison, WI, **2018**.

S11. SADABS v. 2018.1, Bruker AXS, Madison, WI, **2018**.

S12. Sheldrick, G. M. A short history of *SHELX*. *Acta Cryst*. *A* **2008**, *64*, 112 – 122.

S13. Wang, Y.; Zhang, H.; Pink, M.; Olankitwanit, A.; Rajca, S.; Rajca, A. Radical Cation and Neutral Radical of Aza-thia[7]helicene with SOMO−HOMO Energy Level Inversion. *J. Am. Chem. Soc.* **2016**, *138*, 7298–7304.

S14. Olankitwanit, A.; Rajca, S.; Rajca, A. Aza-*m*-Xylylene Diradical with Increased Steric Protection of the Aminyl Radicals. *J. Org. Chem.* **2015**, *80*, 5035–5044.

S15. Miyasaka, M.; Pink, M.; Olankitwanit, A.; Rajca, S.; Rajca, A. Band Gap of Carbon-Sulfur [*n*]Helicenes. *Org. Lett.* **2012**, *14*, 3076–3079.

S16. Shu, C.; Zhang, H.; Olankitwanit, A.; Rajca, S.; Rajca, A. High-Spin Diradical Dication of Chiral π-Conjugated Double Helical Molecule. *J. Am. Chem. Soc.* **2019**, *141*, 17287–17294.

S17. Gennett, T.; Milner, D. F.; Weaver, M. J. Role of solvent reorganization dynamics in electron-transfer processes. Theory-experiment comparisons for electrochemical and homogeneous electron exchange involving metallocene redox couples. *J. Phys. Chem.* **1985**, *89*, 2787–2794.

S18. Connelly, N. G.; Geiger, W. E. Chemical Redox Agents for Organometallic Chemistry. *Chem. Rev.* **1996**, *96*, 877–910.

S19. Osiecki, J. H.; Ullman, E. F. Studies of free radicals. I. .alpha.-Nitronyl nitroxides, a new class of stable radicals. *J. Am. Chem. Soc.* **1968**, *90*, 1078–1079.

S20. Wang, Y.; Olankitwanit, A; Rajca, S.; Rajca, A. Intramolecular Hydrogen Atom Transfer in Aminyl Radical at Room Temperature with Large Kinetic Isotope Effect. *J. Am. Chem. Soc.* **2017**, *139*, 7144–7147.

S21. Stoll, S.; Schweiger, A. EasySpin, a comprehensive software package for spectral simulation and analysis in EPR *J. Magn. Reson.* **2006**, *178*, 42–55.

S22. Rajca, A.; Olankitwanit, A.; Rajca, S. Triplet Ground State Derivative of Aza-*m*-Xylylene Diradical with Large Singlet-Triplet Energy Gap. *J. Am. Chem. Soc.* **2011**, *133*, 4750–4753.

S23. Gallagher, N.; Zhang, H.; Junghoefer, T.; Giangrisostomi, E.; Ovsyannikov, R.; Pink, M.; Rajca, S.; Casu, M. B.; Rajca, A. Thermally and Magnetically Robust Triplet Ground State Diradical. *J. Am. Chem. Soc.* **2019**, *141*, 4764–4774.

S24. Olankitwanit, A.; Pink, M.; Rajca, S.; Rajca, A. Synthesis of Aza-*m*-Xylylene Diradicals with Large Singlet-Triplet Energy Gap and Statistical Analyses of their EPR Spectra. *J. Am. Chem. Soc.* **2014**, *136*, 14277–14288.

S25. M. J. Frisch, G. W. Trucks, H. B. Schlegel, G. E. Scuseria, M. A. Robb, J. R. Cheeseman, G. Scalmani, V. Barone, G. A. Petersson, H. Nakatsuji, X. Li, M. Caricato, A. V. Marenich, J. Bloino, B. G. Janesko, R. Gomperts, B. Mennucci, H. P. Hratchian, J. V. Ortiz, A. F. Izmaylov, J. L. Sonnenberg, D. Williams-Young, F. Ding, F. Lipparini, F. Egidi, J. Goings, B. Peng, A. Petrone, T. Henderson, D. Ranasinghe, V. G. Zakrzewski, J. Gao, N. Rega, G. Zheng, W. Liang, M. Hada, M. Ehara, K. Toyota, R. Fukuda, J. Hasegawa, M. Ishida, T. Nakajima, Y. Honda, O. Kitao, H. Nakai, T. Vreven, K. Throssell, J. A. Montgomery, Jr., J. E. Peralta, F. Ogliaro, M. J. Bearpark, J. J. Heyd, E. N. Brothers, K. N. Kudin, V. N. Staroverov, T. A. Keith, R. Kobayashi, J. Normand, K. Raghavachari, A. P. Rendell, J. C. Burant, S. S. Iyengar, J. Tomasi, M. Cossi, J. M. Millam, M. Klene, C. Adamo, R. Cammi, J. W. Ochterski, R. L. Martin, K. Morokuma, O. Farkas, J. B. Foresman, and D. J. Fox, *Gaussian 16*, Revision A.03 (Gaussian, Inc., Wallingford CT, 2016).

S26. Allouche, A.-R. Gabedit—A graphical user interface for computational chemistry softwares. *J. Comput. Chem.* **2011**, *32*, 174–182.

S27. Yamaguchi, K.; Jensen, F.; Dorigo, A.; Houk, K. N. A Spin Correction Procedure for Unrestricted Hartree–Fock and Møller–Plesset Wavefunctions for Singlet Diradicals and Polyradicals. *Chem. Phys. Lett.* **1988**, *149*, 537–542.

S28. Noodleman, L.; Case, D. A. Density-Functional Theory of Spin Polarization and Spin Coupling in Iron—Sulfur Clusters. *Adv. Inorg. Chem.* **1992**, *38*, 423–470.

S29. Trinquier, G.; Suaud, N.; Malrieu, J.-P. Theoretical Design of High-Spin Polycyclic Hydrocarbons. *Chem.–Eur. J.* **2010**, *16*, 8762–8772.

S30. Quast, H.; Nüdling, W.; Klemm, G.; Kirschfeld, A.; Neuhaus, P.; Sander, W.; Hrovat, D. A.; Borden, W. T. A Perimidine-Derived Non-Kekulé Triplet Diradical *J. Org. Chem.* **2008**, *73*, 4956–4961.

S31. Winter, A. H.; Falvey, D. E.; Cramer, C. J.; Gherman, B. F. Benzylic Cations with Triplet Ground States: Computational Studies of Aryl Carbenium Ions, Silylenium Ions, Nitrenium Ions, and Oxenium Ions Substituted with Meta π Donors. *J. Am. Chem. Soc.* **2007**, *129*, 10113–10119.

S32. Neese, F. The ORCA program system. *Wiley Interdisciplinary Reviews: Comp. Mol. Sci.* **2012**, *2*, 73–78.

S33. Barone, V. in *Recent Advances in Density Functional Methods, Part I*, Ed. D. P. Chong (World Scientific Publ. Co., Singapore, 1996).

S34. Sinnecker, S.; Neese, F. Spin−Spin Contributions to the Zero-Field Splitting Tensor in Organic Triplets, Carbenes and BiradicalsA Density Functional and Ab Initio Study. *J. Phys. Chem. A* **2006**, *110*, 12267–12275.

F. Conducting High-Spin (S = 1) Organic Diradical with Robust Stability

Conducting High-Spin (S = 1) Organic Diradical with Robust Stability

Shuyang Zhang[†], Maren Pink[#], Tobias Junghoefer[§], Wenchao Zhao[⊥], Sheng-Ning Hsu[⊥], Suchada Rajca[†], Bryan W. Boudouris[⊥,‡], Maria Benedetta Casu*[§], and Andrzej Rajca*[†]

[†]Department of Chemistry, University of Nebraska, Lincoln, Nebraska 68588-0304, United States.

[#]IUMSC, Department of Chemistry, Indiana University, Bloomington, Indiana 47405-7102, United States.

[§]Institute of Physical and Theoretical Chemistry, University of Tübingen, 72076 Tübingen, Germany.

[⊥] Charles D. Davidson School of Chemical Engineering and [‡] Department of Chemistry, Purdue University, West Lafayette, IN 47907

ABSTRACT: Triplet ground-state organic molecules are of interest with respect to several emerging technologies but usually show limited stability, especially, as thin films. We report an organic diradical, based entirely on two Blatter radicals, that possesses triplet ground state ($2J/k \approx 220$ K, $\Delta E_{ST} \approx 0.4$ kcal mol^{-1}) and robust stability, with onset of decomposition above 264 °C (TGA). Polycrystalline diradical is a good electrical conductor with conductivity comparable to the out-of-plane conductivity in highly oriented pyrolytic graphite (HOPG). The diradical is evaporated under ultra-high vacuum to form thin films, which are stable on air for at least 18 and 48 h, as demonstrated by X-ray photoelectron and electron paramagnetic resonance (EPR) spectroscopies, respectively.

The recently reported high spin organic diradicals **1** and **2** have attracted a great interest due to their remarkable thermal stability that permits vapor-based growth of thin films under high- or ultra-high vacuum (UHV).[1,2] The design of the diradicals is based on the 1,2,4-benzotriazinyl (Blatter) radical substituted with a nitronyl nitroxide (NN) radical, taking advantage of the Blatter monoradical's high thermal stability and the NN low molecular weights to facilitate evaporation. However, **1** and **2** possess limited stability with onset of decomposition <180 °C (thermogravimetric analysis, TGA), and consequently, the diradical thin films, in particular of **2**, undergo rapid decomposition in air.[2]

We consider a diradical based entirely on the Blatter radical building block, to fully take advantage of its excellent thermal stability.[3,4] A huge challenge is in the design and synthesis of such diradicals. There are a few molecules that formally incorporate two Blatter radicals reported to date, e.g., zwitterionic TetraPhenylHexaazaAnthracene (TPHA), *ortho*-DiBlatterTrimethylenemethane (*o*-DBT) or Chichibabin-type diradicaloid **3**.[5,6] These molecules exclusively possess low-spin (S = 0) ground states. This is not surprising. According to the Ovchinnikov parity models, TPHA, **3**, and its biphenyl isomers are predicted to possess S = 0 ground states, because of the absence of significant spin sign alternation at the atoms connecting two radicals.[7,8] Although the alternating spin connectivity in *o*-DBT predicts the S = 1 ground state, severe out-of-plane twisting is well-known to lead to an S = 0 ground state.[9]

Examination of the parity models and spin density distribution in the parent Blatter radical leads us to note that a connection at the C3 and C7 position would provide a high-spin diradical (Figure 1). We design the di-Blatter diradical **4** by taking advantage of the negative spin density at C3 within the Blatter radical moiety (green dot, Figure 1). A *tert*-butyl group at the site of the largest spin density in the annelated benzene ring[1] would enhance stability and solubility of the diradical.

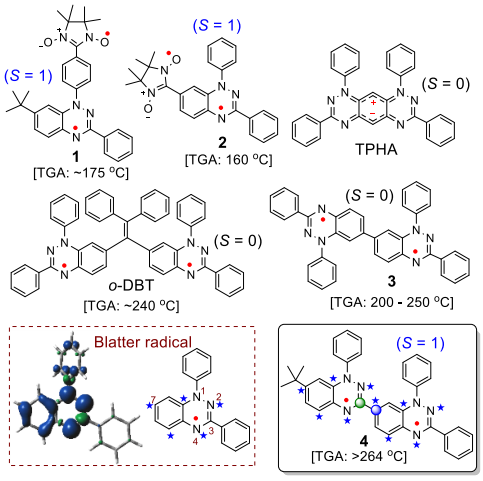

Figure 1. Blatter-based diradicals: TGA onset of decomposition ≈ 1% mass loss. Blatter radical and its spin density map at the UB3LYP/6-31G(d,p) level of theory; positive (blue) and negative (green) spin densities are shown at the isodensity level of 0.002 electron/Bohr.

We set out to explore the synthesis of di-Blatter diradical and faced a tremendous challenge with various unsuccessful convergent synthetic approaches. The breakthrough was achieved after extensive attempts using a divergent route, in which two benzotriazinyl rings are formed in one synthetic step (Scheme 1).

Here we report the synthesis, characterization and thin-film preparation of di-Blatter diradical **4**. The diradical possesses a triplet ground state and robust thermal stability, with an onset of decomposition above 264 °C – the highest temperature among high-spin diradicals studied by TGA. Remarkably,

crystalline **4** exhibits electrical conductivity, with an outstanding $\sigma \approx 0.01$ S cm^{-1} at room temperature and $\sigma \sim 10$ S cm^{-1} in the $T = 294 - 110$ K range, as measured by a two-probe method and estimated by EPR spectroscopy, respectively. This value of σ may be compared to typical neutral π-radicals that are insulators with $\sigma < 10^{-10}$ S cm^{-1} or to recent reports of nitroxide-based glassy polymer with $\sigma \approx 0.3$ S cm^{-1}, or bis(thiazolyl)-related radicals with $\sigma \approx 0.04$ S cm^{-1}, or bis(phenalenyl) radicals with $\sigma \approx 0.3$ S cm^{-1}.[10,11] The diradical can be evaporated under UHV to obtain thin films of **4** on silicon substrates, which remain unchanged after exposure to air for at least 18 – 48 h.

The synthesis of **4** starts with the copper-catalyzed C-N bond coupling reaction of **5** with methyl 4-amino-3-iodo-benzoate to produce **6**. The ester group in **6** is hydrolyzed and the resultant carboxylic acid **7** is activated with 1,1'-carbonyldiimidazole (CDI), followed by the reaction with phenylhydrazine. The resultant synthetic intermediate **8** is subjected to a C-N bond coupling reaction with 4-*tert*-butyl-2-iodo-aniline to provide compound **9**. Acid-catalyzed double cyclization of **9** is followed by air oxidation under basic conditions to produce diradical **4** in about 50% isolated yield. Notably, when the cyclization step is carried out for 24 h, instead of 2 h, an approximately equimolar mixture of diradical **4** and by-product monoradical **10** is isolated (Scheme 1).[12]

Scheme 1. Synthesis of diradical **4** and monoradical **10**.

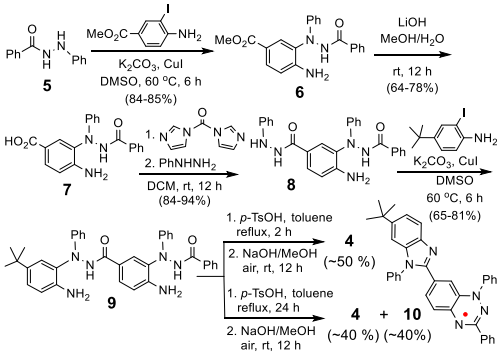

Structures of **4** and **10** are confirmed by X-ray crystallography (Figure 2 and SI). In diradical **4**, two fused-ring Blatter radical moieties are nearly coplanar, as indicated by the mean deviation from plane of 0.0719 Å for the plane defined by the N1-N6 and C1-C20 atoms. Also, the dihedral angle along the C4-C5 bond is 8.20 (0.12)°.[13] Thus, the conformation adopted by **4** in the crystal is near optimum for attaining both strong ferromagnetic coupling and electrical conductivity. Molecules of **4** form one-dimensional (1-D) π-stacks along the crystallographic *a*-axis, which coincides with the longest dimension of the single crystal plate/needle (Figure 2C), with average plane-to-plane distance of 3.482 Å (planes defined by the N1-N6 and C1-C20 atoms). In addition to a short C10···C12 = 3.381 Å contact within the 1-D π-stack, there are multiple C···C and N···C contacts within the sum of van der Waals radii plus 0.1 Å distances (Figs. S1 and S3, SI). Because most of these contacts involve atoms with positive spin densities, relatively strong intermolecular antiferromagnetic interactions, as well as electrical conductivity, are anticipated in crystalline diradical **4**.[2,11]

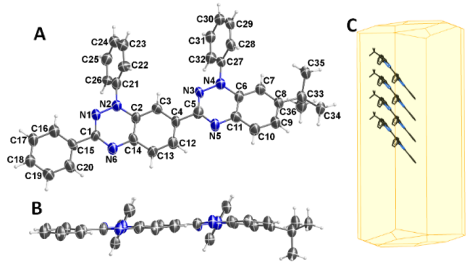

Figure 2. Single crystal X-ray structure of diradical **4** at 100 K, with carbon and nitrogen atoms depicted using thermal ellipsoids set at the 50% probability level (A and B). BFDH crystal morphoplogy (C). Additional data, e.g., for radical **10**, can be found in the SI: Figs. S1-S6 and Tables S1-S6.

EPR spectra of diradical **4** in a frozen glass at 110 K indicate a significant population of the triplet state. The forbidden $|\Delta m_s| = 2$ transition is relatively intense, which is consistent with a large spectral width ($2D = 782$ MHz) of the $|\Delta m_s| = 1$ region (Figure 3 and Table 1). *D*- and *g*-tensor orientations for **1**, **2**, and **4** are similar and the absolute values are well reproduced by DFT-computations for two major conformers, **4**A and **4**B, of **4**, except for the inherently difficult to compute parameter *E*.

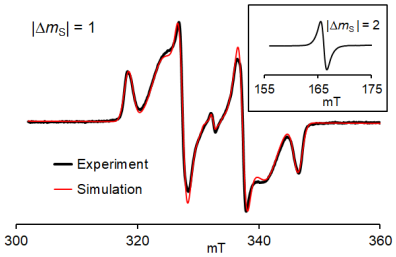

Figure 3. EPR (110 K, ν = 9.3269 GHz) spectrum for 0.54 mM diradical **4** in toluene/chloroform, 3:1 glass; a small center peak corresponds to monoradical impurity (ca. 5 – 7%). Inset: the $|\Delta m_s| = 2$ transition. Spectral simulation of the $|\Delta m_s| = 1$ region (rmsd = 0.0197, see: Table 1 and Fig. S15, SI.

We employ EPR spectroscopy to determine the triplet ground state of **4** in toluene/chloroform (4:1) by measurement of χT,

Table 1. EPR parameters for triplet states of diradicals.

Diradicals	*D* (MHz)	*E* (MHz)	g_x	g_y	g_z	g_{iso}[a]
1	69.6	4.2	2.0069	2.0010	2.0052	2.0044
2	242	35.1	2.0072	2.0026	2.0052	2.0050
3	ca. 75	na	na	na	na	na
o-DBT	126	39	na	na	na	na
4	391	35.9	2.0042	2.0027	2.0041	2.0037
4A[b]	406	71	2.0043	2.0023	2.0041	2.0036
4B[b]	410	60	2.0042	2.0022	2.0042	2.0036

[a] $g_{iso} \approx (g_x + g_y + g_z)/3$. [b] Computed with ORCA, SI, Table S9.[14]

the product of paramagnetic susceptibility (χ) and temperature (T), in the T = 110 – 331 K range. The spectra are acquired at each T at least in triplicate and Tempone in the same solvent is used as a spin counting reference. The numerical fit of χT vs. T to the modified Bleaney-Bowers-like equation (eq. S2, SI)[2,15] suggests the presence of two equilibrating conformations **4**A and **4**B with singlet-triplet energy gaps $2J_A/k$ = 220 ± 70 K and $2J_B/k$ = –340 ± 37 K i.e., $\Delta E_{ST} \approx 0.4$ kcal mol^{-1} for the major conformation **4**A (Figure 4).

Similarly, we study EPR double integrated intensities (DI) vs T for polycrystalline **4**. Notably, a curved plot is obtained in the T = 110 – 280 K range, with a broad maximum slightly above 200 K, rather than the usual $DI \sim 1/T$ paramagnetic behavior. In conjunction with the X-ray-determined crystal packing of **4**, suggesting formation of S = 1 antiferromagnetic π-stacked 1-D chains of diradicals, the DI vs T data are fit to a 1-D chain model (SI, eq. S3A)[2,16] with two variable parameters, exchange coupling constant, J'/k = –157 ± 3 K (mean ± SE), and conversion factor, N, of DI to molar paramagnetic susceptibility χ. Because of the Dysonian line shape for solid **4** (Figure 4),[17ac] J'/k = –157 ± 3 K should be viewed as an order of magnitude estimate. A similar Dysonian line shape is obtained for a crystalline plate of **4** (5 × 2.5 × 0.13 mm^3) with angle-dependent A/B =1.6–1.8 at T = 294 K and polycrystalline **4** (particle size of <75 μm) with A/B =1.5–1.9 at T = 110–279 K. These results suggest that at 9 GHz, the skin depth, δ, of solid **4** is of the order of 0.1 mm, which would imply comparable conductivity to σ = 8.8 S cm^{-1} for HOPG plates (4 × 0.4 × 0.2 mm^3) with δ = 0.19 mm and $A/B \approx 1.8$.[17b]

Two-probe conductivity measurements, which due to contact resistance, may be viewed as lower bounds for actual σ, give σ = 1 × 10^{-4} and 0.01 S cm^{-1} for **4** in spin-coated film and single crystals, respectively.

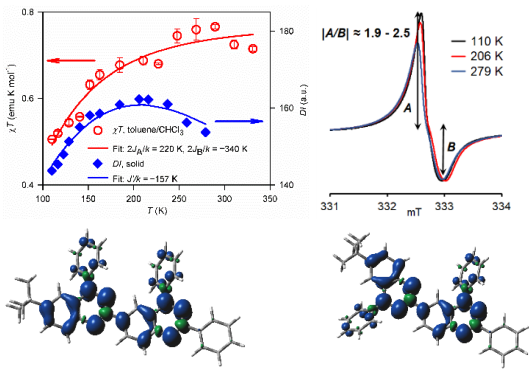

Figure 4. Top left: EPR spectroscopy of diradical **4**: plot and numerical fit of χT vs T in toluene/chloroform (4:1) and DI vs T for polycrystalline **4**. Top right: representative EPR spectra with Dysonian line shape for solid **4**. Further details are reported in the SI: Table S7, Figs. S13–S26, Eqs. S2 and S3A. Bottom: Spin density plots for triplet states of conformations **4**A and **4**B.

As suggested by the EPR-derived χT vs. T data and illustrated by spin density plots (Figure 4), the diradical **4** may exist in two major conformations **4**A and **4**B. Conformation **4**A corresponds to the one found in crystalline **4** (Figure 2). DFT computations at the UB3LYP/6-31G(d,p)+ZPVE level[18] suggest that triplet states of **4**A and **4**B are approximately isoenergetic. ΔE_{ST} values for **4**A and **4**B are surprisingly different, 1.37 and 0.34 kcal mol^{-1}, respectively; in addition, $J'/k \approx$ –100 K is computed in the π-dimer at the X-ray geometry (SI, Tables S8 and S10). Because this level of theory is well-known to overestimate the stability of high-spin states,[1,2,19] it is possible that actual ΔE_{ST} for **4**B is negative, as determined experimentally (Figure 4).

TGA, with parallel IR spectroscopy, of diradical **4** indicates that the onset of decomposition is at T > 264 °C, which is more than ~100 °C higher than recently studied S = 1 diradical **2** (Figure 5).[2] Relying on this result, we deposit thin films of diradical **4** on SiO_2/Si(111) wafers by controlled evaporation under ultra-high vacuum (UHV). Following a well-established method,[4,20] we use X-ray photoelectron spectroscopy (XPS) together with a best fit procedure to assess the intactness and the stability of the diradical in the thin films. The XPS investigation indicate that the films have the expected stoichiometry (Figure 5), i.e., the evaporation of intact radicals was successfully achieved. This is further supported by the direct comparison with the XPS spectra of the powder that did not undergo evaporation and EPR spectroscopy (SI). The films grow following a strong island mode, as seen by atomic force microscopy (AFM, see: SI), indicating a strong interaction between molecules, and very weak interaction with the substrate.

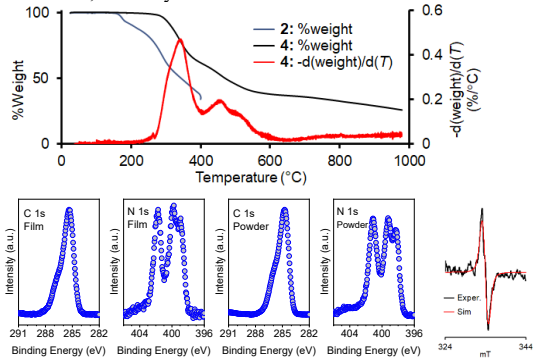

Figure 5. Top: Thermogravimetric analysis with IR spectra of diradicals **2** and **4** under N_2;[2] heating rate = 5 °C min^{-1}. For further details, including IR spectra, see: SI, Figs. S7 and S8. Bottom four left panels: C 1s and N 1s core level XPS spectra of a multilayer of **4** deposited on SiO_2/Si(111) substrate, compared to the powder spectra. Bottom right: preliminary EPR difference spectrum for thin film of **4** at 294 K showing Voigtian line shape with Lorentzian and Gaussian peak-to-peak linewidth of 0.6 and 1.3 mT, respectively. For further details, see: SI, Figs. S27–S37.

The EPR spectrum of nm-thick film of **4** shows a single isotropic peak with a line-shape intermediate between Gaussian and Lorentzian, thus suggesting conductance or exchange coupling in 1-D.[17c,21]

In conclusion, we have prepared the first high-spin (S = 1) diradical, based entirely on two Blatter radical moieties, to attain the robust thermal stability. The crystalline diradical **4** displays good electrical conductivity, observed for the first time in a high-spin diradical. The diradical is evaporated under UHV to form thin films on silicon, which are relatively stable under vacuum (many days) or under air (at least 18 h).

ASSOCIATED CONTENT

Supporting Information

Complete acknowledgment and ref 18, general procedures and materials, additional experimental and computational details. This material is available free of charge via the Internet at http://pubs.acs.org.

AUTHOR INFORMATION

* Corresponding Authors
arajca1@unl.edu and benedetta.casu@uni-tuebingen.de

Notes

The authors declare no competing financial interests.

ACKNOWLEDGMENT

We thank the NSF Chemistry Division for support of this research under Grants CHE-1665256 and CHE-1955349. Support for the acquisition of the Bruker Venture D8 diffractometer through the Major Scientific Research Equipment Fund from the President of Indiana University and the Office of the Vice President for Research is gratefully acknowledged. Financial support from the German Research Foundation (DFG) under the contract CA852/11-1 is gratefully acknowledged. We thank Prof. Letian Dou (Chemical Engineering at Purdue) for the design of the mask for the single crystal measurements of electrical conductivity.

REFERENCES

(1) Gallagher, N. M.; Bauer, J. J.; Pink, M.; Rajca, S.; Rajca, A. High-Spin Organic Diradical with Robust Stability. *J. Am. Chem. Soc.* **2016**, *138*, 9377–9380.

(2) Gallagher, N.; Zhang, H.; Junghoefer, T.; Giangrisostomi, E.; Ovsyannikov, R.; Pink, M.; Rajca, S.; Casu, M. B.; Rajca, A. Thermally and Magnetically Robust Triplet Ground State Diradical. *J. Am. Chem. Soc.* **2019**, *141*, 4764–4774.

(3) (a) Blatter; H. M.; Lukaszewski, H. A new stable free radical. *Tetrahedron Lett.* **1968**, *9*, 22, 2701–2705. (b) Constantinides, C. P.; Koutentis, P. A.; Krassos, H.; Rawson, J. M.; Tasiopoulos, A. J. Characterization and Magnetic Properties of a "Super Stable" Radical 1,3-Diphenyl-7-trifluoromethyl-1,4-dihydro-1,2,4-benzotriazin-4-yl. *J. Org. Chem*. **2011**, 76, 2798– 2806. (c) Zheng, Y.; Miao, M.-S.; Kemei, M. C.; Seshadri, R.; Wudl, F. The Pyreno-Triazinyl Radical – Magnetic and Sensor Properties. *Isr. J. Chem*. **2014**, *54*, 774–778. (d) Ciccullo, F.; Gallagher, N. M.; Geladari, O.; Chasse, T.; Rajca, A.; Casu, M. D. A Derivative of the Blatter Radical as a Potential Metal-Free Magnet for Stable Thin Films and Interfaces. *ACS Appl. Mater. Interfaces* **2016**, *8*, 1805–1812.

(4) Casu, M. B., Nanoscale studies of organic radicals: Surface, interface, and spinterface, *Acc. Chem. Res.* **2018**, *51*, 753–760.

(5) (a) Hutchison, K.; Srdanov, G.; Hicks, R.; Yu, H.; Wudl, F. Tetraphenylhexaazaanthracene: A Case for Dominance of Cyanine Ion Stabilization Overwhelming 16π Antiaromaticity. *J. Am. Chem. Soc.* **1998**, *120*, 2989–2990. (b) Constantinides, C. P.; Zissimou, G. A.; Berezin, A. A.; Ioannou, T. A.; Manoli, M.; Tsokkou, D.; Theodorou, E.; Hayes, S. C.; Koutentis, P. A. Tetraphenylhexaazaanthracenes: 16π Weakly Antiaromatic Species with Singlet Ground States. *Org. Lett.* **2015**, *17*, 4026– 4029. (c) Zheng, Y.; Miao, M.; Dantelle, G.; Eisenmenger, N. D.; Wu, G.; Yavuz, I.; Chabinyc, M. L.; Houk, K. N.; Wudl, F. A Solid-State Effect Responsible for an Organic Quintet State at Room Temperature and Ambient Pressure. *Adv. Mater.* **2015**, *27*, 1718–1723.

(6) (a) Hu, X.; Zhao, L.; Chen, H.; Ding, Y. Zheng, Y.-Z.; Miao, M.; Zheng, Y. Air stable high-spin blatter diradicals: non-Kekulé *versus* Kekulé structures. *J. Mater. Chem. C*, **2019**, *7*, 6559–6563. (b) Hu, X.; Chen, H.; Zhao, L.; Miao, M.; Han, J.; Wang, J.; Guo, J.; Hu, Y.; Zheng, Y. Nitrogen analogues of Chichibabin's and Müller's hydrocarbons with small singlet–triplet energy gaps. *Chem. Commun.* **2019**, *55*, 7812–7815. (c) Hu, X.; Chen, H.; Xue, G.; Zheng, Y. Correlation between the strength of conjugation and spin–spin interactions in stable diradicaloids. *J. Mater. Chem. C* **2020**, Adv. Article, published 03/25/2020. https://doi.org/10.1039/D0TC00868K

(7) (a) Ovchinnikov, A. A. Multiplicity of the ground state of large alternant organic molecules with conjugated bonds. *Theor. Chim. Acta.* **1978**, *47*, 297–304. (b) Gallagher, N. M.; Olankitwanit, A.; Rajca, A. High-Spin Organic Molecules. *J. Org. Chem.* **2015**, *80*, 1291–1298.

(8) (a) Rajca, A.; Rajca, S. Intramolecular Antiferromagnetic vs Ferromagnetic Spin Coupling Through the Biphenyl Unit. *J. Am. Chem. Soc.* **1996**, *118*, 8121–8126. (b) A. Rajca, J. Wongsriratanakul, S. Rajca, S. High-Spin Organic Polyradicals as Spin Clusters: Ferromagnetic Spin Coupling through Biphenyl Unit in Polyarylmethyl Tri-, Penta-, Hepta-, and Hexadecaradicals. *J. Am. Chem. Soc*. **1997**, *119*, 11674–11686.

(9) Shultz, D. A.; Fico, R. M., Jr.; Lee, H.; Kampf, J. W.; Kirschbaum, K.; Pinkerton, A. A.; Boyle, P. D. Mechanisms of Exchange Modulation in Trimethylenemethane-type Biradicals: The Roles of Conformation and Spin Density. *J. Am. Chem. Soc.* **2003**, *125*, 15426–15432.

(10) Joo, Y.; Agarkar, V.; Sung, S. H.; Savoie, B. M.; Boudouris, B. W. A nonconjugated radical polymer glass with high electrical conductivity. *Science* **2018**, *359*, 1391–1395,

(11) (a) Mailman, A.; Wong, J. W. L.; Winter, S. M.; Claridge, R. C. M.; Robertson, C. M.; Assoud, A.; Yong, W.; Steven, E.; Dube, P. A.; Tse, J. S.; Desgreniers, S.; Secco, R. A.; Oakley, R. T. Fine tuning the performance of multiorbital radical conductors by substituent effects. *J. Am. Chem. Soc.* **2017**, *139*, 1625–1635. (b) Pal, S. K.; Itkis, M. E.; Tham, F. S.; Reed, R. W.; Oakley, R. T.; Haddon, R. C. Resonating valence-bond ground state in a phenalenyl-based neutral radical conductor. *Science* **2005**, *309*, 281– 284.

(12) The mechanism for ring contraction to **10** is under investigation.

(13) The dihedral angle is between the C1-N1-N2-C2-C3-C4-C12-C13-C14-N6 and C5-N3-N4-C6-C7-C8-C8-C9-C10-C11-N5 planes.

(14) Neese, F. The ORCA program system. *Wiley Interdisciplinary Reviews: Comp. Mol. Sci.* **2012**, *2*, 73–78.

(15) (a) Rajca, A. Organic diradicals and polyradicals: from spin coupling to magnetism? *Chem. Rev.* **1994**, *94*, 871–893. (b) Shu, C.; Zhang, H.; Olankitwanit, A.; Rajca, S.; Rajca, A. High-Spin Diradical Dication of Chiral π-Conjugated Double Helical Molecule. *J. Am. Chem. Soc.*, **2019**, *141*, 17287–17294.

(16) Meyer, A.; Gleizes, A.; Girerd, J. J.; Verdaguer, M.; Kahn, O. Crystal structures, magnetic anisotropy properties, and orbital interactions in catena - (μ-nitrito) - bis (ethylenediamine) nickel(II) perchlorate and triiodide. *Inorg. Chem.* **1982**, *21*, 1729–1739.

(17) (a) Dyson, F. J. Electron Spin Resonance Absorption in Metals. II. Theory of Electron Diffusion and the Skin Effect. *Phys. Rev.* **1958**, *98*, 349–359. (b) Ziatdinov, A. M.; Skrylnik, P. G. Graphite intercalation by nitric acid: conduction ESR and theoretical studies. *Chem. Phys.* **2000**, *261*, 439–448. (b) Krinichnyi, V. I. Dynamics of spin charge carriers in polyaniline. *Appl. Phys. Rev.* **2014**, *1*, 021305.

(18) Frisch, M. J.; et al, *Gaussian 16*, Revision A.1 (Gaussian, Inc., Wallingford CT, 2016).

(19) Bajaj, A.; Ali, Md. E. First-Principle Design of Blatter's Diradicals with Strong Ferromagnetic Exchange Interactions. *J. Phys. Chem. C* **2019**, *123*, 15186–15194.

(20) Savu, S.-A.; Biswas, I.; Sorace, L.; Mannini, M.; Rovai, D.; Caneschi, A.; Chassé, T.; Casu, M. B., Nanoscale Assembly of Paramagnetic Organic Radicals on Au(111) Single Crystals. *Chem.-Eur. J.* **2013,** *19*, 3445–3450.

(21) Hennessy, M. J.; McElwee, C. D.; Richards, P. M. Effect of interchain coupling on electron-spin resonance in nearly one-dimensional systems. *Phys. Rev. B* **1973**, *7*, 930–947.

Insert Table of Contents artwork here

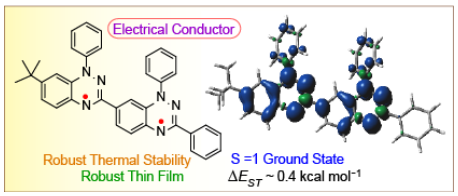

Supporting Information

Conducting High-Spin (*S* = 1) Organic Diradical with Robust Stability

Shuyang Zhang[†], Maren Pink[#], Tobias Junghoefer[§], Wenchao Zhao[⊥], Sheng-Ning Hsu[⊥], Suchada Rajca[†], Bryan W. Boudouris[⊥,‡], Maria Benedetta Casu*[§], and Andrzej Rajca*[†]

[†]Department of Chemistry, University of Nebraska, Lincoln, Nebraska 68588-0304, United States.

[#]IUMSC, Department of Chemistry, Indiana University, Bloomington, Indiana 47405-7102, United States.

[§]Institute of Physical and Theoretical Chemistry, University of Tübingen, 72076 Tübingen, Germany.

[⊥] Charles D. Davidson School of Chemical Engineering and [‡] Department of Chemistry, Purdue University, West Lafayette, IN 47907

.

E-mail address: arajca1@unl.edu and benedetta.casu@uni-tuebingen.de

Table of Contents

1. Complete Acknowledgement.

We thank the NSF Chemistry Division for support of this research under Grants CHE-1665256 and CHE-1955349 (AR). Upgrade of the EPR spectrometer at Nebraska was supported by the National Institutes of Health (NIGMS #R01GM124310-01, AR and SR). Support for the acquisition of the Bruker Venture D8 diffractometer through the Major Scientific Research Equipment Fund from the President of Indiana University and the Office of the Vice President for Research is gratefully acknowledged. NSF's ChemMatCARS Sector 15 is supported by the Divisions of Chemistry (CHE) and Materials Research (DMR), National Science Foundation, under grant number NSF/CHE-1834750. Use of the Advanced Photon Source, an Office of Science User Facility operated for the U.S. Department of Energy (DOE) Office of Science by Argonne National Laboratory, was supported by the U.S. DOE under Contract No. DE-AC02-06CH11357. We also thank Thomas Chassé for accessing the photoelectron laboratory at the University of Tübingen. Financial support from the German Research Foundation (DFG) under the contract CA852/11-1 is gratefully acknowledged. The work at Purdue was supported by the Air Force Office of Scientific Research (AFOSR) through the Organic Materials Chemistry Program (Grant Number: FA9550-19-1-0271, Program Manager: Dr. Kenneth Caster), and we are grateful for this support. We thank Prof. Letian Dou (Chemical Engineering at Purdue) for the design of the mask for the single crystal measurements of electrical conductivity.

2. Complete Reference 18 (Gaussian 16).

M. J. Frisch, G. W. Trucks, H. B. Schlegel, G. E. Scuseria, M. A. Robb, J. R. Cheeseman, G. Scalmani, V. Barone, G. A. Petersson, H. Nakatsuji, X. Li, M. Caricato, A. V. Marenich, J. Bloino, B. G. Janesko, R. Gomperts, B. Mennucci, H. P. Hratchian, J. V. Ortiz, A. F. Izmaylov, J. L. Sonnenberg, D. Williams-Young, F. Ding, F. Lipparini, F. Egidi, J. Goings, B. Peng, A. Petrone, T. Henderson, D. Ranasinghe, V. G. Zakrzewski, J. Gao, N. Rega, G. Zheng, W. Liang, M. Hada, M. Ehara, K. Toyota, R. Fukuda, J. Hasegawa, M. Ishida, T. Nakajima, Y. Honda, O. Kitao, H. Nakai, T. Vreven, K. Throssell, J. A. Montgomery, Jr., J. E. Peralta, F. Ogliaro, M. J. Bearpark, J. J. Heyd, E. N. Brothers, K. N. Kudin, V. N. Staroverov, T. A. Keith, R. Kobayashi, J. Normand, K. Raghavachari, A. P. Rendell, J. C. Burant, S. S. Iyengar, J. Tomasi, M. Cossi, J. M. Millam, M. Klene, C. Adamo, R. Cammi, J. W. Ochterski, R. L. Martin, K. Morokuma, O. Farkas, J. B. Foresman, and D. J. Fox, *Gaussian 16*, Revision A.03 (Gaussian, Inc., Wallingford CT, 2016).

3. Experimental Section: Synthesis, Measurements, and Computations.

3.a. General procedures and materials.

Throughout the following paragraphs labels "SZ_3_48_3_EthylAcetate" and alike correspond to sample or experiment codes directly traceable to the laboratory notebooks or raw data.

Dichloromethane (DCM) was obtained from solvent purification system (LC Technology Solutions). DCM was in addition dried over calcium hydride (CaH_2), and then distilled to a Schlenk vessel, and subsequently degassed by repeated freeze-and-thaw procedure. Per-deuterated solvents for NMR spectroscopy were obtained from Cambridge Isotope Laboratories. Methyl 4-amino-3-iodobenzoate (97%) was purchased from Oakwood Chemical. All other commercially available chemicals were obtained from either Aldrich or Acros, unless indicated otherwise.

The hydrazine amide **5**,[S1-S3] the starting material for synthesis of diradical **4**, and 4-*tert*-butyl-2-iodo-aniline[S4] were prepared according to the published literature procedures.

Column chromatography (0–20 psig pressure) was carried out on silica gel or neutral alumina. Standard techniques for synthesis under inert atmosphere, using Schlenk glassware and argon-filled gloveboxes, were employed. NMR spectra were obtained using commercial spectrometers (^1H, 700 MHz, 500 MHz, and 400 MHz) using chloroform-*d* ($CDCl_3$), benzene-d_6, or acetone-d_6 as solvent. The 500 and 700 MHz instruments were equipped with a cryoprobe. The chemical shift references were the peaks of the solvent with residual proton content. Typical 1D FID was subjected to exponential multiplication with an exponent of 0.1 Hz (for ^1H) and 1.0 – 2.0 Hz (for ^{13}C). IR spectra were obtained using a commercial instrument, equipped with an ATR sampling accessory. MS analyses were carried out at local facilities for mass spectrometry.

3.b. X-ray crystallography.

The single crystals of diradical **4** were obtained by slow solvent evaporation from a solution of **4** in ethyl acetate at about 60 °C (sample label: SZ_3_48_3_EthylAcetate). The single crystals of monoradical **10** were obtained by vapor diffusion method with benzene and pentane (sample label: SZ_3_38_Blatter_monoradical).

The crystals of diradical **4** (sample label: SZ_3_48_3_EthylAcetate) were investigated at the University of Indiana using both Mo Kα radiation (X-ray label: 20029) and Cu Kα radiation (X-ray label: 20036). A very small, black crystal with approximate dimensions, 0.015 × 0.006 × 0.003 mm^3 (Mo Kα) and 0.058 × 0.012 × 0.008 mm^3 (Cu Kα), was placed onto the tip of a MiTeGen loop and mounted on a Bruker Venture D8 diffractometer equipped with a PhotonIII detector at 100(2) K.

The crystal of monoradical **10** (sample label: SZ-3-38-Blatter-monoradical and X-ray label: S19032) was investigated with synchrotron radiation at the ChemMatCARS[S5] 15IDD beamline at the Advanced Photon Source at Argonne National Laboratory, Chicago, utilizing the SCrAPS program.[S6] A dark crystal (approximate dimensions 0.011 × 0.011 × 0.002 mm^3) was placed onto the tip of an glass rod and mounted on a Huber goniometer, equipped with a Pilatus 1M detector, and measured at 100(2) K.

Data collection (Mo Kα) for the crystal of diradical 4. The data collection was carried out using Mo Kα radiation (graphite monochromator) with a frame time of 40 or 80 seconds and a detector distance of 12.00 cm. A collection strategy was calculated and complete data to a resolution of 0.71 Å with a redundancy of 8.7 were collected. Nine major sections of frames were collected with 0.50º ω and φ scans. A total of 2937 frames were collected. The total exposure time was 56.09 hours. The frames were integrated with the Bruker SAINT software package[S7] using a narrow-frame algorithm. The integration of the data using a monoclinic unit cell yielded a total of 42467 reflections to a maximum θ angle of 25.05° (0.84 Å resolution), of which 4743 were independent (average redundancy 8.954, completeness = 99.9%, R_{int} = 40.37%, R_{sig} = 26.18%) and 1435 (30.26%) were greater than $2\sigma(F^2)$. The final cell constants of a = 5.6596(7) Å, b = 20.717(3) Å, c = 22.938(3) Å, β = 95.343(4)°, volume = 2677.8(6) $Å^3$, are based upon the refinement of the XYZ-centroids of 719 reflections above 20 σ(I) with 5.309° < 2θ < 39.52°. Data were corrected for absorption effects using the Multi-Scan method (SADABS).[S8] The ratio of minimum to maximum apparent transmission was 0.733. The calculated minimum and maximum transmission coefficients (based on crystal size) are 0.9990 and 1.0000. *Only 30% of the measured reflections are observed; the weak data are likely due to poor crystal quality and small crystal size.* Please refer to Table S2 for additional crystal and refinement information.

Data collection (Cu Kα) for the crystal of diradical 4. The data collection was carried out using Cu Kα radiation (graphite monochromator) with a frame time of 40 to 120 seconds and a detector distance of 5.00 cm. A collection strategy was calculated and complete data to a resolution of 0.83 Å with a redundancy of 7.1 were collected. Sixteen major sections of frames were collected with 0.50º ω and φ scans. Details are in Table S1 (next page).

Table S1. Summary of data collection (Cu Kα) for diradical **4**.

Axis	2θ/°	ω/°	φ/°	χ/°	Width/°	Frames	Time/s
Phi	97.06	88.05	0.00	-44.50	1.00	360	108.00
Omega	97.06	88.05	90.00	-44.50	1.00	85	108.00
Omega	-12.50	-123.37	180.00	44.50	1.00	120	40.00
Omega	112.06	-3.51	-168.00	65.50	1.00	109	120.00
Phi	112.06	10.92	44.00	24.00	1.00	184	120.00
Phi	-42.50	329.61	4.00	24.00	1.00	184	64.00
Omega	97.06	88.05	180.00	-44.50	1.00	85	108.00
Omega	-42.50	-55.93	80.00	-65.50	1.00	96	64.00
Omega	112.06	-3.51	-40.00	65.50	1.00	109	120.00
Phi	112.06	99.95	-102.60	-24.00	1.00	301	120.00
Omega	112.06	-3.51	128.00	65.50	1.00	109	120.00
Omega	97.06	88.05	270.00	-44.50	1.00	85	108.00
Omega	-27.50	-138.37	180.00	44.50	1.00	120	52.00
Omega	112.06	-3.51	-72.00	65.50	1.00	109	120.00
Omega	112.06	-3.51	32.00	65.50	1.00	109	120.00
Phi	0.00	0.00	0.00	54.74	1.00	180	1.00

A total of 2345 frames were collected. The total exposure time was 60.88 hours. The frames were integrated with the Bruker SAINT software package[S7] using a narrow-frame algorithm. The integration of the data using a monoclinic unit cell yielded a total of 34729 reflections to a maximum θ angle of 67.34° (0.84 Å resolution), of which 4797 were independent (average redundancy 7.240, completeness = 99.4%, R_{int} = 20.92%, R_{sig} = 13.06%) and 2135 (44.51%) were greater than $2\sigma(F^2)$. The final cell constants of a = 5.6659(4) Å, b = 20.7381(12) Å, c = 22.9577(15) Å, β = 95.398(5)°, volume = 2685.6(3) $Å^3$, are based upon the refinement of the XYZ-centroids of 73 reflections above 20 σ(I) with 3.907° < 2θ < 36.95°. Data were corrected for absorption effects using the Multi-Scan method (SADABS).[S8] The ratio of minimum to maximum apparent transmission was 0.785. The calculated minimum and maximum transmission coefficients (based on crystal size) are 0.9640 and 0.9950. *Less than 50% of the measured reflections are observed; the weak data are likely due to poor crystal quality and small crystal size.* Please refer to Table S3 for additional crystal and refinement information.

Data collection for the crystal of monoradical 10. The data collection was carried out using synchrotron radiation (λ = 0.41328 Å, E = 30 keV, silicon 111 and 113 monochromators, two mirrors to exclude higher harmonics) with a frame time of 2 seconds and a detector distance of 13.0 cm. A

randomly oriented region of reciprocal space was surveyed to the extent of two spheres with a detector position (2θ) at 0°, ω at -90°, κ at 0° and 30°, using φ scans. The total exposure time was 120 minutes. The frames were integrated with the Bruker SAINT software package[S7] using a narrow-frame algorithm. The integration of the data using a triclinic unit cell yielded a total of 25835 reflections to a maximum θ angle of 14.28° (0.84 Å resolution), of which 4380 were independent (average redundancy 5.898, completeness = 91.8%, R_{int} = 7.91%, R_{sig} = 5.71%) and 2862 (65.34%) were greater than $2\sigma(F^2)$. The final cell constants of a = 11.059(2) Å, b = 11.856(3) Å, c = 12.713(3) Å, α = 107.607(3)°, β = 98.964(4)°, γ = 116.219(3)°, volume = 1341.2(5) Å^3, are based upon the refinement of the XYZ-centroids of 3233 reflections above 20 σ(I) with 4.905° < 2θ < 28.46°. Data were corrected for absorption effects using the Multi-Scan method (SADABS).[S8] The ratio of minimum to maximum apparent transmission was 0.875. The calculated minimum and maximum transmission coefficients (based on crystal size) are 1.0000 and 1.0000. Please refer to Table S4 for additional crystal and refinement information.

Structure solution and refinement for diradical 4 (Mo Kα). The space group $P2_1/c$ was determined based on intensity statistics and systematic absences. The structure was solved and refined using the SHELX suite of programs.[S9] An intrinsic-methods solution was calculated, which provided most non-hydrogen atoms from the E-map. Full-matrix least squares / difference Fourier cycles were performed, which located the remaining non-hydrogen atoms. All non-hydrogen atoms were refined with anisotropic displacement parameters. The hydrogen atoms were placed in ideal positions and refined as riding atoms with relative isotropic displacement parameters. The structure was solved and refined using the Bruker SHELXTL Software Package, using the space group $P2_1/c$, with Z = 4 for the formula unit, $C_{36}H_{30}N_6$. The final anisotropic full-matrix least-squares refinement on F^2 with 382 variables converged at R1 = 9.65%, for the observed data and wR2 = 31.62% for all data. The goodness-of-fit was 0.955. The largest peak in the final difference electron density synthesis was 0.332 $e^-/Å^3$ and the largest hole was -0.262 $e^-/Å^3$ with an RMS deviation of 0.067 $e^-/Å^3$. On the basis of the final model, the calculated density was 1.356 g/cm^3 and F(000), 1152 e^-.

Structure solution and refinement for diradical 4 (Cu Kα). The space group $P2_1/c$ was determined based on intensity statistics and systematic absences. The structure was solved and refined using the SHELX suite of programs.[S9] An intrinsic-methods solution was calculated, which provided most non-hydrogen atoms from the E-map. Full-matrix least squares / difference Fourier cycles were performed, which located the remaining non-hydrogen atoms. All non-hydrogen atoms were refined with anisotropic displacement parameters. The hydrogen atoms were placed in ideal positions and refined as riding atoms with relative isotropic displacement parameters. The final anisotropic full-matrix least-squares refinement on F^2 with 382 variables converged at R1 = 7.91%, for the observed data and wR2 = 27.63% for all data. The goodness-of-fit was 0.960. The largest peak in the final difference electron density synthesis was 0.285 $e^-/Å^3$ and the largest hole was -0.265 $e^-/Å^3$ with an RMS deviation of 0.062 $e^-/Å^3$. On the basis of the final model, the calculated density was 1.352 g/cm^3 and F(000), 1152 e^-.

Structure solution and refinement for monoradical 10.

The space group P-1 was determined based on intensity statistics and systematic absences. The structure was solved and refined using the Shelx suite of programs.[S9] An intrinsic methods solution was calculated, which provided most non-hydrogen atoms from the E-map. Full-matrix least squares / difference Fourier cycles were performed, which located the remaining non-hydrogen atoms. All non-hydrogen atoms were refined with anisotropic displacement parameters. The hydrogen atoms were placed in ideal positions and refined as riding atoms with relative isotropic displacement parameters. The final anisotropic full-matrix least-squares refinement on F^2 with 373 variables converged at R1 = 5.02%, for the observed data and wR2 = 13.63% for all data. The goodness-of-fit was 0.937. The largest peak in the final difference electron density synthesis was 0.235 $e^-/Å^3$ and the largest hole was -0.231 $e^-/Å^3$ with an RMS deviation of 0.045 $e^-/Å^3$. On the basis of the final model, the calculated density was 1.319 g/cm^3 and F(000), 562 e^-.

BFDH computations.

The Bravais, Friedel, Donnay and Harker (BFDH) morphology for single crystal of diradical **4** (used in the Cu Kα radiation X-ray diffraction) was calculated with Mercury (Fig. S1). It matches very well the faces that could be seen from the tiny needle crystal used for the diffraction. (Some of the smaller top and side faces of the needle were just too small to be seen.) The morphology gives a nice visualization of crystal habit vs structure, and it indicates that the longest dimension of the crystal matches with orientation of crystallographic *a*-axis, along which the molecules are π-stacked.

Table S2. Crystal data and structure refinement for diradical **4** (Mo Kα, X-ray label: 20029).

Empirical formula	$C_{36}\ H_{30}\ N_6$	
Formula weight	546.66	
Crystal color, shape, size	black plate, 0.015 × 0.006 × 0.003 mm^3	
Temperature	100(2) K	
Wavelength	0.71073 Å	
Crystal system, space group	Monoclinic, $P2_1/c$	
Unit cell dimensions	a = 5.6596(7) Å	α = 90°.
	b = 20.717(3) Å	β = 95.343(4)°.
	c = 22.938(3) Å	γ = 90°.
Volume	2677.8(6) $Å^3$	
Z	4	
Density (calculated)	1.356 Mg/m^3	
Absorption coefficient	0.082 mm^{-1}	
F(000)	1152	
Data collection		
Diffractometer	Kappa Apex II Duo, Bruker	
Theta range for data collection	1.966 to 25.045°.	
Index ranges	-6<=h<=6, -24<=k<=24, -27<=l<=27	
Reflections collected	42467	
Independent reflections	4743 [R_{int} = 0.4037]	
Observed Reflections	1435	
Completeness to theta = 25.045°	99.9 %	
Solution and Refinement		
Absorption correction	Semi-empirical from equivalents	
Max. and min. transmission	0.7452 and 0.5462	
Solution	Intrinsic methods	
Refinement method	Full-matrix least-squares on F^2	
Weighting scheme	$w = [\sigma^2Fo^2 + AP^2]^{-1}$, with $P = (Fo^2 + 2\ Fc^2)/3$, A = 0.0955	
Data / restraints / parameters	4743 / 0 / 382	
Goodness-of-fit on F^2	0.955	
Final R indices [I>2σ(I)]	R1 = 0.0965, wR2 = 0.2161	
R indices (all data)	R1 = 0.2870, wR2 = 0.3162	
Largest diff. peak and hole	0.332 and -0.262 $e.Å^{-3}$	

Goodness-of-fit = $[\Sigma[w(F_o^2 - F_c^2)^2]/N_{observns} - N_{params})]^{1/2}$, all data.

$R1 = \Sigma(|F_o| - |F_c|) / \Sigma\ |F_o|$. $wR2 = [\Sigma[w(F_o^2 - F_c^2)^2] / \Sigma\ [w(F_o^2)^2]]^{1/2}$.

Table S3. Crystal data and structure refinement for diradical **4** (Cu Kα, X-ray label: 20036).

Empirical formula	$C_{36}\ H_{30}\ N_6$	
Formula weight	546.66	
Crystal color, shape, size	black needle, 0.058 × 0.012 × 0.008 mm^3	
Temperature	100(2) K	
Wavelength	1.54178 Å	
Crystal system, space group	Monoclinic, $P2_1/c$	
Unit cell dimensions	a = 5.6659(4) Å	α = 90°.
	b = 20.7381(12) Å	β = 95.398(5)°.
	c = 22.9577(15) Å	γ = 90°.
Volume	2685.6(3) $Å^3$	
Z	4	
Density (calculated)	1.352 Mg/m^3	
Absorption coefficient	0.640 mm^{-1}	
F(000)	1152	

Data collection

Diffractometer	Venture D8, Bruker
Source	IμS Diamond, Incoatec
Theta range for data collection	2.877 to 67.338°.
Index ranges	-6<=h<=6, -24<=k<=24, -27<=l<=27
Reflections collected	34729
Independent reflections	4797 [R_{int} = 0.2092]
Observed Reflections	2135
Completeness to theta = 67.338°	99.4 %

Solution and Refinement

Absorption correction	Semi-empirical from equivalents
Max. and min. transmission	0.7528 and 0.5910
Solution	Intrinsic methods
Refinement method	Full-matrix least-squares on F^2
Weighting scheme	$w = [\sigma^2 Fo^2 + AP^2]^{-1}$, with $P = (Fo^2 + 2\,Fc^2)/3$, A = 0.1395
Data / restraints / parameters	4797 / 0 / 382
Goodness-of-fit on F^2	0.960
Final R indices [I>2σ(I)]	R1 = 0.0791, wR2 = 0.2091
R indices (all data)	R1 = 0.1662, wR2 = 0.2763
Largest diff. peak and hole	0.285 and -0.265 $e.Å^{-3}$

Goodness-of-fit = $[\Sigma[w(F_o^2 - F_c^2)^2]/N_{observns} - N_{params})]^{1/2}$, all data.

$R1 = \Sigma(|F_o| - |F_c|) / \Sigma |F_o|$. $wR2 = [\Sigma[w(F_o^2 - F_c^2)^2] / \Sigma [w(F_o^2)^2]]^{1/2}$.

Table S4. Crystal data and structure refinement for monoradical **10** (synchrotron, X-ray label: S19032).

Empirical formula	$C_{36}\ H_{30}\ N_5$	
Formula weight	532.65	
Crystal color, shape, size	red needle, 0.011 × 0.011 × 0.007 mm^3	
Temperature	100(2) K	
Wavelength	0.41328 Å	
Crystal system, space group	Triclinic, P-1	
Unit cell dimensions	a = 11.059(2) Å	α = 107.607(3)°.
	b = 11.856(3) Å	β = 98.964(4)°.
	c = 12.713(3) Å	γ = 116.219(3)°.
Volume	1341.2(5) $Å^3$	
Z	2	
Density (calculated)	1.319 Mg/m^3	
Absorption coefficient	0.036 mm^{-1}	
F(000)	562	
Data collection		
Diffractometer	Huber 6-circle, Huber	
Detector	Pilatus 1M, Dectris	
Theta range for data collection	1.038 to 14.971°.	
Index ranges	-13<=h<=13, -14<=k<=14, -15<=l<=15	
Reflections collected	29057	
Independent reflections	5065 [R_{int} = 0.0843]	
Observed Reflections	3055	
Completeness to theta = 14.357°	92.4 %	
Solution and Refinement		
Absorption correction	Semi-empirical from equivalents	
Max. and min. transmission	0.7439 and 0.6475	
Solution	Intrinsic methods	
Refinement method	Full-matrix least-squares on F^2	
Weighting scheme	$w = [\sigma^2 Fo^2 + AP^2 + BP]^{-1}$, with	
	$P = (Fo^2 + 2\ Fc^2)/3$, A = 0.0806	
Data / restraints / parameters	5065 / 0 / 373	
Goodness-of-fit on F^2	0.888	
Final R indices [I>2σ(I)]	R1 = 0.0521, wR2 = 0.1286	
R indices (all data)	R1 = 0.0847, wR2 = 0.1395	
Largest diff. peak and hole	0.246 and -0.222 $e.Å^{-3}$	

Goodness-of-fit = $[\Sigma[w(F_o^2 - F_c^2)^2]/N_{observns} - N_{params})]^{1/2}$, all data.

$R1 = \Sigma(|F_o| - |F_c|) / \Sigma |F_o|$. $wR2 = [\Sigma[w(F_o^2 - F_c^2)^2] / \Sigma [w(F_o^2)^2]]^{1/2}$.

Table S5. π-Stacked planes in diradical **4** (Cu Kα, X-ray label 20036).

Least-squares plane number 1 (XO = orthogonal, x = Crystal coordinates) -0.5377 XO + 0.0080 YO + 0.8431 ZO = 9.0106 -3.482 x + 0.166 y + 19.356 z = 9.0106	Least-squares plane number 2 (XO = orthogonal, x = Crystal coordinates) -0.5377 XO + 0.0080 YO + 0.8431 ZO = 5.5282 -3.482 x + 0.166 y + 19.356 z = 5.5282
Deviation Weight	Deviation Weight
+ -0.0085 1.0000 N1A	+ -0.0085 1.0000 N1B
+ 0.0363 1.0000 N2A	+ 0.0363 1.0000 N2B
+ -0.0392 1.0000 N3A	+ -0.0392 1.0000 N3B
+ 0.0095 1.0000 N4A	+ 0.0095 1.0000 N4B
+ 0.2055 1.0000 N5A	+ 0.2055 1.0000 N5B
+ -0.0348 1.0000 N6A	+ -0.0348 1.0000 N6B
+ -0.0146 1.0000 C1A	+ -0.0146 1.0000 C1B
+ 0.0247 1.0000 C2A	+ 0.0247 1.0000 C2B
+ 0.0537 1.0000 C3A	+ 0.0537 1.0000 C3B
+ 0.0463 1.0000 C4A	+ 0.0463 1.0000 C4B
+ 0.0764 1.0000 C5A	+ 0.0764 1.0000 C5B
+ -0.0119 1.0000 C6A	+ -0.0119 1.0000 C6B
+ -0.2144 1.0000 C7A	+ -0.2144 1.0000 C7B
+ -0.2678 1.0000 C8A	+ -0.2678 1.0000 C8B
+ -0.0155 1.0000 C9A	+ -0.0155 1.0000 C9B
+ 0.1671 1.0000 C10A	+ 0.1671 1.0000 C10B
+ 0.1483 1.0000 C11A	+ 0.1483 1.0000 C11B
+ 0.0075 1.0000 C12A	+ 0.0075 1.0000 C12B
+ -0.0192 1.0000 C13A	+ -0.0192 1.0000 C13B
+ -0.0027 1.0000 C14A	+ -0.0027 1.0000 C14B
+ -0.0135 1.0000 C15A	+ -0.0135 1.0000 C15B
+ 0.0956 1.0000 C16A	+ 0.0956 1.0000 C16B
+ 0.0637 1.0000 C17A	+ 0.0637 1.0000 C17B
+ -0.0457 1.0000 C18A	+ -0.0457 1.0000 C18B
+ -0.1297 1.0000 C19A	+ -0.1297 1.0000 C19B
+ -0.1170 1.0000 C20A	+ -0.1170 1.0000 C20B
Mean deviation from plane = 0.0719 Å	**Mean deviation from plane = 0.0719 Å**
	Average distance = 3.482 Å
	Angle to previous plane = 0.0°

Table S6. Dihedral angles (°) between the least-squares planes (x,y,z in crystal coordinates) and deviations from plane (Å) for diradical **4** (Cu Kα, X-ray label: 20036). (* indicates atom used to define plane.)

- 3.5083 (0.0013) x – 0.3531 (0.0187) y + 19.2803 (0.0039) z = 5.1992 (0.0117)

* -0.0120 (0.0034) N1
* 0.0477 (0.0034) N2
* -0.0035 (0.0035) N3
* 0.0591 (0.0035) N4
* 0.1850 (0.0038) N5
* -0.0940 (0.0035) N6
* -0.0523 (0.0040) C1
* 0.0169 (0.0042) C2
* 0.0608 (0.0043) C3
* 0.0327 (0.0043) C4
* 0.0778 (0.0046) C5
* 0.0176 (0.0043) C6
* -0.1713 (0.0041) C7
* -0.2462 (0.0041) C8
* -0.0290 (0.0043) C9
* 0.1401 (0.0042) C10
* 0.1420 (0.0043) C11
* -0.0417 (0.0043) C12
* -0.0832 (0.0043) C13
* -0.0465 (0.0042) C14

Rms deviation of fitted atoms = 0.1011

- 3.4145 (0.0041) x + 0.5820 (0.0257) y + 19.5296 (0.0107) z = 5.8753 (0.0178)

Angle to previous plane (with approximate esd) = 2.844 (0.085)°

* 0.0104 (0.0036) C1
* -0.0146 (0.0031) N1
* 0.0049 (0.0032) N2
* -0.0011 (0.0040) C2
* 0.0022 (0.0036) C3
* 0.0019 (0.0035) C4
* -0.0033 (0.0037) C12
* -0.0046 (0.0039) C13
* 0.0052 (0.0041) C14
* -0.0010 (0.0033) N6

Rms deviation of fitted atoms = 0.0064

- 3.7906 (0.0037) x – 1.7400 (0.0267) y + 18.3237 (0.0134) z = 4.3783 (0.0169)

Angle to previous plane (with approximate esd) = 8.197 (0.115)°

* -0.0916 (0.0037) C5
* -0.0619 (0.0032) N3
* 0.1079 (0.0033) N4
* 0.0620 (0.0042) C6
* -0.0183 (0.0037) C7
* -0.1043 (0.0037) C8
* -0.0085 (0.0039) C9
* 0.0544 (0.0038) C10
* 0.0626 (0.0043) C11
* -0.0024 (0.0034) N5

Rms deviation of fitted atoms = 0.0677

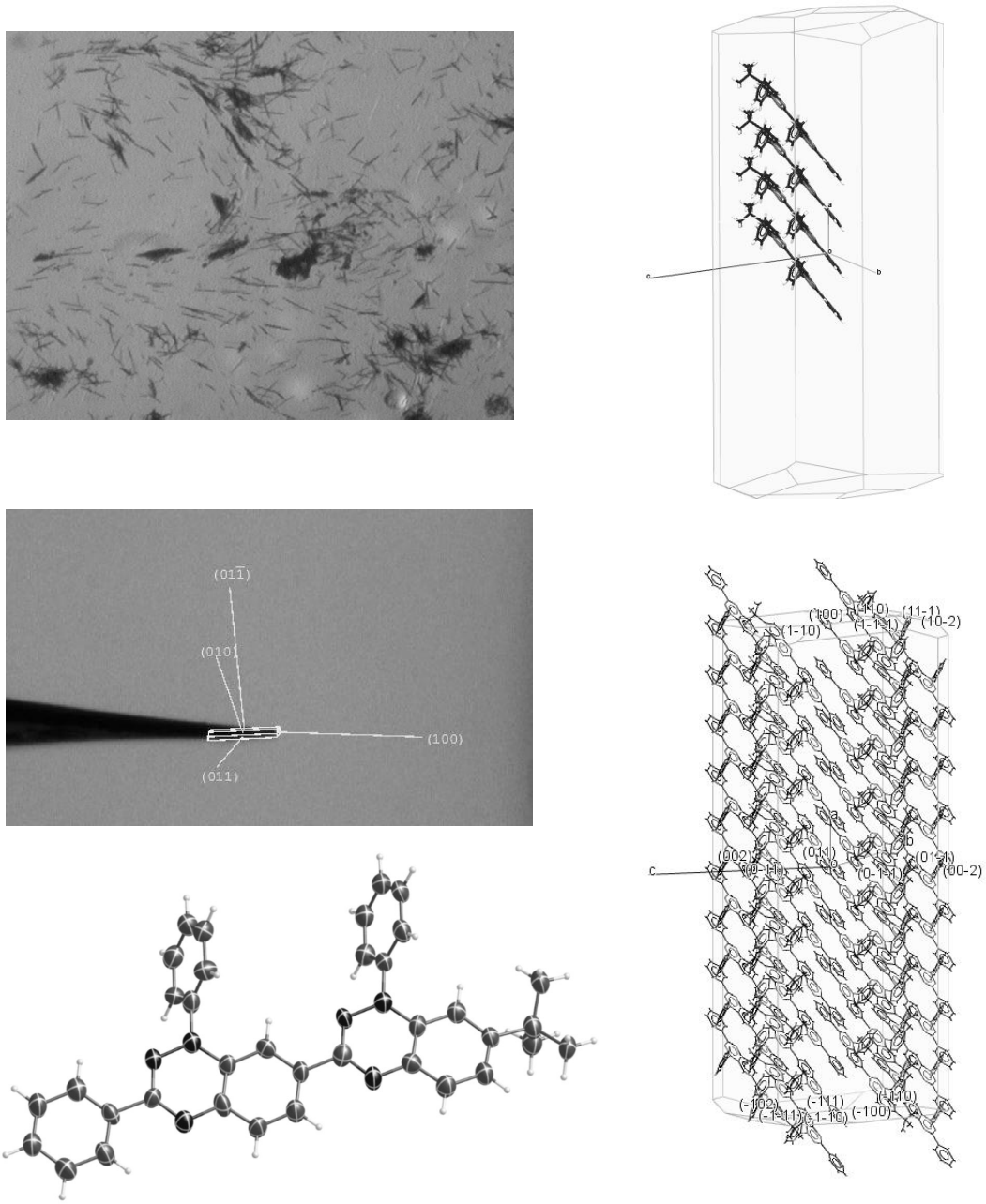

Fig. S1. X-ray crystallography of diradical **4** (Cu Kα, X-ray label: 20036). Left panels top-to-bottom: bulk crystal sample, mounted sample, and formula unit. Right panels: the BFDH morphologies with π-stacked tetramer with crystallographic axes (top) and with the molecules packed in *a*-axis (red line) from -4 to 4 and in *b*- (green) and *c*-axes (blue) from -0.5 to 0.5 (bottom).

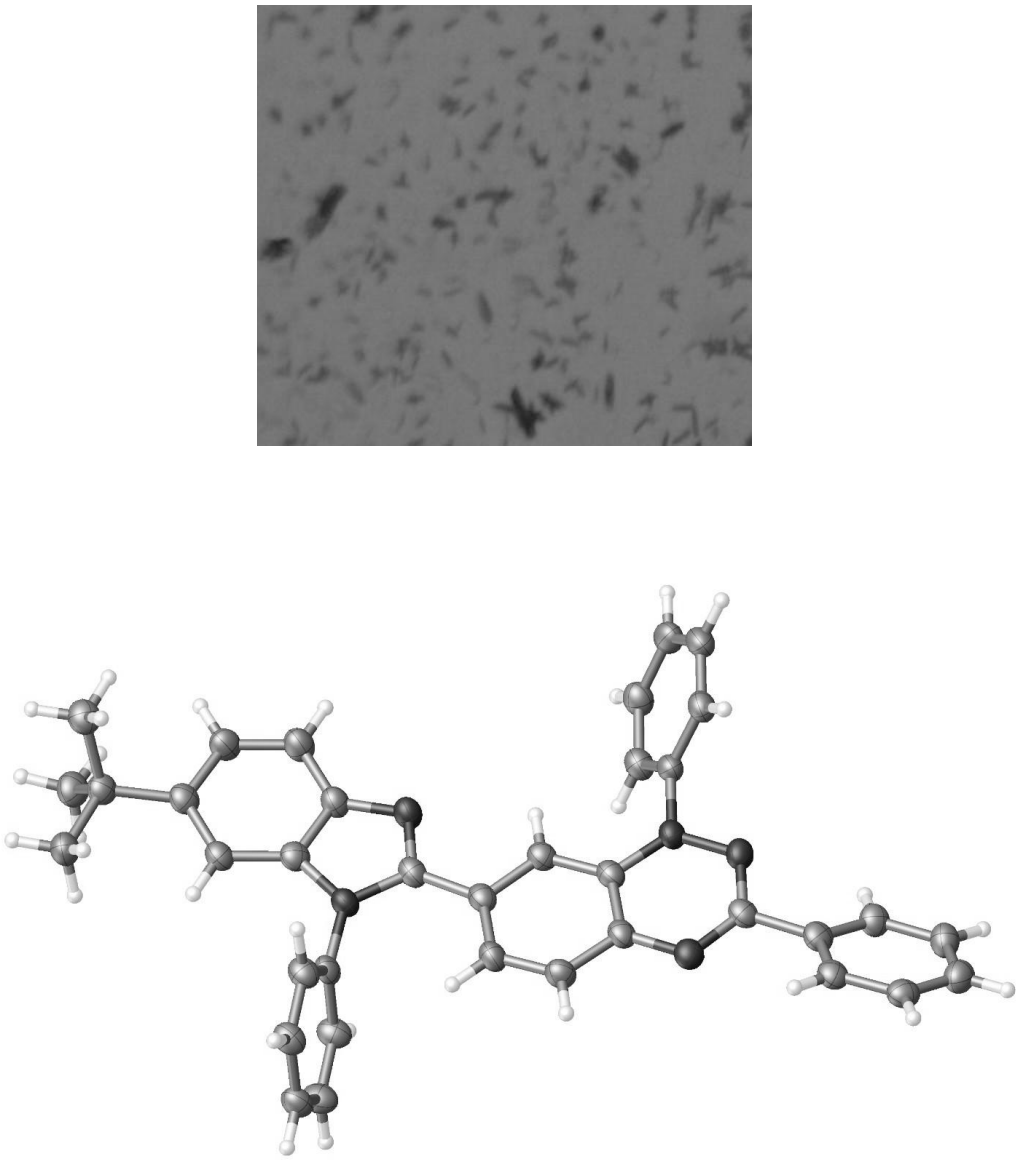

Fig. S2. X-ray crystallography of monoradical **10** (synchrotron, X-ray label: S19032). Top panel: bulk crystal sample. Bottom panel: formula unit.

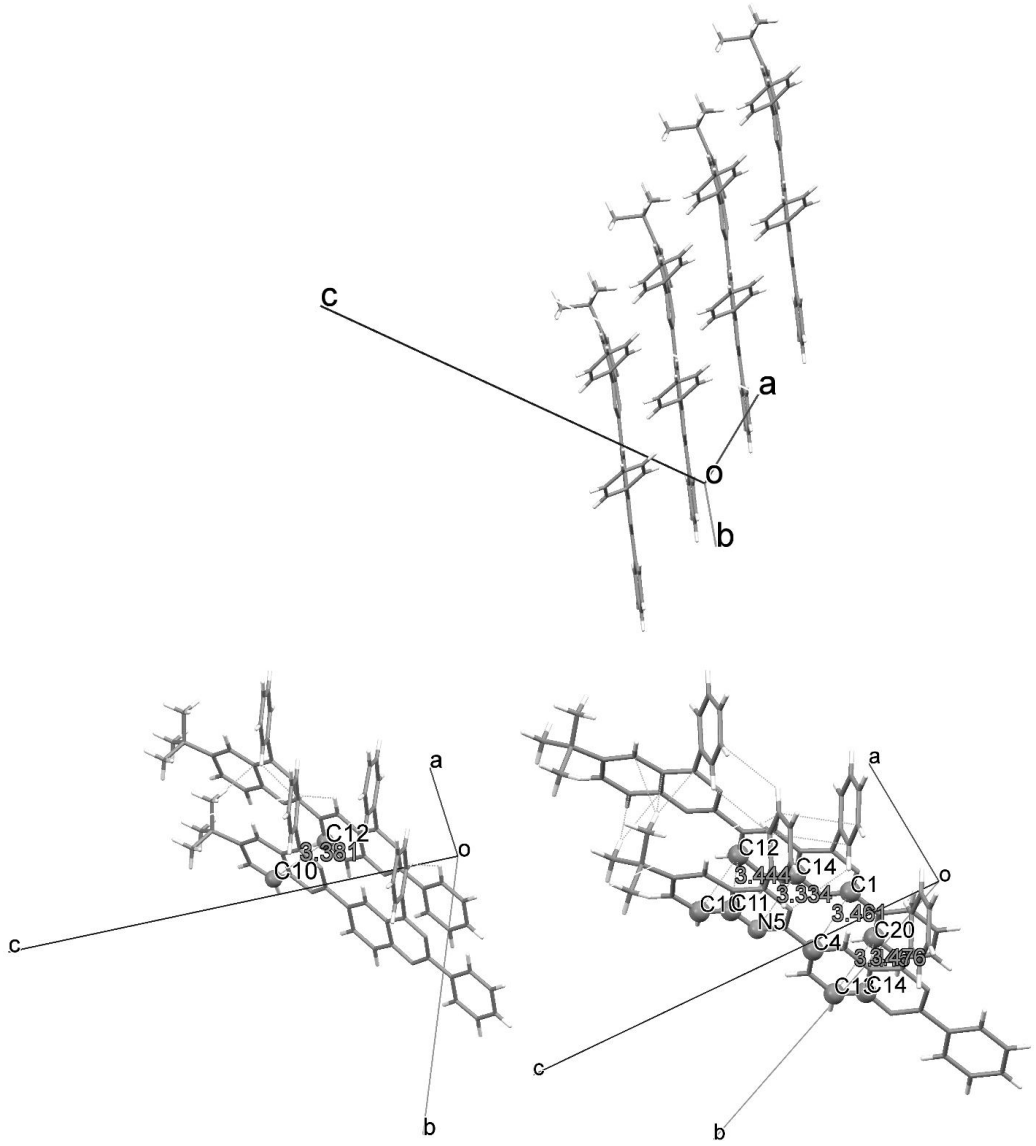

Fig. S3. X-ray crystallography of diradical **4** (Cu Kα, X-ray label: 20036): tetramers and dimers that are fragments of one-dimensional π-stacked chains. Top plot: π-stacked tetramer along *a*-axis. Bottom plot: π-stacked dimers along *a*-axis showing short C10···C12 contact of 3.381 Å (left) and multiple C···C and N···C contacts within sum of van der Waals radii plus 0.1 Å distances, in particular C11···C12 = 3.444, N5···C14 = 3.334, C4···C1 = 3.461, C13···C20 = 3.446, C14···C20 = 3.476 Å (right).

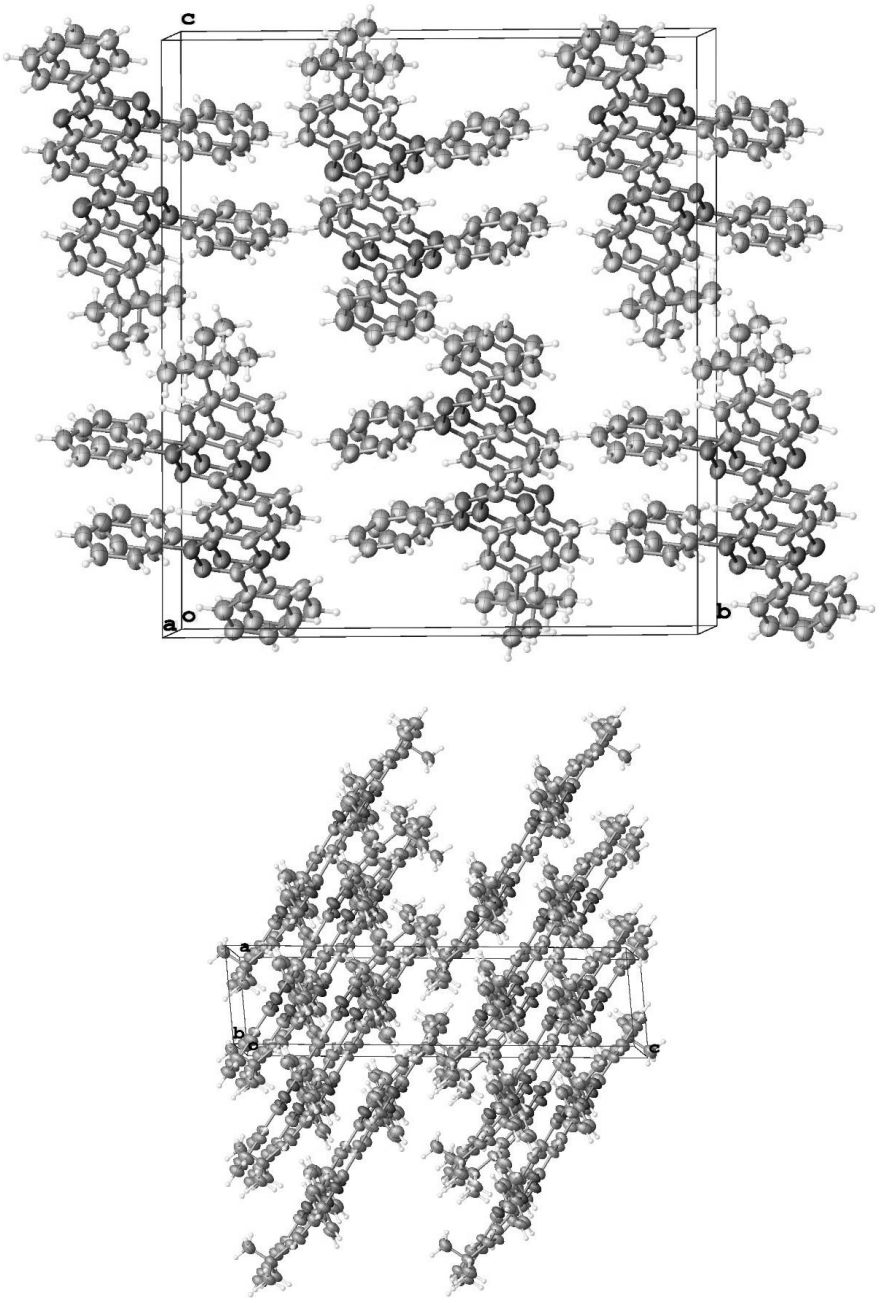

Fig. S4. X-ray crystallography of diradical **4** (Cu Kα, X-ray label: 20036): cell plots. Top plot: a view along the *a*-axis. Bottom plot: a view along the *b*-axis.

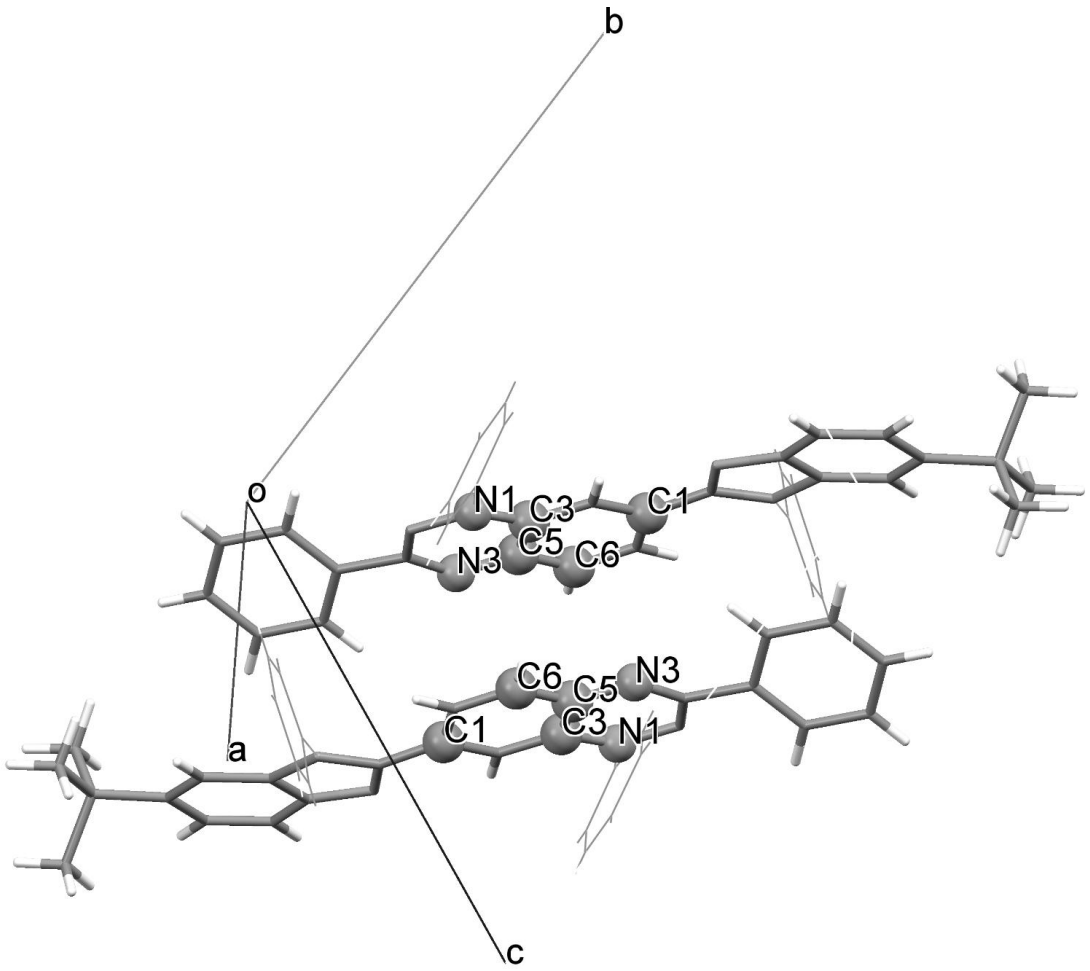

Fig. S5. X-ray crystallography of monoradical **10** (synchrotron, X-ray label: S19032): isolated π-stacked dimers along *c*-axis. Contacts between the atoms with significant spin density: C5···C5 = 3.595, C3···C6 = C6···C3 = 3.615, N1···C6 = C6···N1 = 3.691, C1···N3 = N3···C1 = 3.672 Å; the atoms are shown in ball-and-stick. *N*-phenyl rings are shown in wireframe for clarity.

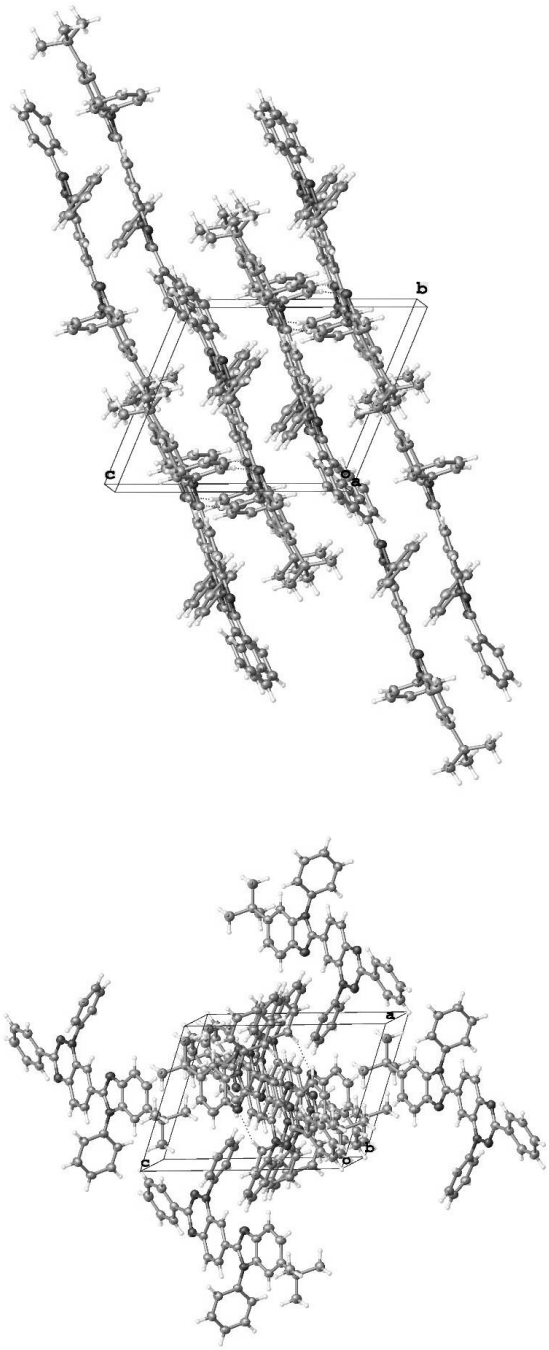

Fig. S6. X-ray crystallography of monoradical **10** (synchrotron, X-ray label: S19032): cell plots. Top plot: a view along the *a*-axis. Bottom plot: a view along the *b*-axis.

3.c. Synthesis of diradical 4 and monoradical 10.

Methyl 4-amino-3-(2-benzoyl-1-phenylhydrazinyl) benzoate (6)

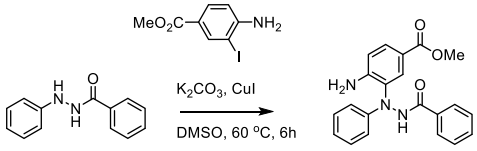

Run	Hydrazine amide SM (g/mmol/eq)	Iodoaniline (g/mmol/eq)	K_2CO_3 (g/mmol/eq)	CuI (mg/mmol/eq)	DMSO (mL)	Yield (g/%)
SZ-2-36	2.027/9.55/1	2.645/9.55/1	1.45/10.5/1.1	181/0.955/0.1	13.4	2.813/85
SZ-2-70	1.930/9.10/1	2.522/9.1o/1	1.383/10.01/1.1	346/1.82/0.2	50	2.795/85
SZ-2-94	3.86/18.20/1	5.044/18.20/1	2.766/20.02/1.1	692/3.64/0.2	100	5.377/83.4

Procedure for methyl 4-amino-3-(2-benzoyl-1-phenylhydrazinyl) benzoate **6** (label: SZ-3-36):

The hydrazine amide starting material **5** was synthesized according to the published literature.[S1-S3] Compound **6** was prepared by adopting the previously reported Cu-catalyzed C–N coupling.[S3,S10] The starting material (2.027 g, 9.55 mmol), methyl 4-amino-3-iodobenzoate (2.645 g, 9.55 mmol, purchased from Oakwood chemical, 97%), K_2CO_3(1.45 g, 10.5 mmol), and CuI (181 mg, 0.955 mmol) were charged in a 250 mL Schlenk flask under N_2 environment. The reaction was stirred at 60 °C for 6 h and formed a dark solution. The reaction mixture was diluted with EA (300 mL) and washed with H_2O (50 mL x 3), brine (50 ml). Following drying over Na_2SO_4 and evaporation of the organic layer, the resulting brown oil crude product was added with Et_2O (10 mL), which caused the formation of grey solid within 1 min. The solid was then filtered and washed with Et_2O (20 mL) to yield the desired material as the white-grey powder (2.813 g, 85% yield). The TLC analysis was performed with regular silica, DCM: MeOH = 20:1, the product R_f = 0.4. IR (SZ369-Me-Ester-Run4, powder, cm^{-1}): 3333, 3269, 1700, 1654, 1618, 1597, 1494, 1439, 1331, 1278, 1233, 1172, 1150, 1103, 1021, 768, 750, 715, 691, 632, 608. ^{1}H NMR (700 MHz, acetone-d_6, SZ-2-94): 8.349 (s, 1H), 7.864 (s, 2H), 7.845 (d, 1H, J = 2.1 Hz), 7.806 (dd, 1H, J_{ab} = 2.8 Hz, J_{ac} = 14.7 Hz), 7.563 (t, 1H, J = 12.6 Hz), 7.453 (t, 2H, J = 14.0 Hz), 7.223 (dd, 2H, J_{ab} = 13.3 Hz, J_{ac} = 14.7 Hz), 6.893 (t, 1H, J = 12.6 Hz), 6.744 (t, 2H, J = 14.0 Hz), 5.323 (s, 2H), 3.786 (s, 3H). ^{13}C NMR (175 MHz, acetone-d_6, SZ-2-94): 167.9, 166.8, 150.7, 146.8, 132.7, 132.0, 131.2, 130.8, 129.6, 129.4, 129.0, 127.4, 120.6, 119.5, 115.3, 113.4, 51.8. HRMS (ESI/TOF-Q) *m/z*: [M + Na^+] calcd for $C_{21}H_{19}N_3O_3Na$ 384.1324; found 384.1319. M.p. (5 °C/min) 161-166 °C.

Amino-benzoic acid 7.

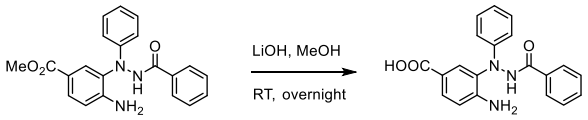

6 **7**

Run	Ester SM (g/mmol/eq)	LiOH·H2O (mg/mmol/eq)	MeOH/H2O=2/1 (mL)	Yield (g/%)
SZ-2-40	3/8.3/1	697/16.6/2	70	1.893/64
SZ-2-71	2/5.54/1	465.4/11.08/2	45	1.35/65
SZ-2-95	6.576/18.22/1	1730/59/2.5	90	4.931/78

Procedure for hydrolysis of methyl ester to prepare the amino-benzoic acid **7** (SZ-2-95):

The starting material ester **6** (6.576 g, 18.22 mmol) and the LiOH·H2O (1.730 g, 2.5 mmol) were weighed in a 250 mL RBF. A mixture of MeOH/H2O = 2/1 (90 mL) was poured into the flask. The reaction was stirred at RT for 12 h. The MeOH was removed *in vacuo*. The residue was added with H2O (300 mL) then extracted by DCM (75 mL x 2). The aqueous layer was treated with excess of NaHSO4 1 M solution until pH 1 was obtained and the dark aqueous solution turned to a white cloudy mixture. The aqueous layer was extracted by EA (300 mL x 4). The combined organic layers were dried over Na2SO4 and evaporated *in vacuo*. The TLC analyses with regular silica, DCM/MeOH = 20/1 indicated that starting material was still observed in the basic extracts (DCM) and the creation of a new spot with higher polarity in the acidic extracts (EA). The crude dark brown solid could be recrystallized by EA to afford a white powder solid (4.93 g, 78%). IR (SZ372-1-acid-run1, powder, cm^{-1}): 3227, 3005, 1647, 1670, 1615, 1596, 1569, 1525, 1489, 1456, 1413, 1296, 1275, 1253, 1152, 802, 747, 732, 688, 634, 607. ^{1}H NMR (700 MHz, acetone-d_6, SZ-2-95): 10.314 (s, 1H), 8.045 (d, 2H, J = 7.7 Hz), 7.940 (s, 1H), 7.791 (dd, 1H, J_{ab} = 1.4 Hz, J_{ac} = 8.4 Hz), 7.604 (d, 1H, J = 3.5 Hz), 7.526 (t, 2H, J = 7.7 Hz), 7.215 (t, 2H, J = 7.7 Hz), 6.921 (d, 1H, J = 8.4 Hz), 6.827 (t, 1H, J = 7 Hz), 6.772 (d, 2H, 8.4 Hz), 6.171 (br, 2H). ^{13}C NMR (175 MHz, acetone-d_6, SZ-2-95): 205.5, 167.3, 166.8, 151.8, 147.8, 132.5, 132.2, 131.8, 130.9, 129.4, 128.9, 128.7, 127.5, 119.5, 118.3, 114.6, 113.2. HRMS (ESI/TOF-Q) *m/z*: [M + Na^+] calcd for $C_{21}H_{19}N_3O_3Na$ 370.1168; found 370.1157. M.p. (5 °C/min): 205-208 °C.

Phenyl hydrazine amide 8.

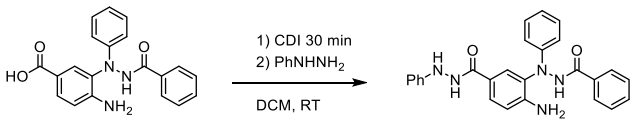

7 **8**

Run	Acid SM (mg/mmol/eq)	CDI (mg/mmol/eq)	$PhNHNH_2$ (mg/mmol/eq)	DCM (mL)	Yield (mg/%)
SZ-2-77[a]	100/0.288/1	47/0.288/1	37/0.346/1.2	3	96/77
SZ-2-98[a]	1000/2.88/1	560/3.45/1.2	466/4.32/1.5	5	806/64
SZ-3-9	1000/2.88/1	720/4.44/1.5	466/4.32/1.5	5	1179/94
SZ-3-31	1900/5.476/1	1332/8.213/1.5	887/8.231/1.5	9.5	1995/84

[a] These two initial reactions are not included in the yield estimates in Scheme 1, main text; the low yield may be lowered, due to the moisture in the starting material, which could compete with the hydrazine as a nucleophile during the reaction.

The amide **8** (label: SZ-3-31) was synthesized by adaptation of the literature procedure.[S11]

The carboxylic acid starting material **7** (1.9 g, 5.476 mmol) and the carbonyl diimidazole (CDI) (1.332 g, 8.213 mmol) were loaded in a 50 mL RBF under N_2 atmosphere. After the injection of DCM (9.5 mL), the reaction was stirred at RT for 30 min. During which time, the reaction mixture was brown and heterogeneous, with a lot of gas bubbles being generated. Then, the neat phenyl hydrazine (0.807 mL) was added to the reaction mixture dropwise. The reaction turned to orange within 5 min and became homogeneous later. After 18 h, the TLC analysis with regular silica, DCM/MeOH = 4/1 indicated no starting material existed with the product R_f = 0.25. The reaction was diluted with DCM (100 mL) and Et_3N (0.5 mL), washed with sat. Na_2CO_3 (30 mL), brine (30 mL). The organic layer was dried over Na_2SO_4 and evaporated to give the orange oil crude. The column chromatography was performed with EA in DCM (5%-20%) to afford the product as a pale orange solid (1.995 g, 84%). IR (SZ375-run1, powder, cm^{-1}): 3454, 3347, 3307, 3248, 1643, 1598, 1492, 1337,1305, 1281, 1250, 892, 775, 744, 716, 687, 666, 634593, 472. ^1H NMR (700 MHz, acetone-d_6, SZ-3-31): 10.313 (s, 1H), 9.392 (s, 1H), 8.029 (d, 2H, J = 7.7 Hz), 7.918 (s, 1H), 7.807 (d, 1H, J = 8.4 Hz), 7.600 (t, 1H, J = 7.0 Hz), 7.511 (t, 2H, J = 7.0 Hz), 7.196 (t, 2H, J = 7.7 Hz), 7.133 (t, 2H, J = 7.0 Hz), 7.054 (s, 1H), 6.920 (d, 1H, J = 8.4 Hz), 6.881 (d, 2H, J = 7.7 Hz), 6.810 (t, 1H, 7 Hz), 6.750 (d, 3H, J = 3.5 Hz), 5.984 (s, 2H). ^{13}C NMR (175 MHz, acetone-d_6, SZ-3-31): δ = 205.4, 170.1, 167.3, 166.2, 150.7, 150.1, 147.7, 132.6, 132.1, 129.8, 129.7, 128.9, 128.7, 128.6, 127.8, 127.6, 121.3, 119.4, 119.3, 114.7, 113.13, 113.06. HRMS (ESI/TOF-Q) m/z: [M + Na^+] calcd for $C_{26}H_{23}N_5O_2Na$ 460.1749; found 460.1751. M.p. (5 °C/min): 148-159 °C.

***N*-phenylbenzohydrazide 9.**

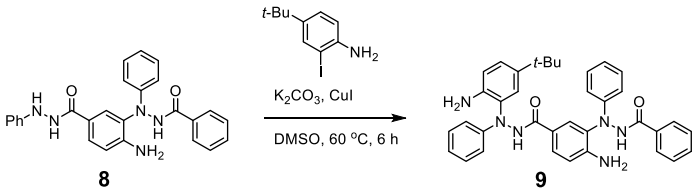

8 **9**

Run	SM (mg/mmol/eq)	*t*-Bu iodo aniline (mg/mmol/eq)	K_2CO_3 (mg/mmol/eq)	CuI (mg/mmol/eq)	DMSO (mL)	Yield (mg/%)
SZ-2-81	70/0.160/1	74/0.268/1.67	31/0.288/1.6	6/0.04/0.25	1	65/69
SZ-2-96	526/1.202/1	363.6/1.323/1.1	199/1.44/1.2	46/0.24/0.2	6.6	488/69
SZ-2-99	100/0.229/1	63/0.229/1	32.2/0.252/1.1	8.7/0.046/0.2	2.3	107/80
SZ-3-1[a]	200/0458/1	126/0.458/1	64/0.504/1.1	16/0.092/0.2	4.6	164/61
SZ_3-34	826/1.888/1	571/2.077/1.1	313/2.266/1.2	72/0.378/0.2	12.6	722/65
SZ-3-55	83/0.189/1	57/0.207/1.1	60/0.434/2.2	10/0.053/0.27	1.6	90/81

[a] This reaction is not included in the yield estimates in Scheme 1, main text; the low yield of the reaction may be, problems with removal of DMSO during workup.

Procedure for C-N coupling reaction to prepare the *N*-phenylbenzohydrazide **9** (label: SZ-2-99):

Compound **9** was prepared by adopting the previously reported Cu-catalyzed C–N coupling.[S3,S10] The starting material **8** (100 mg, 0.229 mmol), K_2CO_3 (32 mg, 0.252 mmol), and CuI (8.7 mg, 0.046 mmol) were loaded in a Schlenk tube and dried under high vacuum overnight. 4-*tert*-Butyl-2-iodo-aniline (63 mg, 0.299 mmol), which was synthesized according to published literature,[S4] was weighed in a vial, dissolved by DMSO (2.3 mL), and then transferred to the Schlenk tube at RT. The reaction was stirred at 60 °C for 6 h and formed a dark solution. Then, the reaction mixture was diluted with EA (20 mL) and washed with H_2O (10 mL x 3) and brine (10 mL). Following drying over Na_2SO_4 and evaporation of the organic layer, the resulting dark brown solid crude product was purified by column chromatography. The desired material was isolated as the white-grey powder (107 mg, 80% yield) (regular silica, DCM/EA = 6/1, R_f = 0.3). To remove the trace amount of impurities, the isolated product was recrystallized by EA and pentane to give a white powder. IR (SZ368-run1, powder, cm^{-1}): 3439, 3334, 3243, 2950, 1658, 1642, 1612, 1597, 1507, 1490, 1339, 1304, 1277, 1258, 764, 719, 690, 617, 509, 495. ^{1}H NMR (700 MHz, acetone-d_6, SZ-2-99): 10.295 (s, 1H), 9.913 (s, 1H), 8.031 (d, 2H, J = 7.0 Hz), 7.898 (s, 1H), 7.795 (dd, 1H, J_{ab} = 8.4 Hz, J_{ac} = 2.1 Hz), 7.607 (t, 1H, J = 7.0 Hz), 7.519 (t, 2H, J = 7.7 Hz), 7.260 (d, 1H, J = 1.4 Hz), 7.204 (dd, 2H, J_{ab} = 8.7 Hz, J_{ac} = 7.0 Hz), 7.139 (t, 3H, J = 2.8 Hz), 6.919 (d, 1H, J = 9.1 Hz), 6.818 (t, 1H, J = 7.0 Hz), 6.770 (t, 3H, J = 8.4 Hz), 6.723 (t, 1H, J = 7 Hz), 6.644 (d, 2H, J = 7.7 Hz), 6.042 (s, 2H), 5.199 (s, 2H), 1.200 (s, 9H). ^{13}C NMR (175 MHz, acetone-d_6, SZ-2-99): δ = 205.3, 167.2, 166.3, 150.9, 148.2, 147.7, 144.6, 139.8, 132.6, 132.1, 130.0, 129.7, 128.9, 128.64, 128.58, 128.0, 127.5, 125.7, 125.5, 120.6, 119.4, 118.3, 115.5, 114.7, 113.2, 112.7. HRMS (ESI/TOF-Q) *m/z*: [M + Na^+] calcd for $C_{36}H_{36}N_6O_2Na$ 607.2797; found 607.2795. M.p. (5 °C/min): 175-179 °C.

Forming "one ring closed" intermediate 11 with the catalytic amount of *p*-TsOH.

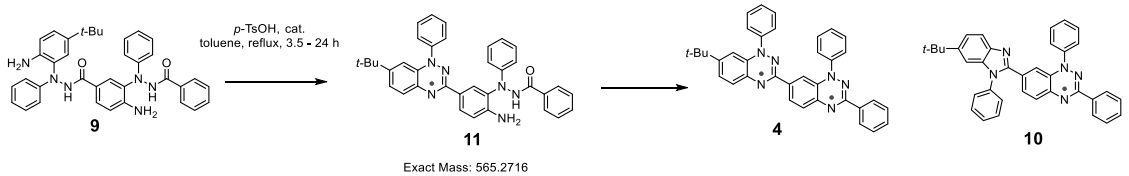

Run	SM (mg/μmol/eq)	*p*-TsOH·H_2O (mg/μmol/eq)	Toluene (mL)	Time (h)	EtOH/2 M NaOH, 1:1 (mL)	Yield (mg/ %)	Spin conc.	Notes
SZ-3-8	50/91/1	2/10.5/0.12	4	3.5	10	**11**: 10 mg/19%, **4:** trace	93%	
SZ-3-16	50/91/1	10/53/0.62	4	2.5	No	**11** is the major	N/D	No SM and TM
SZ-3-24	40.5/69.3/1	5/26.3/0.37	4	24 then 72	30	**4**: 3.5 mg/9%,	TM:124% Mono:62%	

Reaction condition optimization: (label: SZ-3-8)

The starting material **9** (50 mg, 91 μmol) was loaded with a catalytic amount of *p*-TsOH•H_2O (2 mg, 10.5 μmol) in a 10 mL RBF. After the addition of toluene (4 mL), the reaction was refluxed and stirred in the darkness for 3.5 h. the reaction mixture changed to a black homogeneous condition. After oxidation by EtOH/ 2M NaOH = 1/1 (10 mL), the crude mixture showed a trace amount of TM **4,** a green spot as major on TLC with R_f = 0.15, and leftover starting material. (neutral alumina, pentane/DCM = 1/5). The green spot was isolated (10 mg); *m/z* 565.93 from LRMS (ESI-LCQ) was found. EPR (X-band, 9.32 GHz, Toluene/$CHCl_3$ = 4/1, label: SZ310) spectra show that the spin concentration at room temperature is 93%. 2 mg of the green compound was mixed with 10 mg of $Na_2S_2O_4$ in DMSO-d_6 0.5 mL. The mixture was heated by a heat gun and the green solution changed to yellow. The ^{1}H-NMR spectrum (SZ-3-08-reduced)(Fig. S56) showed only one NH_2 group present and the small *J* 1H doublet peak at downfield chemical shift (7.3 ppm), which is from the *meta* coupling on the aromatic ring with *t*-Bu group, is missing compared to the ^{1}H-NMR of SM **9**, suggesting the compound should be the monoblatter radical structure **11** with only one ring closed.

The reaction was repeated (label: SZ-3-24) with 0.37 equivalent of *p*-TsOH•H_2O and monitored by the ESI-LCQ. After 24 h, the reaction crude mixture contained **11**, based on ESI LCQ spectrum (SZ-3-24-cr) (Fig. S54). After addiitonal 24 h of reflux, ESI LCQ spectrum indicated that the crude mixture not only contained **11**, but also the TM **4** (*m/z* 547.20, [M + H^+]) and monoradical **10** (*m/z* 533.33, [M + H^+], see structure in the next scheme) (ESI-LCQ: SZ-3-24-48h-cr) (Fig. S55). After total of 72 h reflux, the TLC showed TM **4** as the major product and many side-products. This result indicated that although the catalytic amount of *p*-TsOH•H_2O worked for the formation of TM **4**, it is not efficient and the long reaction time would lead to complex mixtures including monoradical **10**. The stoichiometric amount of the acid would accelerate the formation of diradical **4** as well as reduce side-products, see: next set of reactions.

Forming diradical 4 and monoradical 10 with the stoichiometric amount of *p*-TsOH.

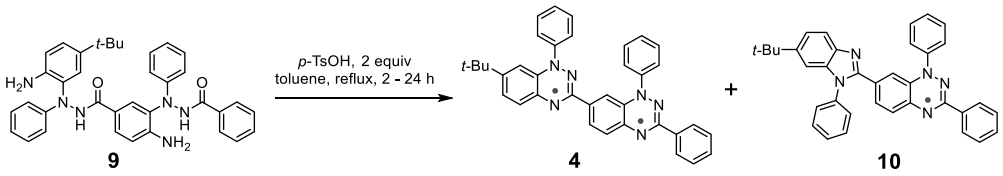

9 **4** **10**

Run	SM (mg/μmol/eq)	*p*-TsOH · H_2O (mg/μmol/eq)	Toluene (mL)	Time (h)	EtOH/2 M NaOH, 1:1 (mL)	Yield of TM **4** (mg/ %)	Spin conc.	Notes
SZ-3-30	22/38/1	18/95/2.5	6/6	18	30	**4**: 11 mg / 50%	TM: 130%	TLC: TM is major, mono minor
SZ-3-33	107/183/1	74/385/2.1	37/5	24	60	**4**: 42 mg / 42% **10**: 43 mg / 44%	TM: 219% Mono: 103%	
SZ-3-46	103/176/1	65/342/1.94	35/5	3.5	60	**4**: 42 mg / 44%	TM: 131%	TLC showed TM was dominant but isolated yield was only 44%

Procedure for diradical **4** and monoradical **10** (label: SZ-3-33).

The starting material **9** (107 mg, 183 μmol), *p*-TsOH · H_2O (74 mg, 385 μmol) was loaded in a 10 mL RBF. After the addition of toluene (37 mL), the reaction was refluxed with the custom-made micro Dean-Stark apparatus[S12] and stirred in the darkness for 24 h. The reaction mixture changed to a black homogeneous solution. Then, after evaporation of the solvent, the dark green-black residue was dissolved in EtOH/ 2M NaOH = 1/1 (60 mL) and immediately turned to a dark brown-red solution. The reaction mixture was stirred on air for 12 h, then extracted by DCM (60 mL x 4). The organic extract was dried over Na_2SO_4, and then evaporated to afford a black solid crude, which was purified by column chromatography (pentane/DCM = 1/8, then pure DCM). The desired diradical product was isolated as dark brown red solid (42 mg, 42%) with R_f = 0.3. The major side product is a monoradical as black red solid (43 mg, 44%) with R_f = 0.1 (neutral alumina, pentane/DCM = 1/4). The diradical **4** could be recrystallized as black plate/needle solid by slow evaporation method with EA. 15 mg diradical was dissolved in ethyl acetate 18 mL under heat. The solution was filtered in hot by a glass pippet with a small piece of cotton then collected in a 20 mL vial. The vial was heated below 80 °C in sand bath and closed with septum cap and needles. After 7 days of evaporation, the remaining liquid was removed and the solid was washed several times with pentane. The crystal sample was put under high vacuum at 80 °C for 2 days. EPR (X-band, 9.32 GHz, Toluene/$CHCl_3$ = 4/1, label: SZ336) The spin concentration at room temperature is 219%. 25-mg recrystalized sample was dissoved in 5 mL $CDCl_3$ with one drop of di-*tert*-butyl nitroxide and checked for ^{1}H NMR, the *tert*-butyl group from the diradical is at 9.860 ppm, the di-*tert*-butyl group from nitroxide is at –5.378 ppm. HRMS (ESI/TOF-Q) *m/z*: [M^+] calcd for $C_{36}H_{30}N_6$ 546.2532; found 546.2546. TGA thermal stability >264 °C with 99% original weight. M.p. 250 – 251 °C (on air, some decomposition after 10 min at 230 °C, see: Fig. S10).

A small sample of **4** was reduced with excess of $Na_2S_2O_4$ in DMSO-d_6 , using the procedure analogous to that for **11**. ^{1}H NMR (700 MHz, Fig. S57) showed two broadened and partially D-exchanged singlets at 9.08 ppm (0.57 H) and 8.61 ppm (0.41 H), assigned to the NH moieties. LRMS ESI showed the most intense peak at *m/z* 547.4 (Fig. S58), one unit above *m/z* 546.4 in the control MS

of diradical **4** (Fig. S59), thus suggesting partial oxidation fo the reduced **4** in the MeOH/HCOOH mixture during ESI.

The monoradical **10** could be recrystallized by vapor diffusion method with ethyl acetate and pentane. HRMS (ESI/TOF-Q) *m/z*: [M$^+$] calcd for $C_{36}H_{30}N_5$ 532.2501; found 532.2481. EPR (X-band, 9.32 GHz, Toluene/$CHCl_3$ = 4/1, label: SZ335) spin concentration 103%.

Optimized conditions for diradical 4.

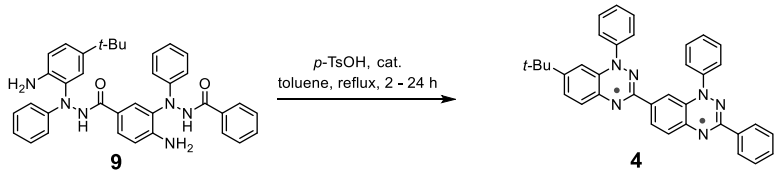

9 **4**

Run	SM (mg/μmol/eq)	*p*-TsOH·H_2O (mg/μmol/eq)	Toluene (mL)	Time (h)	EtOH/2 M NaOH, 1:1 (mL)	Yield of TM **4** (mg/ %)	Spin conc. at RT	Notes
SZ-3-97	40/68.5/1	26/137/2	14	2	24	**4**: 19.6 mg/52%,	Isolated: 200%	
SZ-3-98	40/68.5/1	26/137/2	14	2	24	**4**: 20.3 mg/54%,	Isolated: 198% Recystalized: 213%	68 mg 4A molecular sieves

Procedure for diradical **4** (label: SZ-3-97).

The starting material **9** (40 mg, 68.5 μmol), *p*-TsOH·H_2O (26 mg, 137 μmol) was loaded in a 50 mL RBF. After the addition of toluene (14 mL), the reaction was refluxed with the custom-made micro Dean-Stark apparatus and stirred in the darkness for 2 h. The reaction mixture changed to a black homogeneous condition. Then, after evaporation of the solvent, the dark green-black residue was dissolved into EtOH/ 2M NaOH = 1/1 (60 mL) and immediately turned to a dark brown-red solution. The reaction mixture was stirred with air for 4 h, then extracted by DCM (20 mL x 3). After the removal of the solvent, the TLC analysis showed diradical **4** as the major with R_f = 0.2 (neutral alumina, DCM/pentane = 10/4). The isolated yield was 52% with 200% spin concentration at room temperature. The SZ-3-98 was set up in the identical conditions, except for adding 68 mg 4A molecular sieves, with the hope to absorb water as the by-product. The results were hardly different. The diradical **4** could be recrystallized by the vapor diffusion method with ethyl acetate and pentane to increase purity. EPR (X-band, 9.32 GHz, Toluene/$CHCl_3$ = 4/1, label: SZ406).

3.d. Thermal stability of diradical 4: TGA/IR study and annealing in air/EPR spectroscopic study.

TGA/IR. Thermal stability of diradical **4** was tested using TGA instrument (TA Instruments TGA 550) that was run with IR attachment (Thermo NICOLET Is50 NIR). Polycrystalline diradical **4** (recrystallized from EtOAc) was placed was placed under vacuum (1 mTorr) overnight at 90 °C. A sample of **4** (1.28 mg) was placed in the TGA/IR instrument; TGA was carried out under N_2 with heating at 5 °C/min to 1000 °C (Figs. S7 and S8).

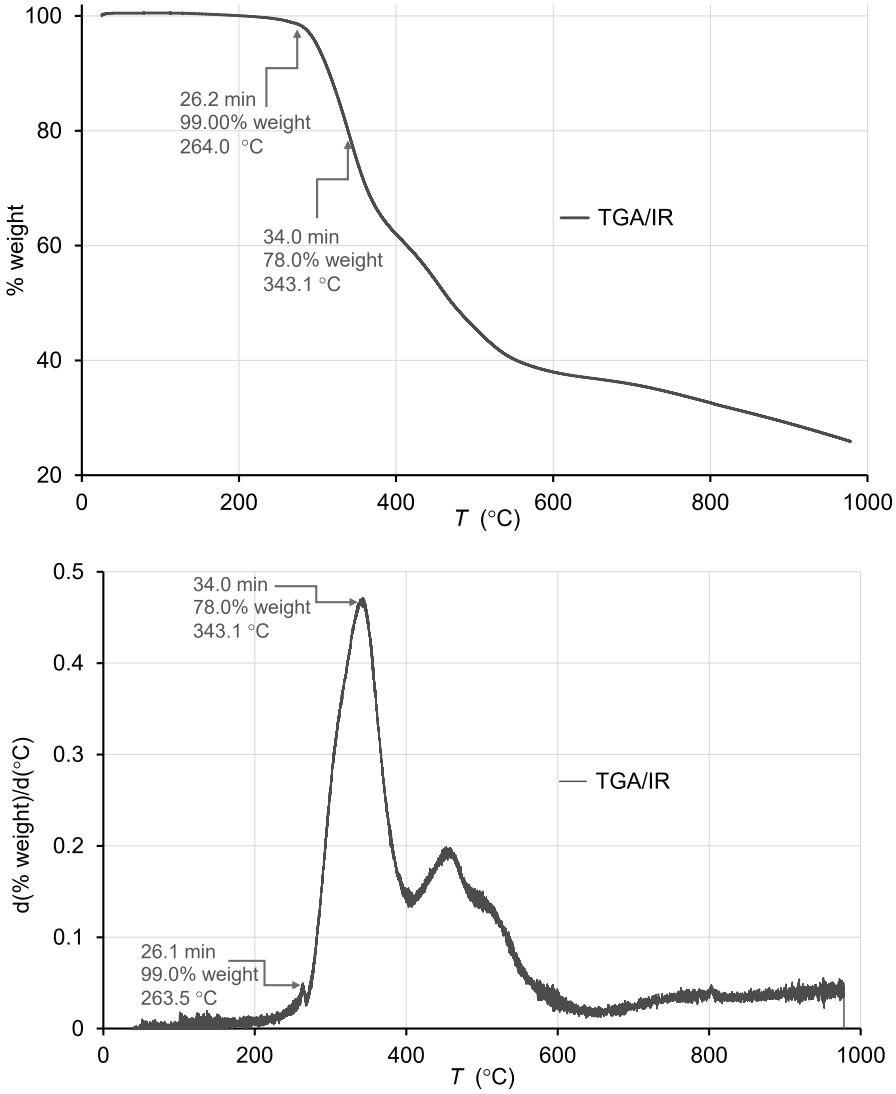

Fig. S7. Thermogravimetric analysis (TGA) with IR spectrosocopy (for IR spectra, see: next Fig.). Top panel: plot for retained %weight vs. temperature. Bottom panel: plot for rate of weight loss, d(% weight)/d(°C), vs. temperature.

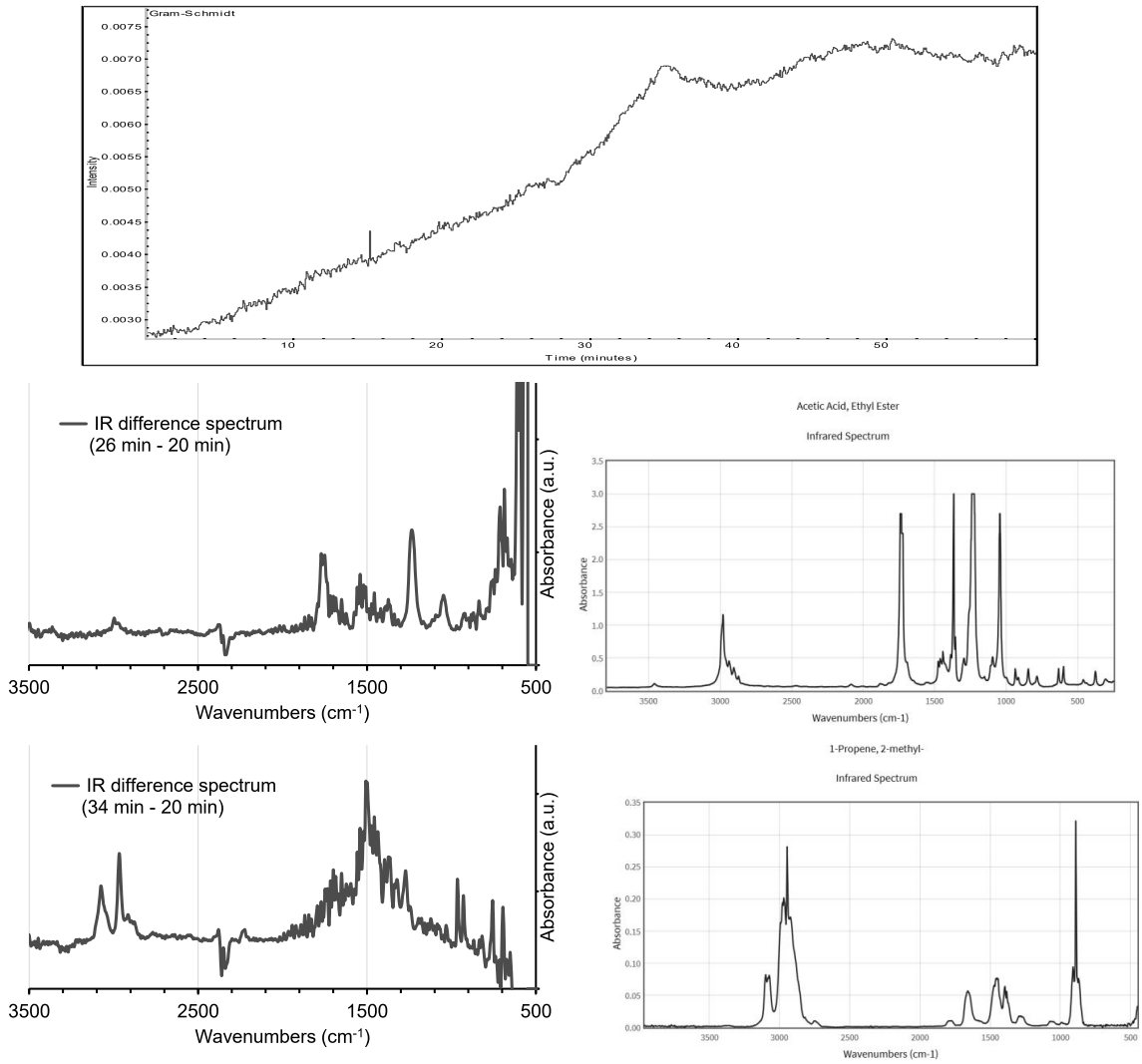

Fig. S8. Top panel: Plot of IR intensity vs. time during the TGA. Middle panel: IR difference spectrum at 26 min, corresponding to onset of weight loss (99% weight retained) at 264 °C and the NIST reference IR spectrum for ethyl acetate (EtOAc). Bottom panel: IR difference spectrum at 34 min, corresponding to maximum rate of weight loss [d(% weight/d(°C) ≈ 0.5] at 343 °C and the NIST reference IR spectrum for *iso*-butylene. Reference IR spectra for EtOAc and *iso*-butylene were obtained from NIST (NIST Chemistry WebBook) website: EtOAc, https://webbook.nist.gov/cgi/cbook.cgi?ID=C141786&Type=IR-SPEC&Index=2 and *iso*-butylene, https://webbook.nist.gov/cgi/cbook.cgi?ID=C115117&Mask=80.

TGA data suggest an outstanding thermal stability for **4**, with apparent onset of thermal decomposition (1 % mass loss) at T = 264 °C. However, at T = 264 °C, a small spike in the rate of weight loss vs T; d(weight)/d(T), is found and parallel IR spectroscopy suggests evolution of EtOAc into the head space (Figure 5 main text and Fig. S7, SI). Thus, actual onset of decomposition of **4** is at T > 264 °C, which is more than 104 °C higher than recently studied S = 1 diradical **2**.[2] At T = 343 °C, which corresponds to the maximum of rate of decomposition, -d(weight) / d(T) ≈ 0.5 % / °C (Figure 5 main text and Fig. S7, SI), IR spectra suggest evolution of *iso*-butylene into the head space, i.e., decomposition of **4** accompanied by the loss of its *tert*-butyl group (Fig. S8, SI). With such outstanding thermal stability, it is not surprising that **4** is stable at ambient conditions on typical chromatographic packing materials such as silica gel or neutral alumina.

Annealing in air with EPR spectroscopic follow up. A small sample of crystalline diradical **4** was placed in a melting point capillary (open to air) and placed in a melting point apparatus. Onset of melting was observed at 255 °C; the liquid was allowed to reach 263 °C, and then it was annealed at 256 °C for 10 min. Subsequently, the capillary was taken out and its bottom part, containing the melt was broken off and crushed into small pieces in a vial. The sample was extracted with toluene/chloroform (3 : 1), and after a brief degassing, EPR spectrum at 117 K was obtained; the spectral simulation indicated that the ratio of S = ½ decomposition product to S = 1 diradical (triplet state) is 1.9 : 1 (Fig. S9). Similar experiments were carried out by heating **4** on air at 200 (Fig. S11), 230 (Fig. S10), 240, and 250 °C for 10 min.

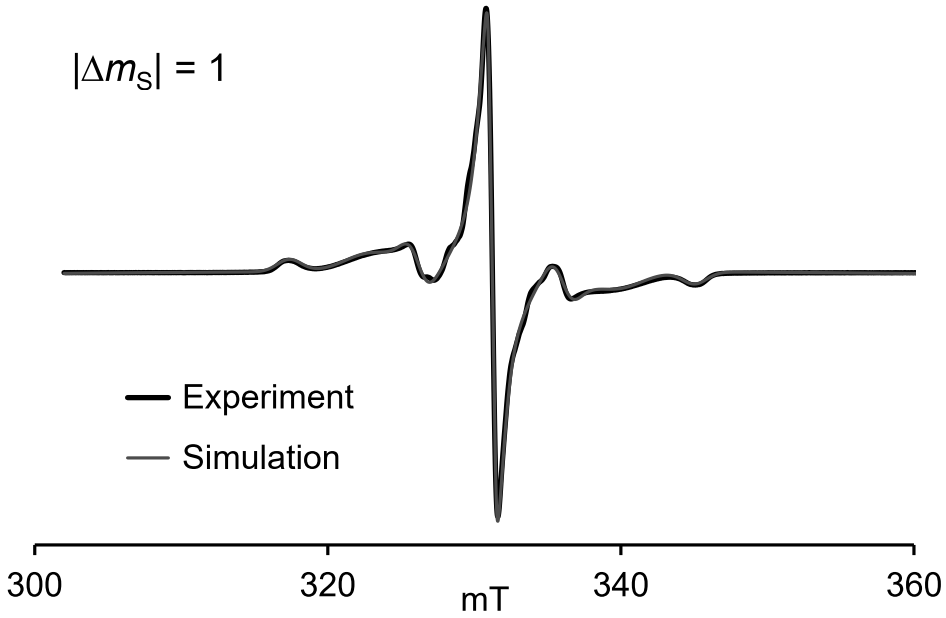

Fig. S9. EPR (117 K, ν = 9.2900 GHz, EPR label: SZ425R2) spectrum for diradical **4** in toluene/chloroform, 3:1 glass, following melting and heating in air up to 263 °C and then following by annealing at 256 °C for 10 min. The ratio of $S = ½$ decomposition product to $S = 1$ diradical (triplet state) is 1.9 : 1. Simulation $|\Delta m_s| = 1$ region (pepper, EasySpin, rmsd = 0.009974): Component A, weight = 1.0000, $S = 1$, $D = 387.5$ MHz, $E = 35.5$ MHz, $g_{xx} = 2.0041$, $g_{yy} = 2.0032$, $g_{zz} = 2.0040$; H-strain (MHz): $H_x = 43.50$, $H_y = 105.36$, $H_z = 54.67$; g-strain: $g_x = 0.0000098$, $g_y = 0.0000077$, $g_z = 0.00000010$, D-strain (MHz): $D = 12.39$, $E = 0.058$; component B, $S = ½$, weight = 1.8958, $g_{xx} = 2.0039$, $g_{yy} = 2.0041$, $g_{zz} = 2.0011$; H-strain (MHz): $H_x = 5.43$, $H_y = 32.24$, $H_z = 132.74$.

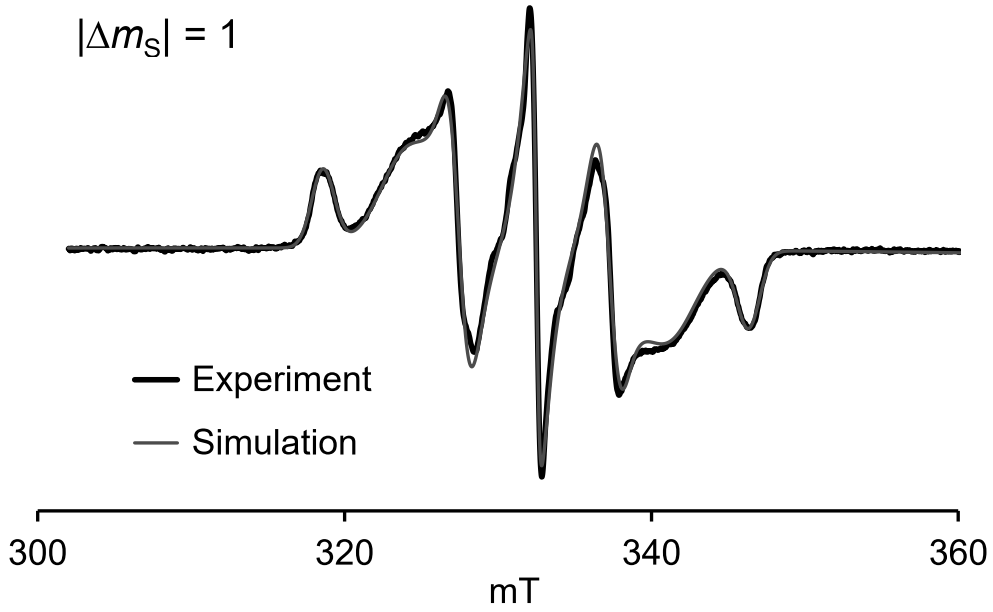

Fig. S10. EPR (117 K, ν = 9.3255 GHz, EPR label: SZ425R11) spectrum for diradical **4** in toluene/chloroform, 3:1 glass, following heating in air up at 230 °C for 10 min. The ratio of S = ½ decomposition product to S = 1 diradical (triplet state) is 0.29 : 1. Simulation $|\Delta m_s| = 1$ region (pepper, EasySpin, rmsd = 0.026443): Component A, weight = 1.0000, S = 1, D = 388.5 MHz, E = 35.6 MHz, g_{xx} = 2.0043, g_{yy} = 2.0030, g_{zz} = 2.0041; H-strain (MHz): H_x = 41.48, H_y = 110.74, H_z = 48.75; g-strain: g_x = 0.0000190, g_y = 0.0000065, g_z = 0.0000067, D-strain (MHz): D = 3.5, E = 0.0438; component B, S = ½, weight = 0.29104, g_{xx} = 2.0039, g_{yy} = 2.0044, g_{zz} = 2.0011; H-strain (MHz): H_x = 9.61, H_y = 41.55, H_z = 180.01.

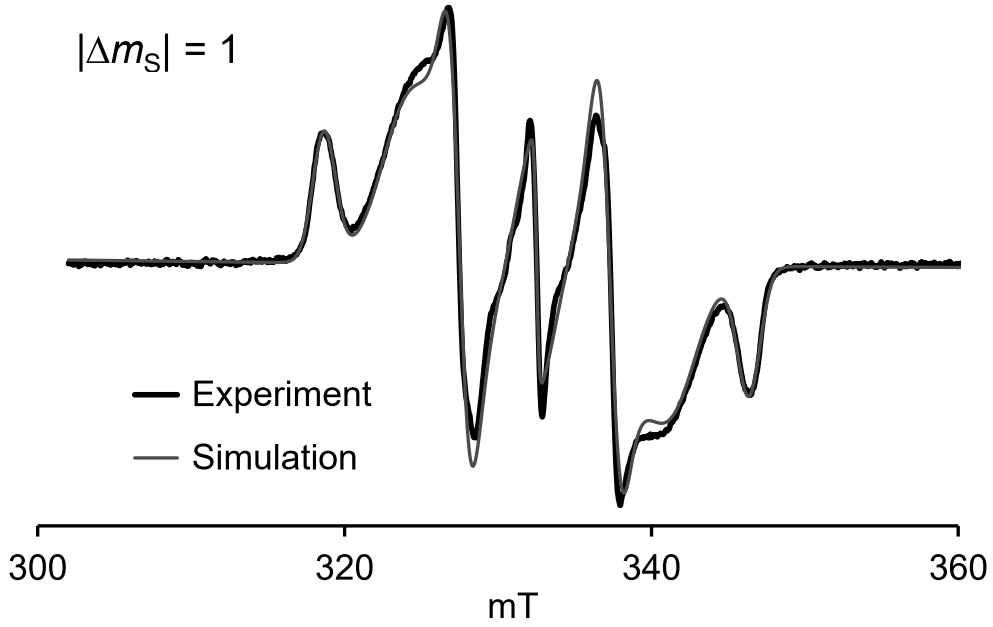

Fig. S11. EPR (117 K, ν = 9.3272 GHz, EPR label: SZ425R9) spectrum for diradical **4** in toluene/chloroform, 3:1 glass, following heating in air up at 200 °C for 10 min. The ratio of S = ½ decomposition product to S = 1 diradical (triplet state) is 0.13 : 1. Simulation |Δm_s| = 1 region (pepper, EasySpin, rmsd = 0.04153): Component A, weight = 1.0000, S = 1, D = 387.9 MHz, E = 35.2 MHz, g_{xx} = 2.0044, g_{yy} = 2.0030, g_{zz} = 2.0044; H-strain (MHz): H_x = 42.42, H_y = 111.60, H_z = 49.09; g-strain: g_x = 0.0000015, g_y = 0.0000091, g_z = 0.00000015, D-strain (MHz): D = 3.22, E = 0.0151; component B, S = ½, weight = 0.1306, g_{xx} = 2.0041, g_{yy} = 2.0045, g_{zz} = 2.0016; H-strain (MHz): H_x = 7.63, H_y = 64.70, H_z = 160.82.

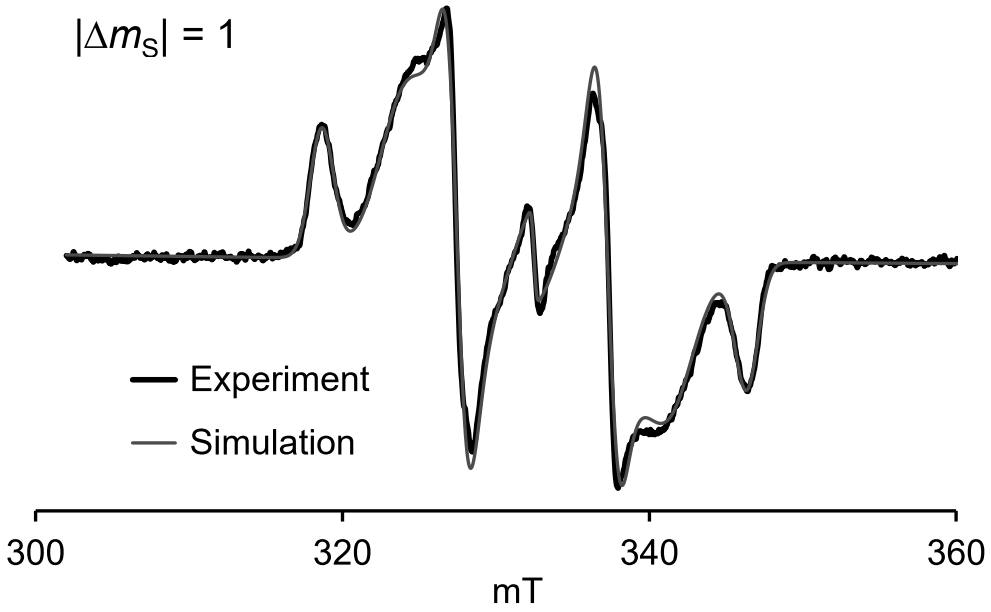

Fig. S12. Control experiment: EPR (117 K, ν = 9.3267 GHz, EPR label: SZ425R10) spectrum for diradical **4** in toluene/chloroform, 3:1 glass; sample was not heated. The ratio of $S = ½$ decomposition product to $S = 1$ diradical (triplet state) is 0.04 : 1. Simulation $|\Delta m_s| = 1$ region (pepper, EasySpin, rmsd = 0.03433): Component A, weight = 1.0000, $S = 1$, $D = 387.8$ MHz, $E = 35.2$ MHz, $g_{xx} = 2.0043$, $g_{yy} = 2.0030$, $g_{zz} = 2.0041$; H-strain (MHz): $H_x = 42.83$, $H_y = 107.68$, $H_z = 49.93$; g-strain: $g_x = 0.0000144$, $g_y = 0.00000014$, $g_z = 0.0000155$, D-strain (MHz): $D = 0.504$, $E = 0.626$; component B, $S = ½$, weight = 0.04240, $g_{xx} = 2.0042$, $g_{yy} = 2.0045$, $g_{zz} = 2.0013$; H-strain (MHz): $H_x = 7.64$, $H_y = 72.74$, $H_z = 120.44$.

3.e1. EPR spectroscopy: general description, spectral simulations, microwave saturation plots, determination of ΔE_{ST}, spectra of solid diradical, and electrical conductivity.

General description. EPR spectra were obtained using Bruker CW EPR spectrometer (X-band EMXplus). For temperature control (400–105 K), EPR spectrometer was equipped with custom-made nitrogen flow system. Temperatures were calibrated using an additional thermocouple inserted to the EPR tube containing solvent (toluene/chloroform or dibutylphthalate). DPPH powder (g = 2.0037) was used as a g-value reference. Quantitative EPR spectroscopy for diradical in toluene/choroform, 3:1 and 4:1 glass was carried using tempone in in the same solvent mixture as a reference.[S13,S14]

Spectral simulations. EPR spectra were simulated using EasySpin.[S15] Simulations for triplet state of diradical **4** (using pepper of EasySpin) are presented in Figs. S15 and S17. Simulation for monoradical **10** (using pepper or garlic of EasySpin) is presented in Fig. S16.

MW saturation. Since at low temperatures required for quantitative EPR spectra obtained in the determination of singlet-triplet gap for the diradical, slow electron spin relaxation rates may affect signal intensities, we have checked for microwave saturation at 110 K for diradical **4**. In Fig. S13 below, absence of microwave saturation at 110 K is found down to attenuation of 30 dB (from 200 mW) for diradical **4**. (The Tempone reference showed no sign of microwave saturation in the 28 – 60 dB power attenuation range at 117 K.)[S16] Therefore, the quantitative EPR can be carried out at attenuation of more than 30 dB – we have exclusively used attenuation of 40 dB to obtain double integrated intensities (see: below). For polycrystalline diradical **4**, the situation is a bit more complicated because of significant electrical conductivity; nevertheless, attenuation of 40 dB was judged not to lead to signigifcant saturation effects, based on saturation plot at 117 K (Fig. S14).

First determination of ΔE_{ST} for diradical **4** (Table S7, Fig. S18, and Eq. S1). The EPR spectra, at least in triplicate at each temperature (T) were obtained in toluene/chloroform, 3:1 in the 129 – 331 K temperature range; the spectra were obtained by rapidly quenching the sample in liquid nitrogen. Because of temperature dependent microwave quality factor (Q = 1700 – 7500), which affects directly the signal intensity, i.e., double integrated signal intensity (DI = 2700 – 25000), both Q and DI were averaged at each T, and then the resultant averages were divided to provide DI_{avg}/Q_{avg}, which should be proportional to magnetic susceptibility χ. Conseqently, $\chi T \approx (DI_{avg}/Q_{avg})^* T/500$ where factor of 500 approximately accounts for instrumental factors other than Q-value. As described in Fig. S14 caption, the average values of $(DI_{avg}/Q_{avg})^* T/500$ vs. T (approximately χT vs T) were fit to the Bleaney–Bowers-like equation (Eq. S1)[S3,S17] in the T = 129 – 331 K range with two variable parameters, J/k = 112 ± 34 K (mean ± SE), exchange coupling constant and N = 0.987 ± 0.032 (mean ± SE), χT correction factor (parameter dependence = 0.998). External magnetic field H was set to 0.3 Tesla (X-Band EPR).

$$\chi T = T^*[(1.118^* N^*\{2\sinh(a)/[1 + 2\cosh(a) + \exp((-2J/k)/T)]\})]/H \qquad \text{(S1)}$$
$$a = 1.345(H/(T - \theta))$$

Then, the value of N = 0.987 can be used to correct the experimental values of $(DI_{avg}/Q_{avg})^* T/500$ to provide corrected χT. Subsequently one-parameter (J/k) fit of corrected χT vs T to the Bleaney–Bowers equation gave J/k = 113 ± 1 K (mean ± SE). Value of corrected χT = 0.842 ± 0.047 at 290 K,

obtained from the (DI_{avg}/Q_{avg})*T/500 vs. T fit, was validated (by using the eidentical sample of **4**) by $\chi T \approx 0.82$ emu K mol^{-1} at $T = 294$ K, obtained by quantitative EPR spectroscopy using Tempone reference.[S13,S14]

Second determination of ΔE_{ST} for diradical **4** (Figure 4, main text and Fig. S19, Eq. S2, SI). The quantitative EPR spectra were obtained in toluene/chloroform, 4:1 in the 110 – 331 K temperature range; the spectra were obtained by slowly quenching the sample in liquid nitrogen. Under these conditions, equilibrium between the conformers of diradical **4** is expected to be established. To account for temperature dependent Q-factor, Tempone in the same solvent was used as a spin counting reference. The spectra were obtained in triplicate by alternating between the sample and the reference, i.e., sample-ref-sample-ref-sample-ref at each T. For each sample-ref pair of measurements, χT was obtained;[S13,S14] subsequently, at each T, average $\chi T \pm$ standard error was calculated as reported in Figure 4, main text and Fig. S19, SI. The χT vs. T data were fit to the modified Bleaney-Bowers-like equation, to allow for two equilibriating conformations with different singlet-triplet energy gaps (eq. S2, SI). The fit is consistent with the presence of two equilibrating conformations **4**A and **4**B with singlet-triplet energy gaps $2J_A/k = 220 \pm 70$ K and $2J_B/k = -340 \pm 37$ K.

$$\chi T = \chi T_A + \chi T_B$$
$$\chi T_A = T^*[(1.118^* x_A \{2\sinh(a)/[1 + 2\cosh(a) + \exp((-2J/k)/T)]\})]/H$$
$$\chi T_B = T^*[(1.118^* x_B \{2\sinh(a)/[1 + 2\cosh(a) + \exp((-2J/k)/T)]\})]/H \qquad \text{(S2)}$$
$$a = 1.345(H/(T - \theta))$$

Molar fractions, x_A and x_B, for **4**A and **4**B are related at equilibrium **4**B ↔ **4**A as follows:
$x_A = a_S^*(\exp(-a_H/T))/[1 + a_S^*(\exp(-a_H/T))]$ and $x_B = 1-\{a_S^*(\exp(-a_H/T))/[1 + a_S^*(\exp(-a_H/T))]\}$
with $a_S = 3.404$ (corresponding to entropy $\Delta S = 2.4$ cal mol^{-1} K^{-1}) and $a_H = 160.31$ (corresponding to enthalpy, $\Delta H = 0.32$ kcal mol^{-1}) obtained from a well-defined 4-parameter fit with Standard Error of Estimate = 0.0256. (The following two-parameter fit, shown in Figure 4, main text and Fig. S19, SI has Standard Error of Estimate = 0.0234.) These values of a_S and a_H correspond to $x_A = 0.68$ and $x_B = 0.32$ at 331 K and $x_A = 0.44$ and $x_B = 0.56$ at 110 K; thus, the conformation **4**A is the major one at temperatures near ambient conditions.

Solid diradical. EPR spectra of solid diradical **4** were typically obtained in the 110–280 K temperature range. Microwave power attenuation of 40 dB was used to minimize the saturation effects. Since the Q-values were approximately constant within this temperature range the double integrated signal intensities (DI) were used directly. Because X-ray crystallography suggested packing of molecules of **4** in the crystal compatible with strongly coupled $S = 1$ antiferromagnetic one-dimensional (1-D) chains, both DI/60000 vs T and DI^*T/60000 vs T data were fit to equations S3A&B.[S3,S12,S18,S19] External magnetic field H was set to 0.3 Tesla (X-Band EPR).

$$DI/60000 = N\{[3/(2k(T-\theta))][(2 + a_1\times K + a_2\times K^2)/(3 + b_1\times K + b_2\times K^2 + b_3\times K^3)]\}$$
$$+ N_{imp}(1.118/H)\{2\sinh(a)/[1 + 2\cosh(a)]\} \qquad \text{(S3A)}$$
$$DI^*T/60000 = N^*T\{[3/(2k(T-\theta))][(2 + a_1\times K + a_2\times K^2)/(3 + b_1\times K + b_2\times K^2 + b_3\times K^3)]\}$$
$$+ N_{imp}(1.118/H)\{2\sinh(a)/[1 + 2\cosh(a)]\} \qquad \text{(S3B)}$$
$$a_1 = 0.0194,\ a_2 = 0.777,\ b_1 = 4.346,\ b_2 = 3.232,\ b_3 = 5.634,$$

$K = -J'/kT$ and $a = 1.345(H/(T-\theta))$

Initial fitting revealed negligible amount of paramagnetic impurity (N_{imp}). Therefore, the term describing $S = 1$ paramagnetic impurity, N_{imp}, was not included in further fitting. Two variable parameters, exchange coupling constatnt, J'/k, and conversion factor, N, of DI/60000 (or DI) to molar paramagnetic susceptibility χ are used (Fig. S19). The model in eqs. S3A&B assumes that intramolecular ferromagnetic exchange coupling (J/k) in the diradical is much stronger than intermolecular antiferromagnetic exchange coupling (J'/k), i.e., $J/k >> |J'/k|$.[S18] Because diradical **4** may adopt different conformations in solution/glass vs. crystalline solid, we may not exclude the possibility that the relationship, $J/k >> |J'/k|$, is holding in the solid **4**, even though $J/k \approx 112 \pm 34$ K for **4** in toluene/chloroform (3:1) solution/glass or $J/k \approx 111 \pm 35$ K in toluene/chloroform (4:1) for major conformer **4**A and $|J'/k| \approx 150 \pm 3$ K for **4** in the crystalline solid are found (Figs. S18 and S19). If however, the conformations of **4** are the same in the solid and solution/glass, then and $|J'/k| \approx 150 \pm 3$ K for **4** (Fig. S19) should be viewed as an order of magnitude estimate. Another source of uncertainty is the quality of the DI values for Dysonian line shapes. As illustrated in the spectral fit for Si/SiO_2 substrate (Fig. S29), which shows a Dysonian line shape, the spectra may be fit well (with linear baseline correction). The spectral fits then were double integrated to provide well behaved double integral lines, with flat baselines at both ends.

Electrical conductivity. EPR line of unpaired electrons in electrically conducting solids is complex because of eddy currents induced by the exciting magnetic field of the microwave irradiation. These currents confine the magnetic flux to a thin surface layer, with thickness referred to as skin depth (δ). The value of $\delta = \mathrm{sqrt}(1/\pi\mu_0\nu\sigma)$, where μ_0 is the magnetic permeability for vacuum, ν is microwave frequency (9.3×10^9 Hz), and σ is conductivity (10 ohm^{-1} cm^{-1} = 10 S/cm). When constants μ_0 and π are accounted for, then δ (in mm) = 50330*[sqrt(1/$\nu\sigma$)] ≈ 0.16 mm; for σ = 27 S/cm, δ = 0.10 mm. According to classic theory of EPR spectroscopy in metals, developed by Dyson,[S20] when (1) δ is comparable or smaller than a characteristic size of the sample (d) and (2) the time of charge carrier diffusion through the skin depth is smaller than a spin relaxation time, then the Dysonian line with characteristic asymmetry factor $A/B > 1$ will appear, as shown in Figure 4 (main text) and Figs. S20 – S24, SI. Asymmetry factor will depend on the ratio d/δ and shape of the object/particle, and for shapes such as plates (or cuboids) on the orientation with respect to the exciting magnetic field, even if conductivity is essentially isotropic at the molecular/atomic level.[S21,S22] In particular, for a plate with thickness $2d$, oriented at the angle of 0 ° (as defined in the caption of Fig. S22), theory predicts A/B = 1.5 and 2 for $2d/\delta \approx 1$ and 1.3-1.4, respectively. Thus, for our diradical, $\delta \approx 0.10$ mm may be estimated, i.e., conductivity σ = 27 S/cm or σ is on the order of 10 S/cm.

For a plate-like sample with $2d/\delta < 2.7$, A/B will increase with increasing conductivity σ (before reaching a maximum of $A/B \sim 6$ at $2d/\delta \approx 2.7$–2.8).[S21] Thus, our diradical samples, which exhibit increasing A/B with lowering of T, are likely showing metallic-like conductivity down to at least T = 150 K, see: Figs. S20 – S24. For samples with metal-like conductivity, $\sigma_{AC} = \sigma_{DC}$.[S21,S23]

3.e2 EPR spectra of 4 and 10, and determination of singlet-triplet energy gap in 4 and electrical conductivity of solid 4.

Table S7. Summary of EPR data for first determination of ΔE_{ST} for diradical **4** (Fig. S18)

T (K)	DI_{avg}	SE (DI)	Q_{avg}	SE (Q)	$(DI_{avg}/Q_{avg})^* T/500$	SE	χT[a]	SE (χT)
128.65	24926.14	30.31	6933.33	296.27	0.9250	0.0395	0.9372	0.0497
140.55	22440.53	239.03	6166.67	88.19	1.0229	0.0182	1.0364	0.0374
151.65	18365.92	156.08	5700.00	0	0.9773	0.0083	0.9901	0.0322
162.65	14222.81	118.86	4500.00	0	1.0282	0.0086	1.0417	0.0339
184.65	7012.12	132.91	2600.00	0	0.9960	0.0189	1.0091	0.0370
206.10	4092.18	110.72	2060.00	24.49	0.8188	0.0242	0.8296	0.0358
227.15	3186.89	115.72	1700.00	0	0.8517	0.0309	0.8629	0.0414
247.85	2940.45	97.33	1740.00	24.49	0.8377	0.0301	0.8487	0.0405
268.75	3403.63	136.32	1900.00	0	0.9629	0.0386	0.9756	0.0497
289.50	3445.66	192.35	2400.00	0	0.8313	0.0464	0.8422	0.0539
310.45	3809.61	21.64	2900.00	0	0.8157	0.0046	0.8264	0.0264
331.15	4508.06	121.49	3500.00	57.74	0.8531	0.0270	0.8643	0.0385

[a] $\chi T = [(DI_{avg}/Q_{avg})^* T/500]/N$ where $N = 0.987 \pm 0.31$ was obtained from two-parameter fit of $(DI_{avg}/Q_{avg})^* T/500$ vs T, using eq. S1.

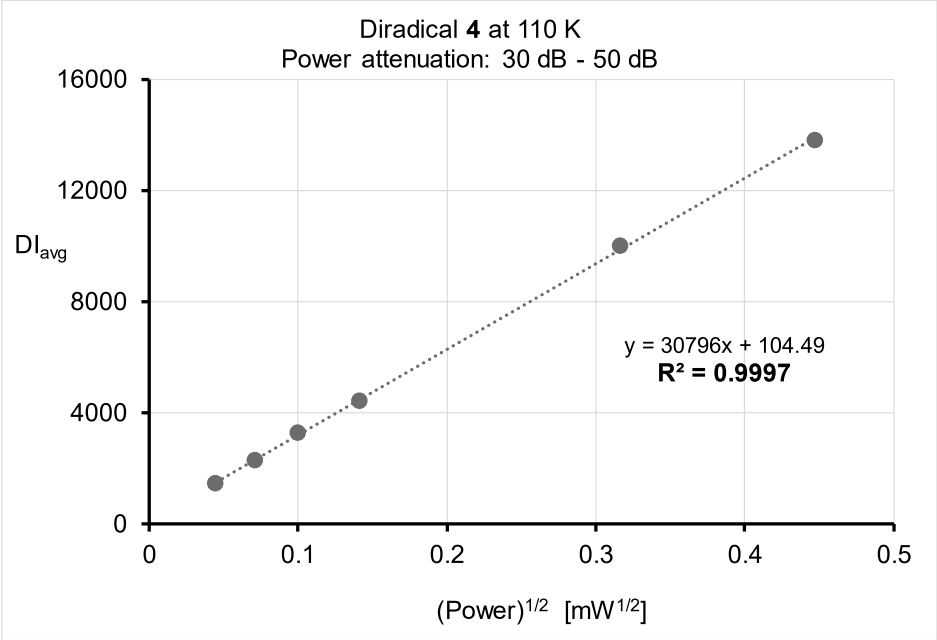

Fig. S13. Plots of EPR double integrated signal intensity (DI) versus the square root of microwave power for 0.54 mM diradical **4** in toluene/chloroform at 110 K, 30–50 dB (EPR labels: SZ373R16–R36).

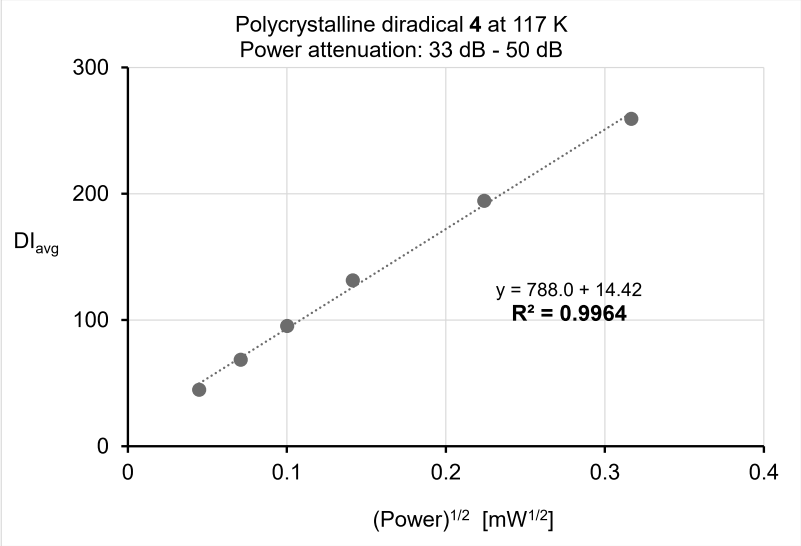

Fig. S14. Plots of EPR double integrated signal intensity (DI) versus the square root of microwave power for polycrystalline diradical **4** at 117 K, 33–50 dB (EPR labels: SZ408R16–R36). DI's are subject to a significant error because of Dysonian line shape.

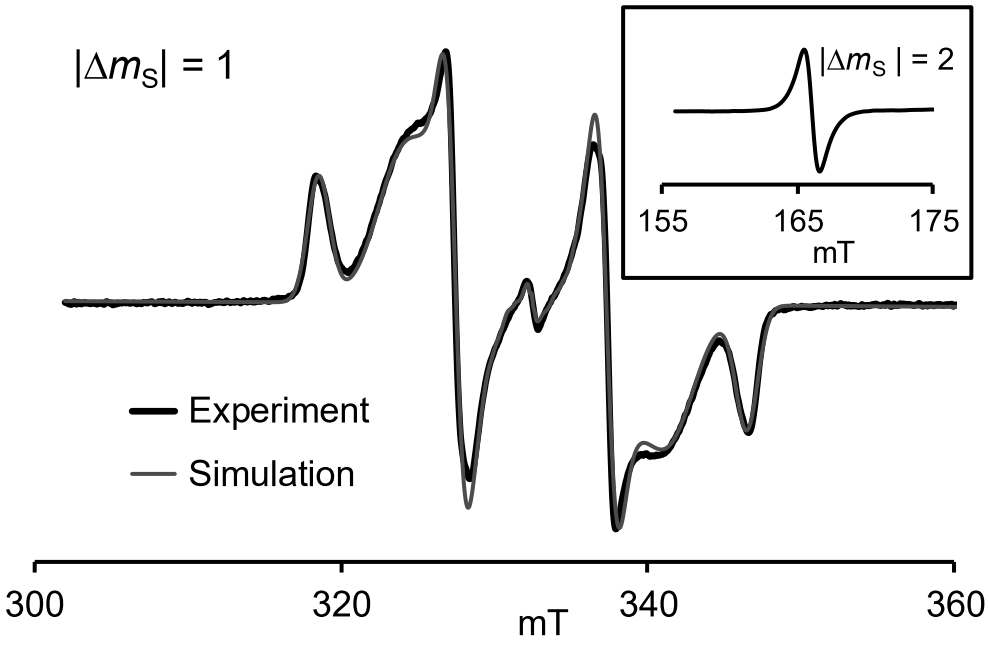

Fig. S15. Complete set of fitting parameters for the spectrum in Figure 3 (main text): EPR (110 K, ν = 9.3269 GHz, EPR label: SZ373R36) spectrum for 0.54 mM diradical **4** in toluene/chloroform, 3:1 glass. Inset: the $|\Delta ms|$ = 2 transition (110 K, ν = 9.3264 GHz, EPR label: SZ373R37). Simulation $|\Delta ms|$ = 1 region (pepper, EasySpin, rmsd = 0.0197): Component A, weight = 1.0000, S = 1, D = 391.2 MHz, E = 35.9 MHz, g_{xx} = 2.0042, g_{yy} = 2.0027, g_{zz} = 2.0041; H-strain (MHz): H_x = 38.65, H_y = 109.96, H_z = 47.32; g-strain: g_x = 0.000026, g_y = 0.000010, g_z = 0.0000015; D-strain (MHz): D = 45.546, E = 0.110; component B, S = ½, weight = 0.0671, g_{xx} = 2.0042, g_{yy} = 2.0042, g_{zz} = 2.0022; H-strain (MHz): H_x = 2.457, H_y = 193.88, H_z = 10.82. Fixed parameters for component B, S = ½ (based on simulation for monoradical **10**, see: next Fig.), ^{14}N $\boldsymbol{A}$-tensors: $A_{xx}(1)$ = 5.324, $A_{yy}(1)$ = 8.527, $A_{zz}(1)$ = 36.220; $A_{xx}(2)$ = 0.095, $A_{yy}(2)$ = 0.144, $A_{zz}(2)$ = 39.216; $A_{xx}(3)$ = 0.003, $A_{yy}(3)$ = 0.014, $A_{zz}(3)$ = 52.586.

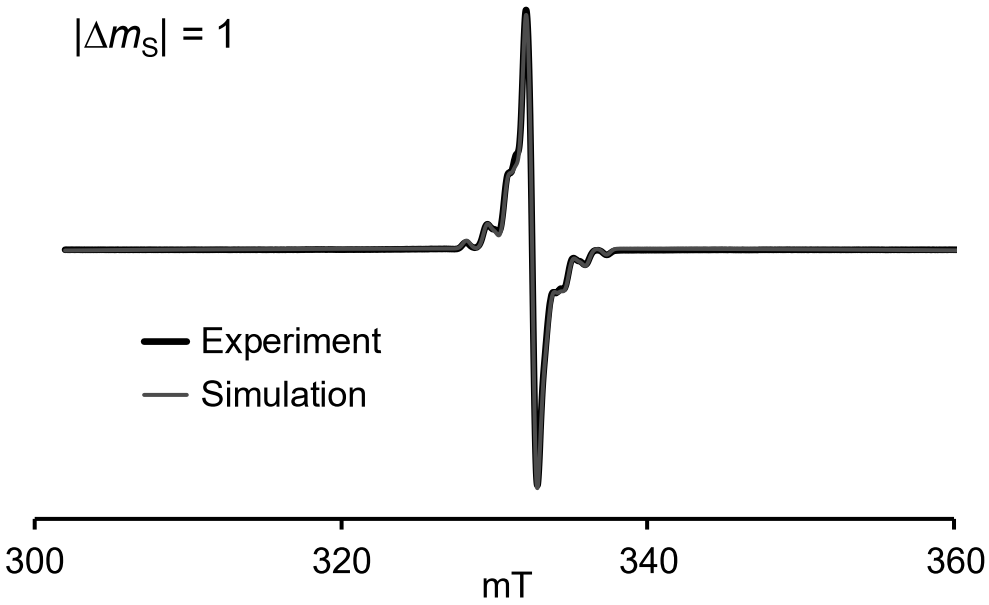

Fig. S16. Complete set of fitting parameters for $S = 1/2$ component (component B) for the spectrum in the preceding Figure. EPR (117 K, ν = 9.3255 GHz, EPR label: SZ343R14) spectrum for 3.12 mM monoradical **10** in toluene/chloroform, 3:1 glass. Simulation $|\Delta m_S| = 1$ region (pepper, EasySpin, rmsd = 0.00597): $S = ½$, $g_{xx} = 2.0042$, $g_{yy} = 2.0043$, $g_{zz} = 2.0023$; H-strain (MHz): $H_x = 9.69$, $H_y = 19.27$, $H_z = 16.13$; ^{14}N $\boldsymbol{A}$-tensors: $A_{xx}(1) = 5.324$, $A_{yy}(1) = 8.527$, $A_{zz}(1) = 36.220$; $A_{xx}(2) = 0.095$, $A_{yy}(2) = 0.144$, $A_{zz}(2) = 39.216$; $A_{xx}(3) = 0.003$, $A_{yy}(3) = 0.014$, $A_{zz}(3) = 52.586$.

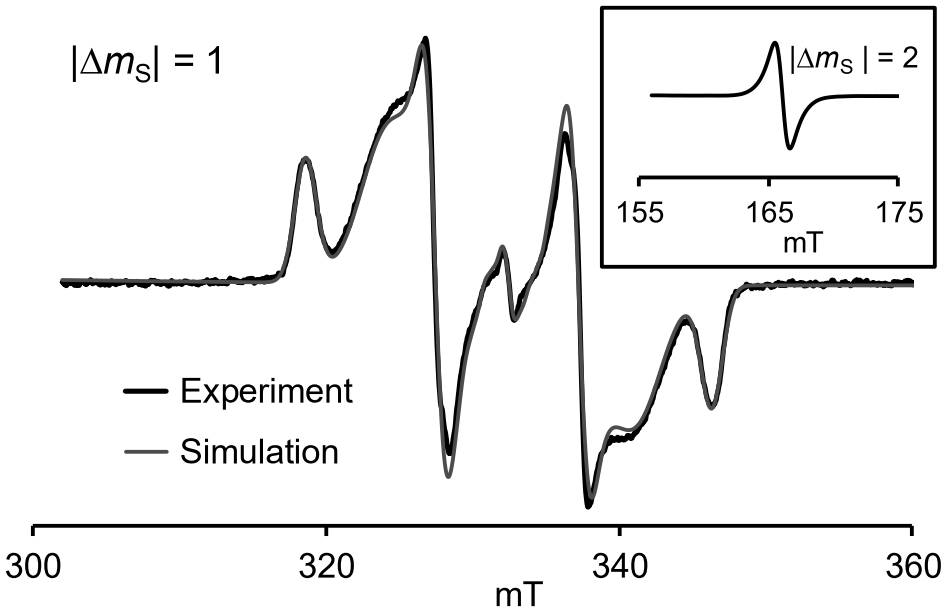

Fig. S17. Repeat spectrum for diradical **4** in toluene/chloroform, 3:1 glass: EPR (117 K, ν = 9.3264 GHz, EPR label: SZ343R11). Insets: the $|\Delta ms|$ = 2 transition (117 K, ν = 9.3266 GHz, EPR label: SZ343R4). Simulation $|\Delta ms|$ = 1 region (pepper, EasySpin, rmsd = 0.0116): Component A, weight = 1.0000, S = 1, D = 388.2 MHz, E = 35.4 MHz, g_{xx} = 2.0044, g_{yy} = 2.0030, g_{zz} = 2.0042; H-strain (MHz): H_x = 41.73, H_y = 112.68, H_z = 48.46; g-strain: g_x = 0.00000069, g_y = 0.00000021, g_z = 0.00000025; D-strain (MHz): D = 2.70, E = 0.006; component B, S = ½, weight = 0.05954, g_{xx} = 2.0043, g_{yy} = 2.0042, g_{zz} = 2.0022; H-strain (MHz): H_x = 13.46, H_y = 80.79, H_z = 15.64. Fixed parameters for component B, S = ½ (based on simulation for monoradical **10**, see: Fig. S16), ^{14}N $\boldsymbol{A}$-tensors: $A_{xx}(1)$ = 5.324, $A_{yy}(1)$ = 8.527, $A_{zz}(1)$ = 36.220; $A_{xx}(2)$ = 0.095, $A_{yy}(2)$ = 0.144, $A_{zz}(2)$ = 39.216; $A_{xx}(3)$ = 0.003, $A_{yy}(3)$ = 0.014, $A_{zz}(3)$ = 52.586.

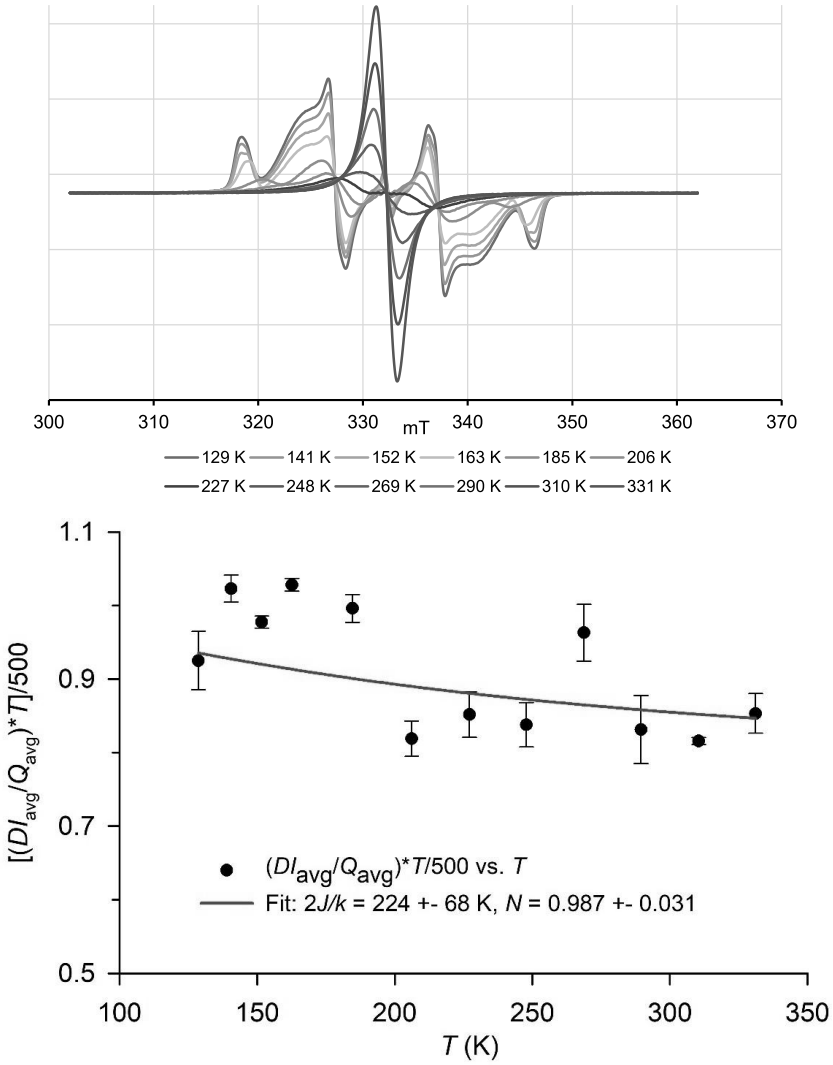

Fig. S18. First determination of ΔE_{ST} for diradical **4**; data are summarized in Table S7 (p. S37). Top panel: selected EPR spectra of 1.01 mM diradical **4** (EPR labels: SZ396r24–r87) in toluene/chloroform in the 129–331 K temperature range. Bottom panel: plot of $(DI_{avg}/Q_{avg})^*T/500$ vs. T, i.e., average double integrated intensity (DI_{avg}) divided by microwave cavity average quality factor (Q_{avg}), and then multiplied by temperature (T), divided by a factor of 500. Temperature range is T = 129–331 K. Error bars are standard errors (SE's) propagated from DI_{avg} and Q_{avg}, with errors in temperature assumed to be negligible. The average values of $(DI_{avg}/Q_{avg})^*T/500$ vs. T (approximately χT vs T) were fit to the Bleaney–Bowers-like equation (eq. S1) with two variable parameters, J/k = 112 ± 34 K (mean ± SE), exchange coupling constant and N = 0.987 ± 0.031 (mean ± SE), DI/Q correction factor (parameter dependence = 0.998). Then, the value of N = 0.987 can be used to correct the experimental values of $(DI_{avg}/Q_{avg})^*T/500 \approx$ "χT". Subsequently one-parameter (J/k) fit of corrected "χT" vs T to the Equation S1 gave J/k = 113 ± 1 K (mean ± SE).

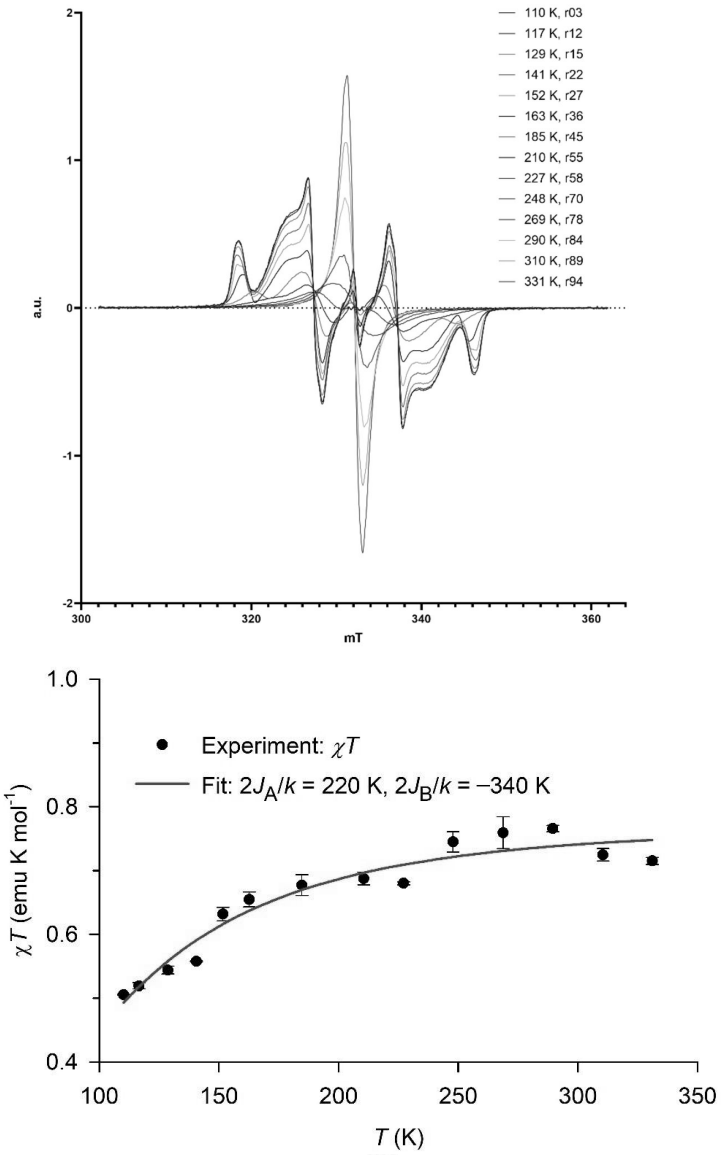

Fig. S19. Second determination of ΔE_{ST} for diradical **4** (same data as in Figure 4, main text). Top panel: selected EPR spectra of 1.01 mM diradical **4** (EPR labels: SZ442r3–r94) in toluene/chloroform (4:1) in the 110–331 K temperature range. Bottom panel: plot of χT vs T, i.e., the product of paramagnetic susceptibility (χ) and temperature (T), in the 110–331 K temperature range. Error bars are standard errors (SE's) for average χT values, obtained from at least triplicate pairs of sample/reference measurements. The fit line corresponds to two-parameter fit to Eq. S2, giving J_A/k = 111.1 ± 34.8 K and J_B/k = –169.4 ± 18.7 K (mean ± SE) with R^2 = 0.937 and standard error of estimate, SEE = 0.0234. No weighing was used in the fit; note that weighing the fit with weight, $w = 1/\chi$ or $1/\chi^2$, leads to much smaller (by a factor of several) error bars for J_A/k and J_B/k.

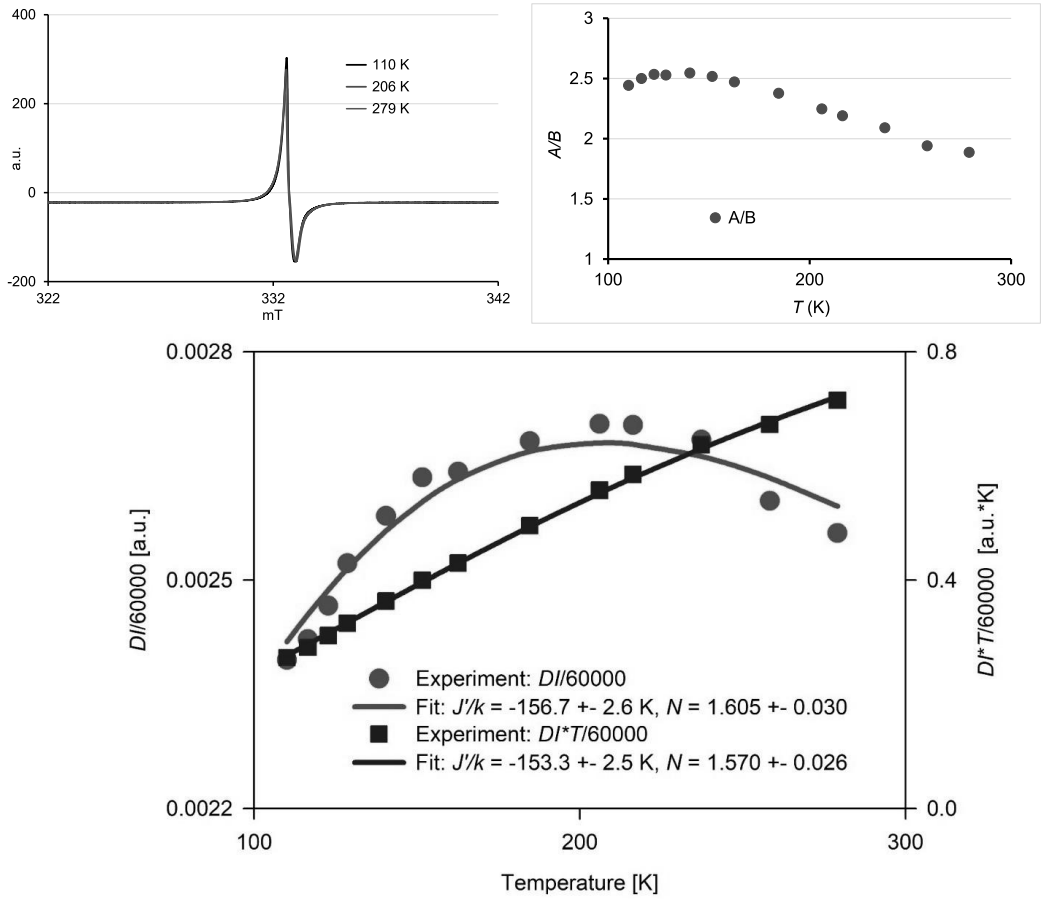

Fig. S20. EPR spectroscopy (EPR labels: SZ387R19–R55) of solid diradical **4** in the 110–279 K temperature (*T*) range; same data as reported in Figure 4 main text. Top panels: representative spectra with Dysonian line shape and plot of *A*/*B* vs temperature. Bottom panel: Plots of approximate double integrated intensities (*DI*) divided by 60000 (*DI*/60000) vs *T* and *DI***T*/60000 vs *T* (symbols) with corresponding numerical fits to to *S* = 1 antiferromagnetic 1D chain model (eq. S3A & B) (solid lines). Fit parameters to *DI*/60000 vs *T* data: exchange coupling, *J*/*k* = 157 ± 3 K, conversion parameter, *N* = 1.61 ± 0.03, parameter dependence = 0.979, R^2 = 0.941, *SSE* = 0.0000. Fit parameters to *DI***T*/60000 vs *T* data: exchange coupling, *J*/*k* = 153 ± 3 K, conversion parameter, *N* = 1.57 ± 0.03, parameter dependence = 0.973, R^2 = 0.9991, *SSE* = 0.0048.

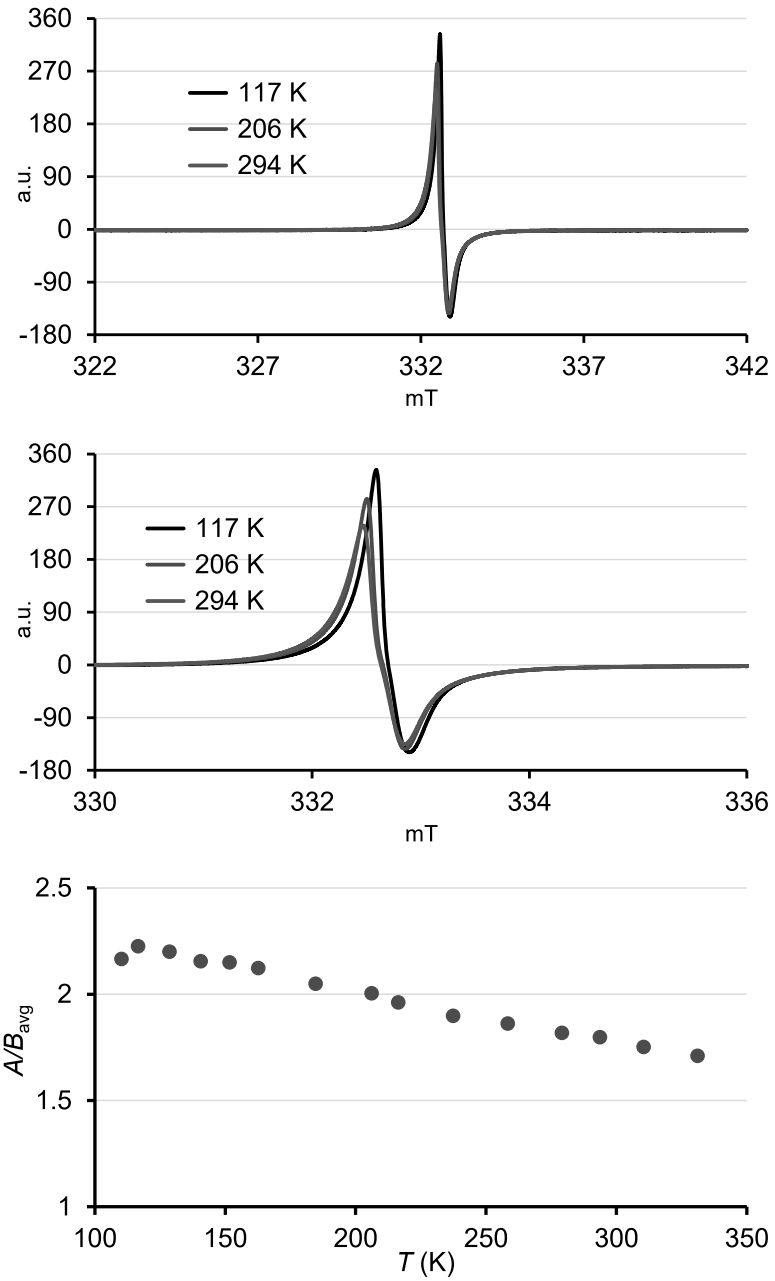

Fig. S21. Repeat EPR spectra (EPR labels: SZ404R1–R35) of solid diradical **4** in the 110–330 K temperature (T) range, showing representative spectra with Dysonian line shape and plot of A/B vs temperature.

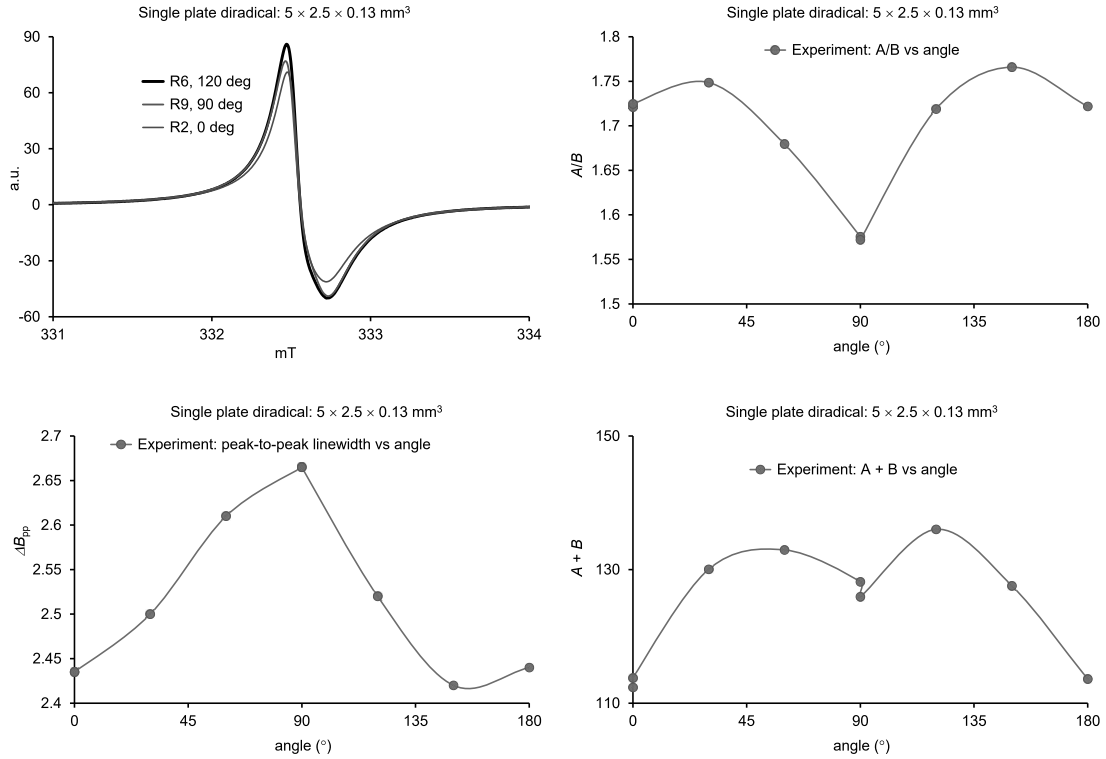

Fig. S22. EPR spectroscopy (EPR labels: SZ421R2–R10) of solid diradical **4** (single plate 5 × 2.5 × 0.13 mm³) at room temperature, T = 294 K. Panels clockwise from left top to left bottom: horizontally expanded spectra at selected angles with Dysonian line shape, plot of A/B vs. angle, plot of $A + B$ (intensity) vs. angle, and plot of peak-to-peak linewidth, ΔB_{pp} (Gauss) vs. angle. In the last three plots, connecting lines are guides to the eye; angles are defined as between the normal to the largest face of the plate and the external magnetic field.

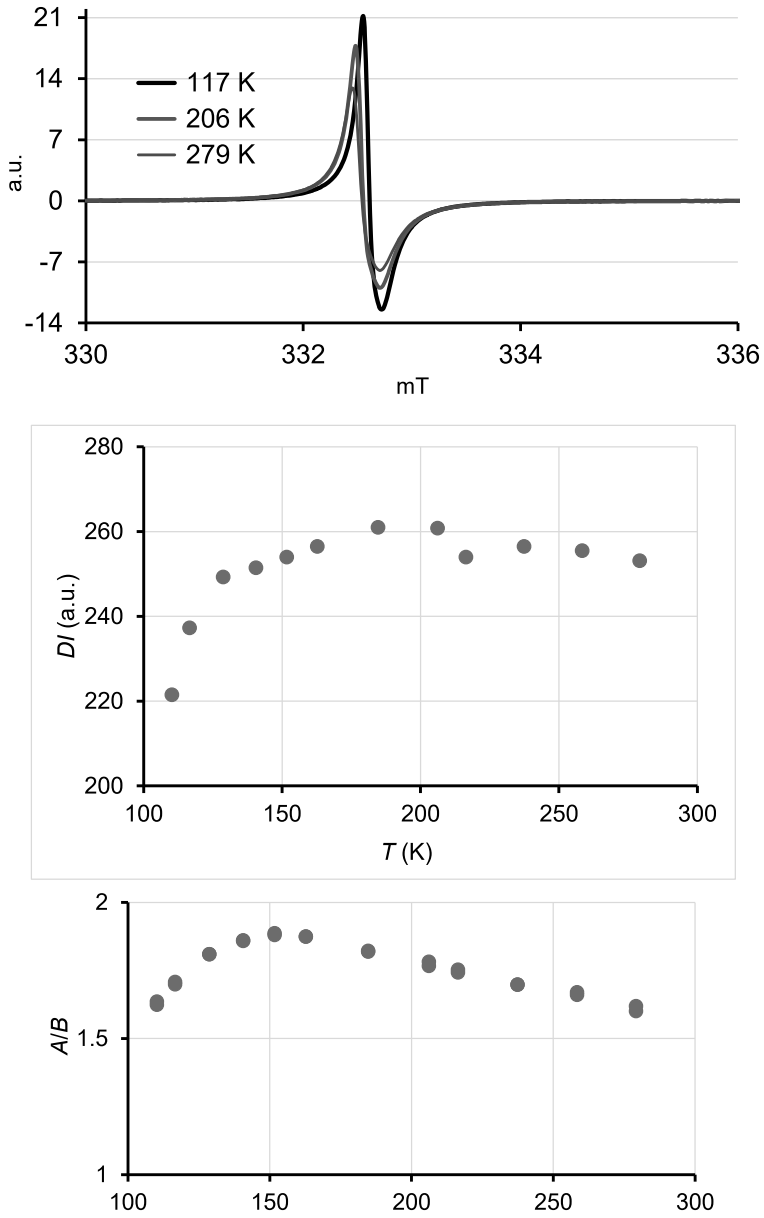

Fig. S23. Variable temperature (T = 110–279 K) EPR spectroscopy (EPR labels: SZ422R9–R32) of solid diradical **4** polycrystalline powder with particle size of less 75 microns (0.075 mm). Examination under microscope reveals that the sample largely consists of separated single crystals on the wall of the EPR sample tube. Panels top to bottom: horizontally expanded spectra at T = 110, 206, and 279 K; double integrated intensity (DI) versus T, and asymmetry factor, A/B versus T.

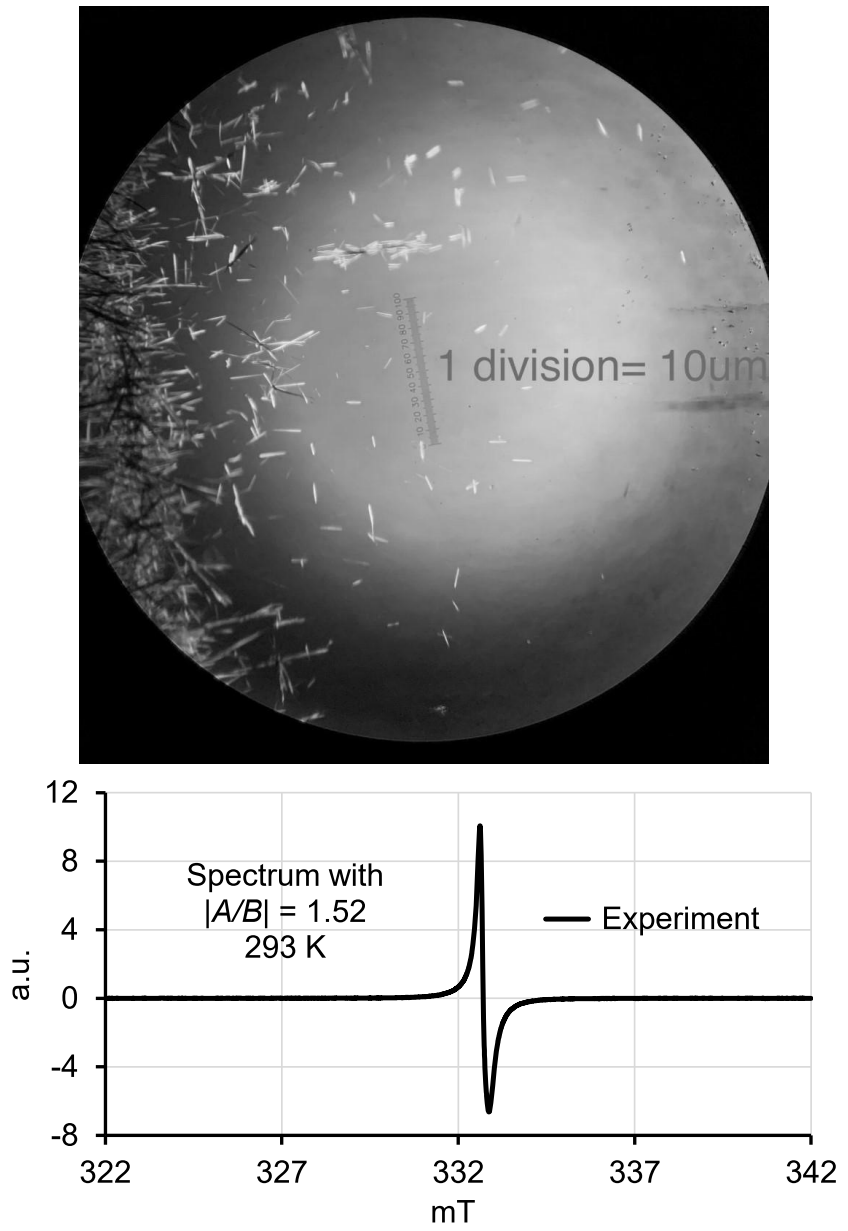

Fig. S24. Single crystal sample of diradical **4** used for conductivity measurements at Purdue. Top panel: picture under microscope with polarized light taken prior to the shipment to Purdue. Bottom panel: EPR spectrum at room temperature (EPR label: SZ431R1) of solid diradical **4** polycrystalline powder.

3.f Electrical conductivity of diradical 4 in spin coated films and single crystals

Microscopic crystal device fabrication. The device architecture was that of Si/SiO_2/single crystal (~1400 nm)/Au (150 nm)/Ag (1600 nm), as shown in Fig. S25a. The silicon substrates were cleaned with water, acetone, and isopropyl alcohol in a sequential manner using an ultrasonic bath with the substrates immersed in each solvent for 20 min. The single crystals (label: SZ431R1, see: Fig. S24, preceding page) were dispersed using hexanes as the suspension solvent. The diradical crystal solution was then cast onto the Si/SiO_2 substrates. The solvent was allowed to evaporate to leave single crystals of the diradical small molecule deposited across the substrate. Then, a copper screen was used as a shadow mask prior to depositing 150 nm of Au and 1600 nm of Ag using thermal evaporation under vacuum at a pressure of ~10^{-4} Pa to complete the device (Fig. S25b). The approximate lengths and widths of the channel used were ~30 μm and ~10 μm, respectively, and varied from sample to sample depending on the orientation of the shadow mask relative to the crystal.

Amorphous thin film device fabrication. The diradical powder was dissolved in chloroform with concentration of 12 mg mL^{-1}, and it was stirred at 50 °C. The silicon substrates were cleaned in the same manner as described previously. The substrates were treated with UV-ozone for 15 min and preheated to 90 °C. The diradical solution was then spun-coat at 2,000 rpm for 60 s onto the preheated silicon substrates. After the film dried, it was baked for 5 min at 100 °C on a hot plate in nitrogen-filled glovebox. The resulting thin films were continuous with an average thickness of 150 ± 20 nm. After coating the diradical thin film, two Au contacts (~ 50 nm) were deposited by thermal evaporation using a shadow mask under high vacuum (~10^{-4} Pa). The channel length and width were 80 μm and 2.75 mm, respectively.

Electrical conductivity measurements. A two-point probe method was used to measure the conductivity value of the diradical crystals and amorphous thin films of the diradicals according to Ohm's law. That is, $\sigma = \frac{L}{W \times h \times R} = \frac{L \times I}{W \times h \times V}$, where σ is the conductivity, L is the effective contacted length, I is current, V is voltage, W is the width of single crystal or the width of the electrodes (in the thin film device cases), and h is the thickness of the single crystal or the thin film. The conductivity values of crystals of the diradical were evaluated, and the current-voltage (I–V) measurements were performed by sweeping the voltage from –5 V ≤ V ≤ 5 V. A representative I–V curve of a single crystal is shown in Fig. S25c. The average conductivity values of the diradical crystals are ~0.01 S cm^{-1}. A representative I–V curve of the amorphous diradical thin film is shown in Fig. S26, and the conductivity is ~10^{-4} S cm^{-1}.

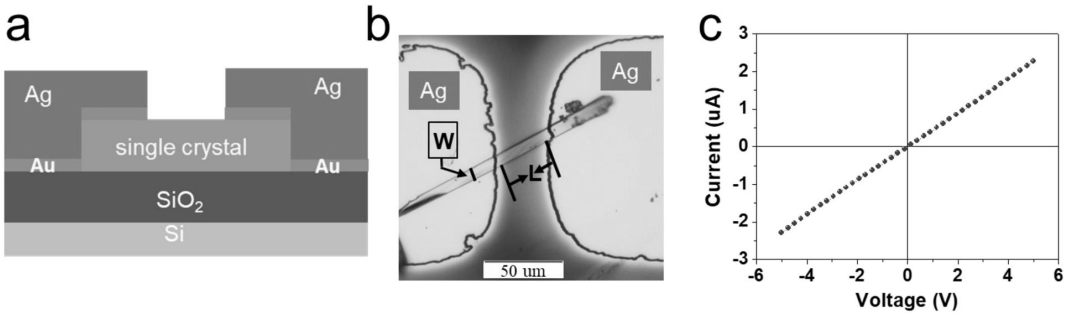

Fig S25. (a) A schematic diagram of the diradical crystal measurement device setup. (b) A representative optical image of single crystal of the diradical species with Au/Ag contacts evaporated atop the organic crystal. (c) A representative *I*–*V* trace of a device based on a single crystal of the diradical compound.

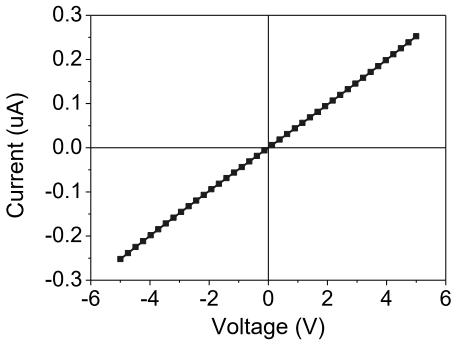

Fig. S26. A representative *I*–*V* trace of a device based on the amorphous diradical thin film.

3.g Thin films of diradical 4.

3.g1 Preparation of films, their XPS spectra, and AFM

Experimental: Thin film growth and investigations. Thin films were prepared in situ under UHV conditions by organic molecular beam deposition (OMBD) using a calibrated Knudsen cell.

Native SiO_2 grown on single-side polished n-Si(111) wafers were used as a substrate. The wafers were cleaned in an ultrasonic bath by immersion in ethanol and acetone for one hour each and annealed at around 500 K for several hours. Cleanness was verified by XPS. The nominal film thicknesses were calculated from the attenuation of the substrate signal. The deposition rate was ~0.01-0.02 nm/min and the substrate was kept at room temperature. The OMDB chamber was installed in a UHV system with an analysis chamber ($2x10^{-10}$ mbar base pressure), equipped with a monochromatic Al Kα source (SPECS Focus 500) and a SPECS Phoibos 150 hemispherical electron analyser. Survey spectra were measured at 50 eV pass energy and individual core level spectra at 20 eV pass energy. In both case the binding energy was calibrated using the Si 2p signal at 99.8 eV. To avoid potential radiation damage, only freshly prepared films were measured, and the radiation exposure was minimized. For the measurements probing stability, the beam exposure was further limited after air exposure to attribute the damage exclusively to the degradation by air exposure. This results in a worse signal to noise ratio in those spectra.

Atomic force microscopy was measured under ambient conditions with a Digital Instrument Nanoscope III Multimode microscope using tapping mode.

Thin film stoichiometry. Precise information on film stoichiometry can be obtained by the analysis of the survey XPS spectra: the ratio of the integrated signal intensities of the spectroscopic lines in XPS curves of a film deposited with intact molecules is directly proportional to the theoretical percentages expected on the basis of radical stoichiometry. This is a powerful tool to determine whether the deposition occurs without degradation.[S24] The results are given in Table S8.

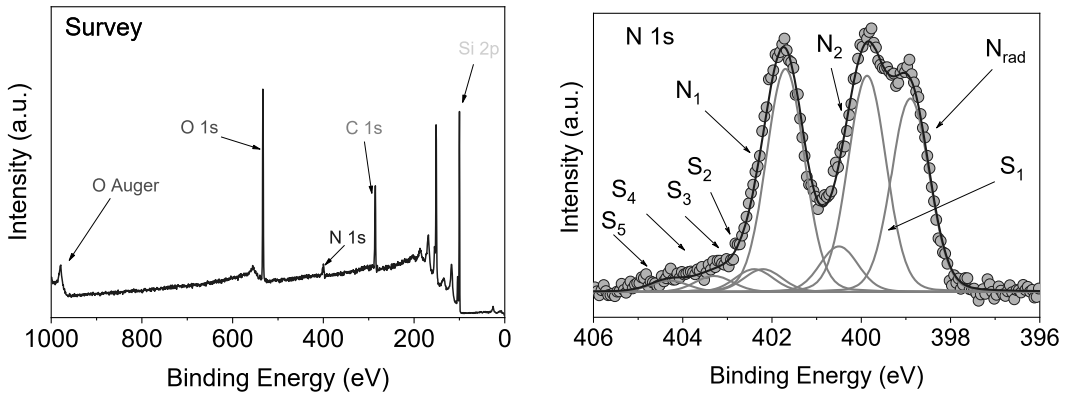

Fig. S27. Left panel: Survey XPS spectra. Right panel: N 1s XPS spectra (together with its best fit) diradical **4** (photon energy = 1486.6 eV).

Table S8. Stoichiometric and experimental elemental ratios for diradical **4.**

	Theoretical value	Film
C	0.86	0.89 ± 0.03
N	0.14	0.11 ± 0.03

The sensitivity factors (σ) are: $\sigma_{C\ 1s}$ = 0.25 and $\sigma_{N\ 1s}$ =0.42.[S25]

We find that the integrated signal intensities obtained analyzing the survey XPS curves (Fig. S27) are in agreement with the theoretical elemental analyses. This means that the stoichiometry of the deposited thin films corresponds to the quantitative composition of the molecule, indicating deposition without degradation.

N 1s core level spectra: fit results for the energy positions and relative intensities of the photoemission lines. A careful best-fit procedure with constraints based on stoichiometry and electronegativity[S26-S28] is a powerful tool to gain a deeper insight into the XPS core level spectra, also when looking at the single spectroscopic lines that have features own to the different chemical environment seen from the same element in a molecule. We focus on the quantitative analysis of the N1s core level spectra (Fig. S27, right panel, and Table S9). These spectra are the most important from the magnetic point of view since their signal depends on the photoelectrons emitted from the nitrogen atoms of the Blatter radicals that carry the unpaired electrons.

We used Voigt profiles, with fixed constant Lorentzian width. The Voigt profile considers both the finite core-hole lifetime (Lorentzian profile) and the broadening due to the finite experimental resolution and various inhomogeneities, e.g., molecular packing and local morphology (Gaussian profile).[S28,S29] To calculate the stoichiometry of the films, we also considered the intensity of the satellites,[S30] typical features in photoemission that appear as an effect of the relaxation processes due to the creation of a core-hole.[S31] The fit that we use is based on the procedure adopted for closed-shell molecules.[S28,S32] The final fit is the result of several self-consistent interactions of sequential fits done taking into account all physical and chemical information and adding more constraints at each interaction, with the goal to keep the parameter dependency very low. As we were more interested in the stoichiometry than in physical phenomena related to photoemission, we kept the number of satellites as low as possible to have a very simplified fit. However, satellite intensities cannot be neglected, especially in case of radicals because the simultaneous presence of a core-hole and a singly occupied molecular orbital on the time-scale of photoemission enhances the relaxation phenomena.[S33,S34] The fit procedure systematically holds for all samples of a specific molecules, prepared and measured under the same conditions. In this way, we can also identify the samples that do not correspond to the expected stoichiometry. We work on sets of measured samples that are big enough to be statically significant. We obtain an excellent agreement between the theoretical and the fit values that indicates that diradical **4** films follow the expected stoichiometry.

The three nitrogen atoms in the Blatter radical are assigned to the pyridine-like nitrogen ($N_{1/3}$) that has a carbon atom and a nitrogen atom as neighbors and to the nitrogen bound also to the phenyl ring ($N_{2/4}$) in agreement with previous works. Due to the delocalization of the unpaired electron, the peak at lower binding energy) can be related to photoelectron emitted from the nitrogen radical ($N_{5/6}$=N_{rad}). Thus, the intensity ratio of the sum of the contributions to the N 1s main line are set to have an intensity ratio 1:1:1 as in the molecule for $N_{1/3}$:$N_{2/4}$:$N_{5/6}$.[S26,S35]

Table S9. Summary of fit results to N 1s core level spectra.

	Energy (eV)	Lorentzian Width (eV)	Gaussian Width (eV)	Intensity (%)
N_{rad}	398.9	0.100	0.950	25.8
$N_{1/3}$	399.9	0.100	0.950	28.8
$N_{2/4}$	401.7	0.100	0.950	29.7
S_1	400.5	0.100	0.950	6.1
S_2	402.2	0.100	0.950	3.0
S_3	402.4	0.100	0.950	3.0
S_4	403.3	0.100	0.950	2.1
S_5	404.3	0.100	0.950	1.5

N_{rad} + ½(S_1 + S_2) + S_4 + S_5 = 33.95 %

$N_{1/3}$ + ½(S_1 + S_2) = 33.35 %

$N_{2/4}$ + S_3 = 32.70 %

Film stability (persistence). We have monitored the stability (persistence) of the films exposed to air at room temperature and kept in darkness by using XPS, focusing on the N 1s core level spectra that are those of interest in our work, carrying the information on the radical state. Fig. S27 shows the N 1s core level spectra of a thick film of diradical **4** exposed to air for 18 and 24 hours.

We have observed changes after 24 hours air exposure (Fig. S28, right panel). The major change is the increase of the intensity at around 401 eV (Fig. S28, right panel see arrow). In our previous work, we found changes in the intensity in the spectra of films of the Blatter radical derivatives in the same binding energy range. These phenomena were related to a very slow degradation of the films under ambient conditions due to changes hinting at a possible hydrogenation of the Blatter radical.[S26,S35]

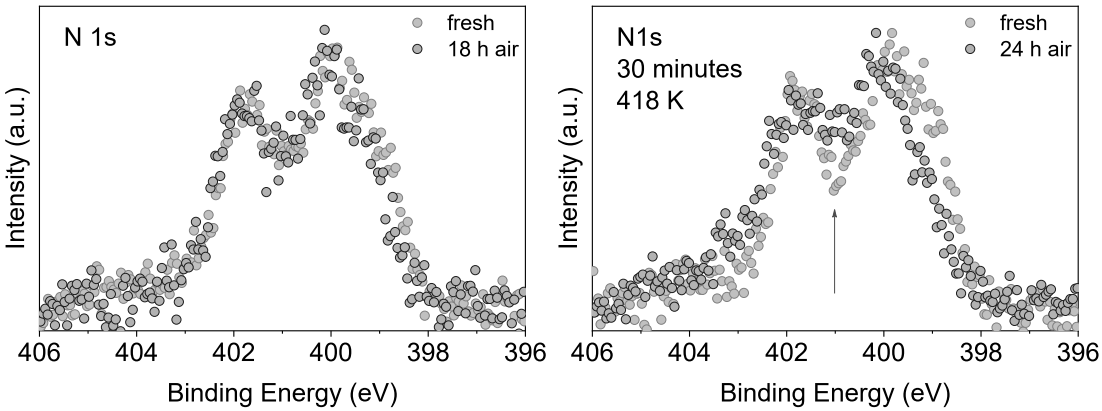

Fig. S28. Comparison of N 1s core level spectra of a freshly evaporated film and after (left panel) 18 hours and (right panel) 24 hours of air exposure.

Comparison between XPS spectra for powder and films: conductivity of polycrystalline diradical 4. Comparing the XPS spectra of the films and the powder, we note that their similarity is remarkable. Usually, the XPS lines of the powder are characterised by a larger bandwidth when compared to the spectra of the films because of charging effects.[S36] Analysing the broadening of the powder C 1s line, we see that it is 0.08 eV larger than the one of the film. This is a very small value in comparison with other radicals. In fact, we have previously investigated a derivative of the Blatter radical that shows a similar but slightly larger difference (0.09 eV).[S26] On the contrary, in the spectra of nitronyl nitroxide radical derivatives this difference is large (0.50 eV).[S27,S37]

This observation supports the result that polycrystalline diradical **4** is a good electrical conductor, being able to screen the core-hole created upon photoemission more efficiently than nitronyl nitroxide radical derivatives[S27,S37] and various closed-shell systems.[S36]

Film morphology. We investigated the film morphology *in-situ* by using XPS and *ex-situ* using AFM. By XPS, it is possible to look at the substrate signal attenuation upon film deposition (Fig. S29, left panel). The curve is characterised by a very slow decay. This intensity trend hints at a Volmer-Weber (VW) growth mode, i.e., island growth. This result is consistent with the atomic force microscopy (AFM) *ex-situ* images obtained on diradical **4** films (Fig. S29, right panel) clearly showing a film morphology dominated by islands. The VW growth mode occurs when the interaction between the deposited molecules is much stronger than between the molecules and the substrate.

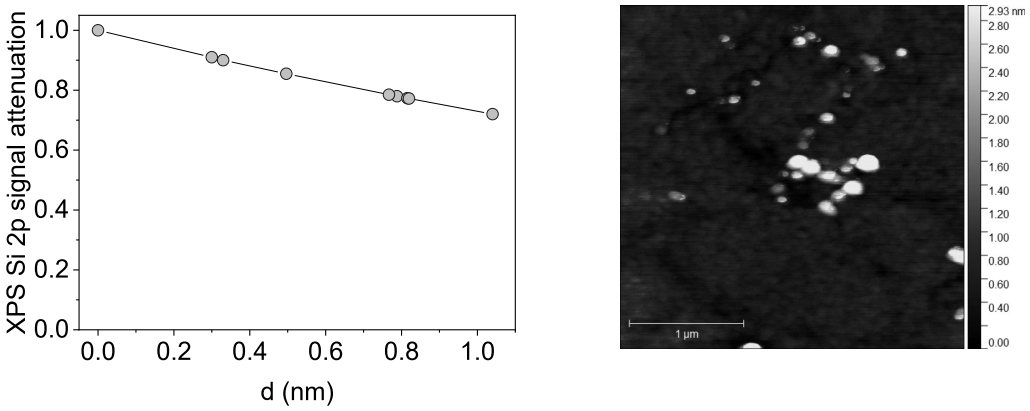

Fig. S29. Attenuation of the Si 2p XPS signal, normalized to the corresponding saturation signal, as a function of film nominal thickness, deposition at room temperature (left panel). A typical 3 mm x 3 mm AFM image (right panel).

3.g2 Preliminary EPR spectra and ESI MS of thin films

EPR spectra of thin films were obtained at the University of Nebraska, using Bruker CW EPR spectrometer (X-band EMXplus), as described in Section 3.e. The films were shipped in several batches from the Casu lab to the Rajca lab via express mail in custom-made Schlenk vessels (under vacuum at ambient temperature). Upon arrival at Nebraska, the films and empty substrate were rapidly transferred on air to custom made Schlenk 5-mm OD EPR tubes, and then placed under high vacuum (ca. 1×10^{-4} Torr). Prior to the measurements the tubes were filled with argon gas under partial pressure (ca. 500 – 1000 mTorr), to ensure adequate thermal conductivity in the 300 – 110 K temperature range. Additional EPR signals, compared to that of empty substrate, were observed only for films of **4** evaporated for ≥2 h.

Angular dependence of EPR spectra of diradical **4** on silicon substrate at room temperature (294 K) was found negligible (checked at 0, 30, 60, and 90 ° angles between the normal to the surface and the external magnetic field). Thus, all subsequent spectra were obtained at 0 ° angle.

EPR difference spectra (diradical **4** on silicon minus the silicon substrate) were obtained by spectral subtraction, after the spectra were shifted by a small magnetic field, to account for small differences in microwave frequencies (if needed). For each spectrum, 64 scans were acquired to ensure adequate signal-to-noise after subtraction. In order to eliminate artifacts from quartz tubes, the spectra for the film of **4** and the empty substrate were obtained in the identical sample tube with identical instrument settings (Fig. S30). The resultant difference spectrum shows a single peak that can be simulated as largely Gaussian line with a significant Lorentzian contribution. This is compatible with predominantly one-dimensional (1D) line narrowing by conductance or exchange coupling.[S21,S38] At lower temperatures, spectral subtraction become more problematic as the relative intensity of the empty substrate peak increases greatly (Figs. S31, S33, S34).

Following EPR experiments both diradical **4** on silicon and empty silicon substrate were extracted with dichloromethane (DCM). The extracts were examined by ESI MS, with the extract from **4** on silicon showing a peak at *m/z* 546.5, corresponding to molecular ion of diradical **4** (Fig. S35).

In another experiment, stability (persistence) of the films, after exposure to air for a total of 18 and 48 h, was followed by EPR spectroscopy (Fig. S32). Following these EPR spectra (film samples under vacuum), the film was extracted with DCM and the extract evaporated, and then dissolved in toluene/chloroform (4:1) for examination by ESI MS – a peak at *m/z* 546.3, corresponding to molecular ion of diradical **4** was observed (Fig. S36), though S/N was lower than for the previous sample in Fig. S35. (Attempted EPR spectroscopy on this extracted sample in toluene/chloroform, 4:1 at 117 K (label: SZ412R17) failed to detect any radical as the background signal from the EPR tube was too strong to permit adequate subtraction.)

Finally, residue of diradical **4**, following three cycles of evaporation under UHV was examined by EPR spectroscopy in toluene/chloroform, 3:1 glass at 117 K (Fig. S37). The spectrum and its simulation shows practically intact diradical **4**.

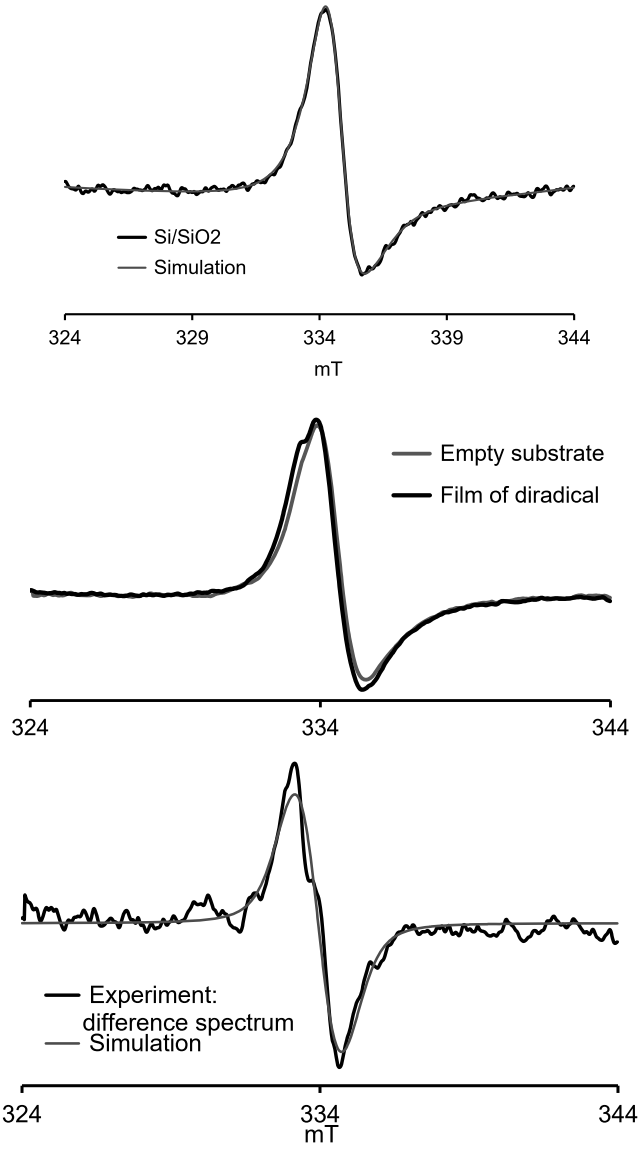

Fig. S30. EPR spectroscopy at room temperature, 294 K. Top panel: EPR spectrum (ν = 9.3613 GHz) of empty Si/SiO_2 substrate (EPR label: SZ392r5), which is characteristic of paramagnetic defects in silicon. Simulation should be viewed as approximate because of significant Dysonian line shape contribution to the spectrum (label: Try639, S = ½, rmsd = 0.005488, g_{xx} = 1.9979, g_{yy} = 1.9963, g_{zz} = 1.9358; H-strain (MHz): H_x = 24.5, H_y = 63.4, H_z = 315.5. Middle panel: overlayed EPR spectra of the film (label: SZ413r1) and the substrate (label: SZ416r4) prior to subtraction. Bottom panel: same data as in Figure 7, main text. EPR difference spectrum (film minus substrate); simulation (label: Try814, S = 1/2, rmsd = 0.07126, g = 2.0006, lwpp (Gaussian) = 1.26 mT and lwpp (Lorentzian) = 0.56 mT.

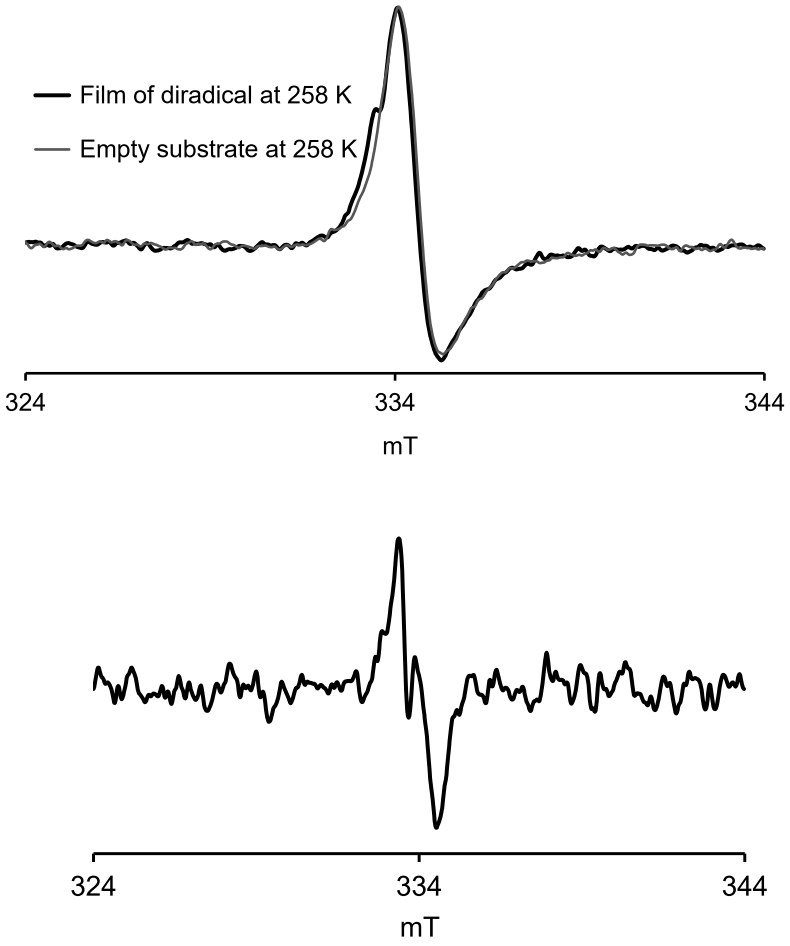

Fig. S31. EPR spectroscopy at 258 K. Top panel: overlayed EPR spectra of the film (ν = 9.35367 GHz, label: SZ414r28) and the substrate (label: SZ414r5) prior to subtraction. Bottom panel: EPR difference spectrum (film minus substrate); simulation is not reliable because of too low S/N.

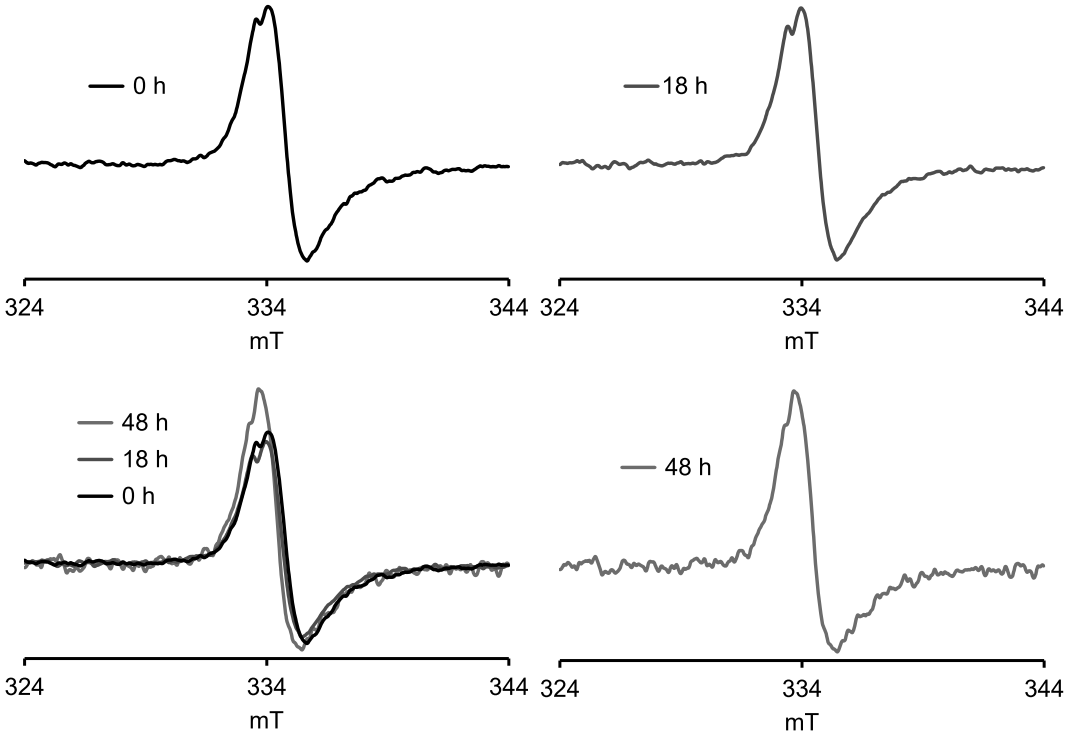

Fig. S32. EPR spectroscopy at room temperature, 293 K: film stability on air in the darkness. Panels clockwise from top left: EPR spectra before exposure to air (label: SZ414r33), after 18 h on air (label: SZ414r39), after 48 h on air (label: SZ414r41), and overlay plot.

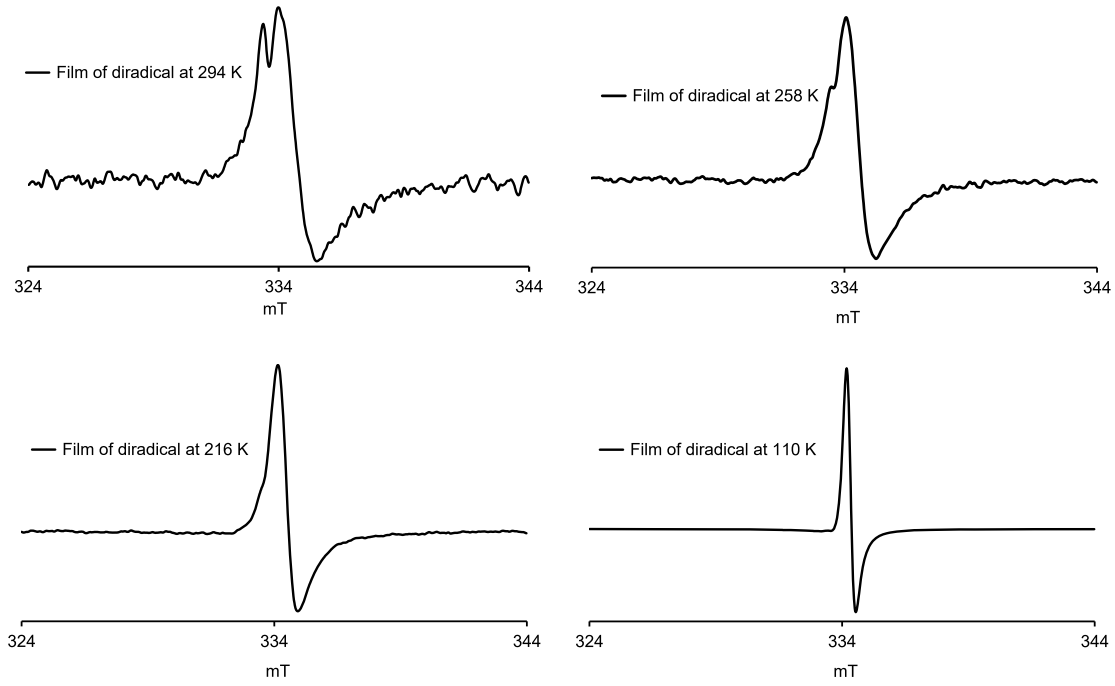

Fig. S33. Variable temperature EPR spectroscopy on thin film of diradical **4**: 294 K (SZ412r13), 258 K (SZ414r28), 216 K (SZ414r24), and 110 K (SZ414r18). The sample tube containing the film had a paramagnetic defect, resulting in an extra peak visible at T = 293 and 258 K. The spectrum at 125 K is partially saturated because of relatively high microwave power (0.2 mW) used.

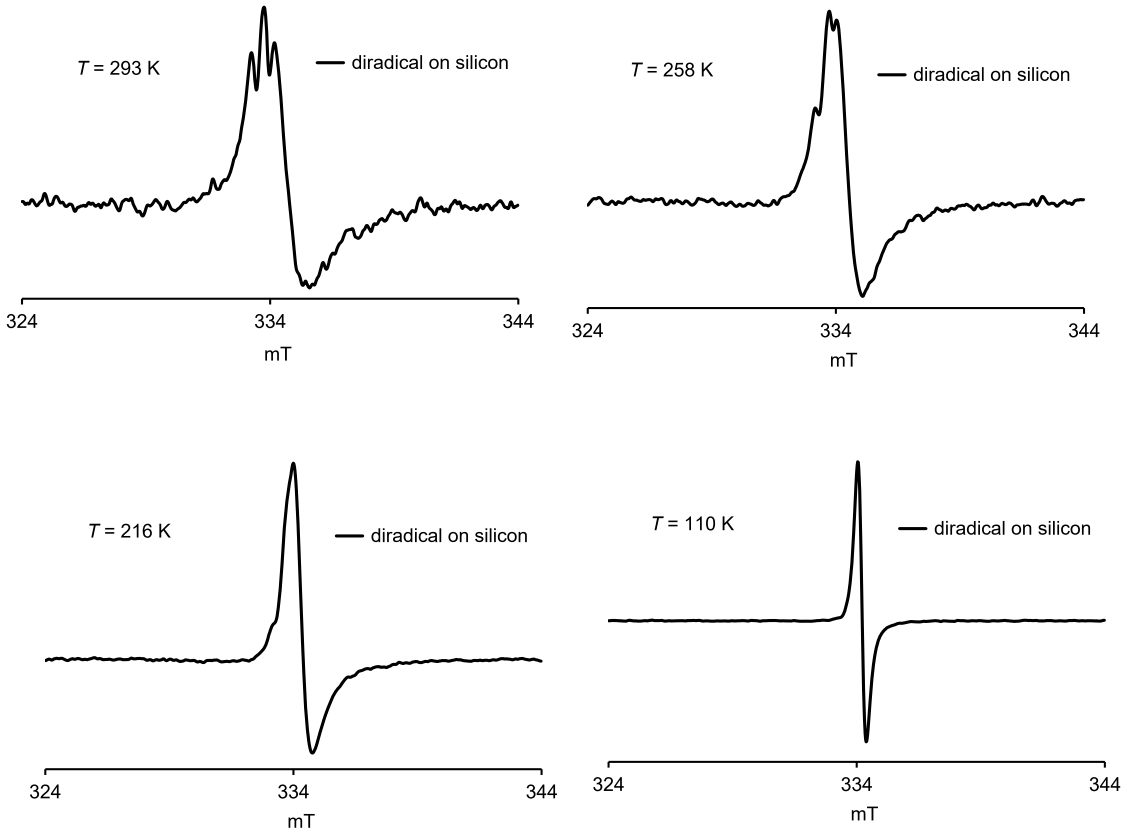

Fig. S34. Repeat variable temperature EPR spectroscopy on thin film of diradical **4**: 293 K (SZ3-83R5), 258 K (SZ3-83R13), 216 K (SZ3-83R16), and 110 K (SZ3-83R10). The sample tube containing the film had a paramagnetic defect, resulting in an extra peak visible at T = 293 and 258 K. The spectrum at 125 K is obtained at low microwave power (0.02 mW) to minimize on saturation effects.

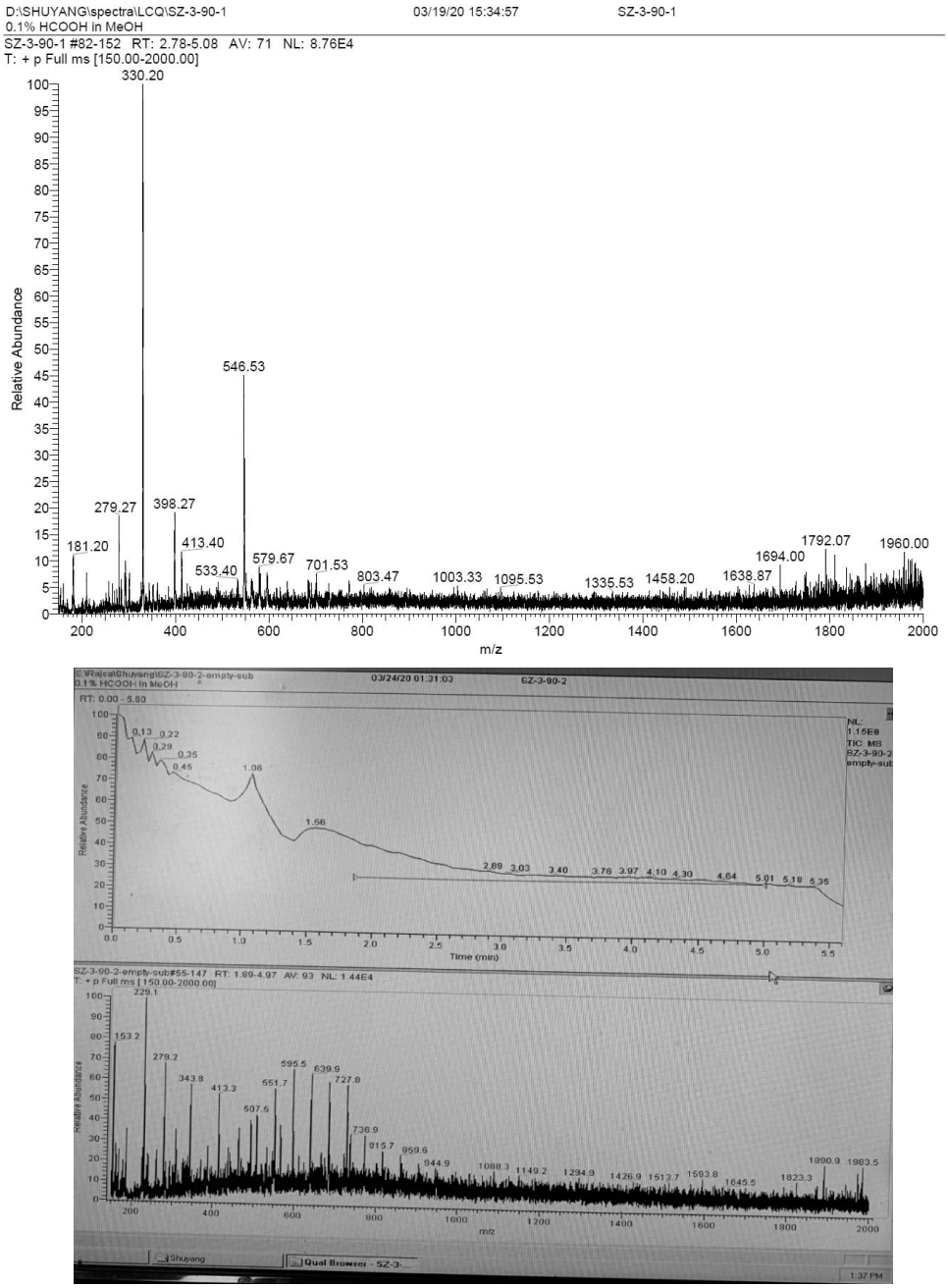

Fig. S35. LR ESI-MS (0.1% HCOOH in MeOH, labels: SZ390-1 and SZ390-2-empty sub) of diradical **4** thin film, with minimal exposure to air (top plot) and of empty silicon substrate (bottom plot), following extraction with DCM. The peak at *m/z* 546.53 is close to calculated *m/z* for molecular ion of **4** ($C_{36}H_{30}N_6$) is 546.25.

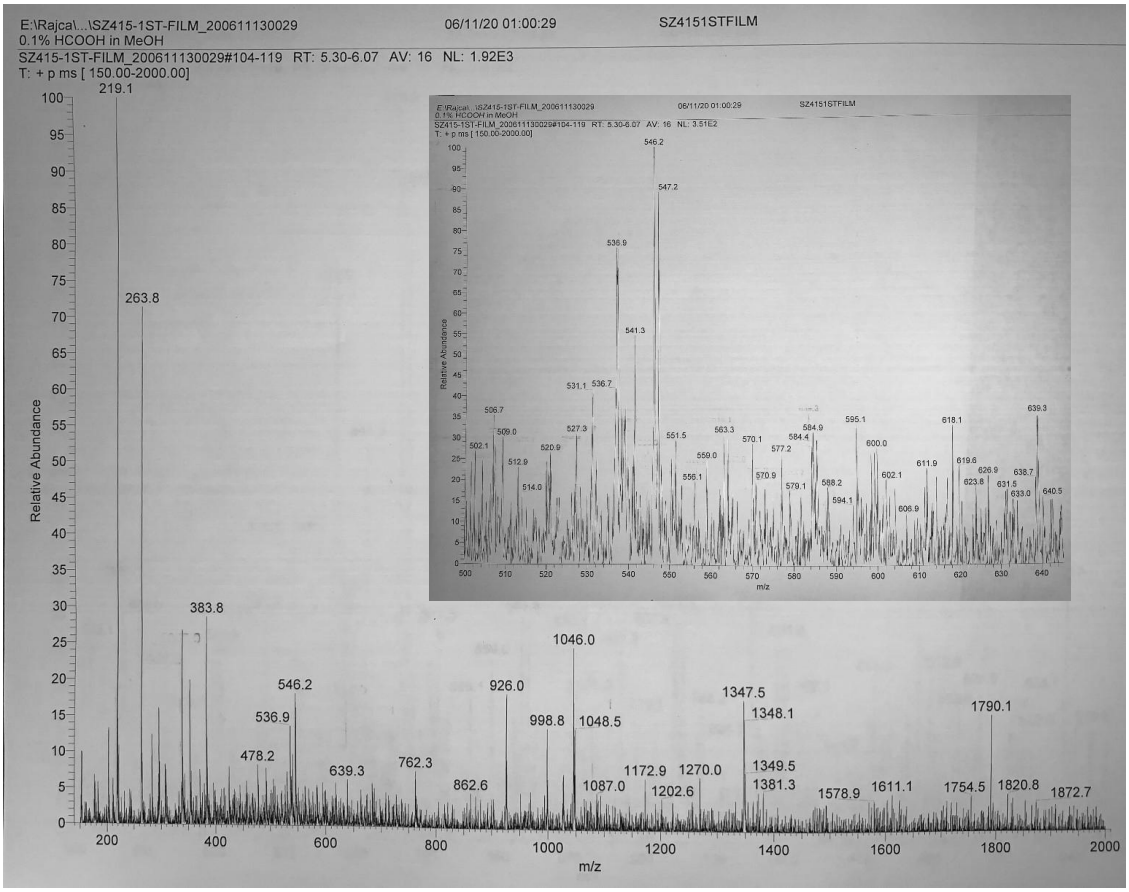

Fig. S36. LR ESI-MS (0.1% HCOOH in MeOH, label: SZ415-1ST-FILM_200611130029) of diradical **4** thin film, following 48 hr exposure to air, and then extraction with DCM. Inset plot: spectral expansion. The peak at *m/z* 546.2 is close to calculated *m/z* for molecular ion of **4** ($C_{36}H_{30}N_6$) is 546.25.

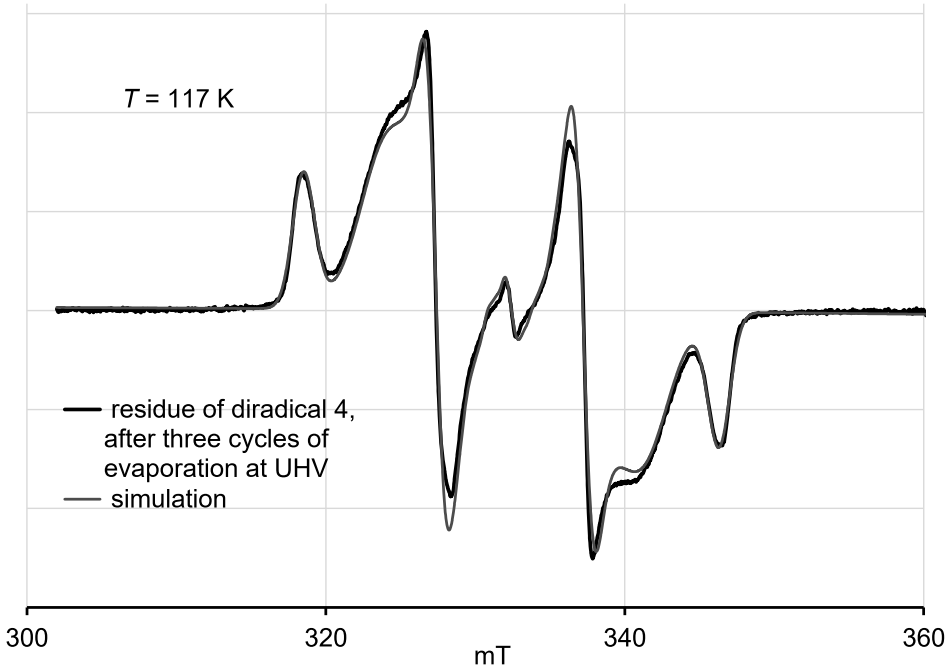

Fig. S37. EPR pectrum for residue of diradical **4** following three cycles of evaporation under UHV: toluene/chloroform, 4:1 glass, 117 K, ν = 9.3251 GHz, EPR label: SZ419R3. The spectrum was obtained at 10 times larger MW power (0.2 mW, attenuation of 30 dB), compared to other spectra, because of small amount sample available; therefore slight oversaturation (line shape distortion) is possible. Simulation $|\Delta m_s| = 1$ region (pepper, EasySpin, rmsd = 0.03464): Component A, weight = 1.0000, $S = 1$, $D = 389.3$ MHz, $E = 35.3$ MHz, $g_{xx} = 2.0045$, $g_{yy} = 2.0029$, $g_{zz} = 2.0043$; H-strain (MHz): $H_x = 41.73$, $H_y = 112.68$, $H_z = 48.46$; g-strain: $g_x = 0.0000134$, $g_y = 0.0000028$, $g_z = 0.0000013$; D-strain (MHz): $D = 9.645$, $E = 0.095$; component B, $S = ½$, weight = 0.050, $g_{xx} = 2.0046$, $g_{yy} = 2.0039$, $g_{zz} = 2.0019$; H-strain (MHz): $H_x = 14.60$, $H_y = 82.79$, $H_z = 14.70$. Fixed parameters for component B, $S = ½$ (based on simulation for monoradical **10**, see: Fig. S16), ^{14}N $\boldsymbol{A}$-tensors: $A_{xx}(1) = 5.324$, $A_{yy}(1) = 8.527$, $A_{zz}(1) = 36.220$; $A_{xx}(2) = 0.095$, $A_{yy}(2) = 0.144$, $A_{zz}(2) = 39.216$; $A_{xx}(3) = 0.003$, $A_{yy}(3) = 0.014$, $A_{zz}(3) = 52.586$.

3.h DFT calculations.

Geometry optimizations and frequency calculations were performed using the Gaussian 16 program packages[S39] running on a 16-cpu workstation under Linux operating system.

Geometries were fully optimized for diradical **4** at the UB3LYP/6-31G(d,p) level of theory in the gas phase and at the UB3LYP/6-31G(d,p)/IEF-PCM-UFF level of theory, using solvent models for toluene and tetrahydrofuran (THF). Optimized geometries (C_1 point group) for both conformations, **4**A and **4**B, were determined to be minima (zero imaginary frequencies) on the potential energy surface (PES). Broken symmetry wavefunctions were employed for singlet ($S = 0$) states of the diradical, and were checked for stability (stable=opt), following geometry optimization. For all geometry optimizations of diradical **4** (and monoradical **10**), RMS forces in Cartesian coordinates are less than 0.3×10^{-6} a.u. (and significantly lower in internal coordinates) that is typically better than the "tight" criterion for RMS forces in geometry optimization in Gaussian 16.

Singlet-triplet energy gaps, ΔE_{ST}, for diradical **4** (Table S10) are computed using eq. S4, where $\Delta E_U = E_{BS} - E_T$, i.e., the energy difference between broken symmetry singlet and triplet states at their optimized geometries after ZPVE corrections at the UB3LYP/6-31G(d,p)+ZPVE theory level:[S40-S42]

$$\Delta E_{ST} = \Delta E_U[<S^2_T>/(<S^2_T> - <S^2_{BS}>)] \qquad \text{(S4)}$$

Values of ΔE_{ST} at this level of theory are typically slightly overestimate the experiment or high level computations accounting for electron correlation more accurately.[S3,S42-S45]

EPR parameters (g-tensor, D-tensor and ^{14}N A-tensor) for diradical **4** were calculated using the B3LYP density functional (as implemented in ORCA[S46]) and Barone's EPR-II basis set.[S47,S48] All calculations used the gas phase optimized UB3LYP/6-31G(d,p) geometries for **4**A and **4**B. Input files were prepared using Gabedit.[S49] Quasi-restricted B3LYP density functional was used ("uno" option in ORCA). Calculations of D-tensor employed spin-spin dipolar coupling only,[S48] with absolute values of D and E being somewhat overestimated compared to the experiment (Table S11).[S3,S48,S50]

Similarly, geometries were optimized for monoradical **10**; geometry optimization starting from the X-ray structure of **10** gave the lowest energy conformation **10**A. Another conformation, **10**B, which is analogous to **4**A, was also found to be a local minimum on the PES, about 0.18 kcal mol^{-1} above **10**A in the gas phase at the UB3LYP/6-31G(d,p)+ZPVE level of theory (Table S10).

Spin density surfaces for radicals were calculated at the UB3LYP/6-31G(d,p) level. Cube files were obtained using "medium" setting in Gaussian 16 (cubegen utility), and surfaces were plotted with isodensity of 0.002 and 0.004 electron/Bohr^3 (Tables S10 and S12).

DFT computations of intra-chain exchange coupling constant, J', were carried out for dimers of diradical **4** at the experimental X-ray geometry, obtained at 100 K (Table S12). Computations were carried out at the UB3LYP/6-31G(d) and UB3LYP/6-311++G(d,p) levels of theory. Intramolecular coupling constant J for the monomers at the X-ray geometries were computed as well. Equations S5 – S7 were used to extract values of J and J',[S51] employing Yamaguchi spin contamination correction.[S40] Equation S5 refers to triplet (T) and broken symmetry singlet (BS)

of the monomer **4**. Equations S6 and S7 refer to high-spin quintet (Q), broken symmetry triplet (BT), and broken symmetry singlet (BS) of the dimers of **4**.[S3,S19,S51] In contrast to the previous work,[S3,S19,S51] we were able to compute a special low-energy BS singlet state (through judicious use of guess command and orbital permutation in G16), which is below the high-spin quintet state; based on its spin density distribution (see: Table 12), monomeric parts of the dimer possess intramolecular ferromagnetic coupling but they are coupled through intermolecular antiferromagnetic coupling. Consequently, equation S7 takes a different form than analogous equations in the previous work.

$$J = (E_{BS} - E_{T})/(\langle S^2\rangle_{T} - \langle S^2\rangle_{BS}) \quad \text{(S5)}$$

$$J + 2J' = [(E_{BT} - E_{Q})*3.0000]/(\langle S^2\rangle_{Q} - \langle S^2\rangle_{BT}) \quad \text{(S6)}$$

$$J' = [(E_{BS} - E_{Q})*4.0000]/(\langle S^2\rangle_{Q} - \langle S^2\rangle_{BS}) \quad \text{(S7)}$$

Table S10. Diradical **4** (two conformations, **4**A and **4**B) and monoradical **10** (two conformations, **10**A and **10**B): spin density surfaces at the UB3LYP/6-31G(d,p) level (in the gas phase) and plotted with isodensity of 0.002 electron/Bohr^3. UB3LYP/6-31G(d,p)+ZPVE (in the gas phase) and UB3LYP/6-31G(d,p)/IEF-PCM-UFF+ZPVE (in toluene and THF) energies (hartree), zero point vibrational energies (hartree), RMS gradient norms (a.u.) in Cartesian coordinates, lowest vibrational frequencies (cm^{-1}), S-T splittings (ΔE_{ST} in kcal mol^{-1}, Eq. S4), and relative energies (e.g., for triplet states of **4**) (kcal mol^{-1}).[a]

Diradical **4**A

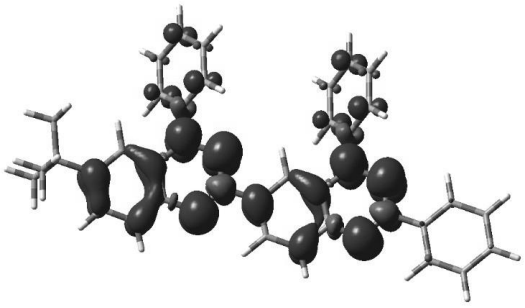

Diradical **4**B

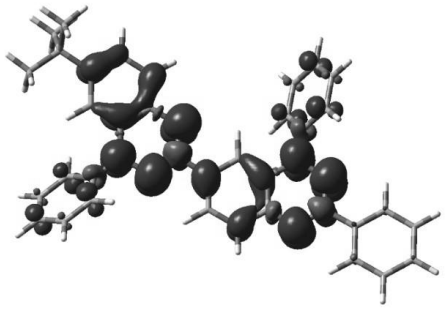

DFT	Medium	Conformation	State	Geometry	E^o (gas phase)	ZPVE	E^o + ZPVE	$\langle S^2 \rangle$	RMS gradient norm (×10^{-6})[b]	Lowest vibrational frequencies	ΔE_{ST}(S-T)	ΔE_{ST}	Relative triplet energies, ΔE_T
UB3LYP	Gas phase	**4**A	Triplet	Triplet	–1718.40694503	0.578996	–1717.827949	2.0363	0.07	9.2, 13.6, 29.7	0.000	**0.000**	**0.000**
			BS-singlet	BS-singlet	–1718.40584035	0.578972	–1717.826868	1.0283	0.17	8.7, 13.6, 29.6	0.678	**1.370**	-
		4B	Triplet	Triplet	–1718.40685760	0.578991	–1717.827866	2.0359	0.04	9.4, 15.9, 27.5	0.000	**0.000**	**0.052**[c]
			BS-singlet	BS-singlet	–1718.40662509	0.579036	–1717.827589	1.0014	0.24	9.8, 15.8, 27.4	0.174	**0.342**	-
UB3LYP	Toluene	**4**A	Triplet	Triplet	–1718.41254507	0.578798	–1717.833747	2.0350	0.16	9.6, 13.4, 28.9	0.000	**0.000**	**0.000**
			BS-singlet	BS-singlet	–1718.41149204	0.578776	–1717.832716	1.0276	0.12	9.1, 13.5, 28.0	0.647	1.307	-
		4B	Triplet	Triplet	–1718.41242723	0.578866	–1717.833561	2.0347	0.30	9.3, 16.6, 27.6	0.000	**0.000**	**0.117**
			BS-singlet	BS-singlet	–1718.41225393	0.578920	–1717.833334	1.0004	0.29	9.9, 16.5 27.6	0.142	0.280	-
UB3LYP	THF	**4**A	Triplet	Triplet	–1718.41718698	0.578611	–1717.838576	2.0339	0.16	9.3, 13.0, 28.5	0.000	**0.000**	**0.000**
			BS-singlet	BS-singlet	–1718.41617315	0.578587	–1717.837586	1.0271	0.15	8.8, 13.0, 28.1	0.621	1.255	-
		4B	Triplet	Triplet	–1718.41704371	0.578695	–1717.838349	2.0338	0.30	9.2, 16.3, 27.6	0.000	**0.000**	**0.142**
			BS-singlet	BS-singlet	–1718.41692009	0.578747	–1717.838173	0.9993	0.26	9.8, 16.3, 27.6	0.110	0.217	-

Monoradical **10**A

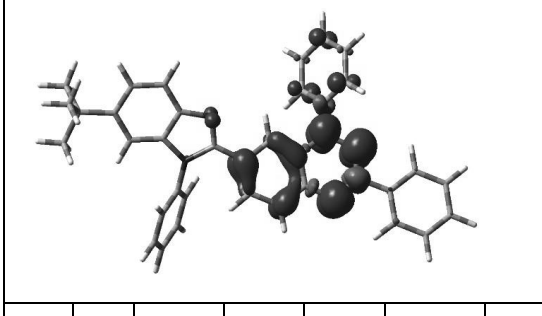

Monoradical **10**B

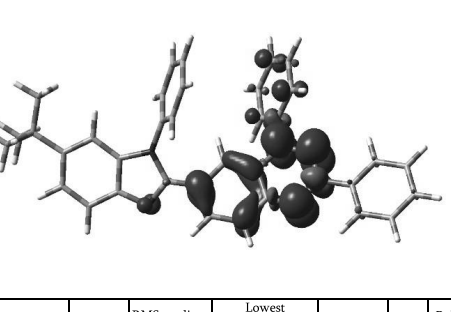

DFT	Medium	Conformation	State	Geometry	E^o (gas phase)	ZPVE	E^o + ZPVE	$\langle S^2 \rangle$	RMS gradient norm (×10^{-6})[b]	Lowest vibrational frequencies			Relative energies
UB3LYP	Gas Phase	**10**A	Doublet	Doublet	–1663.70551128	0.575047	–1663.130464	0.7667	0.17	11.2, 16.2, 27.3			**0.000**
		10B	Doublet	Doublet	–1663.70515223	0.574976	–1663.130176	0.7672	0.08	10.5, 14.8, 26.3			**0.181**

[a] Gas phase dipole moments for triplet states are 6.47 and 5.84 D for **4**A and **4**B, respectively; 1 Hartree = 627.51 kcal mol^{-1}. [b] In Cartesian coordinates. [c] In the gas phase, relative energy of triplets **4**B vs **4**A is 0.072 kcal mol^{-1} at the ROMP2/6-31G(d,p)//UB3LYP/6-31G(d,p) level of theory, i.e., slightly greater than the UB3LYP value of 0.052 kcal mol^{-1}.

Table S11. Diagonalized D-matrix (D-tensor), g-matrix (g-tensor), and the largest component of the ^{14}N A-tensors with corresponding orientations in the molecular system of coordinates (x, y, z) are computed at the UB3LYP/EPR-II level of theory using ORCA for triplet (S = 1) ground states of diradical **4**: conformations **4**A and **4**B, and quintet (S = 2) state of the dimer of **4**A (X-ray geometry). The principal axes (X, Y, Z) are labeled so the components for the diagonalized D-matrix follow the usual relationship: $|D_{ZZ}| > |D_{YY}| > |D_{XX}|$. In this case, E/D is always positive and lies between 0 and 1/3, where for comparison with experiment, $D = D_{ZZ} - (D_{YY} + D_{XX})/2 = 3D_{ZZ}/2$ and $E = (D_{XX} - D_{YY})/2$. The reported largest components of the ^{14}N A-tensors, scaled by the factor of 1/2S, are taken directly from the ORCA outputs, after rounding to two significant digits after the decimal point.[a,b]

	Diradical **4**A					Diradical **4**B					Dimer of **4**A (X-ray geom)				
	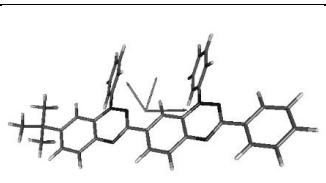					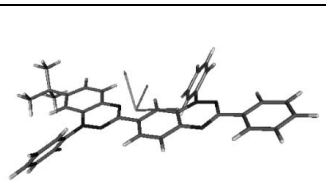					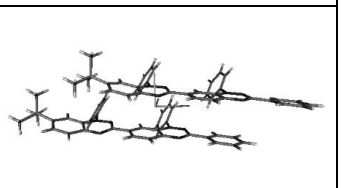				
		$D_{xx} = D_{ZZ}$	$D_{yy} = D_{XX}$	$D_{zz} = D_{YY}$	D (E)		$D_{xx} = D_{ZZ}$	$D_{yy} = D_{XX}$	$D_{zz} = D_{YY}$	D (E)		$D_{xx} = D_{YY}$	$D_{zz} = D_{XX}$	$D_{yy} = D_{ZZ}$	D (E)
D-tensor (cm^{-1})		-0.009031	0.002148	0.006883	–0.013546 (–0.00237)		-0.009135	0.002577	0.006558	–0.013703 (–0.00199)		-0.003272	-0.000061	+0.003332	+0.004999 (0.00161)
	x	0.9981	-0.0596	-0.0126		x	-0.9988	-0.0450	0.0169		x	0.9786	-0.2042	-0.0264	
	y	-0.0581	-0.9936	0.0972		y	0.0452	-0.9989	0.0126		y	-0.0312	-0.0204	-0.9993	
	z	-0.0183	-0.0963	-0.9952		z	0.0163	0.0133	0.9998		z	0.2036	0.9787	-0.0263	
		$g_{zz} = g_{YY}$	$g_{xx} = g_{ZZ}$	$g_{yy} = g_{XX}$	g_{iso}		$g_{zz} = g_{YY}$	$g_{yy} = g_{XX}$	$g_{xx} = g_{ZZ}$	g_{iso}		$g_{zz} = g_{XX}$	$g_{xx} = g_{YY}$	$g_{yy} = g_{ZZ}$	g_{iso}
g-tensor		2.00225	2.00406	2.00434	2.00355		2.00225	2.00418	2.00423	2.00355		2.0023	2.0042	2.0044	2.00365
	x	0.0735	0.7683	-0.6359		x	0.0829	-0.4913	0.8670		x	0.1874	0.8261	-0.5314	
	y	-0.1207	0.6398	0.7590		y	0.0051	-0.8698	-0.4934		y	-0.0382	0.5467	0.8365	
	z	0.9900	0.0210	0.1398		z	0.9965	0.0454	-0.0696		z	0.9815	-0.1365	0.1340	
^{14}N A-tensor (MHz)	N1	N2	N3	N4	N5 (N6)	N1	N2	N3	N4	N5 (N6)	-	-	-	-	-
$A_{zz} = A_{YY}$	20.72	20.61	22.12	19.02	18.20 (22.22)	20.77	20.52	19.13	18.27	22.50 (22.04)	-	-	-	-	-

[a] x, y, and z axes are shown in red, green, and blue, respectively. Note that for **4**A and **4**B, the largest component of D-tensor, D_{ZZ}, is oriented along x-axis of the molecules "connecting" two Blatter radical moieties. The largest components of A-tensor, A_{YY}, are oriented along z-axis of the molecules, which coincides with the $2p_\pi$ orbital axis. Smallest g-tensor component, g_{YY}, is oriented along the z-axis of the molecules, which coincides with the $2p_\pi$ orbital axis, as expected. Notably, the largest g-tensor components for **4**A, g_{XX}, and for **4**B, g_{ZZ}, are oriented along the y- and x-axes of the molecules, respectively. [b] For dimer of **4**A, the largest component of D-tensor, D_{ZZ}, is oriented along y-axis, i.e., it is approximately orthogonal to D_{ZZ} for monomer **4**A and to the $2p_\pi$ orbital axis.

Table S12. Diradical **4** and its dimer from single point calculations at the X-ray structure geometry (X-ray label: 20036): spin density surfaces for dimer, quintet and broken-symmetry singlet at the UB3LYP/6-311+G(d,p) level (in the gas phase), as well as broken-symmetry triplet at the UB3LYP/6-31G(d) level (in the gas phase); all plotted with isodensity of 0.004 electron/Bohr^3. Computed total energy in Hartrees and $\langle S^2 \rangle$ using 6-31G(d) and 6-311+G(d,p) as the basis sets. Computed values of J and J' (i.e., J/k and J'/k in Kelvin) using equations S5–S7. All broken-symmetry states were checked for stability (stable=opt command in G16).

quintet		BS triplet		BS singlet		
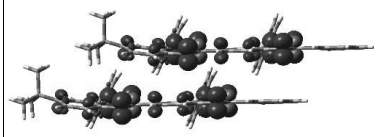		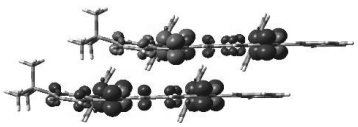				
UB3LYP/6-31G(d)	$2S+1$	Energy [Hartree]	$\langle S^2 \rangle$	J [K]	$J+2J'$ [K]	J' [K]
Monomer	3	-1717.92495124	2.0355	-	-	-
	1	-1717.92362309	1.0242	288.2	-	-
Dimer	5	-3435.84298263	6.0715	-	-	-
	3	-3435.84229814	3.0432	-	148.8	–69.7
	1	-3435.84330857	2.0330	-	-	–70.9
UB3LYP/6-311+G(d,p)	$2S+1$	Energy [Hartree]	$\langle S^2 \rangle$	J [K]	$J+2J'$ [K]	J' [K]
Monomer	3	-1718.36975681	2.0349	-	-	-
	1	-1718.36853398	1.0265	266.1	-	-
Dimer	5	-3436.72434189	6.0705	-	-	-
	3	-3436.72382029	3.0349	-	113.1	–72.4[a]
	1	-3436.72483663	2.0444	-	-	–107.9

[a] A lower energy BS triplet, with spin distribution analogous to that at the UB3LYP/6-31G(d) level, as shown above, could not be located at the UB3LYP/6-311+G(d,p) level.

3. ^{1}H-, ^{13}C NMR, IR Spectra and HR MS Data for Synthetic Intermediates, 4, and 10.

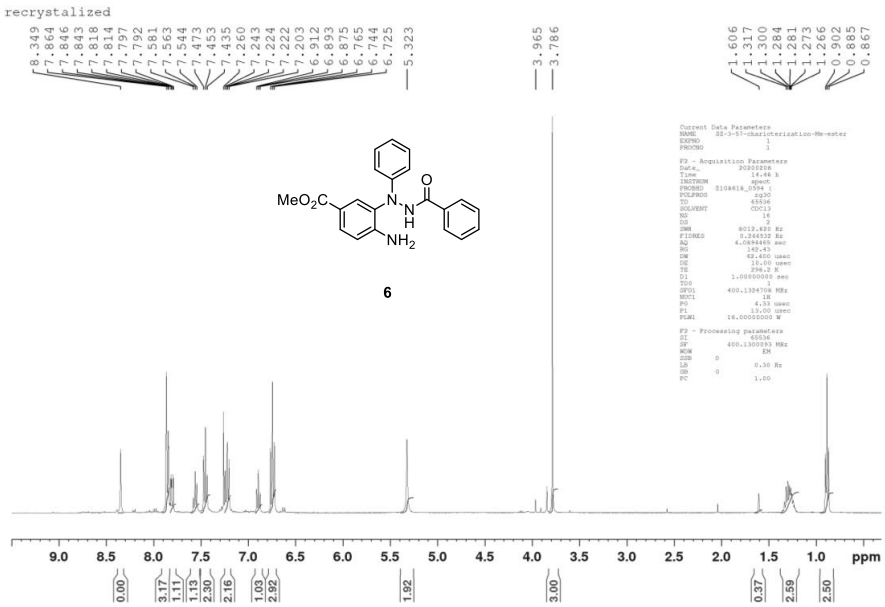

Fig. S38. ^{1}H NMR (400 MHz, $CDCl_3$) spectrum of methyl 4-amino-3-(2-benzoyl-1-phenylhydrazineyl) benzoate **6** (label: SZ-2-94).

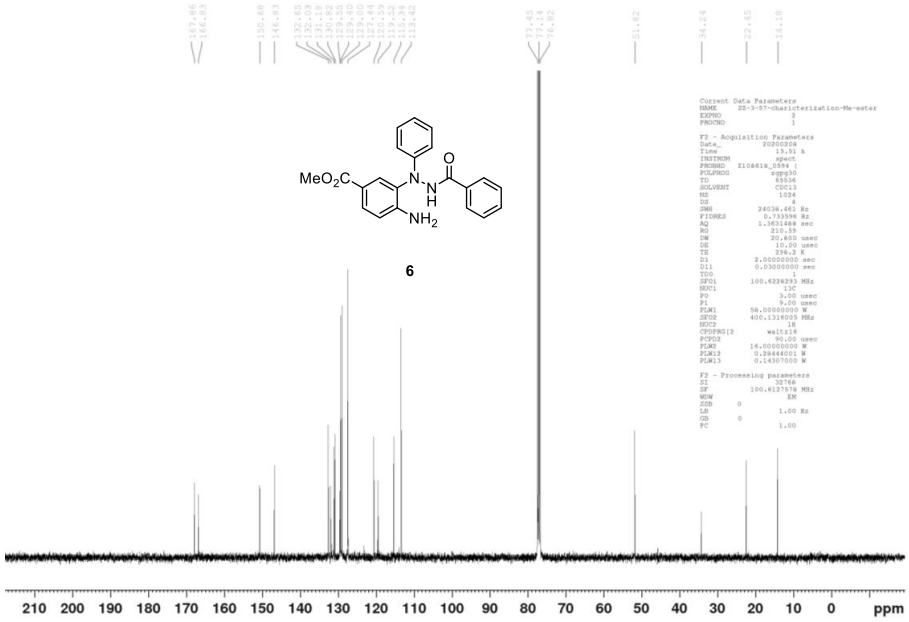

Fig. S39. ^{13}C NMR (100 MHz, $CDCl_3$) spectrum of methyl 4-amino-3-(2-benzoyl-1-phenylhydrazineyl) benzoate **6** (label: SZ-2-94).

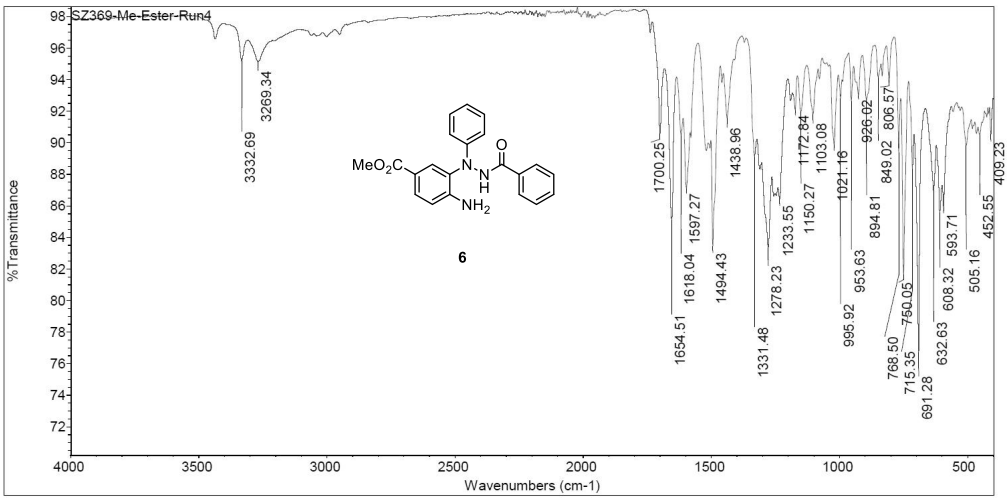

Fig. S40. IR spectrum of 4-amino-3-(2-benzoyl-1-phenylhydrazineyl) benzoate **6** (label: SZ-3-69).

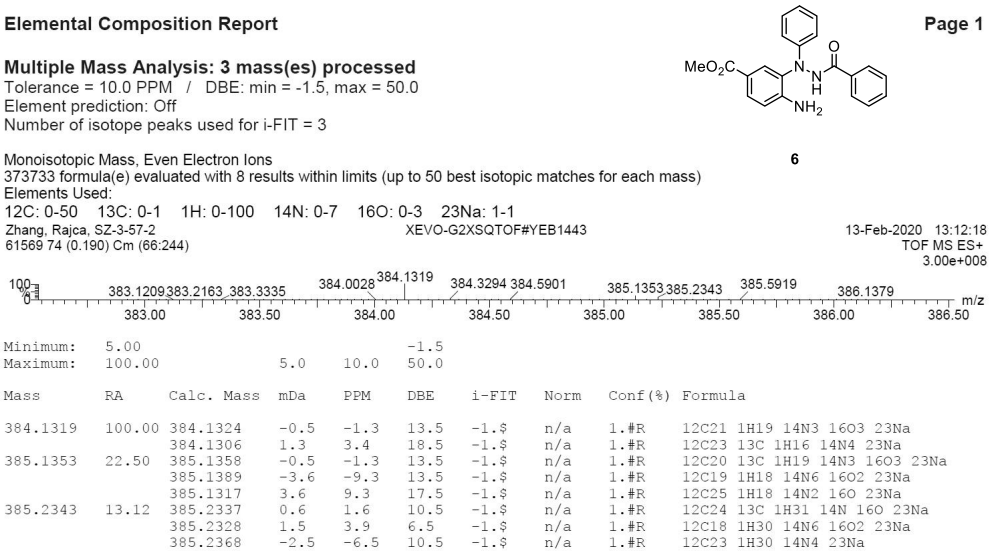

Elemental Composition Report Page 1

Multiple Mass Analysis: 3 mass(es) processed
Tolerance = 10.0 PPM / DBE: min = -1.5, max = 50.0
Element prediction: Off
Number of isotope peaks used for i-FIT = 3

Monoisotopic Mass, Even Electron Ions
373733 formula(e) evaluated with 8 results within limits (up to 50 best isotopic matches for each mass)
Elements Used:
12C: 0-50 13C: 0-1 1H: 0-100 14N: 0-7 16O: 0-3 23Na: 1-1

Zhang, Rajca, SZ-3-57-2 XEVO-G2XSQTOF#YEB1443 13-Feb-2020 13:12:18
61569 74 (0.190) Cm (66:244) TOF MS ES+
3.00e+008

Minimum:	5.00				-1.5				
Maximum:	100.00		5.0	10.0	50.0				
Mass	RA	Calc. Mass	mDa	PPM	DBE	i-FIT	Norm	Conf(%)	Formula
384.1319	100.00	384.1324	-0.5	-1.3	13.5	-1.$	n/a	1.#R	12C21 1H19 14N3 16O3 23Na
		384.1306	1.3	3.4	18.5	-1.$	n/a	1.#R	12C23 13C 1H16 14N4 23Na
385.1353	22.50	385.1358	-0.5	-1.3	13.5	-1.$	n/a	1.#R	12C20 13C 1H19 14N3 16O3 23Na
		385.1389	-3.6	-9.3	13.5	-1.$	n/a	1.#R	12C19 1H18 14N6 16O2 23Na
		385.1317	3.6	9.3	17.5	-1.$	n/a	1.#R	12C25 1H18 14N2 16O 23Na
385.2343	13.12	385.2337	0.6	1.6	10.5	-1.$	n/a	1.#R	12C24 13C 1H31 14N 16O 23Na
		385.2328	1.5	3.9	6.5	-1.$	n/a	1.#R	12C18 1H30 14N6 16O2 23Na
		385.2368	-2.5	-6.5	10.5	-1.$	n/a	1.#R	12C23 1H30 14N4 23Na

Fig. S41. HRMS ESI spectrum of 4-amino-3-(2-benzoyl-1-phenylhydrazineyl) benzoate **6** (0.1% HCOOH in MeOH, label: SZ-3-57-2).

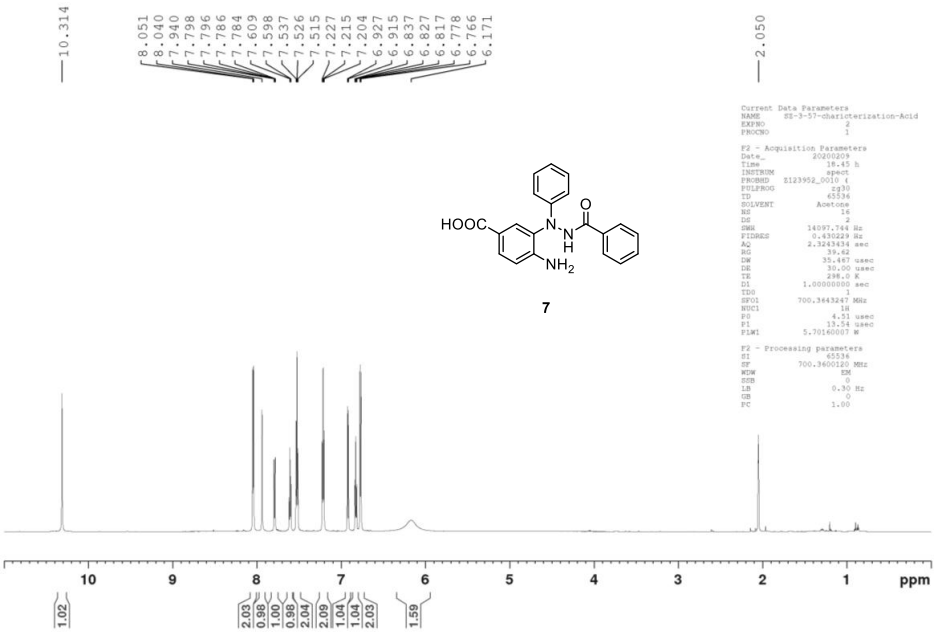

Fig. 42. ^{1}H NMR (700 MHz, acetone-d_6) spectrum of amino-benzoic acid **7** (label: SZ-2-95).

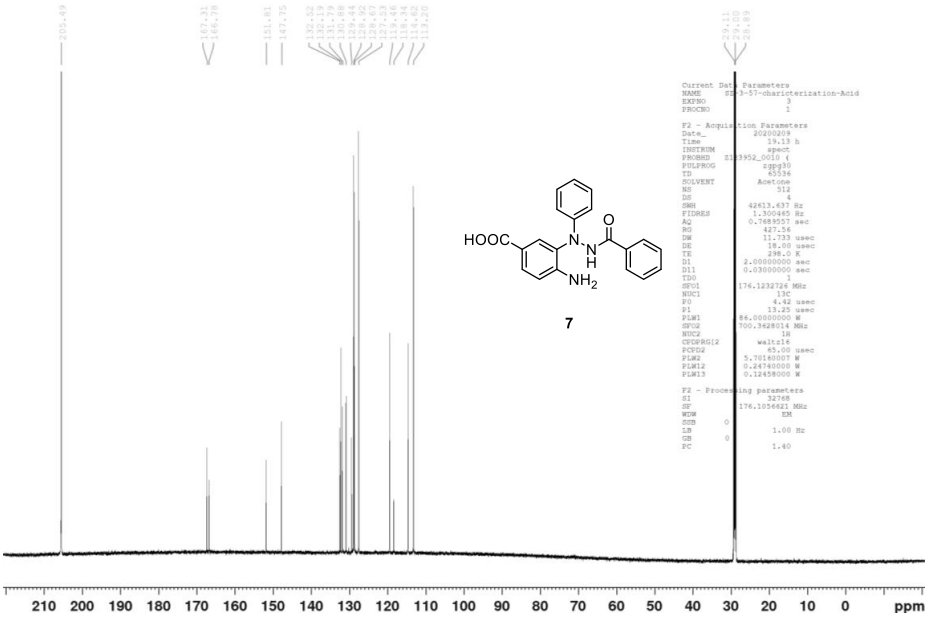

Fig. 43. ^{13}C NMR (175 MHz, acetone-d_6) spectrum of amino-benzoic acid **7** (label: SZ-2-95).

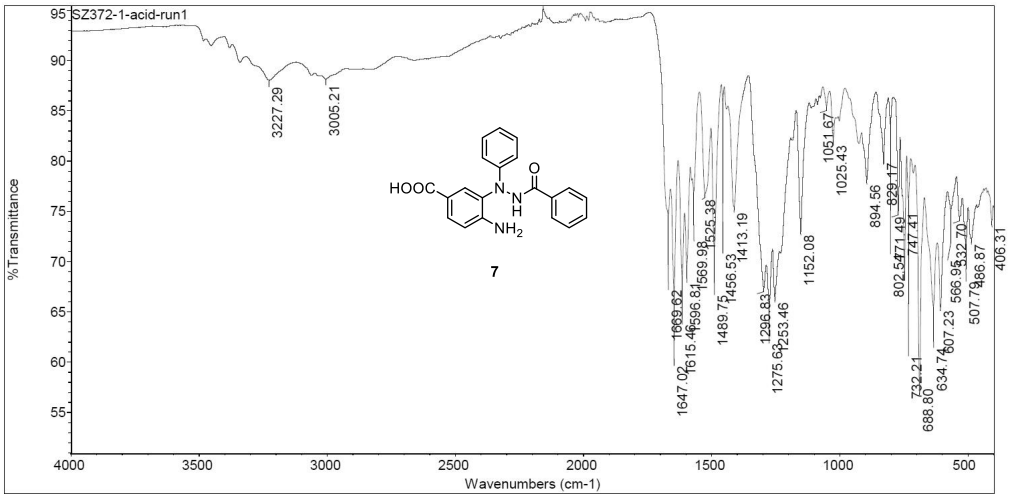

Fig. 44. IR spectrum of amino-benzoic acid **7** (label: SZ-3-72).

Elemental Composition Report Page 1

Multiple Mass Analysis: 7 mass(es) processed
Tolerance = 10.0 PPM / DBE: min = -1.5, max = 50.0
Element prediction: Off
Number of isotope peaks used for i-FIT = 3

Chemical Formula: $C_{20}H_{17}N_3O_3$
Exact Mass: 347.1270

Monoisotopic Mass, Even Electron Ions
818335 formula(e) evaluated with 18 results within limits (up to 50 best isotopic matches for each mass)
Elements Used:
12C: 0-50 13C: 0-1 1H: 0-100 14N: 0-7 16O: 0-3 23Na: 1-1

7

Zhang, Rajca, SZ-3-57-3 XEVO-G2XSQTOF#YEB1443 13-Feb-2020 13:27:49
61570-1 331 (0.779) Cm (48:341) TOF MS ES+
5.06e+007

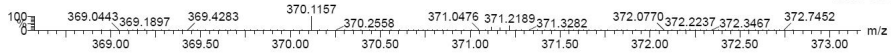

Minimum:	5.00				-1.5				
Maximum:	100.00		5.0	10.0	50.0				
Mass	RA	Calc. Mass	mDa	PPM	DBE	i-FIT	Norm	Conf(%)	Formula
369.1501	6.47	369.1481	2.0	5.4	9.5	-1.$	n/a	1.#R	12C14 13C 1H19 14N7 16O3 23Na
		369.1521	-2.0	-5.4	13.5	-1.$	n/a	1.#R	12C19 13C 1H19 14N5 16O 23Na
		369.1467	3.4	9.2	12.5	-1.$	n/a	1.#R	12C23 1H22 16O3 23Na
369.1897	8.47	369.1903	-0.6	-1.6	7.5	-1.$	n/a	1.#R	12C18 1H26 14N4 16O3 23Na
		369.1885	1.2	3.3	12.5	-1.$	n/a	1.#R	12C20 13C 1H23 14N5 23Na
370.1157	100.00	370.1150	0.7	1.9	18.5	-1.$	n/a	1.#R	12C22 13C 1H14 14N4 23Na
		370.1168	-1.1	-3.0	13.5	-1.$	n/a	1.#R	12C20 1H17 14N3 16O3 23Na
371.1189	22.33	371.1201	-1.2	-3.2	13.5	-1.$	n/a	1.#R	12C19 13C 1H17 14N3 16O3 23Na
		371.1160	2.9	7.8	17.5	-1.$	n/a	1.#R	12C24 1H16 14N2 16O 23Na
371.1638	15.01	371.1637	0.1	0.3	8.5	-1.$	n/a	1.#R	12C14 13C 1H21 14N7 16O3 23Na
		371.1623	1.5	4.0	11.5	-1.$	n/a	1.#R	12C23 1H24 16O3 23Na
		371.1605	3.3	8.9	16.5	-1.$	n/a	1.#R	12C25 13C 1H21 14N 23Na
371.2189	32.54	371.2180	0.9	2.4	10.5	-1.$	n/a	1.#R	12C23 13C 1H29 14N 16O 23Na
		371.2171	1.8	4.8	6.5	-1.$	n/a	1.#R	12C17 1H28 14N6 16O2 23Na
		371.2212	-2.3	-6.2	10.5	-1.$	n/a	1.#R	12C22 1H28 14N4 23Na
372.2237	8.12	372.2245	-0.8	-2.1	10.5	-1.$	n/a	1.#R	12C21 13C 1H28 14N4 23Na
		372.2263	-2.6	-7.0	5.5	-1.$	n/a	1.#R	12C19 1H31 14N3 16O3 23Na
		372.2205	3.2	8.6	6.5	-1.$	n/a	1.#R	12C16 13C 1H28 14N6 16O2 23Na

Fig. 45. HRMS-ESI spectrum of amino-benzoic acid **7** (0.1% HCOOH in MeOH, label: SZ-3-57-3). HRMS (ESI/TOF-Q) *m/z*: [M + Na^+] calcd for $C_{20}H_{17}N_3O_3Na$ 370.1168; found 370.1157.

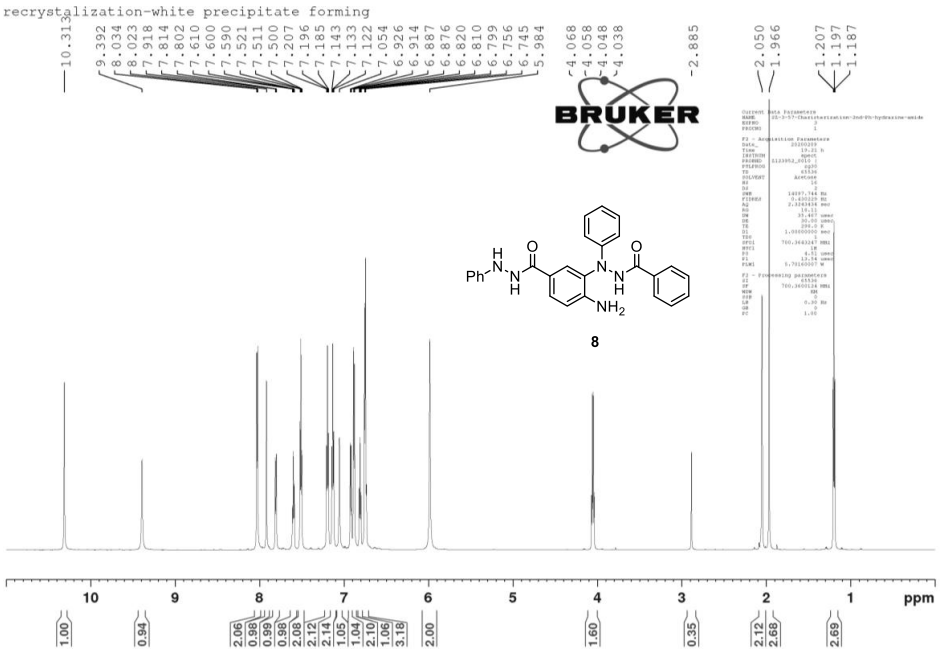

Fig. 46. ^{1}H NMR (700 MHz, acetone-d_6) spectrum of the phenyl hydrazine amide **8** (label: SZ-3-31).

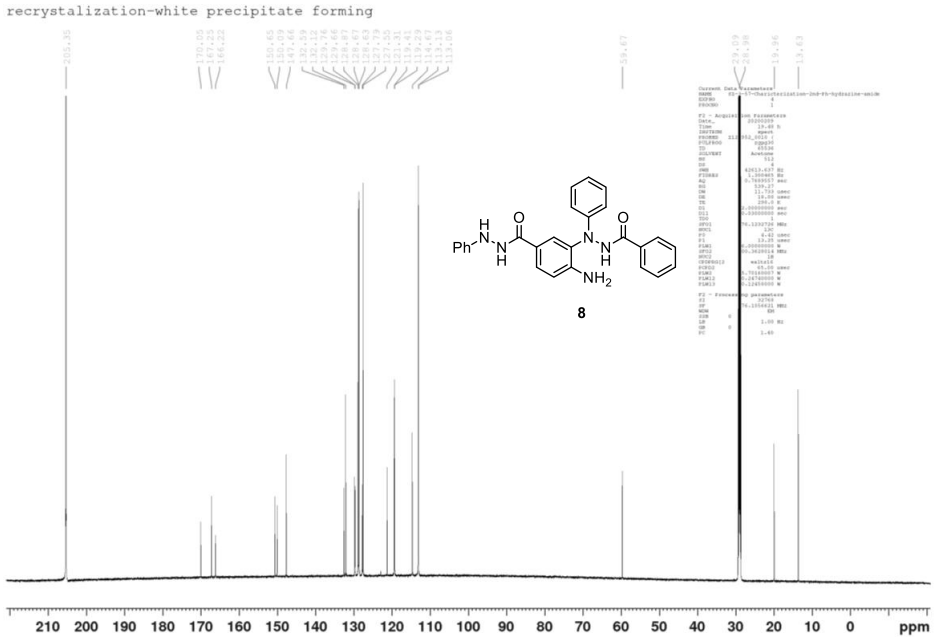

Fig. 47. ^{13}C NMR (175 MHz, acetone-d_6) spectrum of the phenyl hydrazine amide **8** (label: SZ-3-31).

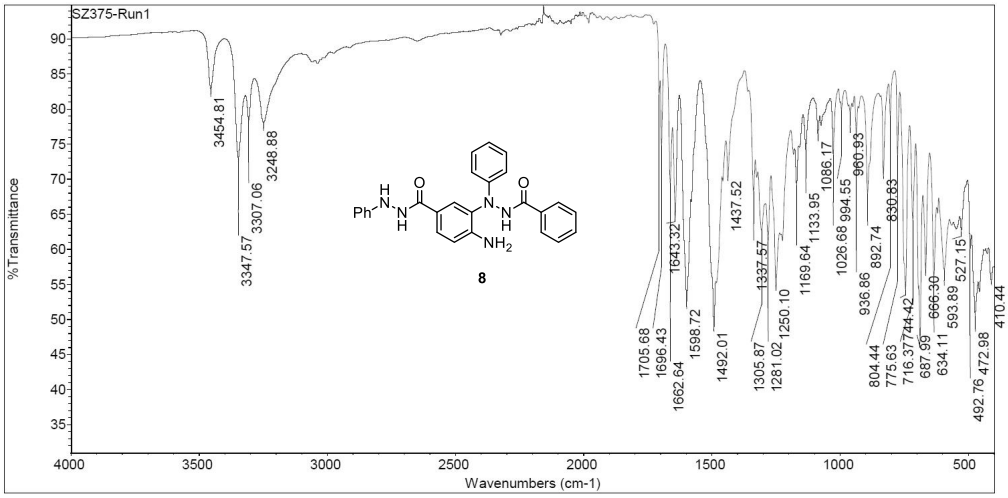

Fig. 48. IR spectrum of the phenyl hydrazine amide **8** (label: SZ-3-75).

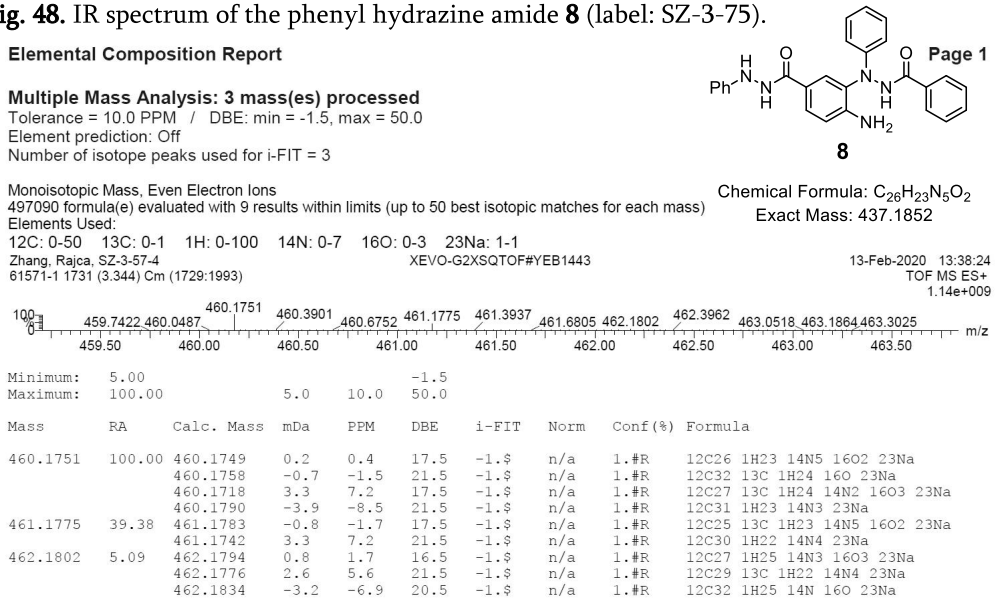

Fig. 49. HRMS-ESI spectrum of the phenyl hydrazine amide **8** (0.1% HCOOH in MeOH, label: SZ-3-57-4); *m/z*: [M + Na^+] calcd for $C_{26}H_{23}N_5O_2Na$ 460.1749; found 460.1751.

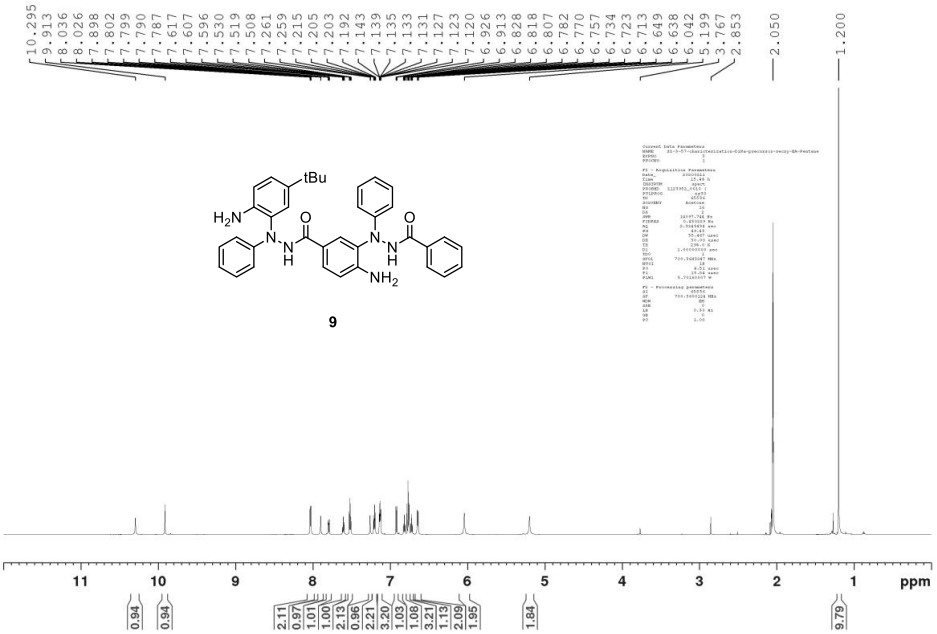

Fig. 50. [1]H NMR (700 MHz, acetone-d_6) spectrum of the N-phenylbenzohydrazide **9** (label: SZ-3-75-characterization-Dira-precursor-recy-EA-Pentane, sample: SZ-2-99).

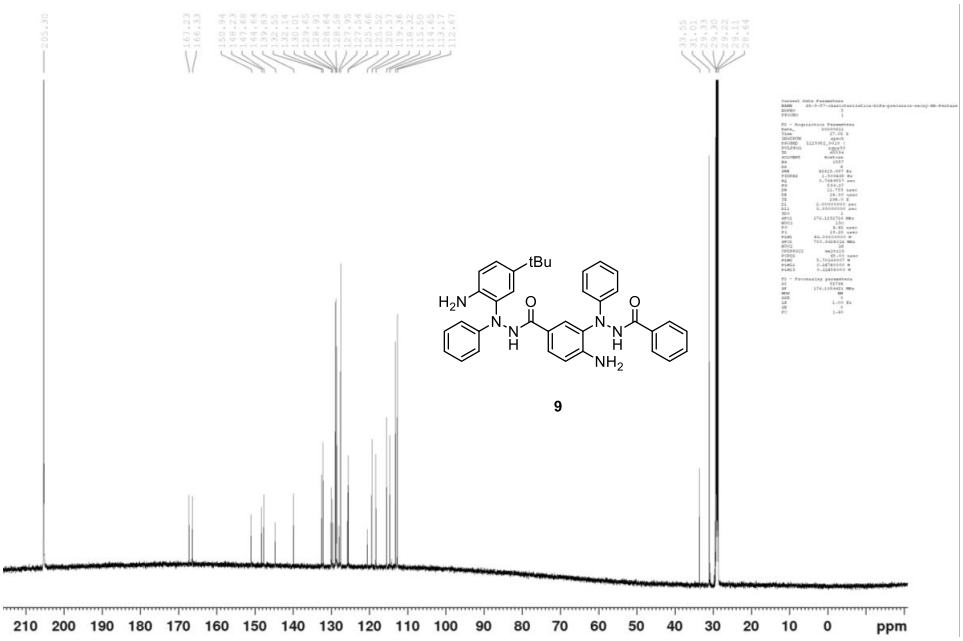

Fig. 51. [13]C NMR (175 MHz, acetone-d_6) spectrum of the N-phenylbenzohydrazide **9** (label: SZ-3-75-characterization-Dira-precursor-recy-EA-Pentane, sample: SZ-2-99).

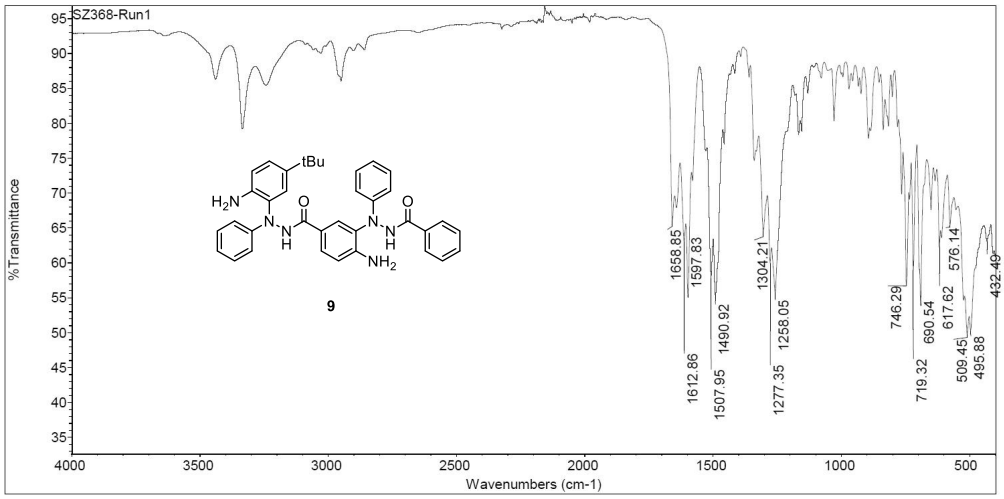

Fig. 52. IR spectrum of the N-phenylbenzohydrazide **9** (sample: SZ-3-68).

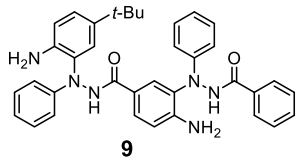

Elemental Composition Report **Page 1**

Multiple Mass Analysis: 3 mass(es) processed
Tolerance = 10.0 PPM / DBE: min = -1.5, max = 50.0
Element prediction: Off
Number of isotope peaks used for i-FIT = 3

Chemical Formula: $C_{36}H_{36}N_6O_2$
Exact Mass: 584.2900

Monoisotopic Mass, Even Electron Ions
734858 formula(e) evaluated with 10 results within limits (up to 50 best isotopic matches for each mass)
Elements Used:
12C: 0-50 13C: 0-1 1H: 0-100 14N: 0-7 16O: 0-3 23Na: 1-1

Zhang, Rajca, SZ-3-57-5 XEVO-G2XSQTOF#YEB1443 13-Feb-2020 13:05:16
61572 397 (0.878) Cm (123:410) TOF MS ES+
1.19e+009

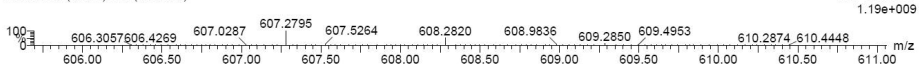

Minimum:	5.00				-1.5				
Maximum:	100.00		5.0	10.0	50.0				
Mass	RA	Calc. Mass	mDa	PPM	DBE	i-FIT	Norm	Conf(%)	Formula
607.2795	100.00	607.2838	-4.3	-7.1	25.5	-1.$	n/a	1.#R	12C41 1H36 14N4 23Na
		607.2806	-1.1	-1.8	25.5	-1.$	n/a	1.#R	12C42 13C 1H37 14N 16O 23Na
		607.2797	-0.2	-0.3	21.5	-1.$	n/a	1.#R	12C36 1H36 14N6 16O2 23Na
		607.2766	2.9	4.8	21.5	-1.$	n/a	1.#R	12C37 13C 1H37 14N3 16O3 23Na
608.2820	50.12	608.2871	-5.1	-8.4	25.5	-1.$	n/a	1.#R	12C40 13C 1H36 14N4 23Na
		608.2831	-1.1	-1.8	21.5	-1.$	n/a	1.#R	12C35 13C 1H36 14N6 16O2 23Na
		608.2790	3.0	4.9	25.5	-1.$	n/a	1.#R	12C40 1H35 14N5 23Na
609.2850	10.54	609.2882	-3.2	-5.3	24.5	-1.$	n/a	1.#R	12C42 1H38 14N2 16O 23Na
		609.2842	0.8	1.3	20.5	-1.$	n/a	1.#R	12C37 1H38 14N4 16O3 23Na
		609.2824	2.6	4.3	25.5	-1.$	n/a	1.#R	12C39 13C 1H35 14N5 23Na

Fig. 53. HRMS-ESI spectrum of the *N*-phenylbenzohydrazide **9** (0.1% HCOOH in MeOH, sample: SZ-3-57-5); *m/z*: [M + Na^+] calcd for $C_{36}H_{36}N_6O_2Na$ 607.2797; found 607.2795.

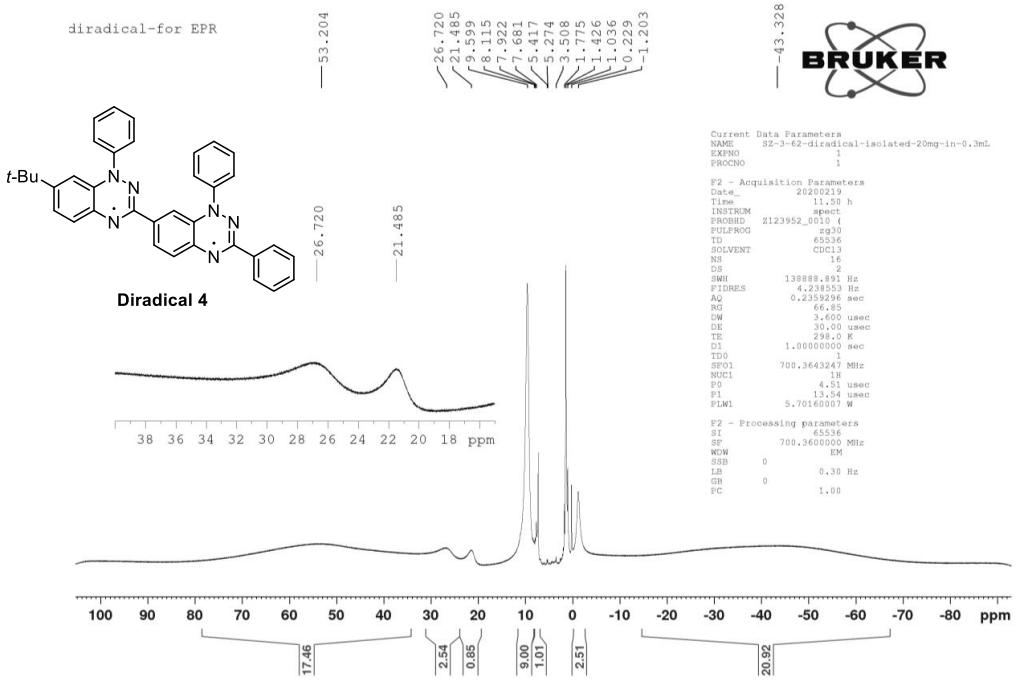

Fig. S54. [1]H NMR (400 MHz, chloroform-*d*) spectrum of 0.12 M diradical **4** (label: SZ-3-62-diradical-20mg-in-0.3mL).

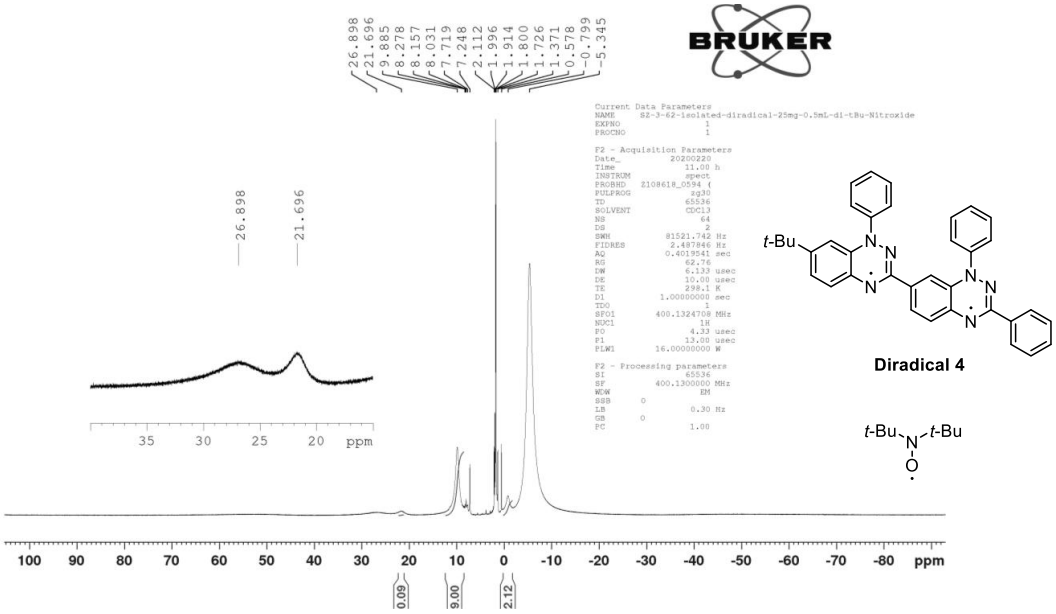

Fig. S55. [1]H NMR (400 MHz, chloroform-*d*) spectrum of 0.092 M diradical **4** with di-*tert*-butyl nitroxide (1 drop) (label: SZ-3-62).

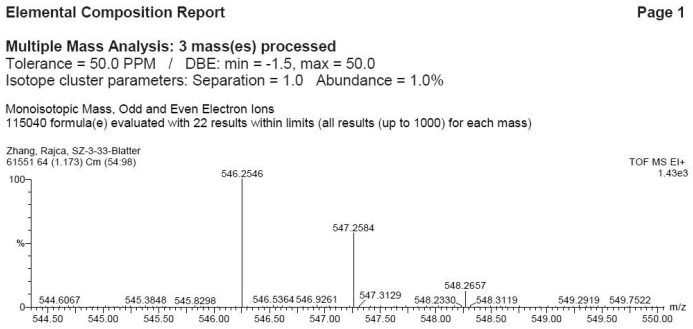

Fig. 56. HRMS-ESI spectrum of diradical **4** (0.1% HCOOH in MeOH, label: SZ-3-33-Blatter); *m/z*: [M⁺] calcd for $C_{36}H_{30}N_6$ 546.2532; found 546.2546.

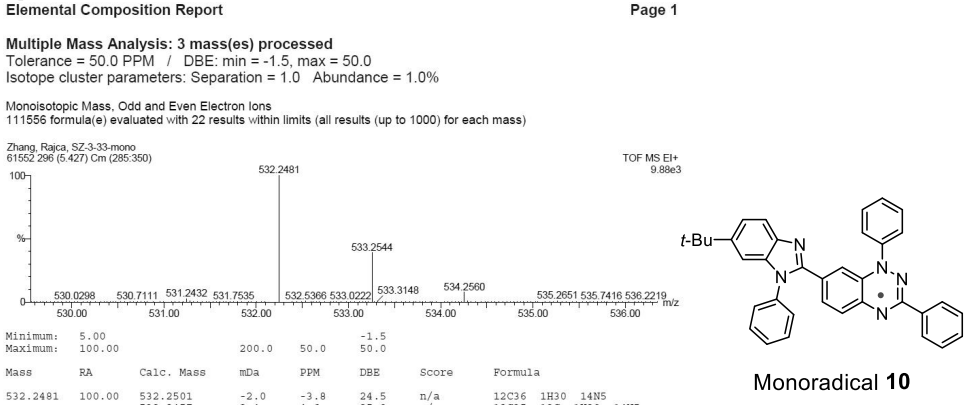

Fig. 57. HRMS-ESI spectrum of monoradical **10** (0.1% HCOOH in MeOH, label: SZ-3-33-mono); *m/z*: [M⁺] calcd for $C_{36}H_{30}N_5$ 532.2501; found 532.2481.

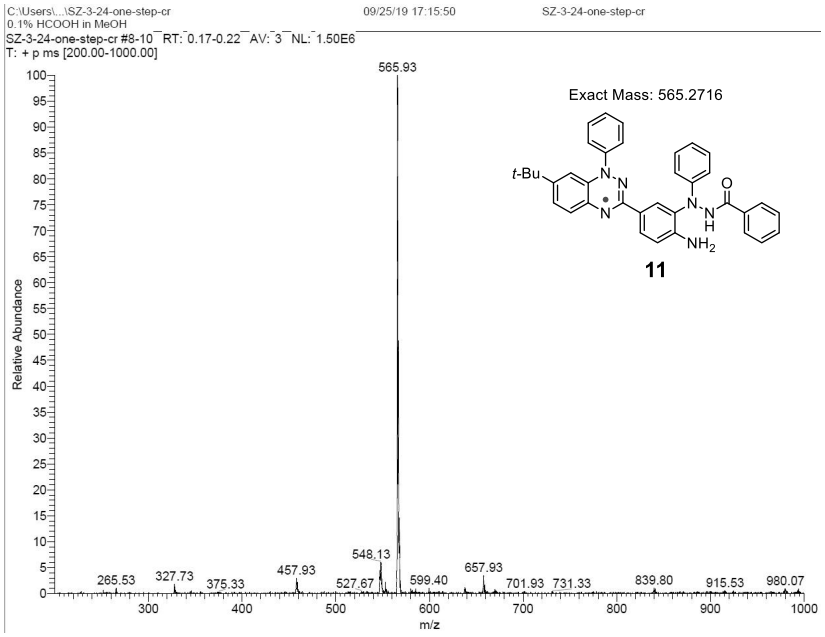

Fig. S58. LRMS-ESI spectrum of crude reaction mixture containing "one ring closed" intermediate **11**, following 24 h of reflux (0.1% HCOOH in MeOH, label: SZ-3-24-one-step-cr).

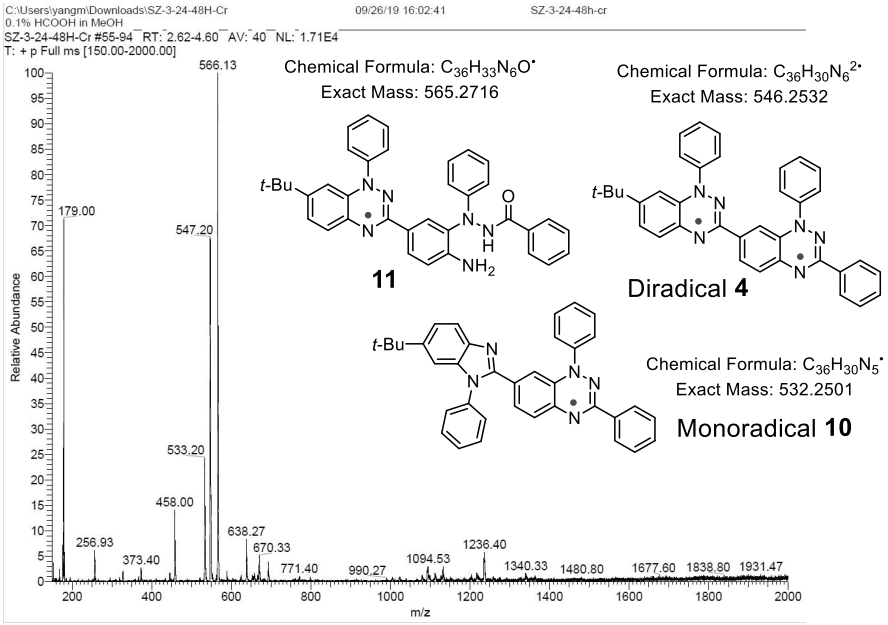

Fig. S59. LRMS-ESI spectrum of crude mixture containing "one ring closed" intermediate **11**, diradical **4**, and monoradical **10**, following 48 h of reflux (0.1% HCOOH in MeOH, label: SZ-3-24-48H-cr).

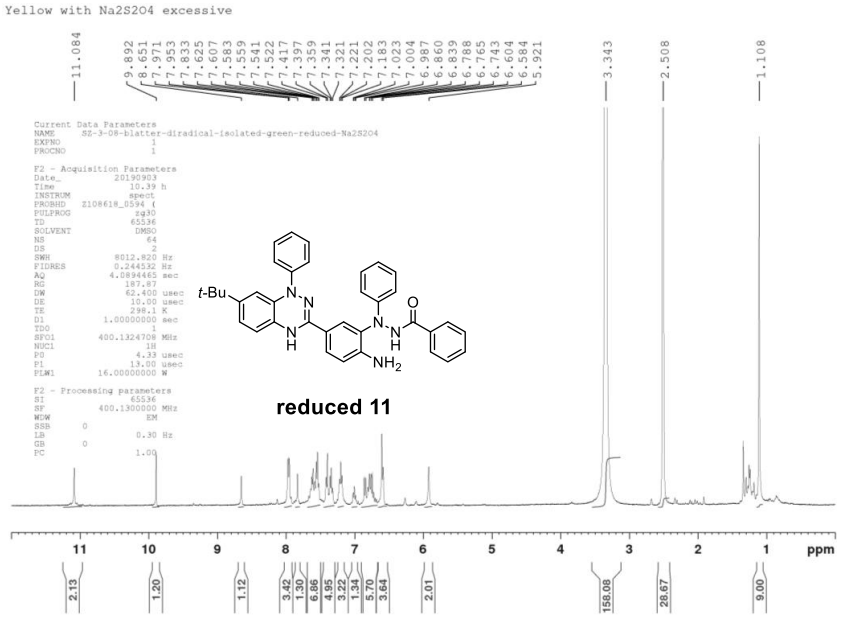

Fig. S60. ^{1}H NMR (400 MHz, DMSO-d_6) spectrum of 7.07 mM "one ring closed" intermediate **11** with 10 mg $Na_2S_2O_4$ (label: SZ-3-08-reduced).

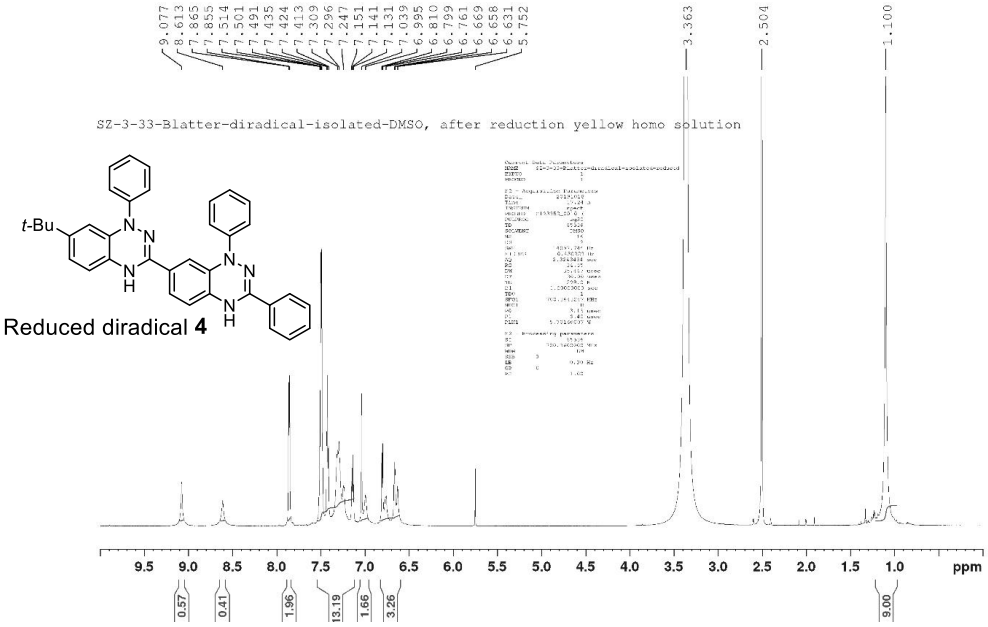

Fig. S61. ^{1}H NMR (700 MHz, DMSO-d_6) spectrum of diradical **4**, following reduction with $Na_2S_2O_4$ (label: SZ-3-33-Blatter-diradical-isolated-reduced). The singlets at 5.752, 3.363, and 2.504 ppm correspond to residual DCM, water, and DMSO-d_5.

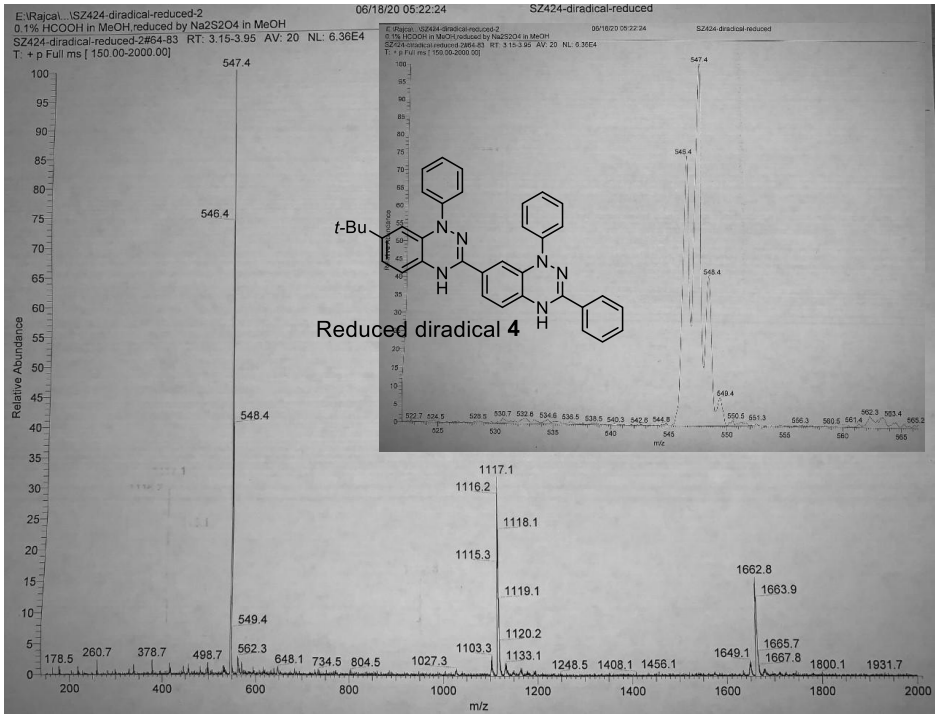

Fig. S62. LRMS-ESI spectrum of crude reaction mixture of reduced diradical 4, using $Na_2S_2O_4$ (label: SZ-4-24-diradical-reduced2). The sample was taken out as DMSO solution. Inset: expansion.

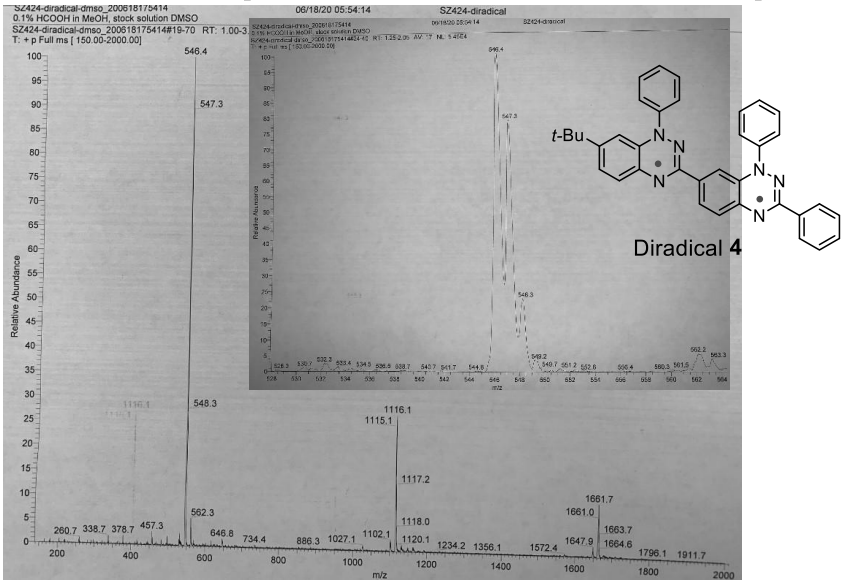

Fig. S63. Control experiment for LRMS in the preceding figure. A follow up LRMS-ESI spectrum of diradical **4** dissolved in DMSO (label: SZ-4-24-diradical-DMSO). Inset: expansion.

4. Outputs of DFT Calculations for Blatter Radical, Diradical 4 and Monoradical 10.

Blatter radical at UB3LYP/6-31G(d,p) in the gas phase

Stoichiometry C19H14N3(2)
Framework group C1[X(C19H14N3)]
Deg. of freedom 102
Full point group C1 NOp 1
Largest Abelian subgroup C1 NOp 1
Largest concise Abelian subgroup C1 NOp 1
Standard orientation:

Center Number	Atomic Number	Atomic Type	Coordinates (Angstroms) X	Y	Z
1	6	0	-2.645413	3.224482	-0.297449
2	6	0	-1.543064	4.077885	-0.142896
3	6	0	-2.483481	1.842904	-0.268263
4	6	0	-0.272451	3.546303	0.015023
5	1	0	-1.683542	5.154167	-0.160393
6	6	0	-1.205341	1.297786	-0.073069
7	1	0	-3.338823	1.193235	-0.403493
8	6	0	-0.069331	2.151652	0.036324
9	1	0	0.604725	4.177151	0.110800
10	6	0	1.324115	0.325415	0.049311
11	7	0	1.202917	1.655018	0.131306
12	7	0	0.330423	-0.568168	-0.024628
13	7	0	-0.941276	-0.073745	-0.010076
14	6	0	-1.955025	-1.080672	0.010150
15	6	0	-1.840990	-2.178567	-0.850001
16	6	0	-3.020111	-1.001864	0.915106
17	6	0	-2.805109	-3.183086	-0.815743
18	1	0	-0.996309	-2.232184	-1.526493
19	6	0	-3.982309	-2.010707	0.935923
20	1	0	-3.081402	-0.169783	1.607676
21	6	0	-3.881116	-3.101496	0.071043
22	1	0	-2.716268	-4.031287	-1.487776
23	1	0	-4.804274	-1.948676	1.642629
24	1	0	-4.631099	-3.886058	0.092924
25	6	0	2.698085	-0.246703	0.054745
26	6	0	3.806960	0.612124	0.071187
27	6	0	2.908703	-1.634328	0.042634
28	6	0	5.099769	0.092764	0.073710
29	1	0	3.634017	1.681842	0.082368
30	6	0	4.202913	-2.149067	0.044524
31	1	0	2.051532	-2.297394	0.036181
32	6	0	5.303009	-1.288503	0.059690
33	1	0	5.950626	0.767929	0.086003
34	1	0	4.353750	-3.224784	0.036520
35	1	0	6.311513	-1.692235	0.061743
36	1	0	-3.637760	3.638417	-0.446600

Rotational constants (GHZ): 0.3919630 0.2106159 0.1408482
Standard basis: 6-31G(d,p) (6D, 7F)
SCF Done: E(UB3LYP) = -896.698454984 A.U. after 4 cycles
NFock= 4 Conv=0.49D-08 -V/T= 2.0097
<Sx>= 0.0000 <Sy>= 0.0000 <Sz>= 0.5000 <S**2>= 0.7667 S= 0.5083
<L.S>= 0.00000000000
Annihilation of the first spin contaminant:
S**2 before annihilation 0.7667, after 0.7502
-- Stationary point found.

Item	Value	Threshold	Converged?
Maximum Force	0.000001	0.000015	YES
RMS Force	0.000000	0.000010	YES
Maximum Displacement	0.000059	0.000060	YES
RMS Displacement	0.000011	0.000040	YES

Predicted change in Energy=-9.105791D-12
Optimization completed.
-- Stationary point found.

Diradical 4, conformation 4A triplet ground state at UB3LYP/6-31G(d,p) in the gas phase

Stoichiometry C36H30N6(3)
Framework group C1[X(C36H30N6)]
Deg. of freedom 210
Full point group C1 NOp 1
Largest Abelian subgroup C1 NOp 1
Largest concise Abelian subgroup C1 NOp 1
Standard orientation:

Center Number	Atomic Number	Atomic Type	Coordinates (Angstroms) X	Y	Z
1	6	0	-5.502201	-2.860288	-0.084650
2	6	0	-4.145749	-3.051351	-0.274960
3	6	0	-3.248746	-1.965275	-0.251066
4	6	0	-3.791141	-0.665137	-0.061996
5	6	0	-5.164986	-0.489766	0.166960
6	6	0	-6.041959	-1.576639	0.156741
7	1	0	-6.158914	-3.723921	-0.108391
8	1	0	-3.728477	-4.040351	-0.432168
9	1	0	-5.536540	0.505668	0.361819
10	6	0	-1.121324	-1.105696	-0.246322
11	6	0	0.345999	-1.313317	-0.281054
12	6	0	0.861802	-2.618292	-0.428138
13	6	0	1.226918	-0.231006	-0.163578
14	6	0	2.225457	-2.836718	-0.431941
15	1	0	0.162879	-3.440179	-0.524229
16	6	0	2.606799	-0.442933	-0.202620
17	1	0	0.818910	0.762321	-0.042185
18	6	0	3.136448	-1.766126	-0.300543
19	1	0	2.641270	-3.834785	-0.518135
20	6	0	5.266307	-0.956742	-0.029148
21	7	0	-1.903850	-2.184564	-0.376242
22	7	0	-1.520645	0.164862	-0.101515
23	7	0	-2.867683	0.386105	-0.083405
24	6	0	-3.226982	1.767920	-0.031777
25	6	0	-4.192536	2.286545	-0.902967
26	6	0	-2.560545	2.612335	0.863316
27	6	0	-4.506673	3.644078	-0.854530
28	1	0	-4.676558	1.635624	-1.622565
29	6	0	-2.878221	3.968032	0.898040
30	1	0	-1.799461	2.196690	1.512905
31	6	0	-3.854777	4.488371	0.045773
32	1	0	-5.252929	4.043173	-1.534838
33	7	0	4.473589	-2.018086	-0.242955
34	7	0	4.887138	0.320960	0.044105
35	7	0	3.558541	0.581238	-0.116451
36	6	0	3.238006	1.973569	-0.122181
37	6	0	3.835824	2.811861	0.826124
38	6	0	2.383503	2.506984	-1.094260
39	6	0	3.561368	4.177053	0.809533
40	1	0	4.511578	2.383012	1.556381
41	6	0	2.111539	3.874306	-1.096567
42	1	0	1.950596	1.861135	-1.849569
43	6	0	2.695568	4.713265	-0.146332
44	1	0	4.024103	4.823321	1.549388
45	1	0	1.450188	4.283534	-1.854087
46	1	0	2.483143	5.777929	-0.154601
47	1	0	-4.100837	5.545231	0.078176
48	1	0	-2.362163	4.619011	1.597216
49	6	0	6.724516	-1.204837	0.130535
50	6	0	7.208901	-2.521271	0.125993
51	6	0	7.630550	-0.144220	0.287826
52	6	0	8.571283	-2.770832	0.277833
53	1	0	6.502090	-3.333233	0.001808
54	6	0	8.991339	-0.398494	0.439671
55	1	0	7.256439	0.872912	0.284819
56	6	0	9.467236	-1.711875	0.435851
57	1	0	8.934170	-3.794691	0.273268
58	1	0	9.683182	0.430449	0.559065
59	1	0	10.529220	-1.907742	0.553948
60	6	0	-7.552827	-1.417842	0.400989
61	6	0	-8.327036	-1.921440	-0.840950
62	1	0	-9.406577	-1.825119	-0.680189
63	1	0	-8.062809	-1.339727	-1.730051
64	1	0	-8.115755	-2.972964	-1.055413
65	6	0	-7.964351	-2.255810	1.635380
66	1	0	-7.436097	-1.916920	2.532329
67	1	0	-9.040480	-2.159687	1.817605
68	1	0	-7.744187	-3.318520	1.499850
69	6	0	-7.957767	0.045515	0.658921
70	1	0	-7.465895	0.454869	1.547278
71	1	0	-7.720976	0.691845	-0.192626
72	1	0	-9.038013	0.103959	0.825002

Rotational constants (GHZ): 0.1595248 0.0358724 0.0299603
Standard basis: 6-31G(d,p) (6D, 7F)
SCF Done: E(UB3LYP) = -1718.40694503 A.U. after 4 cycles
NFock= 4 Conv=0.19D-08 -V/T= 2.0097
<Sx>= 0.0000 <Sy>= 0.0000 <Sz>= 1.0000 <S**2>= 2.0363 S= 1.0121
<L.S>= 0.00000000000
Annihilation of the first spin contaminant:
S**2 before annihilation 2.0363, after 2.0007

Item	Value	Threshold	Converged?
Maximum Force	0.000000	0.000015	YES
RMS Force	0.000000	0.000010	YES
Maximum Displacement	0.000069	0.000060	NO
RMS Displacement	0.000012	0.000040	YES

Predicted change in Energy=-1.624344D-12
Optimization completed on the basis of negligible forces.
-- Stationary point found.

Diradical 4, conformation 4A BS singlet state at UB3LYP/6-31G(d,p) in the gas phase

Stoichiometry C36H30N6
Framework group C1[X(C36H30N6)]
Deg. of freedom 210
Full point group C1 NOp 1
Largest Abelian subgroup C1 NOp 1
Largest concise Abelian subgroup C1 NOp 1
Standard orientation:

Center Number	Atomic Number	Atomic Type	Coordinates (Angstroms) X	Y	Z
1	6	0	-5.505608	-2.856769	-0.093881
2	6	0	-4.149546	-3.049393	-0.285611
3	6	0	-3.250637	-1.965107	-0.256714
4	6	0	-3.791454	-0.664961	-0.061736
5	6	0	-5.165105	-0.488248	0.169023
6	6	0	-6.043608	-1.573480	0.154107
7	1	0	-6.163697	-3.719256	-0.121525
8	1	0	-3.734171	-4.038408	-0.447587
9	1	0	-5.534776	0.506872	0.369046
10	6	0	-1.123527	-1.108845	-0.247299
11	6	0	0.347627	-1.318776	-0.281482
12	6	0	0.863015	-2.622835	-0.425947
13	6	0	1.226576	-0.236498	-0.166033
14	6	0	2.228217	-2.840015	-0.428864
15	1	0	0.164885	-3.445546	-0.520610
16	6	0	2.608101	-0.448166	-0.205049
17	1	0	0.818372	0.756859	-0.045192
18	6	0	3.137098	-1.769567	-0.300646
19	1	0	2.644320	-3.838210	-0.512532
20	6	0	5.266560	-0.959218	-0.027831
21	7	0	-1.905955	-2.185206	-0.382872
22	7	0	-1.519756	0.160666	-0.097713
23	7	0	-2.866412	0.384495	-0.079473
24	6	0	-3.223083	1.766795	-0.024441
25	6	0	-4.189613	2.288804	-0.892580
26	6	0	-2.552918	2.608212	0.870754
27	6	0	-4.500924	3.646836	-0.840929
28	1	0	-4.676346	1.640222	-1.612431
29	6	0	-2.868132	3.964362	0.908849
30	1	0	-1.791227	2.189861	1.517858
31	6	0	-3.845531	4.488149	0.059648
32	1	0	-5.247796	4.048666	-1.518933
33	7	0	4.478611	-2.019855	-0.242630
34	7	0	4.885743	0.321023	0.045150
35	7	0	3.557084	0.578213	-0.118760
36	6	0	3.233840	1.969810	-0.129542
37	6	0	3.829458	2.812346	0.816460
38	6	0	2.379378	2.498440	-1.104330
39	6	0	3.552225	4.176861	0.795257
40	1	0	4.505445	2.387031	1.548538
41	6	0	2.104722	3.865221	-1.111238
42	1	0	1.949042	1.849440	-1.858409
43	6	0	2.686187	4.708311	-0.163118
44	1	0	4.013037	4.826438	1.533408
45	1	0	1.443460	4.270763	-1.870809
46	1	0	2.471792	5.772543	-0.175064
47	1	0	-4.089536	5.545398	0.094606
48	1	0	-2.349408	4.613022	1.608195
49	6	0	6.725604	-1.202395	0.134216
50	6	0	7.213731	-2.517479	0.133510
51	6	0	7.628265	-0.138793	0.289965
52	6	0	8.576528	-2.762780	0.287526
53	1	0	6.509123	-3.331566	0.010549
54	6	0	8.989711	-0.388801	0.444135
55	1	0	7.251191	0.877195	0.283878
56	6	0	9.469269	-1.700742	0.444065
57	1	0	8.942432	-3.785574	0.285948
58	1	0	9.679054	0.442394	0.562323
59	1	0	10.531664	-1.893315	0.563944
60	6	0	-7.554074	-1.413851	0.400117
61	6	0	-8.329836	-1.910095	-0.843814
62	1	0	-9.409138	-1.813136	-0.681828
63	1	0	-8.065423	-1.324256	-1.730148
64	1	0	-8.120145	-2.960809	-1.063743
65	6	0	-7.966030	-2.257401	1.630556
66	1	0	-7.436761	-1.923731	2.528862
67	1	0	-9.041917	-2.160733	1.813920
68	1	0	-7.747418	-3.319726	1.489590
69	6	0	-7.956710	0.048777	0.665654
70	1	0	-7.463653	0.452936	1.555739
71	1	0	-7.719527	0.699029	-0.182798
72	1	0	-9.036757	0.107995	0.832743

Rotational constants (GHZ): 0.1597073 0.0358749 0.0299705
Standard basis: 6-31G(d,p) (6D, 7F)
SCF Done: E(UB3LYP) = -1718.40584035 A.U. after 4 cycles
NFock= 4 Conv=0.39D-08 -V/T= 2.0097
<Sx>= 0.0000 <Sy>= 0.0000 <Sz>= 0.0000 <S**2>= 1.0283 S= 0.6306
<L.S>= 0.00000000000
Annihilation of the first spin contaminant:
S**2 before annihilation 1.0283, after 0.2300

Item	Value	Threshold	Converged?
Maximum Force	0.000000	0.000015	YES
RMS Force	0.000000	0.000010	YES
Maximum Displacement	0.000054	0.000060	YES
RMS Displacement	0.000011	0.000040	YES

Predicted change in Energy=-9.672495D-12
Optimization completed.
-- Stationary point found.

Diradical 4, conformation 4B triplet ground state at UB3LYP/6-31G(d,p) in the gas phase

Stoichiometry C36H30N6(3)
Framework group C1[X(C36H30N6)]
Deg. of freedom 210
Full point group C1 NOp 1
Largest Abelian subgroup C1 NOp 1
Largest concise Abelian subgroup C1 NOp 1
Standard orientation:

Center Number	Atomic Number	Atomic Type	Coordinates (Angstroms) X	Y	Z
1	6	0	-5.105881	-2.560287	-1.090843
2	6	0	-4.045345	-2.484647	-0.180115
3	6	0	-3.720742	-0.015476	0.002754
4	6	0	-5.075121	0.285049	0.219404
5	6	0	-1.061985	-0.527268	-0.151962
6	6	0	0.385924	-0.846942	-0.174445
7	6	0	0.839420	-2.183096	-0.220330
8	6	0	1.316614	0.197436	-0.144213
9	6	0	2.191185	-2.464066	-0.209011
10	1	0	0.109476	-2.982672	-0.255939
11	6	0	2.685244	-0.080972	-0.172025
12	1	0	0.946677	1.212049	-0.096191
13	6	0	3.152042	-1.429734	-0.165294
14	1	0	2.560063	-3.484023	-0.219874
15	6	0	5.318259	-0.702603	0.037059
16	7	0	-1.884043	-1.583469	-0.113061
17	7	0	-1.413582	0.764808	-0.185908
18	6	0	-3.210545	2.352759	0.006523
19	6	0	-4.552471	2.635283	0.184423
20	7	0	4.476719	-1.739806	-0.091471
21	7	0	4.999079	0.593313	0.009781
22	7	0	3.683514	0.902307	-0.169727
23	6	0	3.427404	2.302555	-0.290565
24	6	0	4.073758	3.188705	0.579157
25	6	0	2.587347	2.791661	-1.297927
26	6	0	3.862103	4.558927	0.449368
27	1	0	4.736428	2.791664	1.338757
28	6	0	2.379067	4.165154	-1.413863
29	1	0	2.115643	2.105708	-1.992097
30	6	0	3.011527	5.052867	-0.542224
31	1	0	4.361433	5.242681	1.129270
32	1	0	1.729143	4.539806	-2.198738
33	1	0	2.847707	6.121776	-0.638368
34	6	0	6.764400	-1.004375	0.213695
35	6	0	7.188353	-2.338048	0.309834
36	6	0	7.718587	0.022567	0.287559
37	6	0	8.538709	-2.637342	0.478326
38	1	0	6.444630	-3.123886	0.249588
39	6	0	9.067124	-0.281314	0.456560
40	1	0	7.391097	1.052477	0.206736
41	6	0	9.482738	-1.611507	0.553048
42	1	0	8.854621	-3.674067	0.551977
43	1	0	9.796553	0.521825	0.510843
44	1	0	10.535290	-1.846130	0.684268
45	7	0	-3.224137	-1.317266	-0.115028
46	6	0	-2.752291	1.022729	-0.071542
47	6	0	-3.741751	-3.577637	0.639347
48	6	0	-5.514492	1.607345	0.310404
49	1	0	-2.468571	3.141308	-0.061990
50	1	0	-4.864144	3.673184	0.241848
51	1	0	-5.777513	-0.528894	0.324434
52	6	0	-5.875703	-3.720848	-1.157425
53	6	0	-4.513868	-4.734087	0.559300
54	6	0	-5.585751	-4.809163	-0.332986
55	1	0	-2.901968	-3.508098	1.320503
56	1	0	-5.310656	-1.725986	-1.752535
57	1	0	-6.694196	-3.777617	-1.868621
58	1	0	-6.185683	-5.712056	-0.390758
59	1	0	-4.278098	-5.578639	1.199688
60	6	0	-6.991517	1.969842	0.544155
61	6	0	-7.503631	2.818546	-0.644541
62	1	0	-7.434897	2.259715	-1.583527
63	1	0	-8.552490	3.094942	-0.489574
64	1	0	-6.930789	3.742698	-0.763597
65	6	0	-7.118254	2.789689	1.850726
66	1	0	-6.768753	2.210742	2.711581
67	1	0	-6.535286	3.714265	1.811385
68	1	0	-8.164443	3.063404	2.026947
69	6	0	-7.891254	0.726271	0.669548
70	1	0	-7.871440	0.113861	-0.237895
71	1	0	-7.600212	0.095210	1.515536
72	1	0	-8.927704	1.037689	0.832979

Rotational constants (GHZ): 0.1431917 0.0352883 0.0290063
Standard basis: 6-31G(d,p) (6D, 7F)
SCF Done: E(UB3LYP) = -1718.40685760 A.U. after 4 cycles
NFock= 4 Conv=0.13D-08 -V/T= 2.0097
<Sx>= 0.0000 <Sy>= 0.0000 <Sz>= 1.0000 <S**2>= 2.0359 S= 1.0119
<L.S>= 0.00000000000
Annihilation of the first spin contaminant:
S**2 before annihilation 2.0359, after 2.0007

Item	Value	Threshold	Converged?
Maximum Force	0.000000	0.000015	YES
RMS Force	0.000000	0.000010	YES
Maximum Displacement	0.000031	0.000060	YES
RMS Displacement	0.000007	0.000040	YES

Predicted change in Energy=-1.022234D-12
Optimization completed.
-- Stationary point found.

Diradical 4, conformation 4B BS singlet state at UB3LYP/6-31G(d,p) in the gas phase

Stoichiometry C36H30N6
Framework group C1[X(C36H30N6)]
Deg. of freedom 210
Full point group C1 NOp 1
Largest Abelian subgroup C1 NOp 1
Largest concise Abelian subgroup C1 NOp 1
Standard orientation:

Center Number	Atomic Number	Atomic Type	Coordinates (Angstroms) X	Y	Z
1	6	0	-5.096289	-2.563458	-1.090873
2	6	0	-4.037376	-2.484031	-0.178726
3	6	0	-3.720063	-0.011726	0.000804
4	6	0	-5.075008	0.283017	0.218132
5	6	0	-1.061962	-0.518579	-0.154102
6	6	0	0.386107	-0.844822	-0.174571
7	6	0	0.836873	-2.180713	-0.217076
8	6	0	1.315840	0.198983	-0.145728
9	6	0	2.189867	-2.462562	-0.203137
10	1	0	0.106562	-2.979807	-0.252278
11	6	0	2.685747	-0.081010	-0.170534
12	1	0	0.945695	1.213657	-0.100227
13	6	0	3.150295	-1.430187	-0.161237
14	1	0	2.557521	-3.482988	-0.211202
15	6	0	5.317545	-0.703631	0.037645
16	7	0	-1.881195	-1.575230	-0.115339
17	7	0	-1.413950	0.772581	-0.190160
18	6	0	-3.217121	2.355803	0.000732
19	6	0	-4.560514	2.633567	0.179017
20	7	0	4.477866	-1.739457	-0.086983
21	7	0	4.998693	0.594558	0.009284
22	7	0	3.682160	0.901200	-0.167355
23	6	0	3.424712	2.302042	-0.286391
24	6	0	4.065240	3.186219	0.589333
25	6	0	2.590158	2.792168	-1.297532
26	6	0	3.852518	4.556515	0.461975
27	1	0	4.724157	2.787787	1.351481
28	6	0	2.380916	4.165733	-1.411227
29	1	0	2.123325	2.107183	-1.995958
30	6	0	3.007186	5.051767	-0.533456
31	1	0	4.346974	5.239207	1.146458
32	1	0	1.735123	4.541699	-2.198842
33	1	0	2.842643	6.120722	-0.627836
34	6	0	6.764715	-1.003134	0.211343
35	6	0	7.190391	-2.336122	0.309408
36	6	0	7.717713	0.025138	0.280507
37	6	0	8.541427	-2.633463	0.475146
38	1	0	6.447223	-3.122779	0.252818
39	6	0	9.067119	-0.276801	0.446819
40	1	0	7.388747	1.054439	0.198236
41	6	0	9.484433	-1.606236	0.545196
42	1	0	8.858820	-3.669621	0.550342
43	1	0	9.795758	0.527284	0.497505
44	1	0	10.537584	-1.839362	0.674306
45	7	0	-3.218493	-1.314351	-0.115057
46	6	0	-2.753612	1.027752	-0.075534
47	6	0	-3.732428	-3.574242	0.643725
48	6	0	-5.519690	1.603928	0.307376
49	1	0	-2.478599	3.147444	-0.069289
50	1	0	-4.875128	3.670776	0.234807
51	1	0	-5.774072	-0.533645	0.324874
52	6	0	-5.862908	-3.726169	-1.156588
53	6	0	-4.501596	-4.732740	0.564707
54	6	0	-5.571584	-4.812107	-0.329462
55	1	0	-2.894274	-3.501121	1.326562
56	1	0	-5.302195	-1.730594	-1.753982
57	1	0	-6.680145	-3.786376	-1.868918
58	1	0	-6.169244	-5.716549	-0.386447
59	1	0	-4.265066	-5.575360	1.207324
60	6	0	-6.997804	1.961950	0.541171
61	6	0	-7.513830	2.806557	-0.648714
62	1	0	-7.443776	2.246156	-1.586676
63	1	0	-8.563510	3.079916	-0.493693
64	1	0	-6.944030	3.732326	-0.769955
65	6	0	-7.127138	2.783769	1.846218
66	1	0	-6.775292	2.207655	2.708026
67	1	0	-6.547206	3.710191	1.804891
68	1	0	-8.174154	3.054440	2.022415
69	6	0	-7.892920	0.715319	0.669360
70	1	0	-7.871323	0.101333	-0.237002
71	1	0	-7.598969	0.086862	1.516305
72	1	0	-8.930470	1.023063	0.832861

Rotational constants (GHZ): 0.1433468 0.0352956 0.0290162
Standard basis: 6-31G(d,p) (6D, 7F)
SCF Done: E(UB3LYP) = -1718.40662509 A.U. after 4 cycles
NFock= 4 Conv=0.25D-08 -V/T= 2.0097
<Sx>= 0.0000 <Sy>= 0.0000 <Sz>= 0.0000 <S**2>= 1.0014 S= 0.6187
<L.S>= 0.00000000000
Annihilation of the first spin contaminant:
S**2 before annihilation 1.0014, after 0.2149

Item	Value	Threshold	Converged?
Maximum Force	0.000001	0.000015	YES
RMS Force	0.000000	0.000010	YES
Maximum Displacement	0.000060	0.000060	YES
RMS Displacement	0.000012	0.000040	YES

Predicted change in Energy=-1.381507D-11
Optimization completed.
-- Stationary point found.

Monoradical 10, conformation 10A at UB3LYP/6-31G(d,p) in the gas phase

Stoichiometry C36H30N5(2)
Framework group C1[X(C36H30N5)]
Deg. of freedom 207
Full point group C1 NOp 1
Largest Abelian subgroup C1 NOp 1
Largest concise Abelian subgroup C1 NOp 1
Standard orientation:

Center Number	Atomic Number	Atomic Type	Coordinates (Angstroms) X	Y	Z
1	7	0	-3.298295	1.054645	0.165780
2	7	0	-4.604593	0.695665	0.014641
3	7	0	-3.949507	-1.576877	-0.351045
4	7	0	2.612590	-0.762337	-0.118288
5	7	0	1.796119	1.256115	-0.721750
6	6	0	0.090386	-0.445539	-0.309409
7	6	0	-0.903893	0.522722	-0.102631
8	1	0	-0.598662	1.554264	0.007414
9	6	0	-2.250326	0.155960	-0.064010
10	6	0	-4.853326	-0.594050	-0.232586
11	6	0	-2.640708	-1.197473	-0.295172
12	6	0	-1.624236	-2.151435	-0.505079
13	1	0	-1.932792	-3.174923	-0.687923
14	6	0	-0.288935	-1.791191	-0.508627
15	1	0	0.462373	-2.546928	-0.699392
16	6	0	-3.110757	2.430111	0.508985
17	6	0	-2.258279	2.794158	1.557291
18	1	0	-1.726605	2.030684	2.113823
19	6	0	-2.115075	4.139833	1.892107
20	1	0	-1.454044	4.418607	2.706947
21	6	0	-2.825807	5.119898	1.197885
22	1	0	-2.711928	6.166394	1.463158
23	6	0	-3.688782	4.747401	0.164912
24	1	0	-4.247983	5.503764	-0.377424
25	6	0	-3.835405	3.406836	-0.182730
26	1	0	-4.505874	3.101923	-0.977384
27	6	0	-6.289736	-0.954560	-0.372172
28	6	0	-7.300753	0.003206	-0.195715
29	1	0	-7.024488	1.021133	0.053186
30	6	0	-8.639610	-0.354214	-0.334388
31	1	0	-9.413412	0.395154	-0.194275
32	6	0	-8.988467	-1.669623	-0.649507
33	1	0	-10.033515	-1.946081	-0.756847
34	6	0	-7.987473	-2.627061	-0.824509
35	1	0	-8.251495	-3.651876	-1.069485
36	6	0	-6.646694	-2.274088	-0.687201
37	1	0	-5.859313	-3.006679	-0.820011
38	6	0	1.481067	0.023898	-0.373705
39	6	0	3.714561	0.066941	-0.328171
40	6	0	5.087367	-0.157115	-0.198956
41	1	0	5.455665	-1.127611	0.108090
42	6	0	5.955639	0.902831	-0.474113
43	6	0	4.043554	2.375663	-0.982718
44	1	0	3.650055	3.342934	-1.277844
45	6	0	5.407602	2.153391	-0.866409
46	1	0	6.081948	2.975712	-1.083378
47	6	0	3.173630	1.313175	-0.702155
48	6	0	2.695184	-2.068196	0.455037
49	6	0	2.176998	-2.311298	1.731319
50	1	0	1.699480	-1.503658	2.275754
51	6	0	2.276993	-3.586388	2.285773
52	1	0	1.868212	-3.774620	3.273783
53	6	0	2.908199	-4.613559	1.580993
54	1	0	2.988431	-5.603901	2.018460
55	6	0	3.436785	-4.363722	0.313557
56	1	0	3.927899	-5.158649	-0.239361
57	6	0	3.328094	-3.093996	-0.254832
58	1	0	3.720752	-2.891711	-1.246036
59	6	0	7.485545	0.756466	-0.364161
60	6	0	7.909855	-0.657961	0.073938
61	1	0	7.508602	-0.917221	1.059153
62	1	0	9.001328	-0.712304	0.138180
63	1	0	7.583954	-1.420927	-0.640695
64	6	0	8.027585	1.762883	0.678894
65	1	0	7.592501	1.574693	1.665806
66	1	0	7.798412	2.796803	0.405749
67	1	0	9.116641	1.674578	0.764499
68	6	0	8.133271	1.046201	-1.739312
69	1	0	9.223274	0.951468	-1.675376
70	1	0	7.907527	2.056514	-2.092005
71	1	0	7.774554	0.341354	-2.496462

Rotational constants (GHZ): 0.1549945 0.0391026 0.0328713
Standard basis: 6-31G(d,p) (6D, 7F)
SCF Done: E(UB3LYP) = -1663.70551128 A.U. after 2 cycles
NFock= 2 Conv=0.80D-08 -V/T= 2.0097
<Sx>= 0.0000 <Sy>= 0.0000 <Sz>= 0.5000 <S**2>= 0.7667 S= 0.5083
<L.S>= 0.00000000000
Annihilation of the first spin contaminant:
S**2 before annihilation 0.7667, after 0.7502

Item	Value	Threshold	Converged?
Maximum Force	0.000000	0.000015	YES
RMS Force	0.000000	0.000010	YES
Maximum Displacement	0.000048	0.000060	YES
RMS Displacement	0.000011	0.000040	YES

Predicted change in Energy=-4.065502D-12
Optimization completed.
-- Stationary point found.

Monoradical 10, conformation 10B at UB3LYP/6-31G(d,p) in the gas phase

Stoichiometry C36H30N5(2)
Framework group C1[X(C36H30N5)]
Deg. of freedom 207
Full point group C1 NOp 1
Largest Abelian subgroup C1 NOp 1
Largest concise Abelian subgroup C1 NOp 1
Standard orientation:

Center Number	Atomic Number	Atomic Type	Coordinates (Angstroms) X	Y	Z
1	7	0	2.960688	0.501925	-0.497102
2	7	0	4.301359	0.375422	-0.277009
3	7	0	4.043715	-1.990925	-0.033923
4	7	0	-2.326508	-2.521616	-0.680196
5	7	0	-2.368223	-0.422705	0.157126
6	6	0	-0.125201	-1.578038	-0.201197
7	6	0	0.686335	-0.442841	-0.329417
8	1	0	0.241034	0.535675	-0.437130
9	6	0	2.079414	-0.573167	-0.336578
10	6	0	4.762267	-0.858887	-0.056327
11	6	0	2.692840	-1.846562	-0.146636
12	6	0	1.853309	-2.977700	-0.051509
13	1	0	2.331213	-3.943679	0.070241
14	6	0	0.479626	-2.851532	-0.089999
15	1	0	-0.163256	-3.721434	-0.025011
16	6	0	2.553404	1.824069	-0.852995
17	6	0	1.695968	2.037518	-1.938952
18	1	0	1.330553	1.194378	-2.514524
19	6	0	1.339817	3.338951	-2.289749
20	1	0	0.680320	3.500294	-3.137095
21	6	0	1.843257	4.426728	-1.574640
22	1	0	1.567461	5.438619	-1.855139
23	6	0	2.712863	4.206975	-0.503971
24	1	0	3.114266	5.048093	0.053260
25	6	0	3.070988	2.911356	-0.139883
26	1	0	3.752029	2.725853	0.682087
27	6	0	6.229168	-0.966525	0.165941
28	6	0	7.061511	0.161316	0.090288
29	1	0	6.623523	1.124898	-0.142445
30	6	0	8.431957	0.039348	0.305766
31	1	0	9.066564	0.918719	0.242938
32	6	0	8.990698	-1.207136	0.598126
33	1	0	10.060072	-1.299953	0.765088
34	6	0	8.168274	-2.332859	0.672717
35	1	0	8.596041	-3.305388	0.898756
36	6	0	6.796574	-2.215619	0.458435
37	1	0	6.146406	-3.080875	0.512175
38	6	0	-1.592230	-1.522417	-0.232007
39	6	0	-3.635103	-2.094898	-0.593309
40	6	0	-4.828315	-2.749260	-0.928604
41	1	0	-4.806223	-3.754701	-1.336174
42	6	0	-6.024094	-2.078938	-0.718362
43	6	0	-4.898546	-0.113826	0.152548
44	1	0	-4.895679	0.883891	0.572472
45	6	0	-6.089236	-0.766955	-0.177398
46	6	0	-3.695336	-0.787061	-0.071894
47	6	0	-1.972616	0.750030	0.870740
48	6	0	-2.216907	2.010579	0.315998
49	6	0	-1.375604	0.639111	2.130932
50	6	0	-1.859405	3.158894	1.023363
51	1	0	-2.676084	2.080834	-0.664717
52	6	0	-1.008875	1.791238	2.824547
53	1	0	-1.202851	-0.344407	2.554696
54	6	0	-1.251704	3.051905	2.275062
55	1	0	-2.048186	4.136266	0.590129
56	1	0	-0.540608	1.702826	3.800076
57	1	0	-0.968613	3.946739	2.820659
58	6	0	-7.467185	-0.108958	0.028429
59	6	0	-7.358098	1.307774	0.622948
60	1	0	-6.875411	1.301528	1.605702
61	1	0	-6.795459	1.982051	-0.031176
62	1	0	-8.359026	1.732365	0.750381
63	6	0	-8.198033	-0.002620	-1.331397
64	1	0	-7.626653	0.611497	-2.035115
65	1	0	-8.348301	-0.983230	-1.791742
66	1	0	-9.183682	0.458256	-1.200033
67	6	0	-8.311935	-0.970517	0.997354
68	1	0	-8.466974	-1.982878	0.613726
69	1	0	-7.821969	-1.055299	1.972747
70	1	0	-9.298145	-0.517456	1.149978
71	1	0	-6.948645	-2.585040	-0.977291

Rotational constants (GHZ): 0.1855704 0.0406592 0.0359449
Standard basis: 6-31G(d,p) (6D, 7F)

SCF Done: E(UB3LYP) = -1663.70515223 A.U. after 4 cycles
NFock= 4 Conv=0.17D-08 -V/T= 2.0097
<Sx>= 0.0000 <Sy>= 0.0000 <Sz>= 0.5000 <S**2>= 0.7672 S= 0.5086
<L.S>= 0.00000000000
Annihilation of the first spin contaminant:
S**2 before annihilation 0.7672, after 0.7502

Item	Value	Threshold	Converged?
Maximum Force	0.000000	0.000015	YES
RMS Force	0.000000	0.000010	YES
Maximum Displacement	0.000078	0.000060	NO
RMS Displacement	0.000014	0.000040	YES

Predicted change in Energy=-2.038251D-12
Optimization completed on the basis of negligible forces.
-- Stationary point found.

5. Supporting References

S1. Thevis, M.; Schänzer, W.; Schmickler, H. Effect of the Location of Hydrogen Abstraction on the Fragmentation of Diuretics in Negative Electrospray Ionization Mass Spectrometry. *J. Am. Soc. Mass Spectrom.* **2003**, *14*, 658–670.

S2. Bazian, A.; Taheri, M.; Alavi, H. Synthesis of 4'-[3-Methyl-5-thioxo-1*H*-1,2,4-triazol-4(5*H*)-yl]-2',5'-diphenyl-2',4'-dihydro-spiro[indolin-3,3'[1,2,4]triazol]-2-one Derivatives. *Russ. J. Gen. Chem.* **2014**, *84*, 586–592.

S3. Gallagher, N.; Zhang, H.; Junghoefer, T.; Giangrisostomi, E.; Ovsyannikov, R.; Pink, M.; Rajca, S.; Casu, M. B.; Rajca, A. Thermally and Magnetically Robust Triplet Ground State Diradical. *J. Am. Chem. Soc.* **2019**, *141*, 4764–4774.

S4. Brad Wan, W.; M. Haley, M. Carbon Networks Based on Dehydrobenzoannulenes. 4. Synthesis of "Star" and "Trefoil" Graphdiyne Substructures via Sixfold Cross-Coupling of Hexaiodobenzene. *J. Org. Chem.* **2001**, *66* (11), 3893–3901.

S5. http://chemmatcars.uchicago.edu/

S6. http://www.iumsc.indiana.edu/projects/SCrAPS/index.html

S7. SAINT v. 2018.1, Bruker AXS, Madison, WI, 2018.

S8. SADABS v. 2018.1, Bruker AXS, Madison, WI, 2018.

S9. Sheldrick, G. M. A short history of SHELX. *Acta Cryst. A* **2008**, *64*, 112–122.

S10. Xiong, X.; Jiang, Y.; Ma, D. Assembly of *N*,*N*-Disubstituted Hydrazines and 1-Aryl-1*H*-indazoles via Copper-Catalyzed Coupling Reactions. *Org. Lett.* **2012**, *14*, 2552–2555.

S11. D. Baucom, K.; C. Jones, S.; W. Roberts, S. 1,1'-Carbonyldiimidazole (CDI) Mediated Coupling and Cyclization To Generate [1,2,4]Triazolo[4,3-a]Pyridines. *Org. Lett.* **2016**, *18*, 560–563.

S12. Rajca, A.; Takahashi, M.; Pink, M.; Spagnol, G.; Rajca, S. Conformationally constrained, stable, triplet ground state ($S = 1$) nitroxide diradicals: antiferromagnetic chains of ($S = 1$) diradicals. *J. Am. Chem. Soc.* **2007**, *129*, 10159–10170.

S13. Olankitwanit, A.; Pink, M.; Rajca, S.; Rajca, A. Synthesis of Aza-*m*-Xylylene Diradicals with Large Singlet-Triplet Energy Gap and Statistical Analyses of their EPR Spectra. *J. Am. Chem. Soc.* **2014**, *136*, 14277–14288.

S14. Gallagher, N. M.; Bauer, J. J.; Pink, M.; Rajca, S.; Rajca, A. High Spin Organic Diradical with Robust Stability. *J. Am. Chem. Soc.* **2016**, *138*, 9377–9380.

S15. Stoll, S.; Schweiger, A. EasySpin, a comprehensive software package for spectral simulation and analysis in EPR *J. Magn. Reson.* **2006**, *178*, 42–55.

S16. Shu, C.; Zhang, H.; Olankitwanit, A.; Rajca, S.; Rajca, A. High-Spin Diradical Dication of Chiral π-Conjugated Double Helical Molecule. *J. Am. Chem. Soc.* **2019**, *141*, 17287–17294.

S17. Rajca, A. Organic diradicals and polyradicals: from spin coupling to magnetism? *Chem. Rev.* **1994**, *94*, 871–893.

S18. Meyer, A.; Gleizes, A.; Girerd, J. J.; Verdaguer, M.; Kahn, O. Crystal structures, magnetic anisotropy properties, and orbital interactions in catena - (μ-nitrito) - bis (ethylenediamine) nickel(II) perchlorate and triiodide. *Inorg. Chem.* **1982**, *21*, 1729–1739.

S19. Wang, W.; Chen, C.; Shu, C.; Rajca, S.; Wang, X.; Rajca, A. *S* = 1 Tetraazacyclophane Diradical Dication with Robust Stability: a Case of Low Temperature One-Dimensional Antiferromagnetic Chain. *J. Am. Chem. Soc.* **2018**, *140*, 7820–7826.

S20. Dyson, F. J. Electron Spin Resonance Absorption in Metals. II. Theory of Electron Diffusion and the Skin Effect. *Phys. Rev.* **1958**, *98*, 349–359.

S21. Krinichnyi, V. I. Dynamics of spin charge carriers in polyaniline. *Appl. Phys. Rev.* **2014**, *1*, 021305-1–021305-40.

S22. Tadyszak, K.; Strzelczyk, R.; Coy, E.; Maćkowiak, M.; Augustyniak-Jabłokow, M. A. Size effects in the conduction electron spin resonance of anthracite and higher anthraxolite. *Magn. Reson. Chem.* **2016**, *54*, 239–245.

S23. Kon'kin, A. L.; Shtyrlin, V. G.; Garipov, R. R.; Aganov, A. V.; Zakharov, A. V.; Krinichnyi, V. I.; Adams, P. N.; Monkman, A. P. EPR, charge transport, and spin dynamics in doped polyanilines. *Phys. Rev. B* **2002**, *66*, 075203-1 – 075203-11.

S24. Casu, M. B., Nanoscale Studies of Organic Radicals: Surface, Interface, and Spinterface. *Acc. Chem. Res.* **2018**, *51* (3), 753-760.

S25. Wagner, C. D., Sensitivity factors for XPS analysis of surface atoms. *J. Electron Spectrosc. Relat. Phenom.* **1983**, *32* (2), 99-102.

S26. Ciccullo, F.; Gallagher, N. M.; Geladari, O.; Chasse, T.; Rajca, A.; Casu, M. B., A Derivative of the Blatter Radical as a Potential Metal-Free Magnet for Stable Thin Films and Interfaces. *ACS Appl. Mater. Interfaces* **2016,** *8* (3), 1805–1812.

S27. Savu, S.-A.; Biswas, I.; Sorace, L.; Mannini, M.; Rovai, D.; Caneschi, A.; Chassé, T.; Casu, M. B., Nanoscale Assembly of Paramagnetic Organic Radicals on Au(111) Single Crystals. *Chem.-Eur. J.* **2013,** *19* (10), 3445-3450.

S28. Savu, S.-A.; Casu, M. B.; Schundelmeier, S.; Abb, S.; Tonshoff, C.; Bettinger, H. F.; Chassé, T., Nanoscale assembly, morphology and screening effects in nanorods of newly synthesized substituted pentacenes. *RSC Adv.* **2012,** *2* (12), 5112-5118.

S29. Casu, M. B.; Schuster, B.-E.; Biswas, I.; Raisch, C.; Marchetto, H.; Schmidt, T.; Chassé, T., Locally Resolved Core-hole Screening, Molecular Orientation, and Morphology in Thin Films of Diindenoperylene Deposited on Au(111) Single Crystals. *Adv. Mater.* **2010,** *22* (33), 3740-3744.

S30. Enkvist, C.; Lunell, S.; Sjögren, B.; Brühwiler, P. A.; Svensson, S., The C1s shakeup spectra of Buckminsterfullerene, acenaphthylene, and naphthalene, studied by high resolution x-ray photoelectron spectroscopy and quantum mechanical calculations. *J. Chem. Phys.* **1995,** *103* (15), 6333-6342.

S31. Sjögren, B.; Svensson, S.; Brito, A. N. d.; Correia, N.; Keane, M. P.; Enkvist, C.; Lunell, S., The C1s core shake-up spectra of alkene molecules: An experimental and theoretical study. *The Journal of Chemical Physics* **1992,** *96* (9), 6389-6398.

S32. Schöll, A.; Zou, Y.; Jung, M.; Schmidt, T.; Fink, R.; Umbach, E., Line shapes and satellites in high-resolution x-ray photoelectron spectra of large π-conjugated organic molecules. *J. Chem. Phys.* **2004,** *121* (20), 10260-10267.

S33. Arantes, C.; Chernick, E. T.; Gruber, M.; Rocco, M. L. M.; Chasse, T.; Tykwinski, R. R.; Casu, M. B., Interplay between solution-processing and electronic structure in metal-free organic magnets based on a TEMPO pentacene derivative. *J. Phys. Chem. C.* **2016,** *120* (6), 3289–3294.

S34. Kakavandi, R.; Savu, S.-A.; Sorace, L.; Rovai, D.; Mannini, M.; Casu, M. B., Core-Hole Screening, Electronic Structure, and Paramagnetic Character in Thin Films of Organic Radicals Deposited on SiO2/Si(111). *J. Phys. Chem. C* **2014,** *118* (15), 8044-8049.

S35. Ciccullo, F.; Calzolari, A.; Bader, K.; Neugebauer, P.; Gallagher, N. M.; Rajca, A.; van Slageren, J.; Casu, M. B., Interfacing a Potential Purely Organic Molecular Quantum Bit with a Real-Life Surface. *ACS Appl. Mater. Interfaces* **2019**, *11* (1), 1571-1578.

S36. Barth, G.; Linder, R.; Bryson, C., Advances in charge neutralization for XPS measurements of nonconducting materials. *Surf. Interface Anal.* **1988,** *11* (6-7), 307-311.

S37. Kakavandi, R.; Ravat, P.; Savu, S. A.; Borozdina, Y. B.; Baumgarten, M.; Casu, M. B., Electronic Structure and Stability of Fluorophore–Nitroxide Radicals from Ultrahigh Vacuum to Air Exposure. *ACS Appl. Mater. Interfaces* **2015,** *7* (3), 1685-1692.

S38. Hennessy, M. J.; McElwee, C. D.; Richards, P. M. Effect of interchain coupling on electron-spin resonance in nearly one-dimensional systems. *Phys. Rev. B* **1973**, *7*, 930–947.

S39. M. J. Frisch, G. W. Trucks, H. B. Schlegel, G. E. Scuseria, M. A. Robb, J. R. Cheeseman, G. Scalmani, V. Barone, G. A. Petersson, H. Nakatsuji, X. Li, M. Caricato, A. V. Marenich, J. Bloino, B. G. Janesko, R. Gomperts, B. Mennucci, H. P. Hratchian, J. V. Ortiz, A. F. Izmaylov, J. L. Sonnenberg, D. Williams-Young, F. Ding, F. Lipparini, F. Egidi, J. Goings, B. Peng, A. Petrone, T. Henderson, D. Ranasinghe, V. G. Zakrzewski, J. Gao, N. Rega, G. Zheng, W. Liang, M. Hada, M. Ehara, K. Toyota, R. Fukuda, J. Hasegawa, M. Ishida, T. Nakajima, Y. Honda, O. Kitao, H. Nakai, T. Vreven, K. Throssell, J. A. Montgomery, Jr., J. E. Peralta, F. Ogliaro, M. J. Bearpark, J. J. Heyd, E. N. Brothers, K. N. Kudin, V. N. Staroverov, T. A. Keith, R. Kobayashi, J. Normand, K. Raghavachari, A. P. Rendell, J. C. Burant, S. S. Iyengar, J. Tomasi, M. Cossi, J. M. Millam, M. Klene, C. Adamo, R. Cammi, J. W. Ochterski, R. L. Martin, K. Morokuma, O. Farkas, J. B. Foresman, and D. J. Fox, *Gaussian 16*, Revision A.03 (Gaussian, Inc., Wallingford CT, 2016).

S40. Yamaguchi, K.; Jensen, F.; Dorigo, A.; Houk, K. N. A Spin Correction Procedure for Unrestricted Hartree–Fock and Møller–Plesset Wavefunctions for Singlet Diradicals and Polyradicals. *Chem. Phys. Lett.* **1988**, *149*, 537–542.

S41. Noodleman, L.; Case, D. A. Density-Functional Theory of Spin Polarization and Spin Coupling in Iron—Sulfur Clusters. *Adv. Inorg. Chem.* **1992**, *38*, 423–470.

S42. Trinquier, G.; Suaud, N.; Malrieu, J.-P. Theoretical Design of High-Spin Polycyclic Hydrocarbons. *Chem.–Eur. J.* **2010**, *16*, 8762–8772.

S43. Quast, H.; Nüdling, W.; Klemm, G.; Kirschfeld, A.; Neuhaus, P.; Sander, W.; Hrovat, D. A.; Borden, W. T. A Perimidine-Derived Non-Kekulé Triplet Diradical *J. Org. Chem.* **2008**, *73*, 4956–4961.

S44. Winter, A. H.; Falvey, D. E.; Cramer, C. J.; Gherman, B. F. Benzylic Cations with Triplet Ground States: Computational Studies of Aryl Carbenium Ions, Silylenium Ions, Nitrenium Ions, and Oxenium Ions Substituted with Meta π Donors. *J. Am. Chem. Soc.* **2007**, *129*, 10113–10119.

S45. Bajaj, A.; Ali, Md. E. First-Principle Design of Blatter's Diradicals with Strong Ferromagnetic Exchange Interactions. *J. Phys. Chem. C* **2019,** *123* (24) , 15186–15194.

S46. Neese, F. ORCA – an ab initio, Density Functional and Semiempirical program package, Version

2.6. University of Bonn, **2008**.

S47. Barone, V. in *Recent Advances in Density Functional Methods, Part I*, Ed. D. P. Chong (World Scientific Publ. Co., Singapore, **1996**).

S48. Sinnecker, S.; Neese, F. Spin–Spin Contributions to the Zero-Field Splitting Tensor in Organic Triplets, Carbenes and Biradicals — A Density Functional and Ab Initio Study. *J. Phys. Chem. A* **2006**, *110*, 12267–12275.

S49. Allouche, A.-R. Gabedit – A graphical user interface for computational chemistry softwares. *J. Comput. Chem.* **2011**, *32*, 174–182.

S50. Rajca, A.; Olankitwanit, A.; Rajca, S. Triplet Ground State Derivative of Aza-*m*-Xylylene Diradical with Large Singlet-Triplet Energy Gap. *J. Am. Chem. Soc.* **2011**, *133*, 4750–4753.

S51. Sadhukhan, T.; Hansda, S.; Latif, I. A.; Datta, S. N. Metaphenylene-Based Nitroxide Diradicals: A Protocol To Calculate Intermolecular Coupling Constant in a One-Dimensional Chain. *J. Phys. Chem. A* **2013**, *117*, 13151−13160.

G. Magnetic Behavior in Metal-Free Radical Thin Films

Magnetic ordering in metal-free radical thin films

Tobias Junghoefer,[1†] Arrigo Calzolari,[2†] Ivan Baev,[3†] Mathias Glaser,[1] Francesca Ciccullo,[1] Erika Giangrisostomi,[4] Ruslan Ovsyannikov,[4,] Fridtjof Kielgast,[3] Matz Nissen,[3] Julius Schwarz,[3] Nolan M. Gallagher,[5] Andrzej Rajca,[5] Michael Martins,[3] Maria Benedetta Casu[1*]

[1]Institute of Physical and Theoretical Chemistry, University of Tübingen, 72076 Tübingen, Germany

[2]CNR-NANO Istituto Nanoscienze, Centro S3, 41125 Modena, Italy

[3]Department of Physics, University of Hamburg, 22761 Hamburg, Germany

[4]Helmholtz-Zentrum Berlin, 12489 Berlin, Germany

[5]Department of Chemistry, University of Nebraska, Lincoln, United States

*benedetta.casu@uni-tuebingen.de

[†]These authors contributed equally to this work

Magnetism in organic materials is very intriguing: the realization of long-range magnetic order in completely metal-free systems means that magnetic moments are coupled to useful properties of organic materials, such as optical transparency, low-cost fabrication, and flexible chemical design. Magnetic ordering in purely organic thin films is unknown so far since most of the investigations show this effect due to the proximity of light atoms to heavy metals, impurities, or vacancies. Here, we unravel X-ray magnetic circular dichroism at the carbon and nitrogen K-edges in purely organic radical thin films. Our results show a different behaviour depending on preparation than the magnetic signature of the single crystals. Atomistic simulations indicate that the reason for this is the molecular arrangement in the films compared to that in the single crystal. Our work opens a new avenue towards understanding magnetic properties in purely organic materials. The tuning of the film magnetic properties by the molecular arrangement is an exciting perspective towards revealing new properties and applications.

Magnetic ordering in light elements, such as nitrogen and carbon, has been studied in magnetic-edged graphene nanoribbons[1] or bilayers[2], and polymers[3] while in hybrid organic thin films most of the investigations show this effect as due to the proximity of light atoms to heavy metals, impurities, or vacancies[4]. Purely organic radicals are molecules that carry one unpaired electron giving rise to a permanent magnetic moment, in the complete absence of metal ions.[5-7] Inspired by their tremendous potential, here we investigate thin films of an exceptionally chemically stable Blatter radical derivative[8] by using X-ray magnetic circular dichroism (XMCD)[9-12]. Here we observe XMCD at the nitrogen and carbon K-edges in the thin films: our results show a magnetic behaviour different than in the single crystals depending on the preparation conditions.

Purely organic radicals are exceptionally promising in various fields. Consequently, the needs arose to go beyond the limit of the first attempts to grow films by wet preparations that is prone

to the presence of contaminants. The controlled radical thin film growth using evaporation was believed to be not practicable because of their reactivity that would cause their degradation during evaporation[13]. Once proved that several families of radicals are stable enough to be evaporable,[14] scientific curiosity and potential applications are driving the research on their thin film,[15-18] identifying their potential use in applications ranging from quantum computing to organic spintronics[16,17,19]. While several radicals are synthetized with high enough chemical stability to stand evaporation, their film forming properties are often very poor because of their high vapour pressure at room temperature and the low molecular weight that make them highly volatile and characterized by very low sticking coefficients[8,20]. Willing to investigate the magnetic behaviour of radical thin films, we faced several challenges. To achieve reproducible films and, thus, reproducible results, controlled conditions during growth are necessary to avoid any artefacts (contaminants, degradation due to film aging and air-exposure). The investigations require high signal sensitivity: a single magnetic moment is associated to the large molecular volume. The high sensitivity is furthermore necessary because we investigate very thin films (the nominal thickness varies in the 4-9 nm range). An important issue is also achieving very low temperature, simultaneously to the presence of high magnetic fields to reach magnetic saturation. In fact, purely organic radicals are predicted to have very low Curie temperatures[5-7,21]. We selected a chemically super stable Blatter radical[22,23] derivative, (Blatter-pyr, Figure 1a)[8] explicitly designed to have very good film forming properties and film stability.[8] XMCD was the experimental technique of our choice. It is an element-specific technique based on the absorption of polarized X-rays due to electron transitions from core levels to unoccupied states, a well-established method to access spin and orbital angular momenta in transition metals, identifying their magnetic behaviour [9-12]. Despite the XMCD well-known capabilities, the measurements of metal-free organic films required exceptional facilities to overcome all challenges. The experiments were performed using a newly developed ultra-low temperature setup equipped with a superconducting vector magnet allowing magnetic fields up to ±7 T in

the horizontal direction and ±0.5 T in the vertical direction, and a cryogen free ^{3}He-^{4}He dilution refrigerator, allowing experiments reaching the lowest temperature of 100 mK.[24] This unique portable setup features an ultra-high vacuum (UHV) preparation chamber that allowed growing the radical films by organic molecular beam deposition under controlled conditions, and transferring them to the measuring chamber without breaking the UHV. This led to the investigation of thin films free from contaminants because catalysts, solvents and air exposure may affect the intrinsic film properties.

Results and Discussion

We applied a magnetic field at very low temperature, to align the magnetic moments in the direction of the field that was collinear to the incoming circularly polarized photon beam. The absorption spectra (XAS) once with left and once with right circularly polarized light were measured (Figure 1b). XMCD is defined as the difference between the two absorption signals. We focus on the N K-edge absorption spectra measured at 1.1 K with a magnetic field of +7 T. The films in Figure 2 (nominal thickness 9 nm) were prepared by using controlled evaporation keeping the substrate at 290 K. We observe a clear dichroic signal (Figure 2). The signal reverses sign upon reversal of the magnetic field (Supplementary Information, Figure S1) confirming that the dichroism is real (magnetization reversal is equivalent to switching the helicity of the polarized light). We also measured the absorption at the C K-edge: a XMCD signal is visible also in this case. This behaviour is surprising because the Blatter-pyr single crystal is antiferromagnetic[25], in which case no XMCD should be observable. Discrepancies in the intensity of the XMCD for the two signs of the magnetic field suggests the presence of uncompensated spins that do not follow the external magnetic field[26-28]. Also, the curves are normalised considering the total absorption of the beamline (see the experimental section for details), as it is usually done for XMCD[10,29,30]. This method cannot compensate for possible substrate contaminants contributing to absorption.

To understand the origin of this unexpected behaviour we deposited and investigated a second set of Blatter-pyr thin films with different thicknesses (4 and 9 nm, the latter as in the measurements in Figure 2), at 0.15, 10 and 15 K in order to span a larger temperature range. We prepared the samples keeping the substrate temperature slightly higher (300 K). This increased the kinetic energy of the Blatter-pyr on the substrate during film growth.[8] We measured the X-ray absorption spectra of the films as previously done and we could not detect any XMCD (Figure 3). Also, we did not detect any dichroism spanning a large temperature range from 0.15 to 15 K. This result is concomitant with the antiferromagnetic behaviour of the Blatter-pyr crystalline bulk. Therefore, we found that, depending on the growth conditions, a few samples resemble the crystalline character, others a spin-uncompensated magnetic behaviour. We note that the different preparation conditions cause not only a different XMCD but also the presence of a new feature (Figure 3, and S3 in the Supplementary Information) when the samples are grown on the substrate at 300 K indicating differences in the electronic structure, expected when a different molecular arrangement occurs[31,32].

Thin films can have considerably different structural, transport, electronic and magnetic properties with respect to their bulk counterpart.[33,34] Polymorphism is particularly enhanced in organic materials because of the degree of freedom of the molecules in a film. Molecules have 3N degrees of freedom with N being the number of atoms in a molecule. This has pronounced consequences for all properties of the system. For example, molecular packing has been invoked to explain the different magnetic behaviour ranging from antiferro- to ferromagnetic[21,35] in the different crystallographic phases of the crystals of the first purely organic ferromagnet ever reported, the *p*-nitrophenyl nitronyl nitroxide radical[7]. In our experiments we observe that different preparation conditions play a role: decreasing the kinetic energy of the molecules on the substrates influences their adjustment in the films[33,36,37] with clear consequences on the magnetic interactions, since the antiferromagnetic character of the Blatter-pyr crystals depends on a delicate adjustment of the slippage angle[38,39].

Energetically, the antiferro- (AF) and the ferromagnetic (FM) interactions in the bulk are very close: we performed first-principles density functional theory calculations for the Blatter-pyr derivative that indicate that the antiferromagnetic configuration is more stable by only ~2 meV/cell. The electronic and magnetic properties of the crystalline bulk along with those of the single Blatter-pyr molecule are summarized in the Supplementary Information (Figure S4 and S5). The minimization of electronic problem for a non-magnetic state (para or diamagnetic) does not converge to a minimum, that means that the zero magnetization is not a (either total or local) minimum for the total energy, indicating that the non-magnetic phase is not the ground state for the system.

To shed light on the correlation between structural changes, induced by different preparations, and the intermolecular interactions, we have modelled the thin film phase. Starting from the 3D crystalline structure[8] (Figure 4a), we considered a 9 nm-thick film grown along the *c*-axis, as shown in Figure 4b. The film structure stems from the stacking of the four radicals (labelled 1-4 in the following analysis), which form the crystal. As for the crystalline case, the AF and the FM interactions are almost energetically degenerate. Hereafter, we assume the AF as the reference.

The total magnetic moment of the antiferromagnetic case is the sum of the single molecule contributions with antiparallel spin orientation. The antiparallel magnetic arrangement can be distinguished by the non-magnetic spin unpolarized case, through the evaluation of the absolute magnetization $\mu_A = \int |\rho_{up} - \rho_{dw}| d^3r$. Non-magnetic systems have $\mu_T = \mu_A = 0$, while antiparallel spin systems have $\mu_T = 0$ and $\mu_A \neq 0$. In the present case μ_T=0.0 μ_B and μ_A=15.2 Bohr magneton (μ_B)/cell. The spin alternation follows the structural bi-layer arrangement (↑↑ - ↓↓): spin-up for molecules 2 and 3, spin-down for 1 and 4, as shown by the charge spin-density plot (i.e., ρ_{up}-ρ_{dw}) in Figure 4a, where green and blue lobes represent spin-up and spin-down orientation, respectively. This reflects on the density of states (DOS, Figure 4b) that closely derives from

the coherent superposition of the molecule spectra, where each radical exhibit an unpaired single occupied (SOMO, S_O) and the single unoccupied (SUMO, S_U) molecular orbitals[40]. For molecules 2-3, S_O and S_U have a spin-up and spin-down polarization respectively, while the opposite order attains for molecules 1-4. The electronic and magnetic properties of the film do not depend on the molecular orientation of the external layers (see Supplementary Information, Figure S6a). Similar results can be obtained also from films grown along the *a*- and *b*-axis respectively, see, e.g., Figures S6 b and c.

A closer inspection of the electronic properties indicates that, albeit weak, there is a long-range intermolecular coupling in the film. This is evident, e.g., from the band structure (Supplementary Information, Figure S7a): (i) the molecular-derived bands are not fully degenerate, but rather split in a 2-fold manifolds; (ii) the S_O and S_U bands have k-dispersion of ~100 meV across the Brillouin zone. S_O and S_U states, which are responsible for the magnetic character of the radical, are π-orbitals with a net contribution from both carbon and nitrogen atoms. Even though the magnetic origin of the radical is formally due to the presence of an undercoordinated N atom, the spin-density distribution (i.e., ρ_{up}-ρ_{dw}) is spatially delocalized all over the molecule and not centred on the nitrogen site[19]. Near edge X-ray absorption fine structure (NEXAFS) spectra mirror this delocalisation (see Supplementary Information Figure S8 and S9 (b and d)). This also explains the reason why we observed a XMCD signal both at the N and C K-edges in the films in Figure 2.

To unravel the interplay between the molecular packing and the magnetic character we consider a simple model constituted of a 3 nm-thick film, resulting from the stacking of the four molecules 1-4 (Figure 5a). Starting from the crystalline arrangement (θ=0°) we modified the molecular packing by changing the herringbone angle by 5°, 10°, 15° and 20°, with respect to the *c*-axis. The higher is the rotation angle the flatter is the molecular stacking. After full atomic relaxation we recognize very different configurations, as a function of the initial angles. For θ≤10° the systems maintain the structural and electronic characteristics of the 9 nm-thick films

and the crystalline bulk, both AF and FM interactions can be obtained at the same energy. For $\theta \geq 15°$, the molecule-molecule interaction becomes predominant and the structure undergoes a strong spatial redistribution, as shown in Figure 5b for the case of $\theta = 20°$. The external molecules 1 and 4 slightly displace from the centre of the film and rotate back restoring the crystalline ($\theta = 0°$) spatial distribution. The internal molecules 2-3 rotate in the opposite direction (i.e. increasing θ) forming a very ordered and close-packed bi-layer of parallel molecules. The resulting configuration has a total magnetic moment $\mu_T = \mu_A = 2.0\ \mu_B$/cell. This value is not the result of a transition from AF-to-FM interactions (the FM configuration would have $\mu_T = \mu_A = 4.0\ \mu_B$/cell), but rather of a non-complete spin compensation. Indeed, the charge spin density plot (panel 5b) shows the cancellation of the magnetic moment of the central molecules (2-3). The comparison of the magnetic moment per atoms in the limiting cases for $\theta = 0°$ and $\theta = 20°$ (Figure S5) indicates an identical behaviour for external molecules 1-4, and the complete quenching of the magnetic moment, mostly on N atoms, of the two central molecules, which is a fingerprint of a local charge redistribution. As mentioned above, SOMO and SUMO are aromatic π states, delocalized over the entire molecules including nitrogen atoms. The close packed configuration of molecules 2 and 3, caused by the rotation, favours the π–π coupling, which results in the constructive hybridization of the molecular states, to form two new mixed delocalized orbitals across the film (Figure 5c). The intermolecular interaction changes the DOS plot of the system (panel d), where the external molecules (1-4) maintains their original spin-polarized character as in the thick film, while the internal layer gives rise to a spin-unpolarized peak that crosses the Fermi level (M-state in panel 5d and in the band structure of Figure S7b).

The modification of the magnetic properties caused by a different molecular arrangement is the key to understand the differences observed in the experimental results. We have also considered the possible effects of structural changes (e.g., flattening of the molecules in the proximity of a substrate), which may quench the magnetic moment of the first layers. We changed the

molecular arrangement of the bottom part of the 9 nm-thick film, by rotating only the lowest 4 molecules by 20°, 15°, 10° and 5°, respectively, to model the progressive readjustment of the molecules as expected in the experimental samples, with increasing the thickness. The results are summarized in Figure 5e: the bottom 4 molecules rotate and flatten, similarly to the central layer of the 20° model discussed above (panel 5b); the remaining units stay in the θ=20° configuration, as in the thick film. The resulting system has μ_T=0.0 μ_B and μ_A =10.2 μ_B/cell where the rotated molecules have zero magnetic moment, while the rest maintains the AF interactions. Therefore, in the general case, depending on the growth conditions, the films may show magnetic interactions different from the AF, due to the presence of uncompensated spin layers, whose number (i.e., the final magnetization) depends on the specific different stacking (i.e., intermolecular π–π coupling). The molecules in the samples grown at 300 K have sufficient kinetic energy to mimic the crystalline phase, while in samples grown at a lower temperature the molecules assemble adopting a different arrangement that gives rise to a XMCD signal, because of a spin unbalance in the molecular stack. Control of the growth parameters influence thin film growth and properties[41]: the substrate temperature during growth could be used as a tool to tune the magnetic character of purely organic thin films.

Conclusions

We measured the magnetic dichroism in thin films of purely organic radicals and found that the XMCD signature in the films is different than in the bulk depending on the film preparation. We explain this difference in terms of the different arrangement of the molecules in the two cases.

Even though this work presents two fundamental results, i.e., the magnetic character of purely organic radical thin films can be investigated using XMCD, and it is influenced by the preparation conditions, it is only a first step in a largely unknown field. Many more experiments

are needed to catch the intimate nature of magnetic ordering in radical thin films: measuring the magnetization curves and the hysteresis loop versus the applied magnetic field to define a magnetic character, exploring a large set of preparation parameters and different radicals, including high-spin radical systems are the next necessary steps. New experimental approaches to the XMCD measurements suitable for purely carbon-based materials are also necessary: we suggest that, from the experimental point of view, in case of XAS at the absorption edges of light elements, measuring the clean substrate for minimizing the normalisation issues might be beneficial. In fact, in NEXAFS spectroscopy the best way to normalize the curves at the absorption edge of thin films of light elements such as carbon is using the clean substrate signal rather than the taking into account the total absorption of the beamline with a diode or a grid[42]. On the theoretical side, a model to interpret the XMCD results in this class of materials from a general point of view is missing. The present work will certainly stimulate more discussion in the field and provides exciting new avenues to a new generation of experiments, opening fascinating possibilities for magnetism, revealing the importance of synthetizing, chemically tuning and manipulating stable radicals, towards achieving collective magnetic behaviour in purely organic thin films, also at higher temperatures.

Methods

Experimental section. The molecules were synthetized as described in Ref.[8] Thin film were grown in UHV by using organic molecular beam deposition (OMBD). Native SiO_2 grown on single-side polished n-Si(111) wafer was used as the substrate for all thin films. The wafers were cleaned in an ultrasonic bath by immersion in ethanol and acetone for one hour each and annealed in ultra-high vacuum at around 500 K for several hours. The thin films were grown keeping the substrate temperature either at 290 or 300 K during deposition. When available, the cleanness of the substrates was checked by XPS. The Knudsen cell was accurately calibrated, and the same cell was used during all experiments. The cell temperature during evaporation

was 418 K, far below the onset of degradation of the radical as determined with thermal gravimetric analysis.[8] The evaporation rate was 0.2 nm/min. Under these preparation conditions the films follow the Stranski-Krastanov growth mode (layer+islands). Previously to the experiments discussed int this work, the films were characterised by using electron paramagnetic resonance to prove that the chosen preparation conditions allow depositing films of intact radicals.[8,19] All measuring stations were equipped with preparations chambers that allowed installing the same calibrated Knudsen cells, therefore always using the same evaporation protocol. XPS measurements were performed in an UHV system consisting of a substrate preparation chamber, an OMBD-dedicated chamber, and an analysis chamber (base pressure 4 x 10^{-10} mbar) equipped with a SPECS Phoibos 150 hemispherical electron analyser and a monochromatic Al Kα source (SPECS Focus 500). Further information on substrate preparation, film growth, stoichiometry measurements and fit calculations are given in Ref. [8].

UPS and NEXAFS measurements were performed at the third-generation synchrotron radiation source Bessy II (Berlin, Germany) at the LowDose PES end-station, installed at the PM4 beamline ($E/\Delta E$=6000 at 400 eV) that included substrate preparation and film deposition facilities like those described above for the XPS station. The UPS measurements were carried out in single bunch mode with a SCIENTA ArTOF electron energy analyzer, the NEXAFS measurements in multibunch hybrid mode (ring current in top up mode=300 mA, c_{ff}=3, 100 µm exit slit). The NEXAFS spectra were measured using linearly polarised light, in normal and in grazing incidence (30° to the surface) and normalized by taking the substrate signal and the ring current into account[43].

The XMCD experimental setup[24] was installed at the XUV Beamlime P04 at the PETRA III synchrotron (Hamburg, Germany). At the Beamlime P04 each absorption edge could be scanned in a very short time, from few minutes to several seconds, and the beam exposure was minimized with a shutter. A magnetic field (± 7 T) was applied in the horizontal direction, collinear to the incoming photon beam. The measurements were carried out in normal

incidence. Each element-resolved absorption curve was obtained averaging up to 54 scans, each measured on a fresh point on the film surface. All absorption spectra were recorded in total electron yield. To determine XMCD, the adsorption curves were divided by the incoming photon intensity current, I_0, measured with a photodiode, for the two polarisations. An offset was removed to align the c+ and the c- curves, making sure that the pre-edge regions are equal. We subtracted the same linear background to the c+ and the c- curves and we normalised to have the same equal edge jump. The c- and c+ curves obtained in this way were subtracted to calculate XMCD.[29,30]

We have taken all precautions necessary to avoid radiation damage (e.g., short time beam exposure, shutter protection, defocusing of the beam, low dose radiation). All samples were carefully monitored for radiation damage during beam exposure. All measurements were performed on freshly prepared films.

Calculations. Calculations were performed with the Quantum Espresso Package[44,45] which implements a planewave formulation of the Density Functional Theory (DFT). Exchange-correlation was treated in the Perdew–Burke–Ernzerhof (PBE) Generalized Gradient Approximation (GGA)[46], and the spin degrees of freedom were described within the local spin-density approximation (LSDA). Tests on the effect of the exchange and correlation functional and the comparison with hybrids are reported in SI. Ionic potentials were described by using ab initio ultrasoft pseudopotentials of Vanderbilt's type[47]. Single-particle electronic wave functions (charge) were expanded in a plane-wave basis set up to an energy cutoff of 28 Ry (280 Ry). Van der Waals corrections (Grimme formulation[48]) to dispersive forces were included to improve the description of the intra- and inter-molecular interactions. A uniform (4x8x2) k-point mesh was used for sampling the 3D Brillouin zone of the bulk; a (4x8) k-point mesh was used for the 2D Brillouin zone of the films.

The molecular crystal was simulated by using periodic supercell. The initial structure was extracted by X-ray experimental data.

450

The Blatter-pyr 3D crystal was simulated in a monoclinic unitary cell of dimensions a= 13.65 Å, b=5.11 Å, c=28.24 Å, a=90.00°, b=99.47°, g=90.00°, which includes four molecules as shown in Figure 4 and Supporting Information (Figure S4). The films were modelled through periodically repeated monoclinic slabs, each including 12 Blatter-pyr radicals and a vacuum layer (~1.5 nm) in the direction perpendicular to the surface plane, to avoid spurious interactions among the replicas. All structures were fully relaxed until forces on all atoms became lower than 0.03 eV/$Å^{-1}$.

NEXAFS spectra at the nitrogen K-edge were simulated by using the first-principles scheme based on the continued-fraction approach and ultrasoft pseudopotentials as implemented in the Quantum ESPRESSO package[49]. The reference 1s core level states were obtained by replacing the pseudopotential of a selected N atom with another one, which simulates the presence of a screened core hole. Since the molecule includes inequivalent nitrogen atoms, we repeated the NEXAFS calculations for each N atom of the radical and we averaged the resulting spectra. X-ray absorption spectra for each atom were also repeated changing the direction k_i of incident electric field along the three cartesian axes. The results are summarized in the SI.

References

1 Slota, M. *et al.* Magnetic edge states and coherent manipulation of graphene nanoribbons. *Nature* **557**, 691-695, (2018).

2 Sharpe, A. L. *et al.* Emergent ferromagnetism near three-quarters filling in twisted bilayer graphene. *Science* **365**, 605-608, (2019).

3 Rajca, A., Wongsriratanakul, J. & Rajca, S. Magnetic Ordering in an Organic Polymer. *Science* **294**, 1503-1505, (2001).

4 Ohldag, H. *et al.* pi-Electron Ferromagnetism in Metal-Free Carbon Probed by Soft X-Ray Dichroism. *Phys. Rev. Lett.* **98**, 187204, (2007).

5 Miller, J. S. Magnetically ordered molecule-based materials. *Chem. Soc. Rev.* **40**, 3266-3296, (2011).

6 Gatteschi, D., Sessoli, R. & Villain, J. *Molecular Nanomagnets*. (Oxford University Press Inc., 2006).

7 Tamura, M. *et al.* Bulk ferromagnetism in the β-phase crystal of the p-nitrophenyl nitronyl nitroxide radical. *Chem. Phys. Lett.* **186**, 401-404, (1991).

8 Ciccullo, F. *et al.* A Derivative of the Blatter Radical as a Potential Metal-Free Magnet for Stable Thin Films and Interfaces. *ACS Appl. Mater. Interfaces* **8**, 1805–1812, (2016).

9 Stöhr, J. Exploring the microscopic origin of magnetic anisotropies with X-ray magnetic circular dichroism (XMCD) spectroscopy. *J. Magn. Magn. Mater.* **200**, 470-497, (1999).

10 Brune, H. & Gambardella, P. Magnetism of individual atoms adsorbed on surfaces. *Surf. Sci.* **603**, 1812-1830, (2009).

11 Cornia, A., Talham, D. R. & Affronte, M. in *Molecular Magnetic Materials* 187-229 (2016).

12 Schütz, G. *et al.* Absorption of circularly polarized x rays in iron. *Phys. Rev. Lett.* **58**, 737-740, (1987).

13 Huang, Z. *et al.* A chemist's overview of surface electron spins. *Chem. Soc. Rev.* **46**, 1955-1976, (2017).

14 Casu, M. B. Nanoscale Studies of Organic Radicals: Surface, Interface, and Spinterface. *Acc. Chem. Res.* **51**, 753-760, (2018).

15 Zhang, Y. *et al.* Temperature Tunable Self-Doping in Stable Diradicaloid Thin-Film Devices. *Advanced Materials* **27**, 7412-7419, (2015).

16 Ai, X. *et al.* Efficient radical-based light-emitting diodes with doublet emission. *Nature* **563**, 536-540, (2018).

17 Guo, H. *et al.* High stability and luminescence efficiency in donor–acceptor neutral radicals not following the Aufbau principle. *Nat. Mater.* **18**, 977-984, (2019).

18 Mugnaini, V. *et al.* Looking Inside the Perchlorinated Trityl Radical/Metal Spinterface through Spectroscopy. *J. Phys. Chem. Lett.* **6**, 2101-2106, (2015).

19 Ciccullo, F. *et al.* Interfacing a Potential Purely Organic Molecular Quantum Bit with a Real-Life Surface. *ACS Appl. Mater. Interfaces* **11**, 1571-1578, (2019).

20 Savu, S.-A. *et al.* Nanoscale Assembly of Paramagnetic Organic Radicals on Au(111) Single Crystals. *Chem.-Eur. J.* **19**, 3445-3450, (2013).

21 Blundell, S. J. & Pratt, F. L. Organic and molecular magnets. *Journal of Physics: Condensed Matter* **16**, R771-R828, (2004).

22 Blatter, H. M. & Lukaszewski, H. A new stable free radical. *Tetrahedron Letters* **9**, 2701-2705, (1968).

23 Constantinides, C. P., Koutentis, P. A., Krassos, H., Rawson, J. M. & Tasiopoulos, A. J. Characterization and Magnetic Properties of a “Super Stable” Radical 1,3-Diphenyl-7-trifluoromethyl-1,4-dihydro-1,2,4-benzotriazin-4-yl. *J. Org. Chem.* **76**, 2798-2806, (2011).

24 Beeck, T. *et al.* New experimental perspectives for soft x-ray absorption spectroscopies at ultra-low temperatures below 50 mK and in high magnetic fields up to 7 T. *Rev. Sci. Instrum.* **87**, 045116, (2016).

25 Zhou, Z., Chu, S.-I. & Han, S. Quantum computing with superconducting devices: A three-level SQUID qubit. *Phys. Rev. B* **66**, 054527, (2002).

26 Ohldag, H. *et al.* Correlation between Exchange Bias and Pinned Interfacial Spins. *Phys Rev Lett* **91**, 017203, (2003).

27 Nogués, J. & Schuller, I. K. Exchange bias. *J. Magn. Magn. Mater.* **192**, 203-232, (1999).

28 Berkowitz, A. E. & Takano, K. Exchange anisotropy — a review. *J. Magn. Magn. Mater.* **200**, 552-570, (1999).

29 Goering, E., Fuss, A., Weber, W., Will, J. & Schütz, G. Element specific x-ray magnetic circular dichroism magnetization curves using total electron yield. *J. Appl. Phys.* **88**, 5920-5923, (2000).

30 Goering, E., Gold, S., Bayer, A. & Schuetz, G. Non-symmetric influences in the total electron yield X-ray magnetic circular dichroism signal in applied magnetic fields. *J. Synchrotron Rad.* **8**, 434-436, (2001).

31 Duhm, S. *et al.* Orientation-dependent ionization energies and interface dipoles in ordered molecular assemblies. *Nature Materials* **7**, 326-332, (2008).

32 Klett, B., Cocchi, C., Pithan, L., Kowarik, S. & Draxl, C. Polymorphism in α-sexithiophene crystals: relative stability and transition path. *Phys. Chem. Chem. Phys.* **18**, 14603-14609, (2016).

33 Jones, A. O. F., Chattopadhyay, B., Geerts, Y. H. & Resel, R. Substrate-Induced and Thin-Film Phases: Polymorphism of Organic Materials on Surfaces. *Adv. Funct. Mater.* **26**, 2233–2255, (2016).

34 Poulopoulos, P. & Baberschke, K. Magnetism in thin films. *J. Phys. Condens. Matter* **11**, 9495-9515, (1999).

35 Mori, T. *Electronic Properties of Organic Conductors*. (Springer Japan, 2016).

36 Dalal, S. S., Walters, D. M., Lyubimov, I., de Pablo, J. J. & Ediger, M. D. Tunable molecular orientation and elevated thermal stability of vapor-deposited organic semiconductors. *Proceedings of the National Academy of Sciences* **112**, 4227-4232, (2015).

37 Kowarik, S., Gerlach, A. & Schreiber, F. Organic molecular beam deposition: fundamentals, growth dynamics, andin situstudies. *Journal of Physics: Condensed Matter* **20**, 184005, (2008).

38 Zheng, Y., Miao, M.-s., Kemei, M. C., Seshadri, R. & Wudl, F. The Pyreno-Triazinyl Radical – Magnetic and Sensor Properties. *Isr. J. Chem.* **54**, 774-778, (2014).

39 Constantinides, C. P., Koutentis, P. A. & Rawson, J. M. Antiferromagnetic Interactions in 1D Heisenberg Linear Chains of 7-(4-Fluorophenyl) and 7-Phenyl-Substituted 1,3-Diphenyl-1,4-dihydro- 1,2,4-benzotriazin-4-yl Radicals. *Chemistry – A European Journal* **18**, 15433-15438, (2012).

40 The use of higher levels of theory, such as hybrid exchange-correlation (XC) functional does not change this picture. Preliminary tests on the single molecule (Figure S4) show that the inclusion of the B3LYP functional barely opens the energy gap between the SOMO and the SUMO molecular orbitals, while it does not modify the symmetry or the order of the single molecular orbitals.

41 Forrest, S. R. Ultrathin Organic Films Grown by Organic Molecular Beam Deposition and Related Techniques. *Chem. Rev.* **97**, 1793-1896, (1997).

42 Schöll, A., Zou, Y., Schmidt, T., Fink, R. & Umbach, E. Energy calibration and intensity normalization in high-resolution NEXAFS spectroscopy. *J. Electron. Spectros. Relat. Phenomena* **129**, 1-8, (2003).

43 Casu, M. B. *et al.* Nucleation in Organic Thin Film Growth: Perylene on Al2O3/Ni3Al(111). *J. Phys. Chem. C* **113**, 10990-10996, (2009).

44 Giannozzi, P. *et al.* Advanced capabilities for materials modelling with Quantum ESPRESSO. *J. Condens. Matter Phys.* **29**, 465901, (2017).

45 Giannozzi, P. *et al.* QUANTUM ESPRESSO: a modular and open-source software project for quantum simulations of materials. *J. Phys. Condens. Matter* **21**, 395502, (2009).

46 Perdew, J. P., Burke, K. & Ernzerhof, M. Generalized Gradient Approximation Made Simple. *Phys. Rev. Lett.* **77**, 3865-3868, (1996).

47 Vanderbilt, D. Soft self-consistent pseudopotentials in a generalized eigenvalue formalism. *Phys. Rev. B* **41**, 7892-7895, (1990).

48 Grimme, S. Semiempirical GGA-type density functional constructed with a long-range dispersion correction. *J. Comput. Chem.* **27**, 1787-1799, (2006).

49 Gougoussis, C., Calandra, M., Seitsonen, A. P. & Mauri, F. First-principles calculations of x-ray absorption in a scheme based on ultrasoft pseudopotentials: From alpha-quartz to high-Tc compounds. *Phys. Rev. B* **80**, 075102, (2009).

Acknowledgements

This paper is in memory of Wilfried Wurth. He was a brilliant scientist open to new ideas and views. We are deeply saddened that he will not see the result of our work because it was made possible also thanks to Wilfried's unprejudiced scientific approach. He would have appeared as a co-author.

The authors would like to thank Helmholtz-Zentrum Berlin (HZB) for providing beamtime at BESSY II (Berlin, Germany), and DESY (Hamburg, Germany), a member of the Helmholtz Association HGF, for the provision of experimental facilities at PETRA III, Tang Zahng, Moritz Hoesch, Kai Bagschik, Hilmar Adler, Elke Nadler and Sergio Naselli for technical support,

Thomas Chassé for the access to the photoelectron spectroscopy lab at the University of Tübingen. We also thank Eberhard Goering for the XAS normalisation method. Financial support from HZB, DESY, and German Research Foundation (DFG) under the contract CA852/5-2 and CA852/11-1 is gratefully acknowledged. We thank the National Science Foundation (NSF), Chemistry Division for support of this research under Grants No. CHE-1665256 (A.R.) and CHE-1955349 (A.R.).

Author contributions

T.J., I.B., M.G., F.K., M.N., J.S., M.M. and M.B.C. took part in the beamtimes at PETRA III. M.G., F.C., E.G., R.O. and M.B.C. took part in the beamtimes at BESSY II. N.N.G. and A.R. designed and synthetized the radical. A.C. performed the calculations. M.B.C. conceived and supervised the project; interpreted the data and wrote the manuscript together with A.C. All authors contributed to the discussion and commented on the manuscript.

Competing interests The authors declare no competing interests.

Additional information

Supplementary information is available for this paper at

Reprints and permissions information is available at http://www.nature.com/ reprints.

Data availability The datasets generated during and analysed during the current study are available from the corresponding author on reasonable request.

Correspondence and requests for materials should be addressed to benedetta.casu@uni-tuebingen.de.

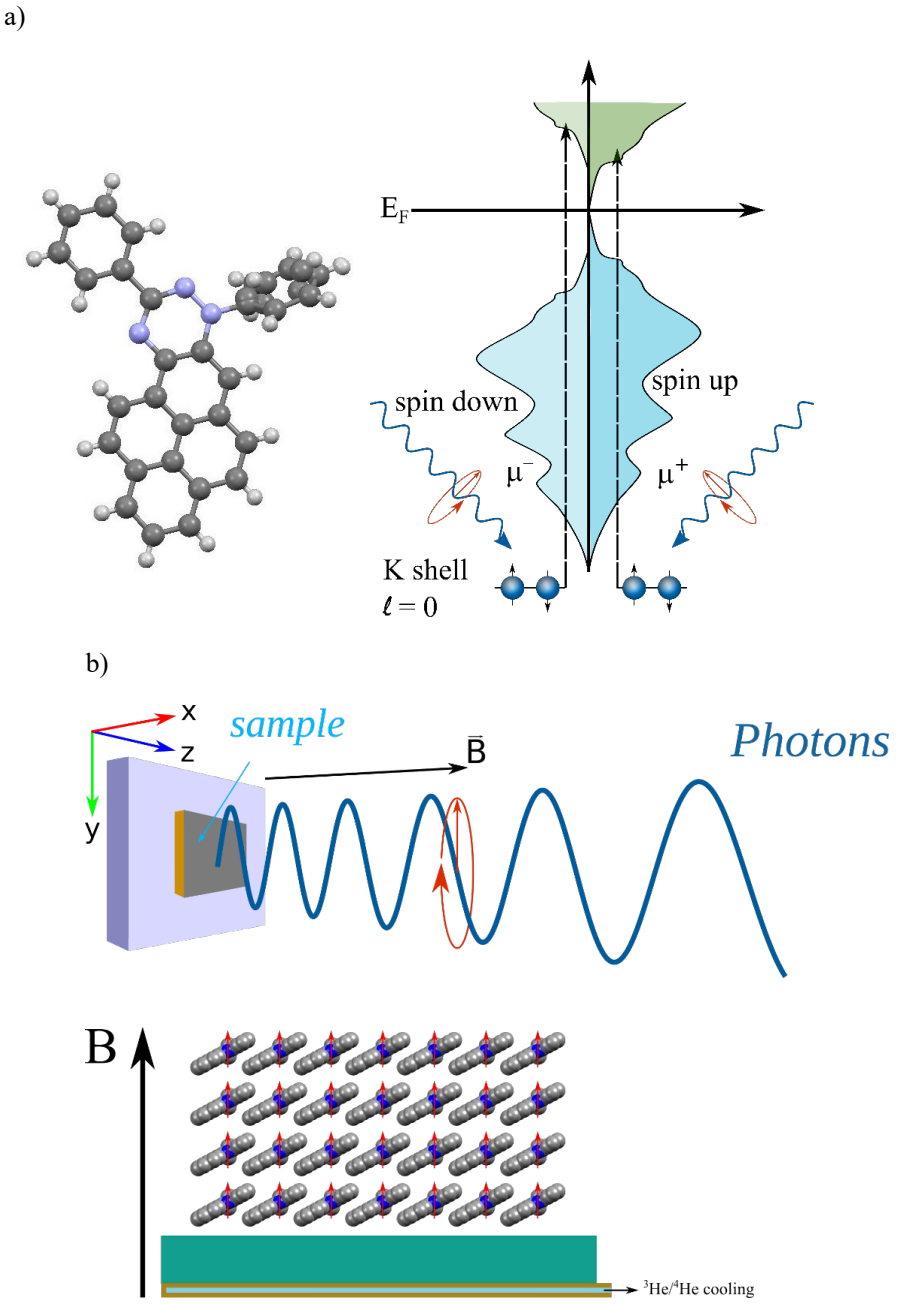

Figure 1 | Molecular structure of the pyrene Blatter derivative and experiment. a. (left panel) Molecular structure ($C_{29}H_{18}N_3^{\bullet}$), carbon atoms in dark grey, nitrogen atoms in blue, and hydrogen atoms in white. (right panel) XMCD principles. **b**. Sketch of the experiment.

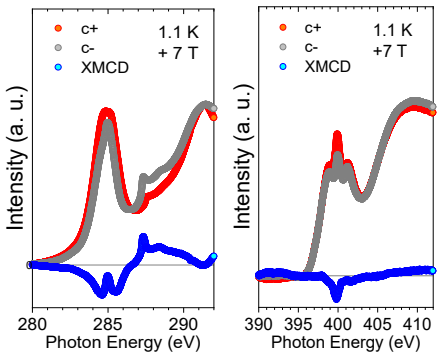

Figure 2 | X-ray absorption measurements. Circularly polarized (left) C K-edge and (right) N- K-edge XAS and XMCD as indicated recorded in normal incidence at B=7 T, at 1.1 K (substrate temperature during preparation at 290 K, nominal thickness 9 nm).

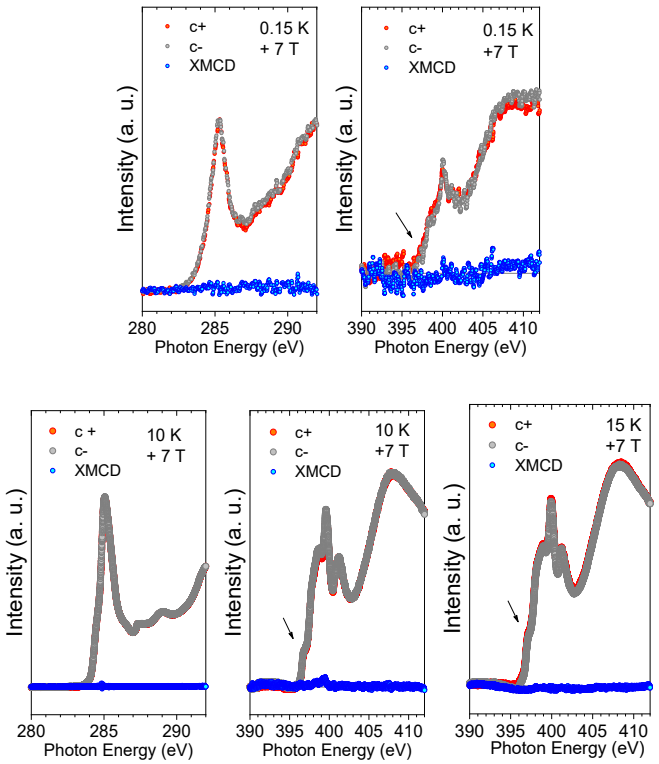

Figure 3 | X-ray absorption measurements. Circularly polarized C K-edge and N- K-edge XAS and XMCD recorded in normal incidence at B=7 T, and temperature as indicated (substrate temperature during preparation at 300 K, nominal thickness 4 (upper panel) and 9 nm (lower panel)). The spectra at 0.15 K were measured with lower resolution. The features are therefore less resolved than at 10 K but still present (see also Supplementary information, Figure S 3)

460

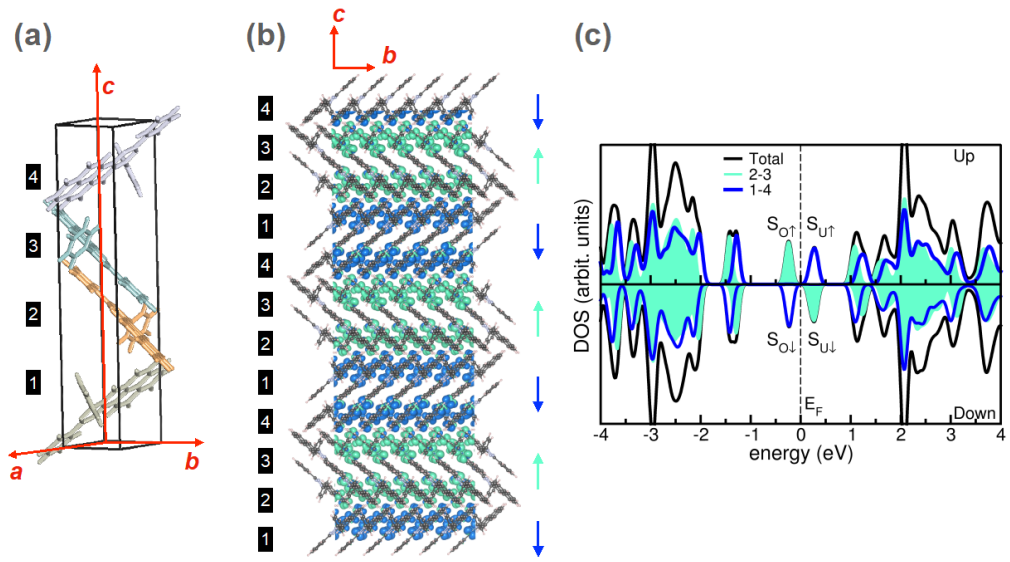

Figure 4 | Calculation results for the Blatter-pyr antiferromagnetic film. a. Primitive cell of monoclinic Blatter-pyr crystal. Labels 1-4 indicate the four molecules in the cell. **b.** Side view of the 9 nm-thick film. Coloured isosurfaces represent the charge spin-density plots for the antiferromagnetic phase. Green (blue) colour indicates the majority (minority) spin-up (spin-down) orientation of single radicals. Atomic positions and charge spin-density have been replicated for clarity. **c.** Total and molecule projected spin-polarized density of states. Total (black line) and molecule projected (shaded green areas for molecules 2-3 and thick blue line for molecules 1-4) spin-polarized density of states (DOS) of the Blatter-pyr film. Vertical dashed line marks the Fermi level of the system assumed as energy reference for the plot. S_O (S_U) indicate the single occupied (unoccupied) molecular orbitals for the spin up (↑) and spin down (↓) channels.

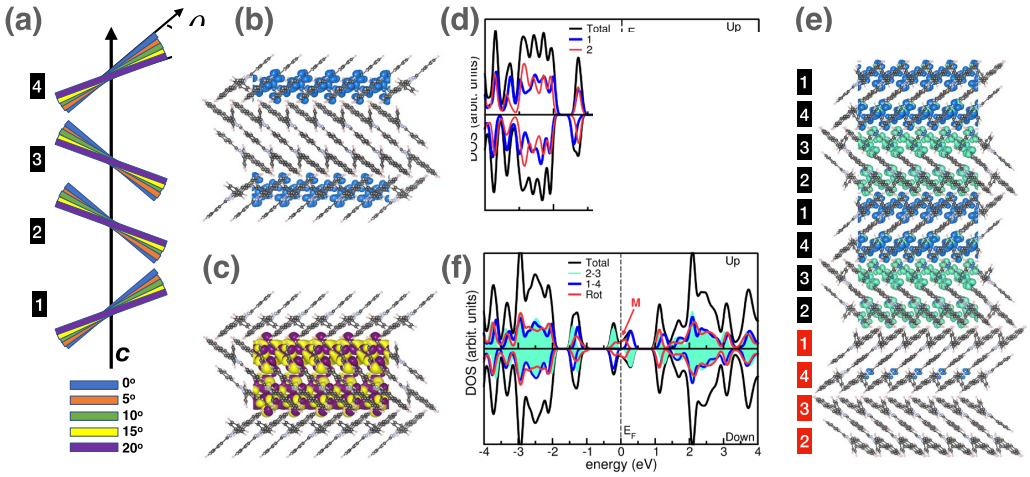

Figure 5 | Calculation results for different molecular orientations in the Blatter-pyr films. **a.** Graphical model for a 3 nm-think film (4 molecules), rotated by angle θ with respect to the crystalline *c*-axis. Colours identify different rotation angles, θ=0° corresponds to the crystalline configuration (no rotation). **b.** Charge spin density plot of rotated model with θ =20°. **c.** Isosurface plot of the mixed M state and **d.** spin polarized DOS corresponding to the model in panel c. **e.** Side view and charge spin density plot for partially 9-nm thick film with a different molecular arrangement at the bottom. Red labels correspond to rotated molecules (20°, 15°, 10°, 5° for molecule 2, 3, 4, 1 respectively); black labels correspond to un-rotated stacked molecules. (f) Spin-polarized DOS corresponding to the structure in panel e). Red lines in panels c and f correspond to the projected DOS from spin-unpolarized molecules.

Supporting Information

Magnetic behavior in metal-free radical thin films

Tobias Junghoefer,[1†] Arrigo Calzolari,[2†] Ivan Baev,[3†] Mathias Glaser,[1] Francesca Ciccullo,[1] Erika Giangrisostomi,[4] Ruslan Ovsyannikov,[4,] Fridtjof Kielgast,[3] Matz Nissen,[3] Julius Schwarz,[3] Nolan M. Gallagher,[5] Andrzej Rajca,[5] Michael Martins,[3] Maria Benedetta Casu[1*]

[1]Institute of Physical and Theoretical Chemistry, University of Tübingen, 72076 Tübingen, Germany

[2]CNR-NANO Istituto Nanoscienze, Centro S3, 41125 Modena, Italy

[3]Department of Physics, University of Hamburg, 22761 Hamburg, Germany

[4]Helmholtz-Zentrum Berlin, 12489 Berlin, Germany

[5]Department of Chemistry, University of Nebraska, Lincoln, United States

*benedetta.casu@uni-tuebingen.de

[†]These authors contributed equally to this work

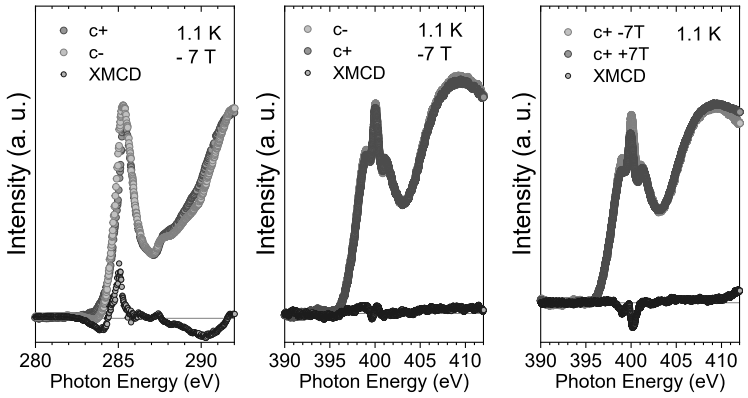

Figure S1. | X-ray absorption measurements performed at B=-7 T. Circularly polarized c and N K-edge XAS and XMCD recorded in normal incidence at B=-7 T, at 1.1 K (substrate temperature during preparation at 293 K, nominal thickness 9 nm). (right) C+ circular polarised N K-edge XAS and XMCD at + 7 T and -7 T.

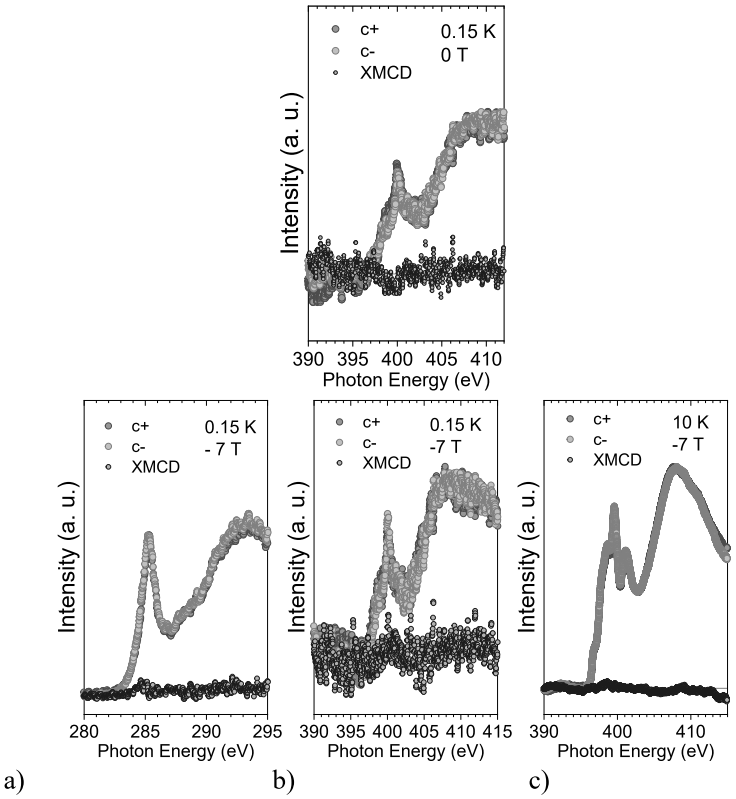

Figure S2. X-ray absorption measurements performed at B= 0 T and B=-7 T. (upper panel) Circularly polarized N K-edge XAS and XMCD recorded in normal incidence at B= 0 T, after cooling at 0.15 K (substrate temperature during preparation 300 K, nominal thickness 4 nm). (lower panel) Circularly polarized C and N K-edge XAS and XMCD recorded in normal incidence at B=-7 T, and temperature as indicated (substrate temperature during preparation 300 K, nominal thickness 4 (a and b) and 9 nm (c)).

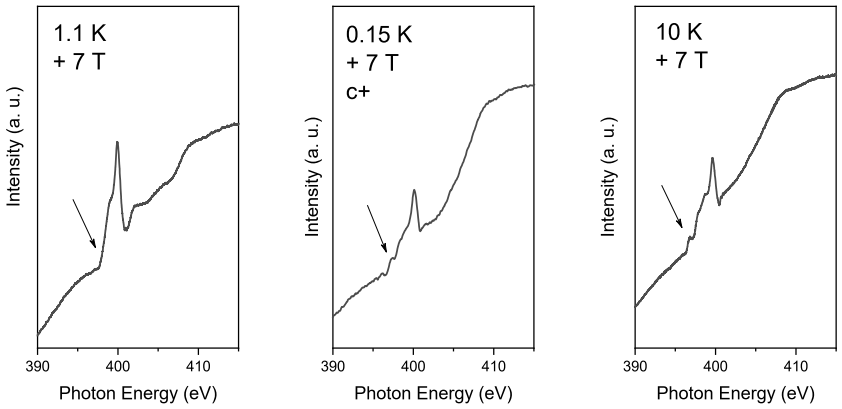

Figure S3. Raw data evidencing the different electronic structure with the absence/presence of the A feature. (left) The samples are grown with substrate at 290 K and (middle and right) at 300 K.

Single molecule characterization.
Figure S4 shows the spin resolved density of states (DOS) DOS of single Blatter-pyr radical, calculated at two levels of accuracy for the description of the exchange correlation functional (XC): (a) standard GGA-PBE and (b) hybrid B3LYP. Except the expected opening of the energy gap between the SOMO and the SUMO for B3LYP XC, the two spectra reproduces the same molecular features. Insets show the molecular spin-density in the two cases.

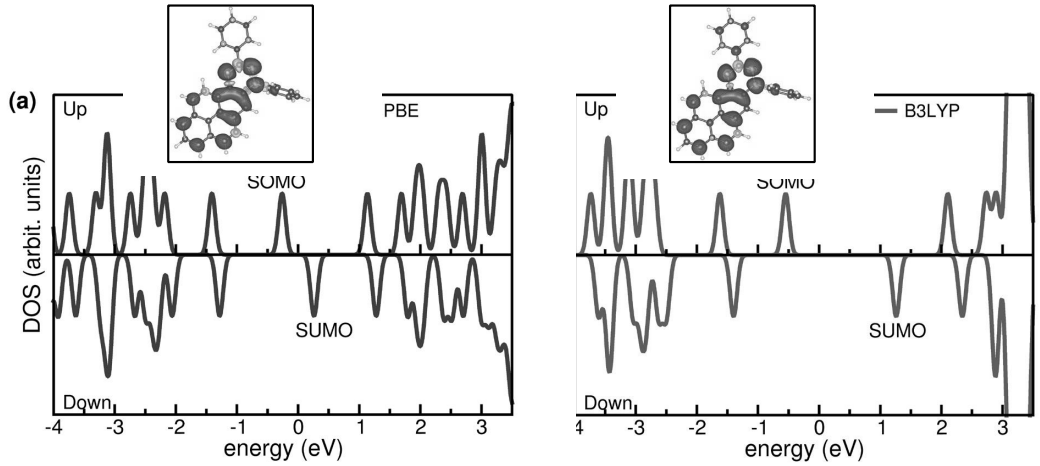

Figure S4. Density of state of the Blatter-pyr single molecule. Both spin-un (top) and spin-down (bottom) channels, calculated with (a) PBE and (b) B3LYP XC functionals. Labels SOMO and SUMO indicate the highest occupied molecular orbitals and the lowest unoccupied molecular orbitals, respectively. Insets show the molecular spin-density in the two cases.

3D extended crystal (bulk).
The primitive cell of bulk crystal has been obtained from experimental X-ray structure. The cell is monoclinic and includes 4 inequivalent Blatter-pyr molecules, whose spatial arrangement is shown in Figure Theo S5a. Molecules are stacked in double layers of molecules 1-4 and 2-3, forming a herring-bone path along the *c*-axis. In the ferromagnetic phase all molecules are magnetically ordered and total magnetic moment of the ferromagnetic phase is μ_B=4.0 Bohr mag/cell, which is the sum of the single molecule contributions per cell (↑↑-↑↑). In the antiferromagnetic phase, molecular spins are alternative oriented, following the structural bi-layer distribution (↑↑ - ↓↓) (see spin-density plots in panel a), resulting in a total magnetic moment μ_T=0.0 Bohr mag/cell (absolute magnetization μ_A=5.4 Bohr mag/cell). The electronic structure of AF bulk is shown in panels (b) and (c) that display the DOS and the band structure, respectively. The DOS is the AF combination of the single molecule contributions: molecules 1-4 and 2-3 are electronically equivalent but magnetically inverted. Band structure indicate that there is a long-range intermolecular coupling in the crystal, responsible for the band dispersion across the Brillouin zone.

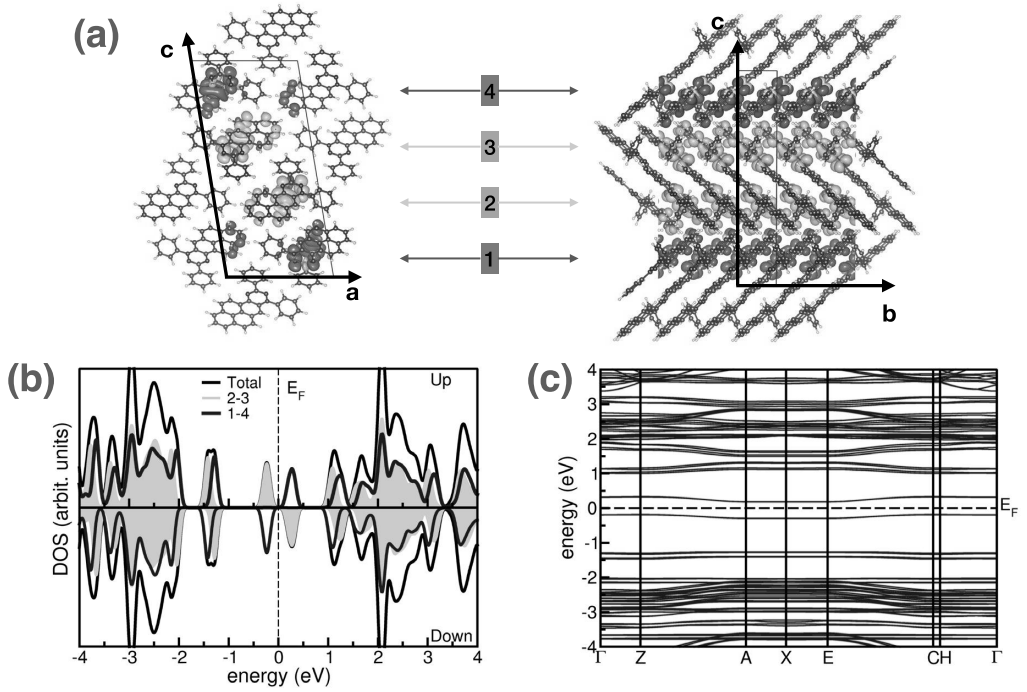

Figure S5. Density of state of the Blatter-pyr bulk. (a) Two side view of the 3D bulk crystal. Thick arrows indicate the axis directions, light lines the primitive crystalline cell. The 4 inequivalent Blatter-pyr molecules are indicated, along with their bi-layer (1-4/ 2-3) stacking arrangement. Colored isosurfaces represent the spin-density plot for the antiferromagnetic phase. Spin-resolved density of states (b) and band structure (c) for the antiferromagnetic phase. Labels refer molecular indexes of panel a. Dashed lines indicate the Fermi level of the system, assumed as zero reference in panels b and c.

Molecular films.

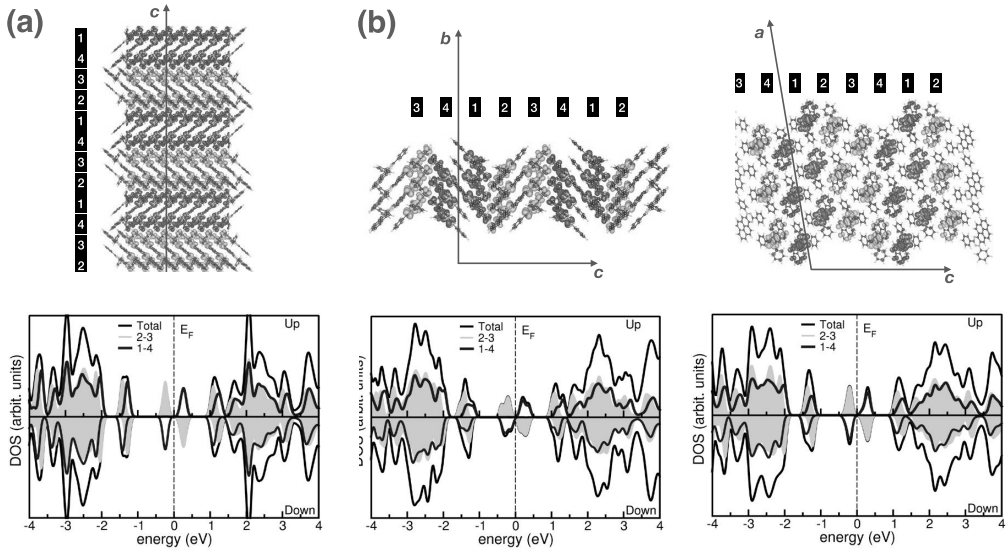

Figure S6. Density of state of the Blatter-pyr film. Atomic structures and spin density (top panels) and DOS spectra (bottom panels) of alternative thin films. (a) Film grown along the c-axis with a different molecular order (-2341-) wrt to the model of main text (-1234-). (b) Film grown along the b-axis and (c) film grown along the a-axis. Each system is composed of 12 radicals, i.e. three primitive units (4 molecules).

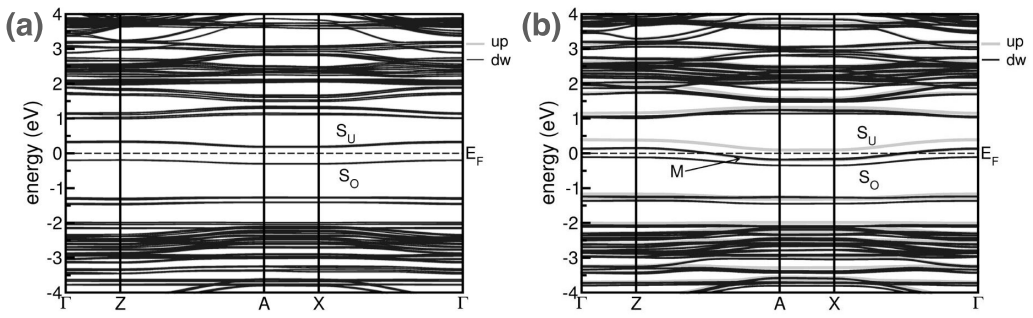

Figure S7. 2D spin-resolved band structure of (a) 9nm-thick (12 molecules) AF film and (b) 3nm-thick film (4 molecules) with θ=20°rotated molecules. Green (blue) lines identify spin-up (spin-down) bands, respectively.

NEXAFS

We performed and simulated near edge X-ray absorption fine structure (NEXAFS) spectroscopy on the films grown at 300 K. By analogy with the C K-edge NEXAFS spectra of pyrene and pyrene-based molecules,[1,2] we identify two main regions: the π* region up to around 290 eV and the σ* region above 290 eV. The main resonance at around 286 eV can be identified as due to the carbon atoms of the pyrene substituent[1]. The average orientation of the molecular pyrene plane calculated on the feature at 286 eV (Figure S8) is 29°.

Even though the magnetic origin of the radical is formally due to the presence of an undercoordinated N atom, the charge spin-density distribution is spatially delocalized all over the molecule and not centred on the nitrogen site[3]. NEXAFS spectra mirror this delocalisation where we superimposed the spin up and spin down components of the electronic density of states projected on the 2p states of C and N species. While the 2p-like components of SOMO and SUMO contribute to the lowest energy peak of C K-edge at the Fermi level, the lowest energy peaks of the N spectrum do not involve electron transitions to frontier unpaired orbitals. This highlights a non-trivial interplay between C and N bonding in the magnetic properties of Blatter-pyr and marks a distinctive difference with respect to most molecular magnets, where the magnetic spin-density is localized around the metal magnetic ion, simply coordinated to the carbon-based molecular skeleton. In our case, the spatial distribution of the frontier orbitals also favours the intermolecular interaction in the packed arrangement, allowing for a long-range magnetic order.

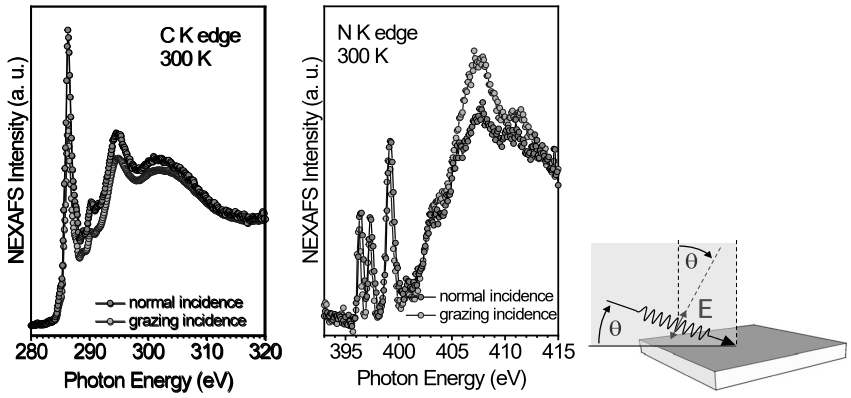

Figure S8. X-ray absorption measurements performed at Bessy II. **a.** C K-edge and **b.** N K-edge NEXAFS spectra of a nominally 3.5 nm thick film at 30 K. **c.** Geometry of the NEXAFS experiment. **d**. Theoretical X-ray absorption at the N K-edge compared to the experimental curve.

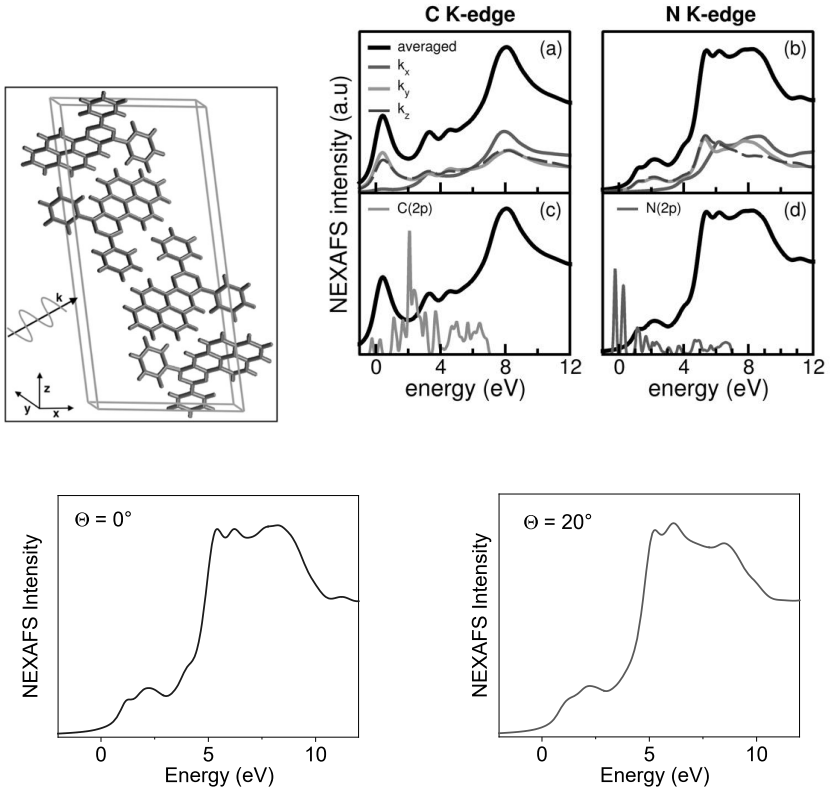

Figure S9. Simulated NEXAFS K-edge spectra for Blatter-pyr crystal and for 3nm-thick films. (Upper panel) left. Primitive crystal cell and atomic structure of the four constituent molecules forming the Blatter-pyr crystal. Coloured waving arrow indicates a generic orientation of the incident X-ray wavevector (**k**) considered for NEXAFS simulations. **a., b.**, carbon, **b., d.**, nitrogen species in the Blatter-pyr molecular crystal. Black lines correspond to spectra averaged over all C (**a, c.**) and N (**b, d.**) atoms of the radical and the three wavevector directions ($\mathbf{k_i}$) of the incident electric field. Grey and blue lines in **c.**, **d.** respectively, are the components of the electronic density of states projected on the 2p states of C and N species. Zero energy reference is set to the Fermi level of the crystal. Negative energies indicate pre-edge contributions. **(Lower panel)** Nitrogen k-edge for two model systems with different angle orientation, averaged over the three direction of the incident radiation.

We observe changes in the relative intensities of the lower energy features for the two different structures, mirroring what we observe in the XAS experiment at PETRA III (Figure 3 and Figure S3).

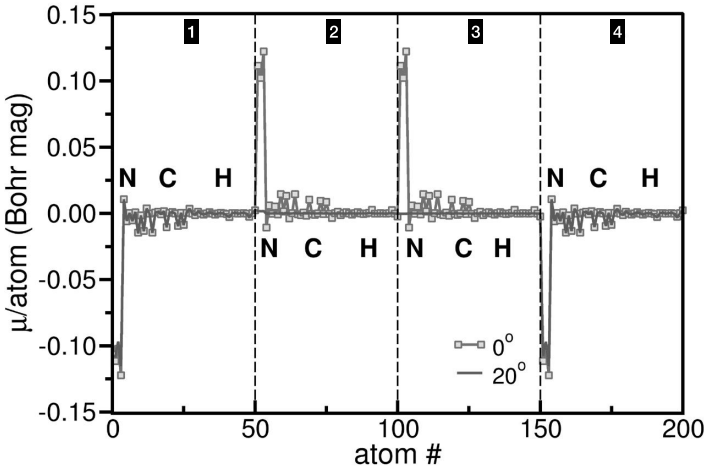

Figure S10. Magnetic moment per atom for 3nm-thick film (4 molecules) with θ=0° (green-dotted line) and θ=20° (pink line) rotated molecules. Vertical dashed lines mark the single molecules; labels identify the chemical species in each molecule.

We also checked the agreement between theoretical and experimental curves for the valence band photoelectron spectra.

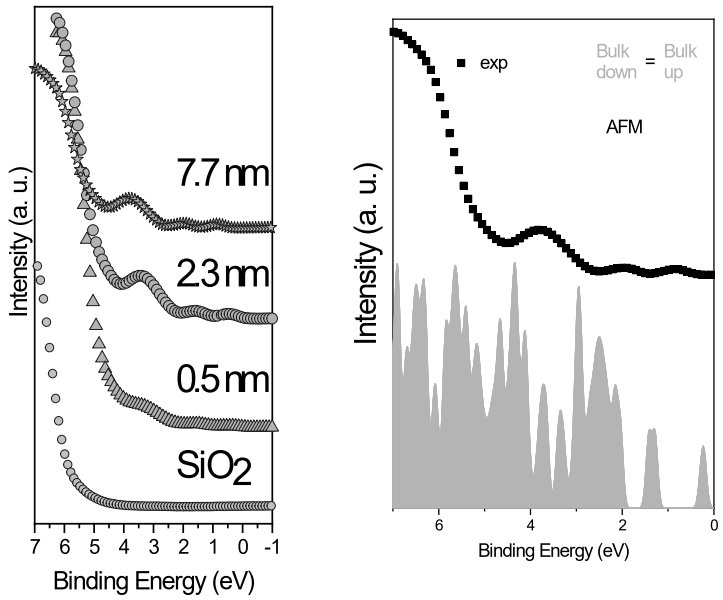

Figure S11. Experimental and theoretical valence band photoemission curves. (left) Ultraviolet photoelectron spectroscopy (UPS) spectrum of the Blatter-pyr films grown with the substrate at 300 K, (right) 7.7 nm spectrum compared to the calculated density of states (DOS) of the spin up (magenta) and spin down (cyan) for the antiferromagnetic configuration. The Fermi energy, theoretical and experimental, respectively, is the zero-binding energy in both cases (i.e., we did not introduce any energy shift, as usually done, to compensate for the difference in the experimental and theoretical energy gap).

References

1 Sandi, G., Song, K., Carrado, K. A. & Winans, R. E. A NEXAFS determination of the electronic structure of carbons for lithium-ion cells. *Carbon* **36**, 1755-1758, (1998).

2 Lucas, L. A. *et al.* Thin film microstructure of a solution processable pyrene-based organic semiconductor. *Chem. Mat.* **20**, 5743-5749, (2008).

3 Ciccullo, F. *et al.* Interfacing a Potential Purely Organic Molecular Quantum Bit with a Real-Life Surface. *ACS Appl. Mater. Interfaces* **11**, 1571-1578, (2019).